# Proton and Lithium Insertion Into Heat-treated Synthetic Manganese Dioxides.

Jason Jones

A Thesis submitted to Middlesex University in partial fulfilment of the requirements for the degree of Doctor of Philosophy.

*March 1996*

The work was carried out at the Energy Technology Centre, Middlesex University, School of Mechanical and Manufacturing Engineering, Bounds Green Road, London N11 2NQ and was funded by the NAB Research Initiative 3 and Sedema SA.

## Abstract

Two electrodeposited and two chemical manganese dioxides were heat-treated in an air or argon environment for 24 hours at temperatures from 120-450°C and the products were characterised by chemical analysis, XRD (X-Ray Diffraction) and FTIR (Fourier Transform Infra-Red) spectroscopy. It was found that the rate of water evolution was identical in air or argon but the weight loss was greater in argon. This was explained on the basis that the x value in $MnO_x$ increased in air but not in argon. Powder X-ray diffraction spectra of the heat-treated materials showed that there was little change in structure from 25-300°C and between 300-400°C the structure changed from a γ-phase to a β-like phase. Application of the latest structural model of γ-$MnO_2$ in terms of de Wolff disorder and microtwinning was applied to the XRD patterns of Faradiser WSLi. It was found that there was decrease in microtwinning from 25-300°C but the amount of de Wolff disorder was essentially unchanged. Simulation of XRD patterns by taking appropriate amounts of two end-members and comparing them with one obtained experimentally showed that the transformation from γ to β like in the temperature range 300-400°C was heterogeneous. FTIR spectra of the same materials showed a progressive shift of the peaks associated with the $MnO_6$ octahedral framework. Comparison of the peak positions with the published data of ramsdellite (γ-$MnO_2$) and pyrolusite (β-$MnO_2$) suggested a ramsdellite phase in the unheated material and a pyrolusite phase at 400°C.

An electrodeposited $MnO_2$ was heat-treated at 200, 300 and 400°C and then H was chemically inserted using propan-2-ol or hydrazine hydrate. XRD spectra showed that a homogeneous reduction occurred with the material that had been heat-treated at 200°C and reduced with propan-2-ol while a heterogeneous reduction occurred with the material heat treated at 400°C and reduced with hydrazine hydrate. Within these extremes of behaviour different regions of homogeneity/heterogeneity were observed. With hydrazine hydrate heterogeneity set in at a lower level of H insertion than with propan-2-ol reduction. This was because the rate of reduction was faster with hydrazine hydrate and the critical value of $r=0.8$ in $MnOOH_r$ was reached earlier at the surface of the $MnO_2$ particles. FTIR spectra of the chemically reduced materials were interpreted in terms of OH bond formation which was revealed by the appearance of peaks centred at 2050 and 2650$cm^{-1}$. With the homogeneous reduction there was no evidence of OH bond formation until $MnOOH_{0.8}$, in the heterogeneous reduction OH bond formation was observed at low levels of H insertion. The onset of OH bond formation was thought to be due to the localisation of the inserted $H^+$ and $e^-$.

H insertion into a range of chemical manganese dioxides heat-treated analogously to EMD was carried out. The non heat-treated CMD material exhibited the largest region of homogeneous H insertion while H insertion for the material heat-treated at 400°C was entirely heterogeneous. Between these extremes of behaviour intermediate levels of homogeneity/heterogeneity were observed. The crystal structure of the most reduced materials formed a similar range of intergrowth structures as was found for the EMD materials. This was δ-MnOOH for the material heat-treated at 200°C and manganite for that heat-treated at 400°C. The boundaries of the homogeneous/heterogeneous behaviour of EMD and CMD were compared and it was found that heterogeneity occurred at a higher level of H insertion for the CMD materials.

A range of chemically Li-inserted $MnOOLi_x$ ($0 \leq x \leq 0.8$) compounds were prepared from an EMD and CMD that had been heat-treated at 200, 300 and 400°C and then reduced in an argon-filled glove box using n-butyllithium. Powder X-ray diffraction revealed that the first stage of the reaction ($0 \leq x \leq 0.3$) was homogeneous and for $x > 0.3$ (EMD) and $x > 0.35$ (CMD) a new phase was formed via a heterogeneous reaction. The X-ray diffraction patterns of the new phase could be indexed to an orthorhombic unit cell and, in contrast to H insertion, the crystal structures of the most reduced Li-inserted materials seemed to be the same regardless of the initial heat-treatment temperature.

A novel applied linear regression analysis was developed to determine possible peak movement in a spectral dataset. The analysis used the coefficient of determination $R^2$ as a parameter for peak movement. In the second part of the analysis it was found that a low value of $R^2$ indicated peak movement. In the XRD patterns of EMD heat-treated at 200°C and reduced with propan-2-ol the low values of $R^2$ correlated with peak movement. Conversely with EMD heat-treated at 400°C and reduced with hydrazine hydrate there was little or no peak movement and the values of $R^2$ were close to 1.

## Acknowledgements

This work would have been impossible without the collaboration of many people. First and foremost I would like to thank Dr. W.C. Maskell for his constant interest and valuable discussions throughout the investigation all of which I enjoyed. I am particularly indebted to my second supervisor, Professor F.L. Tye for his many suggestions and remarks which I have learnt from.

Support from my parents is gratefully acknowledged.

I would like to acknowledge the stimulating conversations that I had with Energy Centre colleagues Jose Larcin and Robert Copcutt and the ideas gleaned from them. Also to Etienne Gehain, for his computer program which was used to aid manipulation and interpretation of XRD patterns and to Lachlan MacLean for discussions pertaining to manganese dioxide. I am especially pleased to thank my other colleagues in the Energy Technology Centre, Andreas Ioannou, Mohiedienne Benammar, Jiri David, Louis Egbe, Chris Walton and Hassan Ipakchi for providing a stimulating environment in which to complete this work. Finally I would like to thank Nick Kollerstrom for interesting remarks and suggestions.

## Table of Contents

## Main Symbols Used.

CMD chemically prepared manganese dioxide

EMD electrodeposited manganese dioxide

OCV open circuit voltage

$R^2$ coefficient of determination

SCE saturated calomel electrode

SHE standard hydrogen electrode

r degree of H insertion (in $MnOOH_r$)

x oxidation degree of manganese dioxide, in $MnO_x$

Greek

$\gamma,\beta,\lambda$ crystal phase of $MnO_2$

$\rho$ density

# Chapter 1 Introduction.

## 1.1 Introduction.

Manganese dioxide ($MnO_2$) is used as the cathode material in aqueous Leclanche and alkaline manganese cells and more recently in non-aqueous lithium cells which, when combined, dominate the world's primary battery market. There are three different types of manganese dioxide, natural (NMD), chemical (CMD) or electrolytic (EMD). Whatever the type of $MnO_2$ it typically contains about 5% water. Whilst this is may be of benefit to the performance of aqueous cells it will react with the lithium electrode in non-aqueous cells and so it must be removed before use. The current investigation is concerned with the water content of EMD and CMD and the effect of that regarding proton and lithium insertion during heat-treatment from 25-450°C. In sections 1.2-1.8 the literature which is of relevance to the current investigation is reviewed.

## 1.2 Heat treatment of manganese dioxide.

### *1.2.1 Heat treatment up to 1000°C.*

When manganese dioxide is heated the following transformations take place;

$$MnO_{2\ (hydrated)} \xrightarrow{\text{waterloss}} MnO_2 \Rightarrow Mn_2O_3 \Rightarrow Mn_3O_4 \qquad (1.1)$$

The decomposition of $MnO_2$ into $Mn_2O_3$ takes place at about 550°C the second transition at about 950°C, the final one is less clear and will depend on the heating atmosphere as shown by Tinsley and Sharp (1971). Battery active manganese dioxide also undergoes a phase change between 300 -400°C from a predominantly $\gamma$-like to $\beta$-like phase. In this study emphasis is on water removal and heating temperatures up to 450°C were used.

The main techniques used to study the heat treatment of manganese dioxide have been; differential thermal analysis (DTA), thermogravimetric analysis (TGA) and X-ray diffraction (XRD). In DTA the difference in temperature between the sample and an inert reference material is measured as a function of temperature. In TGA the change in weight of a sample is recorded as a function of temperature or time. X-ray diffraction will show structural changes during

heat-treatment. The transformation from $\gamma$ to $\beta$ is of particular relevance.

The importance of the water content of manganese dioxide was shown as early as 1954 by Kozawa and Sasaki; they found that the potential decreased linearly with temperature and this was attributed to a lower oxide film formation on the surface of $MnO_2$. Tvarusko (1964) and Freeman *et al.* (1971) investigated the water content of a variety of crystalline modifications of $MnO_2$ , $\gamma$, $\beta$, $\delta$ , and $\rho$ ; the former found that the water content varied from 1% for a highly crystalline $\beta$-$MnO_2$ to 20% for a synthetic hydrous $MnO_2$. The latter authors used TGA to investigate the temperature at which the decomposition of $MnO_2$ to $Mn_2O_3$ took place; a low temperature related to a good discharge performance (called battery activity) on five different discharge regimes. Preisler (1980) reported a linear correlation between the electrode potential of $MnO_2$ and the amount of combined water (this is the difference between the total water and the physisorbed water of $MnO_2$). Although the results were similar to those shown by Kozawa and Sasaki (1954), Preisler related the potential change to water loss causing a change in the free energy of formation of $MnO_2$ and not to a surface phenomenon.

It is well established that manganese dioxide contains three types of water. Lee *et al.* (1973a&b) studied an EMD by temperature programmed desorption and found three kinds of water called 1,2 or 3. Type 1 had a shoulder at 120°C and was associated with the removal of molecular water. Type 2 had a maximum at 200°C and had two components; type 2a which was water dissociatively chemisorbed to surface manganese and oxygen ions and 2b which was associated with the removal of both surface and bulk hydroxyls; this led to the generation of micropores. Brown *et al.* (1975) found that the micropore volume reached a maximum at 278°C. Type 3, which had a shoulder at 360°C, was not clearly ascribed although in a later paper by Lee *et al.* (1978) it was resolved in an oxygen environment into two entities; the first being the elimination of hydroxyl groups from the interior of the lattice and the second being loss of chemisorbed oxygen. Using pyknometric density measurements Brown *et al.* (1981) further investigated type 1 water. Two days outgassing, of an EMD, at 25°C was sufficient to remove water which, in the associated state had a density of normal water (0.997 $gcm^{-3}$), however outgassing at 60-120°C

removed water that had a density of 1.25 $gcm^{-3}$. The manganese dioxide required several days of immersion in water for the high density water to reform. Water evolved by outgassing at 160-280°C was designated type 2 and on immersion of the heat-treated $MnO_2$ in water oxygen was evolved.

Miyazaki (1975) heated sixteen different types of manganese dioxide; examined the evolved gases by mass spectrometry and tested the discharge performance in Leclanche type cells. He tried to find a correlation between the peaks in the water evolution rate and the discharge performance. He found that when the water evolution rate had maxima at 200 and 300°C the discharge performance was superior. Yoshimori and Kato (1980) heated manganese dioxide with infrared radiation and measured the evolved gases by coulometric methods; they found that CMD contained about twice the amount of free water and half the amount of combined water of EMD. Shimzu and Koshiba (1985) found that EMD containing a large quantity of combined water gave a good performance in alkaline cells confirming the results of Miyazaki.

The work by Fillaux *et al.* (1991) was not concerned with the $\gamma$-$\beta$ transformation but with different types of protons found in $\gamma$-$MnO_2$. They used the technique of inelastic neutron scattering (INS) to investigate proton dynamics in $\gamma$-$MnO_2$. An EMD was heat-treated at 150, 250, 350 and 450°C for 16 hours in air. The INS spectra of samples heat-treated at 150 and 350°C were similar to those of non heat-treated $MnO_2$ and $MnO_2$ heat-treated at 450°C. Three different types of bands were distinguished in the INS spectra. (i) A broad continuum rising at $\approx 30cm^{-1}$ and extending over the whole frequency range. These were interpreted in terms of an ideal gas of protons moving almost freely within the crystal. (ii) Bands between 500 and $1100cm^{-1}$ assigned to protons trapped in crystal defects. (iii) Sharp and relatively intense bands between 30 and $90cm^{-1}$ assigned to covalently bonded protons corresponding to MnOOH.

### *1.2.2. Heat treatment concerned with lithium battery performance.*

There is disagreement in the literature about which is the optimum temperature for heat treatment of $MnO_2$ concerning Li cells. This is probably due to the many different crystalline modifications of $MnO_2$ and differences in the duration of the heat treatment. For commercially produced $LiMnO_2$ cells the manganese dioxide is usually heated at 400°C (Tye 1991). This is probably used

because it is known that the $MnO_2$ changes structure to a $\beta$-like structure at this temperature and, most, if not all, of the water is removed. Ikeda (1975) felt that all the water was removed at 700°C whereas Desai *et al.* (1988) give a temperature of 300°C. Ikeda (1975) heat-treated an EMD at 250, 350, 450 and 500°C for 20 hours in air and reported that the maximum discharge capacity was obtained at 350°C. In 1980 the same authors tested a range of International Common (I.C.) samples for use in Li/$MnO_2$ cells, the $MnO_2$ was heat-treated at 400°C; I.C. 2,9 and 10 (EMD) and I.C. 11 (CMD) gave superior discharge characteristics to the other eight I.C. samples. Manev *et al.* (1989) investigated oxygen and water release during the heat-treatment of EMD (Knapsack and Tekkosha) and CMD (Faradiser M and WS) in an argon atmosphere; they reported that up to 300°C the weight loss was due to water while above 300°C it resulted from oxygen evolution. At this temperature the oxygen evolution tended to zero after 20 hours, this suggested a surface loss similar to the type 3 loss reported by Lee *et al.* (1978). Ilchev *et al.* (1989a) found that the optimum temperature, for most types of $MnO_2$, was 300°C for eight hours. Ohzuku *et al.* (1990) showed electrochemical discharge curves for heat-treated EMD (200-450°C for 7 days) and reported that EMD heat-treated at 400°C had the highest capacity.

## 1.3 Crystal structure of manganese dioxide.

The structural properties of $MnO_2$ have been reviewed by Burns and Burns (1975) and Giovanoli (1980) and the X-ray diffraction patterns of the 31 International Battery Association (I.B.A.) samples have been shown by Malpas and Tye (1989). Figure 1.1 shows the X-ray diffraction pattern for a typical electrodeposited manganese dioxide with the Joint Committee on Powder Diffraction Standards (JCPDS) positions of ramsdellite (this is a mineral from Lake valley, Mexico). The structure of ramsdellite was elucidated by Bystrom (1949). In this structure every manganese (Mn) atom was surrounded by six oxygen (O) atoms distributed at the corners of a distorted octahedron. Each oxygen was surrounded by three Mn but there was a difference in the way they were arranged. In one arrangement the O atom was at the centre of an almost equilateral triangle with Mn at its corners (called the planar configuration). The

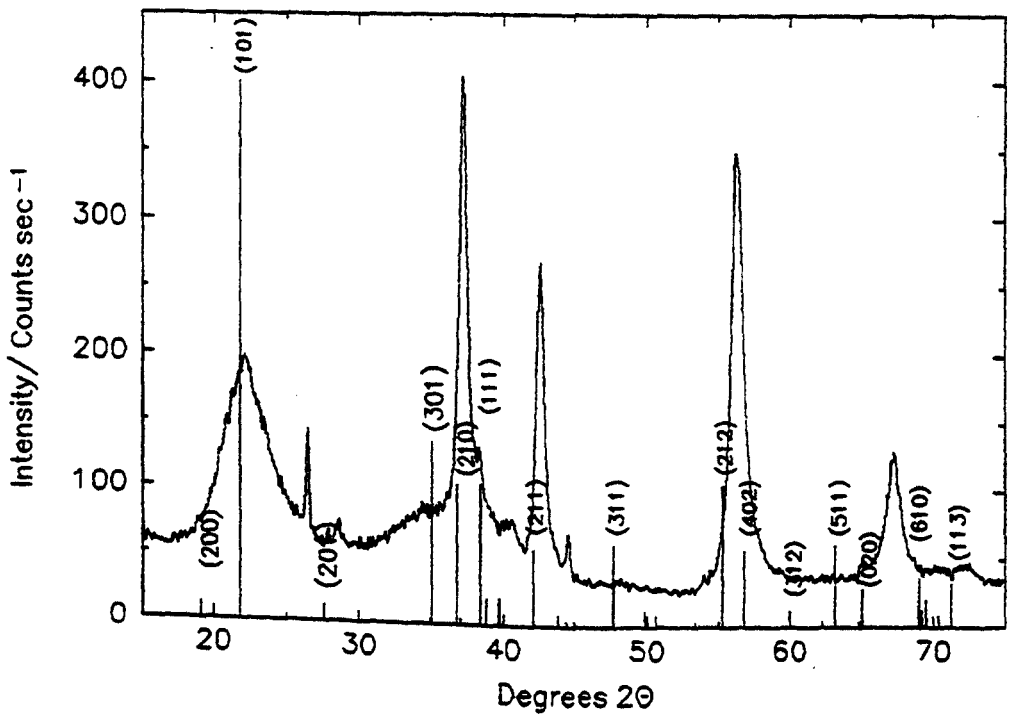


*Figure 1.1* : X-ray diffraction pattern of a typical EMD with the JCPDS pattern of ramsdellite (ref this work)

Mn – O bond lengths were 0.186 (twice) and 0.191nm. In the latter arrangement the O atom was at the apex of a trilateral pyramid (called the pyramidal configuration). The Mn – O bond distances being 0.192 (twice) and 0.189nm. The structure of ramsdellite was therefore built up of distorted oxygen octahedra each with four shared edges. Pyrolusite is the most stable form of $MnO_2$ and it has the rutile structure (Baur 1976). All the octahedra are equivalent and the Mn – O bond distance is 0.188nm. The main difference between ramsdellite and pyrolusite is that in the former the octahedra are linked to form double chains in the c direction, whereas in the latter single chains of octahedra are formed. In the literature these arrangements are referred as "1x2" and "1x1" tunnels respectively. The structures are shown in figure 1.2. Bystrom (1949) also felt that the structure of $\gamma$-$MnO_2$ was an "intermediate product between ramsdellite and pyrolusite." This was further developed with the proposal of a structural model for $\gamma$-$MnO_2$ in the classical paper by de Wolff in 1959. He analysed the X-

ray diffraction pattern of a "line rich"[†] EMD and found the position of the "sharp" lines resembled those of ramsdellite. There were also some "broad" lines whose positions were shifted away from those consistent with the "sharp" lines of ramsdellite. He noted that shifting and broadening of diffraction lines was known to occur for certain types of random layer structures. This shift could be explained by a random succession of layers of pyrolusite and ramsdellite. The structure of $MnO_2$ is dependent on the manufacturing conditions as described by Kozawa (1958) and Preisler (1989a&b). Freund *et al.* (1975) found that $\gamma$-$MnO_2$ obtained from the anodic oxidation of aqueous $Mn^{2+}$ solutions yielded strongly oriented $\gamma$-$MnO_2$ fibres and in 1978 de Wolff *et al.* proposed that this type of $MnO_2$ should be called $\epsilon$-$MnO_2$. It had the same hexagonal close packed structure as $\gamma$-$MnO_2$ except that the $Mn^{4+}$ ions were randomly distributed over 50% of the octahedral sites. The electron diffraction patterns of Charenton *et al.* (1988) were fully compatible with de Wolff but the hexagonal $\epsilon$-$MnO_2$ structure could not account for the diffuse spots in the [101] planes.

The most comprehensive structural model for $\gamma$-$MnO_2$ has been developed in the 1990's by Pannetier and co-workers (1990, 1992 & 1994 by Ripert *et al.* 1991 and Chabre and Pannetier 1995). They found that application of the de Wolff model (1959) could account for most of the features of the XRD patterns of $\gamma$-$MnO_2$ in the way that it predicted both line shifts and broadenings in reasonable agreement with experimental data but it was not able to explain the differences among the XRD patterns of "higher" and "lower" structure $\gamma$-$MnO_2$'s as shown by Malpas and Tye (1989). A constraint of the de Wolff model was that no two pyrolusite (rutile) layers could be nearest neighbours and this meant that the model was only valid for pyrolusite concentrations $<50\%$. The Pannetier model removed that constraint and a second structural defect or parameter called microtwinning was added. This was based upon the following observations: (a) twinning occurred in natural samples of rutile $TiO_2$ and cassiterite $SnO_2$. Twinning modified the cationic array without changing the octahedral environment of $Mn^{4+}$, and (b) EMD often exhibited a fibrous texture and the axis of the fibres corresponded to the (021) or (061) planes of

[†]This refers to samples that have sharp lines (like ramsdellite) in their XRD patterns for example IBA No 11. They were called "higher structure" $MnO_2$'s by Malpas and Tye (1989). This is in contrast to "lower structure" $MnO_2$'s that exhibit about five or six broad lines as shown in figure 1.1

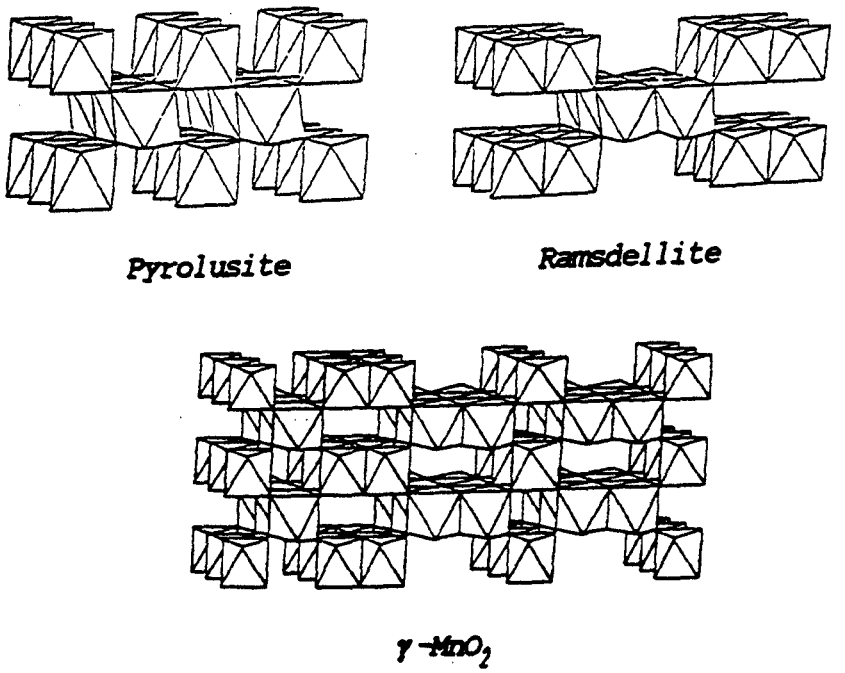


*Figure 1.2* : Structures of ramsdellite, pyrolusite and $\gamma$-$MnO_2$ (from Burns and Burns 1975).

ramsdellite. Pannetier *et al.* found that these two parameters namely de Wolff disorder and microtwinning could explain the features of the XRD patterns of $\gamma$-$MnO_2$'s and that all CMD's and EMD's were $\gamma$-$MnO_2$'s which differed only by the amount of structural defects they contained. Indeed these authors have proposed that instead of having notations such as $\gamma$, $\beta$, $\alpha$ to designate structural forms of $MnO_2$ they can be represented by the parameters Tw (microtwinning) and $P_r$ (fraction of rutile chains in a given sample). Tw varies from 0 for ramsdellite to 100 for a full twinned ramsdellite and $P_r$ varies from 0 for ramsdellite to 1 for pyrolusite with a rutile structure. Using their notation {Tw, $P_r$} therefore ramsdellite is represented as {0,0} and pyrolusite as {0,1}. Finally the calculated XRD pattern of $\epsilon$-$MnO_2$ (this was proposed by de Wolff *et al.* 1978) could not account for the strong (110) peak at 21°2Θ($Cu_{K\alpha}$) but it was suggested by Pannetier (1995) that this name should be retained to describe the XRD patterns of highly disordered samples.

## 1.4 Crystal structure of manganese oxyhydroxides.

The two well-characterised MnOOH modifications are groutite ($\alpha$-MnOOH) and manganite ($\gamma$-MnOOH). The orthorhombic unit cell of groutite was

determined by Gruner (1947) and the structure refined by Dent Glasser and Ingram (1968). In nature groutite occurs in the Cuyuna iron range in Minnesota. It is isostructural with ramsdellite and the large variations in the Mn-O bond lengths (the oxygens in the shared-edge octahedra are 0.1896 and 0.1968 nm distant from the Mn while the apical are 0.2178 and 0.234 nm away) can be attributed to the Jahn-Teller effect associated with the $Mn^{3+}$ ion ($d^4$ electronic configuration). Klingsberg and Roy (1959) investigated the ramsdellite-groutite systems. They found that with heat treatment at 130°C groutite persisted indefinitely, above this it oxidised partly to ramsdellite in 14 days, at 300°C it oxidised in a few hours and above 300°C it went directly to pyrolusite. The manganite ($\gamma$-MnOOH) structure was elucidated by Buerger (1936). It is related to pyrolusite and, like groutite, there are large variations in the Mn-O bond lengths (four short Mn-O from 0.188 to 0.198 and two longer 0.220 to 0.233 nm bonds), which again is the result of the Jahn-Teller distortion.

The reaction that takes place during the discharge of a battery (Tye 1985) may be represented by equation 1.2

$$MnOOH_r + \Delta\ H^+ + \Delta\ e \Rightarrow MnOOH_{r+\Delta} \qquad (1.2)$$

where r varies from 0.1 in the starting material to 1.0 at the theoretical end of discharge. The above reaction takes place in a single phase by the progressive conversion of $Mn^{4+}$ and $O^{2-}$ into $Mn^{3+}$ and $OH^-$ by transfer of $H^+$ and $e^-$ into $MnO_2$ and diffusion of the inserted $H^+$ and $e^-$ throughout the particles. The X-ray diffraction pattern of the reduction product of a $\gamma$-$MnO_2$ in comparison with the JCPDS patterns of groutite and manganite are shown in figures 1.3 and 1.4. It is generally accepted that the reduction of ramsdellite will lead to groutite and the reduction of pyrolusite to manganite. Maskell *et al.* (1981) felt that if the de Wolff model for $\gamma$-$MnO_2$ were accepted (ramsdellite with microdomains of pyrolusite) then the reduction product would be groutite with microdomains of manganite, this was called $\delta$-MnOOH. Fitzpatrick and Tye (1991) prepared 31 materials of composition $MnOOH_r$ where $0.1 < r < 1.0$ and analysed them by powder XRD. They found that up to $MnOOH_{0.8}$ there were no changes in the main features of the XRD patterns except the movement of peak positions due to lattice dilation. After $MnOOH_{0.8}$ new peaks appeared and the original peaks

continued to shift to lower angles in accordance with the conclusion that the solid solution extended over the range $0.1 < r < 1.0$. An important observation was the restricted mobility shown by inserted H in the region $0.8 < r < 1.0$. A number of the properties in the $\gamma$-$MnO_2$-$\delta$-MnOOH solid solution system such as the activation energy for semiconduction, thermal behaviour, magnetic susceptibility , electrode potential and the Jahn-Teller distortion parameter show a change in behaviour at $MnOOH_{0.5}$. This led Maskell *et al.* (1982) to propose that there were two solid solutions in the $\gamma$-$MnO_2$-$\delta$-MnOOH system. Experiments by Pannetier *et al.* (1990) and Chabre (1991) where proton insertion occurred in two steps corresponding to two different hydrogen bonding geometries below and above $MnOOH_{0.5}$ have substantiated that claim.

A series of papers by Fillaux *et al.* (1991, 1992a&b and 1993a&b) have used the technique of inelastic neutron scattering (INS) to study $\gamma$-$MnO_2$. This was used because X-ray or neutron diffraction, nuclear magnetic resonance or infrared do not provide direct information on the location of protons in the $\gamma$-$MnO_2$ lattice. With INS however the spectra are dominated by signals due to protons. Different sites or distinct chemical bonds for the protons give separate bands with intensities depending on the relative amounts of each species. In the papers published in 1993 INS spectra were shown for EMD, CMD, manganite and samples reduced by cinnamyl alcohol in xylene at various levels of reduction ($0.04 < r < 0.96$). The INS spectra of reduced EMD, CMD and manganite showed three main peaks at $\approx$ 1110, 2200 and 3100$cm^{-1}$. The main peak at $\approx$ 1110$cm^{-1}$ in manganite could be split into two components at 1131 and 1095$cm^{-1}$ whereas for EMD and CMD the peak was much broader and could be decomposed into several submaxima at 750, 890, 1010 and 1120$cm^{-1}$. These components were assigned as follows (i) single protons in sites surrounded by empty sites at $\approx$750$cm^{-1}$, (ii) protons in sites nearest neighbour to the $Mn^{4+}$ vacancies at $\approx$890$cm^{-1}$, (iii) protons in sites next nearest neighbour to the $Mn^{4+}$ vacancies at $\approx$1010$cm^{-1}$ and (iv) protons in the ramsdellite/pyrolusite like channels of the intergrowth structure at 1120$cm^{-1}$.

Recent work by MacLean and Tye (1995) has contributed to the knowledge of the structure of chemically prepared fully inserted $\gamma$-$MnO_2$ compounds ($MnOOH_{1.0}$) and the results have been interpreted in terms of the

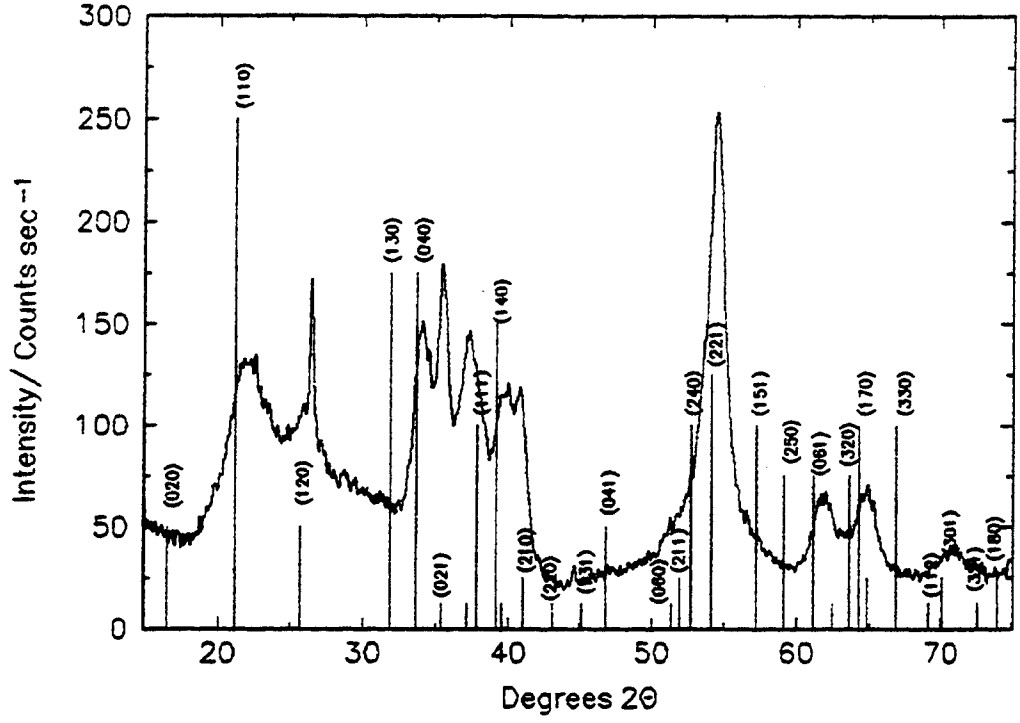


***Figure 1.3*** : Comparison of the reduction product of EMD ($MnOOH_{1.0}$) with the JCPDS pattern of groutite (ref this work).

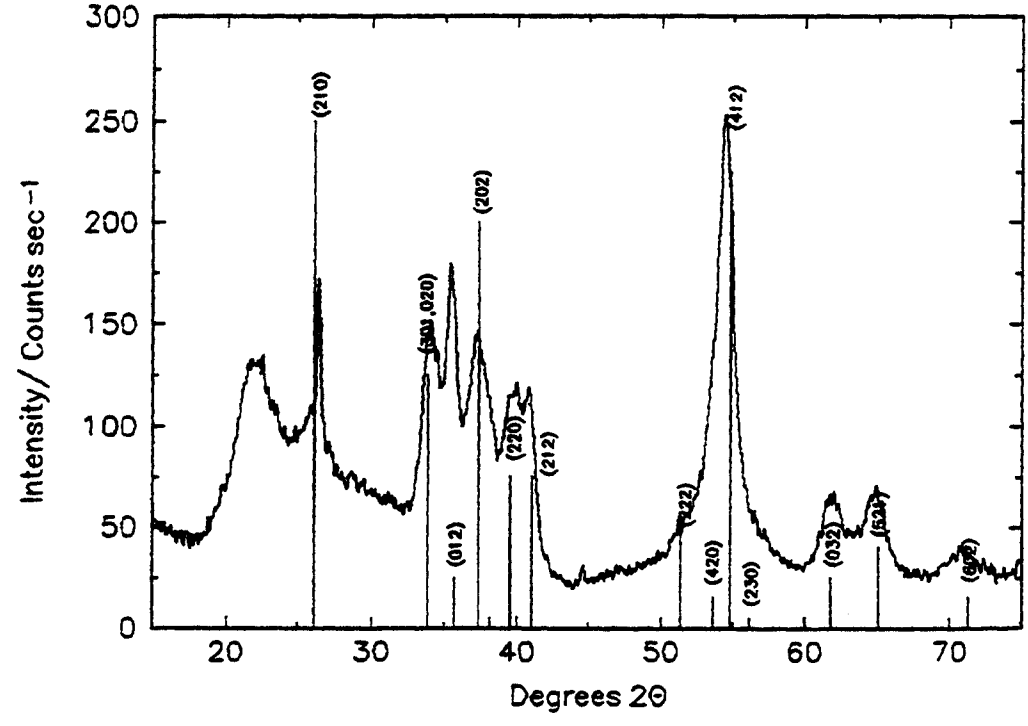


***Figure 1.4*** : Comparison of the reduction product of EMD ($MnOOH_{1.0}$) with the JCPDS pattern of manganite (ref this work).

structural model for $\gamma$-$MnO_2$ developed by Pannetier. The materials being studied formed a structural series from a "line rich" (or "higher structure") $\gamma$-$MnO_2$ to that of a typical EMD having only six broadened reflections in the XRD pattern. The structural parameters of the starting materials had similar de Wolff disorder ($P_r$) but different amounts of microtwinning (Tw). They found that all the lines in the XRD patterns of the starting materials were present in the most H-inserted derivatives and that the structure of the most H-inserted compound was an expanded version of the original structure. The expansion was in the orthorhombic b direction and was of similar dimensions to that of the hypothetical transition ramsdellite to groutite. In agreement with Maskell *et al.* (1981) the end-product was termed $\delta$-MnOOH which was defined as "an unmicrotwinned intergrowth structure having a random alternation of groutite and manganite type layers."

## 1.5 Infra-red studies of manganese dioxide and oxyhydroxides.

Most of the investigations concerning infra-red have been of a qualitative nature in order to differentiate between the different crystalline modifications of $MnO_2$. White and Roy (1964) observed that the broad band of pyrolusite was split into four ill-defined components. The infra-red spectra of $MnO_2$ can be split into two regions from 400-1400 $cm^{-1}$ and 1400-4000$cm^{-1}$ the former is associated with vibrations of the $MnO_6$ framework and the latter with OH stretching and bending vibrational modes. Potter and Rossman (1979) have published I.R. spectra for the manganese oxide minerals. They showed the I.R. spectra of a heat-treated synthetic nsutite (this is a structural intergrowth of pyrolusite and ramsdellite) and found that heat-treatment produces increasing concentrations of randomly distributed pyrolusite microdomains. This was in agreement with the X-ray work of Laudy and de Wolff (1963). An interesting observation was the correlation between the major band position and the number of edges shared per $MnO_6$ octahedron, for example pyrolusite, which had two edges shared per $MnO_6$ octahedron had its main band position at 600$cm^{-1}$ whereas manganosite (MnO) which had eight the band position was at 300$cm^{-1}$. The trend could be used in conjunction with a direct comparison of I.R. patterns

to infer unknown structures.

In recent years Swinkels (1984 & 1989) has been the leading exponent of I.R. spectroscopy. In the first paper he showed that there was a linear relationship between heat-treatment temperature and the major FTIR peak position for EMD, which suggested that $MnO_2$ changed in a linear fashion from one structure into another. He also used the statistical technique of factor analysis to determine the number of components contributing to a spectral region and reported that the number of significant factors was 3 or 4. He was not able to pin-point the nature of the factors but felt that it was related to regions of different energy and hence different electrochemical reactivity in $MnO_2$. In 1989 he showed I.R. spectra for the 31 I.B.A. samples, they were divided into four categories , pyrolusite, NMD, CMD and EMD. Tye (1992) showed FTIR spectra for an EMD that had been reduced from $MnOOH_{0.1}$-$MnOOH_{1.0}$ in a single phase. He found that peaks centred at 1950 and 2600$cm^{-1}$ started to dominate the spectra after $MnOOH_{0.8}$ and this was attributed to the formation of OH bonds.

## 1.6 The potential of manganese dioxide and oxyhydroxides.

The equilibrium potential against degree of reduction curve for $MnO_2$ is shown in Figure 1.5 the data was taken from Maskell *et al.* (1981) and the experiments were performed in specially modified Leclanche cells. The continuously varying potential against composition has been used as evidence of a homogeneous reaction. According to Vetter (1962) a homogeneous reduction may occur if a single phase of variable composition exists which contains both the oxidisable and reducible components and this leads to a progressive change in potential with degree of reduction. In a heterogeneous phase both oxidised and reduced materials exist simultaneously as separate phases which form a physical mixture and this leads to an equilibrium potential that is invariant of the degree of reduction.

The potential of the manganese dioxide electrode is given by (Tye 1985a)

$$E = E_0 - \frac{2.3RT}{F} pH + \frac{RT}{F} \ln \frac{a_{MnO_2}}{a_{MnOOH}} \qquad (1.3)$$

$$E_0 = \frac{G^0_{MnO_2} - G^0_{MnOOH}}{F} \qquad (1.4)$$

in which $G^0$ is the free energy of formation of the subscript species, R is the gas constant, T is temperature and F is the Faraday. Maskell *et al.* (1981, 1982a,b&c and 1983a&b) have developed models to explain the curve in figure 1.5. The basic assumptions in their models were the independent mobility of the inserted proton and electron, different sites for the proton and electron in the first and second half of the reduction and an amount of $Mn^{3+}$ which is present in the original $\gamma$-$MnO_2$ and is inactive regarding the potential determining reaction. Tye (1985b) took the model one stage further by considering that there was a different solid solution on either side of the mid-reduction point. In the present investigation interest is centred around heat-treated manganese dioxides but no potential against degree of reduction curves for such materials were found in the literature. There are, however, papers concerning the potential of $MnO_2$ with heat-treatment (Kozawa 1985 and Preisler 1980). Both authors found that the potential of $MnO_2$ decreases by about 200mV upon heat-treatment from 25-450°C. The cation vacancy model developed by Ruetschi† (1984, 1988a&b) also dealt with the potential of heat-treated $MnO_2$ and explained the results of Kozawa and Preisler.

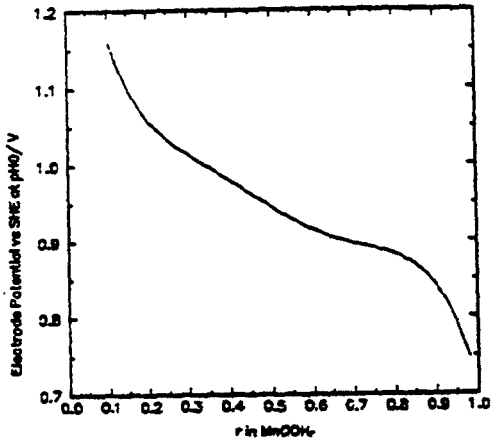


*Figure 1.5*: Variation of the equilibrium potential of $MnO_2$ with degree of reduction (ref Maskell *et al.* 1981)

†In a series of three papers a model was developed which was able to explain, for the first time, a number of aspects of $MnO_2$ electrochemistry. These included, for example, the structural water content of $MnO_2$, density, electrochemical reactivity and electrode potential. The basis of the model was that a fraction of $Mn^{4+}$ ions were missing in the $Mn^{4+}$ lattice and each of these vacancies was co-ordinated to 4 protons present as $OH^-$ ions. Also a fraction of $Mn^{4+}$ ions were replaced by $Mn^{3+}$ and this determined the degree of oxidation of the manganese ions. The model, however, is of little use in the interpretation of the reduction process to MnOOH.

## 1.7 Properties of lithium manganese oxide insertion compounds.

### *1.7.1 Lithium manganese dioxide*

Ikeda (1975) first showed that one mole of manganese dioxide heat-treated at 400°C could accommodate one mole of lithium as shown in equation 1.5.

$$MnO_2 + Li^+ + e^- \Rightarrow MnOOLi \quad (1.5)$$

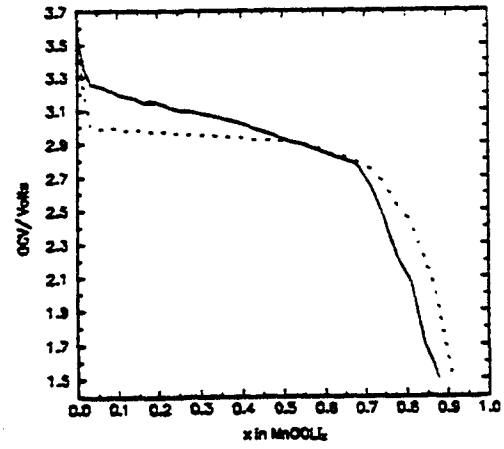


*Figure 1.6* :OCV against Li insertion for the intermittent discharge of an $Li_xMnO_2$ cell (–)EMD heat-treated at 250°C;(...)EMD 400°C.(ref Ohzuku *et al* 1989)

There was, however, no interpretation of the X-ray diffraction patterns. Voinov (1981) investigated the open circuit voltage of $Li/MnO_2$ cells (after electrochemical discharge) and found that for $x<0.04$ in $Li_xMnO_2$ the voltage decreased rapidly from 3.55 to 3.05V for $0.04<x<0.5$ it decreased from 3.05 to 2.95 and for $0.5<x<1$ it decreased towards 2.5V, he came to the conclusion that only cornersharing tetrahedral holes of the hexagonally close packed oxygen layers of $MnO_2$ were occupied by $Li^+$. Figure 1.6 shows how the OCV against Li insertion varies during the intermittent discharge of a $Li/MnO_2$ cell, the data was taken from Ohzuku *et al.* (1989). Ravdel *et al.* (1988) have shown the equilibrium potential against the degree of reduction for $LiMnO_x$ they found a smooth curve up to $x=0.75$-0.8. After this the voltage decreased rapidly and this was attributed to a new phase. The results differed to those shown by Voinov. One reason could be that Voinov did not allow a sufficiently rigorous criterion for the attainment of equilibrium (10mV/24 hours) whereas Ravdel *et al.* (1988) specified ±2mV. Laig-Horstebrock (1990) demonstrated that at high drain the performance of the $Li/MnO_2$ cell was restricted by the depletion of the lithium salt in the organic electrolyte.

David *et al.* (1984) showed that room temperature lithiation of a $\beta$-$MnO_2$

phase (equivalent crystal structure to I.C. No 6) with n-butyllithium formed a spinel phase the driving force for the transformation being the repulsion between $Li^+$ and $Mn^{4+}/Mn^{3+}$ ions. This was in contrast to the results obtained by Murphy *et al.* (1978) who reported that up to 0.3 lithium atoms per formula unit could be inserted into the structure without transforming the rutile framework of $\beta$-$MnO_2$ . Buseck *et al.* (1985) used transmission electron microscopy to examine an electrodeposited manganese dioxide at various levels of lithium insertion; samples with 36 and 50% lithiation were similar with crystals of $Mn_2O_3$ present, The 75% sample was different as the crystal spacings were larger than in other samples and the 100% lithiated sample was much less crystalline than the other samples. Nardi (1985a&b) used open-circuit voltage recovery data to deduce that

(a) the first 10% of discharge i.e. $Li_xMnO_2$ $(0<x<0.1)$ was a homogeneous reduction.

(b) between 10 and 40% was a heterogeneous reaction which was distinguished by a flat portion of the open-circuit and discharge curves, due possibly to a structural change from an hcp to a ccp configuration.

(c) above 40% discharge ($Li_{0.4}MnO_2$) was a homogeneous reaction.

A mechanism of Li insertion into EMD was proposed by Burns and Burns (1985) based on the work of David *et al.* (1984) and Nardi (1985). In the first 10% of discharge $Li^+$ ions entered $Mn^{4+}$ vacancies and in the 10-40% discharge region $Li^+$ ions entered unoccupied octahedral sites between the chains of linked $MnO_6$ octahedra. Charge balance was maintained by conversion of $Mn^{4+}$ to $Mn^{3+}$ and this corresponded to a two-phase region.

The most detailed studies have been reported in a series of four papers by Ohzuku *et al.* (1989, 1990a&b and 1991). In the first paper they showed X-ray diffraction patterns at various levels of Li insertion from electrochemical discharge of an EMD that had been heat-treated for 7 days at 250 and 400°C. In contradiction to Nardi he found that in the first part of the reduction a new phase was formed and in the 30-90% part of the reduction the a axis increased continuously as a function of Li insertion and that this was a homogeneous reaction. The crystal structure of the end product was indexed assuming an orthorhombic unit cell with a = 1.027nm, b = 0.493nm and c = 0.285nm.

The theoretical capacity for insertion of one mole of Li into $MnO_2$ is 308mAh $g^{-1}$, the percentage utilisation found by Ohzuku *et al.* (1989) was 90-95% at 0.1mA $cm^{-2}$ discharge rate. At a discharge rate of 3.5mA $cm^{-2}$ Ilchev (1989b) found that the utilisation was 56% for a CMD (Faradiser WS) and at -20°C and 1.0mA $cm^{-2}$ it was 15% for the same material. Ohzuku *et al.* (1990a) also found that the $Li_xMnO_2$ insertion compound, prepared by the electrochemical reduction of EMD, was rechargeable in the region $0.26 < x < 0.86$, although there was no indication as to how many charge/discharge cycles could be performed. They also reported (1991) evidence of the Jahn-Teller deformation of the $MnO_6$ octahedron at $MnO_{1.75}$. A comparable type of behaviour for proton insertion was found by Gabano *et al.* (1965), Giovanoli *et al.* (1969) and Maskell *et al.* (1981).

A series of papers by Murray *et al.* (1991) and Sleigh *et al.* (1990 & 1991) have investigated various properties of $Li/MnO_2$ cells. They identified two distinct processes in the relaxation of the voltage after a current pulse had been applied, one associated with the electrolyte and one with the intercalation electrode. In the subsequent papers of Murray *et al.* (1991) and Sleigh *et al.* (1991) they looked at heat production (measured in a calorimeter) and hysteresis in $Li/Li_xMnO_2$ cells during charge and discharge over the range of x ($0.4 < x < 1.0$). One of the conclusions they came to was that $Li_xMnO_2$ was a two-phase system over at least part of the range $0.4 < x < 1$. A diffusion coefficient for Li in $MnO_2$ was estimated to be $6x10^{-12}$ $cm^2s^{-1}$. Vondrak (1985) found $3.4x10^{-10}$ $cm^2s^{-1}$ and Dickens and Reynolds (1981) $4x10^{-11}$ $cm^2s^{-1}$. A recent *in situ* X-ray diffraction study of Li insertion into EMD by Crespi *et al.* (1990) reported that it was a homogeneous reaction: at $Li_{0.03}MnO_2$ new peaks appeared in the X-ray pattern which shifted with increasing lithiation. The pattern was indexed using the same orthorhombic cell as Ohzuku *et al.* (1989). These experiments were performed in an argon atmosphere and an interesting observation was an increase of 20% unit cell volume of $Li_{0.7}MnO_2$ when exposed to air. Chen and Greenblatt (1985) used a different approach by studying Li insertion into $Li_2Ti_2O_7$, this material had a ramsdellite type structure, therefore its study served as a model for Li insertion into a ramsdellite material.

Thackeray *et al.* (1993a&b) prepared a highly crystalline form of ramsdellite $MnO_2$ from acid treatment of the spinels $LiMn_2O_4$ and $Li_2Mn_4O_9$. This

material was synthesised in order to achieve the synthetic equivalent to natural ramsdellite that was used in the work of Bystrom (1949)†. Compounds of composition $x=0.3$, 0.5 and 0.9 in $Li_xMnO_2$ were chemically prepared using lithium iodide in acetonitrile. The XRD results indicated that the ramsdellite $MnO_2$ framework remained intact over the whole compositional range of $Li_xMnO_2$ ($0 \leq x \leq 0.9$). The lattice parameters of $Li_{0.9}MnO_2$ were indexed to an orthorhombic unit cell with $a=0.991$, $b=0.5208$ and $c=0.2812$nm in good agreement with Ohzuku. Using electrochemical and structural data the following processes for Li insertion into $MnO_2$ were given (a) $0 \leq x \leq 0.3$ of $Li_xMnO_2$ was characterised by the insertion of lithium into an essentially hexagonally-close-packed $MnO_2$ structure and (b) $0.3 \leq x \leq 0.9$ insertion of lithium into the close-packed oxygen array which was a combination of hexagonal (hcp) and cubic close packing (ccp). A mechanism for the hcp to the pseudo ccp arrangement was thought to be due to a shear of the (2x1) ramsdellite blocks and a buckling of the structure in response to an increase in electrostatic interactions between lithium and manganese ions in face-shared octahedra.

Zachau-Christiansen *et al.* (1994) investigated the electrochemical insertion of lithium into natural ramsdellite, pyrolusite, EMD and CMD. They found that the discharge of ramsdellite proceeded at a higher voltage until $Li_{0.3}MnO_2$ but in the region $x > 0.35$ in $Li_xMnO_2$ the discharges were similar. The behaviour of EMD and CMD corresponded to either the ramsdellite or pyrolusite polymorph.

### *1.7.2 Other lithium manganese oxide phases.*

It is generally accepted that heat-treated $MnO_2$ has limited rechargeability in $Li/MnO_2$ cells and in recent years there has been increasing interest in other lithium manganese oxide phases. In 1981 Hunter synthesised a new crystal form of manganese dioxide called $\lambda$-$MnO_2$. This was made by the solid state reaction of $Li_2CO_3$ and $MnO_2$ at 850°C to form $LiMn_2O_4$ with subsequent removal of the lithium by treatment in acid at pH 2. $\lambda$-$MnO_2$ has the cubic spinel type structure and this provides, as discussed by Thackeray *et al.* (1992), a three dimensional

†Even though Thackeray *et al.* state that "in this particular sample there was an insignificant concentration of $\beta$-$MnO_2$ domains in the ramsdellite structure", a subsequent analysis of the sample according to the method developed by Chabre and Pannetier 1995 (p49) gave a rutile concentration of 29%. Only the natural ramsdellite used by Bystrom had 0% rutile concentration.

interstitial space for $Li^+$ transport that remains intact over a wide compositional range. Hunter and Tudron (1985) compared the discharge characteristics of $\lambda$-$MnO_2$ and heat-treated EMD. The former had two discharge steps (given by equations 1.6 and 1.7) whilst EMD had a single discharge plateau (equation 1.5).

$$2\ \lambda\text{-}MnO_2 + Li^+ + e^- \Rightarrow LiMn_2O_4 \qquad (1.6)$$

$$LiMn_2O_4 + Li^+ + e^- \Rightarrow 2LiMnO_2 \qquad (1.7)$$

This material has been investigated by Tarascon and co-workers (1991, 1993a&b and 1995) and Thackeray *et al.* (1983, 1984, 1987) for use in the new generation of so-called "rocking-chair" or "Li-ion" (this is because Li ions rock back and forth between the intercalation compounds during charge/discharge cycles) rechargeable battery technology. The idea behind these batteries was to replace Li metal with a material that was able to reversibly intercalate Li ions. These authors have investigated lithium insertion using electrochemical and chemical methods. The latter method using n-butyllithium was used in this investigation. Table 1.1 lists some of the Li-Mn-O phases that show promise for rechargeable lithium battery applications. Reviews of manganese oxide materials for use in Lithium cells have been given by Goodenough *et al.* (1984&1985) and Rossouw *et al.* (1990&1991).

***Table 1.1*** : Lithium Manganese Oxide Phases Being Researched For Lithium Battery Applications.

| PHASE | THEORETICAL CAPACITY/ $mAhg^{-1}$ | PRACTICAL CAPACITY/ $mAhg^{-1}$ |
|---|---|---|
| $Mn_3O_4$ | 117 | no data |
| $MnO_2$* | 308 | 150-180 |
| $\lambda$-$MnO_2$ | 308 | no data |
| $LiMn_2O_4$ | 148 | 75 |
| $Li_2Mn_4O_9$ | 213 | 130 |
| $Li_4Mn_5O_{12}$ | 163 | 130 |

## 1.8 Lithium insertion compounds.

An insertion compound consists of a host matrix into/from which a guest

species may be inserted/extracted reversibly without a rearrangement of the host structure. A wide range of transition metal compounds have been investigated in an attempt to find a suitable cathode material for a rechargeable lithium battery, and the purpose of this section is to review briefly the literature concerning the most widely studied of these materials. Comprehensive reviews of lithium insertion electrodes have been given by Whittingham (1978), Jacobsen (1981), Yoffe (1983), Pistoia (1983) Hughes *et al.* (1984), Murphy (1986), Atlung and West (1989), Desilvestro and Haas (1990), Naraukawa and Furukawa (1991), Cisak and Werblan (1993) and Nohma *et al.* (1994).

***Titanium disulphide:*** The reaction of titanium disulphide with n-butyllithium is given in equation 1.8.

$$C_4H_9Li + TiS_2 \Rightarrow LiTiS_2 + \frac{1}{2} C_8H_{18} \qquad (1.8)$$

The structure of $TiS_2$ consists of laminae or "sandwiches" that are stacked upon each other. Each "sandwich" is formed by a layer of Ti atoms between two layers of sulphur atoms in a hexagonally close-packed array. Each "sandwich " is held together by weak van der Waals forces and the reaction takes place homogeneously in the range $Li_xTiS_2$ $0 < x < 1$. During intercalation Li atoms locate in the van der Waals gap between the $TiS_2$ layers. The OCV during discharge ranged from 2.5 to 1.5V as reported by Whittingham (1978). He also demonstrated the rechargeability of the Li/$TiS_2$ cell, showing that there was still 90% utilisation after 76 cycles at 10mAcm$^{-2}$. An important factor for this rechargeability could be the Li diffusion coefficient which did not change as a function of discharge. The results of Dahn *et al.* (1982) who used an *in situ* X-ray diffraction cell confirmed the results of Whittingham.

***Vanadium oxides:*** The most studied have been $V_2O_5$ and $V_6O_{13}$. The incorporation of lithium into $V_2O_5$ is given by equation 1.9:

$$V_2O_5 + xe^- + xLi^+ \Rightarrow Li_xV_2O_5 \qquad (1.9)$$

The maximum stoichiometry of $Li_xV_2O_5$ is $x = 3$. Dickens *et al.* (1979) found three solid phases in the region $0.1 < x < 1.0$ and an OCV versus x plot suggested the following ranges of homogeneity, phase I $0 < x < 0.1$, phase II $0.35 < x < 0.5$ and phase III $0.9 < x < 1.0$. Cartier *et al.* (1990) have also studied the above reaction

and found that for $x > 1$ an amorphous phase was formed which induced irreversibility of the electrochemical process. $V_6O_{13}$ has been studied by West *et al.* (1983 and 1985), like $V_2O_5$ the OCV curve showed several distinct plateaus reflecting the sequential filling of inequivalent sites in the $V_6O_{13}$ lattice. They found that the diffusion coefficient of Li decreased from $8x10^{-10}cm^2s^{-1}$ to $6x10^{-11}cm^2s^{-1}$ during the reaction. The rechargeability of the $V_6O_{13}$ cathode was also demonstrated but inferior results were found in practical cells due to degradation of the electrode structure.

***Titanium dioxide:*** There are three $TiO_2$ modifications anatase, rutile and $TiO_2$(B). The first two are naturally occurring minerals and the third is a synthetic metastable polymorph. Ti is octahedrally co-ordinated to oxygen in all three materials although the packing densities are different being 3.89, 4.25 and 3.76 $gcm^{-3}$ respectively, as discussed by Zachau-Christiansen *et al.* (1988). By chemical reaction with an excess of n-BuLi, the maximum Li uptake at room temperature was 0.6, 0.8 and 0.15 for anatase, $TiO_2$(B) and rutile respectively. In electrochemical discharges the uptake was 0.5 Li/Ti in anatase and $TiO_2$(B) while rutile did not insert Li at all. The reasons for the differing uptakes of Li for the $TiO_2$ modifications were considered by Murphy *et al.* (1983). He found that, for rutile, there were no octahedral or tetrahedral sites for Li insertion that did not share at least one face with a $TiO_6$ octahedra, which is an unfavourable site due to the short distances between $Li^+$ and $Ti^{3+}$.

***Other transition metal oxides:*** Davidson *et al.* (1984) prepared $Li_xRuO_2$ and $Li_xIrO_2$ in the range $0.2 < x < 0.9$ by reaction with n-butyllithium. For $x < 0.9$ two phases were observed with one phase being the host metal oxide. Compounds were indexed on an orthorhombic unit cell and the unit cell volume expanded 12% for $Li_{0.9}RuO_2$ and 15% for $Li_{0.9}IrO_2$ relative to the host material. Ruthenium oxide is of interest because it is isostructural with $\beta$-$MnO_2$. A neutron powder diffraction study of Li insertion into $MoO_2$ was carried out by Cox *et al.* (1982). $MoO_2$ has a distorted rutile type structure with monoclinic symmetry and Li ions are inserted into octahedral sites during the reduction to $LiMoO_2$, a two phase region was also observed.

## 1.9 Aims of the current investigation.

The broad aims of the investigation were as follows.

(a) Heat-treatment of an EMD and a CMD in the range 25-450°C in an air and argon environment. Characterisation of the products by water loss and oxygen loss or uptake and investigation of any structural changes using powder X-ray diffraction and FTIR spectroscopy.

(b) Preparation of a range of H inserted compounds in the range $MnOOH_{0.1}$-$MnOOH_{1.0}$ by application of a suitable reducing agent on products from (a). Investigation of structural changes using X-ray diffraction and FTIR spectroscopy.

(c) Preparation of a matching range of lithium-inserted manganese oxide compounds in an argon filled glove box and their characterisation using X-ray diffraction.

(d) Comparison of the materials prepared in (b) and (c) in order to gain a greater understanding of the H and Li insertion mechanisms.

# Chapter 2 Experimental.

## 2.1 General.

The calibrated glassware was of the class A type, chemicals were either analytical grade, from Merck-BDH, or American Chemical Society grade from Aldrich. Singly distilled water was used throughout the investigation. A Solartron 7150 digital multimeter from Schlumberger was used for the potentiometric titrations and pH measurements were taken with a Philips PW9420 meter calibrated with pH solutions from BDH. A Stanton CL41 analytical balance was used for weighing to the nearest 0.1 mg. An argon filled glove box from Miller Howe Engineering was used for the preparation of the lithium samples this operated at under 25 ppm of water and was kept at 25°C with a constant temperature control unit from Accuron.

## 2.2 Chemical analyses.

### *2.2.1 Preparation of solutions.*

A 0.05 M solution ferrous ammonium sulphate was prepared by dissolving 19.6g of $FeSO_4(NH_4)SO_4.6H_2O$ and 20ml of concentrated sulphuric acid in a 1 litre volumetric flask. A 0.01 M solution potassium permanganate was prepared by dissolving 0.316g of $KMnO_4$ in a 2 litre volumetric flask). A 0.01 M standard solution of sodium oxalate was prepared (after it had been dried at 110°C for two hours), by dissolving 1.34g in 950ml of distilled water and 50 ml of concentrated AnalaR sulphuric acid.

### *2.2.2 Manganese dioxide.*

The method of Vetter and Jaeger (1966) was used to determine the value of x in $MnO_x$. The apparatus is shown in Figure 2.1. Approximately 80 mg of the sample was weighed into a 250 ml beaker and dissolved in an excess of ferrous ammonium sulphate according to equation 2.1.

$$MnOOH_r + (4-r)H^+ + (2-r)Fe^{2+} \Rightarrow Mn^{2+} + (2-r)Fe^{3+} + 2H_2O \qquad (2.1)$$

The excess of ferrous ammonium sulphate ($V_1$) was then potentiometrically back titrated with 0.01 M $KMnO_4$ from a 10ml burette according to equation 2.2. A digital multimeter was used to monitor the platinum

electrode potential.

$$MnO_4^- + 8H^+ + 5Fe^{2+} \Rightarrow Mn^{2+} + 5Fe^{3+} + 4H_2O \qquad (2.2)$$

Enough sodium pyrophosphate was then added so that the pH was between 6.5 and 7 (this gave the maximum potential jump according to Lingane and Karplus 1946). The manganese content of the sample ($V_2$) was then measured by titration according to equation 2.3. A titration ($V_0$) was also carried out with 40 ml of ferrous sulphate and the $KMnO_4$ at the beginning and end of a series of analyses performed on the same day. The stoichiometry of the $MnO_2$ was calculated from equation 2.4. In this investigation the value of r in MnOOHr is normally quoted where r=4-2x.

$$4Mn^{2+} + MnO_4^- + 8H^+ + 15H_2P_2O_7^{2-} \Rightarrow 5Mn(H_2P_2O_7)_3^{3-} + 4H_2O \qquad (2.3)$$

$$X = 1 + \frac{5}{8} * \left[\frac{(V_0 - V_1)}{(V_2 - \frac{V_1}{4})}\right] \qquad (2.4)$$

When the manganese content of the solution was also required the $KMnO_4$ solution was standardised against the sodium oxalate ($Na_2C_2O_4$) solution. 50 ml of the sodium oxalate solution was heated to 70-80°C and titrated by the $KMnO_4$ solution until a pink colouration persisted (equation 2.5). The manganese content was calculated from equation 2.6

$$2MnO_4^- + 5C_2O_4^{2-} + 16H^+ \Rightarrow 2Mn^{2+} + 5CO_2 + 8H_2O \qquad (2.5)$$

$$\% \text{ Mn} = \frac{54.938 \times 4\text{Mol}_{KMnO_4} (V_2 - \frac{V_1}{4})}{Y} \qquad (2.6)$$

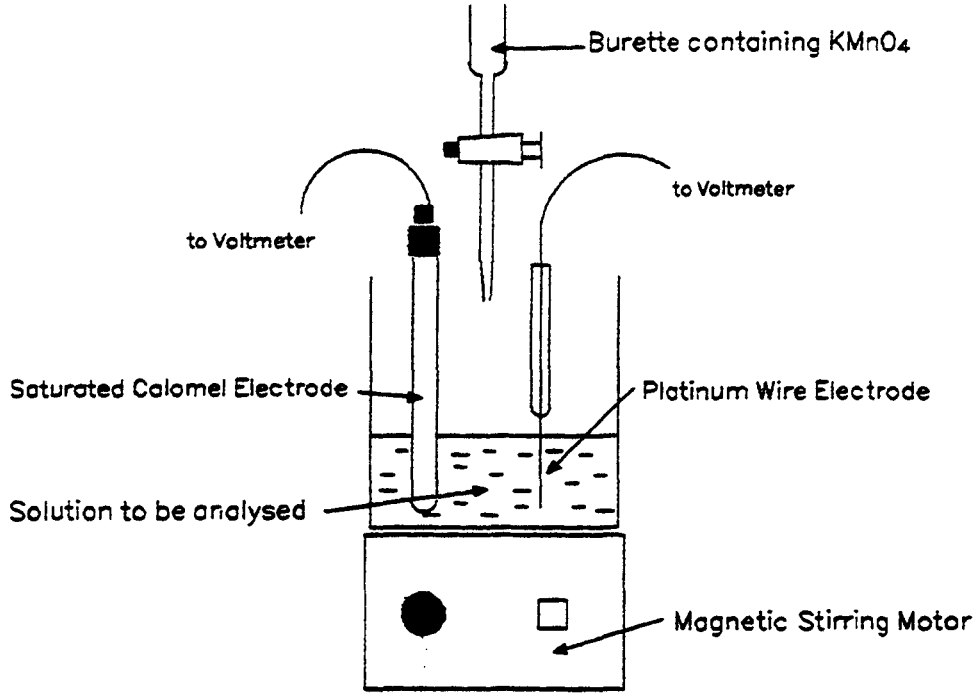


*Figure 2.1* : Apparatus used to determine the stoichiometry of the manganese oxyhydroxide samples.

### *2.2.3 Lithium manganese oxide.*

The lithium content of the lithium inserted manganese oxide samples was determined using the same technique as described in section 2.2.2.

## 2.3 Heat treatment of manganese dioxide.

The physical properties of the manganese dioxides that were used are given in Table 2.1. The apparatus used for heating the $MnO_2$ is shown in figure 2.2. The physisorbed water content of $MnO_2$ depends upon the environment in which the $MnO_2$ has been kept. In order to have comparable results for water loss, the $MnO_2$ was pre-treated by placing it in a vacuum desiccator and evacuating for 24 hours prior to heat-treatment. The effect of the evacuation was to remove most or all of the physisorbed water. After evacuation the $MnO_2$ was put into the furnace and heated for 24 hours at the requisite temperature. Dry air or argon was passed through the glass heating vessel and the evolved water was collected in drying tubes containing magnesium perchlorate. The drying tubes were weighed at hourly intervals to

*Table 2.1:* Physical properties of the manganese dioxides used in the current investigation.

| | Far M | FarWSLi | Chemetals | R2 |
|---|---|---|---|---|
| O/Mn Ratio* | 1.944 | 1.944 | 1.952 | 1.951 |
| $MnO_x$/%† | 95.3 | 96.1 | 93.5 | 93.4 |
| Surface Area/$m^2g^{-1}$† | 97.8 | 42.9 | 35.0 | 38.0 |
| Average Particle Size/$\mu$M† | 32.9 | 23.8 | 41.0 | 36.0 |

* this work
† Data sheets supplied by Sedema

establish the rate of water removal. After heating, the $MnO_2$ was allowed to cool in a desiccator and then weighed to determine the weight loss.

## 2.4 Preparation of manganese oxyhydroxides.

### *2.4.1 Propan-2-ol method.*

This method was developed by MacLean (1993) and the apparatus is shown in figure 2.3. It would take many months for low degrees of reduction to be reached at room temperature, for example Fitzpatrick and Tye (1991) found that after nine months immersion in xylene a material of $MnOOH_{0.89}$ was obtained, so elevated temperatures were used. The reaction stoichiometry is given by equation 2.7.

$$2MnO_2 + CH_3CHOHCH_3 \Rightarrow 2MnOOH + CH_3COCH_3 \qquad (2.7)$$

The reaction was initially very rapid. After 1 hour reaction with refluxing propan-2-ol a material of H insertion level $MnOOH_{0.6}$ was obtained. Approximately 30 hours was needed to obtain the $MnOOH_{1.0}$. After reaction the $MnOOH_t$ sample was filtered on a sintered glass crucible, washed with propan-2-ol and vacuum-dried for 30 minutes and stored in a sample vial.

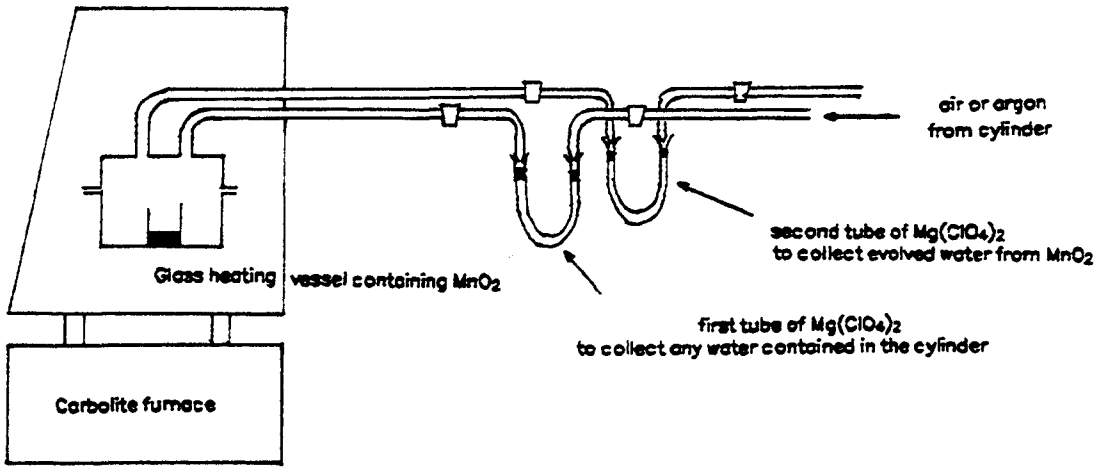


*Figure 2.2* : Apparatus used for the heat-treatment of $MnO_2$ in an air or argon atmosphere.

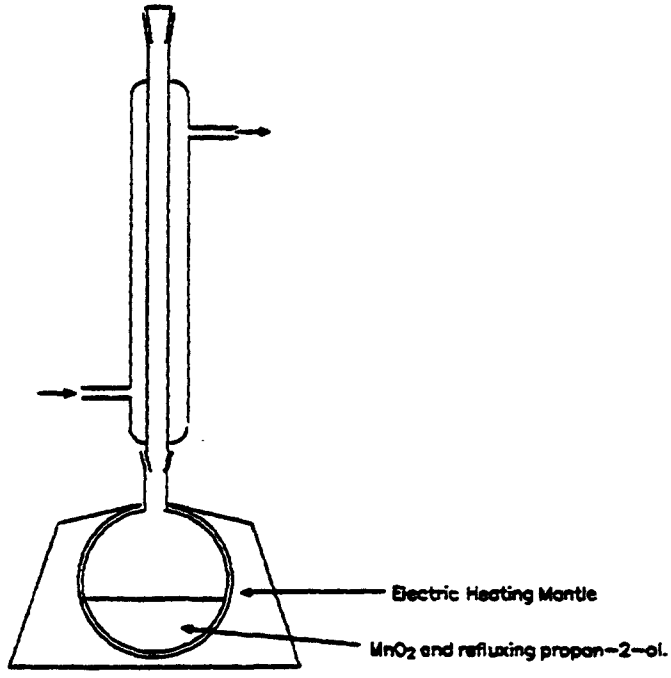


*Figure 2.3* : Apparatus used to reduce manganese dioxide with propan-2-ol.

### *2.4.2 Hydrazine hydrate method.*

This method was developed by Larcin (1991) and also used by Alday (1991). After the $MnO_2$ had been heat-treated at the requisite temperature for 24 hours, 3gm of the sample were immersed in 30 ml of AnalaR hexane in a 50 ml conical flask containing a PTFE stirring bar and 0.2 ml aliquots of a 1.6M solution of hydrazine hydrate in propan-2-ol were added to the $MnO_2$/hexane mixture at hourly intervals. The reaction was carried out so that the reduction steps ran parallel to those obtained for lithium inserted samples (see section 2.5). The stoichiometry is given by equation 2.8.

$$4MnO_2 + N_2H_4.H_2O \Rightarrow 4MnOOH + N_2 + H_2O \qquad (2.8)$$

The least reduced samples needed 7 additions of hydrazine and took 11 hours and the most reduced samples needed 108 additions and the reaction was carried out over one week. Using this method a series of approximately 16 H inserted compounds from $MnOOH_{0.1} - MnOOH_{1.0}$ were prepared. After reaction samples were filtered on a sintered glass crucible and vacuum-dried for thirty minutes and stored in a sample vial.

## 2.5 Preparation of lithium manganese oxide samples.

The preparation of these samples was carried out in an argon filled glove box (section 2.1). Approximately three grams of the heat-treated $MnO_2$ was accurately weighed into a 50 ml conical flask containing a PTFE stirring bar. The $MnO_2$ was then immersed in hexane and 0.2 ml aliquots of 1.6M n-butyllithium were added at hourly intervals and the reaction proceeded according to equation 2.9

$$MnO_2 + C_4H_9Li \Rightarrow LiMnO_2 + \frac{1}{2} C_8H_{18} \qquad (2.9)$$

Approximately 108 additions were required for one mole of lithium to be inserted into $MnO_2$ and this was carried out over one week. The samples were filtered on a sintered glass crucible, washed with hexane and vacuum-dried for 30 minutes. All operations and storage of the samples were carried out in the argon filled glove box.

## 2.6 Fourier Transform Infra-Red spectroscopy of manganese dioxides.

### *2.6.1 Pellet preparation.*

Approximately 3mg of the manganese oxyhydroxide sample was weighed out (the exact weight being recorded) and ground with 450mg of SpectroSol caesium iodide in an agate pestle and mortar for five minutes. The powder was then divided into two equal parts and transferred to a sample vial. The two portions were then pressed into 13mm pellets using a Specac die at a load of 9 tonnes for approximately one minute. A blank pellet of CsI was also made on every occasion that the spectrophotometer was used[††]. Some samples were analysed at BHP in Australia (EMD heat-treated at 200 and 300°C reduced by hydrazine hydrate) and the same procedure was used except that the pellets were pressed under nitrogen so there would be fewer problems with the CsI absorbing water from the atmosphere.

### *2.6.2 Machine operation.*

The infra-red spectra were recorded on a Perkin-Elmer 1710 series spectrophotometer . An average of 50 scans of the background were run in the wavenumber region 400-4000$cm^{-1}$ at a resolution of 2$cm^{-1}$ . The caesium iodide pellet was then scanned and finally the manganese oxyhydroxide sample. The CsI spectrum was subtracted from the MnOOH + CsI spectrum to yield the MnOOH spectrum. A hardcopy of the spectra was produced using the Perkin-Elmer plotter. The spectra were then converted into a digital format and loaded into a Lotus 1-2-3 compatible spreadsheet where they were normalised to a weight of 1mg $cm^{-2}$ of MnOOH, using the weights that were previously recorded. Each spectra consisted of 442 data points (every 5$cm^{-1}$ in the range 400-1200cm-1 and every 10cm-1 from 1200-4000cm-1).The same procedure was used by at BHP except that a Perkin-Elmer 1750 series spectrophotometer was used and the spectra consisted of 902 data points (every 4$cm^{-1}$ in the range 400-4000$cm^{-1}$).

[††]A fresh CsI pellet was made because the CsI FTIR spectrum was subtracted from the MnOOH + CsI FTIR spectrum and as CsI was hygroscopic (a large absoption band at 3400$cm^{-1}$ would appear) this would affect the data in that region.

## 2.7 Powder x-ray diffractometry.

A Philips PW 1710 series Automated Powder Diffractometer (APD) with the following equipment was used: PW 1050/81 goniometer and step motor, PW 2253/20 broad focus copper anode X-ray tube, PW 1730/10 high performance 4kW 60kV constant potential generator and a PW 1711/10 xenon proportional counter.

The operating conditions were: generator set at 45kV and 55mA, proportional counter pulse height selection set between 35 and 70% and settings of 1° for the divergence and scatter slits and 0.2 mm for the receiving slit. Samples were scanned at a speed of 0.01° of $2\theta$ per second between 15 and 75° of $2\theta$.

The sample preparation was similar to that given by Klug and Alexander (1974). The manganese oxyhydroxide was ground in an agate pestle and mortar for five minutes. An aluminum sample holder was attached to a glass slide with sticky tape and the ground $MnO_2$ was carefully placed in the cavity so that a flat surface was produced.

## 2.8 Pyknometric density measurements of manganese dioxides.

The apparatus for this piece of work are shown in figure 2.4. 2.5 g of the manganese dioxide sample were accurately weighed into the calibrated 10 ml density bottle and transferred to the desiccator. This was then attached to a vacuum pump and evacuated for 5 minutes to remove any air that was trapped in the $MnO_2$ pores. Degassed distilled water was then admitted and enough was added to cover the $MnO_2$ surface. The system was then allowed to reach atmospheric pressure, the density bottle was removed and filled with water. The bottle was then transferred to a water bath at 25°C and allowed to equilibrate for 1 hour it was then dried and weighed to 0.1 mg. The equations for calculating the density of $MnO_2$ are given in section 3.5.

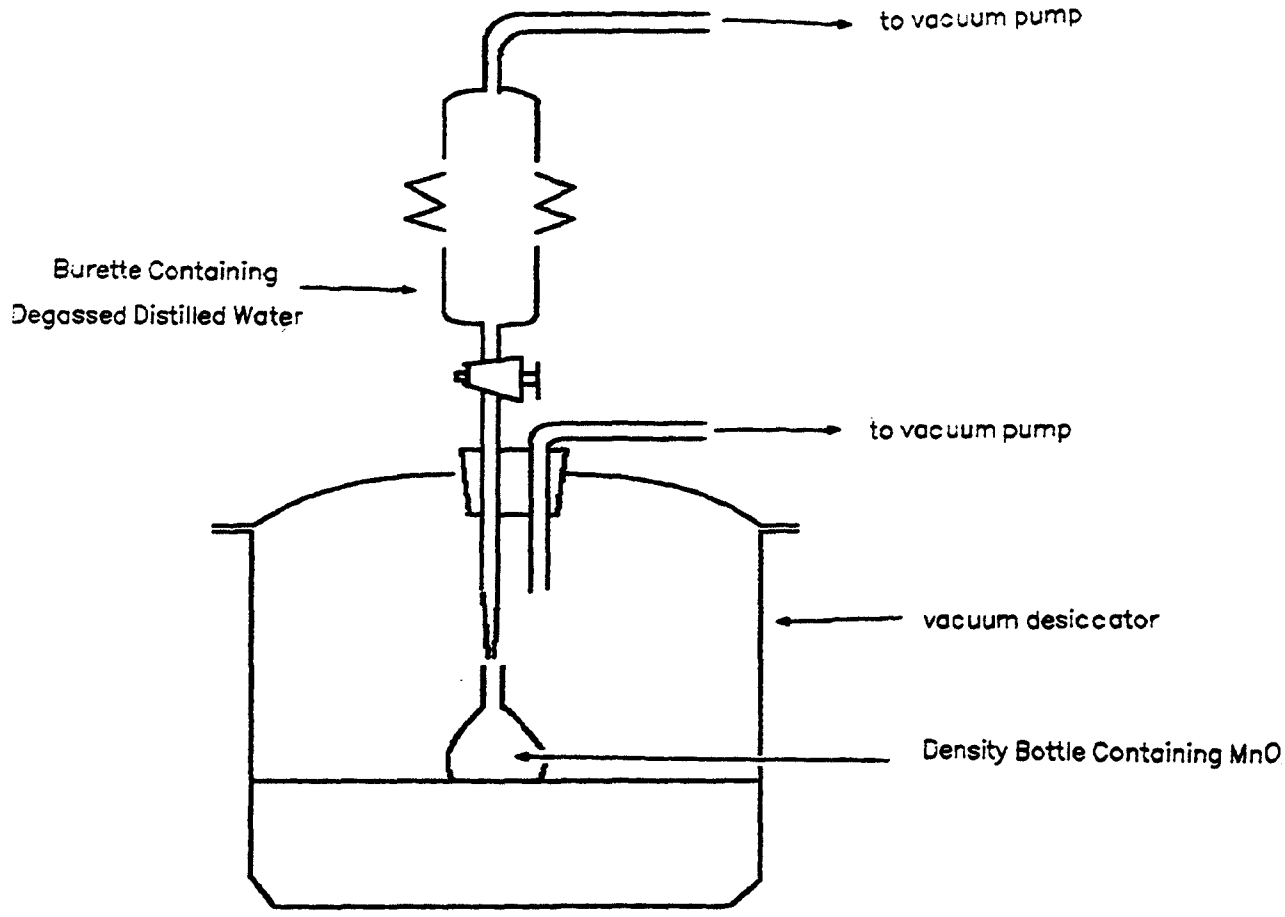


*Figure 2.4* : Apparatus used to determine the density of manganese dioxides at 25 °C.

## 2.9 Electrode potential of manganese dioxides.

The apparatus for this area of work are shown in figure 2.5. Three grams of the $MnO_2$ sample were accurately weighed into the Nalgene test-tube and then 25 ml of the 5M $NH_4Cl$/2M $ZnCl_2$ solution added and allowed to equilibrate at 25°C for three days. A platinum spade electrode was then inserted into the $MnO_2$ and a saturated calomel electrode into the electrolyte. The potential was recorded when a stable potential (± 2mV) was reached. The pH of the electrolyte was also taken and the potential was calculated at pH0 by equation 2.10.

$$E_{MnO_2} = E_M + 0.0592\ pH + 0.2444 \qquad (2.10)$$

where $E_M$ is the measured potential of $MnO_2$ and 0.0592 V $pH^{-1}$ is the slope of the potential pH relationship and 0.2444 is the potential of the saturated calomel electrode versus the standard hydrogen electrode.

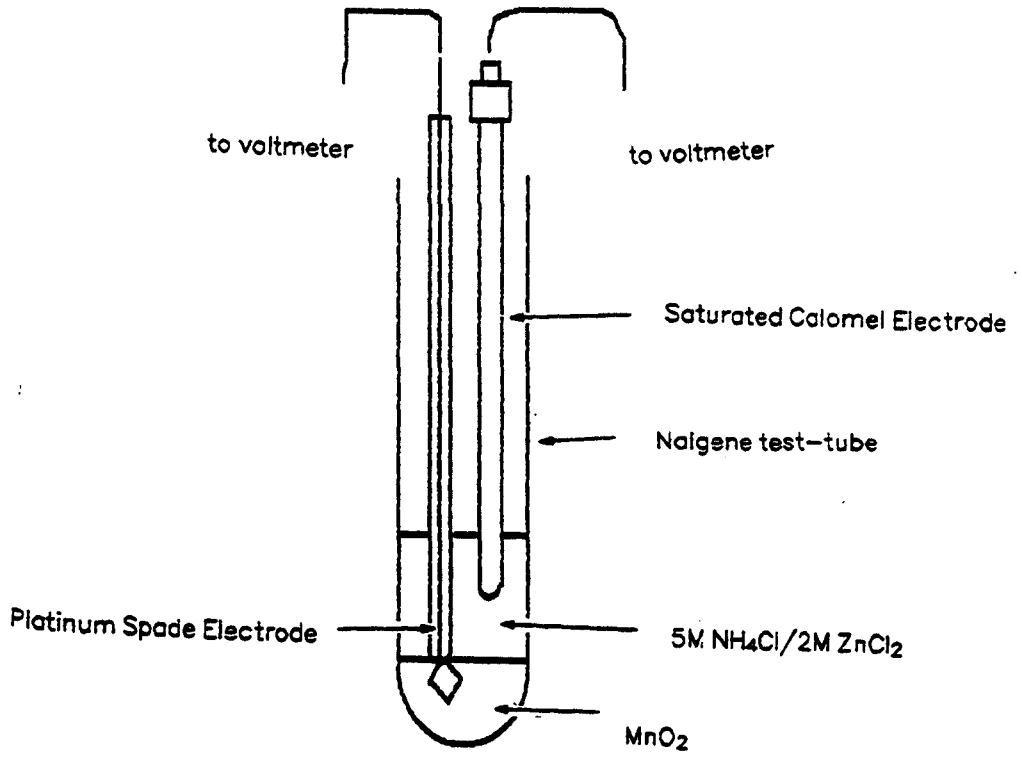


*Figure 2.5* : Apparatus used to determine the potential of manganese dioxides at 25°C.

# Chapter 3 Heat Treatment of Synthetic Manganese Dioxides.

## 3.1 Introduction.

Many investigations have been concerned with the heat-treatment of manganese dioxides and the literature regarding that has been reviewed in section 1.2. The overall aim of this chapter was to create, using a variety of techniques, a clear picture of the chemical and physical changes when $MnO_2$ is heat-treated at temperatures from 25 to 450°C.

## 3.2 Pre treatment procedure.

Prior to heat-treatment the samples were evacuated for 24 hours to remove the water that was dependent on the environment in which the $MnO_2$ was kept. The purpose of this pre-treatment was to bring all samples to a uniform and reproducible state as established by Holton and Tye (1980). The weight loss as a function of pumping time is shown in figure 3.1.

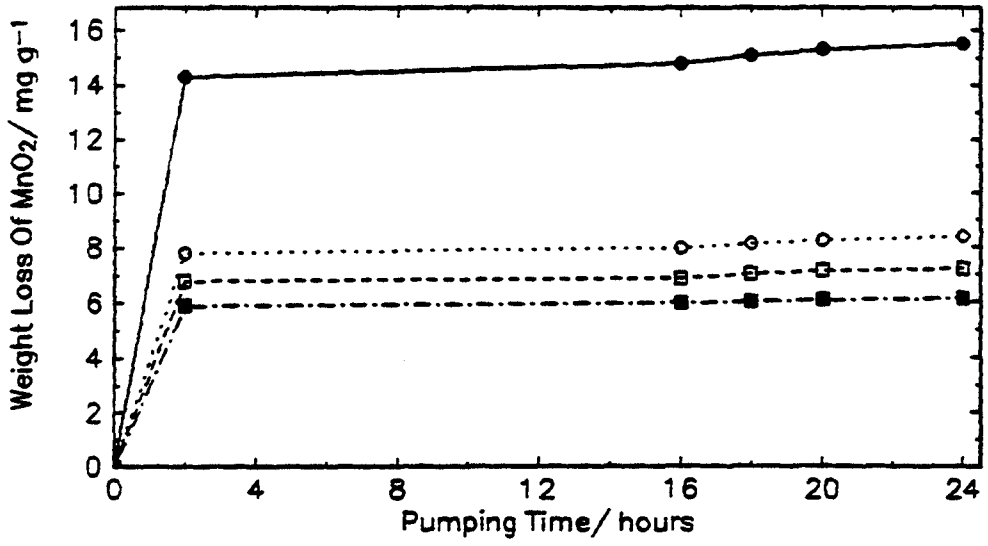


*Figure 3.1* : Weight loss of the $MnO_2$'s prior to heat treatment as a function of the pumping time (●)Far M, (□)Far WSLi, (○)R2 and (●) Chemetals.

Figure 3.1 shows that the weight loss was significantly greater for one of the CMDs (Faradiser M) than for the other three materials. The physisorbed water

content of manganese dioxide is probably dependent on the surface area of the $MnO_2$ and the surface area of Faradiser M is twice as much as the other materials (see Table 2.2). Amlie and Tvarusko (1964) have shown that the dependence of the physisorbed water content of $MnO_2$ with surface area.

## 3.3 Check of the analytical technique to determine the stoichiometry of $MnO_x$.

The method given by Lingane and Karplus (1946) and Maskell (1976) is used here. Examination of equations 2.2 and 2.3 shows that the volume of $KMnO_4$ required by equation 2.2 is four times that required by equation 2.3. Using the apparatus of figure 2.1. 25ml of 0.05M ferrous sulphate was titrated with 0.01M $KMnO_4$ (20ml was added with a calibrated pipette and the remaining added with a 10ml burette). 7 gm of sodium pyrophosphate was added and the second titration performed. The end-points for the two titrations being performed are shown in figure 3.2. This titration is performed with no $MnO_x$ present. The results of five analyses are given in Table 3.1 and they are in good agreement with the theoretical value of 4. Lingane and Karplus (1946) achieved 4.000 ± 0.002.

*Table 3.1:* Check of the analytical technique.

| 1st Titration $(V_1)$ /cm$^{-3}$ | 2nd Titration $(V_2)$ /cm$^{-3}$ | $(V_1/V_2)$ |
|---|---|---|
| 24.229 | 6.031 | 4.017 |
| 23.957 | 6.001 | 3.992 |
| 24.000 | 6.018 | 3.988 |
| 24.282 | 6.071 | 4.000 |
| 24.226 | 6.043 | 4.009 |
| | | Average 4.0012 |
| | | Std Error 0.0119 |

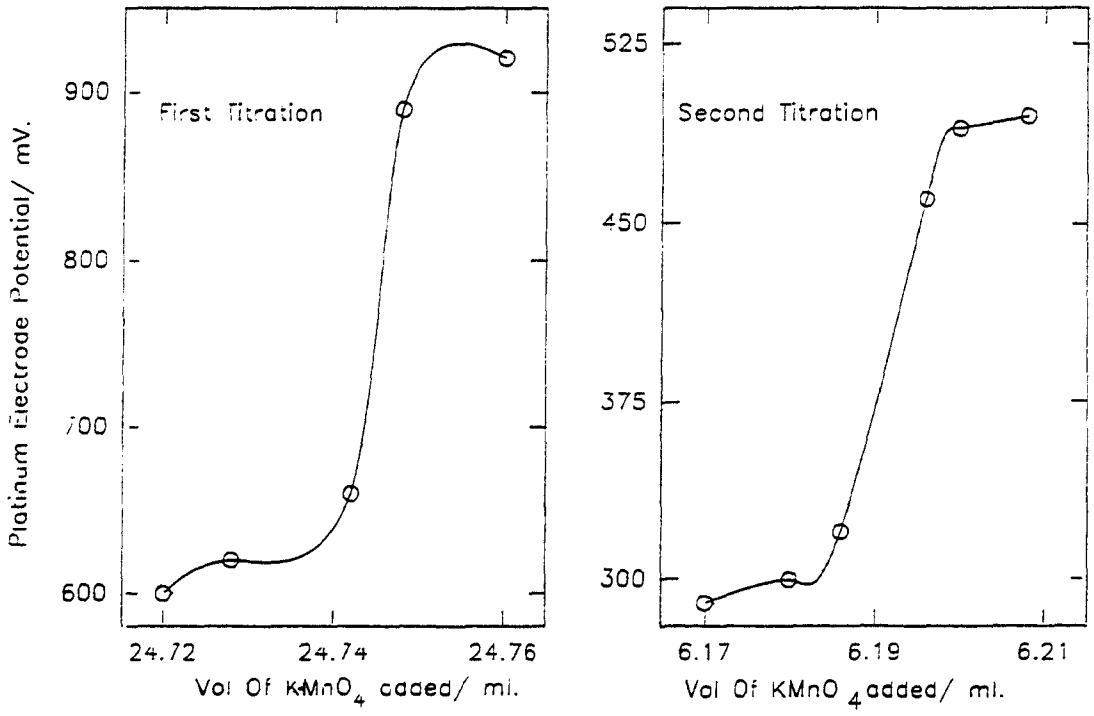


*Figure 3.2*: End-points for the first and second titrations that were used to determine the stoichiometry of manganese oxyhydroxide (x in $MnO_x$ or r in $MnOOH_r$).

## 3.4 Water loss and oxygen changes during heat treatment in an air or argon environment.

The apparatus for this piece of work is shown in section 2.3. In this section results are first of all presented for the four manganese dioxide materials in terms of water loss and oxygen changes and at the end of the section the results are interpreted in the context of the current literature.

**EMD (Chemetals).**

The stoichiometry in air and argon as a function of the heat-treatment temperature is shown in figure 3.3. Figure 3.4 shows the water and weight loss in air and argon against temperature and figure 3.5 shows the rate of water evolution in air and argon respectively.

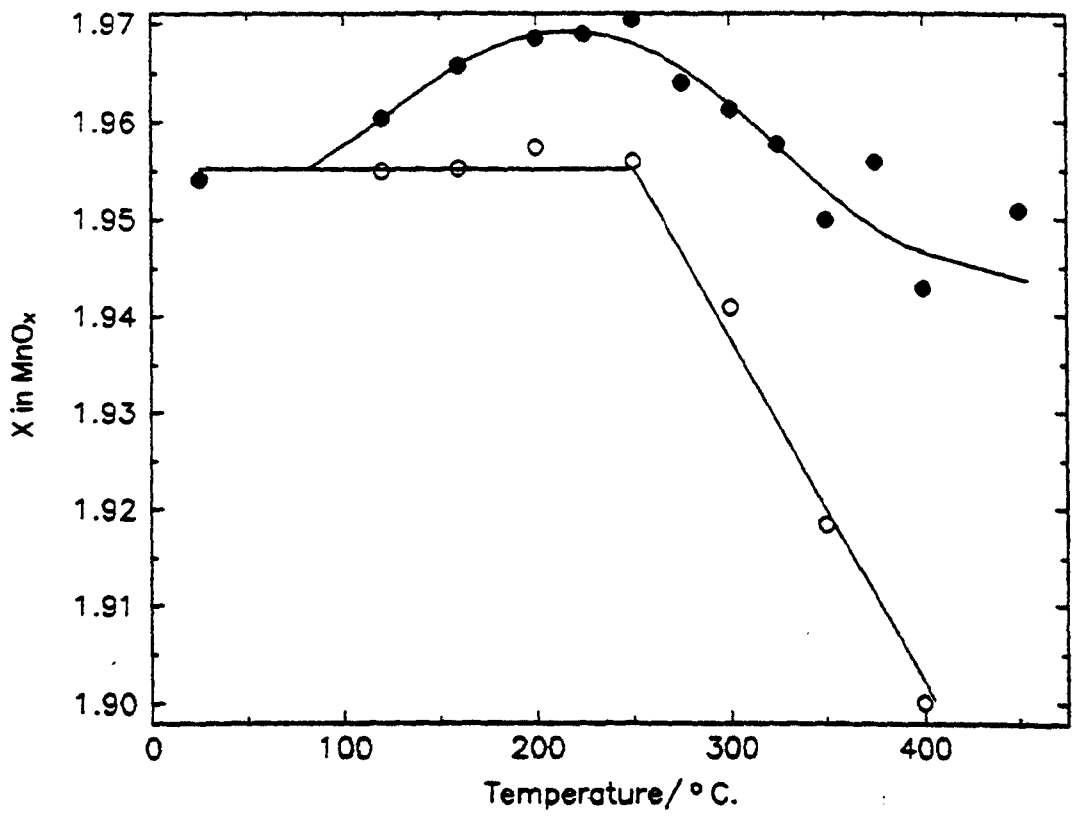


***Figure 3.3*** : Stoichiometry of Chemetals (EMD) after heat-treatment in an air (●) or argon (○) environment for 24 hours.

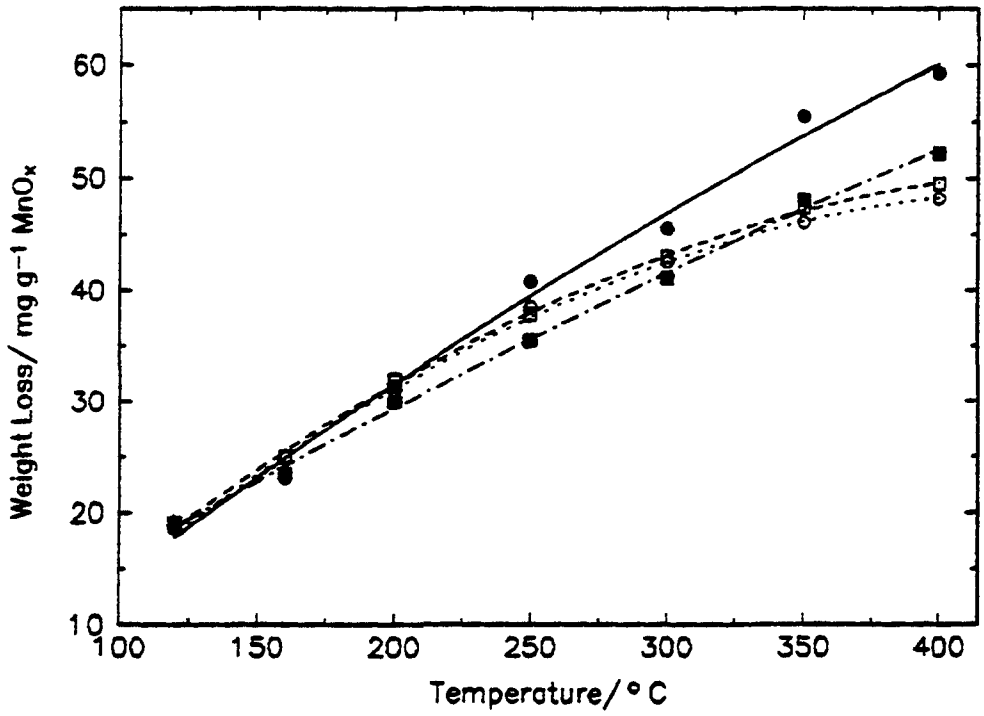


*Figure 3.4* : Sample weight loss and water weight loss for Chemetals EMD (●) weight loss in argon, (○) water loss in argon, (■) weight loss in air, (□) water loss in air.

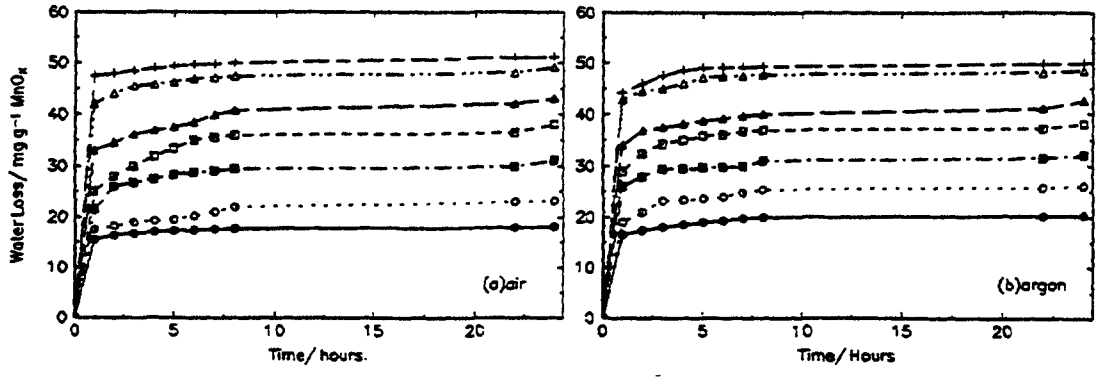


*Figure 3.5* : Water evolution from Chemetals EMD in (a) air and (b) argon. heat-treatment temperatures (●)120°C, (○)160°C,(■)200°C,(□)250°C,(▲)300°C,(Δ)350°C and (+)400°C. Duration 24 hours.

**EMD (R2)**

The stoichiometry in air and argon as a function of the heat-treatment temperature is shown in figure 3.6. Figure 3.7 shows the water and weight loss in air and argon against temperature and figure 3.8 shows the rate of water evolution in air and argon respectively.

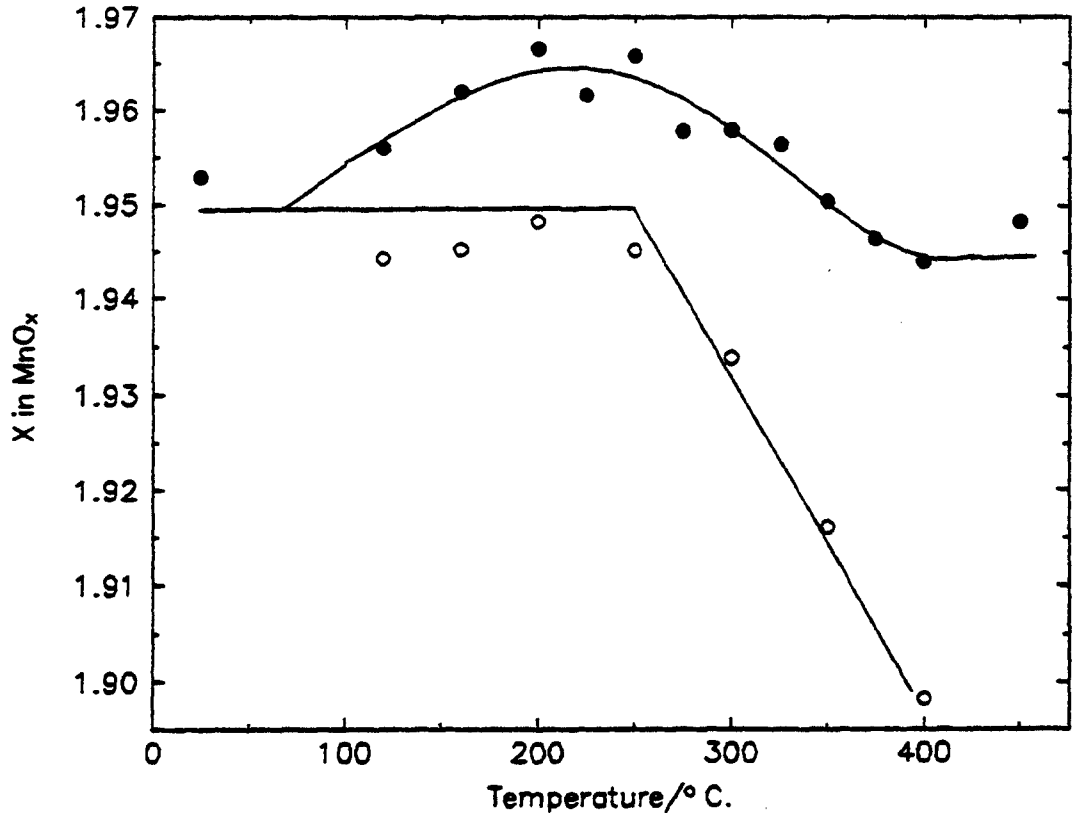


***Figure 3.6*** : Stoichiometry of R2 (EMD) after heat-treatment in an air (●) or argon (○) environment for 24 hours.

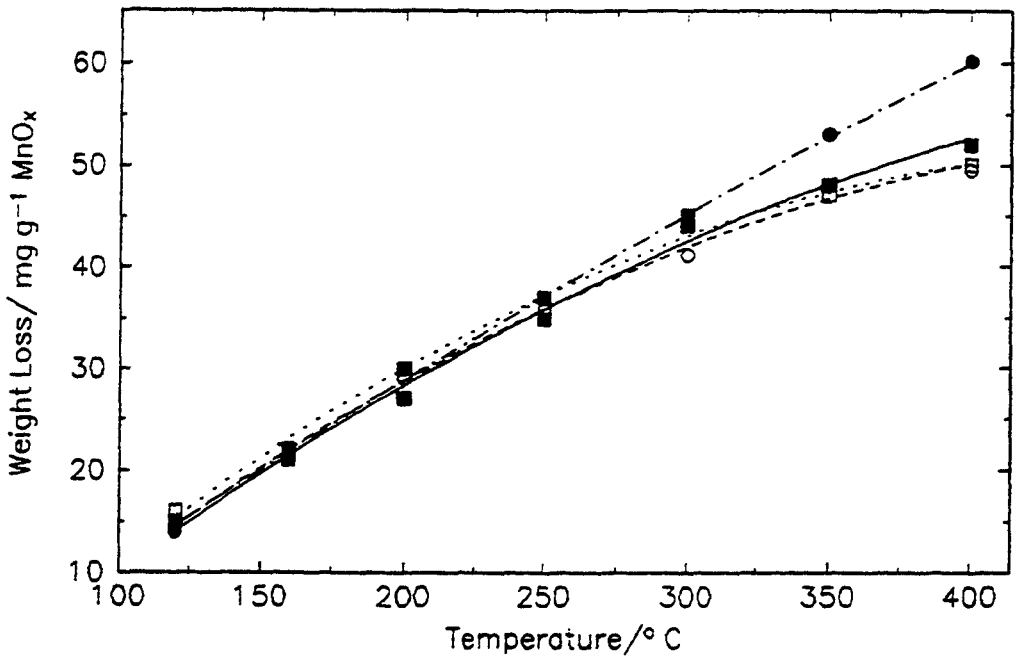


*Figure 3.7* : Sample weight loss and water weight loss for R2 (EMD); (●)weight loss in argon, (○)water loss in argon, (■) weight loss in air, (□) water loss in air.

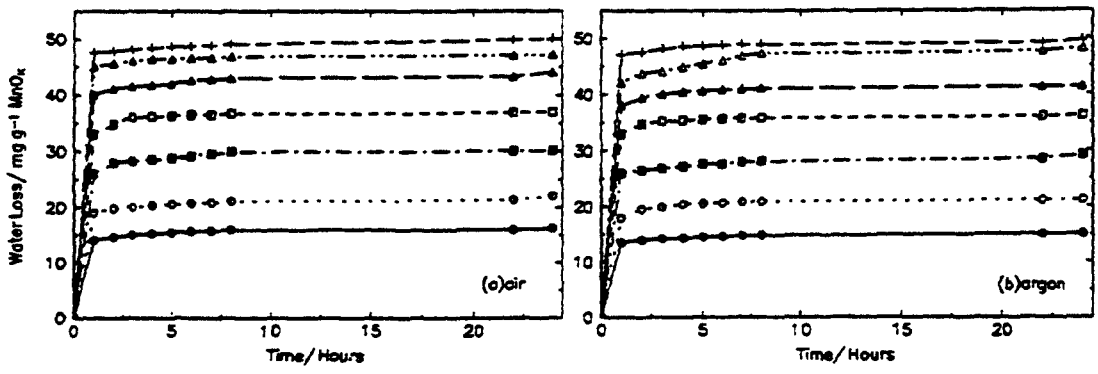


*Figure 3.8* : Water evolution from R2 (EMD) in (a) air and (b) argon. Heat -treatment temperatures (●)120°C,(○)160°C,(■)200°C,(□)250°C,(▲)300°C,(Δ)350°C and (+)400°C. Duration 24 hours.

**CMD (Faradiser WSLi)**

The stoichiometry in air and argon as a function of the heat-treatment temperature is shown in figure 3.9. Figure 3.10 shows the water and weight loss in air and argon against temperature and figure 3.11 shows the rate of water evolution in air and argon respectively.

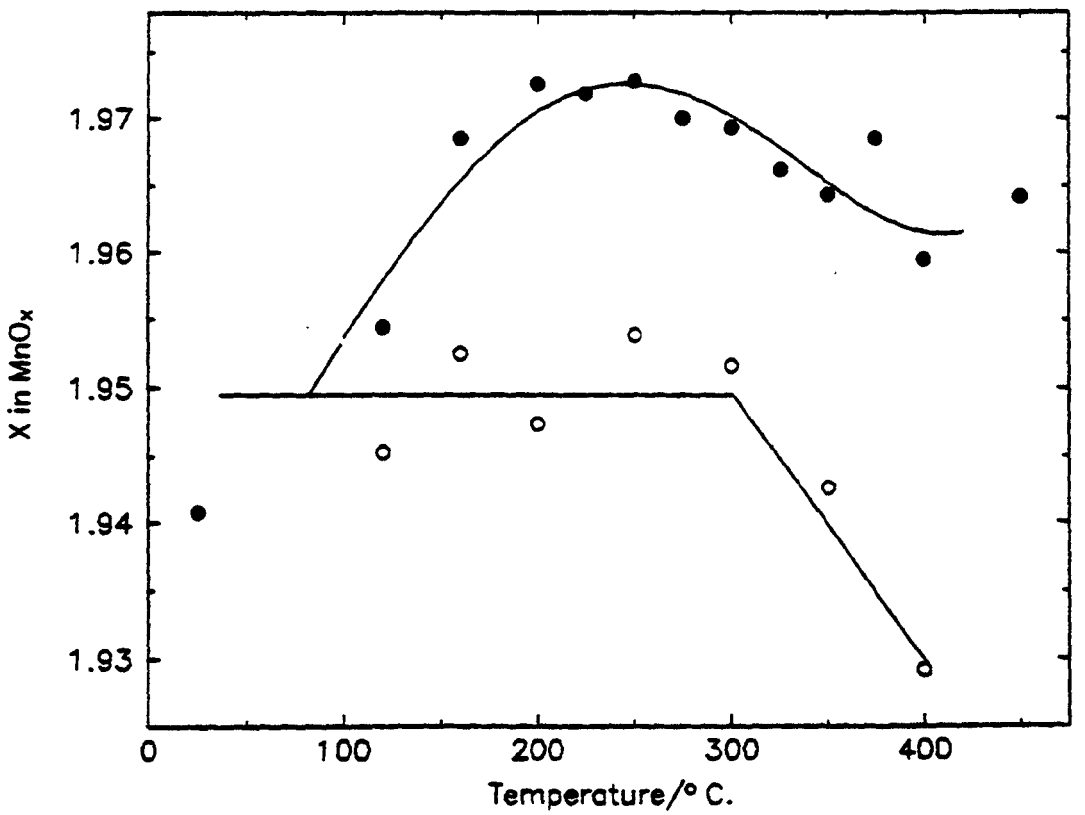


***Figure 3.9*** : Stoichiometry of Faradiser WSLi (CMD) after heat-treatment in an air (●) or argon (○) environment for 24 hours.

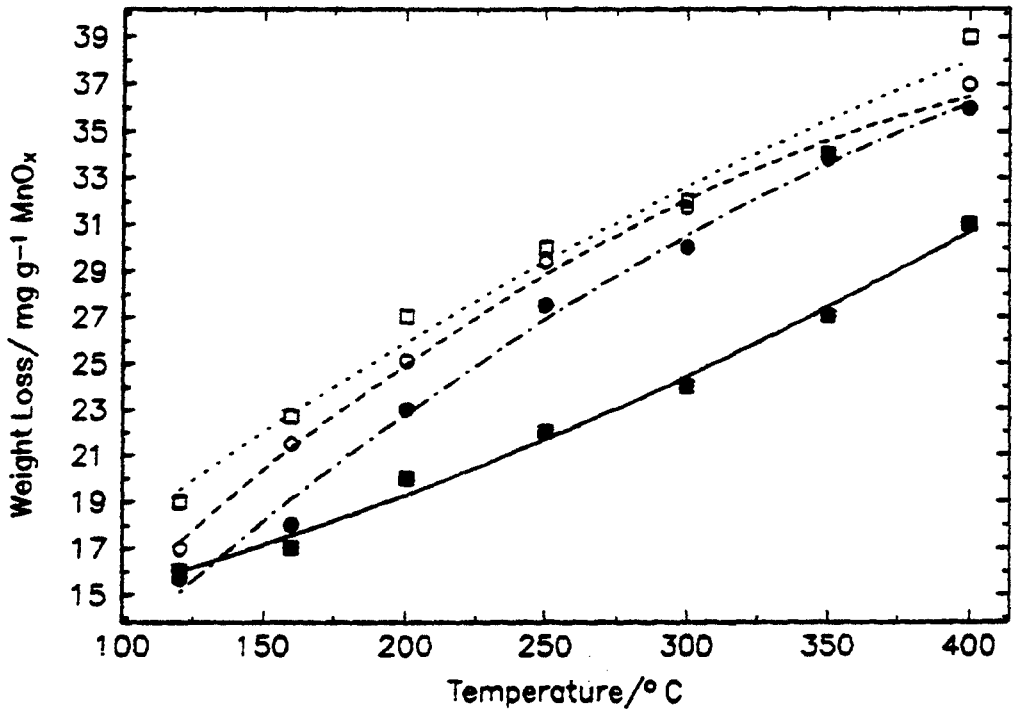


*Figure 3.10* : Sample weight loss and water weight loss for Faradiser WSLi (CMD); (●) weight loss in argon, (○) water loss in argon,(■)weight loss in air and (□)water loss in air.

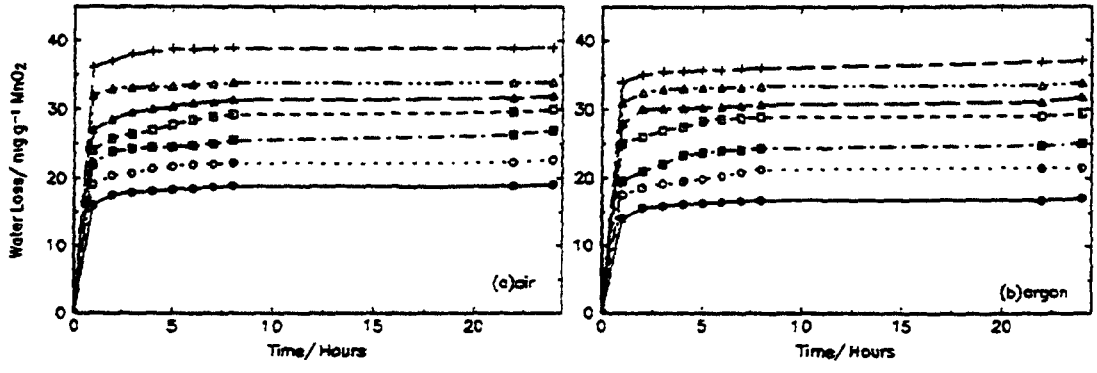


*Figure 3.11* : Water evolution from Faradiser WSLi in (a) air and (b) argon. Heat-treatment Temperatures (●)120°C,(○)160°C,(■)200°C,(□)250°C,(▲)300°C,(Δ)350°C and (+)400°C. Duration 24 Hours.

**CMD (Faradiser M)**

The stoichiometry in air and argon as a function of the heat-treatment temperature is shown in figure 3.12. Figure 3.13 shows the water and weight loss in air and argon against temperature and figure 3.14 shows the rate of water evolution in air and argon respectively.

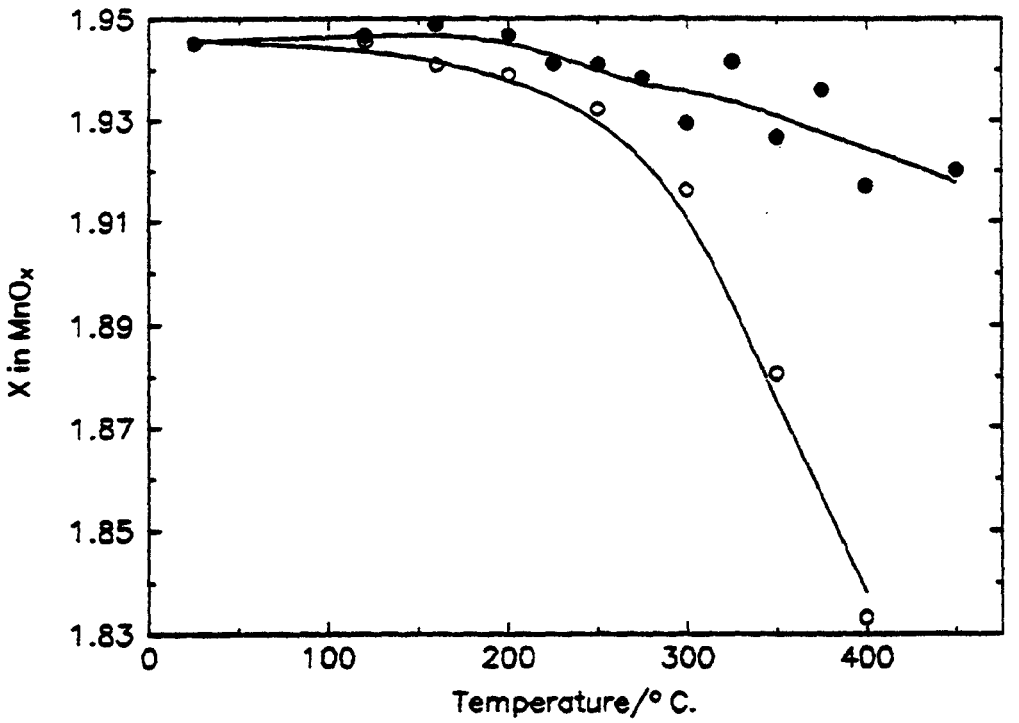


*Figure 3.12* : Stoichiometry of Faradiser M (CMD) after heat-treatment in an air (●) or argon (○) environment for 24 hours.

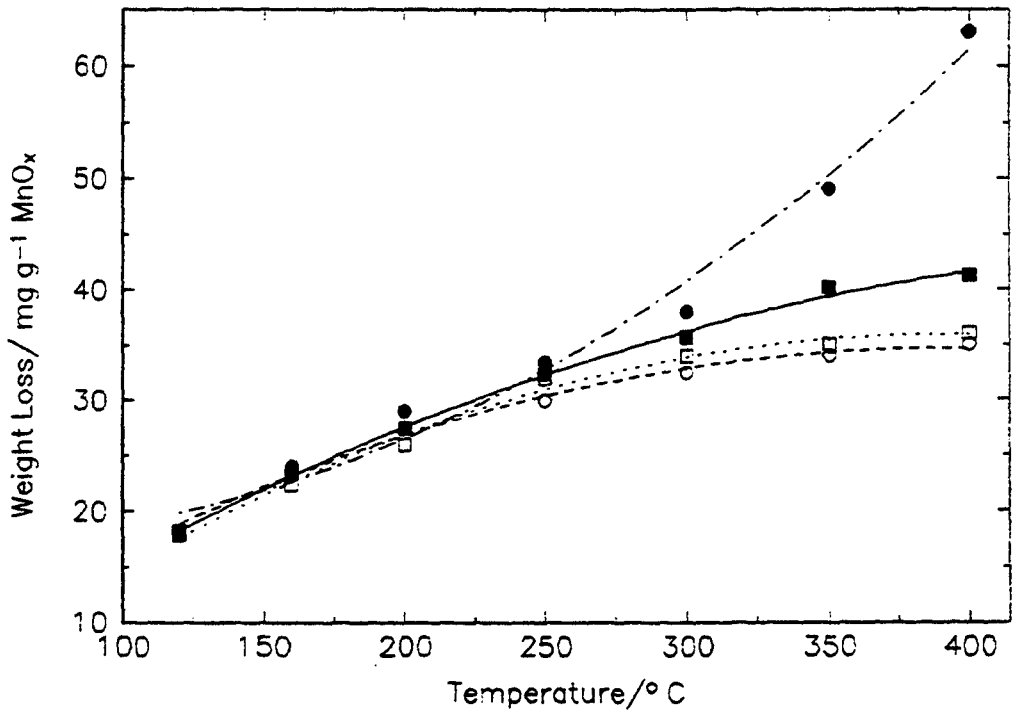


*Figure 3.13* : Sample weight loss and water weight loss for Faradiser M (CMD);(●)weight loss in argon,(○)water loss in argon,(■)weight loss in air,(□)water loss in air.

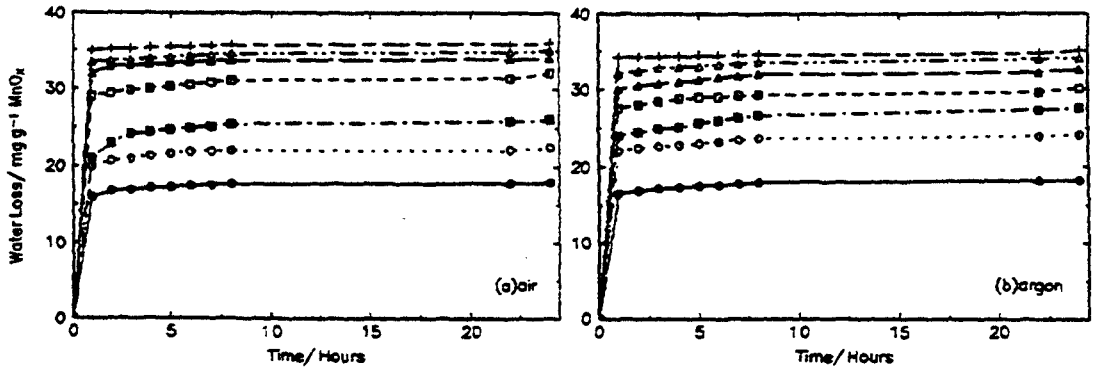


*Figure 3.14*: Water evolution from Faradiser M in (a) air and (b) argon. Heat-treatment temperatures (●)120°C,(○)160°C,(■)200°C,(□)250°C,(▲)300°C,(Δ)350°C and (+)400°C. Duration 24 hours.

**General Comments.**

The following key points can be assimilated from examination of figures 3.3-3.14.

(i) The stoichiometry of $MnO_2$ (except Faradiser M) reached a maximum in air at 250°C. It then decreased from 250-450°C to approximately the same x value of the unheated material. In other words there was no observable oxygen loss when $MnO_2$ was heat-treated up to 450°C in air.

(ii) In an argon atmosphere the stoichiometry of $MnO_2$ remained unchanged on heat-treatment from 25-300°C and decreases thereafter. In other words oxygen loss was observed after 300°C in an argon environment.

(iii) The rate and the amount of water evolution was the same in air and argon (see figures 3.5, 3.8, 3.11 and 3.14).

(iv) In an argon atmosphere the weight and water loss of $MnO_2$ were equivalent up to 300°C. After this the weight loss exceeded the water loss. This was particularly so for Faradiser M (figure 3.13). In an air environment the weight and water loss were comparable up to 400°C, although for Faradiser WSLi the water loss was appreciably more.

**Explanations For The Different Behaviour In Air And Argon**

The increase of x in $MnO_x$ with heat-treatment temperature has been reported in the literature by Preisler (1980) and figure 3.15 compares the results of this work with those found in the literature. Good agreement was found with the data of Preisler and Ohzuku. The results of Ikeda show a similar trend except that the x values were very high[†††] and only pyrolusite had a stoichiometry very close to 2. The results of Parida would seem to be erroneous as he has shown oxygen evolution below 400°C and, as pointed out by Kozawa, $MnO_2$ is thermodynamically stable up to 425°C in air. The cause for the increase of x in $MnO_x$ with heat-treatment temperature is due to the condensation of hydroxyl groups. Oxygen vacancies are then created in the lattice which are available for the uptake of oxygen from the air. This explains why the x value did not increase in argon because there was no oxygen available to go into the vacancies. Equations 3.1 and 3.2 show the different reactions in air and argon.

[†††]This could be a consequence of the method of measuring x in $MnO_x$ because the trend in the data was the same as reported in this work and by Preisler (1980).

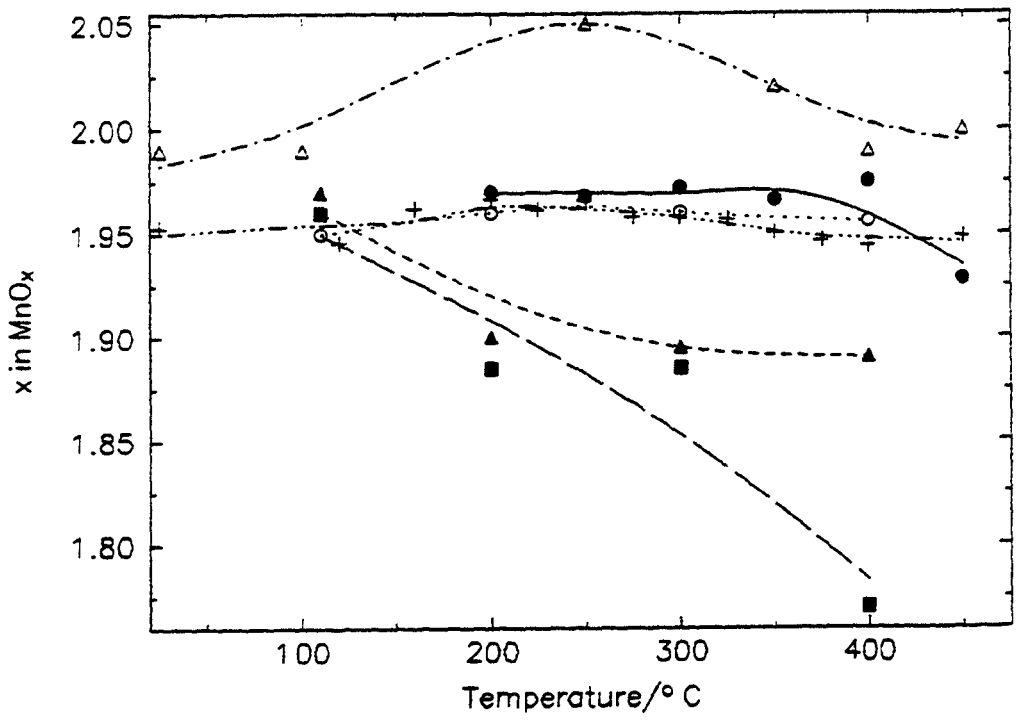


*Figure 3.15* : Published data of x in $MnO_x$ with heat-treatment temperature; (●)Ohzuku 1990,(○)Preisler 1980,(Δ)Ikeda 1975,(▲)Parida (emd) 1983,(■)Parida (cmd) 1983 and (+)this work.

$$4MnOOH + O_2 \Rightarrow 2MnO_2 + 2H_2O \qquad (3.1)$$

$$2MnOOH \Rightarrow Mn_2O_3 + H_2O \qquad (3.2)$$

**Quantification of the differences between the water and weight loss of $MnO_2$ with heat treatment temperature in an air or argon environment.**

Figures 3.4, 3.7, 3.10,and 3.13 show the water and weight loss of $MnO_2$ against heat-treatment temperature and it was noted that in air the water loss was sometimes greater than the weight loss and the opposite behaviour occurred in argon. The purpose of this section is to seek the explanation of those differences. There are two different ways of determining any oxygen changes during the heat-treatment of $MnO_x$. The first is the difference between the weight loss of manganese dioxide (determined by weighing the $MnO_x$ before and after heat-treatment) and the water loss (determined by the change in weight of the drying tube containing magnesium perchlorate). If the weight loss was greater than the water loss then $O_2$ was evolved. The second method is the

stoichiometry of $MnO_x$ as calculated by chemical analysis. Any oxygen changes were calculated from the differences in the molecular weight of $MnO_x$ before and after heat-treatment. The results of this type of analysis are shown in figures 3.16-3.19 for the four materials. Lines of unit slope passing through the origin are drawn on the graphs and if the data from the two sources were identical they would lie on the line From examination of figures 3.16-3.19 it can be seen that there is reasonable correlation between the two sets of data.

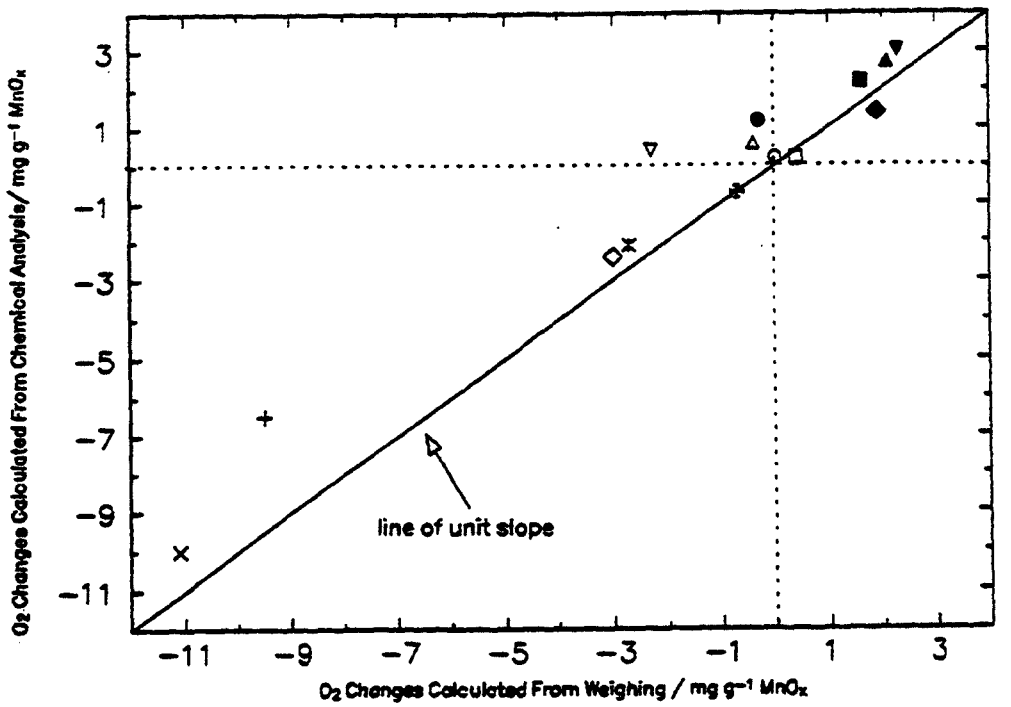


*Figure 3.16* : Correlation between the $O_2$ changes calculated from chemical analysis and weighing $MnO_2$ for Chemetals EMD (positive means $O_2$ gain,negative $O_2$ loss):(○,●)120°C,(□,■)160°C,(Δ,▲)200°C,(▽,▼ )250°C,(◇,◆)300°C,(+,+)350°C and (x,✕)400°C.Open Symbols argon,closed symbols air.

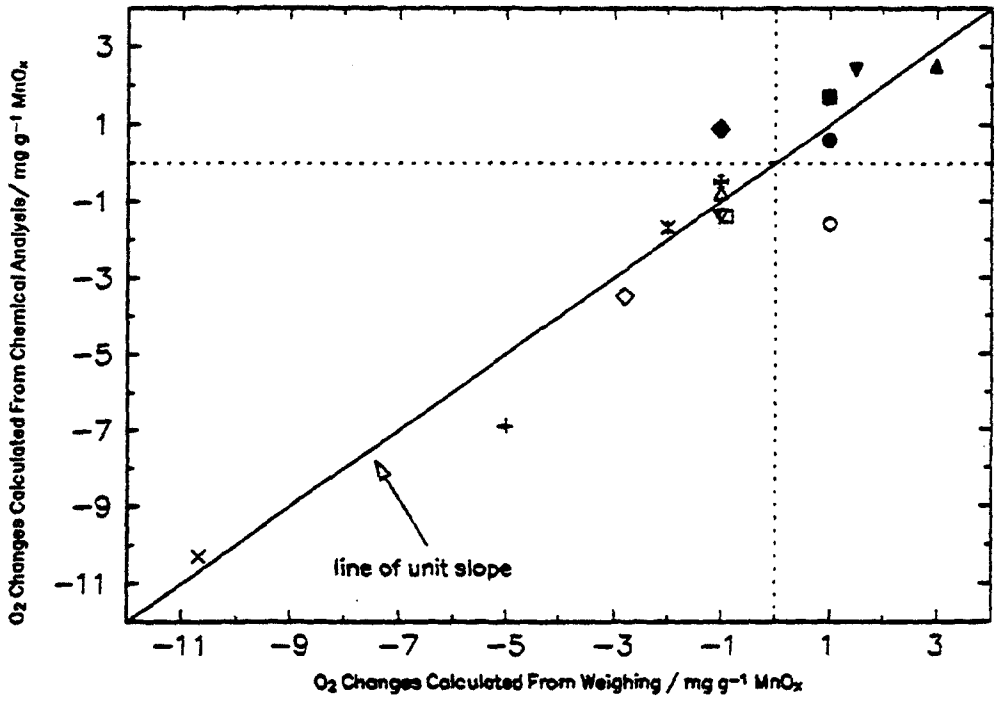


*Figure 3.17* : Correlation between the $O_2$ changes calculated from chemical analysis and weighing $MnO_2$ for R2 EMD (positive means $O_2$ gain, negative means $O_2$ loss):(○,●)120°C,(□,■)160°C,(Δ,▲)200°C,(∇,▼ )250°C,(◇,◆)300°C,(+,+)350°C and (x,✳)400°C. Open symbols argon, closed symbols air.

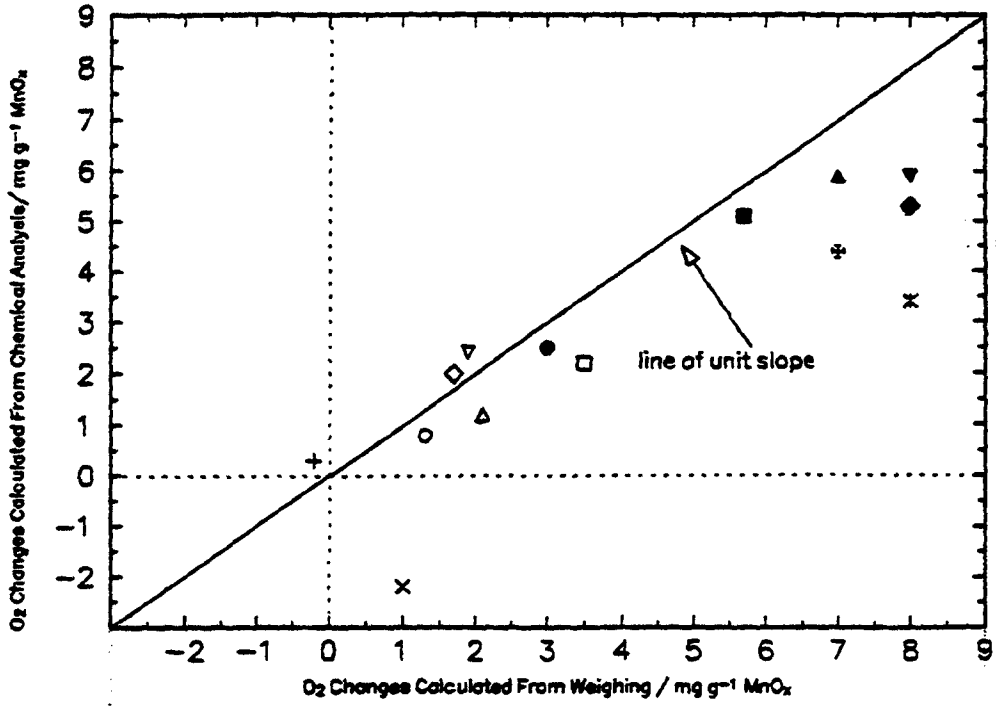


*Figure 3.18*: Correlation between the $O_2$ changes calculated from chemical analysis and weighing $MnO_2$ for Faradiser WSLi (positive means $O_2$ gain, negative means $O_2$ loss): (○,●)120°C,(□,■)160°C,(Δ,▲)200°C,(∇,▼ )250°C,(◇,◆)300°C,(+,+)350°C and (x,✳)400°C. Open symbols argon, closed symbols air.

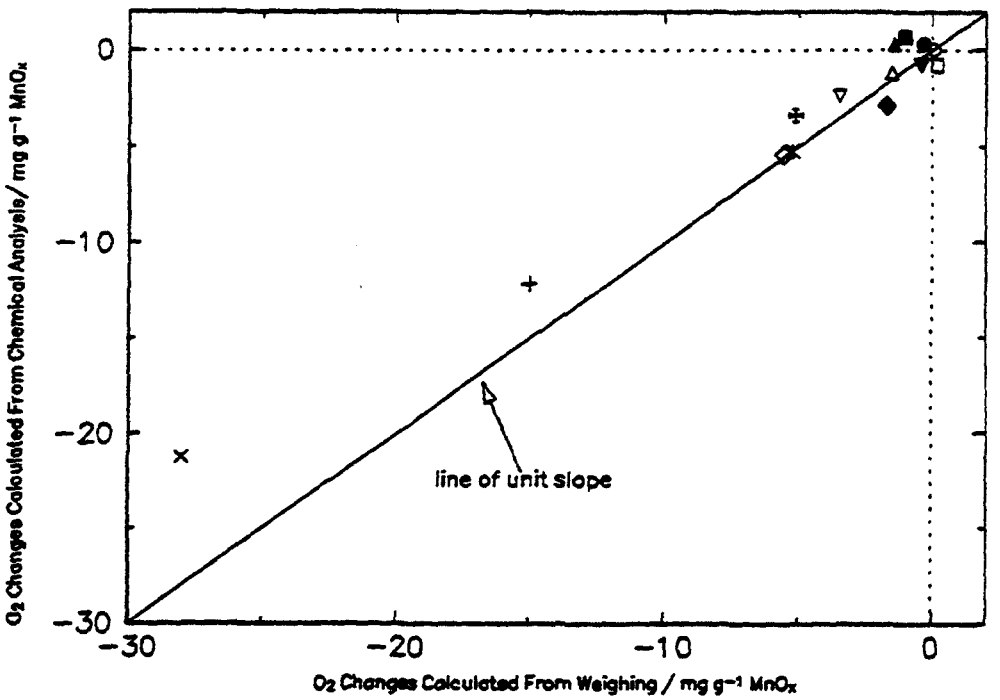


*Figure 3.19* : Correlation between the $O_2$ changes calculated from chemical analysis and weighing $MnO_2$ for Faradiser M (positive means $O_2$ gain, negative means $O_2$ loss): (○,●)120°C,(□,■)160°C,(Δ,▲)200°C,(▽,▼ )250°C,(◇,◆)300°C,(+,+)350°C and (x,✳)400°C. Open symbols argon, closed symbols air.

## Further Data Correlation.

In this section the correlations between further different sets of data are carried out. The data used are the weight loss of $MnO_2$ and the manganese content of the heat-treated material that was determined by potentiometric titration. The expected manganese content was calculated from equation 3.3.

$$\text{Expected \% Mn} = \frac{\text{Mn content of starting material}}{100 - \text{\% weight loss during heat treatment}} \times 100\% \qquad (3.3)$$

The analytical % manganese was calculated from the potentiometric titration[†]. The results of this analysis are shown in figures 3.20-3.23 for the four materials. Lines of unit slope passing through the origin are drawn on the figures. By definition the starting material must lie on that line because the expected manganese content was based on the starting material. As can be seen from figures 3.20-3.23 there is a good correlation between the expected and analytical % Mn.

[†]The KMno4 was standardised against sodium oxalate.

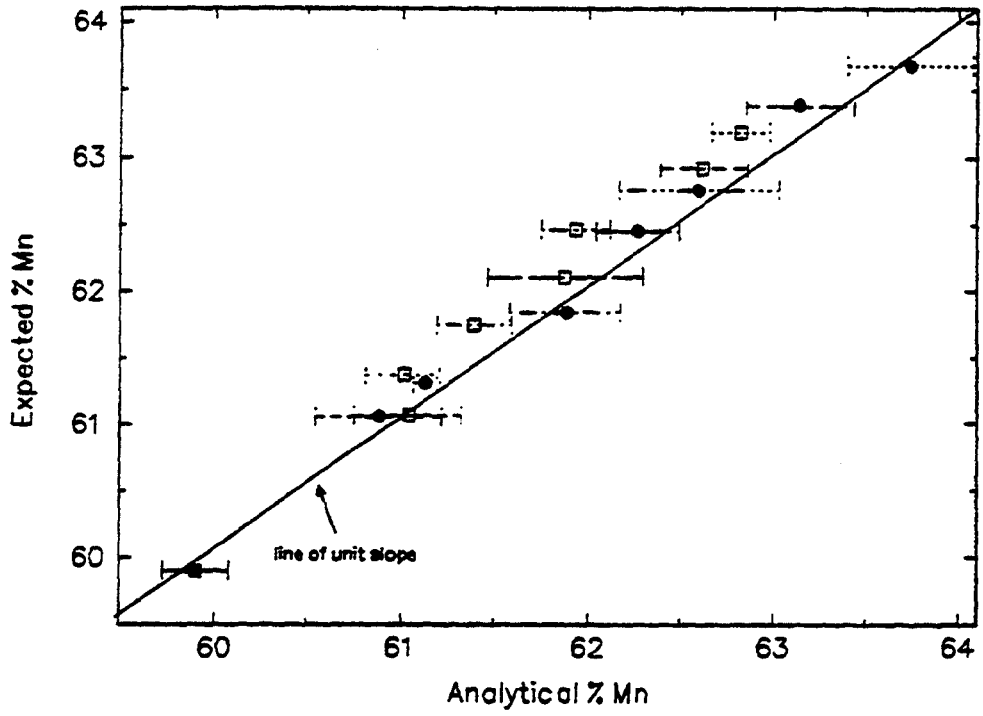


*Figure 3.20* : Correlation between the expected % Mn and analytical % Mn for Chemetals EMD: (□)air, (●)argon; (error bars ± $\sigma_{n-1}$)

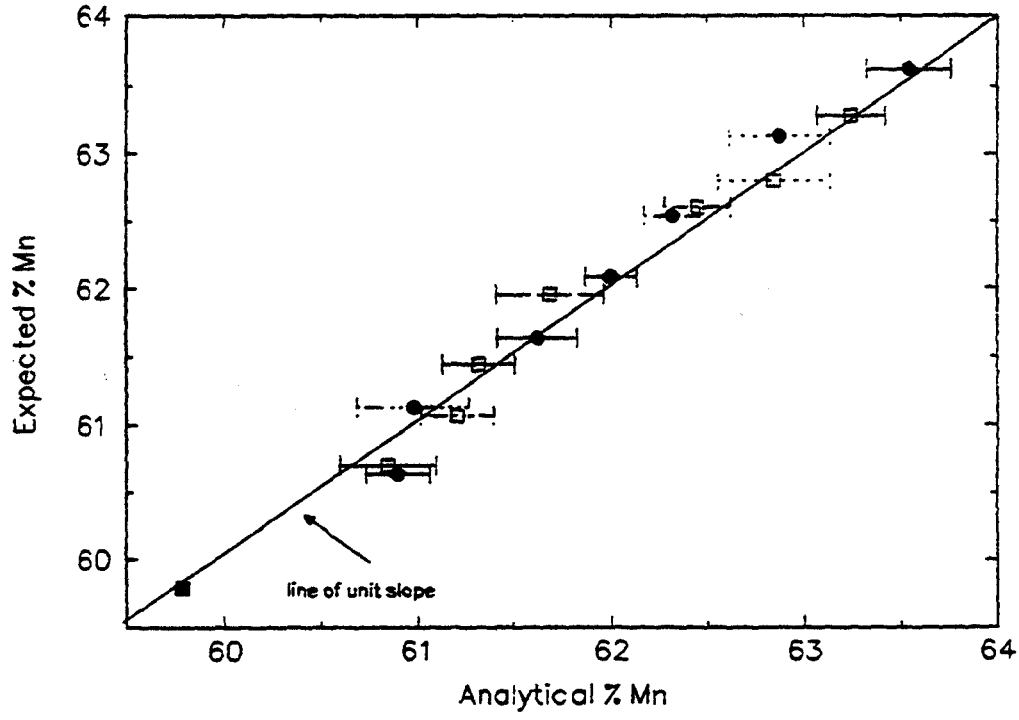


*Figure 3.21* : Correlation between the expected % Mn and the analytical % Mn for R2 EMD: (□)air, (●)argon; (error bars $\pm\sigma_{n-1}$)

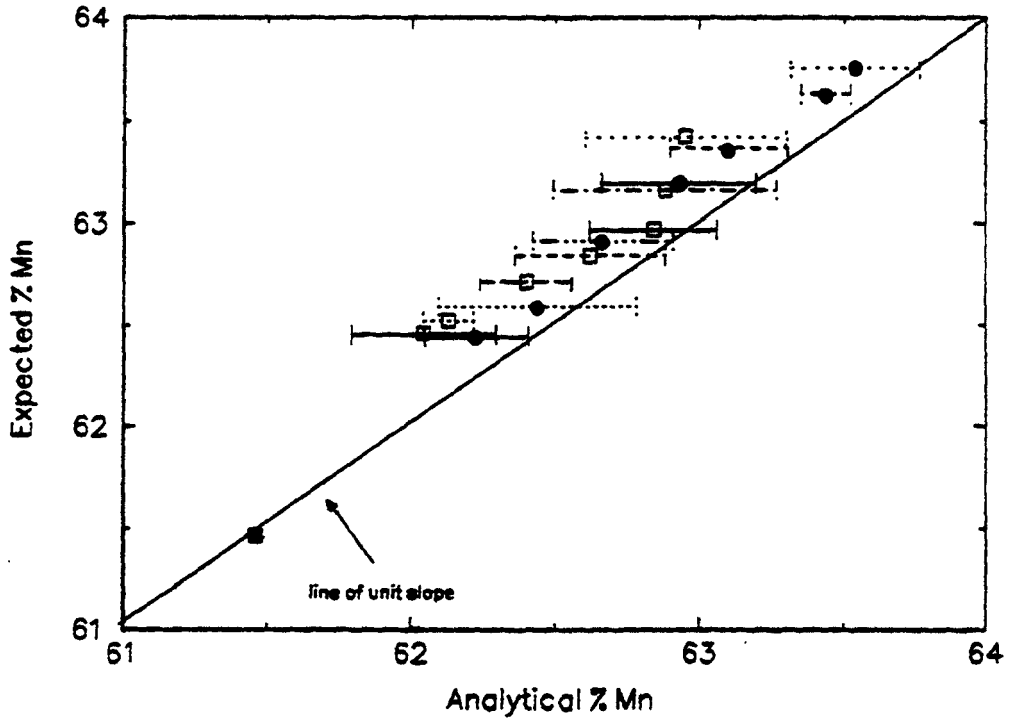


*Figure 3.22* : Correlation between the expected % Mn and the analytical % Mn for Faradiser WSLi: (□)air, (●)argon; (error bars $\pm\sigma_{n-1}$).

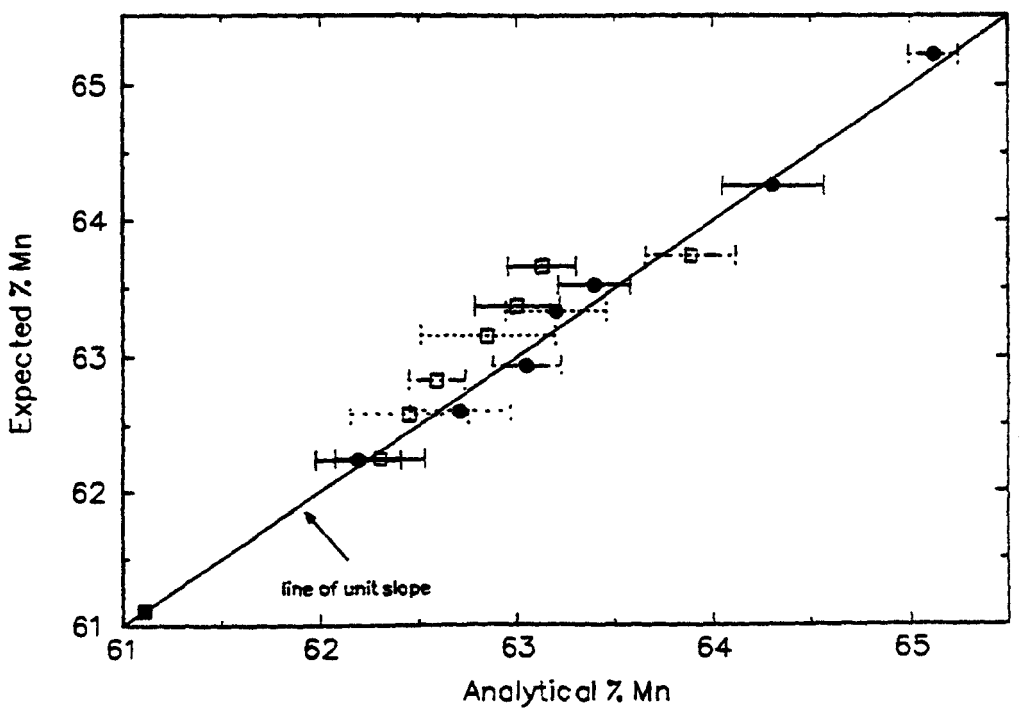


*Figure 3.23* : Correlation between the expected % Mn and the analytical % Mn for Faradiser M: (□)air, (●)argon; (error bars $\pm\sigma_{n-1}$)

## 3.5 Pyknometric density measurements.

The work in this section is based on the work of Brown *et al.* (1981). The advantage of density measurements is that it is possible to differentiate between the types of water in $MnO_2$ which was not possible with the data presented in section 3.4. The experimental details for this area of work were given in section 2.8.

The following measurements were taken in order to calculate the density of manganese dioxide.

(a) weight of density bottle.

(b) weight of density bottle plus $H_2O$ at 25 °C to fill the bottle.

(c) weight of density bottle plus $MnO_2$.

(d) weight of density bottle plus $MnO_2$ plus $H_2O$ at 25 °C to fill the bottle.

(e) weight of $MnO_x$ after heat-treatment.

(f) weight of $MnO_x$ before heat-treatment.

The density of the $MnO_2$ before any heat-treatment ("as received") was calculated from equation 3.4.

$$\rho^{\bullet} = \frac{f\ \rho_{H_2O}}{b + c - a - d} \qquad (3.4)$$

The density of $MnO_2$ after heat-treatment ($\rho_{exp}$) was calculated from equation 3.5.

$$\rho_{exp} = \frac{e\ \rho_{H_2O}}{b + c - a - d} \qquad (3.5)$$

The density may also be calculated from the "as received" density and the weight of water removed by heat-treatment. This is given by equation 3.6.

$$\rho_{calc} = \frac{e\ \rho_{H_2O}\ \rho^{\bullet}}{f\ \rho_{H_2O} - (f - e)\ \rho^{\bullet}} \qquad (3.6)$$

where $\rho_{H2O}$ is the density of water at 25 °C.

The calculated ($\rho$calc) and experimental ($\rho$exp) density of manganese dioxide will be the same if the water removed by heat-treatment had the same density as that of normal water ($\rho_{H2O}$ 0.9970 $gcm^{-3}$). Therefore by plotting the experimental density against the calculated density it is possible to determine

when all the physisorbed water had been removed. The results of the experimental density of $MnO_2$ against the calculated density of $MnO_2$ for the materials under investigation are given in figures 3.24-3.27.

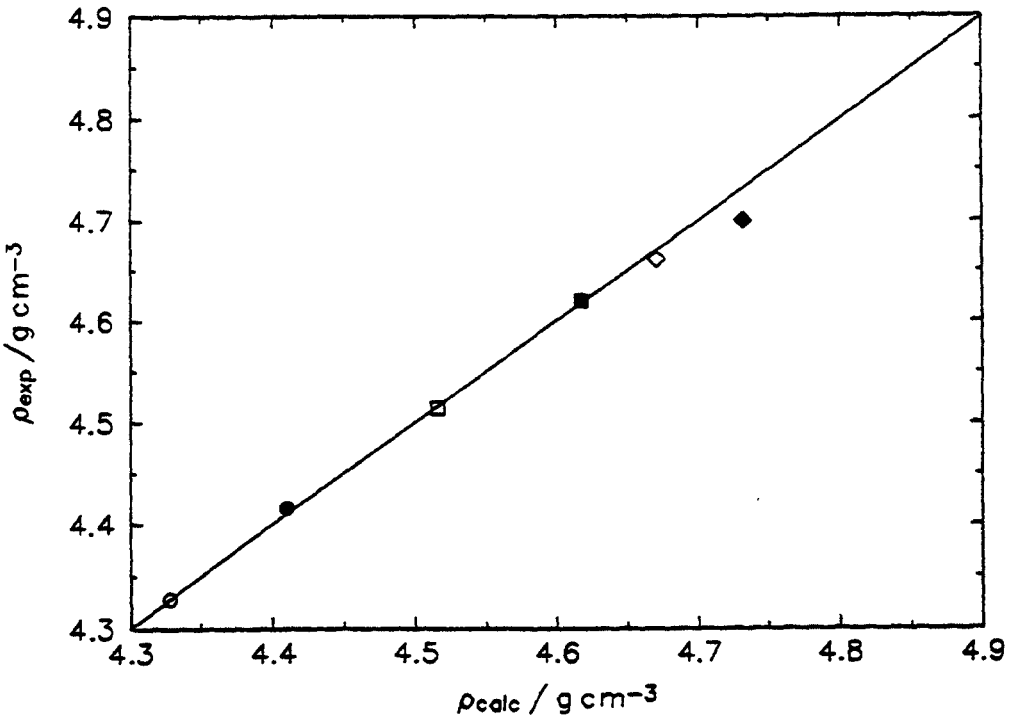


***Figure 3.24*** : Experimental density (ρexp) against calculated (ρcalc) density for Chemetals EMD (○)as received,(●)evacuated 24 hrs,(□)80°C,(■)120°C,(◇)140°C and (◆)160°C. Heat-treatment duration 24 hours in air.

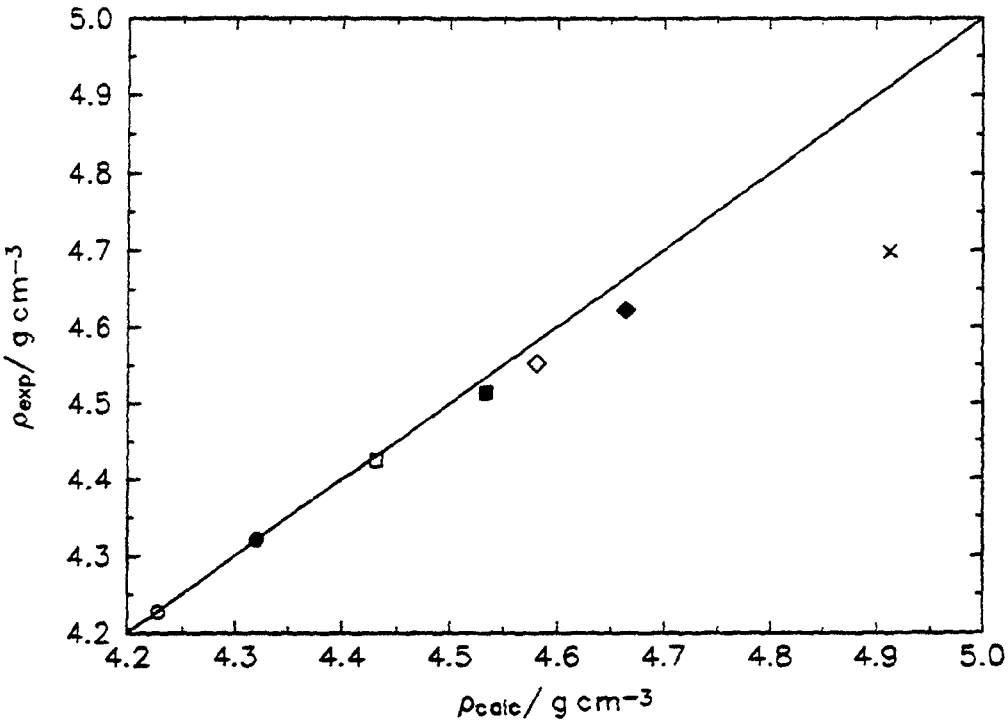


*Figure 3.25* : Experimental density ($\rho_{exp}$) against calculated ($\rho_{calc}$) density for R2 EMD (○)as received,(●)evacuated 24hrs,(□)80°C,(■)120°C,(◇)140°C,(◆)160°C and(x)250°C.Heat-treatment duration 24 Hours in air.

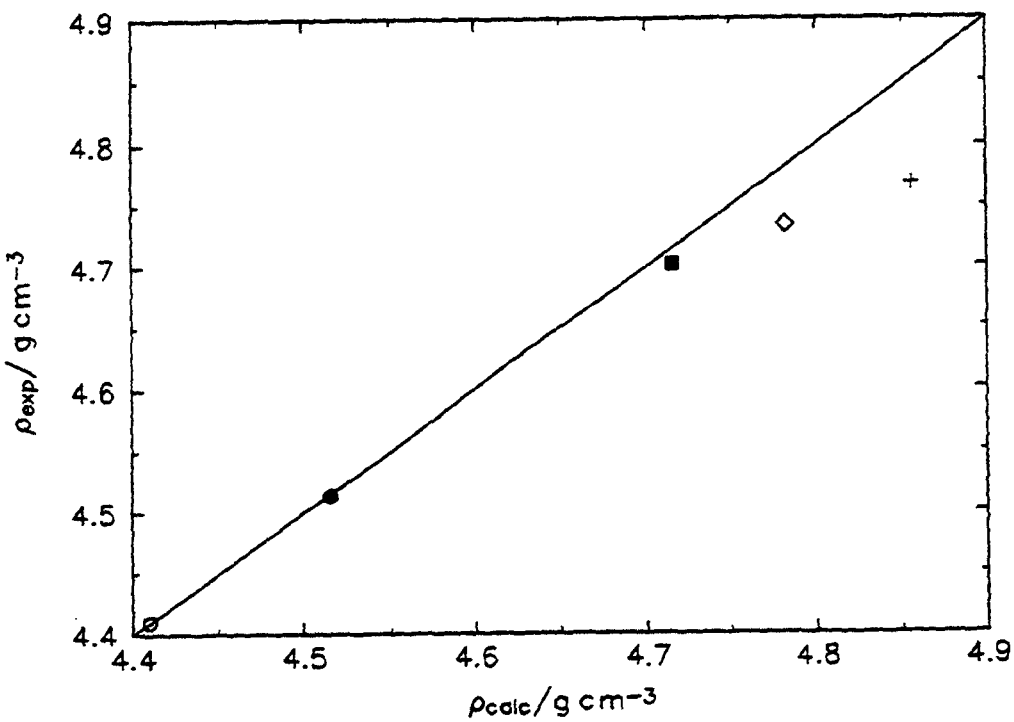


*Figure 3.26* : Experimental density ($\rho_{exp}$) against calculated density ($\rho_{calc}$) for Faradiser WSLi CMD,(○)as received,(●)evacuated 24 hrs,(■)120°C,(◇)140°C and (+)200°C. Heat-treatment duration 24 Hours in air.

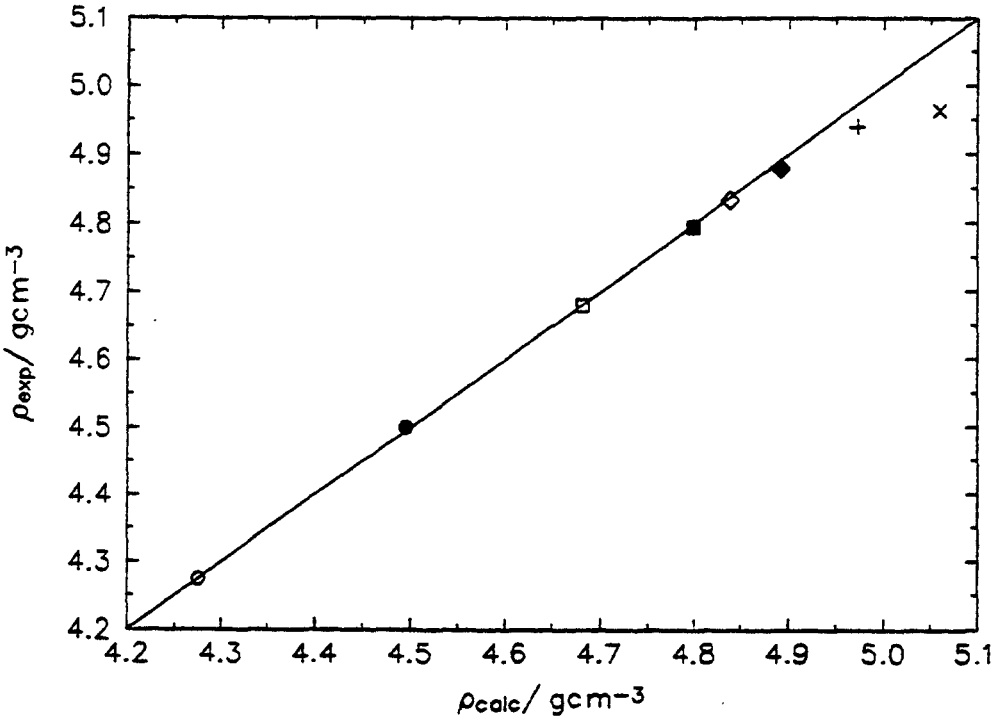


*Figure 3.27* : Experimental density ($\rho_{exp}$) against calculated density ($\rho_{calc}$) for Faradiser M C M D , ( O ) a s r e c e i v e d , ( ● ) e v a c u a t e d 2 4 hrs,(□)80°C,(■)120°C,(◇)140°C,(◆)160°C,(+)200°C and (x)250°C.Heat-treatment duration 24 hours in air.

The following observations can be made from examination of figures 3.24-3.27.

(i) The water that was removed by evacuating at room temperature for 24 hours and heat-treatment at 80°C had the same density as that of normal water (0.9970 $gcm^{-3}$) because the calculated and experimental densities lie on the same line.

(ii) When $MnO_2$ was heat-treated at 120-160°C the calculated and experimental densities were not equivalent. The reason for this type of behaviour is that the water removed at these temperatures had a density that is higher than that of normal water.

(iii) When $MnO_2$ was heat-treated at 200-250°C there was a further departure in the calculated and experimental densities. The water removed at these temperatures was of a different nature to that which was removed at 120-160°C.

In the paper by Brown *et al.* (1981) they attributed the water that was removed in (ii) to strongly bound physisorbed molecular water hydrogen-bonded

with the $MnO_2$ surface. The water that was removed in (iii) was due to the condensation of hydroxyl groups and this generated considerable microporosity in the $MnO_2$. The results shown here agree with those of Brown *et al.* (1981) and it is also worth noting that for samples heat-treated at 200-250°C gas evolution was observed in the density bottles and this was caused by the condensation of hydroxyl groups. The reason for this can be explained by equation 3.7.

$$4MnO_2 + 2H_2O \rightleftharpoons 4MnOOH + O_2 \qquad (3.7)$$

As the number of hydroxyl groups in the heat-treated $MnO_x$ was decreased by heat-treatment at 200-250°C the equilibrium could only be re-established after equation 3.7 had moved to the right to form more hydroxyl ions in the solid phase†. Movement of equation 3.7 to the right generated oxygen.

## 3.6 Intensity standard operation of the x-ray diffractometer.

The intensity of the X-ray tube decreased with time principally due to the degradation of the copper target in the X-ray tube. If the X-ray diffraction patterns taken at the same time are compared then it is not necessary to monitor the intensity of the X-ray tube. It will also depend on the atmospheric pressure, for example Klug and Alexander (1974) showed that a 1% increase in pressure caused a 1% decrease in intensity. In this investigation, however, the X-ray diffraction patterns were taken at various time intervals so the intensity of the tube was monitored each time samples were analysed. The peak area of the main peak of Arkansas stone is measured in order to monitor the tube intensity. As can be seen from figure 3.28 the peak is about 25000 counts $sec^{-1}$ high and so any small variations in the tube will be seen. The intensity of the tube as a function of time is shown in figure 3.29 where it can be seen that the tube intensity has decreased by about 25% over a period of thirteen months. In this study all X-ray diffraction patterns were normalised to a tube intensity of 6000 $cs^{-1}$ (relative to the main peak area of Arkansas stone).

†This is in accordance with Le Chatelier's principle which states that 'If a system in equilibrium is subjected to a change' processes occur which tend to counteract the change imposed.

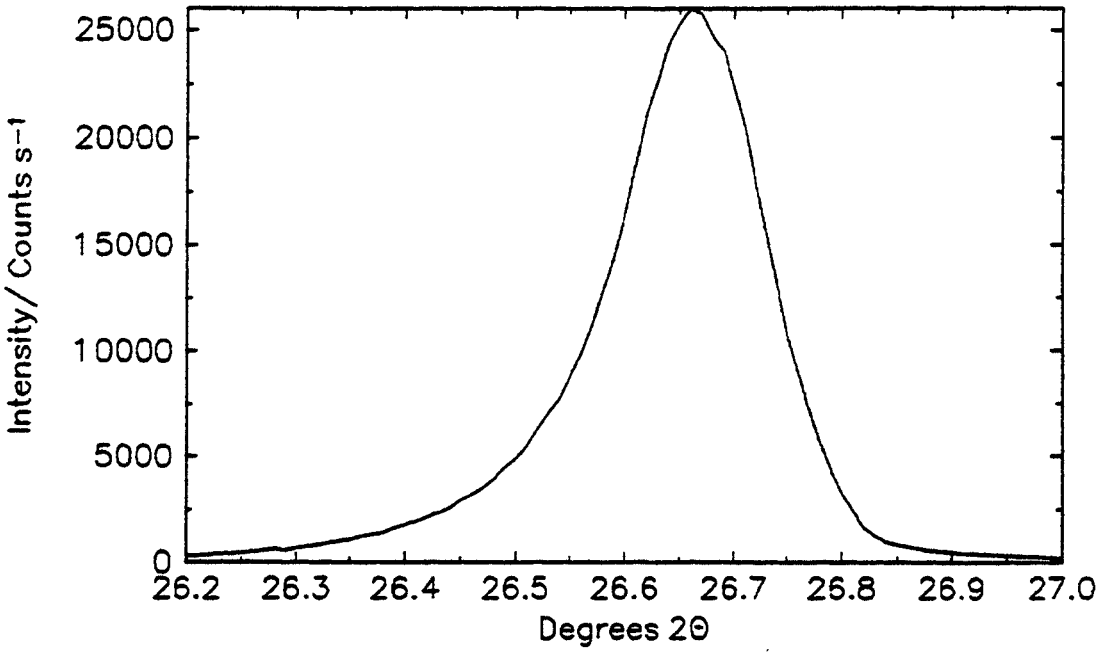


*Figure 3.28*: X-ray diffraction pattern of the main peak of Arkansas stone (this was used to monitor the intensity of the x-ray tube).

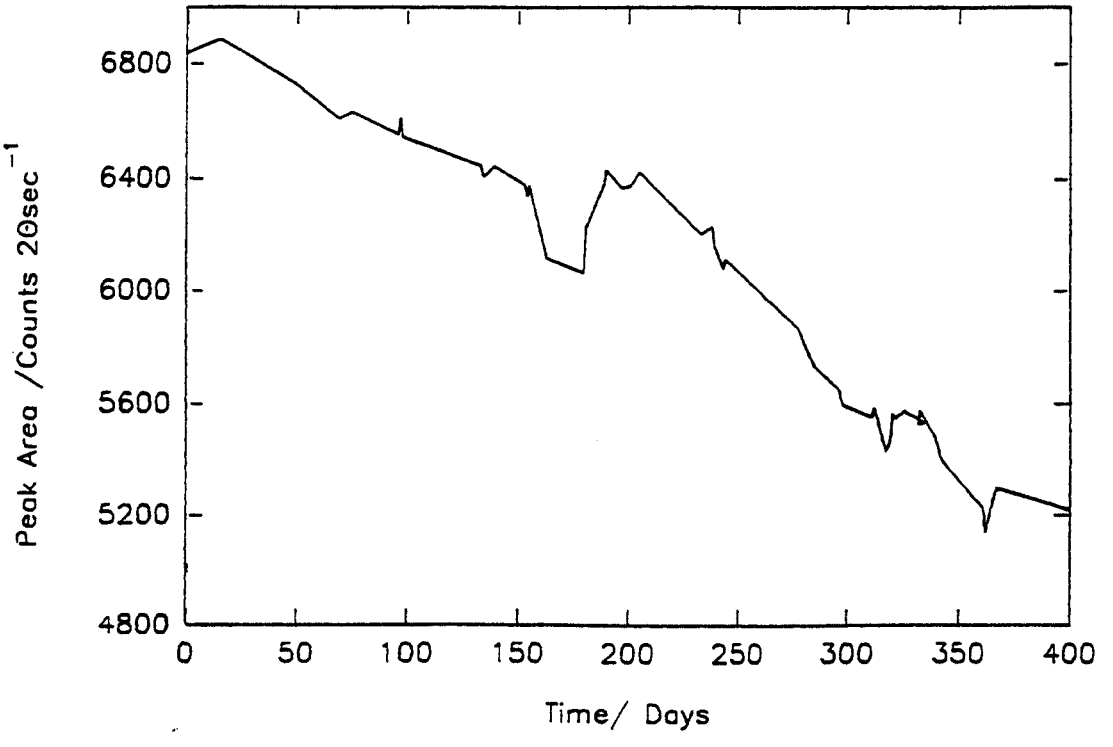


*Figure 3.29* : Measurement of the peak area of Arkansas stone with time (this was used to monitor the intensity of the x-ray tube.

## 3.7 Powder x-ray diffraction spectra of heat-treated manganese dioxides.

Powder X-ray diffraction spectra when $MnO_x$ was heat-treated from 25-450°C are shown in figures 3.30-3.33. From examination of figures 3.30-3.33 it can be seen that the X-ray spectra are essentially unchanged when $MnO_2$ is heat-treated from 25-300°C. From 300-450°C a new peak appears at 28.68°2Θ; this is the $\gamma \rightarrow \beta$ transformation of $MnO_2$. This part of the X-ray diffraction pattern (15-35°2Θ) is shown in more detail in figures 3.34-3.37[†] where the transformation can be seen more clearly. This is further substantiated in figure 3.38 where the peak height intensity at 28.68°2Θ is plotted against heat-treatment temperature. The almost linear increase in intensity after 300°C can be attributed to the change in structure of $MnO_2$. The X-ray diffraction pattern of Faradiser M is virtually identical with that of R2 EMD that had been heat-treated at 300°C for 24 hours (figure 3.39). This is because in the manufacturing process Faradiser M is made from the heat-treatment of manganese carbonate at 320°C. The X-ray diffraction pattern of R2 EMD that had been heat-treated at 400°C is compared with the JCPDS pattern of pyrolusite in figure 3.40. Laudy and de Wolff (1963) carried out an X-ray diffraction investigation of the $\gamma \rightarrow \beta$ transformation of $MnO_2$ and they calculated the X-ray pattern of $\gamma$-$MnO_2$ at various values of pyrolusite concentrations. They found that the computed curves accounted for the main features of the heat-treated materials. The results presented here would suggest that the $\gamma$ phase is predominant to 300°C and the $\gamma \rightarrow \beta$ transformation occurs between 300-400°C. Pistoia (1982) discussed the disagreement in the literature regarding the $\gamma \rightarrow \beta$ transformation. For instance Ikeda (1975) reported a transition from $\gamma \rightarrow \beta$ at 250-350°C whereas Giovanoli (1980) found that there was no change up to 350°C. The discrepancies are probably due to the fact that there are many slightly different crystalline modifications of $MnO_2$ and the duration of the heat-treatment. Figure 3.38 shows a similar behaviour has been found for the $\gamma \rightarrow \beta$ transformation for the materials under investigation .

[†]In 3-D plots the data needs to be equally spaced in the x (degrees 2Θ) and y directions (temperature) and in this case the experimental data was not evenly spaced in the y direction. To overcome this a 3rd or 4th order polynomial equation was fitted to the intensity against temperature data in order to obtain the data in an evenly spaced format. The 3-D plots were performed in the scientific data analysis package called AXUM.

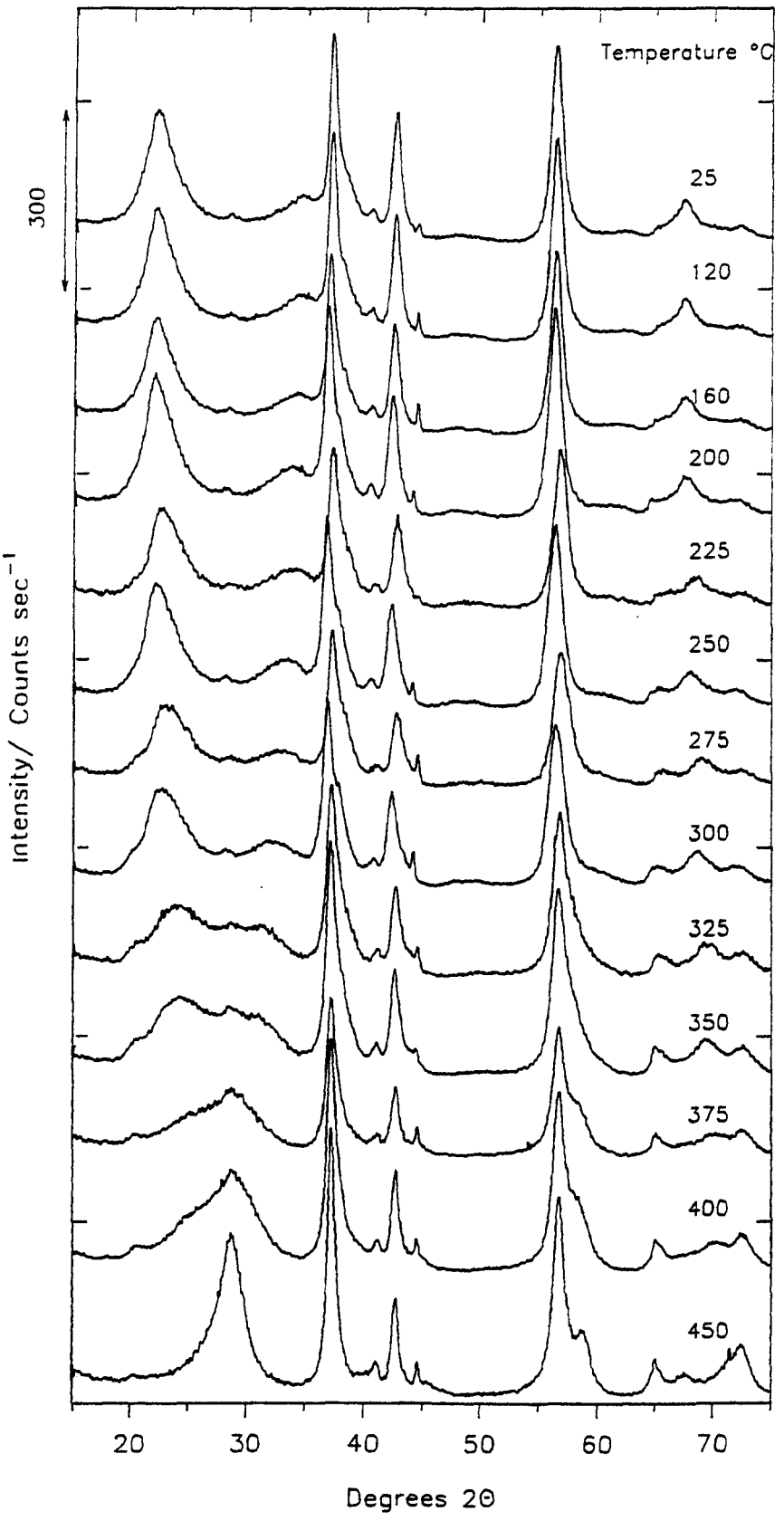


***Figure 3.30*** : **Powder x-ray diffraction spectra for the heat-treatment of Chemetals EMD in the range 25-450°C. Heat-treatment duration 24 hours in air (the heat-treatment temperature is given above the XRD pattern).**

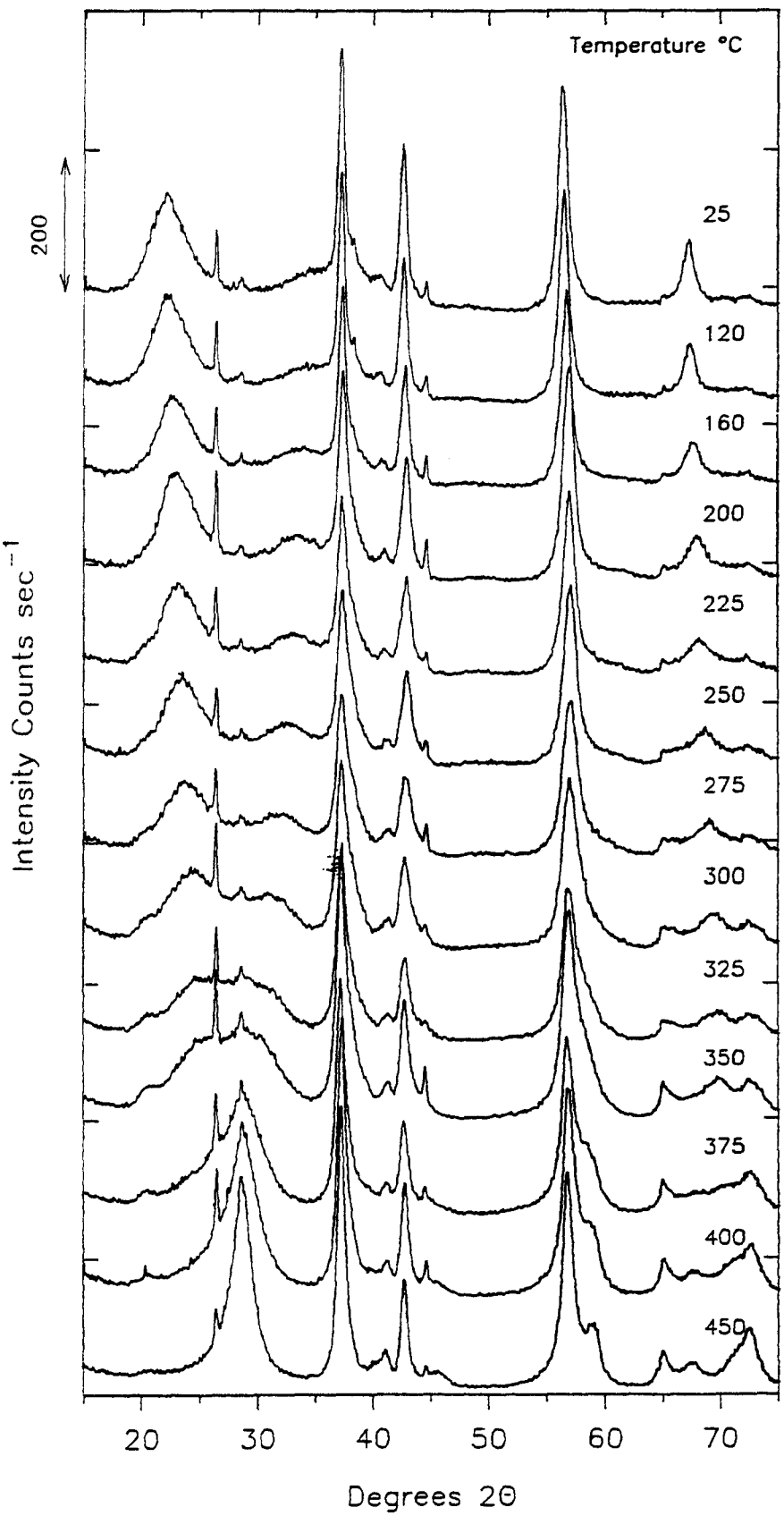


***Figure 3.31*** : Powder x-ray diffraction spectra during the heat-treatment of R2 EMD from 25-450°C. Heat-treatment duration 24 Hours in air (the heat-treatment temperature is given above the XRD pattern).

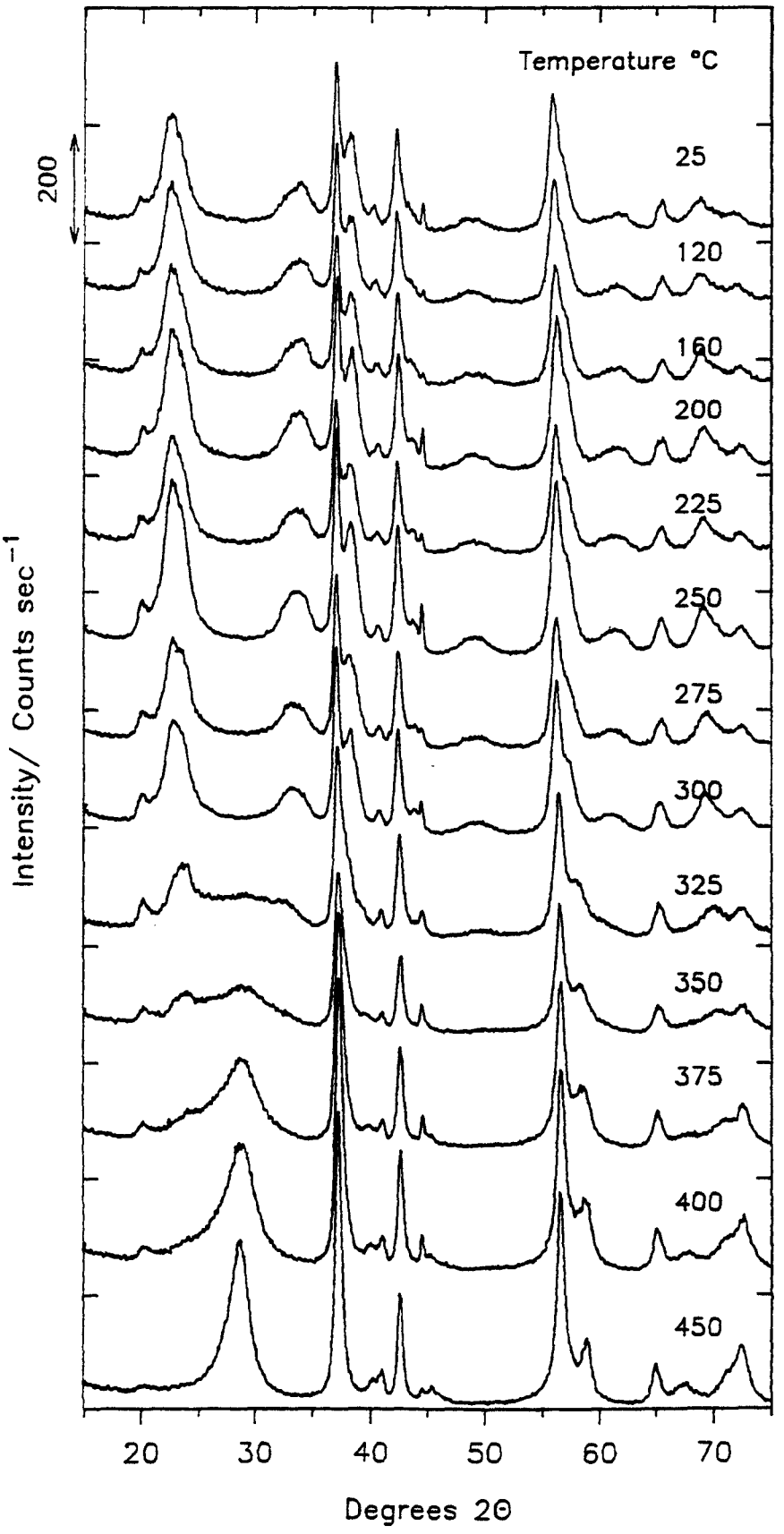


*Figure 3.32* : Powder x-ray diffraction spectra during the heat-treatment of Faradiser WSLi CMD from 25-450°C. Heat-treatment duration 24 Hours in air (the heat-treatment temperature is given above the XRD pattern).

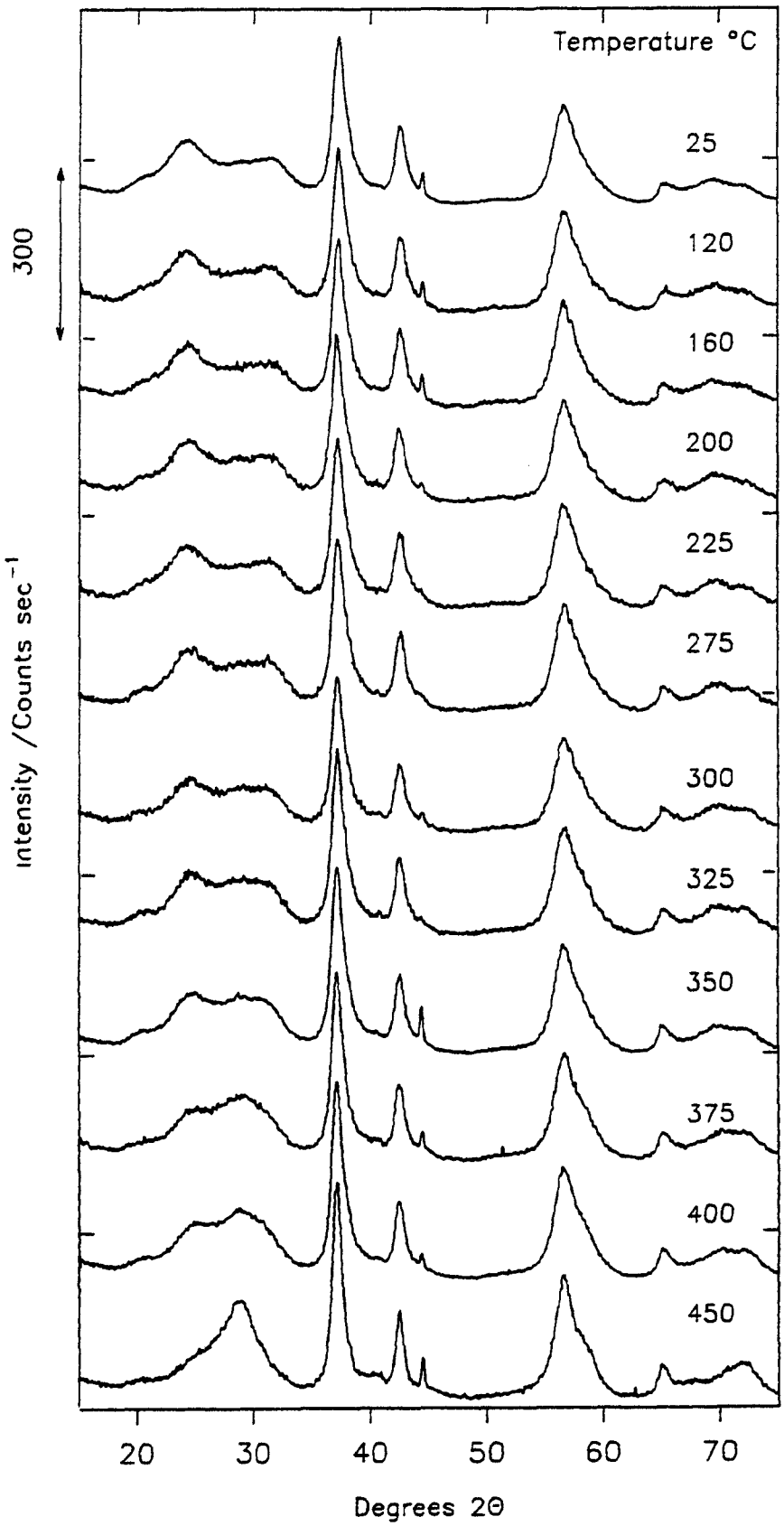


***Figure 3.33*** : Powder x-ray diffraction spectra during the heat-treatment of Faradiser M CMD from 25-450°C. Heat-treatment duration 24 hours in air (the heat-treatment temperature is given above the XRD pattern).

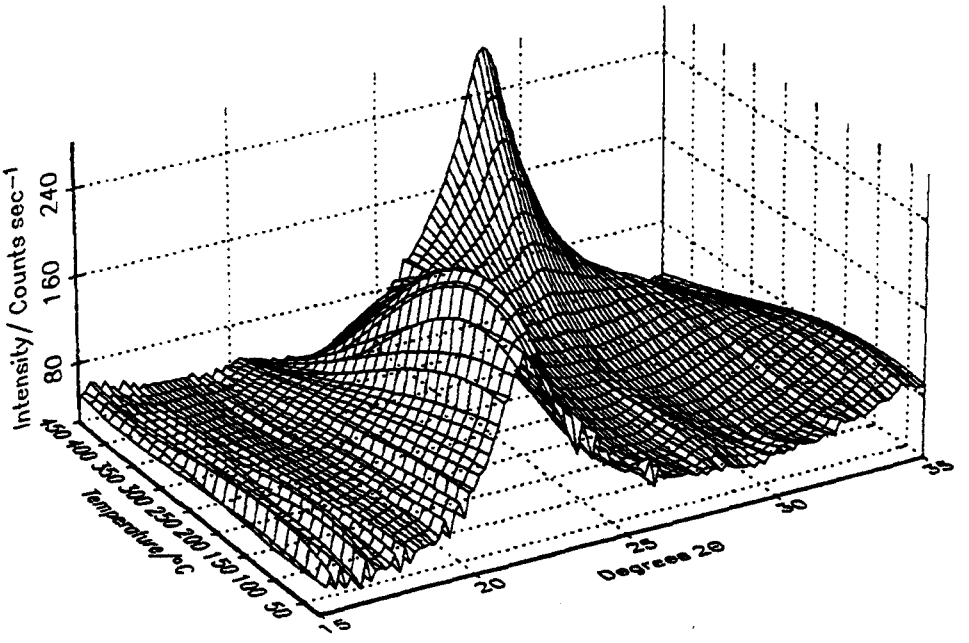


*Figure 3.34*: Powder x-ray diffraction spectra in the region 15-35 degrees 2Θ for Chemetals EMD (data grid from 25-450°C in 25°C intervals and from 15-35 degrees 2Θ in 0.16° intervals).

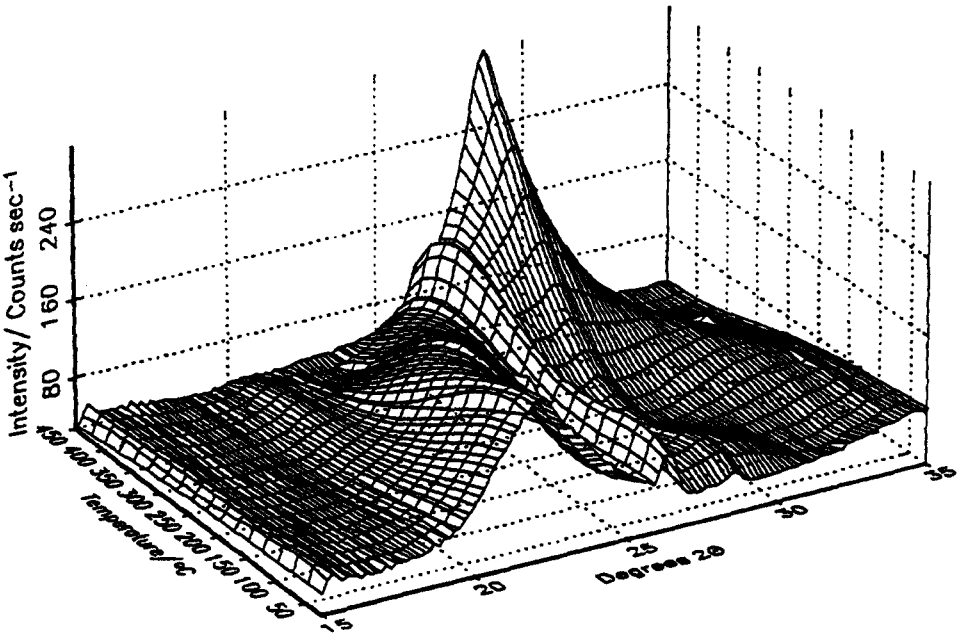


*Figure 3.35* : Powder x-ray diffraction spectra in the region 15-35 degrees 2Θ for R2 EMD (data grid from 25-450°C in 25°C intervals and from 15-35 degrees 2Θ in 0.16° intervals).

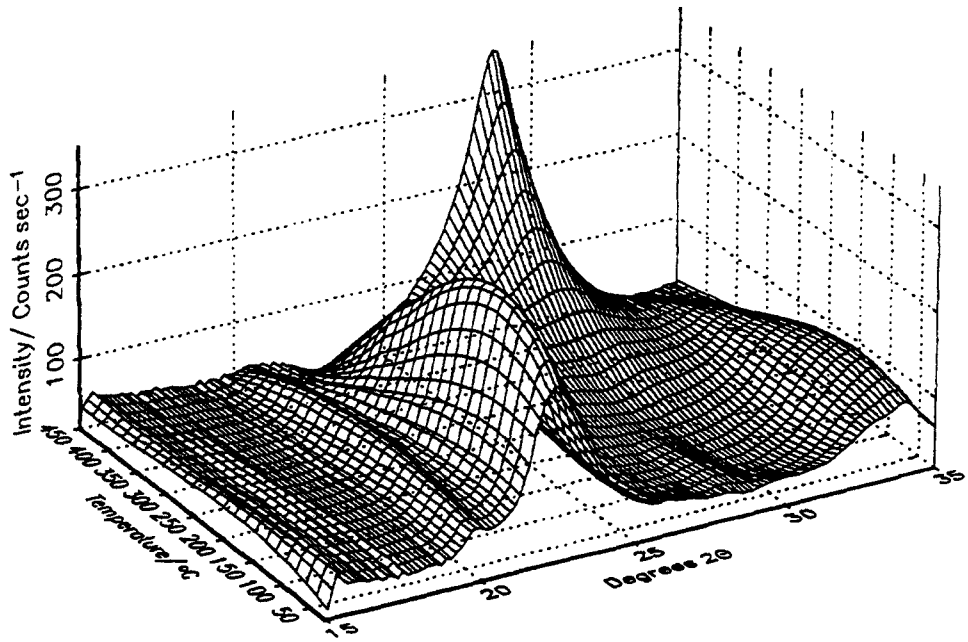


*Figure 3.36* : Powder x-ray diffraction spectra in the region 15-35 Degrees 2Θ for Faradiser WSLi CMD (data grid from 25-450°C in 25°C intervals and from 15-35 degrees 2Θ in 0.16° intervals).

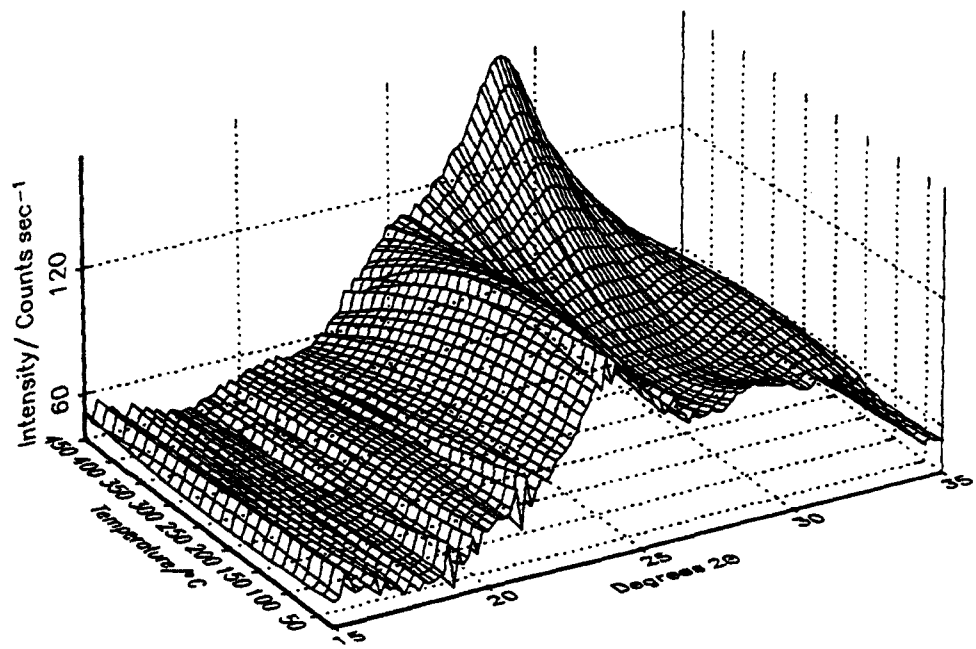


*Figure 3.37* : Powder x-ray diffraction spectra in the region 15-35 degrees 2Θ for Faradiser M CMD (data grid from 25-450°C in 25°C intervals and from 15-35 degrees 2Θ in 0.16° intervals).

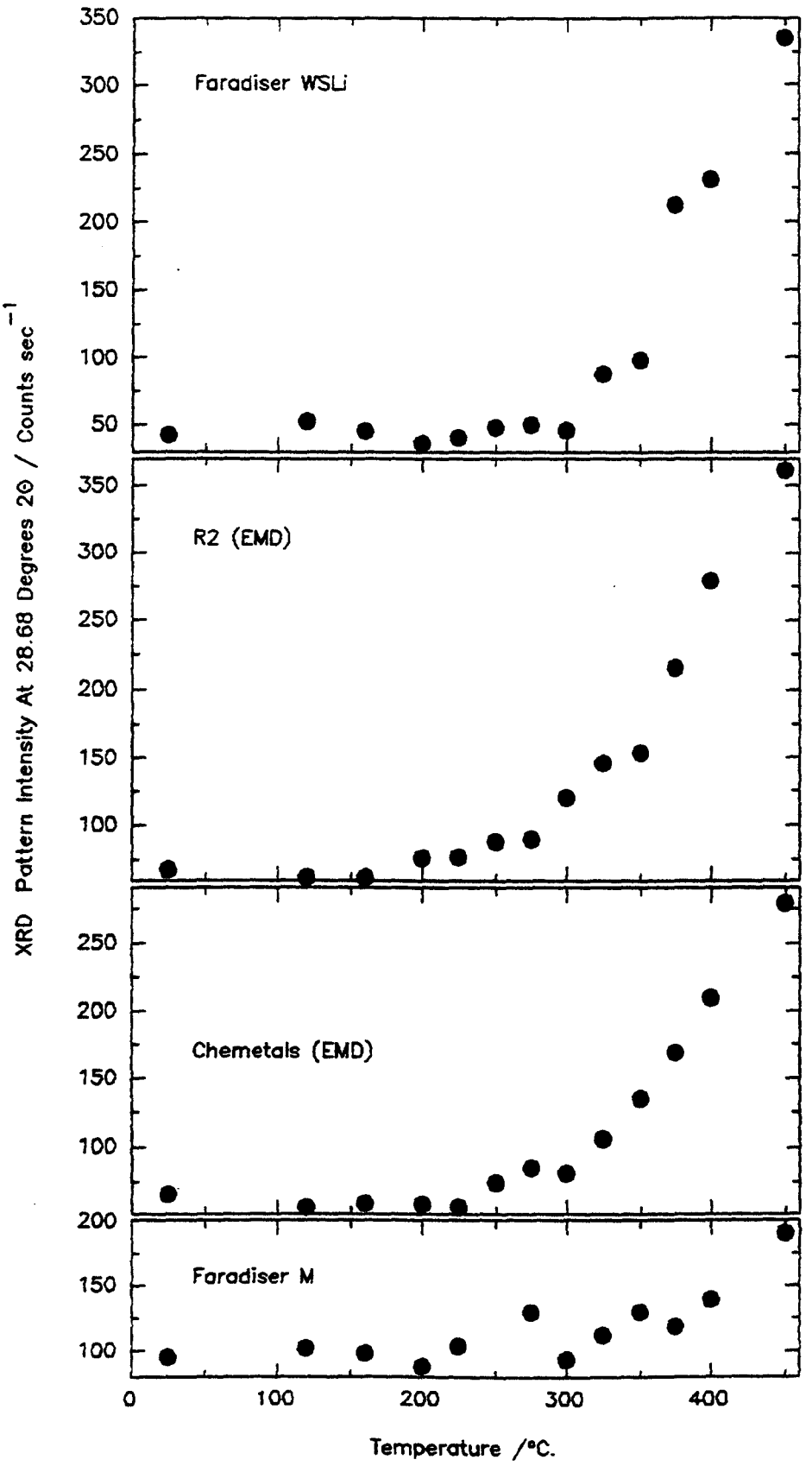


***Figure 3.38*** : X-ray diffraction pattern intensity at 28.68 Degrees 2Θ (the main peak position of $\beta$-$MnO_2$) for the four materials under study.

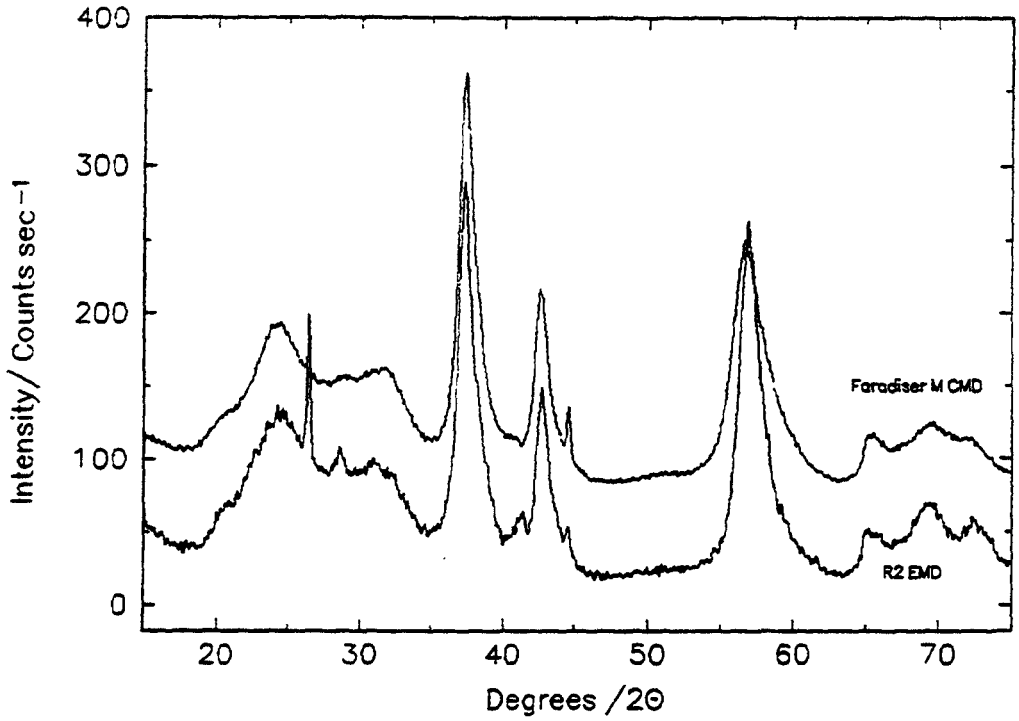


*Figure 3.39* : Comparison of the x-ray diffraction pattern of Faradiser M CMD with R2 EMD that had been heat-treated for 24 hours in air at 300°C (the X-ray pattern of Faradiser M is displaced by 60cs$^{-1}$ for clarity).

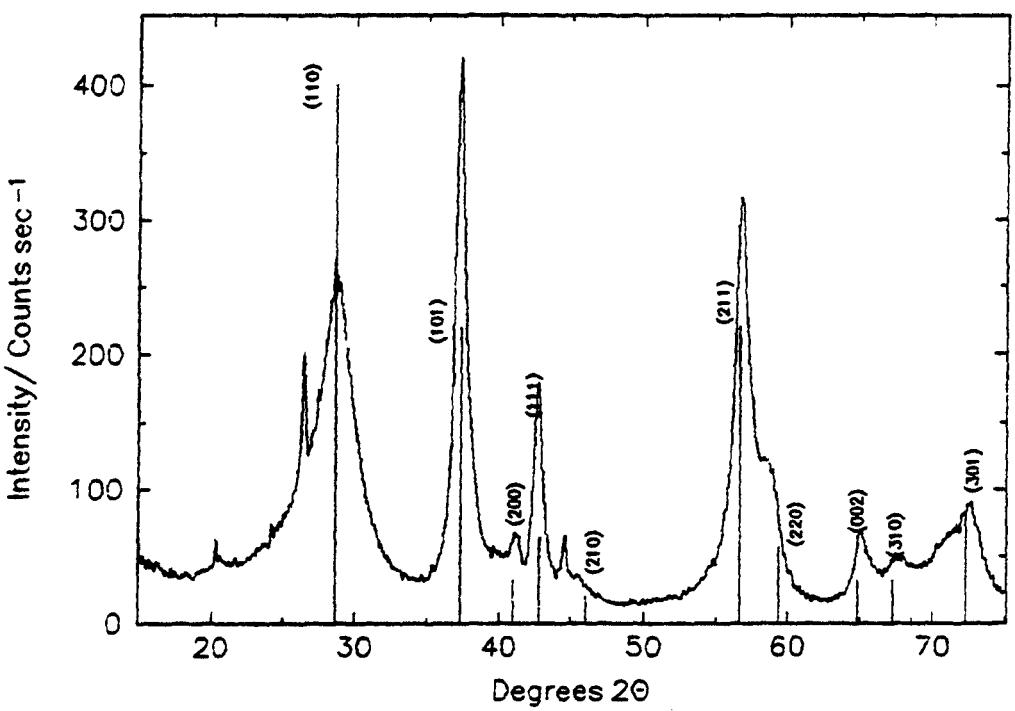


*Figure 3.40* : Comparison of the x-ray diffraction pattern of R2 EMD heat-treated at 400°C for 24 Hours in air with the JCPDS pattern of pyrolusite.

## 3.8 Structural parameter changes during the heat treatment of manganese dioxide.

The work in this section is based on the structural model for γ-$MnO_2$ developed by Pannetier. This model was mentioned in section 1.3 and is used here to investigate structural parameter changes during heat treatment of γ-$MnO_2$ namely increasing de Wolff disorder ($P_r$) and a decrease of the amount of microtwinning (Tw). Comparison of the XRD patterns of unheated Faradiser M, Faradiser WSLi and R2 with ramsdellite line positions are shown in figure 3.41. Four types of manganese dioxide have been identified by Chabre and Pannetier (1995) depending on the amount of $P_r$ and Tw. They are as follows: *Type I*: microtwinning < 50%. This includes patterns that have sharp diffraction patterns close to that of ramsdellite (as investigated by Bystrom 1949). Doublets 221/240 (located at 55.3 and 56.8°2$\theta$) and 002/061 (65.0 and 69.0°2$\theta$) are clearly separated. Faradiser WSLi belongs here. *Type II*: heavily twinned samples (Tw > 50%). These samples contain large amounts of de Wolff disorder. Doublets 221/240 are not resolved but there is measurable line splitting of 002/061. None of the materials in this study are type II but examples are IBA 14 and 15. *Type III*: extensively twinned samples (Tw ≈ 100%). The XRD patterns of these samples are characterised by six broadened reflections in the range 15-75°2$\theta$. Lines 221/240 and 002/061 have completely merged. In this work this is shown in the patterns of Chemetals and R2. *Type IV*: these samples have high levels of de Wolff disorder. In their XRD patterns the closeness of lines 110 and 130 (separated by 7°2$\theta$ instead of 12°$\theta$) is evidence of large $P_r$ values. Faradiser M and most heat-treated CMD's and EMD's belong in this category.

According to de Wolff the introduction of rutile chains into the ramsdellite lattice gives rise to three types of reflections depending on the value of the Miller indices k and l (i) l + ½k even (the "sharp lines") there will be no shift or broadening of the corresponding line, (ii) l + ½k odd these lines are weakened by the presence of rutile faults and (iii) k odd these lines are shifted by a constant value.

The de Wolff model mentioned above was a one parameter model that is the introduction of rutile chains into a ramsdellite lattice. Chabre and Pannetier (1995), however, found that it could not explain all of the features of the XRD

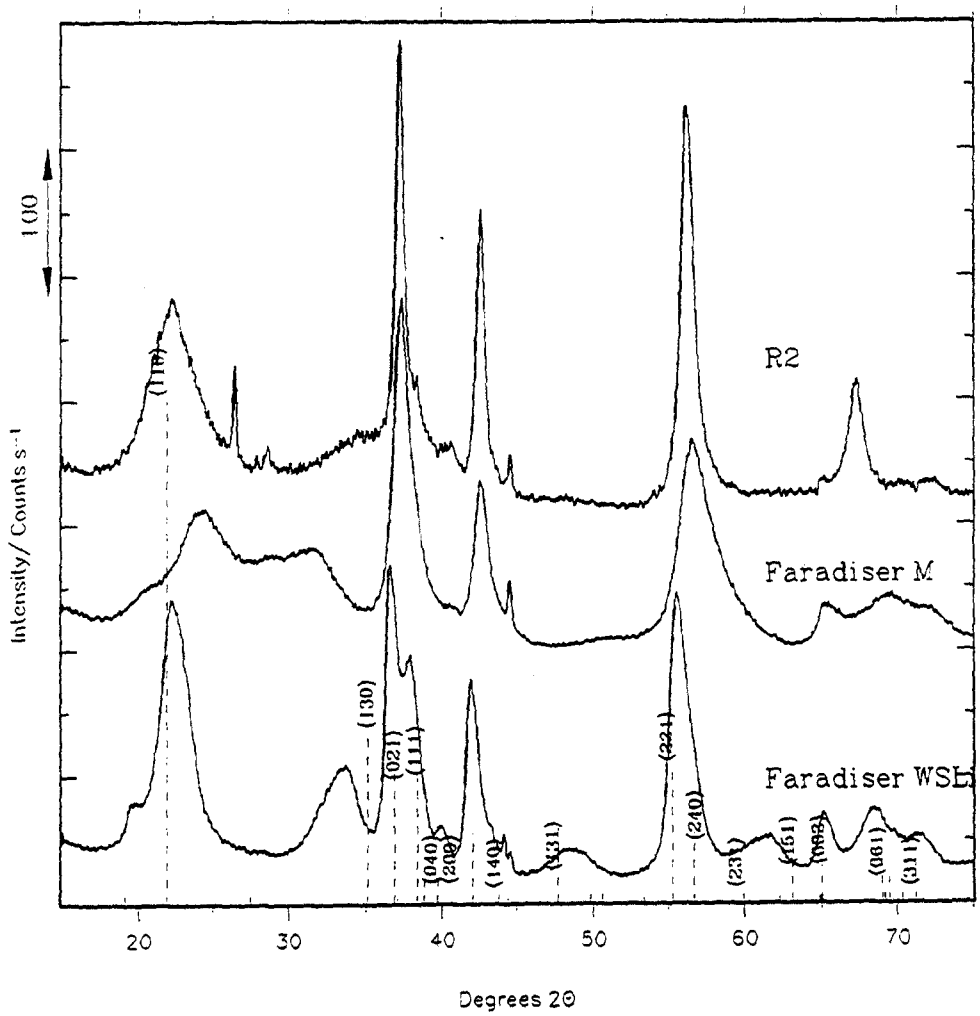


***Figure 3.41***: Comparison of the XRD patterns of R2, Faradiser M and Faradiser WSLi with the JCPDS pattern of ramsdellite.

patterns of $\gamma$-$MnO_2$. The introduction of a second parameter (microtwinning) was able to account for the features of the XRD patterns (see section 1.3). In this work the XRD analysis method developed by Chabre and Pannetier is applied to the heat-treated materials. A full description of the method is given in their paper and the main features are mentioned here.

Analysis of XRD Patterns.

The effect of $P_r$ and Tw on the ramsdellite lattice are given in table 3.2. As mentioned previously lines l + ½k even are not affected by de Wolff disorder. The effect of microtwinning on the ramsdellite lattice has been investigated by Chabre and Pannetier using the computer program DIFFAX (developed by Treacy *et al.* 1991). The XRD patterns were significantly changed by microtwinning which wiped out most of the features of the ramsdellite pattern. The most important modifications were as follows (i) line 110 (21.8°2$\theta$) is shifted to lower

*Table 3.2:* The effect of microtwinning and de Wolff disorder on the ramsdellite line positions.

| h | k | l | 2θ(CuKα) | microtwinning | de Wolff |
|---|---|---|---|---|---|
| 1 | 1 | 0 | 21.8 | θ↓ | θ↑ |
| 1 | 3 | 0 | 35.1 | θ↑ | θ↓ |
| 0 | 2 | 1 | 36.8 | θ↑ | – |
| 1 | 1 | 1 | 38.4 | θ↓ | θ↓ |
| 0 | 4 | 0 | 38.8 | θ↓ | – |
| 2 | 0 | 0 | 39.7 | – | – |
| 1 | 2 | 1 | 42.0 | θ↑ | – |
| 1 | 4 | 0 | 43.8 | θ↓ | – |
| 1 | 3 | 1 | 47.7 | θ↓ | θ↑ |
| 2 | 2 | 1 | 55.3 | θ↑ | – |
| 2 | 4 | 0 | 56.8 | θ↓ | – |
| 2 | 3 | 1 | 60.0 | θ↓ | θ↑ |
| 1 | 5 | 1 | 63.1 | θ↑ | θ↓ |
| 0 | 0 | 2 | 65.0 | θ↑ | – |
| 0 | 6 | 1 | 69.0 | θ↓ | – |
| 3 | 3 | 0 | 69.2 | θ↑ | θ↓ |
| 1 | 1 | 2 | 69.5 | θ↓ | θ↑ |
| 3 | 0 | 1 | 70.4 | θ↓ | – |
| 3 | 1 | 1 | 71.2 | θ↓ | θ↓ |

angles with increasing microtwinning, (ii) line 130 (35.1°2θ) broadens rapidly and shifts to higher angles. It eventually merges with 111 (38.4°2θ).

In this section the analysis of Chabre and Pannetier is applied to Faradiser WSLi CMD, this is because its XRD pattern is most amenable to the analysis. In the calculation of $P_r$ and Tw it is necessary to know the orthorhombic unit cell parameters of γ-$MnO_2$. These are referred to as *apparent* cell parameters by Chabre and Pannetier because, as can be seen from table 3.2, all peaks (except h00) are affected by $P_r$ and Tw. Therefore, to eliminate de Wolff disorder, only reflections with k/2+l even should be used. The apparent orthorhombic cell parameters can be found from equation 3.8.

$$\frac{1}{d^2} = \frac{h^2}{a^2} + \frac{k^2}{b^2} + \frac{l^2}{c^2} \qquad (3.8)$$

where d is the spacing between lattice planes in the crystal and a, b and c are the lattice parameters. These can be found using a linear regression analysis, with $h^2$, $k^2$ and $l^2$ as the independent variables and $1/d^2$ as the dependent variable. This yields $1/a^2$, $1/b^2$ and $1/c^2$ and hence a, b and c. The amount of microtwinning is provided by the ratio b/2c and is found from equation 3.9.

$$Tw\ (\%) = 871\ (\frac{b}{2c}) - 1409 \qquad (3.9)$$

The other method uses the splitting (in °2$\theta$) between the lines 221/240 and 002/061 to provide an approximate measure of the amount of microtwinning. In this work lines 221/240 (of Faradiser WSLi) could not be accurately resolved but lines 002/061 could. The % microtwinning was calculated from equation 3.10.

$$Tw\ (\%) = 100 - 25.20\ \Delta 2\theta \qquad (3.10)$$

Calculation of the amount of de Wolff disorder is also complicated beacuse all lines (except h00) are affected by microtwinning. Chabre and Pannetier found that the most convenient method was based on the displacement of the strong 110 reflection with respect to its position (21.808°2$\theta$) in the pattern of pure ramsdellite. The procedure is as follows: the percentage of microtwinning is calculated as above, then the shift $\delta$(Tw) of line 110 produced by microtwinning is found from:

$$\delta(Tw) = -0.0054\ Tw - 8.9\ 10^{-5}\ Tw^2 \qquad (3.11)$$

The value of $P_r$ can then be found from the observed position $2\theta_{(exp)}$ of line 110 using:

$$P_r = 0.602\ \delta(DW) - 0.198\ \delta^2(DW) + 0.026\ \delta^3(DW) \qquad (3.12)$$

where $\delta(DW) = 2\theta(110)_{exp} - \delta(Tw) - 21.808$. An example calculation of Tw and $P_r$ is given in Appendix B.

Application of the two methods to determine how Tw varies with heat-treatment temperature, in Faradiser WSLi are given in Figure 3.42. The variation of de Wolff disorder with heat-treatment is given in Figure 3.43. The set of lines used in the calculations were 021, 200, 121, 221, 002 and 061. The results for microtwinning when using the splitting of 002/061 is probably overestimated due to the presence of other reflections close to them. The correction used by Chabre and Pannetier was that the value obtained was approximately 80% of the true value of Tw. As mentioned in the introduction to this section Faradiser WSLi belongs to Type 1 $MnO_2$ and has a low degree of microtwinning. During the heat-treatment of Faradiser WS Ripert *et al.* (1991) mention a decrease of the twinning rate of $\gamma$-$MnO_2$ from 120-200°C. A decrease of microtwinning with

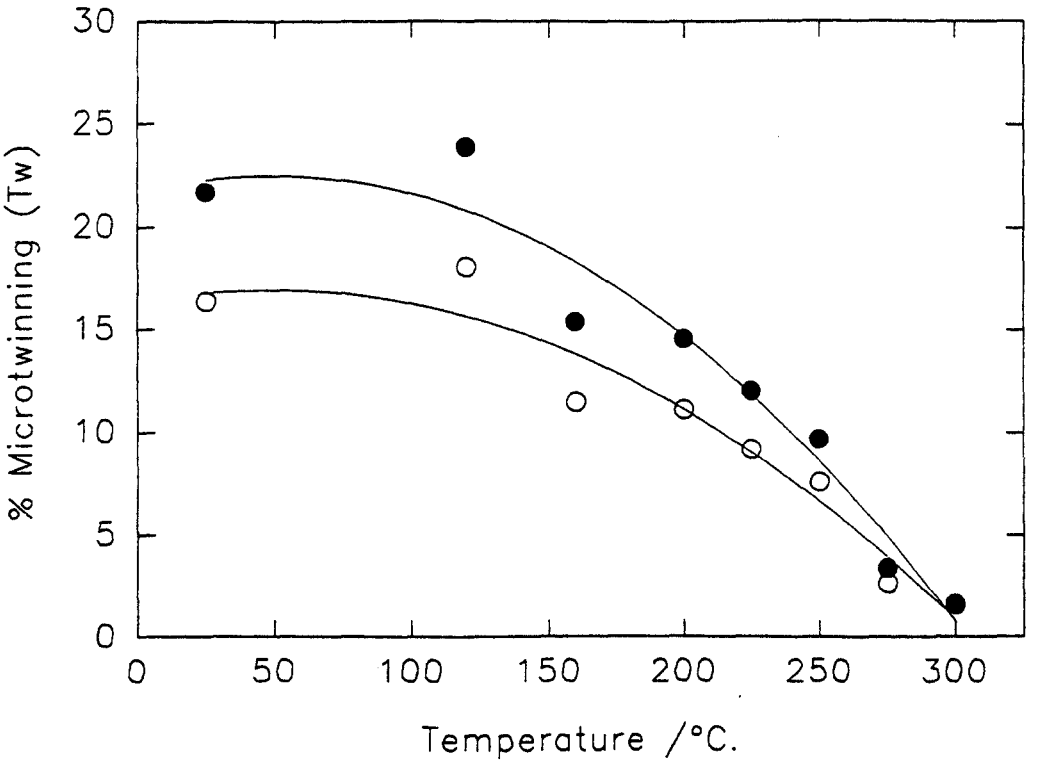


***Figure 3.42***: Variation of Tw with heat-treatment for Faradiser WSLi (○) Tw calculated from the orthorhombic b/2c ratio and (●) from the splitting of the 002/061 planes.

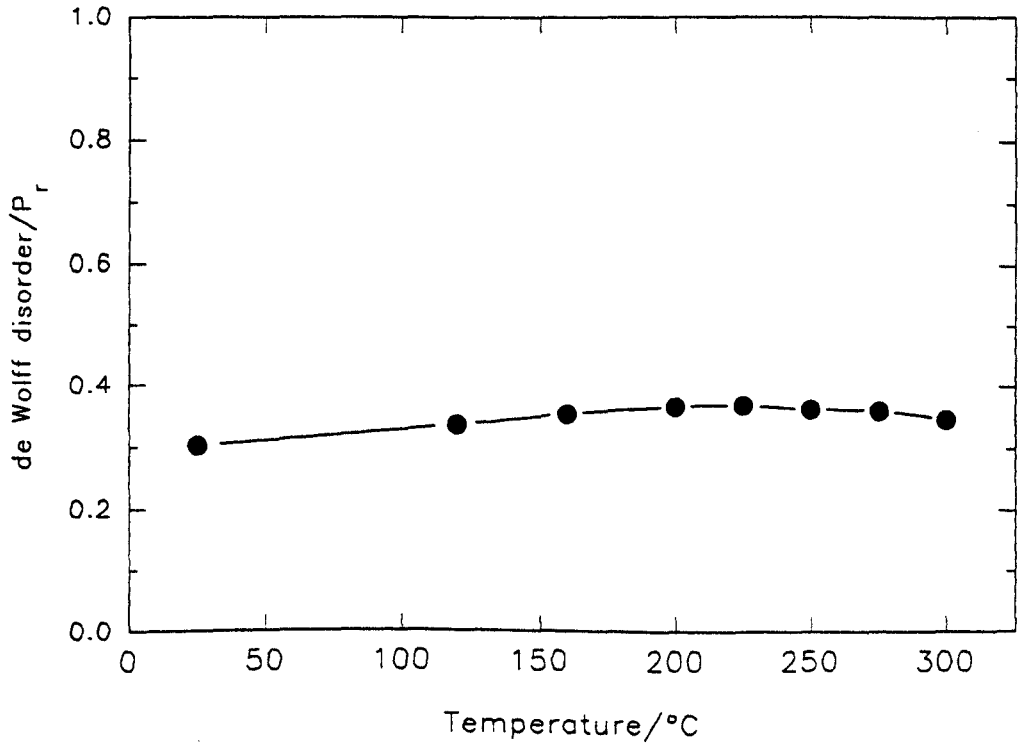


***Figure 3.43*** : Variation of de Wolff disorder with heat-treatment temperature for Faradiser WSLi.

heat-treatment is to be expected in accordance with the acceptance that an $MnO_2$ heat-treated at 400°C has a high $P_r$ value and low microtwinning. The values of Tw for the non heat treated material are significantly different to those obtained by Chabre and Pannetier for Faradiser WSA (36% from the b/2c ratio and 25% from 002/061). The main difference in the analyses was their use of a pattern decomposition program to deconvolute overlapping reflections, whereas in this work the peak detection program in the APD software was used. It is quite conceivable that the former method is more reliable. The calculation of the de Wolff disorder (figure 3.43) is dependent on the position of line 110 and a correction for microtwinning. Examination of figure 3.43 would suggest that $P_r$ is essentially unchanged from 25-300°C, although there is a slight increase from 0.30-0.36. Chabre and Pannetier obtained $P_r$ 0.38 for non heat treated Faradiser WSA. Again these results should be regarded with caution because of the difficulty of obtaining an accurate measure of the broad line 110. The transformation of ramsdellite to pyrolusite necessitates a migration of $Mn^{4+}$ cations within the oxygen framework and results (see figure 3.32) suggest this occurs between 300-400°C.

Synthesis of XRD patterns

The purpose of this section is to investigate changes in the XRD patterns of the heat-treated materials. This is done by taking appropriate amounts of two patterns and comparing the resultant pattern with one obtained experimentally, an example of this is shown schematically in figure 3.44

The reaction scheme can be represented by equation 3.13, where a, b and c are the intensity values at °2$\theta$ (in this dataset the value of x is computed every 0.04°2$\theta$ from 15-75°2$\theta$).

$$xa + (1 - x)\, b = c \qquad (3.13)$$

The value of x is then calculated for the 1,500 values of °2$\theta$ and the mean value is used for the calculation of the simulated XRD pattern. The values of x needed to solve equation 3.13 are given in figure 3.45. The mean value of x (0.745) can then be used to calculate the simulated XRD pattern of EMD heat-treated at 200°C. The results of this are shown in figure 3.46, as expected the

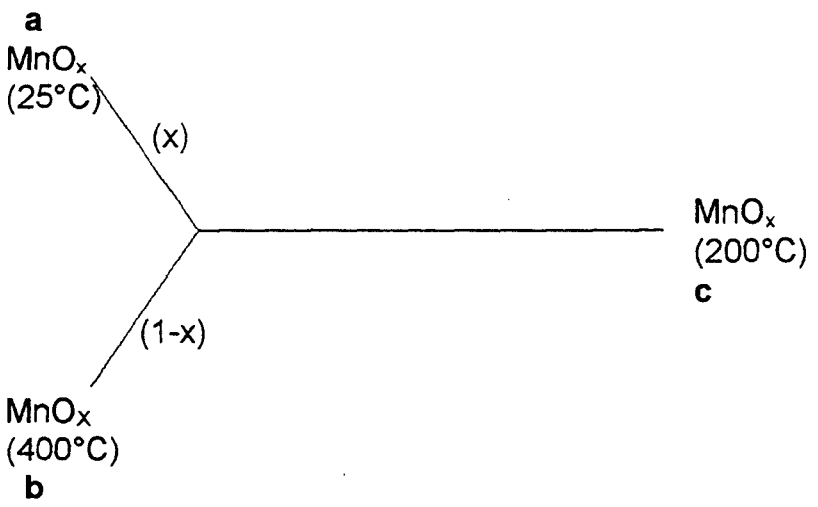


Figure 3.44: Reaction scheme for the synthesis of XRD patterns.

spectra are dissimilar this is particularly so in the region 20-30°2$\theta$. The peak height and area of the "$\beta$" peak at 28.68°2$\theta$ are much greater in the sinulated material. This has already been seen in figure 3.38 where the peak height at 28.68°2$\theta$ increased in a linear fashion from 300-400°C. The best agreement between experimental and simulated spectra was found with a mixture of 67% EMD heat-treated at 300°C and 33% EMD heat-treated at 400°C this is shown in figure 3.47. The results just shown would suggest a heterogeneous transformation from $\gamma$-$\beta$ $MnO_2$ in the temperature range 300-400°C. A similar set of results were obtained for the CMD material Faradiser WSLi and the best match is given in 3.48.

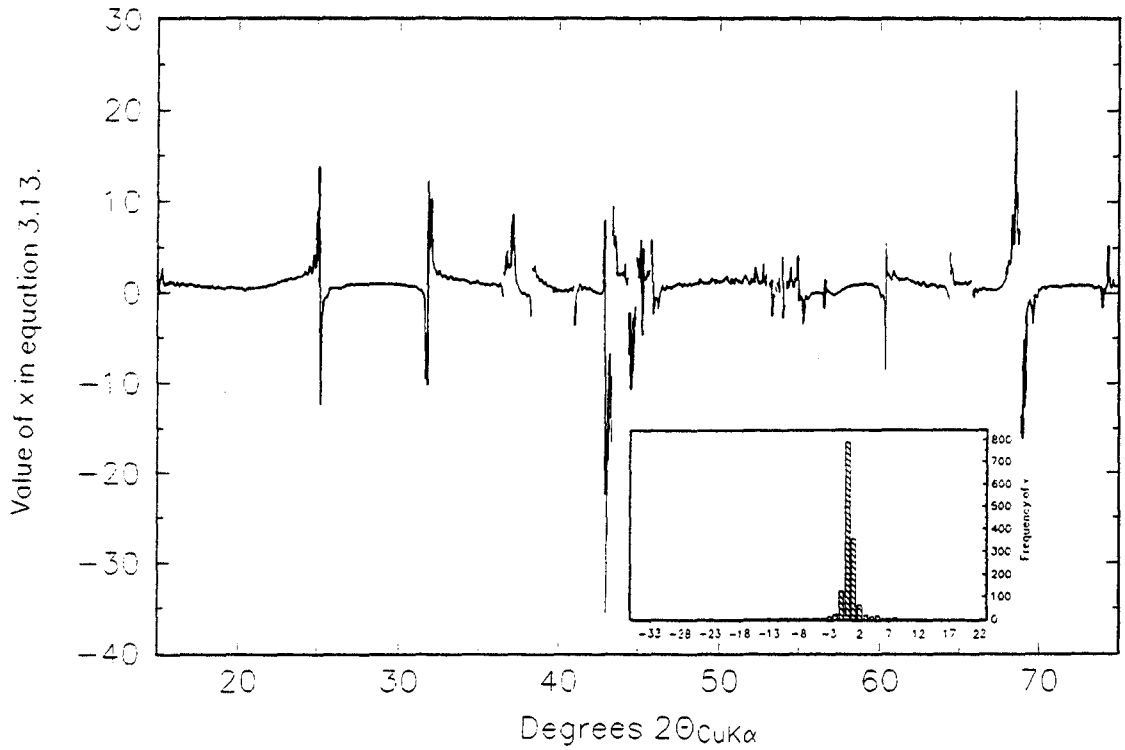


*Figure 3.45*: Values of x needed to satify equation 3.13. The experimental patterns were R2 (EMD) non heat-treated and R2 heat-treated at 400°C. The inset plot shows the frequncy distribution of x values.

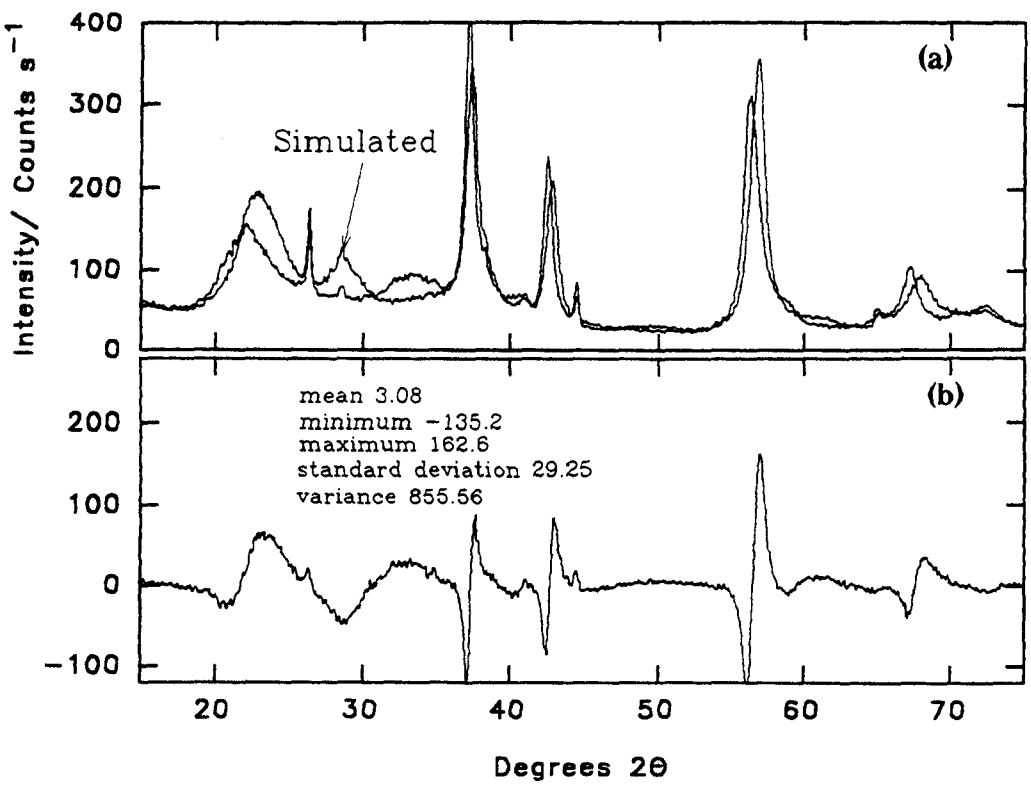


*Figure 3.46* : Comparison of (a) experimental R2 EMD heat-treated at 200°C with a mixture of 74.5% non heat-treated EMD and 25.5% EMD heat-treated at 400°C and (b) experimental-simulated difference spectrum (the statistical analysis is given for (b)).

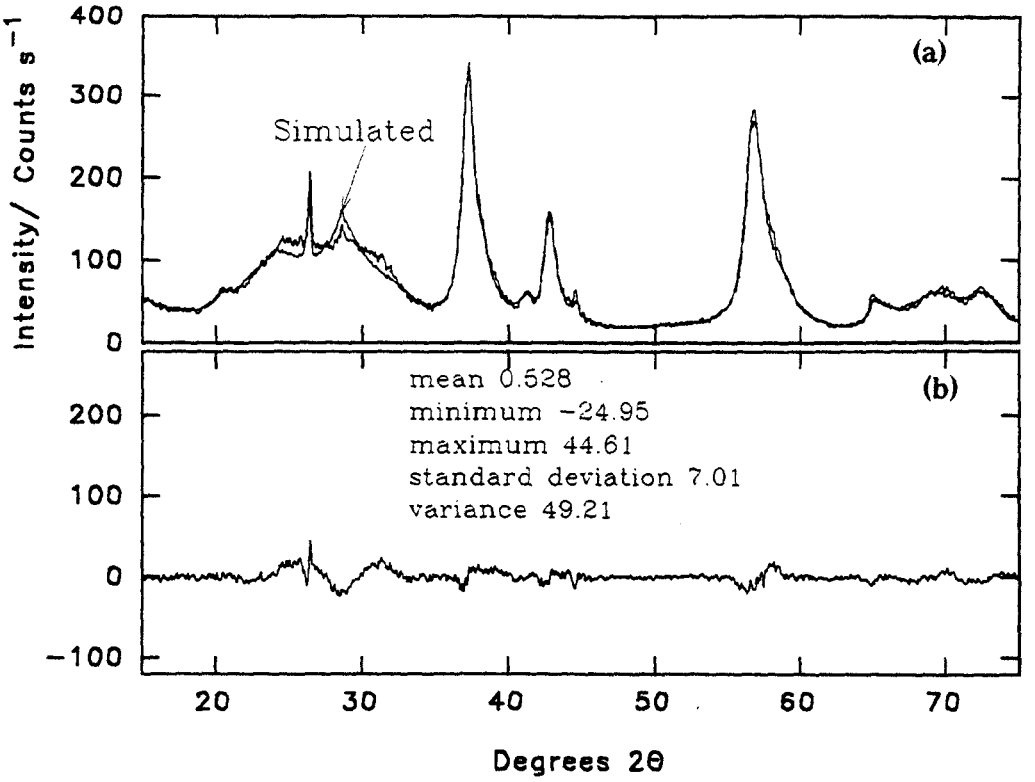


*Figure 3.47*: Comparison of (a) experimental R2 EMD heat-treated at 325°C with a mixture of 67% R2 heat-treated at 300°C and 33% R2 heat-treated at 400°C and (b) experimental-simulated difference spectrum (the statistical analysis is given for (b)).

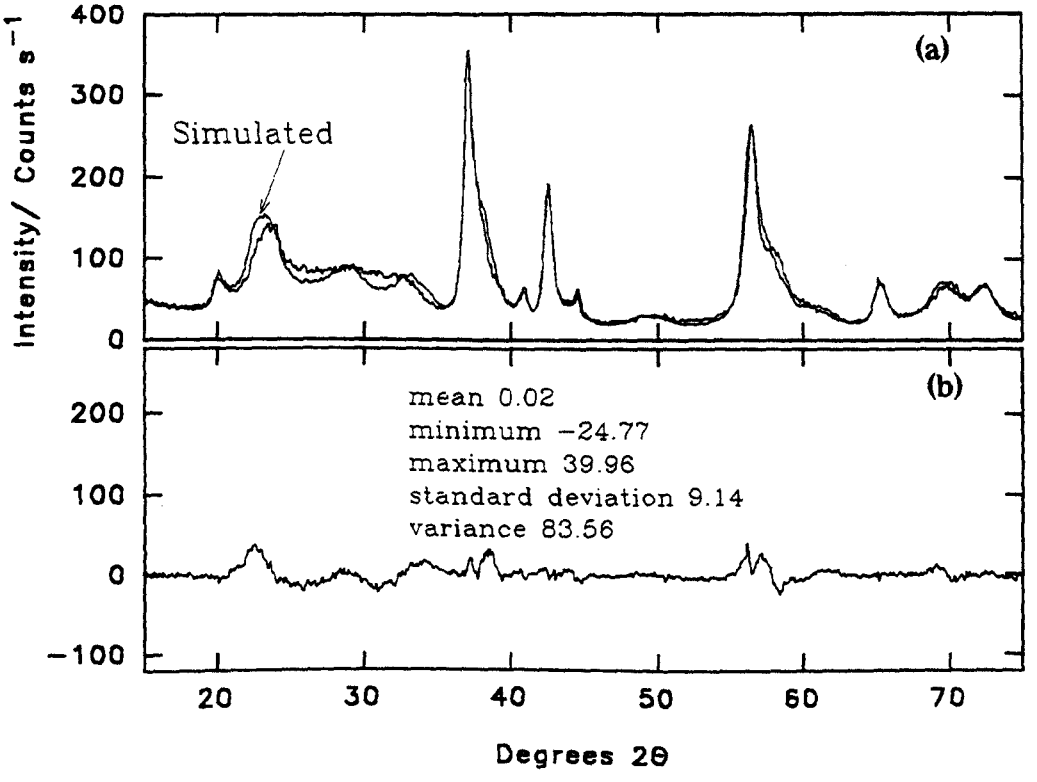


*Figure 3.48*: Comparison of (a) experimental Faradiser WSLi CMD heat-treated at 325°C with a mixture of 77% WSLi heat-treated at 300°C and 23% WSLi heat-treated at 400°C and (b) experimental-simulated difference spectrum (the statistical analysis is given for (b)).

## 3.9 Fourier Transform Infra-Red Spectra of heat-treated manganese dioxides.

The experimental details for this piece of work are given in section 2.6. The FTIR spectra for the heat-treated materials are given in figures 3.49-3.52. In section 1.5 it was discussed that the I.R spectrum of $MnO_2$ was split into two regions from 400-1400cm$^{-1}$ and from 1400-4000cm$^{-1}$. The former region is concerned with vibrations of the $MnO_6$ framework and the latter with OH stretching and bending vibrational modes. The area from 1400-4000cm$^{-1}$ is examined in detail in section 4.4. White and Roy (1964) showed that the I.R. spectrum of ramsdellite was split into four ill-defined peaks at 680,580,530 and 470 cm$^{-1}$ and this probably represents the four different Mn-O bond lengths that are present in the unheated materials. Examination of the FTIR spectra of the unheated materials reveals four ill-defined peaks which is consistent with the starting materials having features in accordance with the ramsdellite structure. The peak position of pyrolusite was given as 606cm-1 by White and Roy (1964) and 620cm$^{-1}$ by Swinkels (1989). The peak position of the main I.R. peak against heat-treatment temperature is given in figure 3.53 where it can be seen that the peak shifted from approximately 570-580cm$^{-1}$ to 605-620cm$^{-1}$ during heat-treatment from 25-450°C. This is in agreement with an increasing concentration of pyrolusite microdomains during the heat-treatment of $MnO_2$. An increase of the I.R. stretching frequency with heat-treatment also indicates increasing Mn-O bond strength and a shortening of the Mn-O bond distance in the transformation from ramsdellite to pyrolusite. Tarte *et al.* (1990) discussed different types of co-ordination and correspondingly different infrared absorption frequencies for Ti-$O_x$ compounds. In octahedral coordination there was a strong band at 600cm$^{-1}$ and in tetrahedral coordination where the average Ti-O bond distance was shorter the I.R. frequency was higher (700cm$^{-1}$). Of course differences of 100cm$^{-1}$ would not be expected in going from ramsdellite to pyrolusite because they have the same hexagonally close packed anion array. It is only the arrangement of the octahedra that differ. It is also worth noting that the peak position of the unheated materials could be used to estimate the concentration of pyrolusite microdomains.

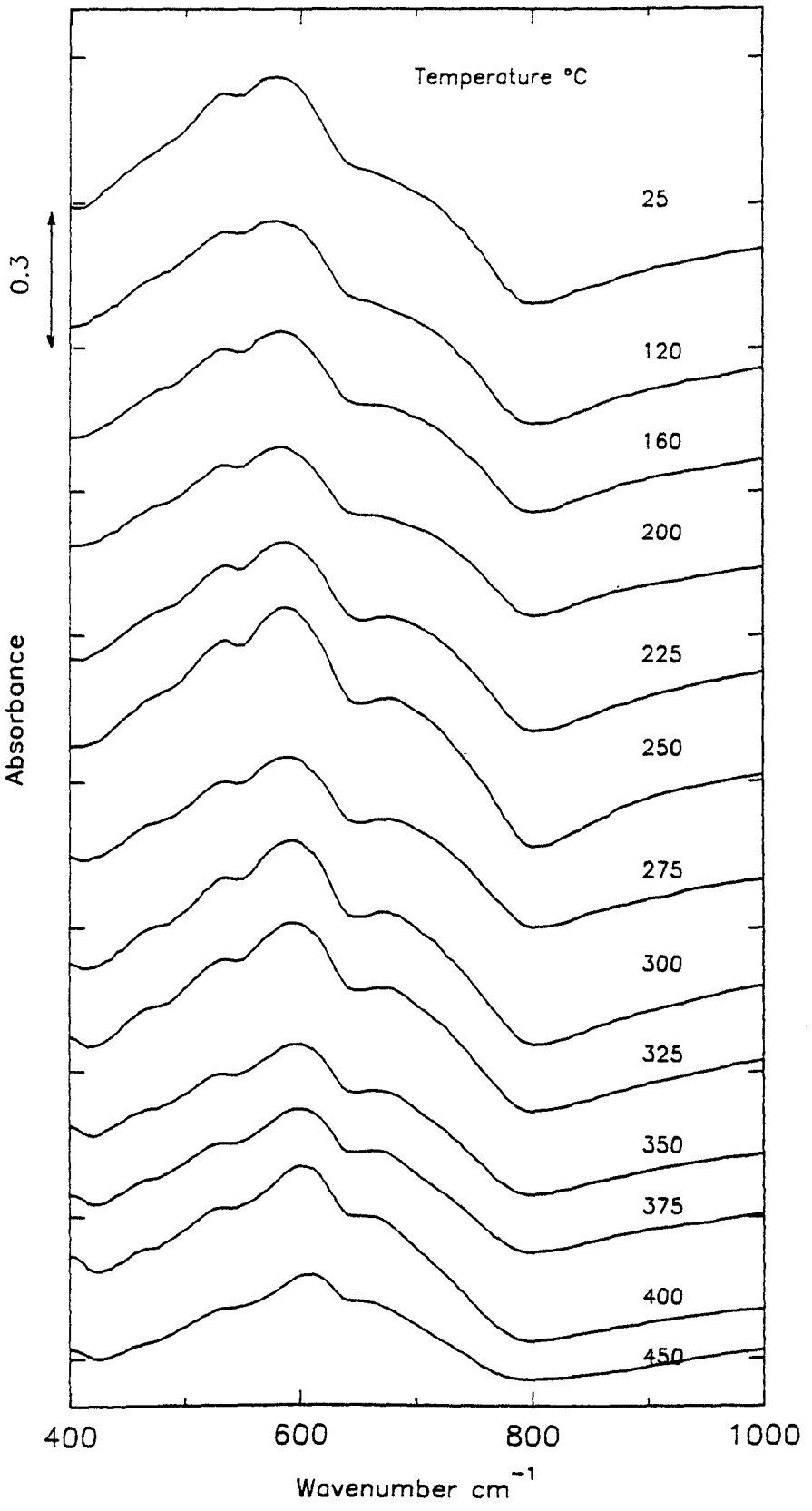


***Figure 3.49*** : FTIR spectra in the wavenumber region 400-1000cm$^{-1}$ during the heat-treatment of Chemetals EMD from 25-450°C. Heat-treatment duration 24 hours in air (the heat-treatment temperature is given above the FTIR spectra).

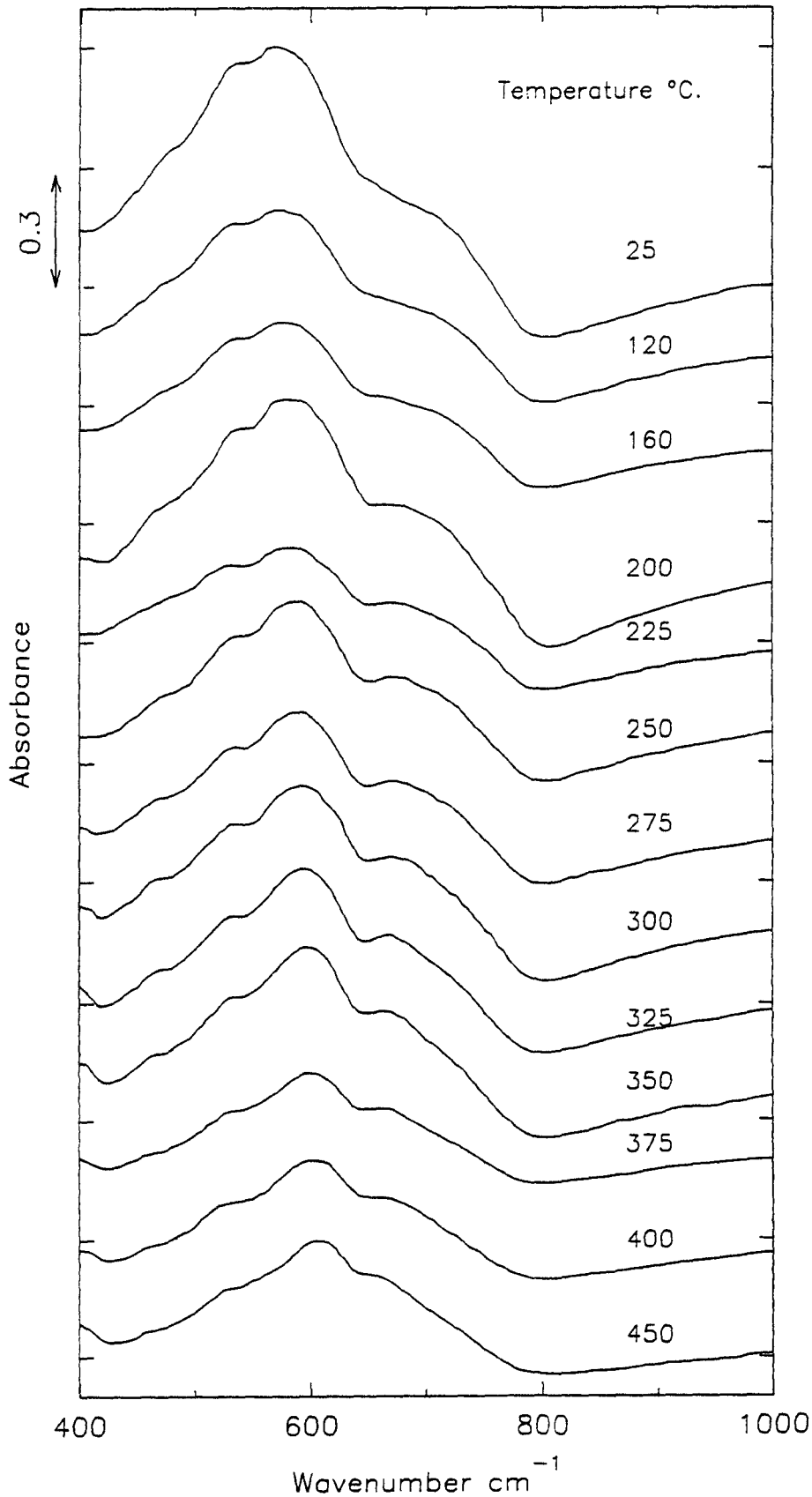


***Figure 3.50*** : FTIR spectra in the wavenumber region 400-1000cm$^{-1}$ during the heat-treatment of R2 EMD from 25-450°C. Heat-treatment duration 24 hours in air (the heat-treatment temperature is given above the FTIR spectra).

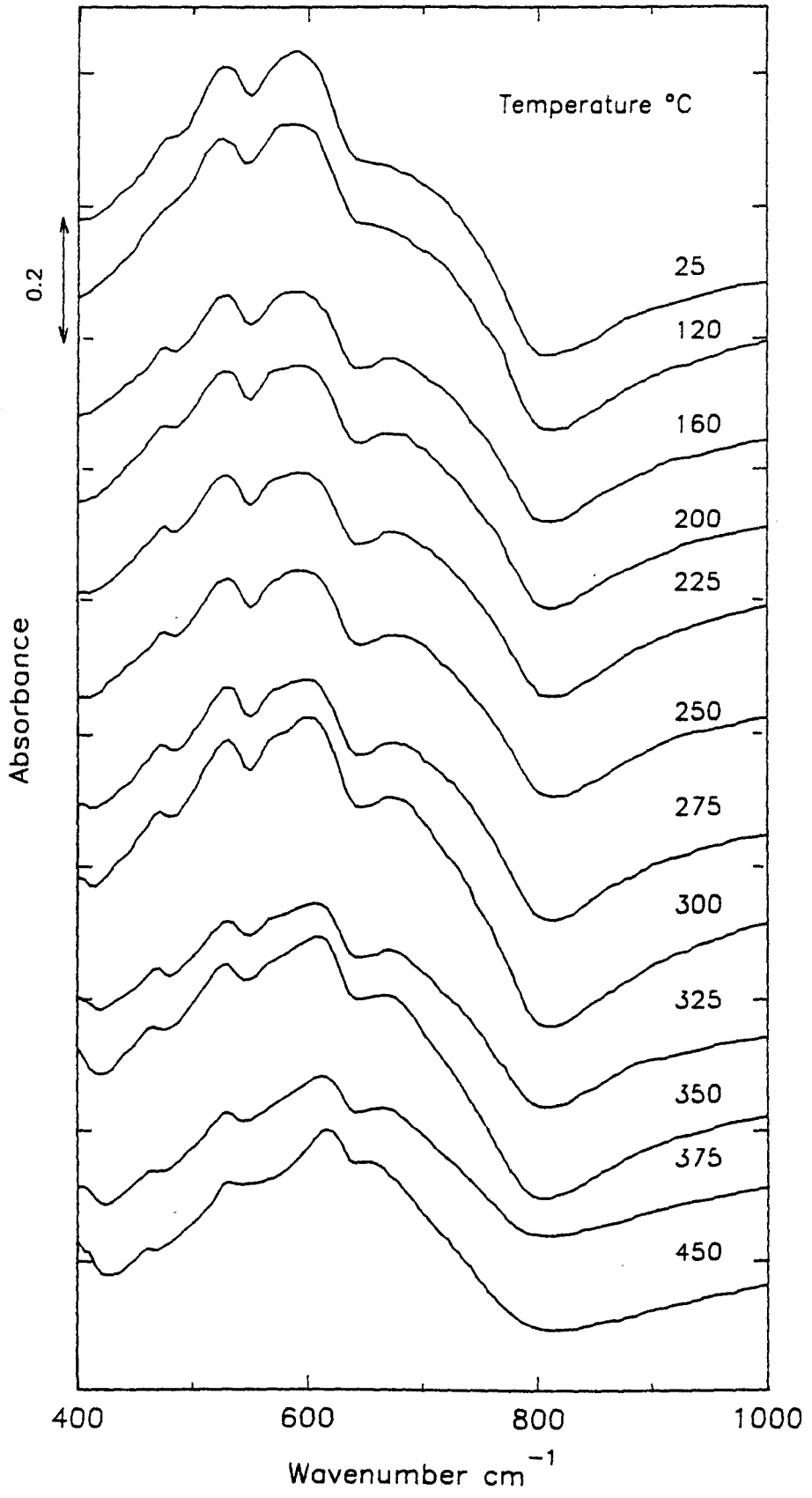


***Figure 3.51*** : FTIR spectra in the wavenumber region 400-1000cm$^{-1}$ during the heat-treatment of Faradiser WSLi CMD from 25-450°C. Heat-treatment duration 24 Hours in air (the heat-treatment temperature is given above the FTIR spectra).

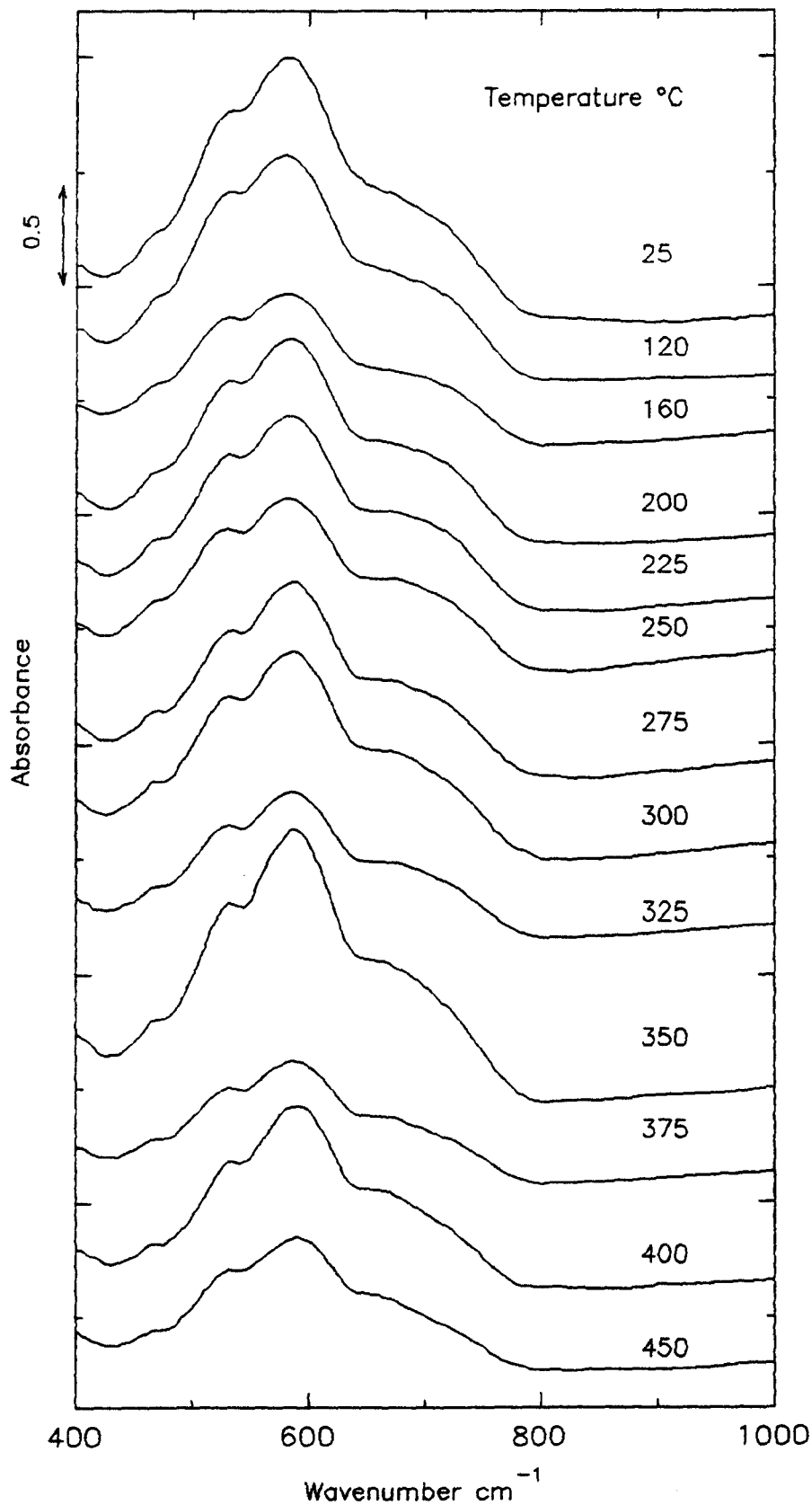


*Figure 3.52* : FTIR spectra in the wavenumber region 400-1000cm$^{-1}$ during the heat-treatment of Faradiser M CMD from 25-450°C. Heat-treatment duration 24 hours in air (the heat-treatment temperature is given above the FTIR spectra).

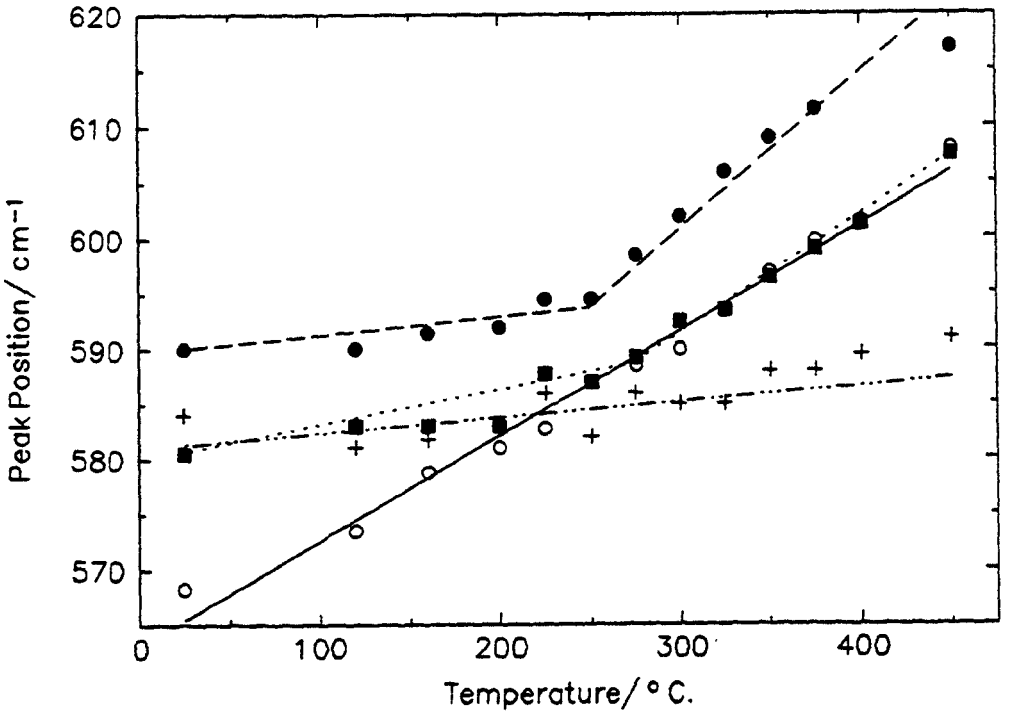


*Figure 3.53* : Peak positions of the major peak in the FTIR spectra of the heat-treated manganese dioxides (■)Chemetals EMD,(○)R2 EMD,(●)Faradiser WSLi and (+) Faradiser M.

## 3.10 The electrode potential of heat-treated manganese dioxides.

The experimental details for this section of work are given in section 2.9. The electrode potentials are quoted relative to the Standard Hydrogen Electrode (SHE) at pH0 and were calculated using equation 2.10. The results for R2 EMD and Faradiser WSLi CMD† are given in figure 3.54. Both materials show similar trends in the temperature range 25-400°C. There is an indication of a greater rate of fall of potential at temperatures higher than 200°C. The pyknometric density measurements that were carried out in section 3.4 showed that water removed at temperatures above 200°C was of a different nature to that removed at 120-160°C. Brown *et al.* (1981) found that water removed at 120-160°C adsorbed after several days immersion in water. In other words very little structural change had occurred during heat-treatment at temperatures up to

†The pH was measured at the time of the potential measurement.

160°C hence there is little change in the $MnO_2$ potential. Heat-treatment at temperatures above 200°C cause the condensation of hydroxyl groups leading to irreversible changes in the $MnO_2$ structure as suggested by Fillaux *et al.* (1991). The potential data shown here are in agreement with the X-ray diffraction data that was presented in section 3.5, which showed structural changes above 250°C. The $MnO_2$ potential is compared with published values found in the literature in figure 3.55. The results found in this work are very similar to those of Kozawa (1985). The results of Ruetschi (1988) show a comparable trend except that the potential is lower. The data of Preisler (1980) show a linear decrease from 120-200°C although his samples were only heat-treated for 2 hours.

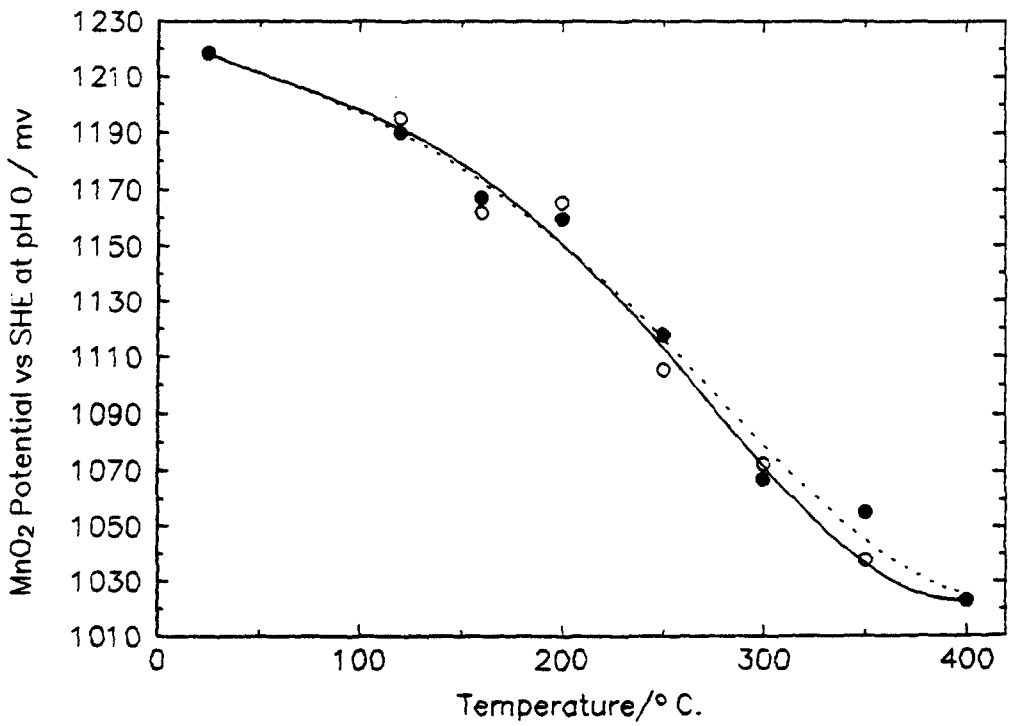


***Figure 3.54*** : Variation of the potential of $MnO_2$ with heat-treatment temperature in 5M $NH_4Cl$/2M $ZnCl_2$; (○)R2 EMD and (●) Faradiser WSLi CMD.

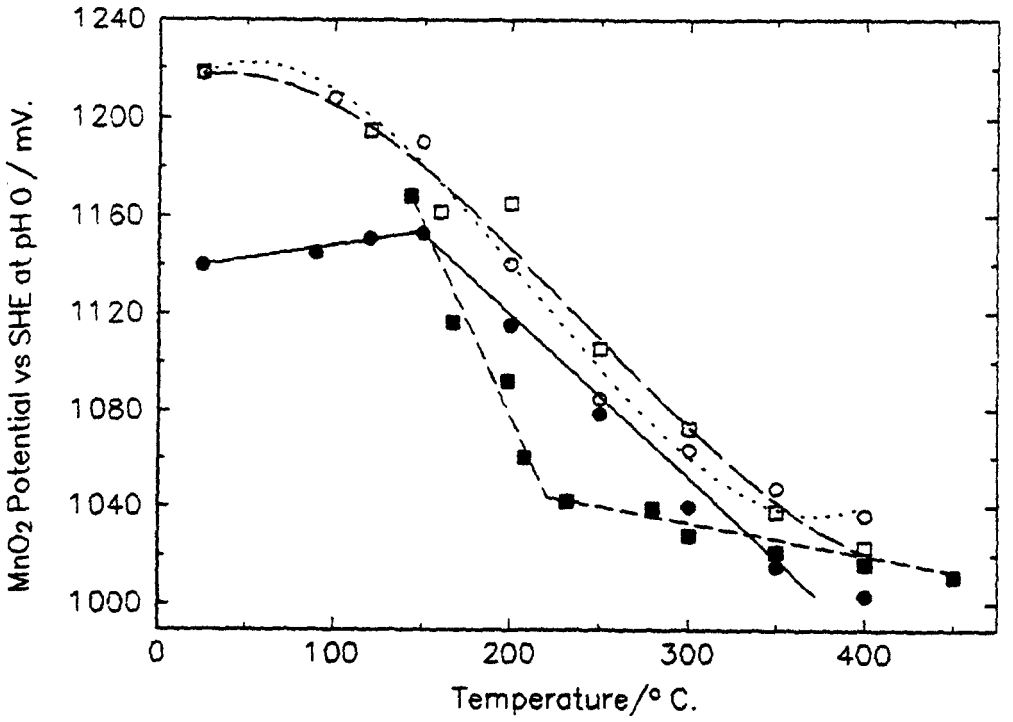


*Figure 3.55*: Published data of the variation of the potential of $MnO_2$ with heat-treatment temperature; (●) Ruetschi 1988,(■)Preisler 1980,(○)Kozawa 1985 and (□) this work.

## 3.11 Conclusions.

Four different types of $\gamma$-$MnO_2$ (two EMD's and two CMD's) were heat-treated in an air or argon environment, in the temperature range 25-450°C. The rate of water evolution was measured by collecting the evolved water in tubes containing magnesium perchlorate and the uptake/loss of oxygen by chemical analysis of the heat-treated material. The rate and amount of water evolution were the same in air and argon. The stoichiometry of $MnO_2$ reached a maximum at 250°C in air whereas in argon the stoichiometry remained unchanged from 25-250°C. Oxygen loss was observed in an argon environment from 300°C whereas in air loss was seen after 350°C.

Pyknometric density measurements of $MnO_2$ revealed that water removed up to 120°C had the same density as that of normal water (0.997 g $cm^{-3}$). Between 120-160°C water of a higher density was removed and the removal of hydroxyl groups between 200-250°C generated microporosity in $MnO_2$ and a surface which reacted with water.

Powder X-ray diffraction spectra of the heat-treated materials showed that there was little change in structure from 25-300°C and between 300-400°C the structure from a $\gamma$-phase to a $\beta$-like phase. It was found that a $\gamma$-$MnO_2$ heat-treated from 300-400°C should not be referred to as $\beta$-$MnO_2$ or $\gamma/\beta$-$MnO_2$ (as is often quoted in the literature) but instead as "$\beta$-like" or "pyrolusites containing random ramsdellite defects". Application of the latest structural model of $\gamma$-$MnO_2$ in terms of de Wolff disorder and microtwinning was applied to the XRD patterns of Faradiser WSLi. It was found that there was decrease in microtwinning from 25-300°C but the amount of de Wolff disorder was essentially unchanged. Simulation of XRD patterns by taking appropriate amounts of two materials and comparing them with one obtained experimentally showed a heterogeneous transformation from $\gamma$ to $\beta$-$MnO_2$ in the temperature range 300-400°C.

FTIR spectra of the heat-treated materials showed a progressive shift of the peak associated with the $MnO_6$ octahedra. Comparison of the peak positions with the published data of ramsdellite and pyrolusite suggested a ramsdellite phase in the unheated material and a pyrolusite phase at 400°C. This was in agreement with the XRD data.

The potential of $MnO_2$ became more negative by approximately 200mV during heat-treatment from 25-450°C. The potential decreased at a greater rate after 200°C and this was attributed to structural changes that had been observed with XRD and FTIR spectra.

# Chapter 4 Proton Insertion Into Electrodeposited Heat-treated Synthetic Manganese Dioxides.

## 4.1 Introduction.

The reaction that takes place during the discharge of a battery can be represented by equation 1.2

$$MnOOH_r + \Delta H^+ + \Delta e \Rightarrow MnOOH_{r+\Delta} \qquad (1.2)$$

where r represents the level of H insertion and varies from approximately 0.1 in the starting material to 1.0 at the end of discharge. The literature regarding the reduction of manganese dioxide has been reviewed in section 1.4. One of the most powerful techniques used to study this reaction has been X-ray diffraction (Gabano *et al.* 1965, Maskell *et al.* 1981 and Fitzpatrick and Tye 1991) although in recent years neutron diffraction (Fillaux *et al.* 1991, 1992a&b and 1993a&b) and EXAFS spectroscopy (Li *et al.* 1988 and Levy-Clement *et al.* 1992) have been used in an attempt to elucidate reaction 1.2. One of the reasons why the reaction has not been fully understood is that manganese dioxide exists in a variety of crystalline modifications (Burns and Burns 1975) and the reaction is dependent on the nature and rate at which the reaction is carried out (Gabano *et al.* 1970). Manganese dioxide can be reduced either electrochemically (as in a battery) or chemically. The latter is preferred here as the X-ray diffraction pattern is not complicated by additional phases such as hetaerolite or acetylene black which might be present in electrochemical reduction. The heat-treatment of manganese dioxide (up to 400°C) has been well investigated in the literature (Ikeda 1975 and Manev *et al.* 1989) particularly in regard to the performance of $MnO_2$ in Li cells The reduction of heat-treated manganese dioxide, however, has received little attention the most notable paper being by Bode and Scheimer (1964). The aim of this chapter is to bridge that gap and results are shown for an X-ray powder diffraction and FTIR study on an EMD that had been heat-treated at 200, 300 and 400°C and then reduced to $MnOOH_{1.0}$ by either hydrazine hydrate or propan-2-ol.

## 4.2 Powder x-ray diffraction spectra of heat-treated manganese oxyhydroxides.

### *4.2.1 Peak position criterion.*

When locating the position of a peak it is not advisable just to take the maximum intensity of a peak because of the variation in the counts of the diffracted X-rays. An objective process is used here and that is the peak detection program available in the APD software. Table 4.1 shows the peak positions for an EMD that had been reduced by propan-2-ol: two reduction levels are shown $MnOOH_{0.178}$ and $MnOOH_{0.882}$. The peak positions shown are for three different X-ray patterns and it can be seen that the percentage standard deviation about 0.1% or less which is acceptable considering the broadness of the $MnO_2$ peaks. Another commonly used method for measuring peak positions is to use an internal standard, this is shown in Figure 4.1, where an EMD was ground in an agate pestle and mortar with potassium chloride (KCl). The procedure is to compare the positions of the KCl peaks (mixed with $MnO_2$) with those of the JCPDS pattern and plot the difference in the peak position against degrees $2\theta$. Using this method it is possible to correct for errors such as sample height displacement that occur in the mounting of the sample. This method was not used partly because, as can be seen from Figure 4.1 the position of one of the Kcl peaks interferes with one of the $MnO_2$ peaks but also because the large number of samples meant that this method was impractical.

*Table 4.1*: Peak positions for an EMD that had been heat-treated at 200°C and reduced by propan-2-ol at two different levels of H insertion.

| r in $MnOOH_r$ | | Peak Position /Degrees 2$\theta$. A | B | C | D |
|---|---|---|---|---|---|
| 0.178 | | 67.7950 | 56.6125 | 42.7275 | 37.2375 |
| | | 67.5825 | 56.6225 | 42.7475 | 37.2600 |
| | | 67.5600 | 56.6550 | 42.7700 | 37.2625 |
| | Average | 67.6460 | 56.6300 | 42.7483 | 37.2533 |
| | $\sigma_{n-1}$ | 0.1297 | 0.02222 | 0.02126 | 0.01377 |
| | % deviation | 0.1917 | 0.03924 | 0.04973 | 0.03696 |
| 0.882 | | 64.7750 | 54.5175 | 40.9125 | 35.5250 |
| | | 64.8950 | 54.4525 | 40.9375 | 35.5250 |
| | | 64.8775 | 54.4800 | 40.9475 | 35.5700 |
| | Average | 64.8492 | 54.4830 | 40.9325 | 35.5400 |
| | $\sigma_{n-1}$ | 0.06482 | 0.03263 | 0.01803 | 0.02598 |
| | % deviation | 0.09995 | 0.05989 | 0.04405 | 0.07310 |

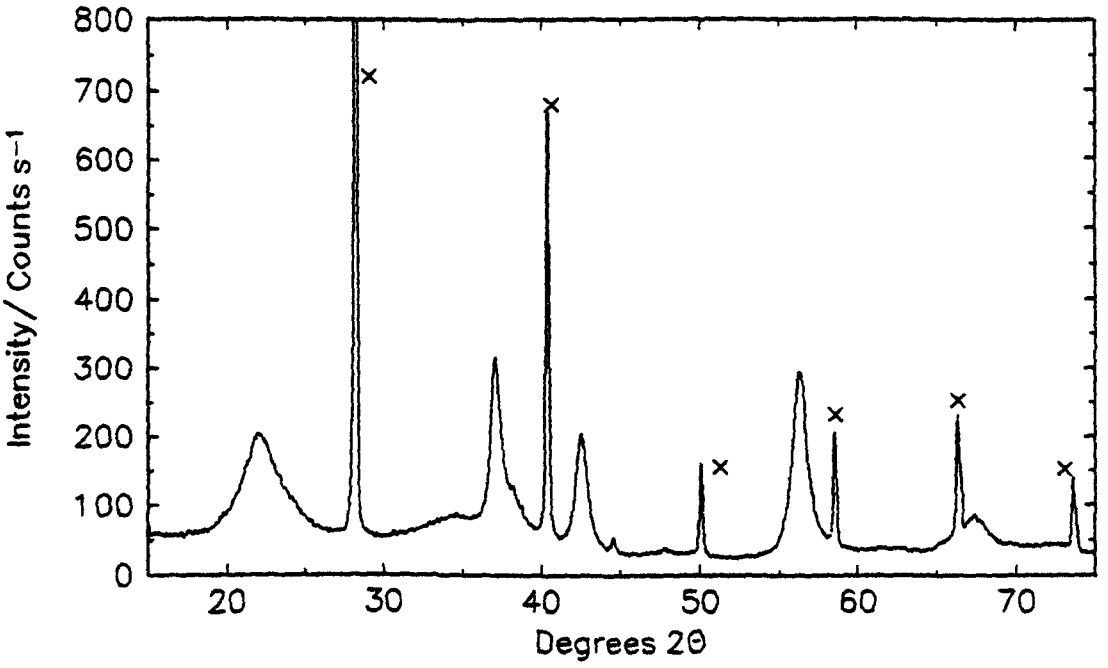


*Figure 4.1* : X-ray diffraction pattern of an EMD mixed with KCl (peaks marked with an x are due to KCl).

## *4.2.2 EMD heat-treated at 200°C.*[††]

### 4.2.2.(i) Propan-2-ol reduction.

The manganese oxyhydroxide samples were prepared using the method

[††]All the H inserted compounds in this work were made from materials heat-treated in air.

given in section 2.4.1. X-ray diffraction patterns are shown in figure 4.2, for materials reduced from $MnOOH_{0.07}$ (the starting material) to $MnOOH_{0.976}$ (the most reduced material). The precise level of H insertion (as determined by chemical analysis) is given on the right hand side of the figure. The results of a series of chemical analysis on these materials is shown in Table 4.2. Throughout this investigation two separate analyses were performed on the H inserted compounds and the average taken. Notice that from $MnOOH_{0.07}$ to $MnOOH_{0.745}$ the five main peaks (labelled A-E) have shifted to lower diffraction angles which indicates lattice dilation which has been reported many times in the literature (Gabano *et al.* 1965, Maskell *et al.* 1981 and Fitzpatrick and Tye 1991). After $MnOOH_{0.745}$ new peaks begin to appear in the X-ray pattern. Interplanar spacings for peaks A-D are plotted in figure 4.3. Peak E also shifts to lower angles with progressive H insertion although it was not possible to the obtain the peak position as accurately as for peaks A-D. Examination of figure 4.3 shows that the peaks move throughout the reduction range which would be consistent with a single phase process. A similar set of data has recently been reported by Fitzpatrick and Tye (1991) for the same EMD but this had not been heat-treated prior to reduction. The actual movement of peaks A-D can be seen more clearly in figures 4.4-4.7. For example peak A moves from 67.9°2Θ to 65°2Θ also the appearance of a new peak is seen at 61.5°2Θ. For peak C it is also possible to see the appearance of a new peak at 39.9°2Θ after $MnOOH_{0.75}$. The heights of peaks A-D are plotted in figure 4.8 where interesting trends in the data are observed. The height of peak D is invariant of H insertion until $MnOOH_{0.69}$ and then it decreases to $MnOOH_{0.976}$. Peak B decreases in a reasonably linear fashion to $MnOOH_{0.70}$ and then increases to the reduction product. It would be reasonable to say that for all the peaks (except C) major changes in peak height behaviour occur around $MnOOH_{0.70}$. If the lattice were expanding isotropically then the ratio of the interplanar spacings would be constant. Ratios derived for peaks A-D are shown in figure 4.9. Examination of this figure shows that the changes in the interplanar spacing ratios are evident after $MnOOH_{0.70}$ and this is correlates with appearance of new lines in the X-ray diffraction pattern. The scales used in figure 4.9 are very small; for example the ratio of peaks D/A changed from 1.746 at $MnOOH_{0.070}$ to 1.731 at $MnOOH_{0.70}$ and this represents

a change of 0.86%. The data presented in this section agree well with the published data on the reduction of EMD (Fitzpatrick and Tye 1991, Giovanoli and Leuenberger 1969 and Maskell *et al.* 1981).

*Table 4.2* : Series of chemical analysis to determine the stoichiometry of manganese oxyhydroxide samples reduced by propan-2-ol (see section 2.2.2 for details of technique).

| Sample No. | 1st analysis of x | 2nd analysis of x | Average x | r in $MnOOH_r$ |
|---|---|---|---|---|
| 1 | 1.965 | 1.965 | 1.965 | 0.070 |
| 2 | 1.924 | 1.923 | 1.923 | 0.153 |
| 3 | 1.910 | 1.912 | 1.911 | 0.178 |
| 4 | 1.906 | 1.910 | 1.908 | 0.184 |
| 5 | 1.902 | 1.906 | 1.904 | 0.192 |
| 6 | 1.890 | 1.896 | 1.893 | 0.214 |
| 7 | 1.884 | 1.884 | 1.884 | 0.232 |
| 8 | 1.875 | 1.872 | 1.873 | 0.253 |
| 9 | 1.866 | 1.870 | 1.868 | 0.264 |
| 10 | 1.840 | 1.856 | 1.848 | 0.304 |
| 11 | 1.814 | 1.814 | 1.814 | 0.371 |
| 12 | 1.794 | 1.810 | 1.802 | 0.396 |
| 13 | 1.775 | 1.772 | 1.773 | 0.454 |
| 14 | 1.751 | 1.753 | 1.752 | 0.496 |
| 15 | 1.742 | 1.747 | 1.745 | 0.511 |
| 16 | 1.735 | 1.737 | 1.736 | 0.528 |
| 17 | 1.713 | 1.715 | 1.714 | 0.572 |
| 18 | 1.708 | 1.709 | 1.708 | 0.582 |
| 19 | 1.680 | 1.680 | 1.680 | 0.640 |
| 20 | 1.641 | 1.644 | 1.643 | 0.714 |
| 21 | 1.629 | 1.626 | 1.627 | 0.745 |
| 22 | 1.616 | 1.616 | 1.616 | 0.767 |
| 23 | 1.607 | 1.608 | 1.607 | 0.785 |
| 24 | 1.589 | 1.593 | 1.591 | 0.818 |
| 25 | 1.587 | 1.585 | 1.586 | 0.828 |
| 26 | 1.559 | 1.558 | 1.558 | 0.882 |
| 27 | 1.519 | 1.524 | 1.521 | 0.958 |
| 28 | 1.512 | 1.512 | 1.512 | 0.976 |

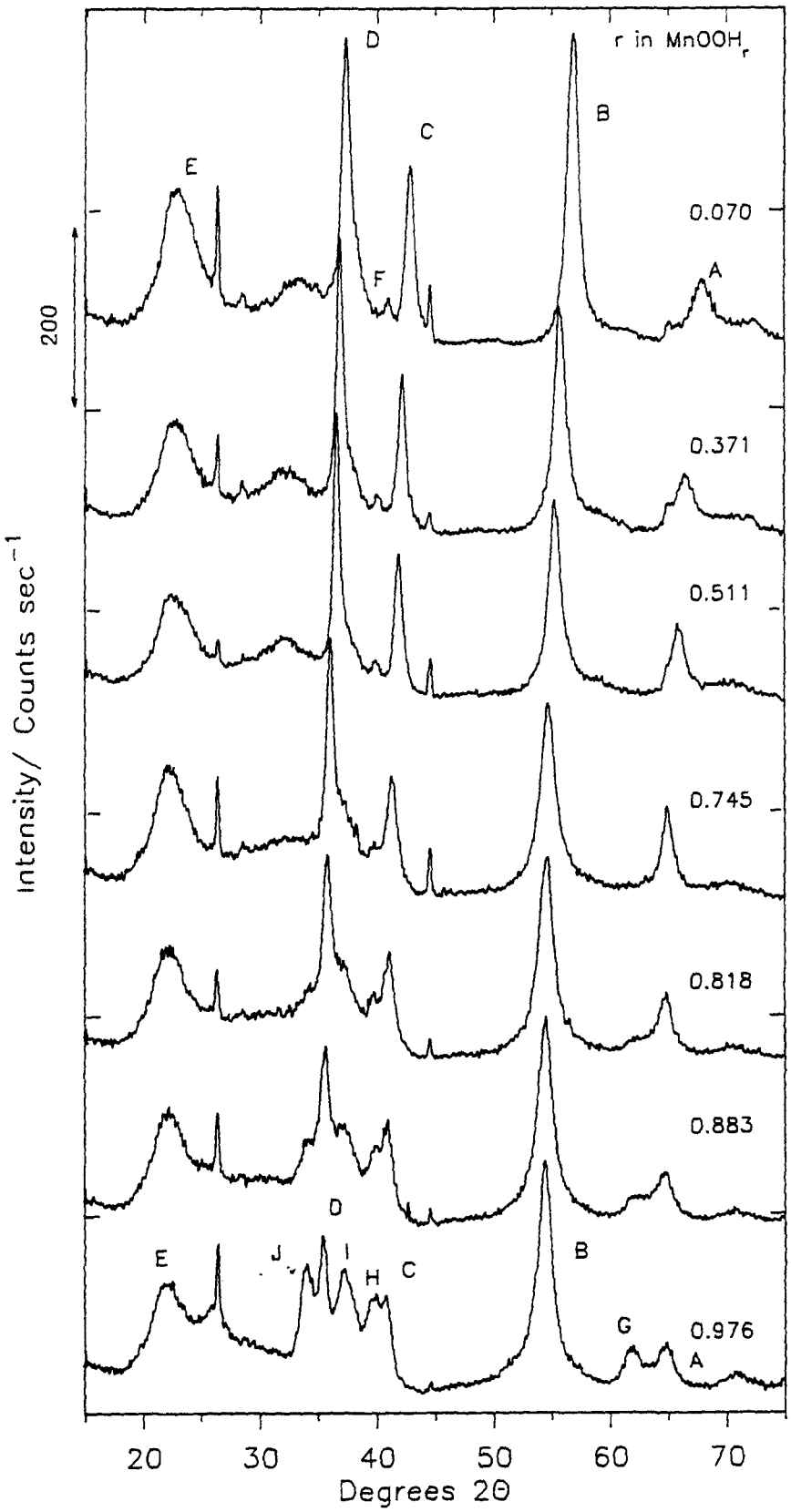


***Figure 4.2*** : X-ray diffraction spectra during the reduction of an EMD heat-treated at 200°C; propan-2-ol reduction method (the level of H insertion is given above the XRD pattern).

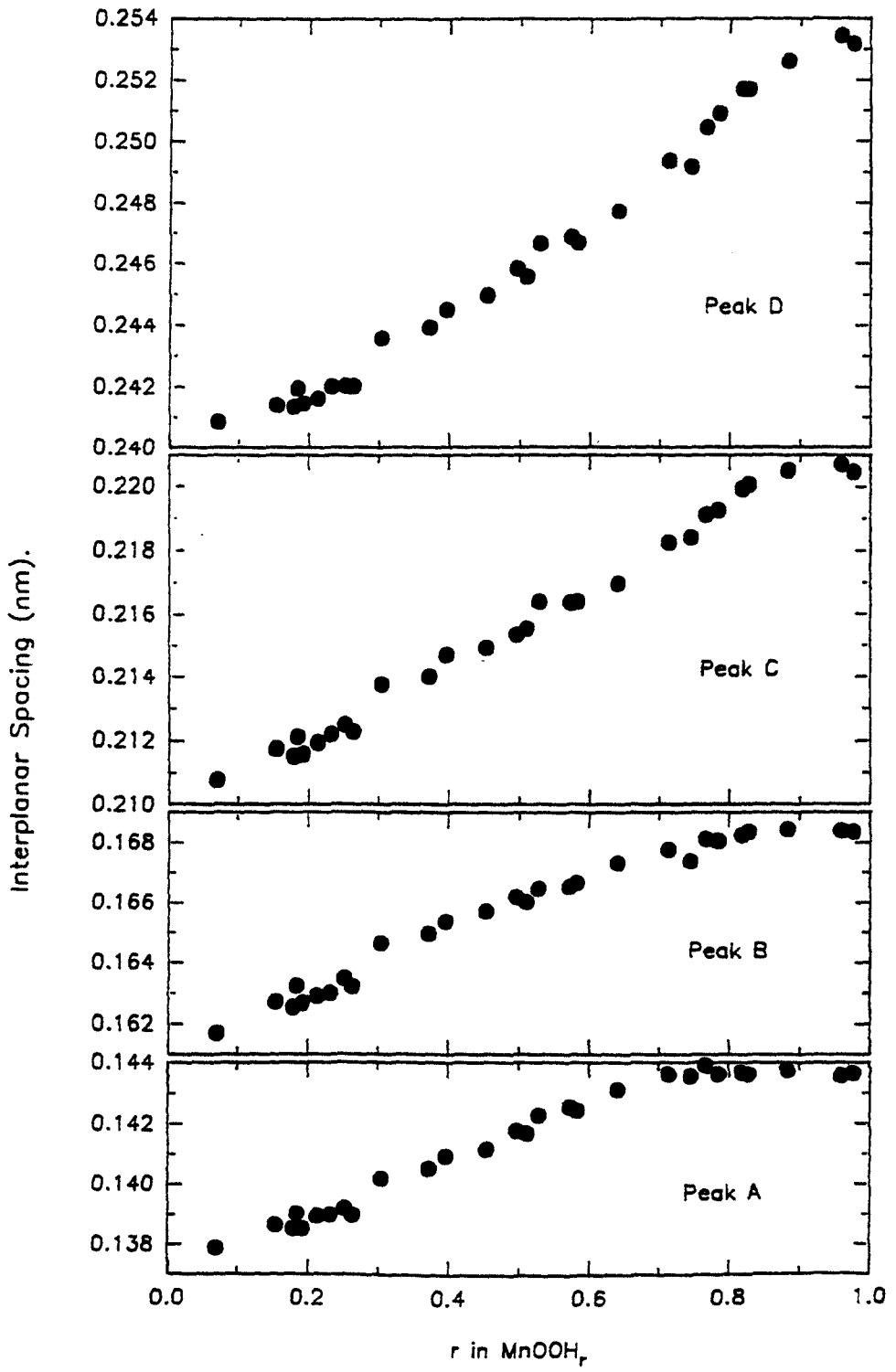


***Figure 4.3***: Interplanar spacing against H insertion level: EMD heat-treated at 200°C; propan-2-ol reduction method (see figure 4.2 for peak labelling).

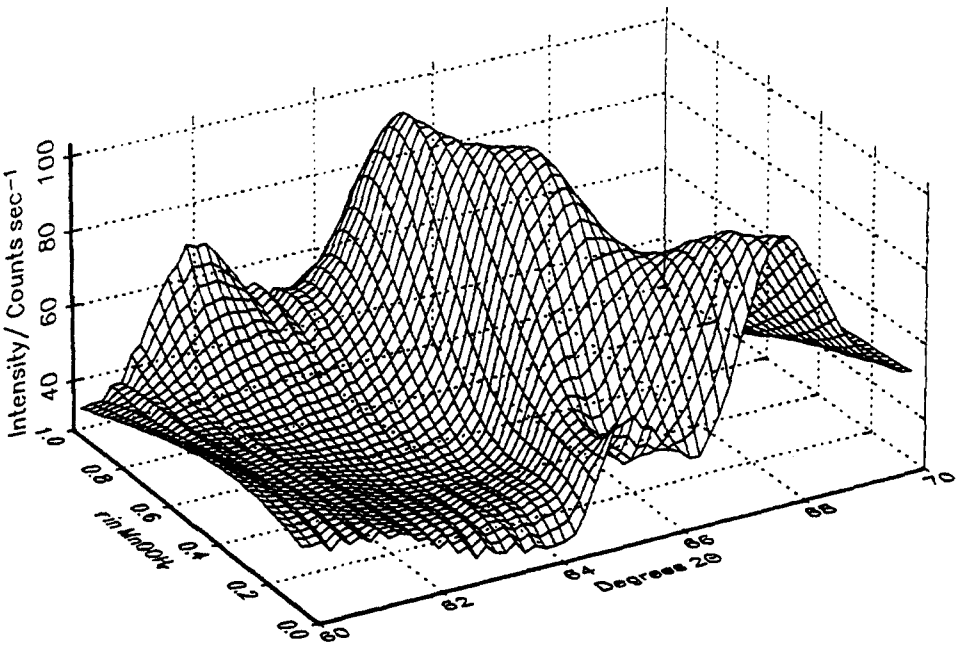


*Figure 4.4* : Movement of Peak A during the reduction of EMD heat-treated at 200°C;propan-2-ol reduction method (data grid from 0.07-0.97 in 0.0225 increments in r in MnOOH, and from 60-70.08°2Θ in 0.16 increments).

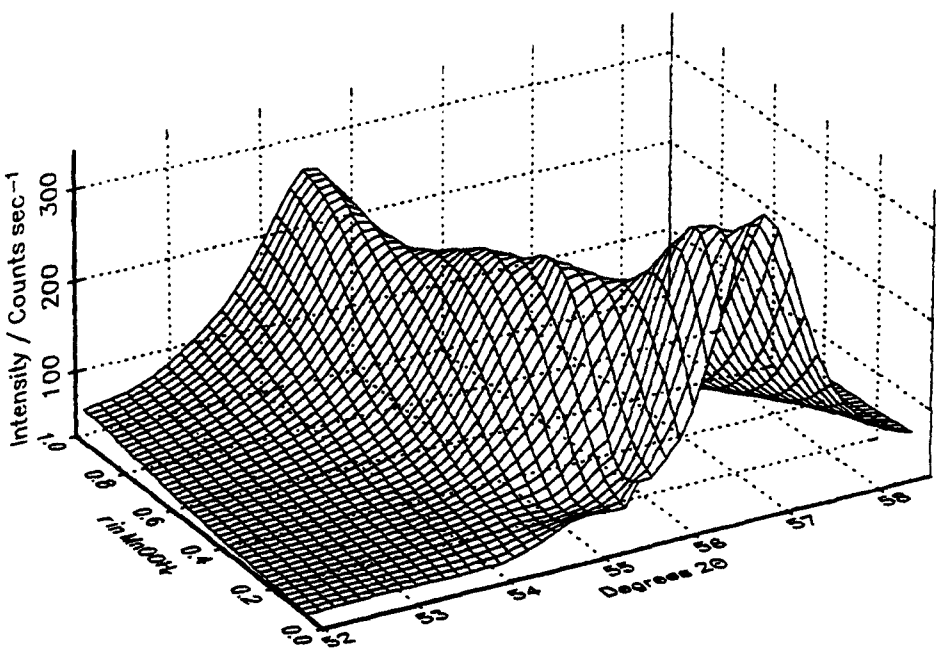


*Figure 4.5* :Movement of peak B during the reduction of EMD heat-treated at 200°C; propan-2-ol method reduction.

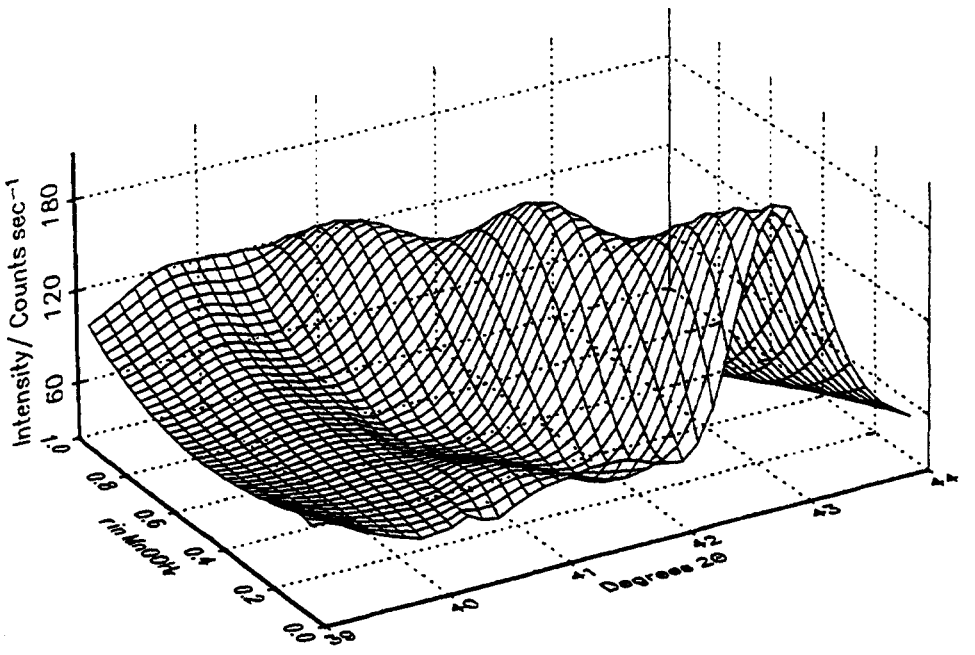


*Figure 4.6* :Movement of peak C during the reduction of EMD heat-treated at 200°C;propan-2-ol reduction method.

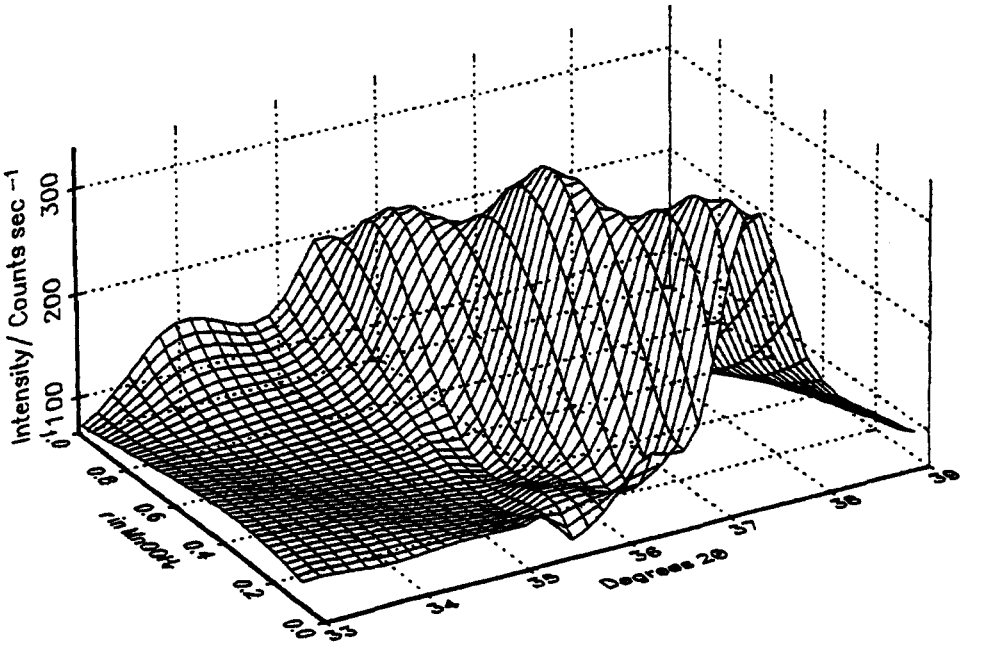


*Figure 4.7*: Movement of peak D during the reduction of EMD heat-treated at 200°C;propan-2-ol reduction method.

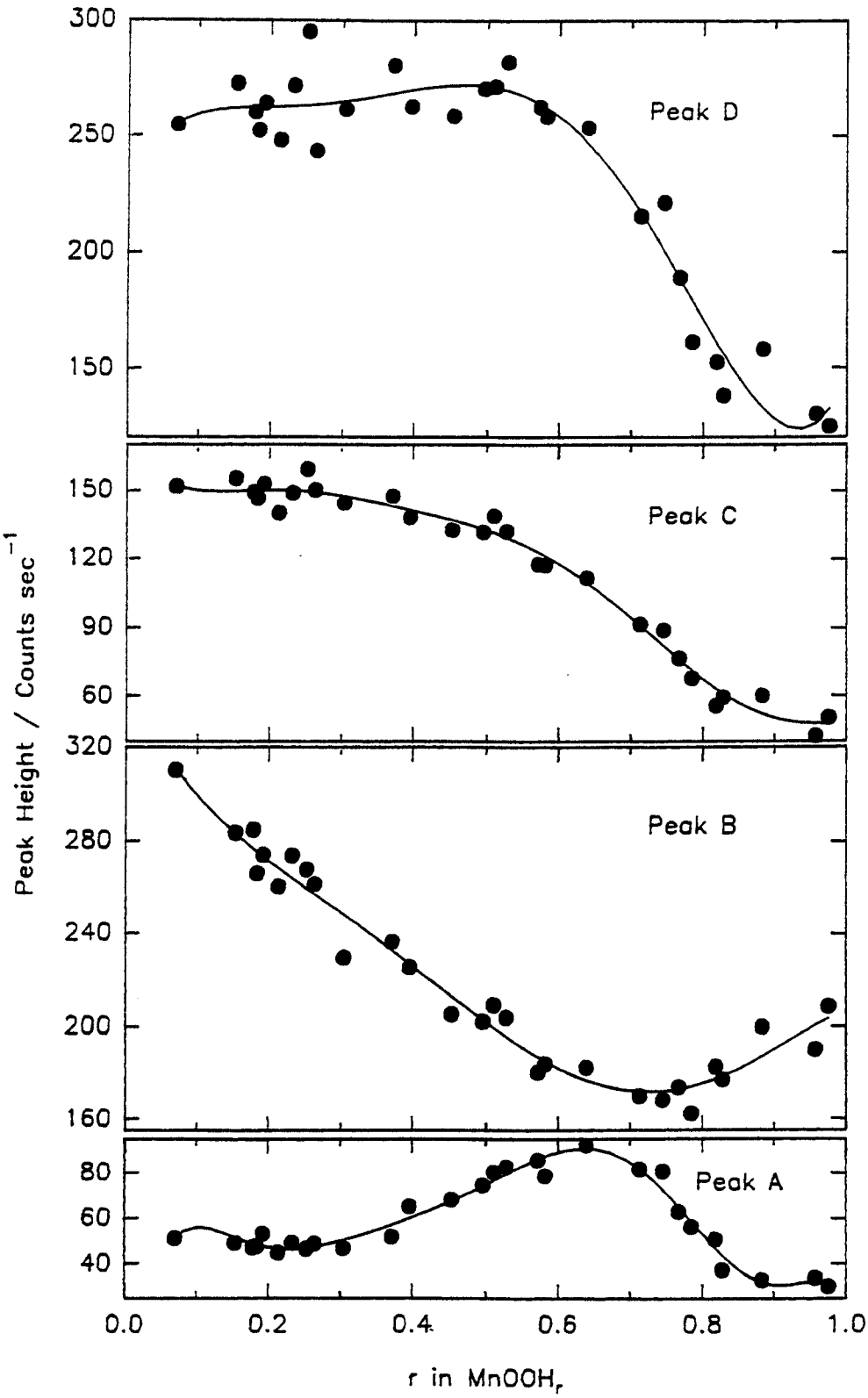


***Figure 4.8*** :Peak height against H insertion level for EMD heat-treated at 200°C;propan-2-ol reduction method.

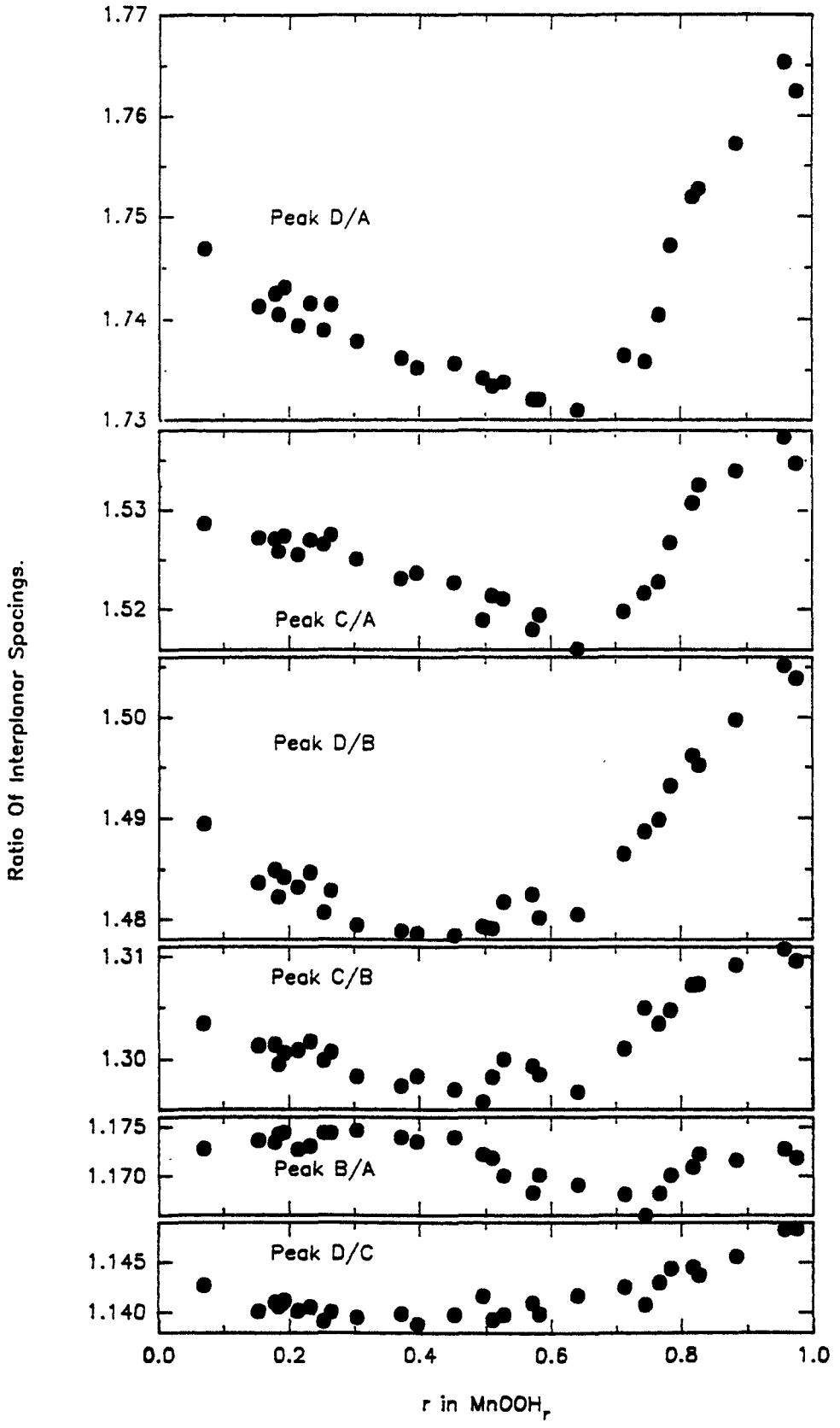


***Figure 4.9*** : Ratio of the interplanar spacings against H insertion level for peaks A-D;EMD heat-treated at 200°C; propan-2-ol reduction method.

4.2.2 (ii) Hydrazine hydrate reduction.

X-ray diffraction spectra for the reduction of the same material as in section 4.2.2.(i) but this time reduced by hydrazine hydrate are shown in figure 4.10. Notice that the patterns from $MnOOH_{0.070}$ to $MnOOH_{0.29}$ are unchanged except that the peaks have shifted to lower angles indicating a homogeneous reaction. Above this level of H insertion new peaks appear in the X-ray diffraction patterns. These peaks increase in intensity and the original lines decrease in intensity indicating a heterogeneous reaction. This is shown more clearly in figure 4.11 where the interplanar spacings are plotted against the H insertion level. It is interesting to compare figures 4.3 and 4.11 where it can be seen that the new lines appear at the same position as those of the most reduced material ($MnOOH_{0.976}$) of the same material but reduced by propan-2-ol. Between $MnOOH_{0.35}$ and $MnOOH_{0.6}$ there is a region where the interplanar spacings associated with peaks pertaining to the reduction product increase. This is because in this region there are particles of manganese dioxide that have different stoichiometries. What is happening is that hydrazine hydrate is reducing the manganese dioxide too quickly[‡] and only the surface of the $MnO_2$ is being reduced. Maskell *et al.* (1981) mentioned the irreversible reduction of $MnO_2$ if reduced at too fast a rate. Even though hydrazine hydrate has been used as a reducing agent by Ohzuku (1985) and Xia Xi (1989) this type of behaviour has not been reported before, although examination of the X-ray patterns of those workers would suggest that heterogeneous behaviour was occurring. The results would also show the importance of having a fairly large number of H insertion compounds and plotting the peak positions with degree of reduction. This approach was not taken by Xia Xi and Ohzuku and hence the possibility of heterogeneous reduction was overlooked. In figure 4.12 peak heights are plotted against H insertion and this can be compared with figure 4.6 for the propan-2-ol reduction. In figures 4.13-4.16 the movement of the individual peaks are shown and the heterogeneous behaviour can be seen clearly. In figure 4.17 the X-ray patterns of $MnOOH_{0.44}$ that had been made by different methods is shown.

[‡]Fitzpatrick and Tye (1991) showed that at r=0.8 the behaviour changed significantly and protons became less mobile or 'frozen' in microcrystalline regions. If the reduction is too fast the critical value of r may be reached on the surface and this new state is not dispersed by diffusion therefore heterogeneity sets in.

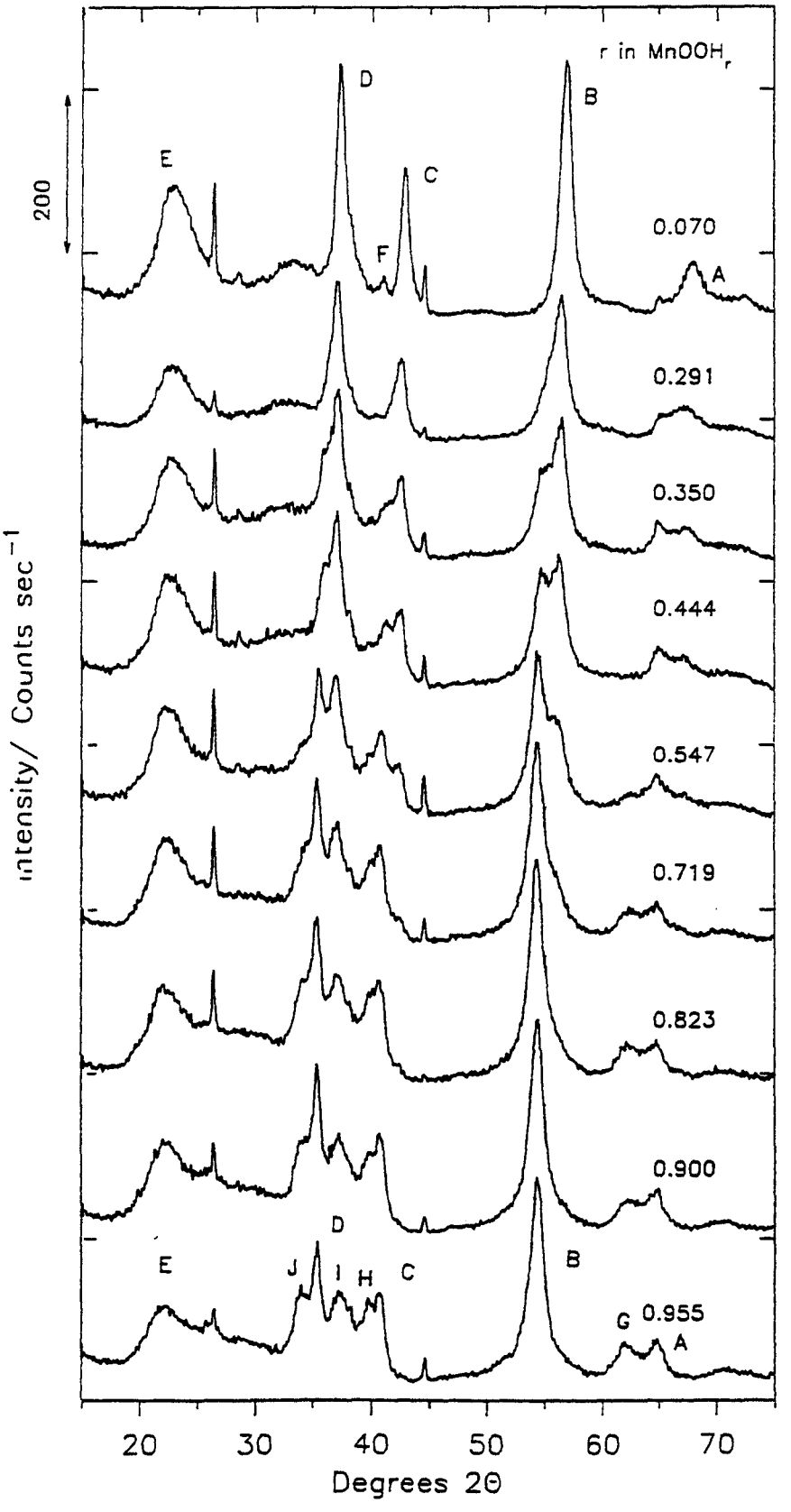


***Figure 4.10*** : X-ray diffraction spectra for the reduction of EMD heat-treated at 200°C; hydrazine hydrate reduction method (the H insertion level is given above the XRD pattern).

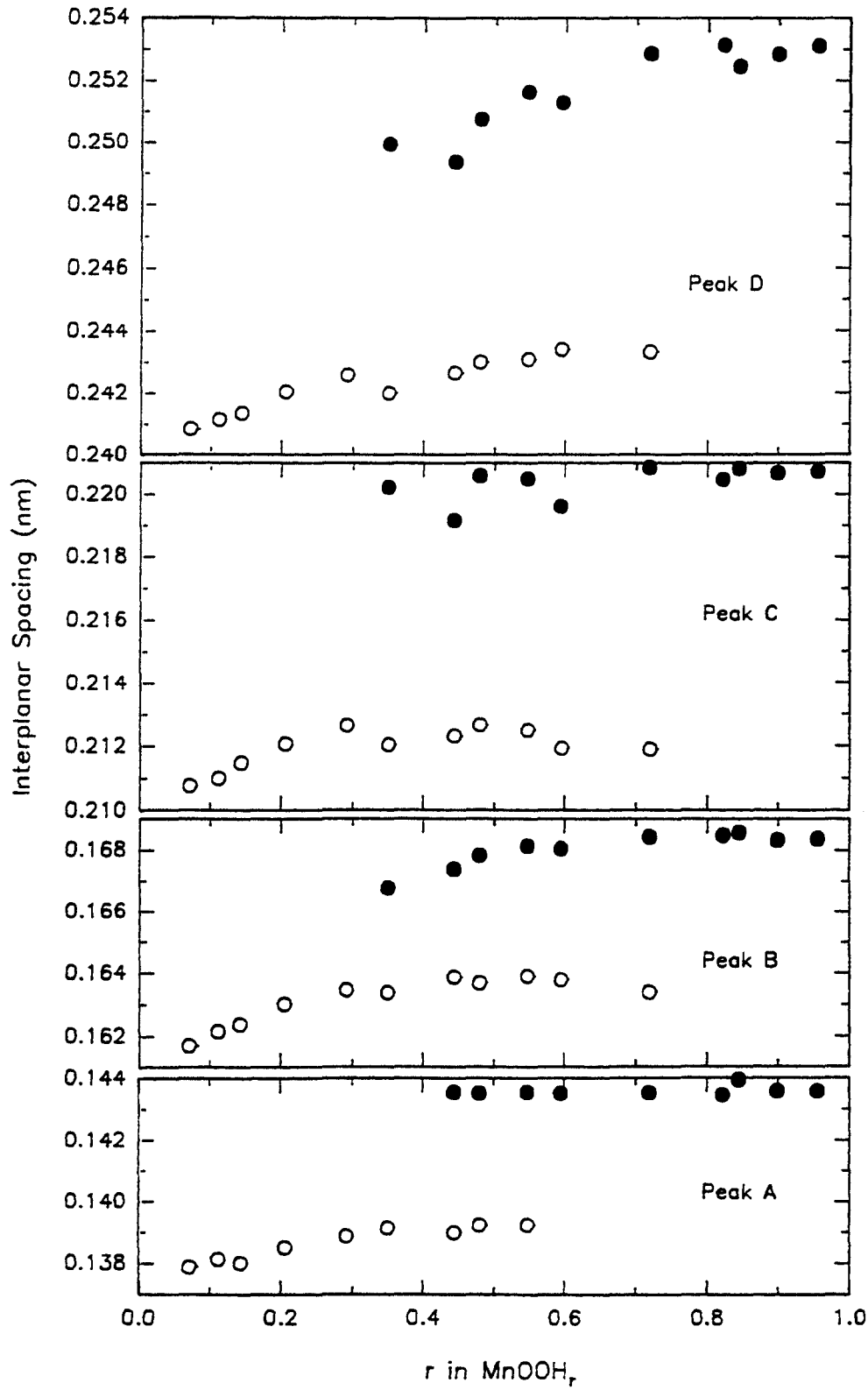


***Figure 4.11*** : Interplanar spacing against H insertion level;EMD heat-treated at 200°C; hydrazine hydrate reduction method (see figure 4.10 for peak labelling).

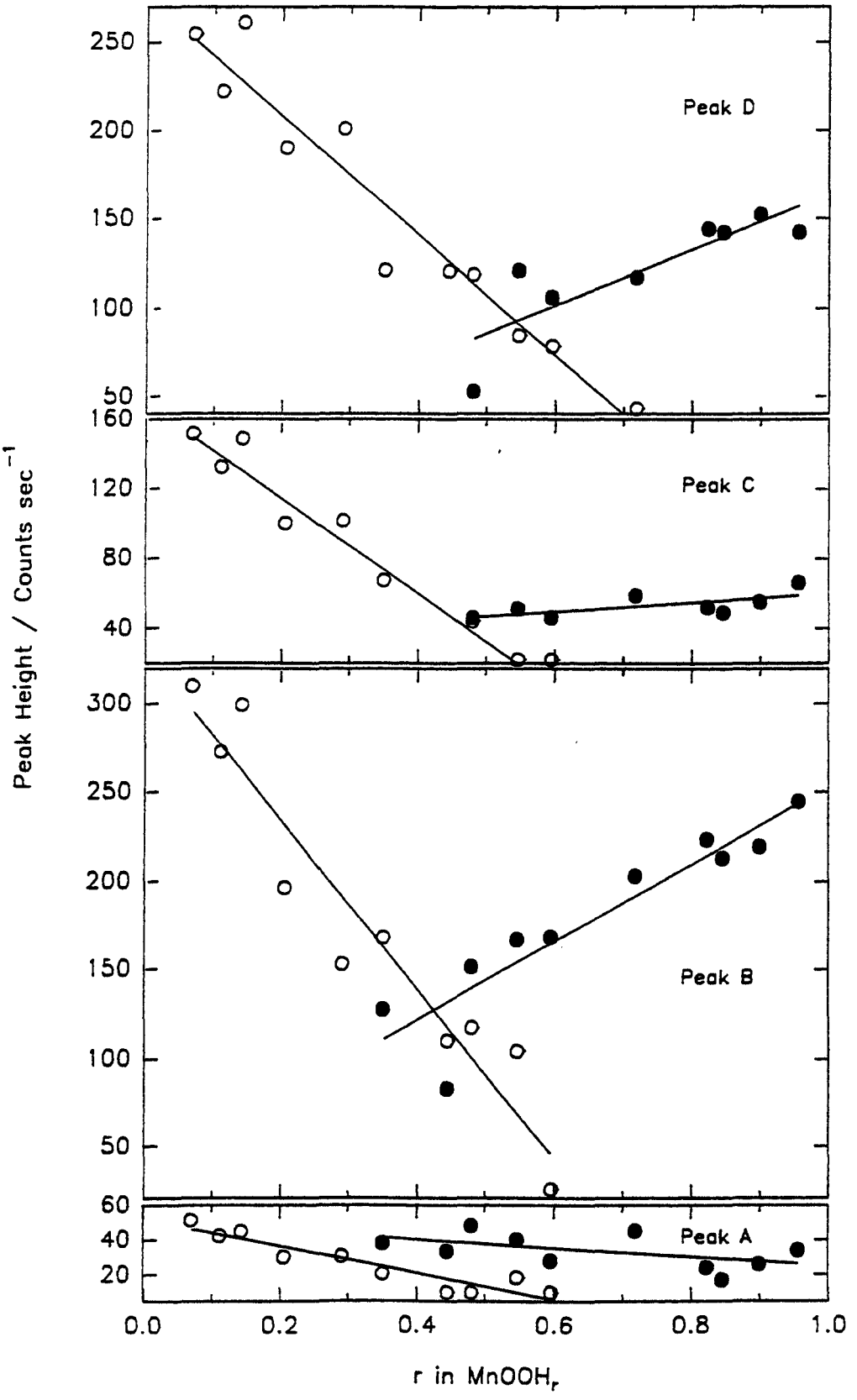


***Figure 4.12***: Peak height against H insertion level;EMD heat-treated at 200°C;hydrazine hydrate reduction method (see figure 4.10 for peak labelling).

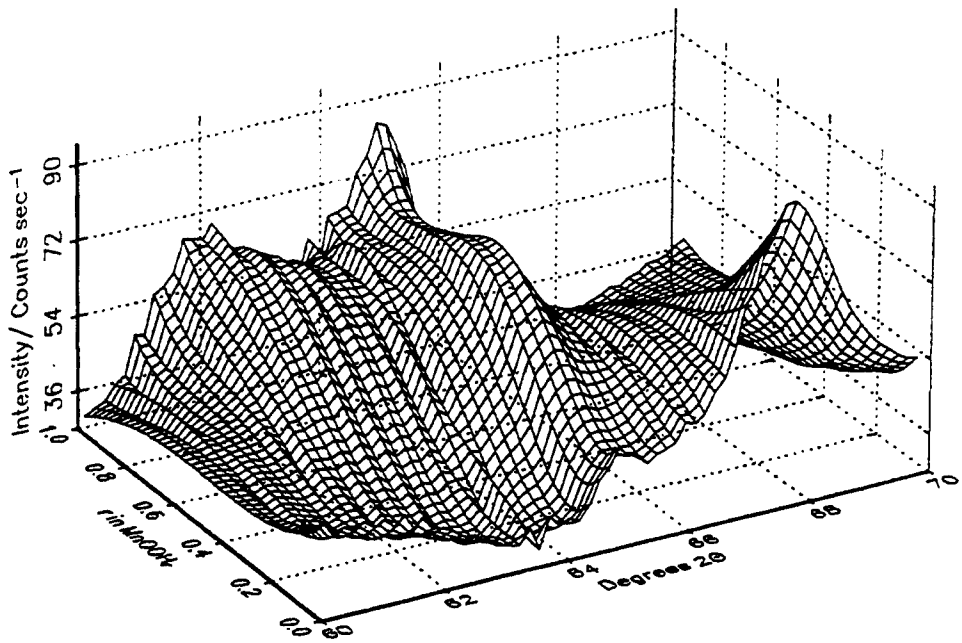


*Figure 4.13* : Movement of Peak A during the reduction of EMD heat-treated at 200°C; hydrazine hydrate reduction method (data grid from 0.07-0.97 in 0.0225 increments in r in $MnOOH_r$ and from 60-70.08°2Θ in 0.16 increments).

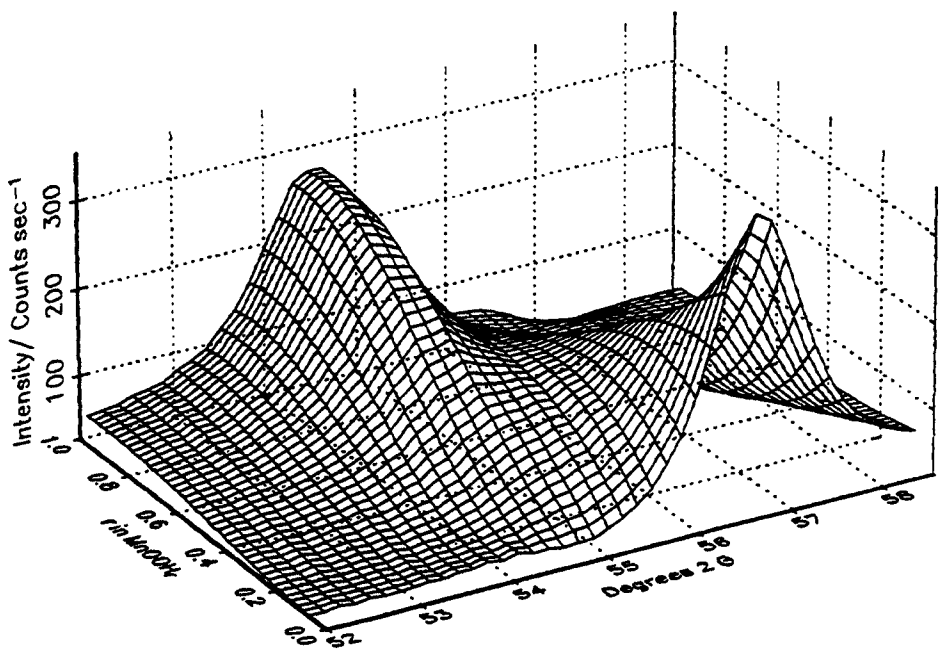


Figure 4.14 : Movement of peak B during the reduction of EMD heat-treated at 200°C; hydrazine hydrate reduction method.

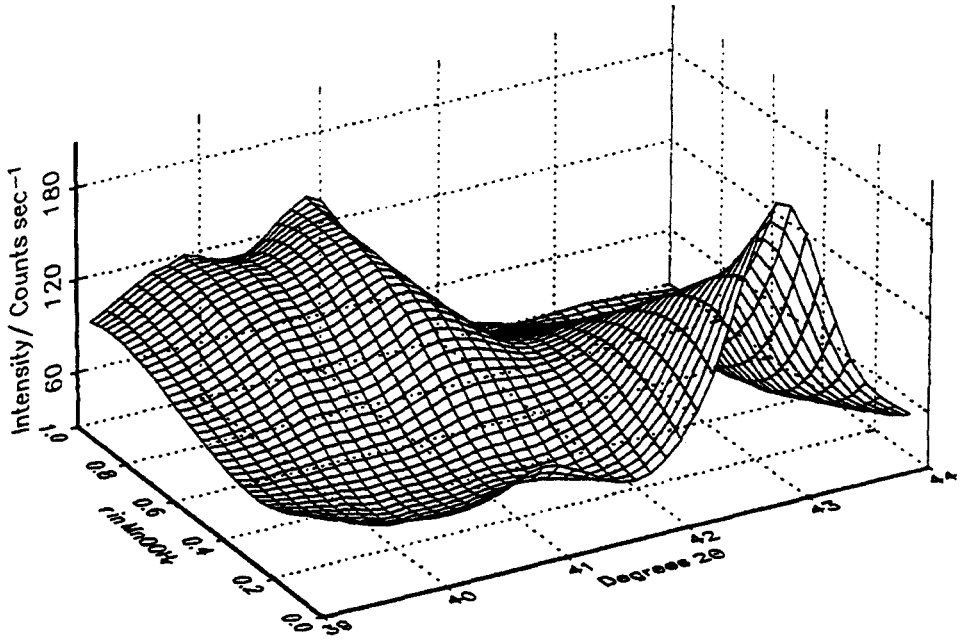


*Figure 4.15*: Movement of peak C during the reduction of EMD heat-treated at 200°C; hydrazine hydrate reduction method.

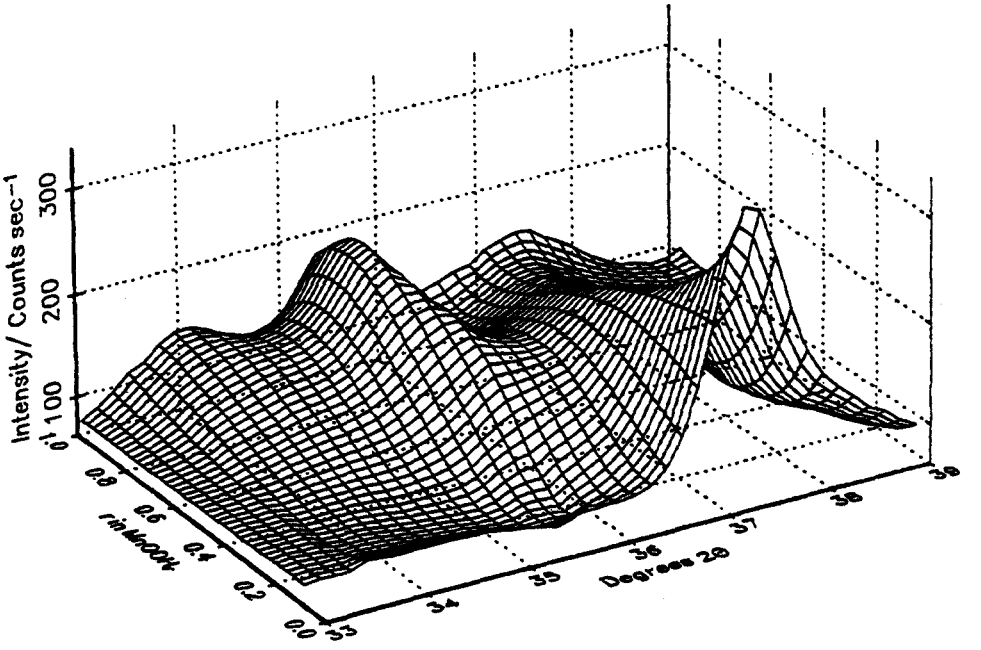


*Figure 4.16* : Movement of peak D during the reduction of EMD heat-treated at 200°C; hydrazine hydrate reduction method.

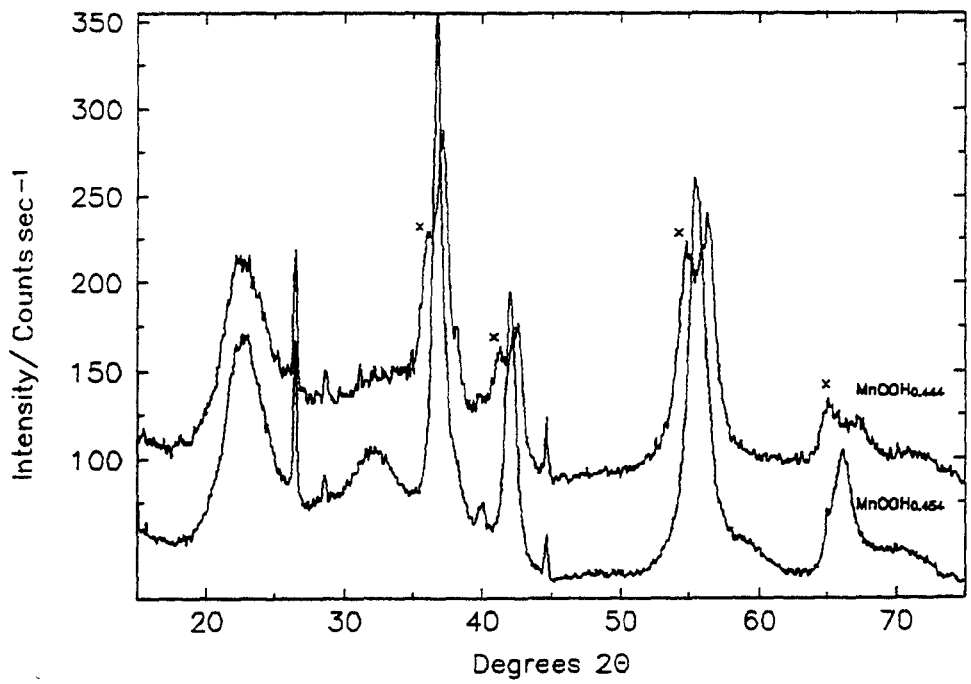


*Figure 4.17* : Comparison of the x-ray diffraction patterns of $MnOOH_{0.444}$ and $MnOOH_{0.454}$ for EMD heat-treated at 200°C and reduced by hydrazine and propan-2-ol respectively (peaks marked with an x are those pertaining to the surface of $MnO_2$). The hydrazine pattern is displaced upwards by 60 $cs^{-1}$.

## *4.2.3 EMD heat-treated at 300°C.*

### 4.2.3 (i) Propan-2-ol reduction.

X-ray diffraction spectra for the reduction of an EMD heat-treated at 300°C and then reduced by propan-2-ol are shown in figure 4.18. If this is compared with the EMD heat-treated at 200°C (figure 4.2) it can be seen that peaks B, C and D of the starting material are of lower intensity and are broader. It can also be seen that the reaction was not homogeneous throughout the range $MnOOH_{0.08}$-$MnOOH_{0.967}$ as was observed with EMD heat-treated at 200°C. In section 3.5 X-ray diffraction patterns were shown for this material when it was heat-treated from 25-450°C and it was noted that $MnO_2$ changed structure between 275-400°C. At 300°C all the physisorbed and most of the combined water have been removed from the $MnO_2$ and the concentration of pyrolusite domains have increased (Laudy and de Wolff 1963). It is therefore not surprising that the H insertion process is different to that observed at 200°C. The

interplanar spacings associated with peaks B, C and D are plotted in figure 4.19 the movement of peaks B, C and D is apparent from $MnOOH_{0.08}$ to $MnOOH_{0.53}$. Within this range, however, the movement of these peaks is less than that of the material heat-treated at 200°C. Above $MnOOH_{0.53}$ new peaks appear . The same type of behaviour was observed for the EMD heat-treated at 200°C and reduced by hydrazine hydrate. The peak heights are plotted in figure 4.20 and this figure can be compared with figure 4.11 for example peak D is invariant of H insertion from $MnOOH_{0.07}$-$MnOOH_{0.64}$ whereas at 300°C the peak has decreased from 250-150 counts $s^{-1}$. Figures 4.21-4.23 show the movement of the individual peaks.

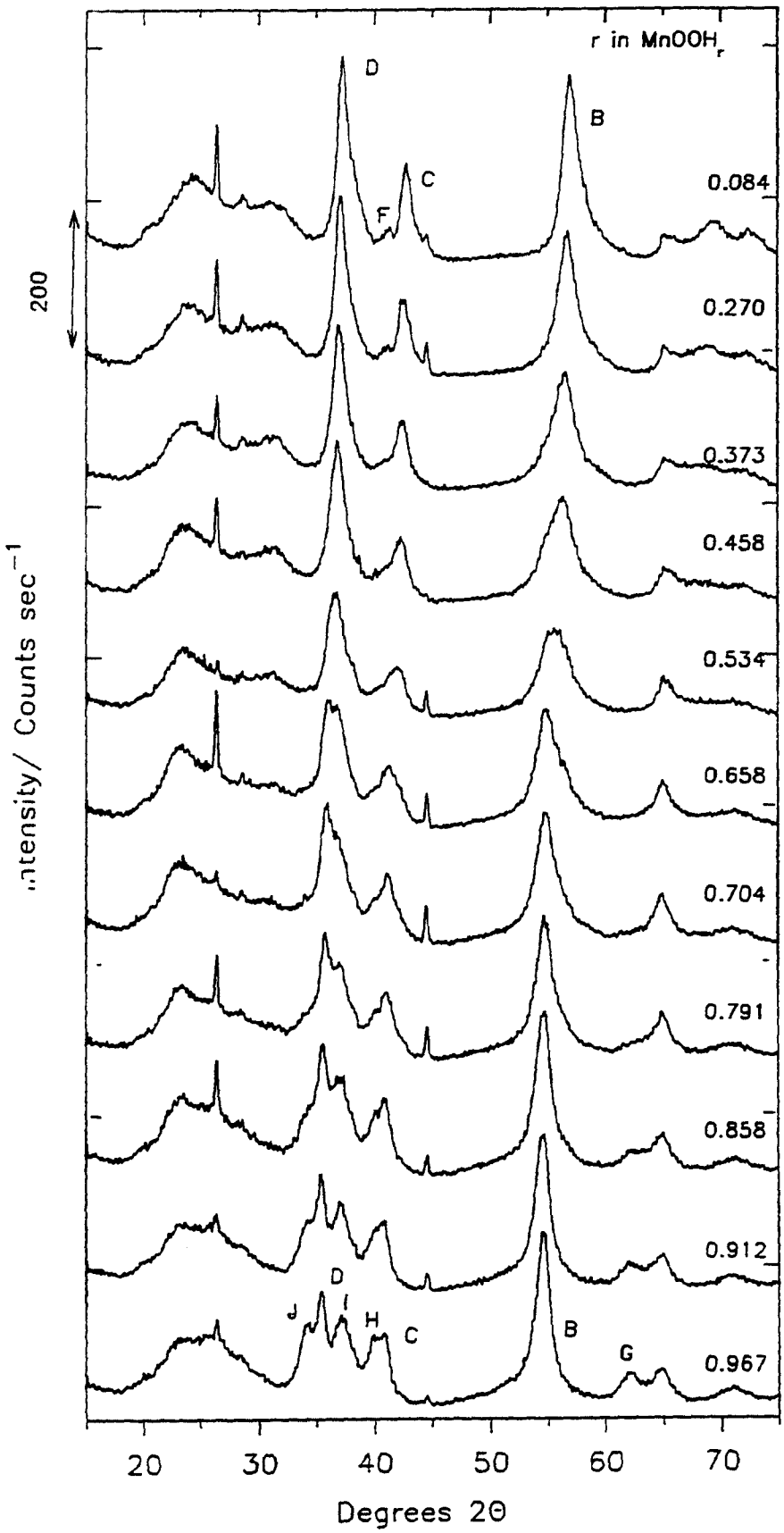


*Figure 4.18* : X-Ray diffraction spectra during the reduction of an EMD heat-treated at 300°C; propan-2-ol reduction method (the level of H insertion is given above the XRD pattern).

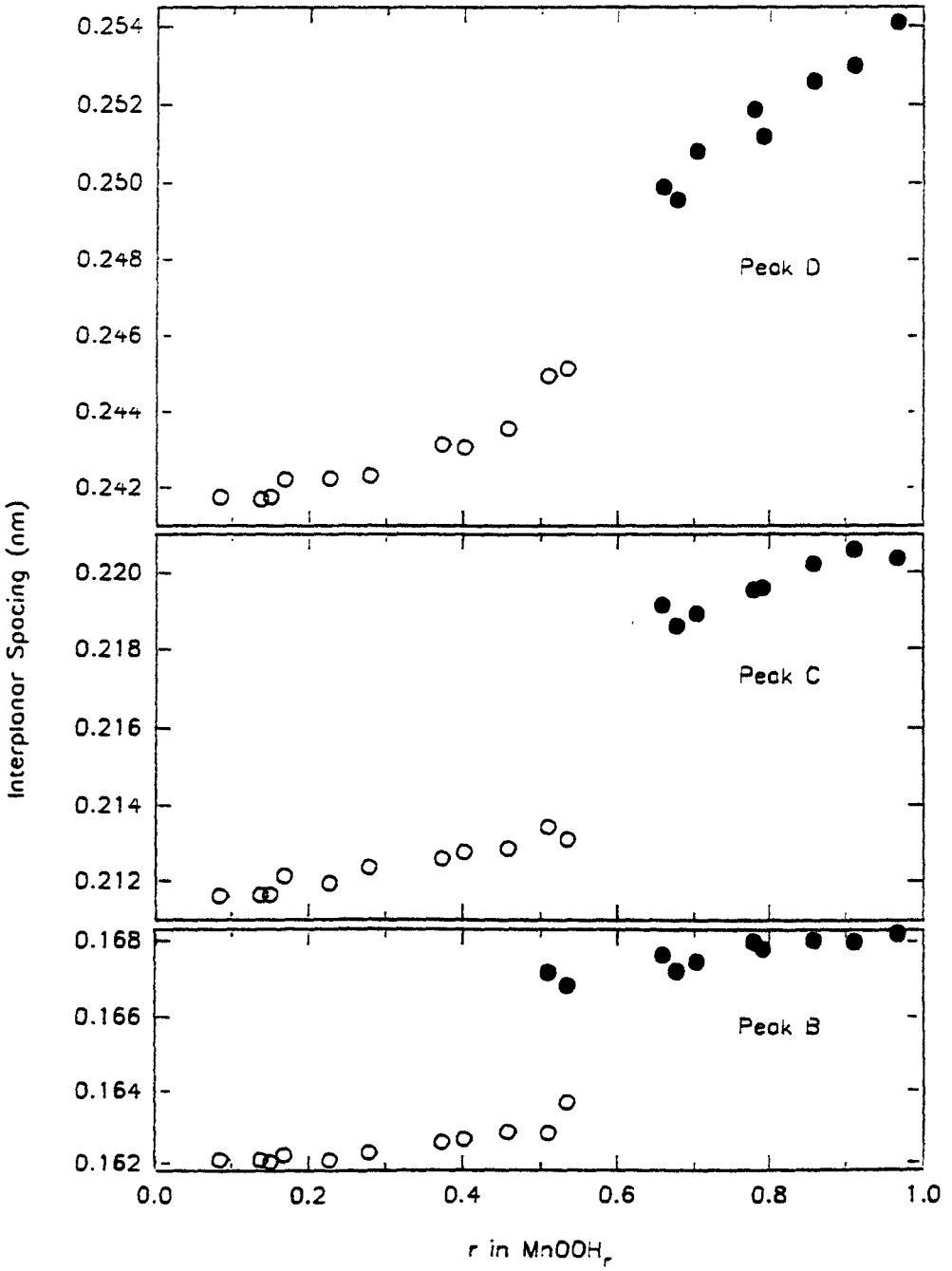


***Figure 4.19*** : Interplanar spacing against H insertion level;EMD heat-treated at 300°C;propan-2-ol reduction method (see figure 4.18 for peak labelling).

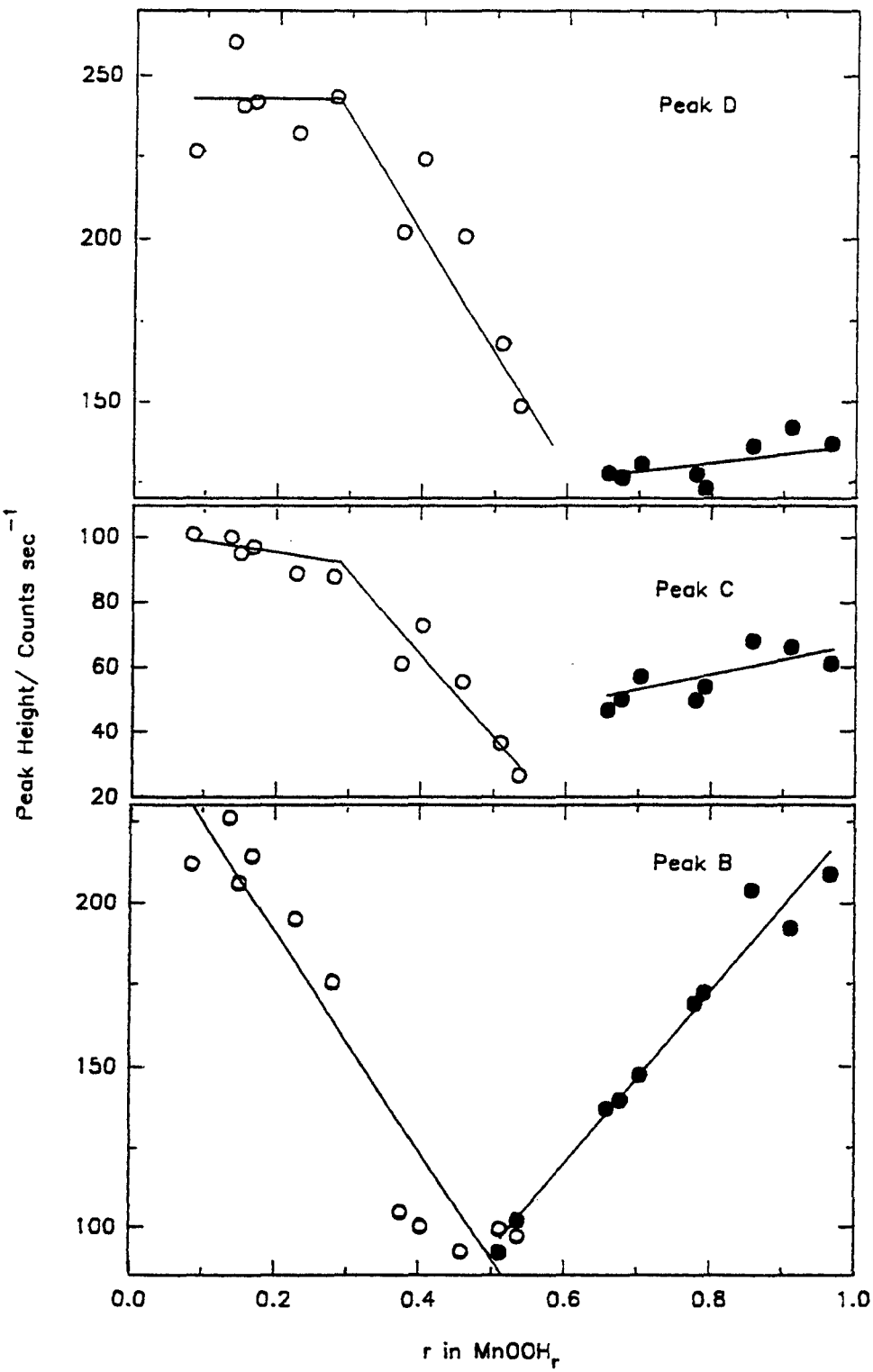


*Figure 4.20* : Peak height against H insertion level; EMD heat-treated at 300°C; propan-2-ol reduction method (see figure 4.18 for peak labelling).

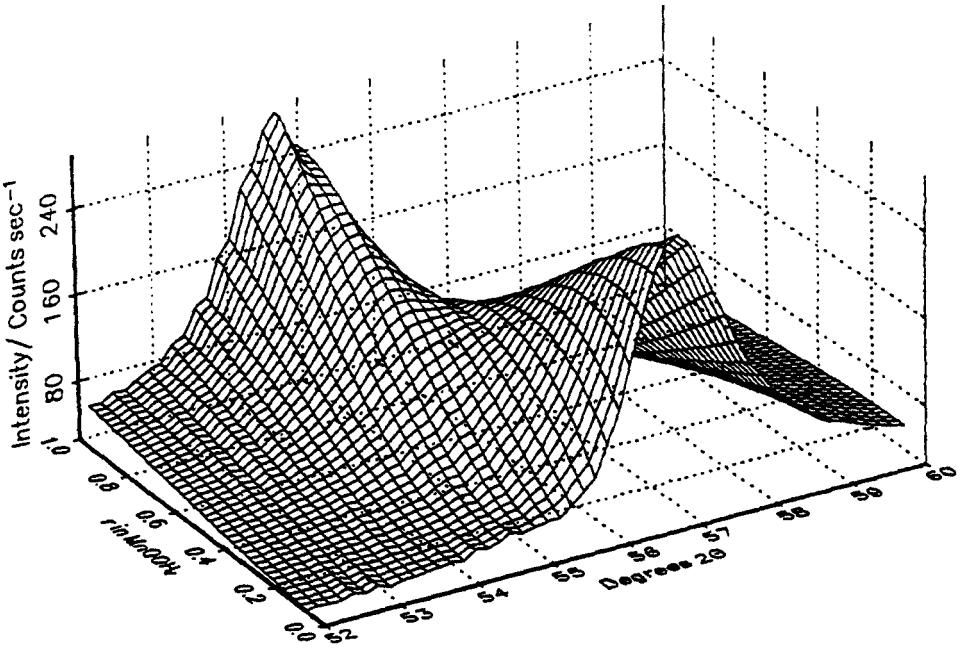


*Figure 4.21* : Movement of Peak B during the reduction of EMD heat-treated at 200°C; propan-2-ol reduction method (data grid from 0.08-0.96 in 0.022 increments in r in MnOOH, and from 52-60°2Θ in 0.16 increments).

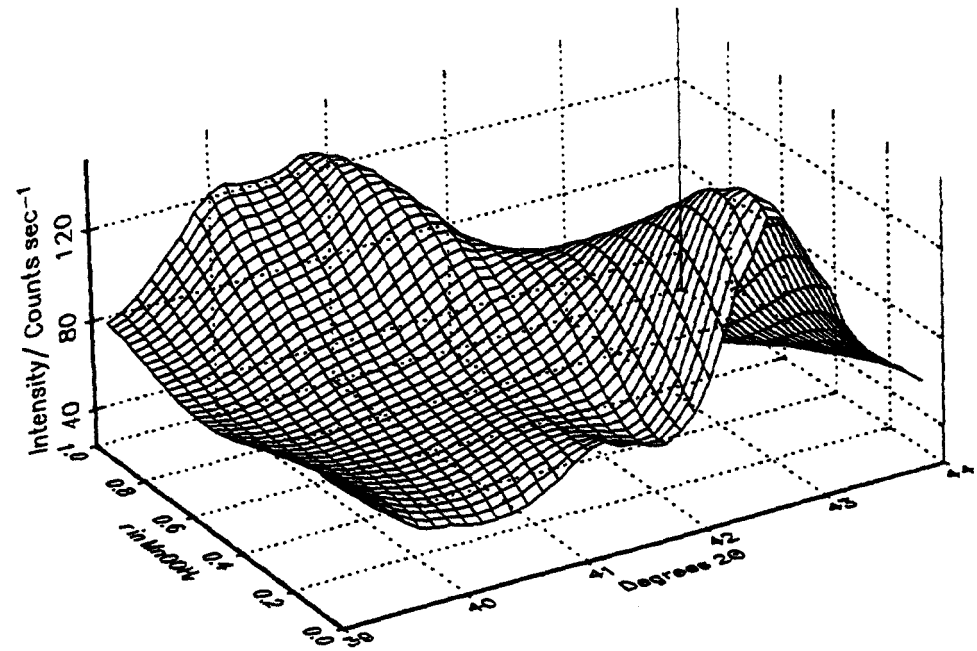


*Figure 4.22* : Movement of peak C during the reduction of EMD heat-treated at 300°C; propan-2-ol reduction method.

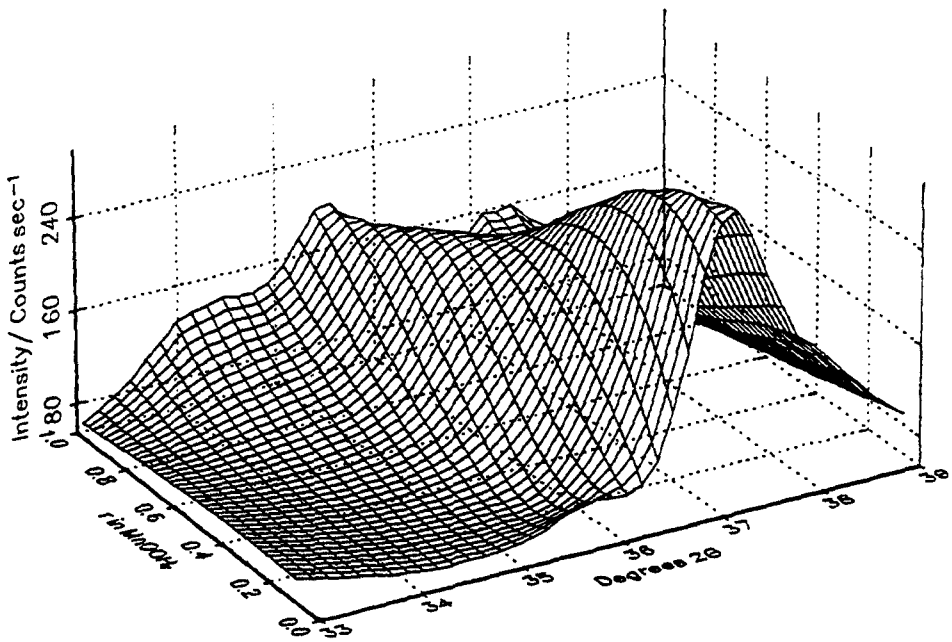


*Figure 4.23* : Movement of peak D during the reduction of EMD heat-treated at 300°C; propan-2-ol reduction method.

4.2.3 (ii) Hydrazine hydrate reduction.

X-ray diffraction spectra for the reduction of an EMD heat-treated at 300°C and reduced by hydrazine hydrate are shown in figure 4.24. If hydrazine can induce heterogeneous behaviour at 200°C from $MnOOH_{0.35}$ then it is not surprising that heterogeneous behaviour is observed from very early on in the reduction process. Examination of the interplanar spacings (figure 4.25) shows that there is very little movement of the solid solution peaks; the same material reduced by propan-2-ol showed movement to $MnOOH_{0.53}$. Figure 4.26 shows the peak height against H insertion level; notice that peaks B, C and D decrease in an almost linear fashion to $MnOOH_{0.70}$. The reduction product is identical to that of the same material reduced by propan-2-ol. The movement of the individual peaks is shown in figures 4.27-4.29. Figure 4.30 compares two compounds of similar a H insertion level but prepared by different methods.

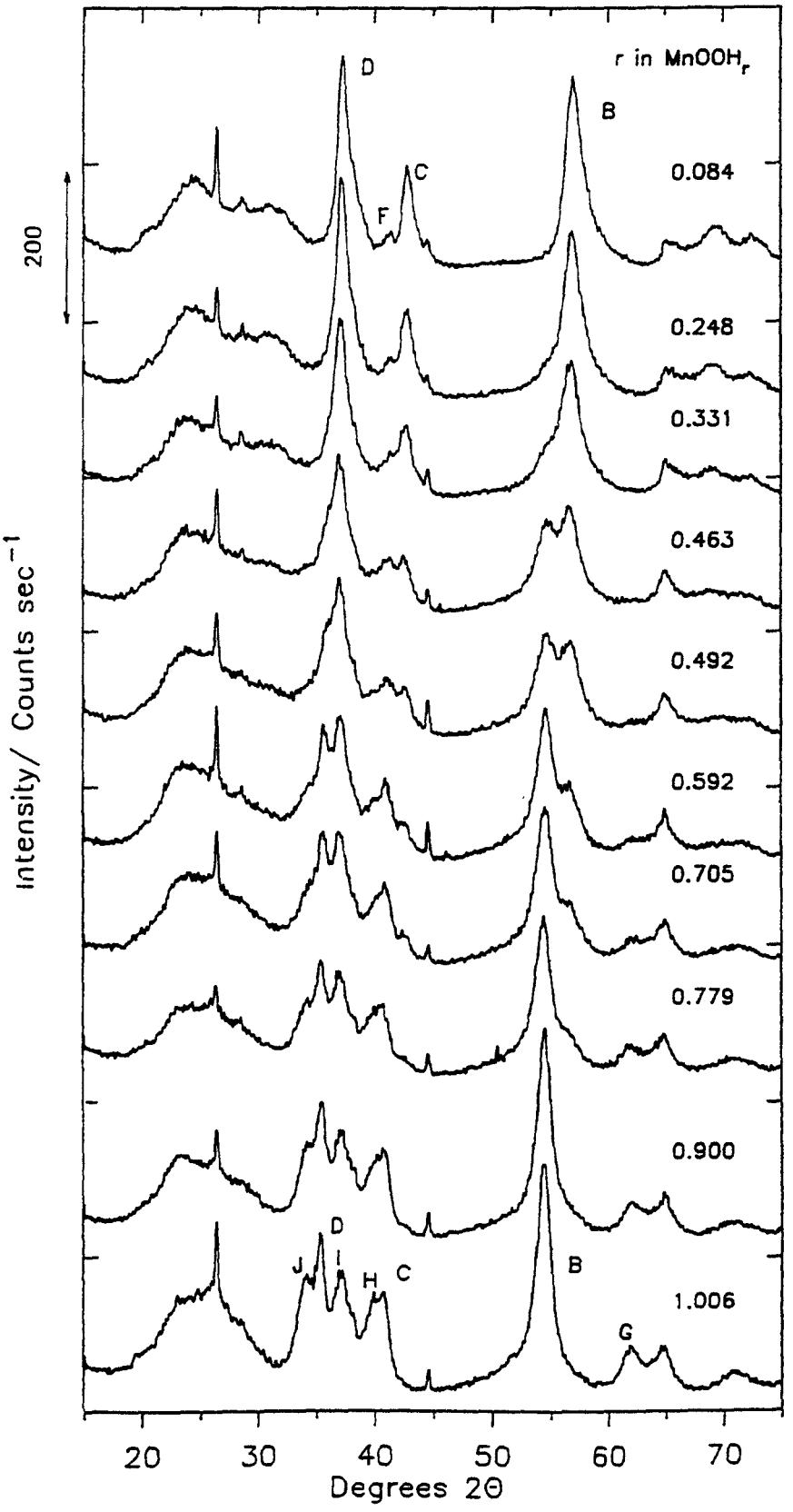


***Figure 4.24*** : X-ray diffraction spectra during the reduction of an EMD heat-treated at 300; hydrazine hydrate reduction method (the level of H insertion is given above the XRD pattern).

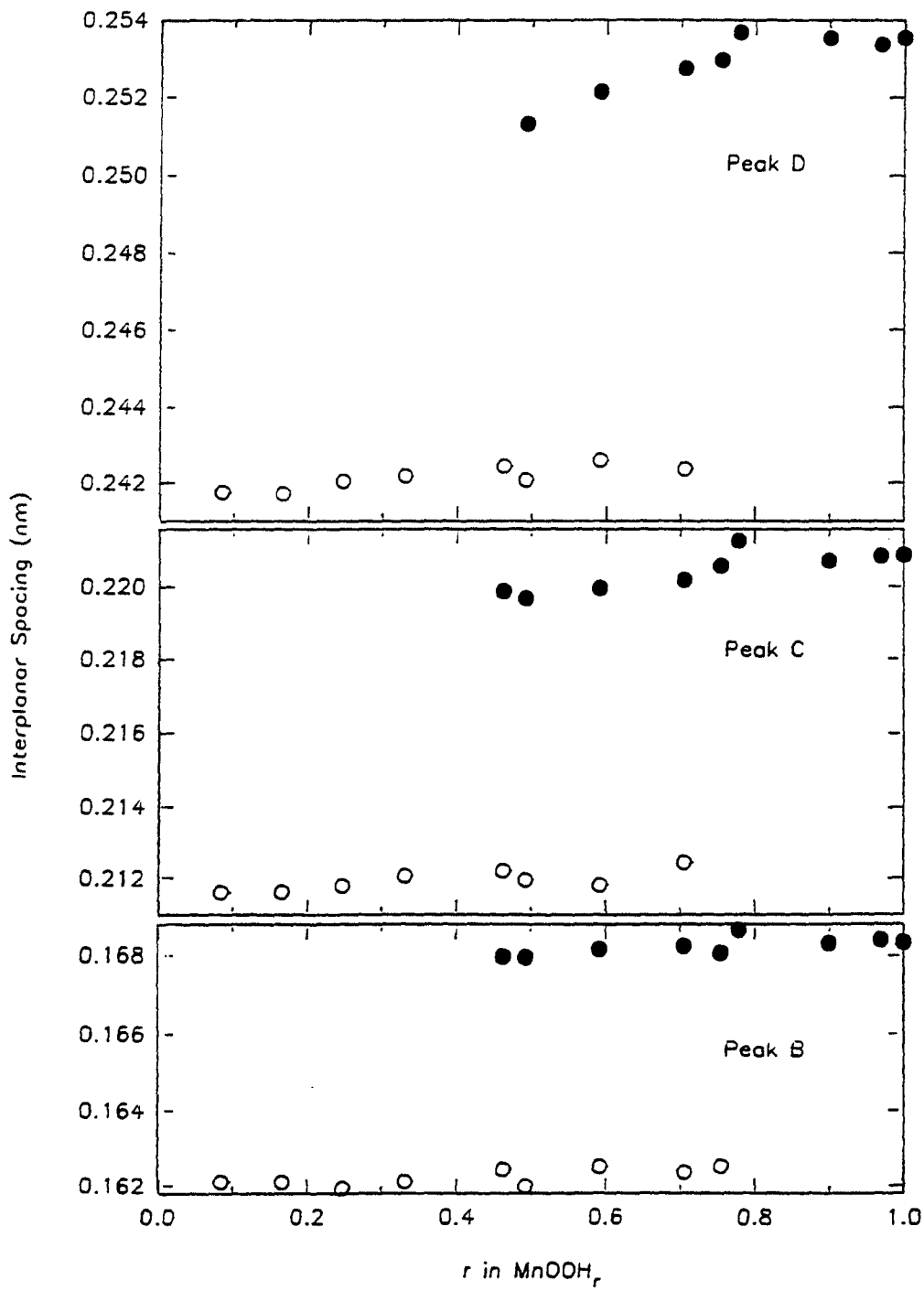


***Figure 4.25***:Interplanar spacing against H insertion level; EMD heat-treated at 300°C;hydrazine hydrate reduction method (see figure 4.24 for peak labelling).

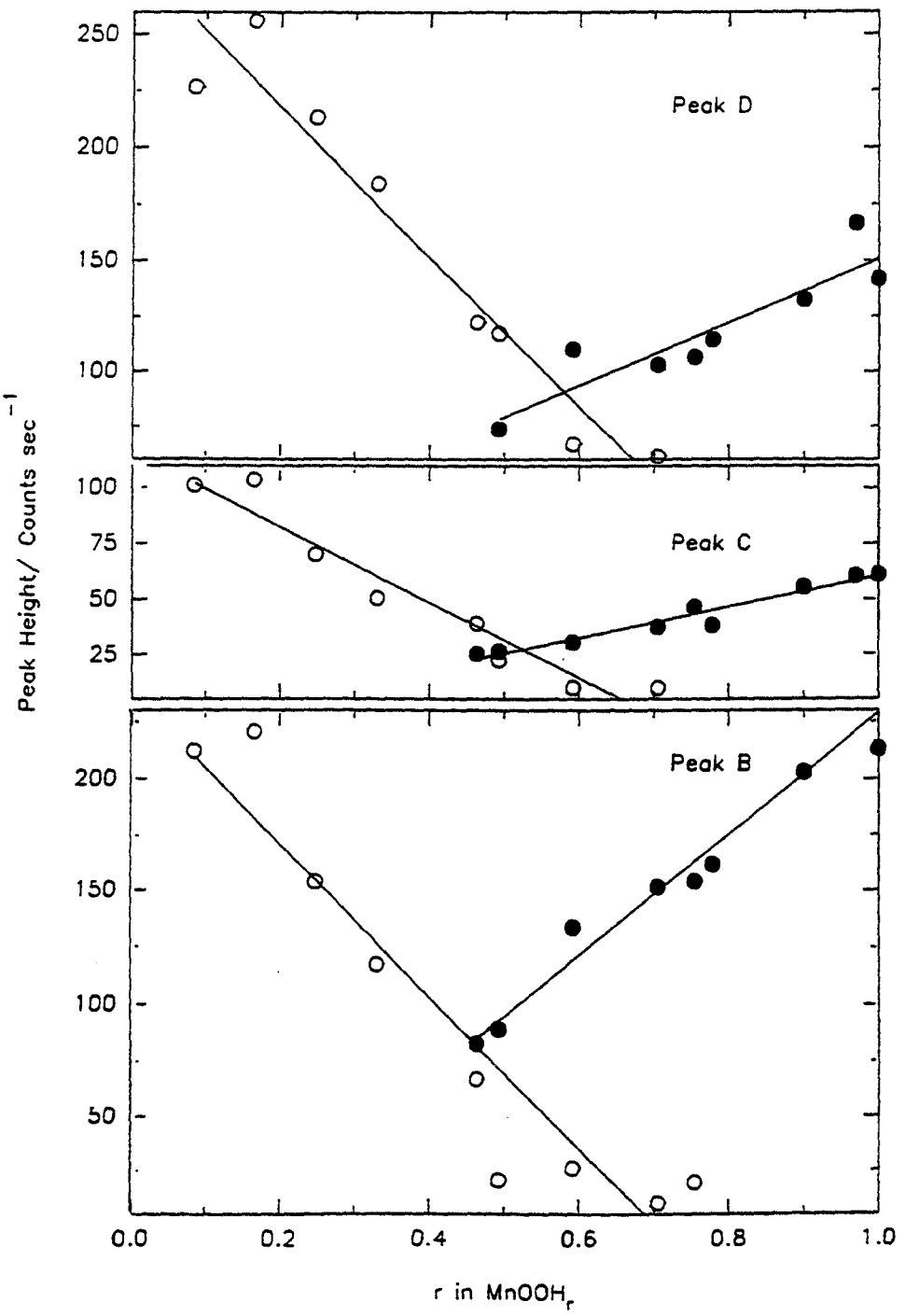


***Figure 4.26***:Peak height against H insertion Level; EMD heat-treated at 300°C;hydrazine hydrate reduction method (see figure 4.24 for peak labelling).

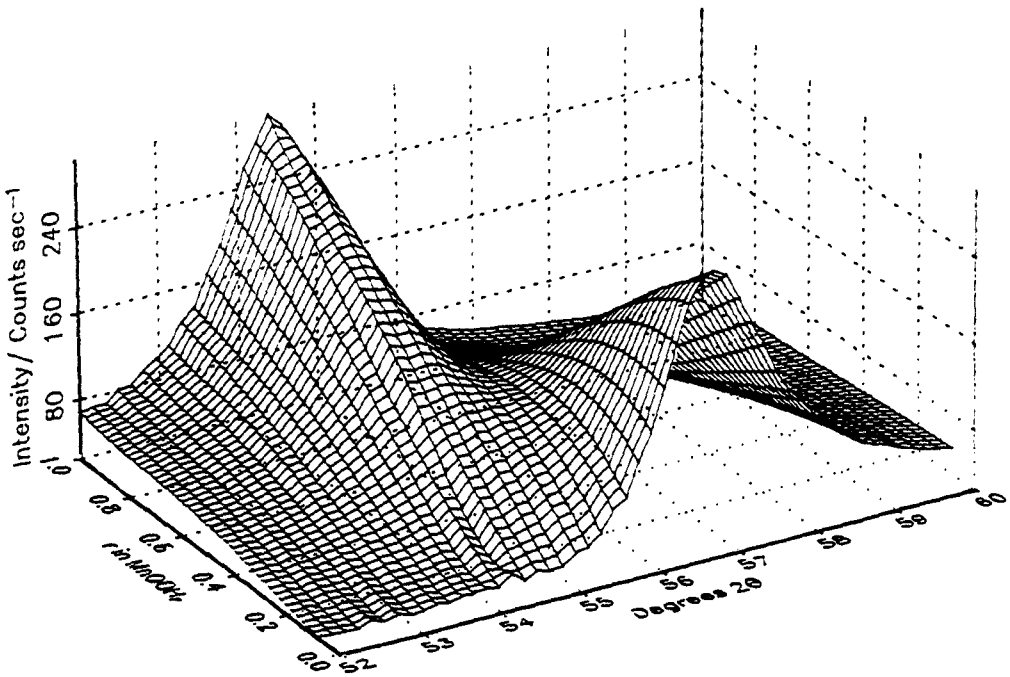


*Figure 4.27* : Movement of Peak B during the reduction of EMD heat-treated at 300°C; hydrazine hydrate reduction method (data grid from 0.08-1.00 in 0.023 increments in r in MnOOH, and from 52-60°2Θ in 0.16 increments).

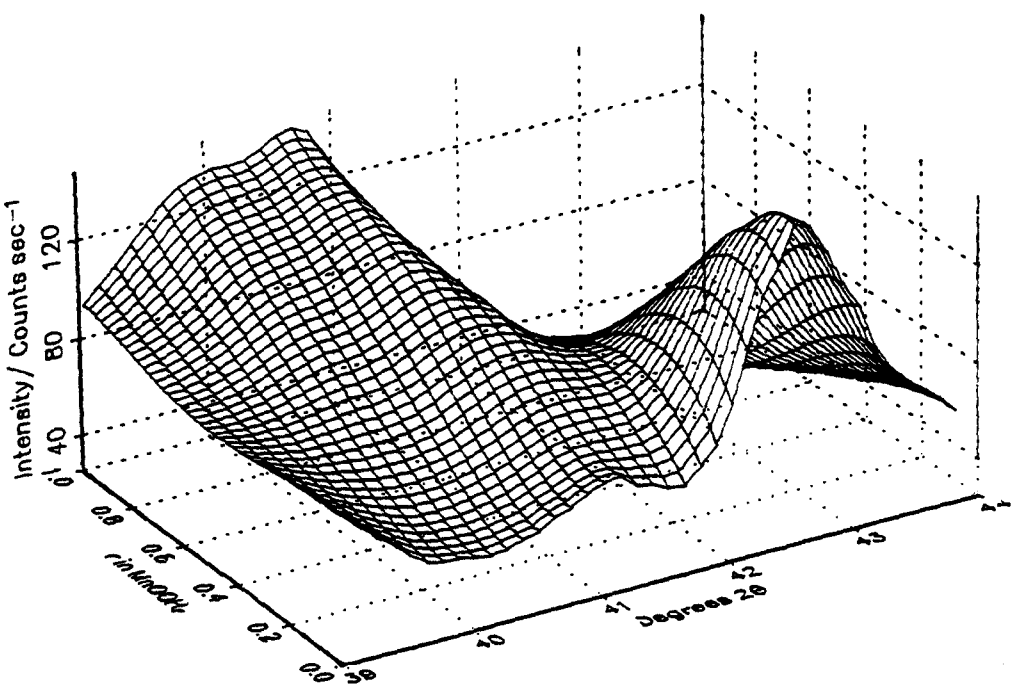


*Figure 4.28* :Movement of Peak C during the reduction of EMD heat-treated at 300°C;hydrazine hydrate reduction method.

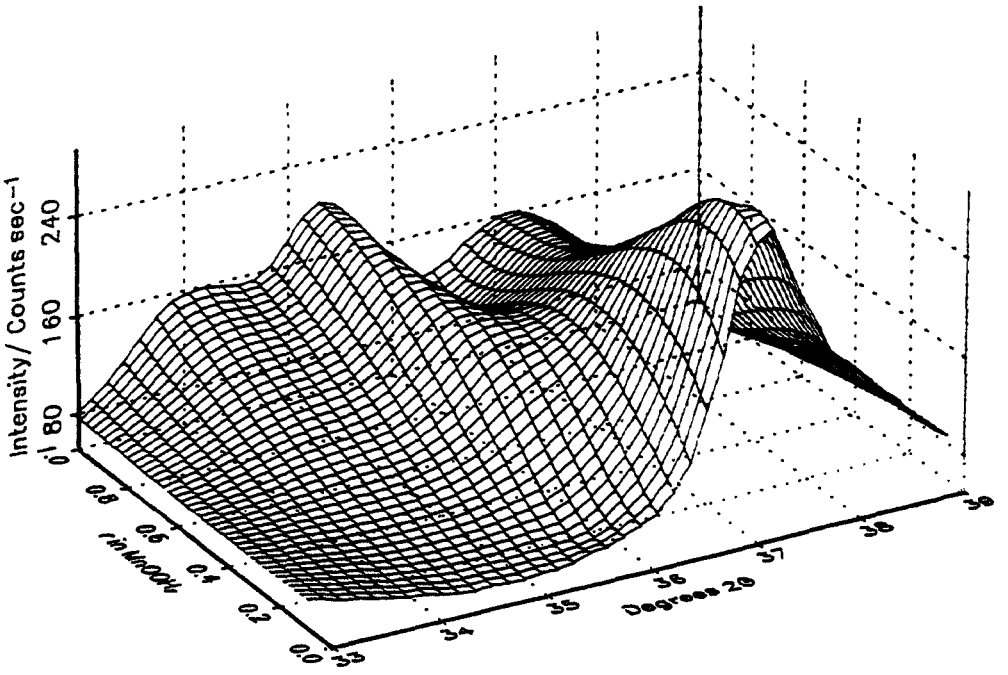


*Figure 4.29* :Movement of Peak D during the reduction of EMD heat-treated at 300°C;hydrazine hydrate reduction method.

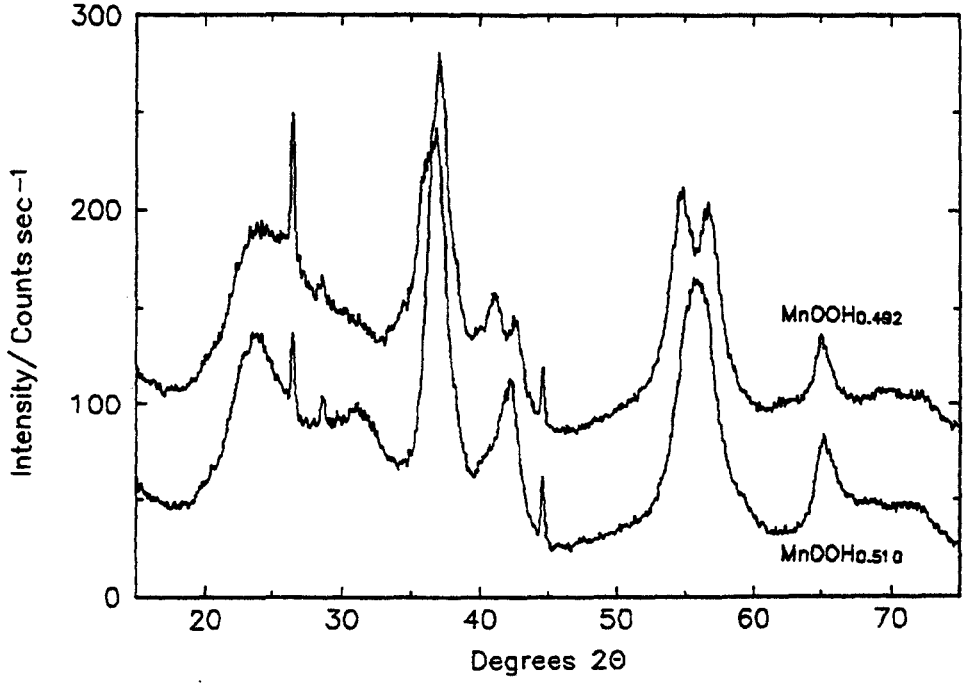


*Figure 4.30* : Comparison of the x-ray diffraction patterns of $MnOOH_{0.492}$ and $MnOOH_{0.510}$ for EMD heat-treated at 300°C and reduced by hydrazine and propan-2-ol respectively. The hydrazine pattern is displaced upwards by 60 counts $s^{-1}$.

## *4.2.4 EMD heat-treated at 400°C*

### 4.2.4 (i) Hydrazine hydrate reduction

X-ray diffraction spectra during the reduction of EMD heat-treated at 400°C and reduced by hydrazine hydrate are shown in figure 4.31. In section 3.5 it was established that an EMD heat-treated at 400°C was a non-stoichiometric pyrolusite phase. In the literature there are conflicting reports on the reduction of pyrolusite Bode and Scheimer (1962) found a heterogeneous process to manganite whereas Kozawa (1967) found that the reduction was homogeneous to $MnOOH_{0.20}$. The results shown here would agree with those of Bode and Scheimer (1962) as can be seen of the plots of the individual peaks (figure 4.32-4.35) there is no movement of the peaks and new peaks start to appear in the spectrum from $MnOOH_{0.228}$. The interplanar spacings and peak heights of peaks B,C, and D are shown in figures 4.36 and 4.37 respectively. The regions of the heterogeneous behaviour are further examined in section 4.5.

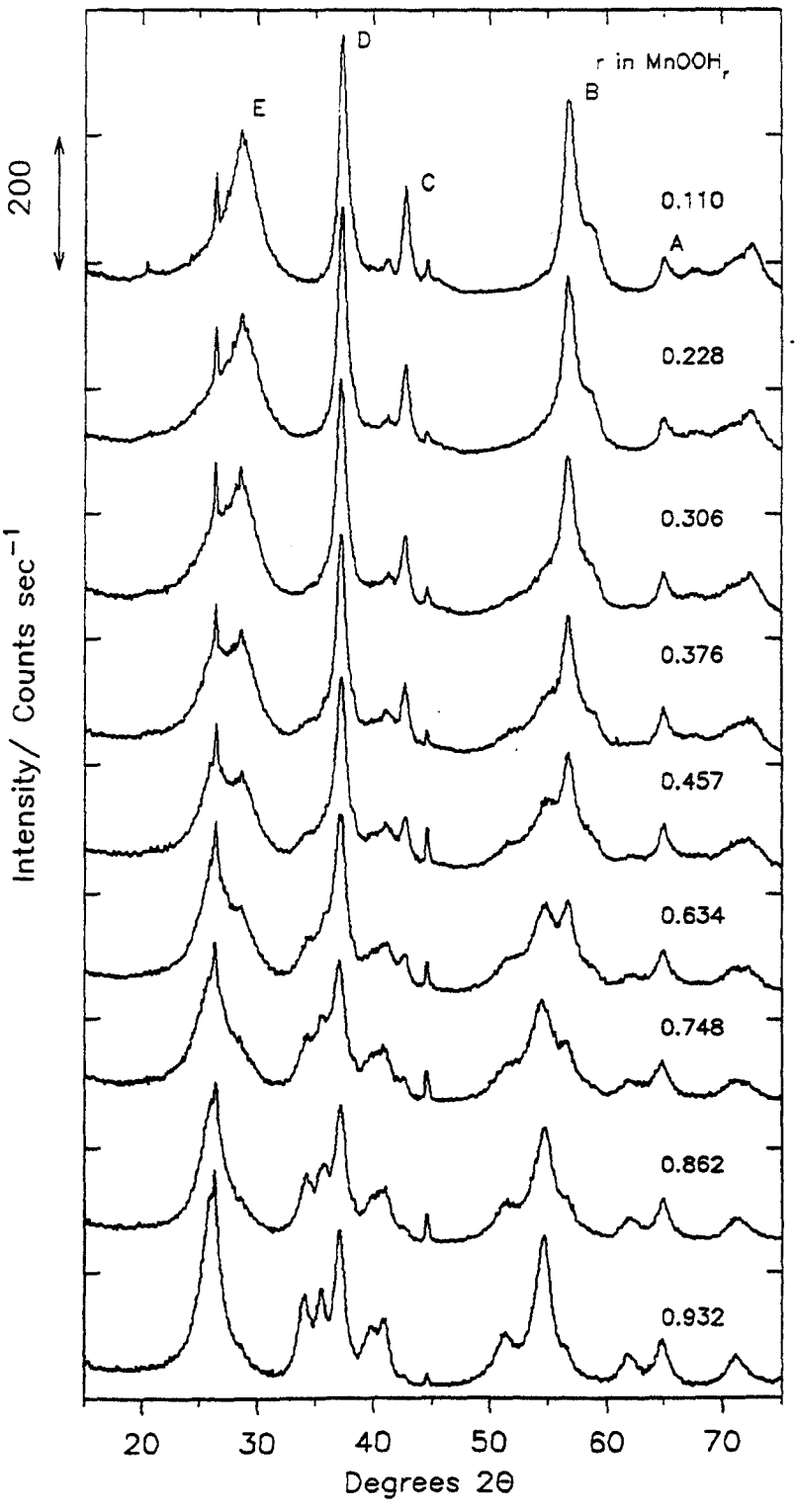


***Figure 4.31*** :X-ray diffraction spectra during the reduction of EMD heat-treated at 400°C;hydrazine hydrate reduction method (the level of H insertion is given above the XRD pattern).

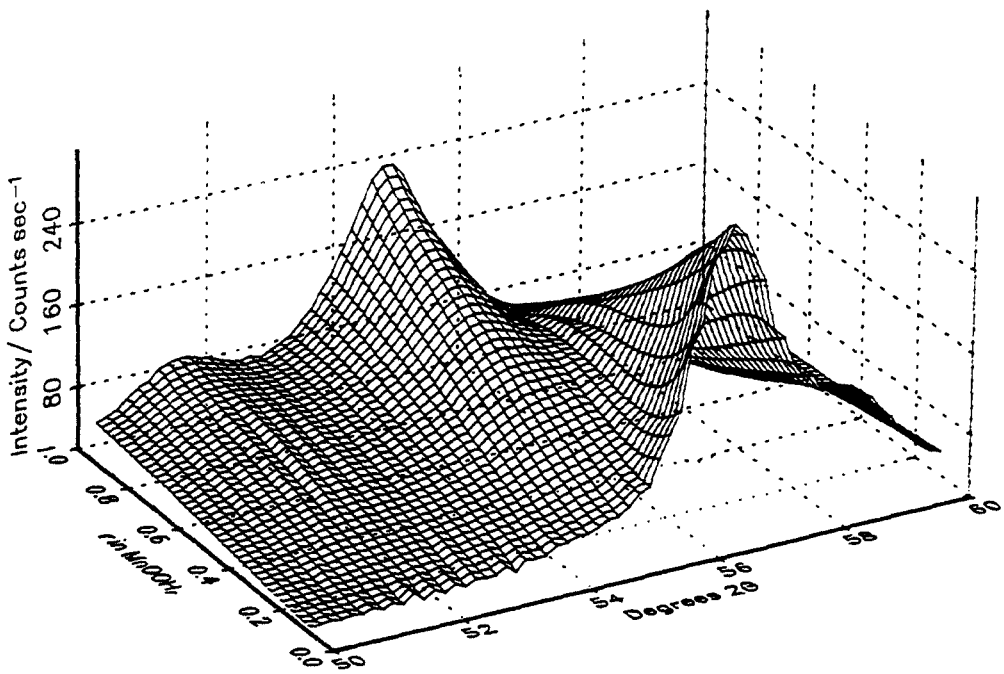


*Figure 4.32* : Movement of Peak B during the reduction of EMD heat-treated at 300°C; hydrazine hydrate reduction method (data grid from 0.11-0.95 in 0.021 increments in r in MnOOH, and from 50-60°2Θ in 0.16 increments).

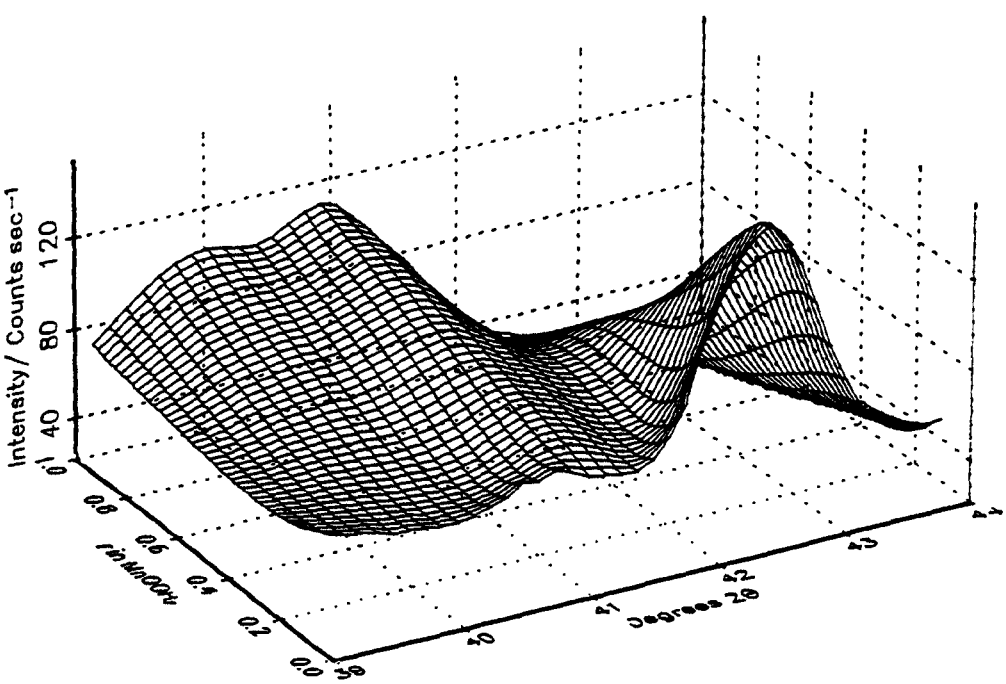


*Figure 4.33* : Movement of Peak C during the reduction of EMD heat-treated at 400°C; hydrazine hydrate reduction method.

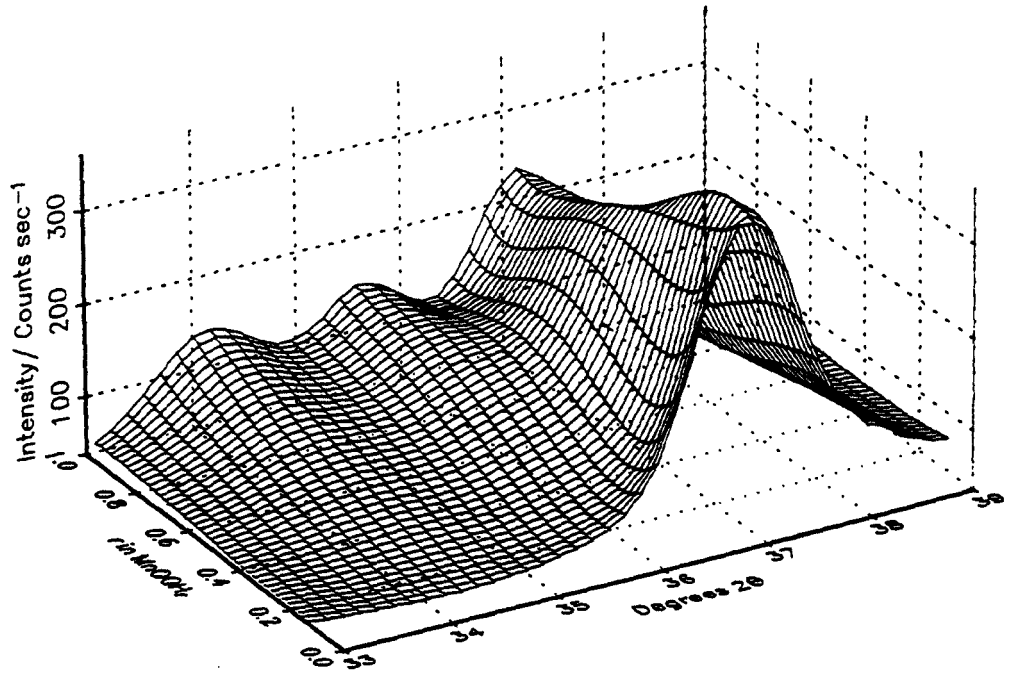


***Figure 4.34*** : Movement of Peak D during the reduction of EMD heat-treated at 400°C; hydrazine hydrate reduction method.

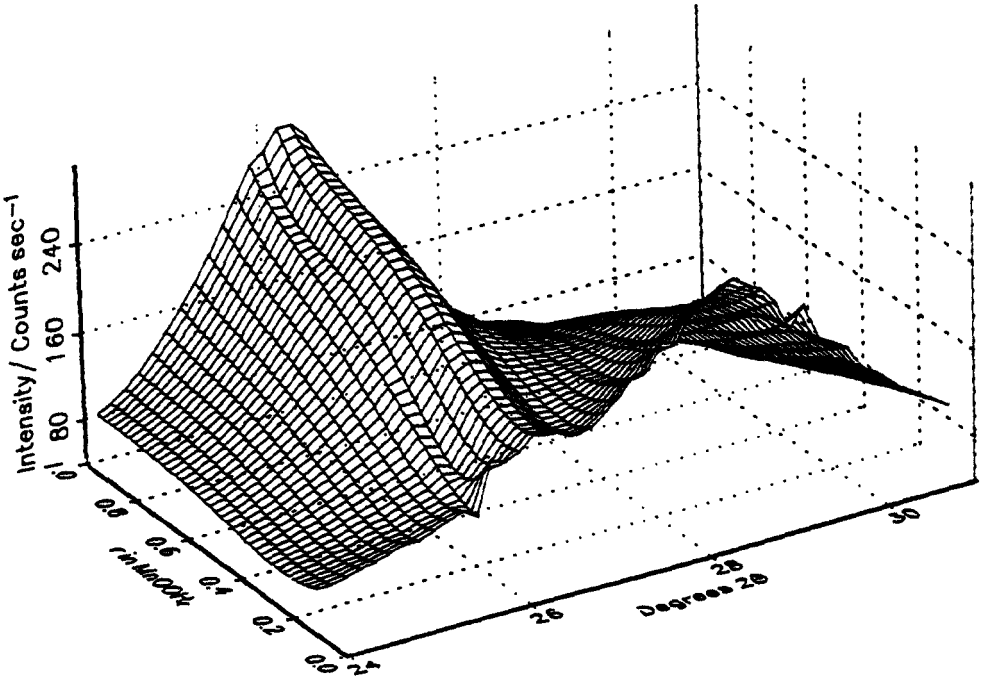


***Figure 4.35*** : Movement of Peak E during the reduction of EMD heat-treated at 400°C; hydrazine hydrate reduction method.

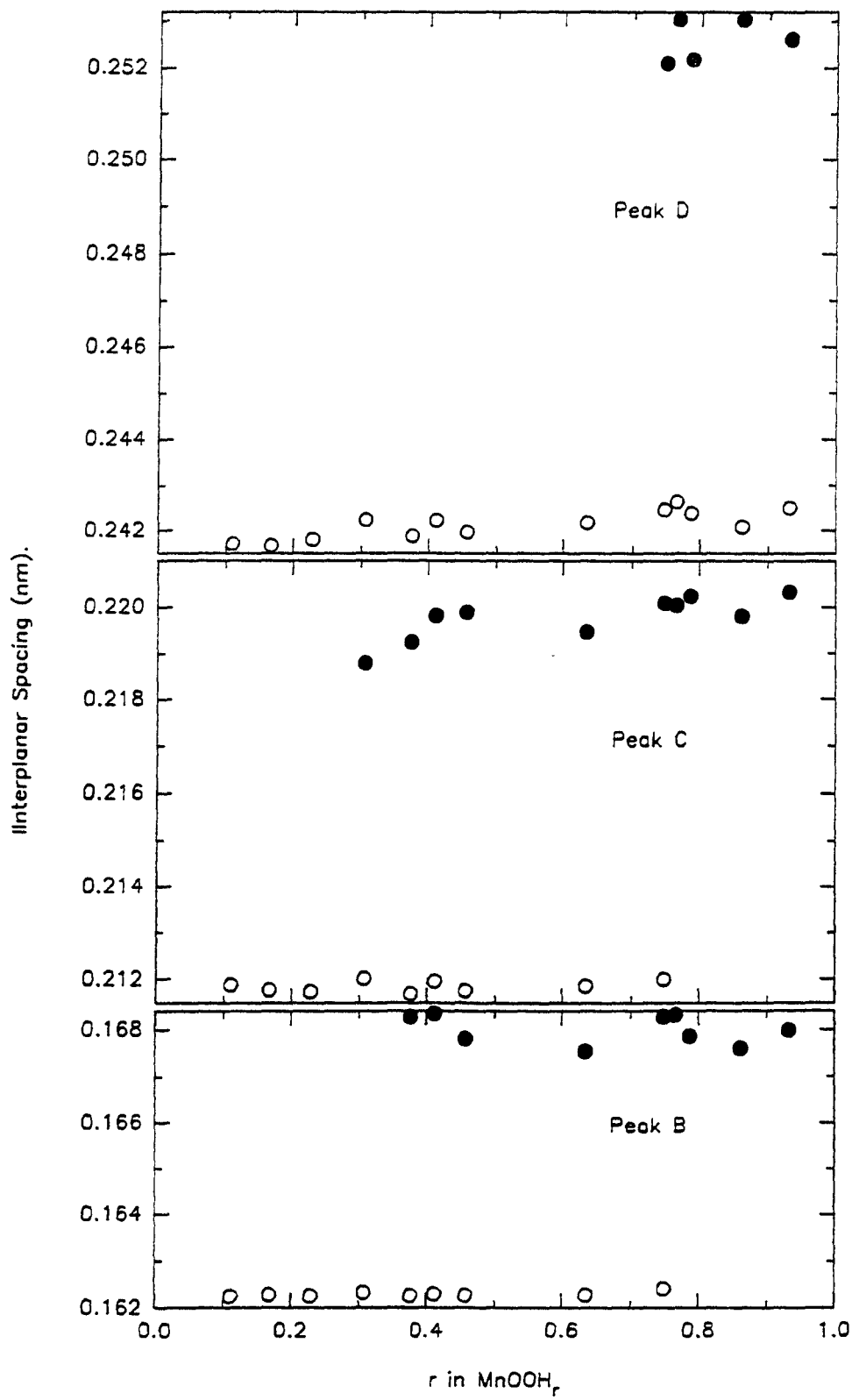


***Figure 4.36*** :Interplanar spacing against H insertion level; EMD· heat-treated at 400°C; hydrazine hydrate reduction method (see figure 4.31 for peak labelling).

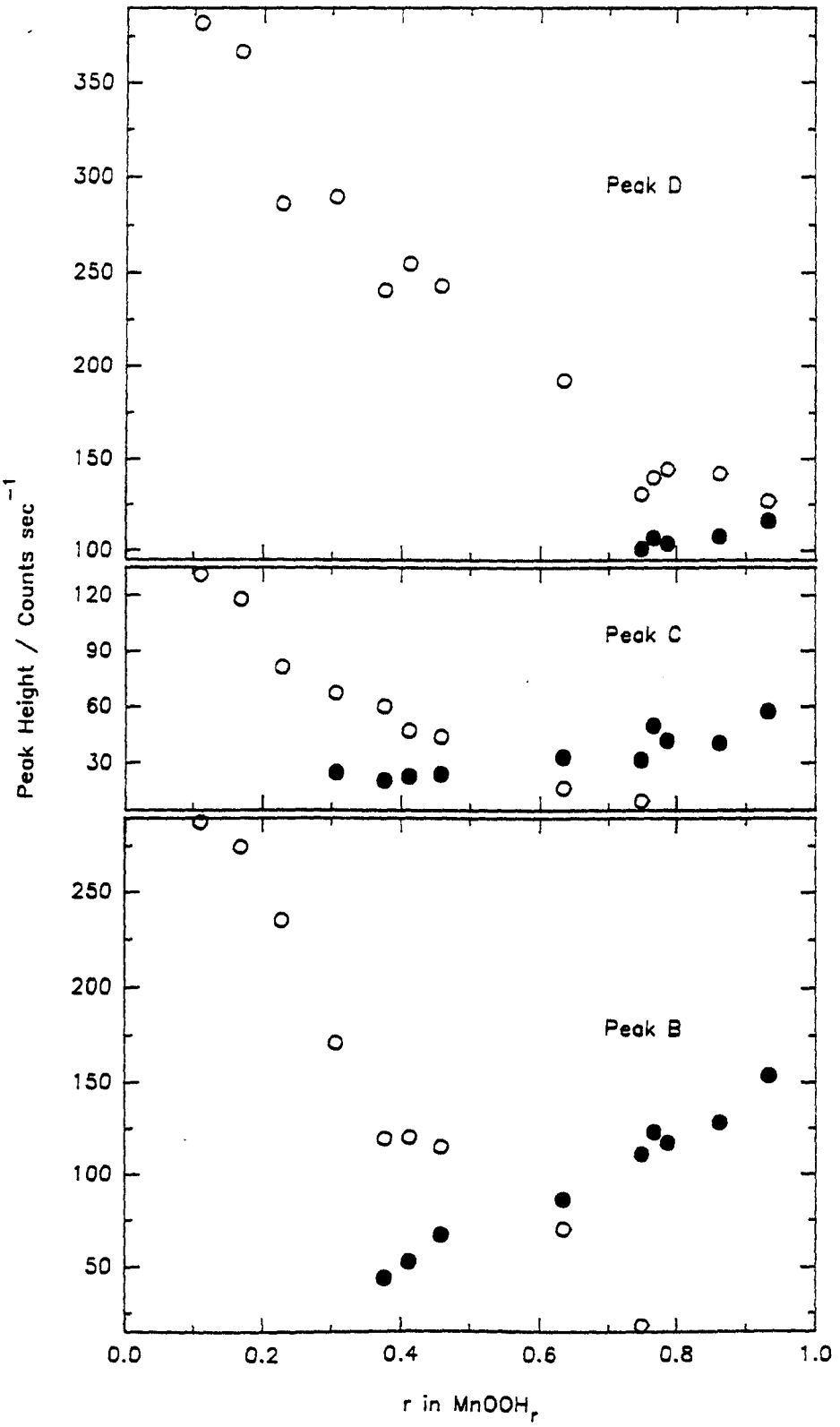


***Figure 4.37*** : Peak height against H insertion level for EMD heat-treated at 400°C;hydrazine hydrate reduction method (see figure 4.31 for peak labelling).

## 4.3 FTIR spectroscopy of manganese oxyhydroxides.

Fourier transform infrared spectroscopy has been shown (Potter and Rossman 1979) to be a complementary technique to X-ray diffraction. The spectra have also been used to distinguish between the different crystalline modifications of manganese dioxide (Fernandes *et al.* 1983, Swinkels 1985), and there are publications relating to the reduction of $\gamma$-$MnO_2$ to $\delta$-MnOOH (Ohzuku *et al.* 1985, Xi Xia *et al.* 1989) In the following sections FTIR spectra are shown for the electrodeposited manganese oxyhydroxides that have been analysed by X-ray diffraction in section 4.2. The literature regarding infrared and experimental details have been given in sections 1.5 and 2.5 respectively.

### *4.3.1 FTIR spectra of EMD heat-treated at 200°C.*

#### 4.3.1.(i) Propan-2-ol reduction.

FTIR spectra for the progressive reduction of EMD from $MnOOH_{0.07}$ to $MnOOH_{0.976}$ are shown in figure 4.38. The main features of the spectra are a broad absorption at 550-750 $cm^{-1}$ and the appearance, with increasing H insertion, of peaks at 1000, 2050 and 2650 $cm^{-1}$. It is generally accepted (Potter and Rossman 1979) that peaks in the region 200-1400 $cm^{-1}$ are associated with the $MnO_6$ octahedral framework of the $\gamma$-$MnO_2$ lattice and peaks between 1400-4000 $cm^{-1}$ with the hydrous components of the oxide. White and Roy (1964) have shown I.R. spectra for ramsdellite and pyrolusite. In ramsdellite the main absorption band was split into four ill-defined peaks at 680, 580, 530 and 470 $cm^{-1}$ whereas in pyrolusite there was a single broad band at 606 cm-1. The absorption band for this sample has features that are similar to ramsdellite and this would be in accordance with the XRD data which was presented in section 3.5. In the paper by Bystrom (1949) it was elucidated that there were four different Mn-O bond lengths in ramsdellite, two at 1.86, two at 1.92, one at 1.91 and one at 1.89 Å. In the I.R. spectrum this could lead to four different vibrational modes as was found by White and Roy and substantiated in this work.

During the reduction of $\gamma$-$MnO_2$ protons and electrons were added to the lattice with the concurrent reduction of $Mn^{4+}$ to $Mn^{3+}$ and the replacement of $O^{2-}$ with $OH^-$. If there were OH bond formation then it would be expected that vibrational modes due to OH stretching and bending vibrations would arise in the

spectra. Examination of Figure 4.38 reveals that the spectra are essentially identical from $MnOOH_{0.07}$ to $MnOOH_{0.745}$. After $MnOOH_{0.745}$ there is evidence of OH bond formation as exemplified by the emergence of the peaks at 2050 and 2650 $cm^{-1}$. In the FTIR spectra there are also changes in the $MnO_6$ octahedral framework at H insertion levels greater than $MnOOH_{0.745}$. The shoulder at 700 $cm^{-1}$ disappears and there is enhancement of peaks at 550 and 450 $cm^{-1}$. The $Mn^{3+}$ ion has the $d^4$ electron configuration and so the Jahn-Teller distortion related with it would lead to differing Mn-O configurations. Tarte *et al.* (1990) noted that in the I.R. spectrum of $NiMoO_4$ the $MoO_6$ octahedra have short and long to very long Mo-O distances which were represented in the spectrum by two groups of bands in the 1000-900 and 700-600 $cm^{-1}$ regions. This type of behaviour is not observed to such an extent in this work, but, nevertheless, there is the emergence of a peak in the latter half of the reduction at 550 $cm^{-1}$.

It is possible to make assumptions concerning OH bond formation by calculating the area under the peaks at 2050 and 2650$cm^{-1}$†. An example of this type of calculation is shown in Figure 4.39 and the results are shown in Figure 4.40. There is a fair scatter in the data and this could obviously be improved by making different pellets and taking an average of two or more FTIR spectra. Nevertheless there is a break in the graph at approximately $MnOOH_{0.70\text{-}0.75}$. A similar break was also observed in the graph of interplanar spacing against H insertion level (Figure 4.3) where new lines start to appear in the X-ray diffraction pattern.

†This type of analysis has not been reported in the literature before.

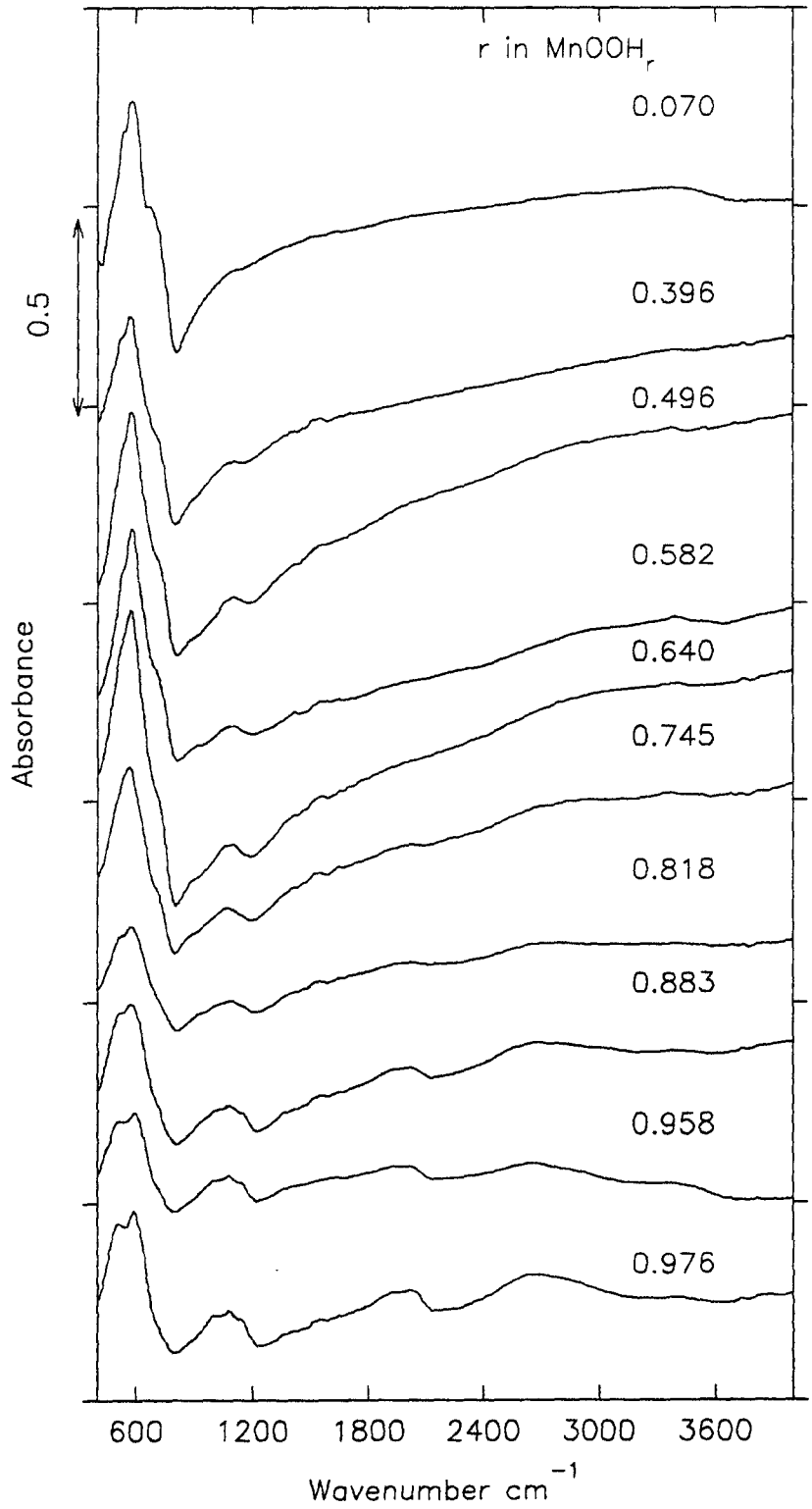


***Figure 4.38*** : FTIR spectra during the reduction of EMD heat-treated at 200°C; propan-2-ol reduction method (the level of H insertion is given above the FTIR spectrum).

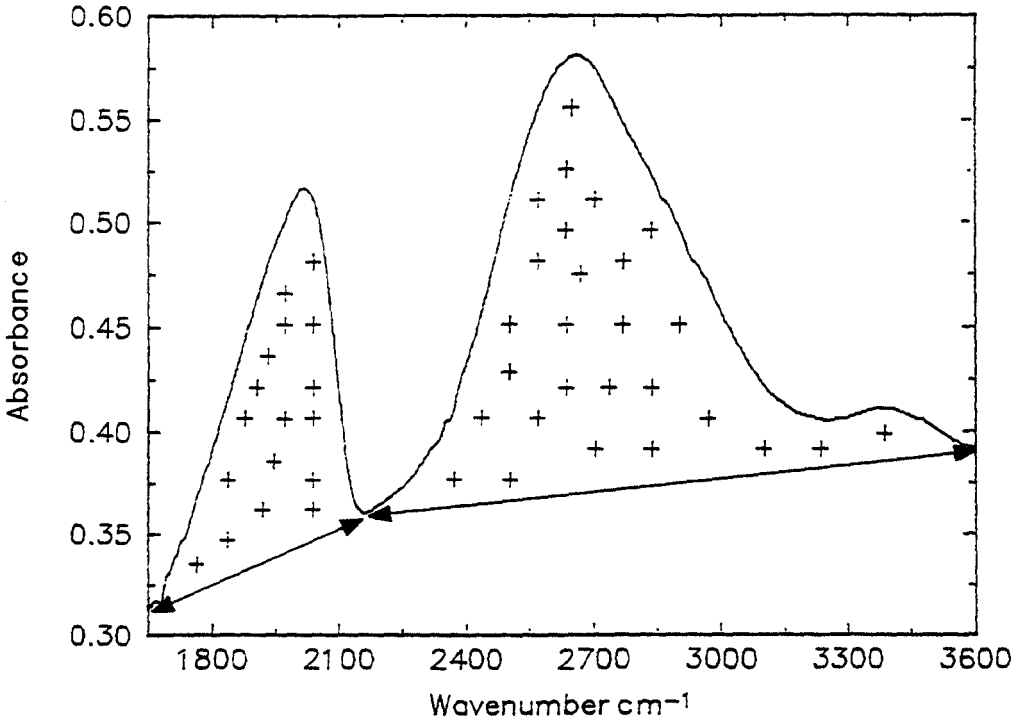


***Figure 4.39*** : An example of how the area of the peaks centred at 2050 and 2650 $cm^{-1}$ was calculated. The arrows indicate the peak boundaries.

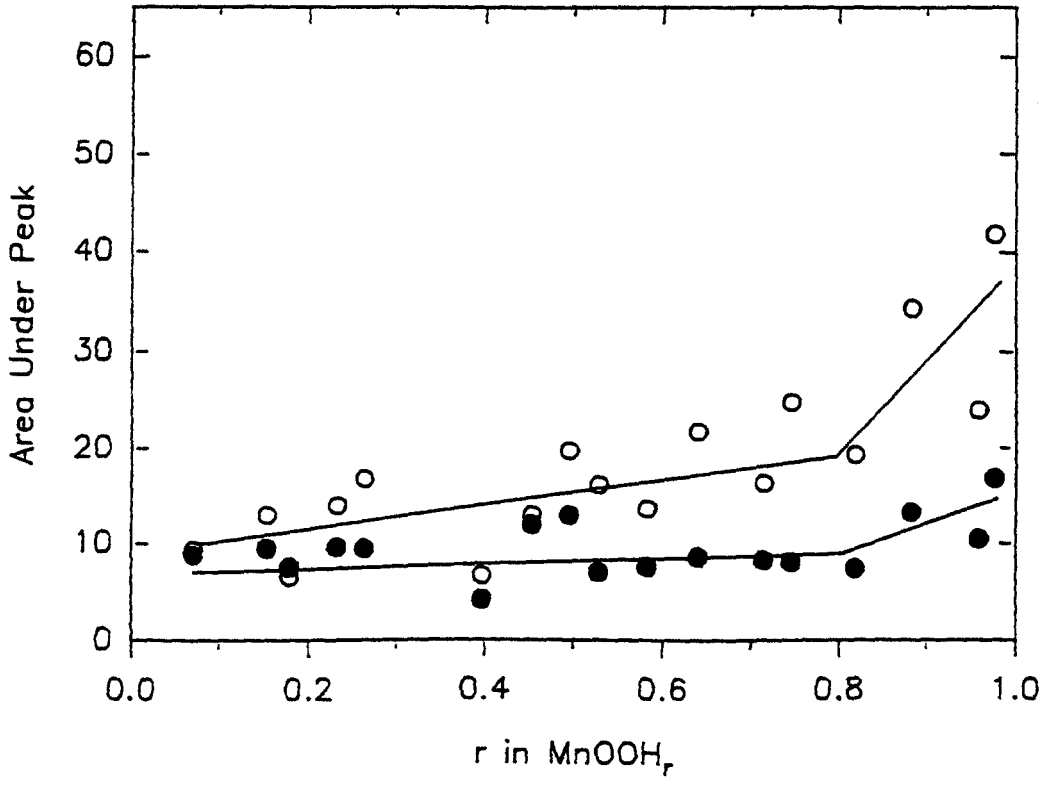


***Figure 4.40*** : Area under the peaks centred At 2050 (●) and 2650 (○) $cm^{-1}$ ; EMD heat-treated at 200°C ; propan-2-ol reduction method.

4.3.1 (ii) Hydrazine hydrate reduction.

FTIR spectra during the reduction of EMD heat-treated at 200°C and reduced by hydrazine hydrate are shown in figure 4.41. If this is compared with figure 4.38 then it can be seen peaks relating to OH bond formation start to appear from $MnOOH_{0.35}$. This is quantified in figure 4.42 where the area has been calculated for the MnOOH samples. As was observed in the previous section the break in the graph is at the same point as the graph of interplanar spacing against H insertion (figure 4.11). The heterogeneous reduction of this material was observed in section 4.2.1(ii).

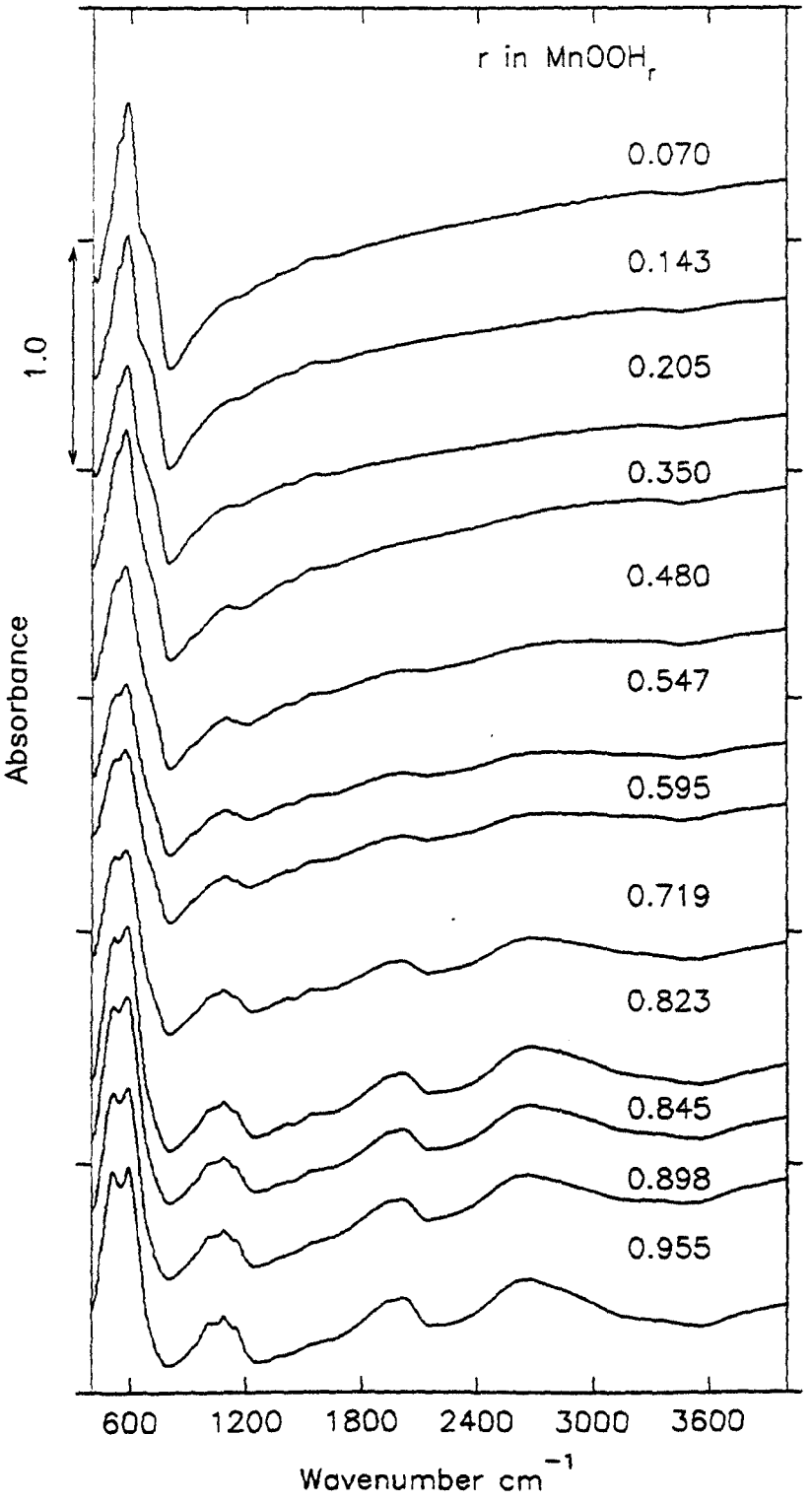


*Figure 4.41* : FTIR spectra during the reduction of EMD heat-treated at 200°C; hydrazine hydrate reduction method (the level of H insertion is given above the FTIR spectrum).

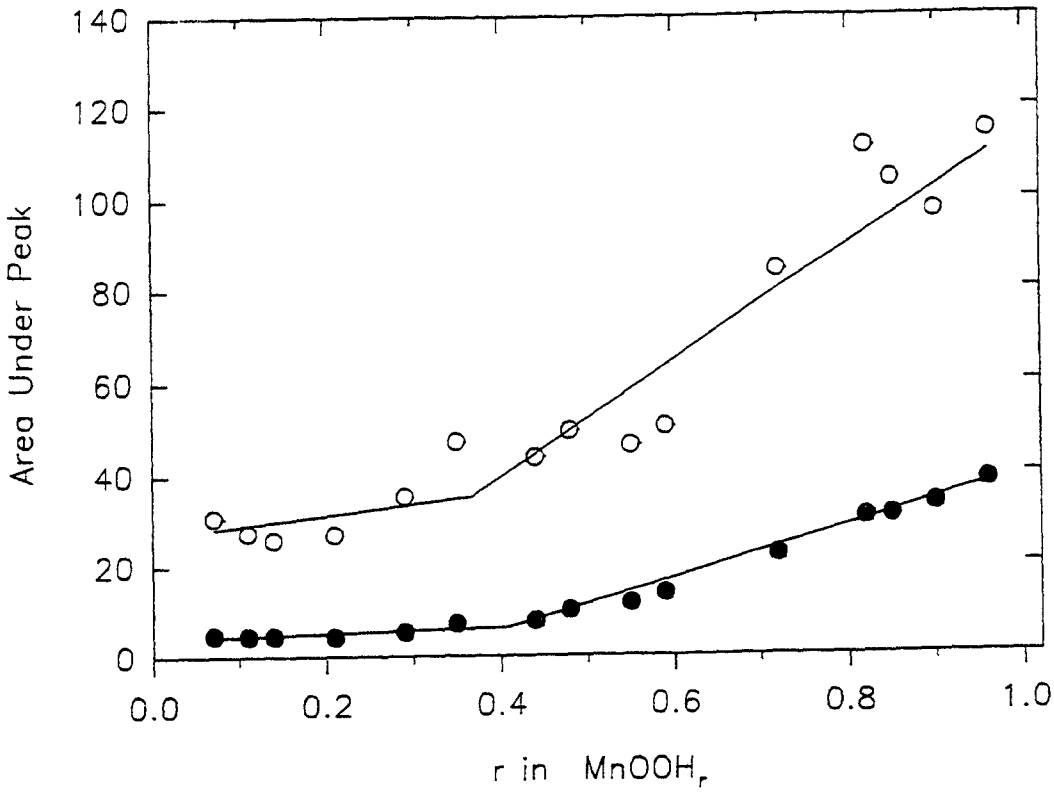


***Figure 4.42*** : Area under the peaks centred at 2050 (●) and 2650 (○) cm-1; EMD heat-treated at 200°C; hydrazine hydrate reduction method.

## *4.3.2 FTIR spectra of EMD heat-treated at 300°C.*

### 4.3.2 (i) Propan-2-ol reduction.

FTIR spectra during the reduction of EMD heat-treated at 300°C and reduced by propan-2-ol are shown in figure 4.43. The spectra are unchanged from $MnOOH_{0.08}$-$MnOOH_{0.458}$ and there is evidence of OH bond formation after $MnOOH_{0.534}$ which is shown more clearly in figure 4.44.

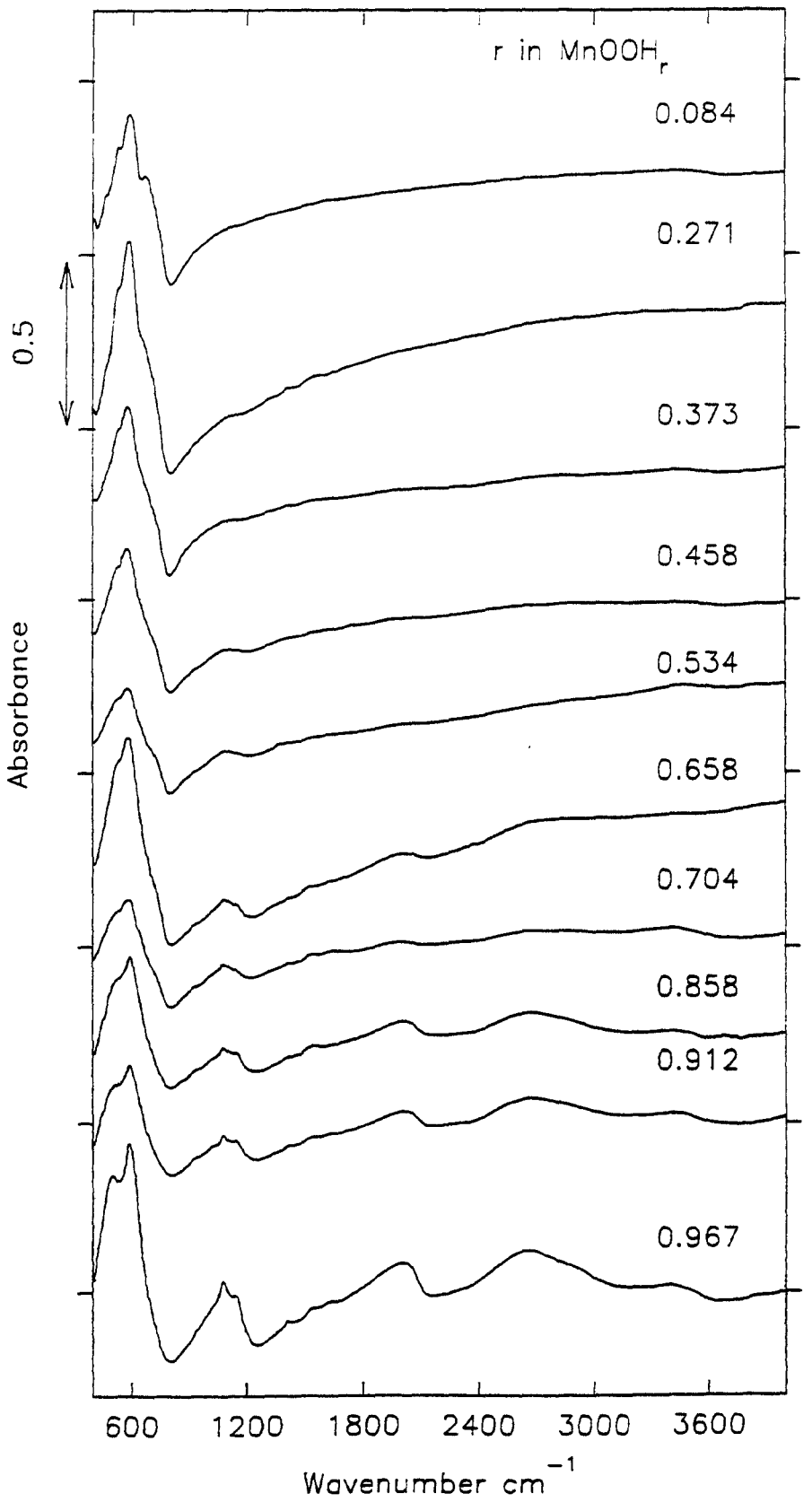


***Figure 4.43*** : **FTIR spectra during the reduction of EMD heat-treated at 300°C; propan-2-ol reduction method.**

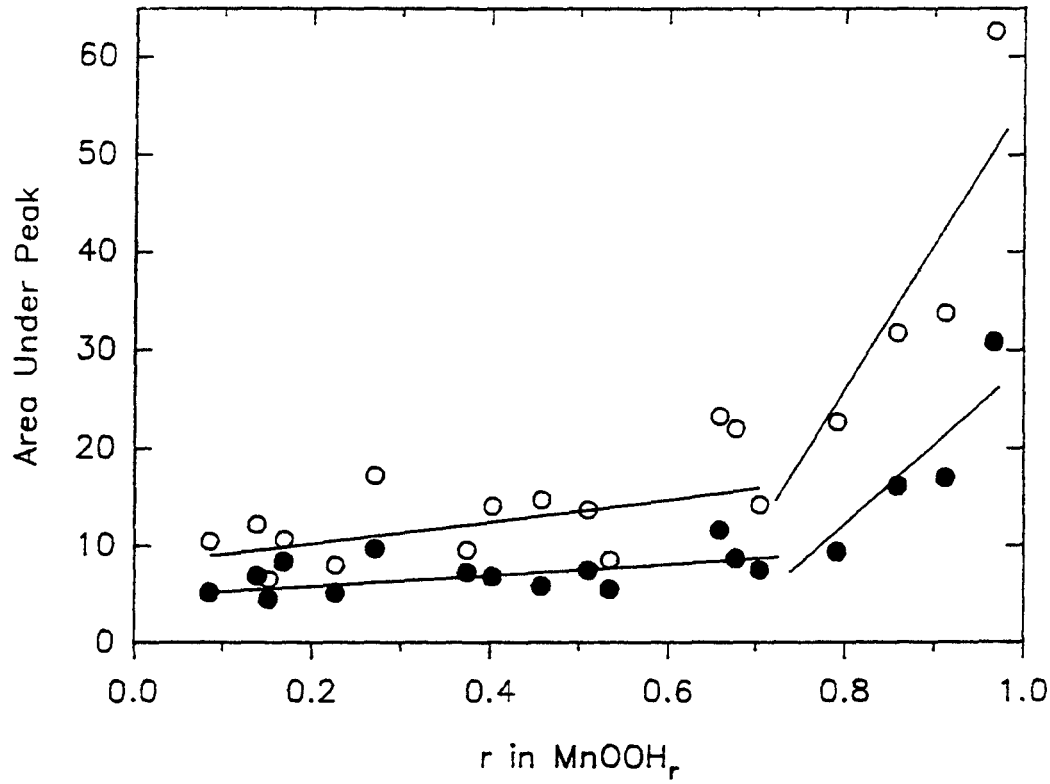


*Figure 4.44* : Area under the peaks centred at 2050 (●) and 2650 (○) cm-1; EMD heat-treated at 300°C; propan-2-ol reduction method.

### *4.3.2 (ii) Hydrazine hydrate reduction.*

FTIR spectra for this material are similar to those shown in figure 4.41 and so are not reproduced. The area under the peaks at 2050 and 2650cm$^{-1}$ is shown in figure 4.45 and, as expected, OH bond formation is seen at an earlier level of H insertion than when the material is reduced with propan-2-ol (figure 4.44).

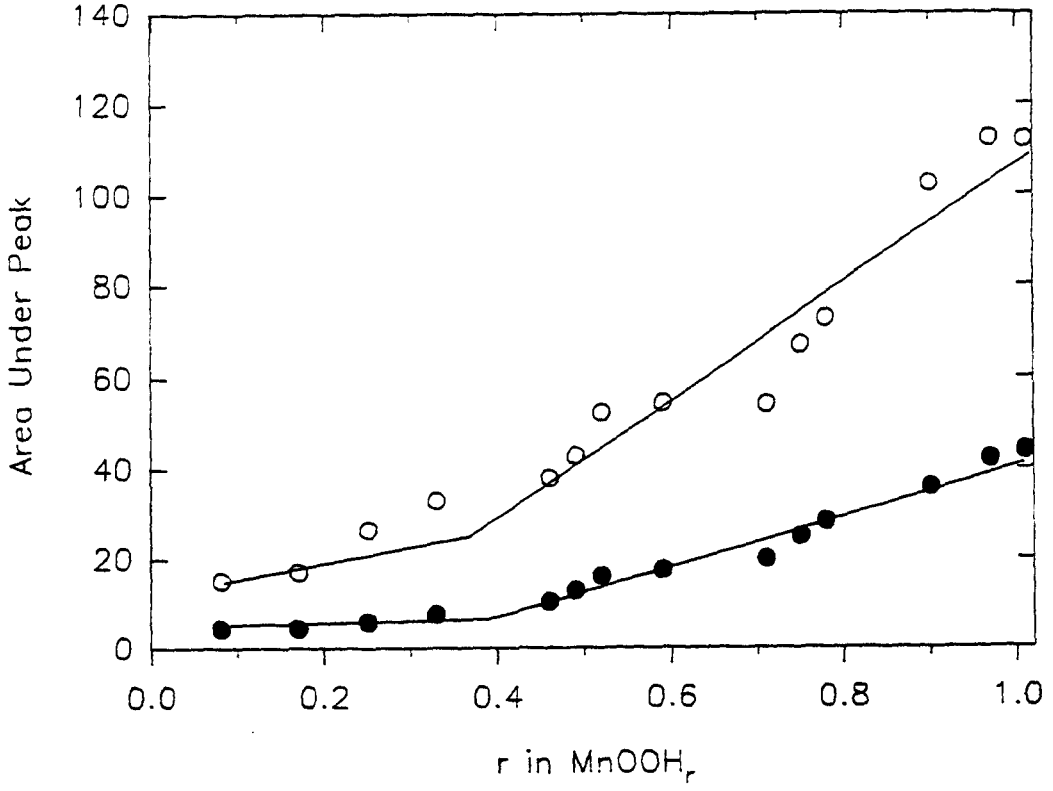


*Figure 4.45* : Area under the peaks centred at 2050 (●) and 2650 (○) cm-1; EMD heat-treated at 300°C; hydrazine hydrate reduction method.

## *4.3.3 FTIR spectra of EMD heat-treated at 400°C.*

### 4.3.3 (i) Hydrazine hydrate reduction

FTIR spectra are shown in figure 4.46 for an EMD that had been heat-treated at 400°C and then reduced by hydrazine hydrate. In figure 4.47 the area under the emerging peaks is plotted against the H insertion level. The area increases in an almost linear fashion from $MnOOH_{0.11}$ to $MnOOH_{0.932}$.

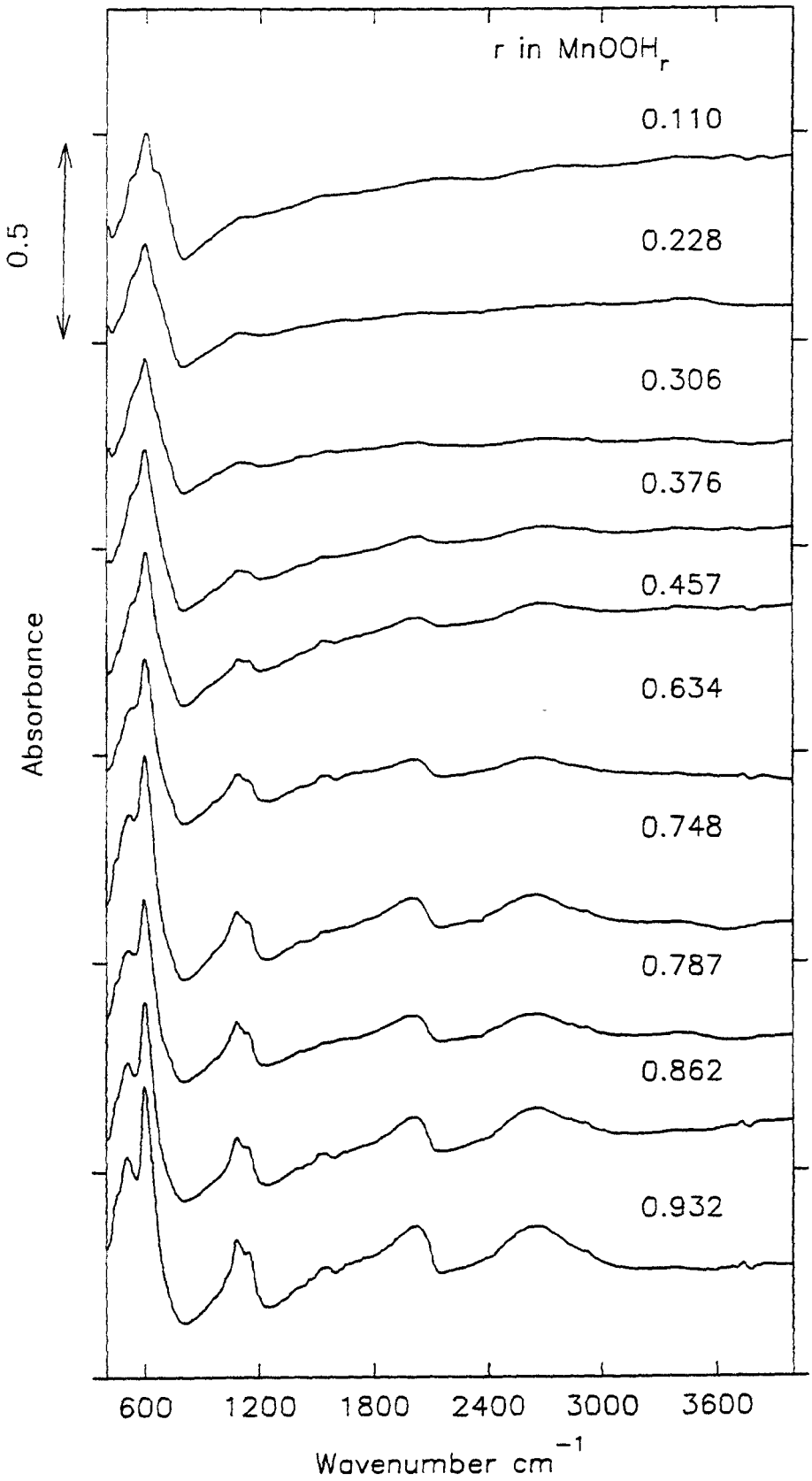


***Figure 4.46*** : FTIR spectra during the reduction of EMD heat-treated at 400°C; hydrazine hydrate reduction method (the level of H insertion is given above the FTIR spectrum).

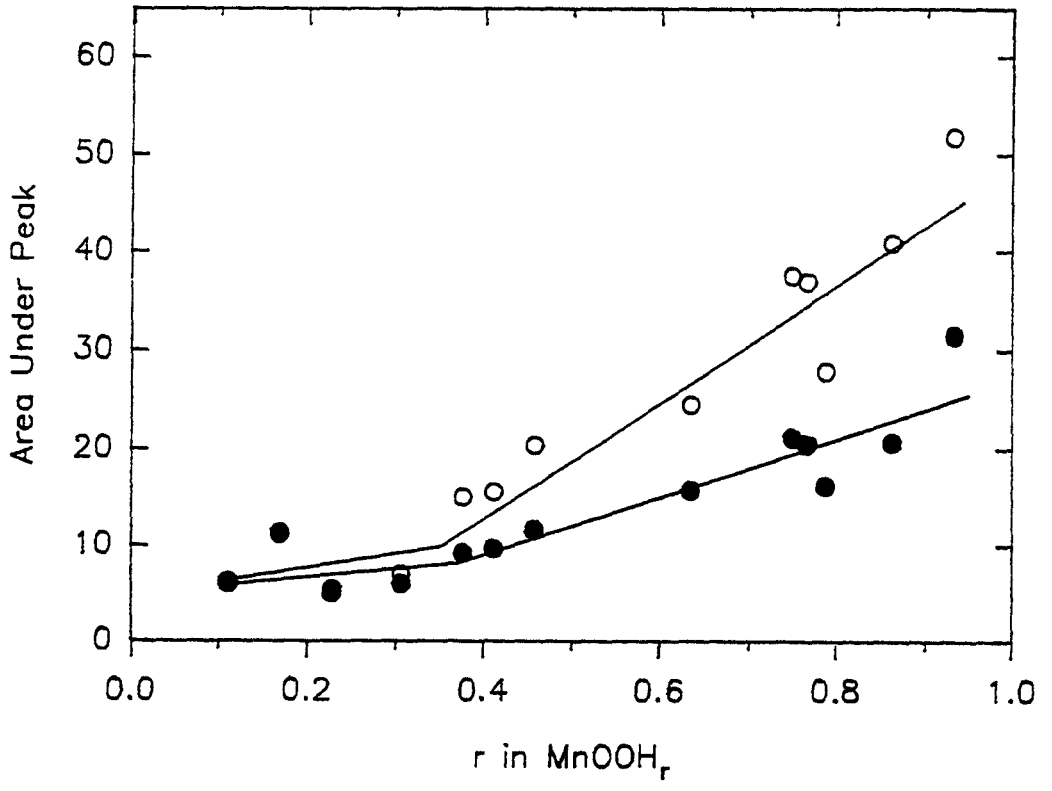


*Figure 4.47* : Area under the peaks centred at 2050 (●) and 2650 (○) $cm^{-1}$; EMD heat-treated at 400°C; hydrazine hydrate reduction method.

## 4.4 Comparison of the XRD and FTIR reduction product spectra with published spectra of manganite and groutite.

The X-ray diffraction patterns of the reduction products that were prepared at various temperatures and with different methods are compared with the JCPDS pattern of (a) manganite and (b) groutite in figure 4.48. It can be seen that the X-ray patterns bear little resemblance to groutite but are similar to manganite. Notice that the patterns of the materials heat-treated at the same temperature are identical although differing regions of homogeneity/heterogeneity were observed in the reduction process. The new lines that appear in the X-ray pattern of EMD heat-treated at 200°C (labelled as G,H,I and J) in figure 4.2 are at the same position as the lines in the 400°C material. The sample heat-treated at 400°C has a pattern that is identical with that of manganite, even the relative intensities of the lines are similar to the JCPDS pattern. For the sample heat-treated at 200°C the main manganite peak at 2Θ 26.1° is absent although the appearance of the new lines correspond with the manganite pattern. Maskell *et al.* (1981) also compared the X-ray pattern of the reduction product and they

found that the new lines correlated with manganite and this led them to term the reduction product as δ-MnOOH. This was taken to mean that the reduction product was essentially groutite with microdomains of manganite.

Figure 4.49 shows the FTIR spectra of the reduction products and figure 4.50 shows the I.R. spectra of groutite and manganite taken from Potter and Rossman (1979) and the peak positions of the reduction products obtained in this work in Table 4.3. Referral to figure 4.50 and Table 4.3 would suggest that in the region $>2000cm^{-1}$ the most reduced materials had peaks that were more in common with manganite than groutite. In the region $400\text{-}1200cm^{-1}$ however the situation is less clear. The most reduced materials products all have peaks at 508 and $596cm^{-1}$ and neither of these peaks are present in groutite or manganite. In the region $950\text{-}1200cm^{-1}$ groutite and manganite are different; the former has peaks at 995 and $1027cm^{-1}$ and the latter peaks at 1087,1119 and $1149cm^{-1}$. Table 4.3 shows that the reduction products at 300 and 400°C have a peak at $1144cm^{-1}$ which is present in manganite. Ohzuku (1985) used a similar type of argument although his conclusions were based on the X-ray diffraction patterns as opposed to the I.R. spectra of Potter and Rossman which are used here. Generally comparisons with groutite and manganite are not conclusive although the reduction products at 300 and 400°C have peaks that are only found in manganite.

*Table 4.3* : Peak positions in the FTIR spectra of the most reduced materials

| Temperature of heat treatment /°C | Reduction method | Peak Position / $cm^{-1}$ |
|---|---|---|
| 200 | propan-2-ol | 511,595,1079,2016,2666 |
| 200 | hydrazine hydrate | 508,595,1084,2016,2650 |
| 300 | propan-2-ol | 508,595,1084,2016,2650 |
| 300 | hydrazine hydrate | 508,596,1081,1145,2015,2650 |
| 400 | hydrazine hydrate | 509,601,1085,1144,2024,2647 |

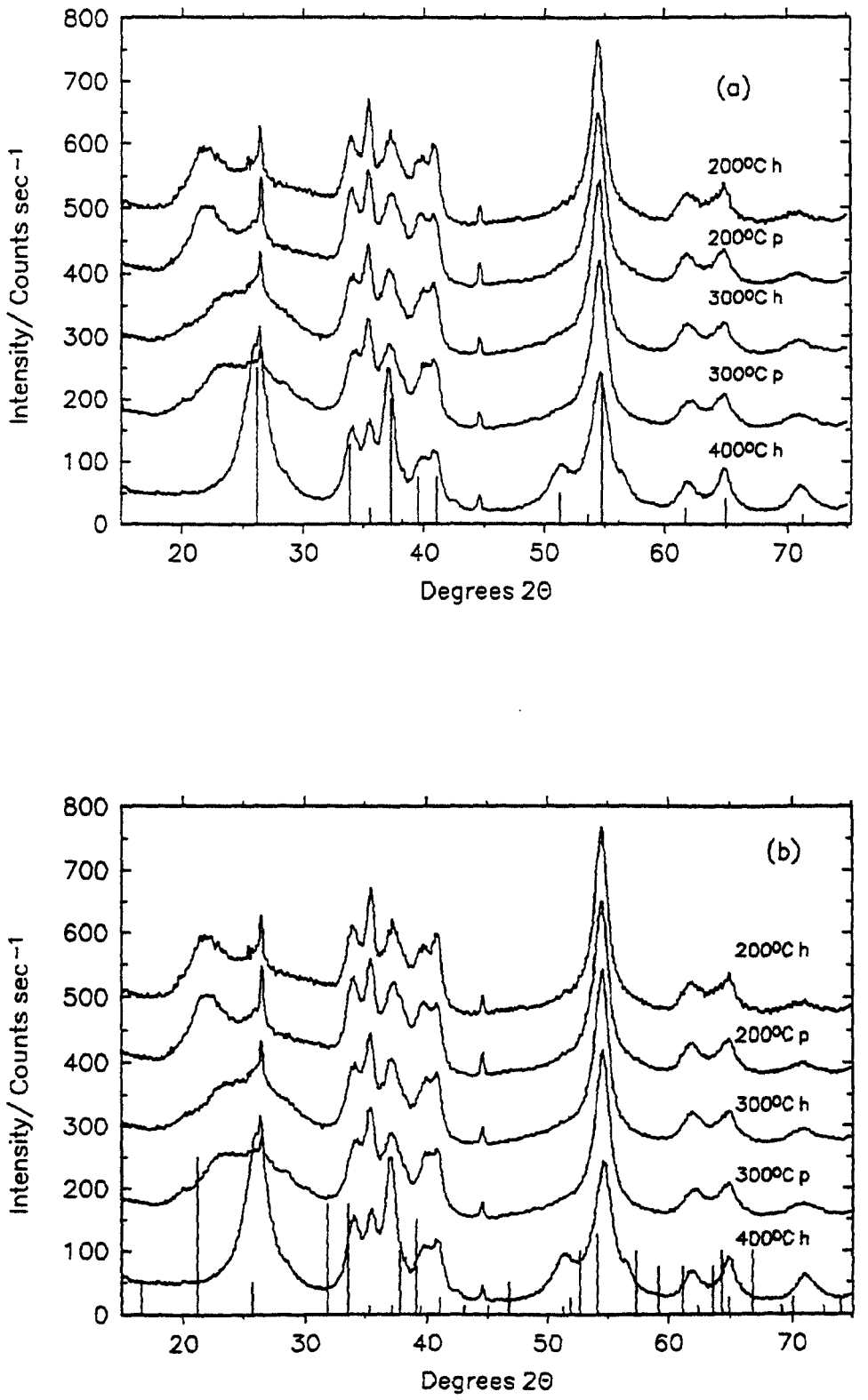


***Figure 4.48*** : Comparison of the X-ray diffraction reduction products with (a) manganite and (b) groutite. h and p refer to hydrazine and propan-2-ol respectively. The stoichiometries of the compounds, from top to bottom, are $MnOOH_{0.955}$, $MnOOH_{0.976}$, $MnOOH_{1.01}$, $MnOOH_{0.967}$ and $MnOOH_{0.932}$.

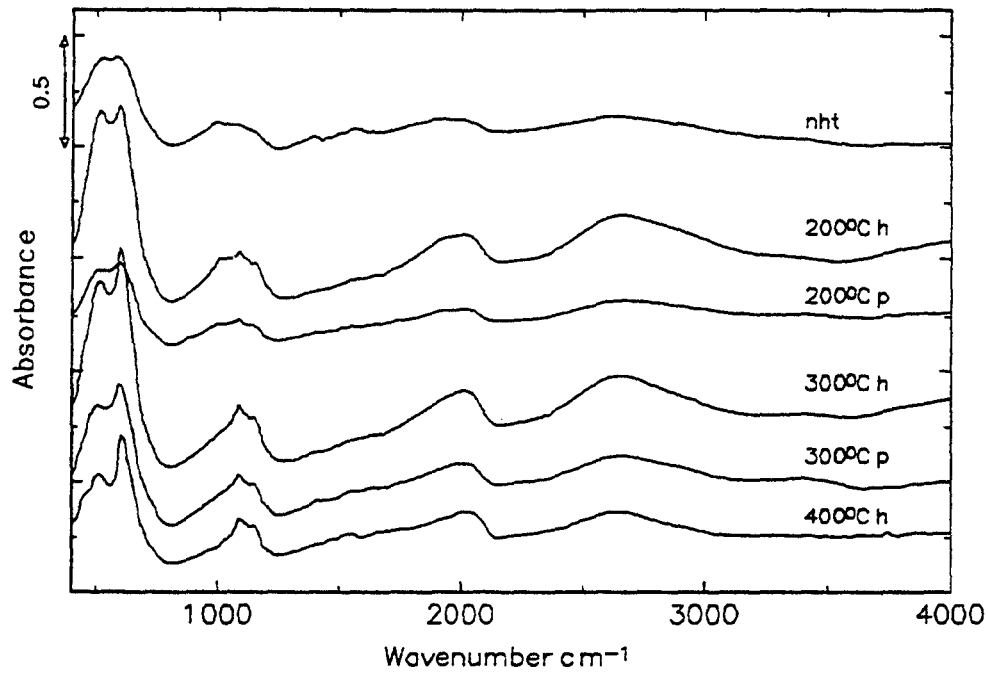


**Figure 4.49** : Comparison of the FTIR reduction product spectra. h and p refer to hydrazine and propan-2-ol respectively, nht is non-heat-treated (ref Tye 1992). The stoichiometries of the compounds, from top to bottom, are $MnOOH_{1.01}$, $MnOOH_{0.955}$, $MnOOH_{0.976}$, $MnOOH_{1.01}$, $MnOOH_{0.967}$ and $MnOOH_{0.932}$.

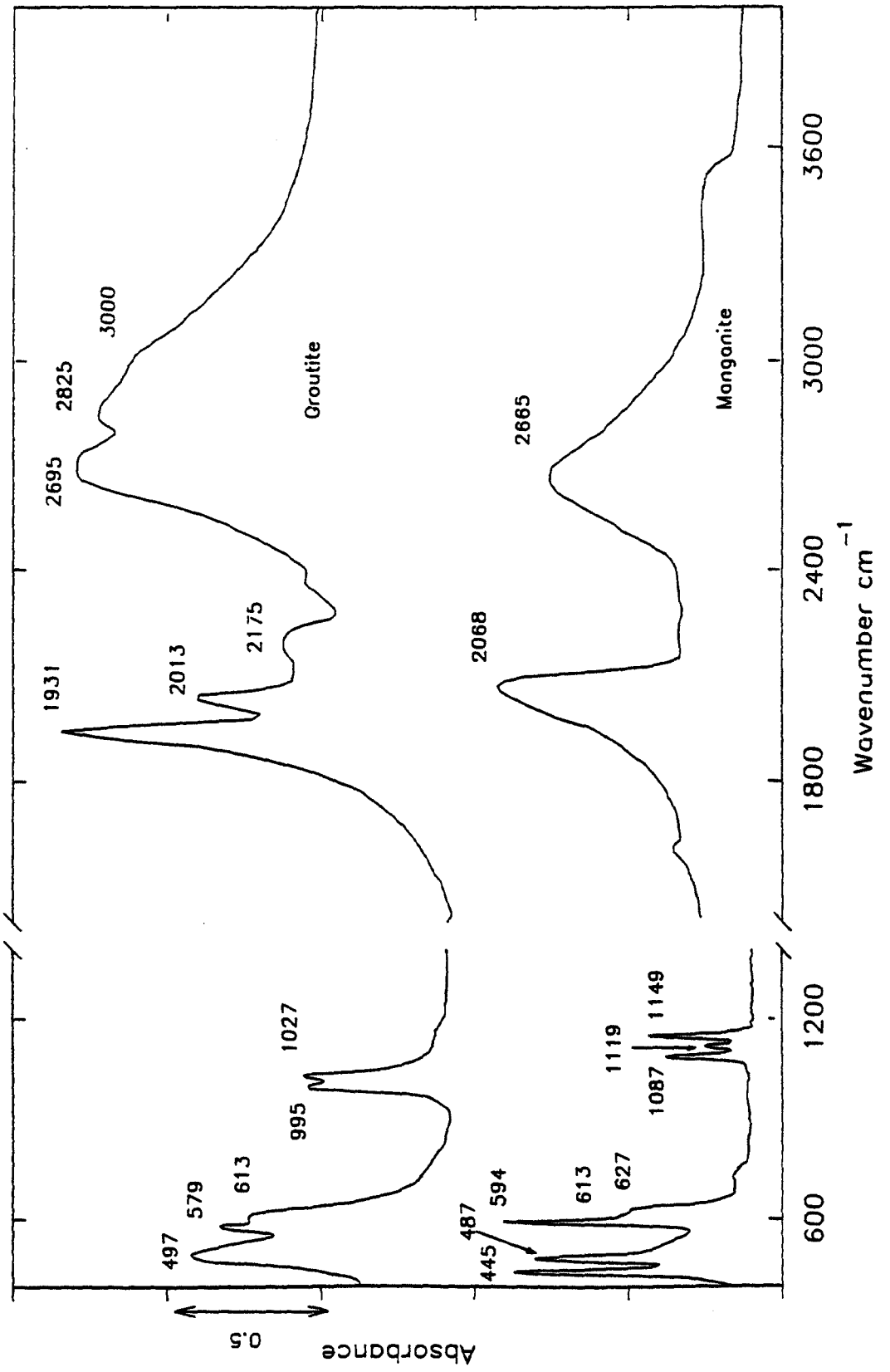


*Figure 4.50* : Infra-red spectra of groutite and manganite (from Potter and Rossman 1979). The spectra were obtained by mixing 0.5 mg of powder in TlBr and KBr pellets from 400-1400cm$^{-1}$ and 2.0 mg in TlBr from 1400-4000cm$^{-1}$.

## 4.5 Computer simulation of XRD spectra[‡]

The purpose of this section is to establish the regions of homogeneity/heterogeneity that have been found in the $MnOOH_{0.1}$-$MnOOH_{1.0}$ reduction process. A single phase (homogeneous) process was found for EMD heat-treated at 200°C (reduced by propan-2-ol) and a heterogeneous process for EMD heat-treated at 400°C (reduced by hydrazine hydrate). In the latter process one phase grows at the expense of another one. In order to demonstrate this figure 4.51 shows the heterogeneous case. A mixture of the starting material and the reduction product (this is called the simulated spectrum) is compared with an experimental compound of the same H insertion level. The difference spectrum is shown beneath the X-ray patterns and it can be seen that the simulated and experimental patterns are almost identical as would be expected for a heterogeneous reaction. Figure 4.52 shows the result of the homogeneous reduction and the differences in the simulated and experimental spectra are significantly greater than the heterogeneous case. The full information is given in the figure legends. Within the two cases just shown reduction processes have been observed with regions of homogeneity/heterogeneity, for example figure 4.53 shows the spectra of EMD heat-treated at 200°C and reduced by hydrazine hydrate the agreement is significantly better than figure 4.52 and this is to be expected because heterogeneous behaviour was observed in this system. Note that the scales on all figures are identical to facilitate comparison. Figures 4.54 and 4.55 show the spectra of the 300°C samples, the difference spectrum is greater for the propan-2-ol data because a larger region of homogeneity was observed. The statistical analysis for the difference spectra depicted in figures 4.51(b) – 4.55(b) is given in Table 4.4.

Figure 4.56 shows the result when appropriate proportions of $MnOOH_{0.479}$ and $MnOOH_{1.006}$ are combined and compared with $MnOOH_{0.718}$. The agreement between the spectra is better than when the starting material and end-product were mixed (figure 4.52) and statistical analysis of the difference spectrum (Table 4.5) shows that the agreement is similar to figure 4.51(b). A similar

[‡]The simulated spectra can be produced easily because the XRD spectra are in a spreadsheet format. For example figure 4.52: the simulated spectra can be made by multiplying the spectra of $MnOOH_{0.11}$ by 0.58 and multiplying the spectra of $MnOOH_{0.932}$ by 0.42 and adding the resultant columns of data together.

*Table 4.4* : Statistical analysis of the difference spectra depicted in Figures 4.51(b)–4.55(b).

| Temperature of heat-treatment/°C | Reduction method | Figure Number | Max | Min | Mean | Var | Standard deviation |
|---|---|---|---|---|---|---|---|
| 400 | hydrazine | 4.51(b) | 32.43 | -40.78 | -2.11 | 50.28 | 7.09 |
| 200 | propan-2-ol | 4.52(b) | 283.47 | -129.1 | 3.03 | 1678 | 40.97 |
| 200 | hydrazine | 4.53(b) | 58.65 | -106.2 | 0.39 | 396.4 | 19.91 |
| 300 | hydrazine | 4.54(b) | 71.87 | -35.62 | 2.56 | 164 | 12.81 |
| 300 | propan-2-ol | 4.55(b) | 112.5 | -48.52 | 1.29 | 433 | 20.80 |

var = variance
max or (min) = maximum or (minimum) value in the difference spectrum

*Table 4.5*: Statistical analysis of the difference spectra depicted in Figures 4.56(b)–4.59(b).

| Temperature of heat-treatment/°C | Reduction method | Figure number | Max | Min | Mean | Var | Standard Deviation |
|---|---|---|---|---|---|---|---|
| 200 | hydrazine | 4.56(b) | 35.52 | -27.84 | -0.89 | 53.28 | 7.30 |
| 200 | propan-2-ol | 4.57(b) | 186.66 | -111.28 | -3.21 | 571.1 | 23.9 |
| 300 | hydrazine | 4.58(b) | 45.07 | -32.32 | -1.19 | 64.16 | 8.01 |
| 300 | propan-2-ol | 4.59(b) | 79.91 | -16.49 | 3.61 | 84.84 | 9.21 |

exercise was performed on EMD heat-treated at 300°C and the region where heterogeneity begins is set at $MnOOH_{0.33}$ and $MnOOH_{0.534}$ for hydrazine and propan-2-ol respectively. The results are shown in figures 4.58 and 4.59 and the analysis in Table 4.5.

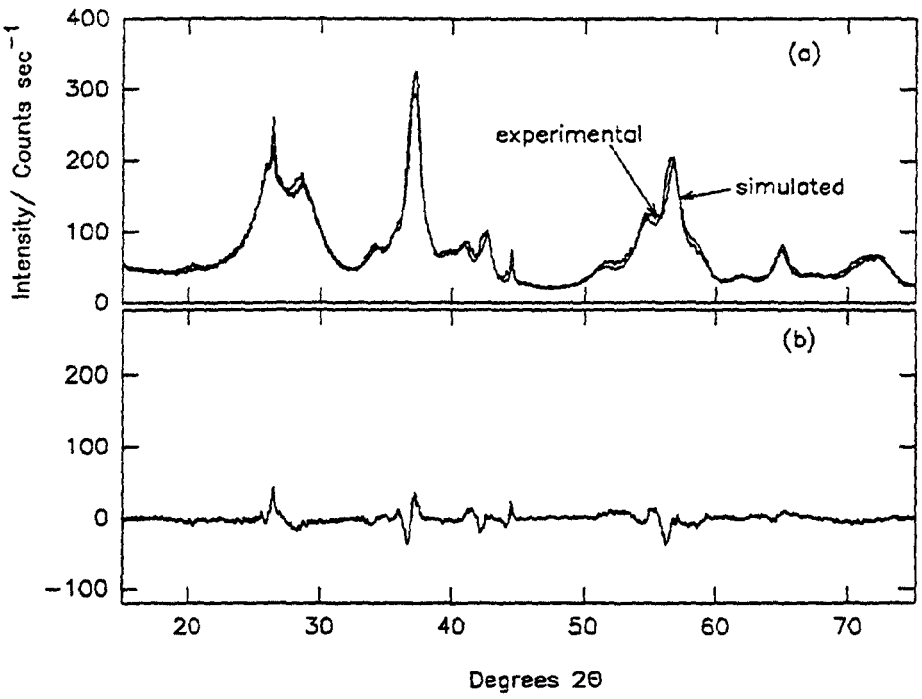


***Figure 4.51*** : Comparison of (a) experimental XRD pattern of $MnOOH_{0.457}$ with a mixture of 58% $MnOOH_{0.11}$ and 42% $MnOOH_{0.932}$ and (b) experimental-simulated difference spectrum; EMD heat-treated at 400°C; hydrazine hydrate reduction method.

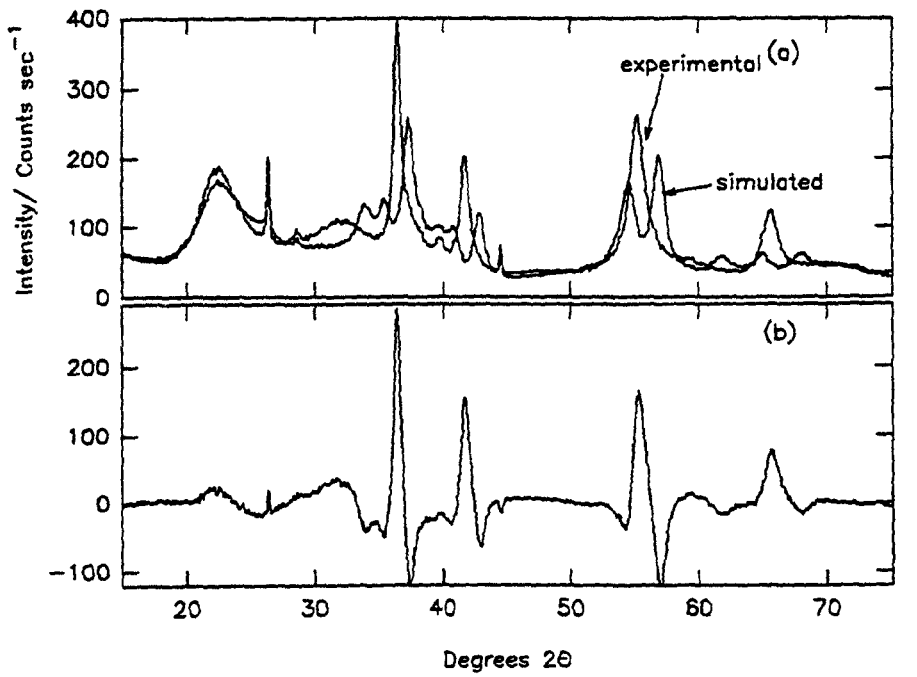


***Figure 4.52*** : Comparison of (a) experimental $MnOOH_{0.528}$ with a mixture of 50% $MnOOH_{0.07}$ and 50% $MnOOH_{0.976}$ (b) experimental-simulated difference spectrum; EMD heat-treated at 200°C; propan-2-ol reduction method.

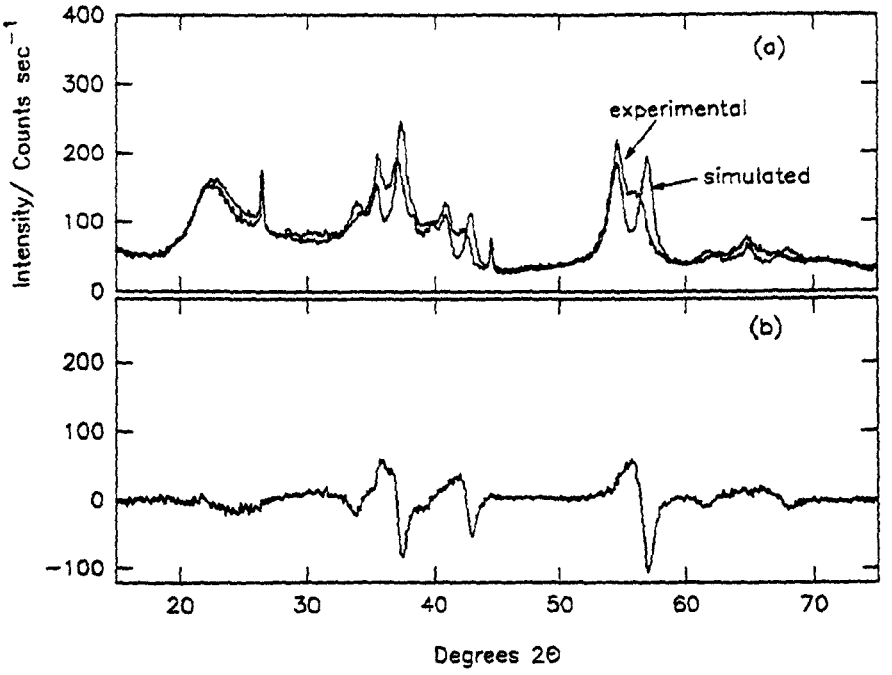


***Figure 4.53*** : Comparison of (a) experimental $MnOOH_{0.547}$ with a mixture of 46.5% $MnOOH_{0.07}$ and 53.5% $MnOOH_{0.955}$ and (b)experimental-simulated difference spectrum; EMD heat-treated at 200°C;hydrazine hydrate reduction method.

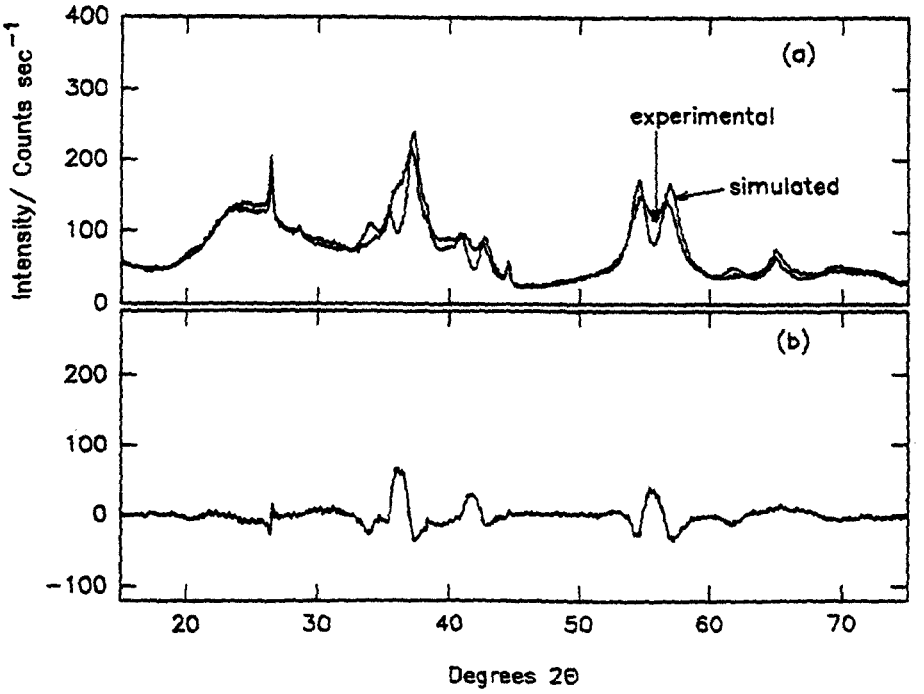


***Figure 4.54*** : Comparison of (a) experimental $MnOOH_{0.497}$ with a mixture of 55% $MnOOH_{0.08}$ and 45% $MnOOH_{1.006}$ and (b) experimental-simulated difference spectrum; EMD heat-treated at 300°C;hydrazine hydrate reduction method.

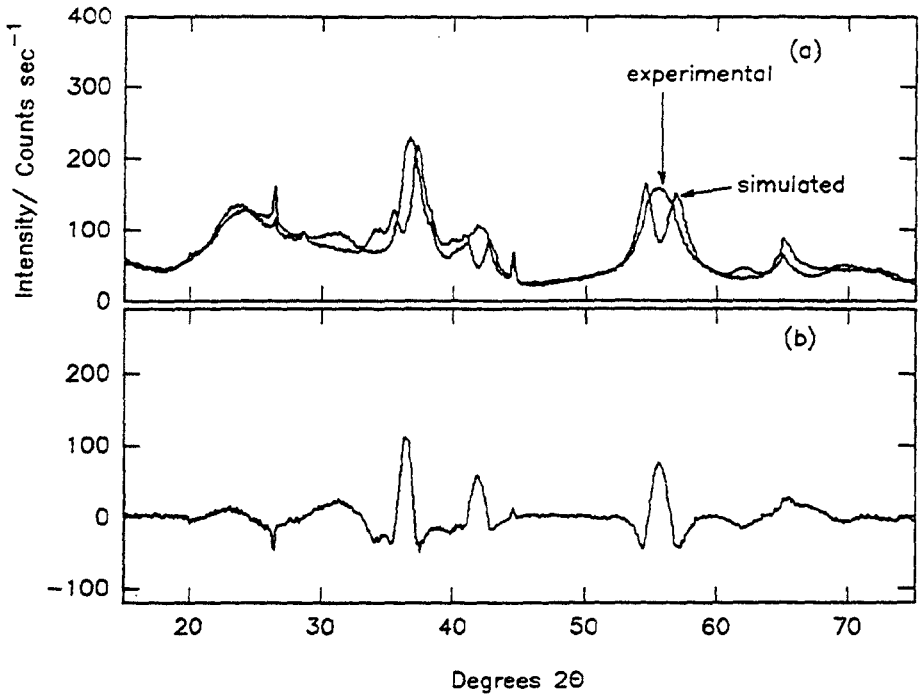


***Figure 4.55*** : Comparison of (a) experimental $MnOOH_{0.532}$ with a mixture of 49% $MnOOH_{0.08}$ and 51% $MnOOH_{0.9668}$ with (b) experimental-simulated difference spectrum; EMD heat-treated at 300°C; propan-2-ol reduction method.

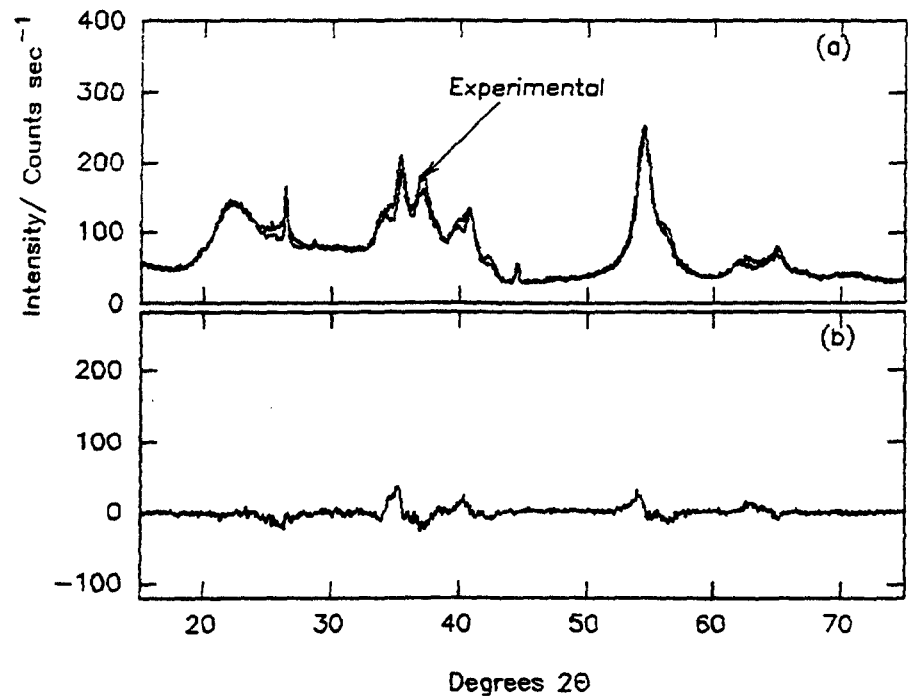


***Figure 4.56*** : Comparison of (a) experimental $MnOOH_{0.718}$ with a mixture of 50% $MnOOH_{0.479}$ and 50% $MnOOH_{0.955}$ with (b) experimental-simulated difference spectrum; EMD heat-treated at 200°C; hydrazine hydrate reduction method.

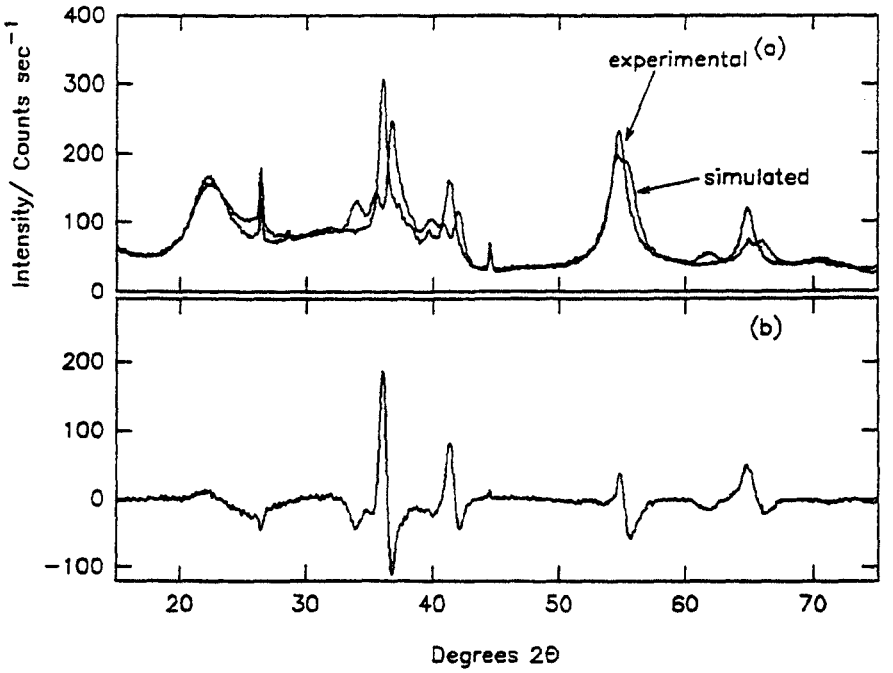


***Figure 4.57*** : Comparison of (a) experimental $MnOOH_{0.713}$ with a mixture of 50% $MnOOH_{0.454}$ and 50% $MnOOH_{0.976}$ with (b) experimental-simulated difference spectrum; EMD heat-treated at 200°C; propan-2-ol reduction method.

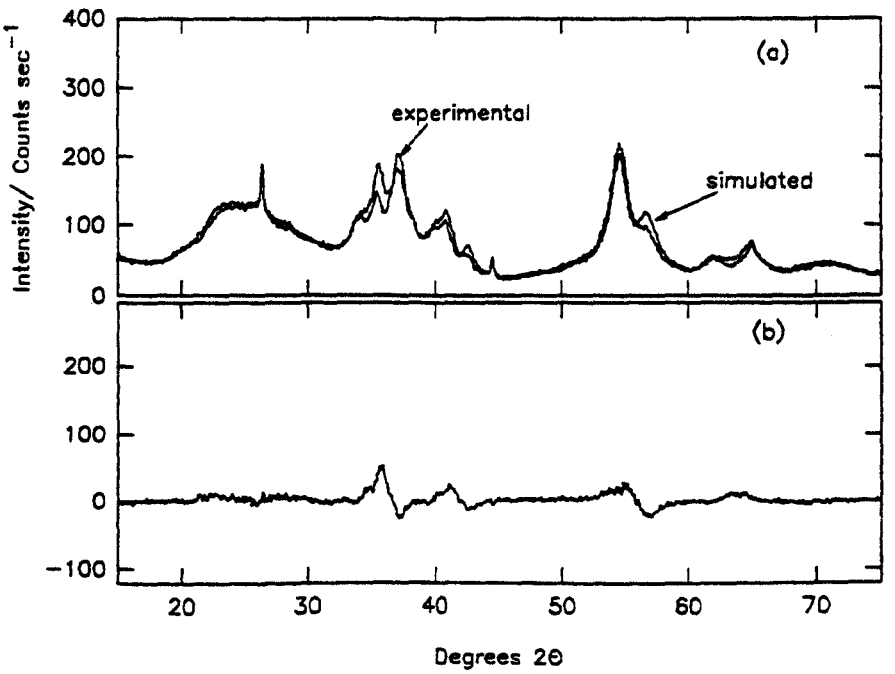


***Figure 4.58*** : Comparison of (a) experimental $MnOOH_{0.705}$ with a mixture of 44% $MnOOH_{0.331}$ and 56% $MnOOH_{1.006}$ with (b) experimental-simulated difference spectrum; EMD heat-treated at 300°C; hydrazine hydrate reduction method.

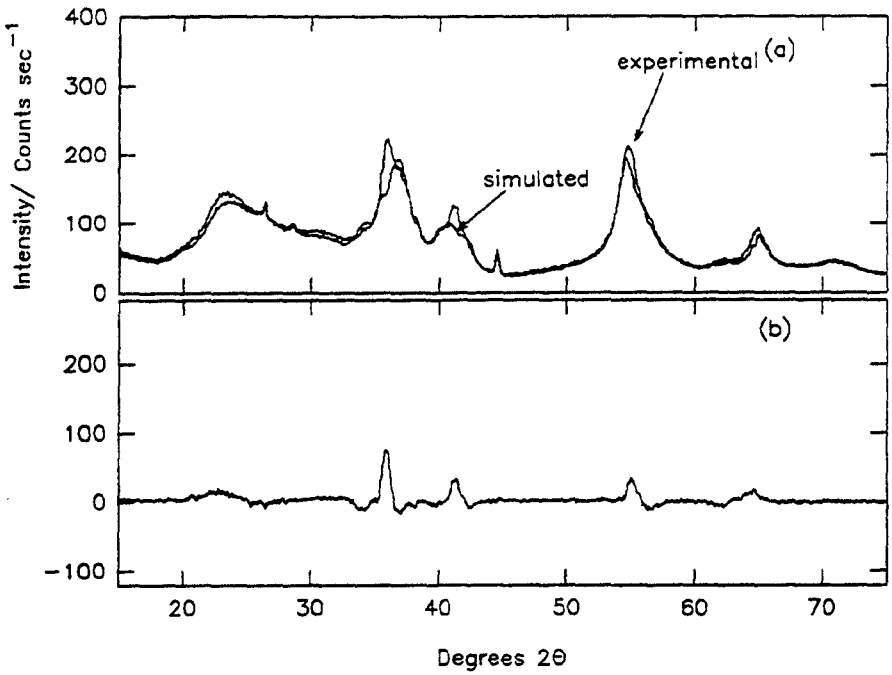


***Figure 4.59*** : Comparison of (a) experimental $MnOOH_{0.704}$ with a mixture of 60% $MnOOH_{0.534}$ and 60% $MnOOH_{0.966}$ with (b) experimental-simulated difference spectrum; EMD heat-treated at 300°C; propan-2-ol reduction method.

## 4.6 Conclusions

An electrodeposited $MnO_2$ was heat-treated at 200, 300 and 400°C and then reduced to $MnOOH_{1.0}$ by either hydrazine hydrate or propan-2-ol. Different behaviour was observed and this depended on the heat-treatment temperature and the reduction method. When EMD was heat-treated at 200°C and reduced by propan-2-ol a homogeneous phase from $MnOOH_{0.07}$-$MnOOH_{0.976}$ was observed in the X-ray diffraction spectra (section 4.2.1(i)). At 400°C the reduction is heterogeneous from $MnOOH_{0.11}$-$MnOOH_{0.932}$ and within these extremes of behaviour different regions of homogeneity/heterogeneity were found. A new finding was that hydrazine hydrate caused the heterogeneous reduction of EMD heat-treated at 200°C (section 4.2.1 (ii)) even though a homogeneous phase was found for the same material reduced with propan-2-ol (section 4.2.1 (i)). At 300°C the reduction of $MnO_2$ was found to be heterogeneous whatever the mode of reduction although heterogeneous reduction was observed at an earlier stage when hydrazine hydrate was used.

FTIR spectroscopy was used as a complementary technique to X-ray

diffraction (section 4.3) and it was found that the spectra could be divided into two regions. Vibrations in the region 400-1400cm$^{-1}$ were due to the $MnO_6$ octahedral framework and from 1400-4000 cm$^{-1}$ they were due to OH bending and stretching vibrational modes. The changes in the $MnO_6$ octahedral framework were related to the Jahn-Teller deformation associated with the $Mn^{3+}$ ion (section 4.3.1 (i)). Peaks relating to OH bond formation centred at 2050 and 2650cm$^{-1}$ dominated the spectra at $MnOOH_{1.0}$. It was found that for a homogeneous reduction (section 4.3.1 (i)) peaks relating to OH bond formation only appeared after $MnOOH_{0.70}$ and this demonstrated delocalisation of the inserted proton and electron without significant OH bond formation which was a new finding (Figure 4.36). When the reduction of $MnO_2$ was heterogeneous peaks relating to OH bond formation appeared much earlier in the reduction process.

Comparison of the X-ray diffraction reduction products with groutite and manganite (Figure 4.48) showed that the new lines that appear in the X-ray diffraction pattern are at the same position as those of manganite. The crystal structure of the sample heat-treated at 200°C was similar to $\delta$-MnOOH which was obtained by Maskell *et al.* (1981) and Fitzpatrick and Tye (1991). At 400°C the crystal structure was the same as manganite. A method (section 4.5) whereby appropriate amounts of two experimental XRD patterns (called a simulated pattern) was compared with one obtained experimentally was used to establish the onset of the heterogeneous behaviour and the following levels of H insertion were found at which heterogeneity set in: 200°C hydrazine $MnOOH_{0.48}$, 300°C hydrazine $MnOOH_{0.33}$ and 300°C propan-2-ol $MnOOH_{0.534}$.

# Chapter 5. Proton Insertion Into Heat-treated Chemical Manganese Dioxide.

## 5.1 Introduction.

Examination of the literature pertaining to manganese dioxide revealed that most of the papers have dealt with electrodeposited manganese dioxide (EMD). It would therefore seem appropriate to investigate the H insertion mechanism using methods that have already been presented in Chapter 4. In this chapter results are reported for a CMD that had been heat-treated at 200, 300 and 400°C and then reduced to $MnOOH_{1.0}$ with hydrazine hydrate.

## 5.2 Powder x-ray diffraction spectra of non heat-treated and heat-treated manganese oxyhydroxides.

### *5.2.1 Non heat-treated CMD*

The reduction of non heat-treated CMD was investigated because there was no literature on the reduction of this material. A selection of X-ray diffraction patterns during the reduction of Faradiser WSLi are shown in Figure 5.1 (the insertion level is given above each pattern) and selected regions of the patterns are shown in 3-D in Figures 5.2-5.5. In Figure 5.6 the variation of interplanar spacing with H insertion is plotted for six of the peaks (see Figure 5.1 for peak labelling). Figure 5.7 shows the variation in peak height with H insertion level. Examination of Figure 5.6 reveals that the peaks move from $MnOOH_{0.116}$ – $MnOOH_{0.70}$. It is difficult to decipher the exact position as there are few samples at high degrees of reduction. MacLean (1993) reported on the reduction of Faradiser WSZ (the same crystal structure as WSLi but with a higher water content) and found that the reduction was homogeneous to $MnOOH_{0.40}$ and heterogeneous from $MnOOH_{0.64}$. In this work the samples were reduced at a slower rate (approximately 5 times) and so it is not unexpected that a greater region of homogeneity was observed (Gabano *et al.* 1970 found that the reduction was dependent on the rate of reaction). In Figure 5.8[†] appropriate amounts of $MnOOH_{0.736}$ and $MnOOH_{1.01}$ are compared with the actual pattern of

[†]see footnote on page 142 and section 4.5.

stoichiometry $MnOOH_{0.894}$ (a similar exercise was performed in section 4.5). This was done in order to find out if the reduction was heterogeneous after $MnOOH_{0.736}$. The patterns in figure 5.8 have similar intensities although the agreement is not as good as demonstrated in figure 4.51. These type of simulations are very dependent on the intensities of the individual patterns (this is minimised by the standardisation procedure given in section 2.7.1) so it is difficult to determine the exact stage where heterogeneity began but it probably occurred between $MnOOH_{0.736}$ and $MnOOH_{0.894}$. To demonstrate the validity of the technique figure 5.9 compares a mixture of 50% of the starting material and 50% of the reduction product and it can be seen that there is little resemblance to the pattern of $MnOOH_{0.560}$.

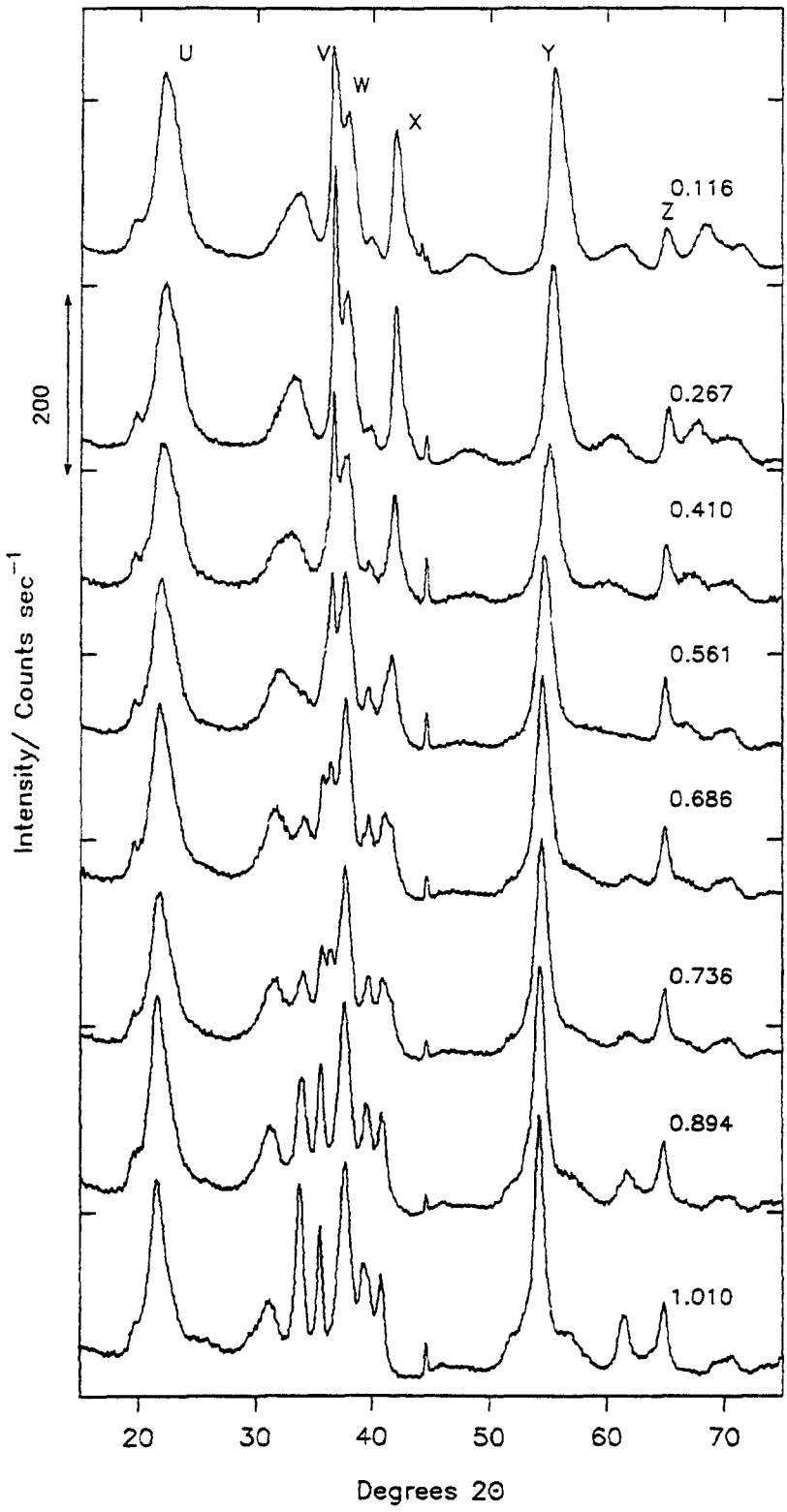


***Figure 5.1*** : X-ray diffraction spectra during the reduction of non heat-treated CMD (Faradiser WSLi); hydrazine hydrate reduction method (the level of H insertion is given above the XRD pattern).

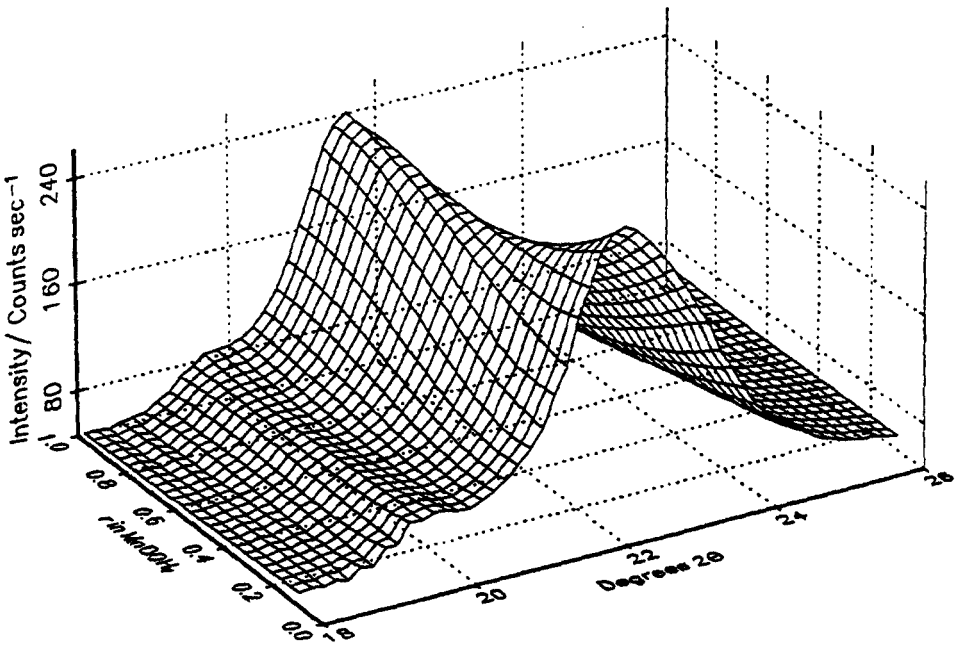


*Figure 5.2* : X-ray diffraction spectra in the region 18-26° 2Θ; non heat-treated CMD; hydrazine hydrate reduction method (data grid from 0.12 – 1.00 in 0.0352 increments in r in $MnOOH_r$).

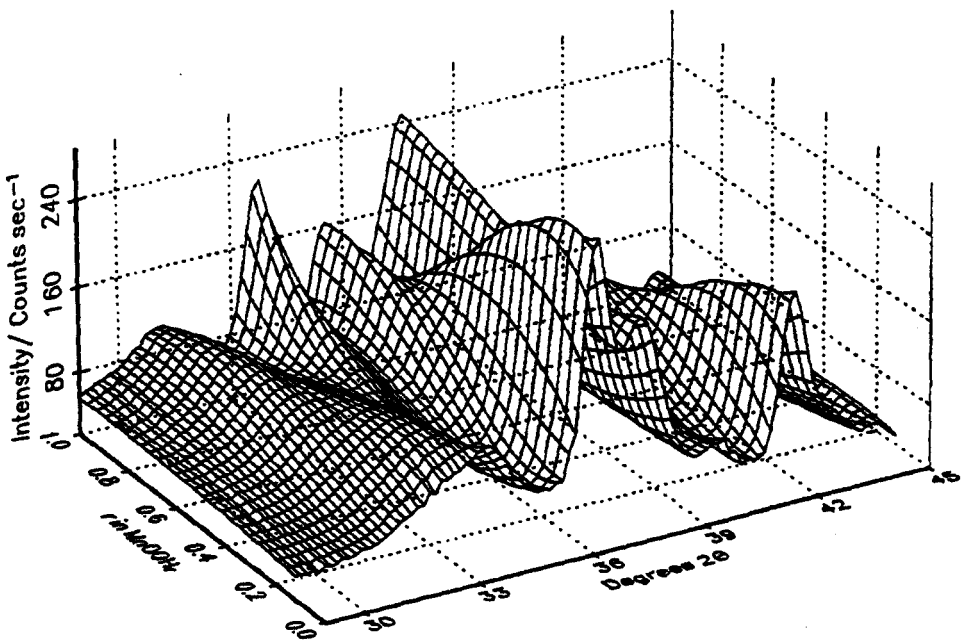


*Figure 5.3* :X-ray diffraction spectra in the region 29-45° 2Θ; non heat-treated CMD; hydrazine hydrate reduction method.

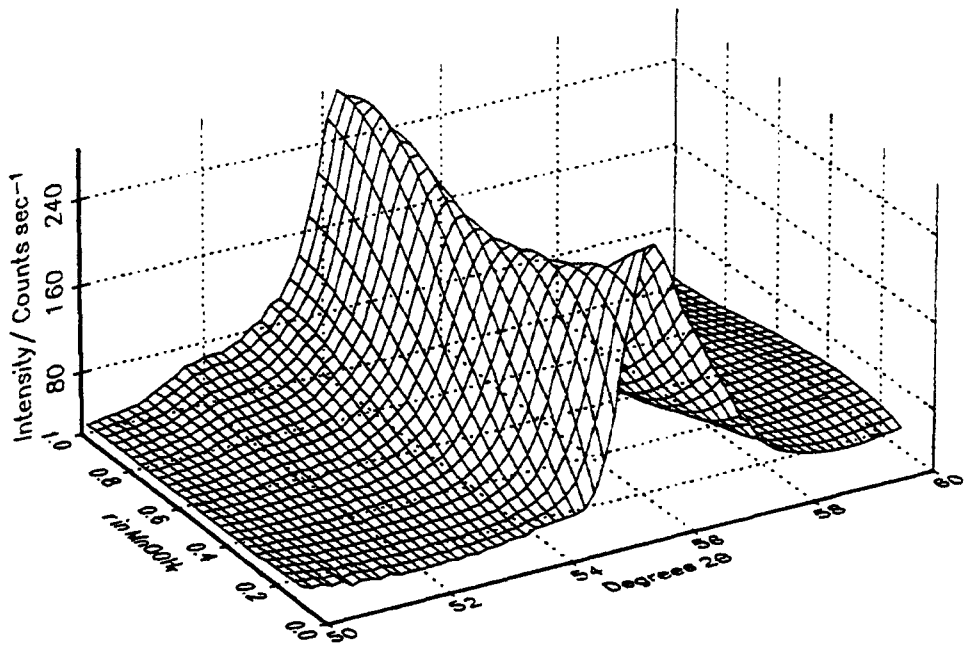


*Figure 5.4* : X-ray diffraction spectra in the region 50-60° 2Θ; non heat-treated CMD; hydrazine hydrate reduction method.

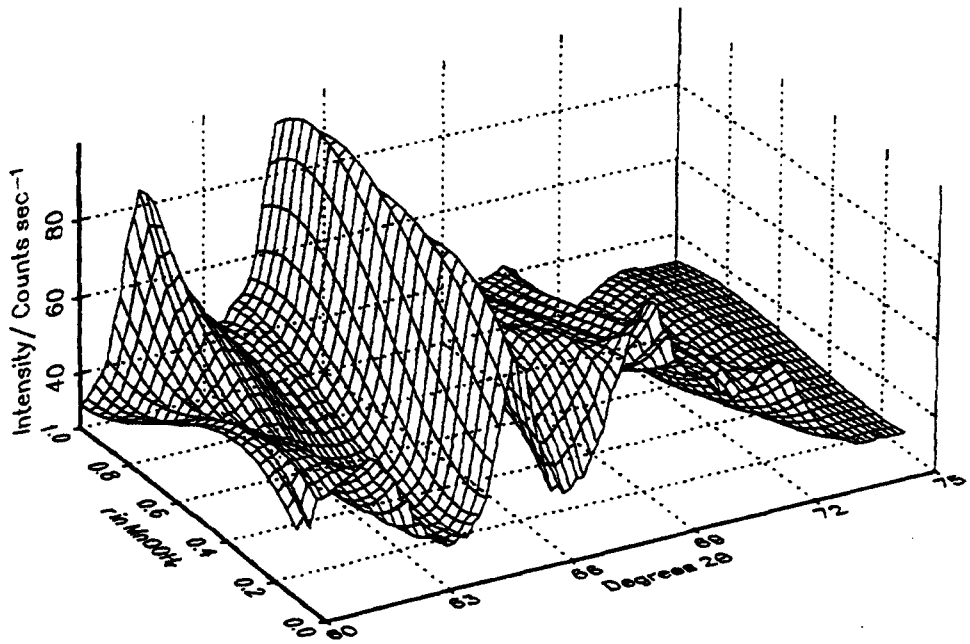


*Figure 5.5* :X-Ray Diffraction Spectra In The Region 60-75° 2Θ; Non Heat-treated CMD; hydrazine hydrate reduction method.

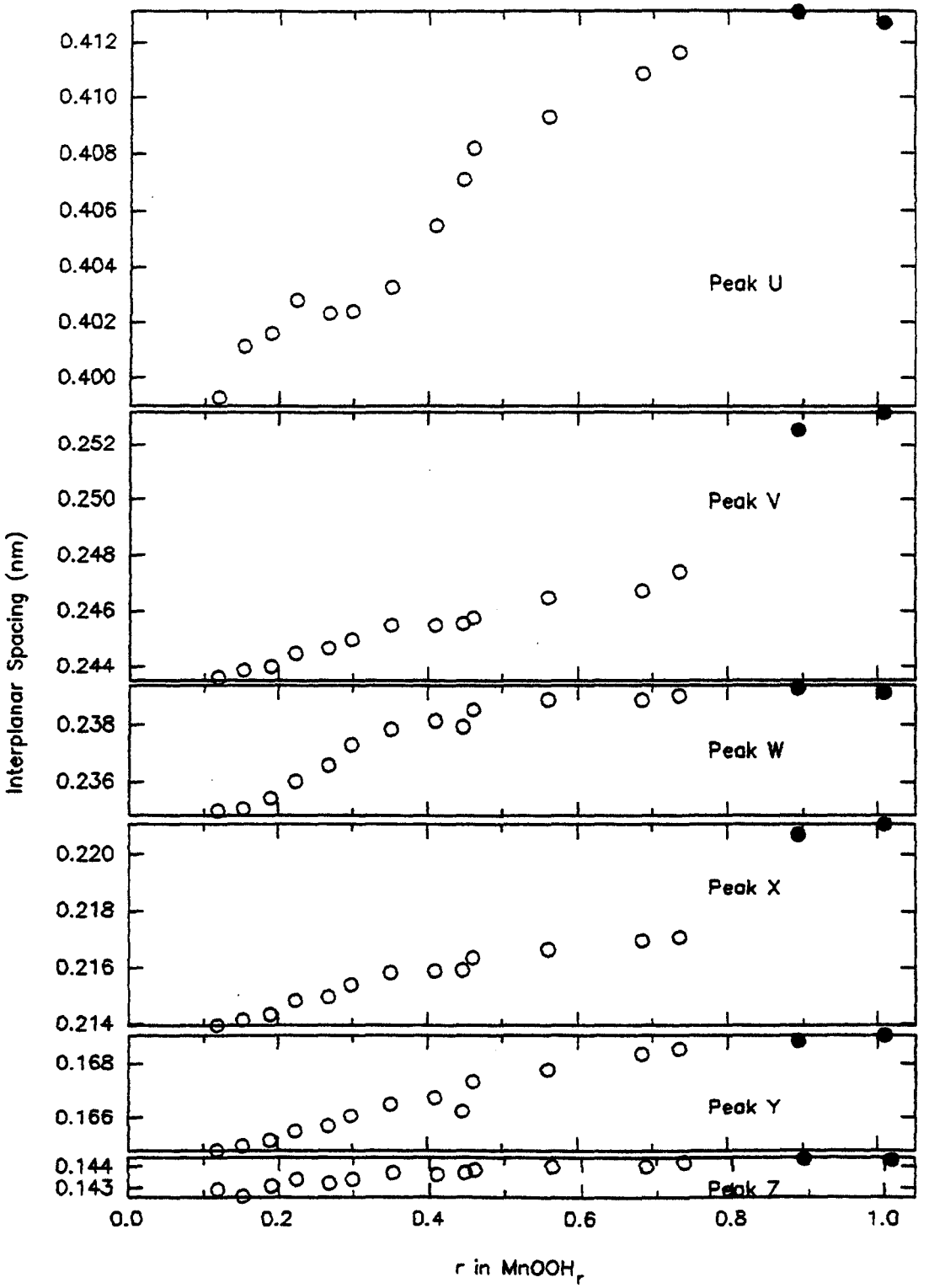


***Figure 5.6*** : Interplanar spacing against H insertion level: non heat-treated CMD (Faradiser WSLi); hydrazine hydrate reduction method.

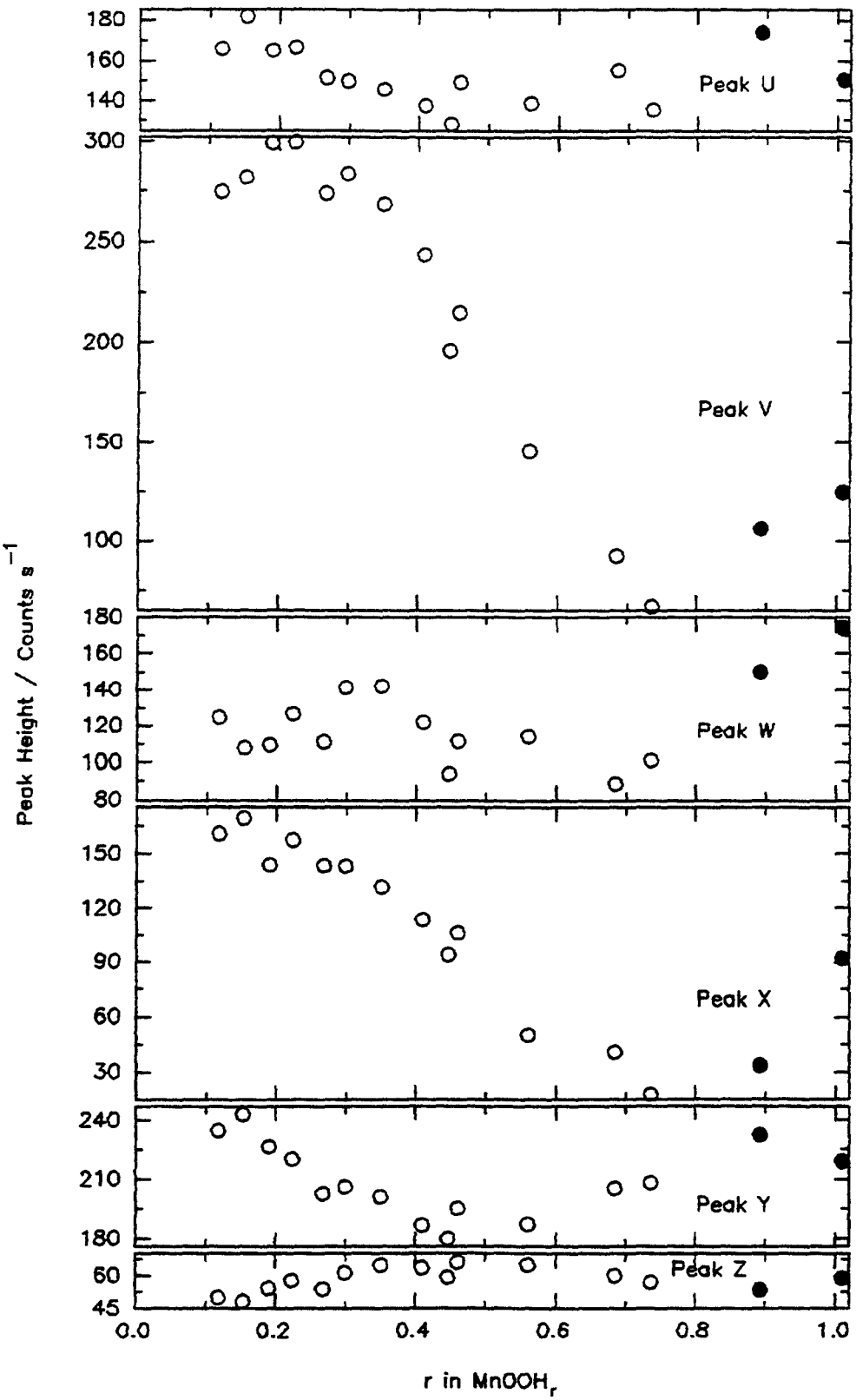


*Figure 5.7*: Peak height against H insertion level non heat-treated CMD (Faradiser WSLi): see figure 5.1 for peak labelling.

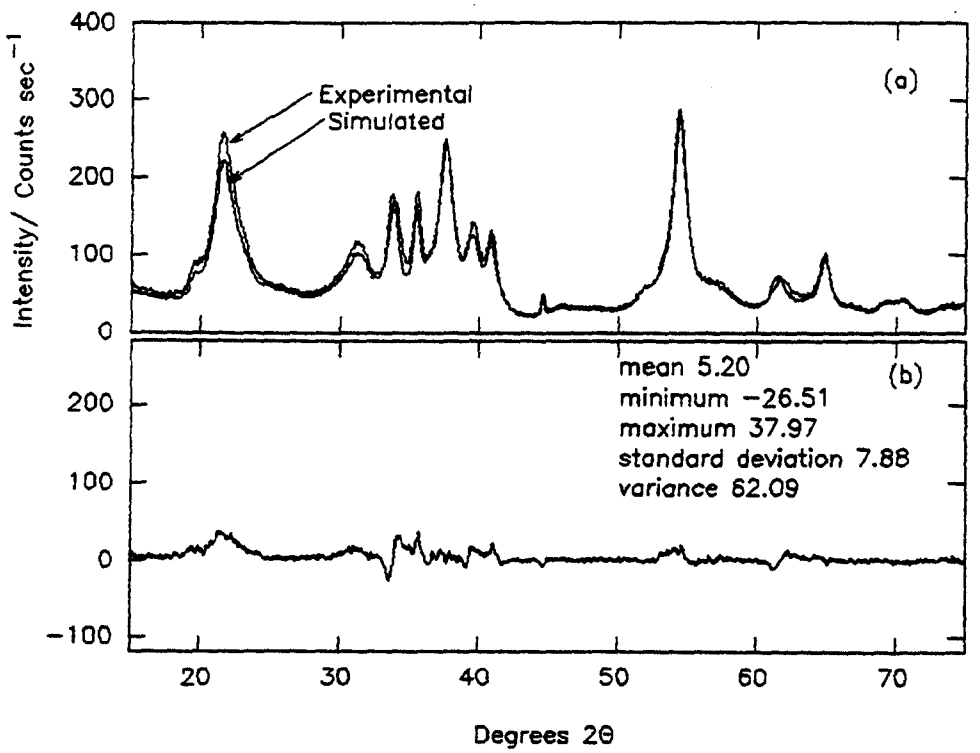


***Figure 5.8*** : Comparison of (a) experimental XRD pattern of $MnOOH_{0.894}$ with a mixture of 42% $MnOOH_{0.736}$ and 58% $MnOOH_{1.01}$ and (b) experimental−simulated difference spectrum; Non heat-treated CMD (statistical analysis is given for (b)).

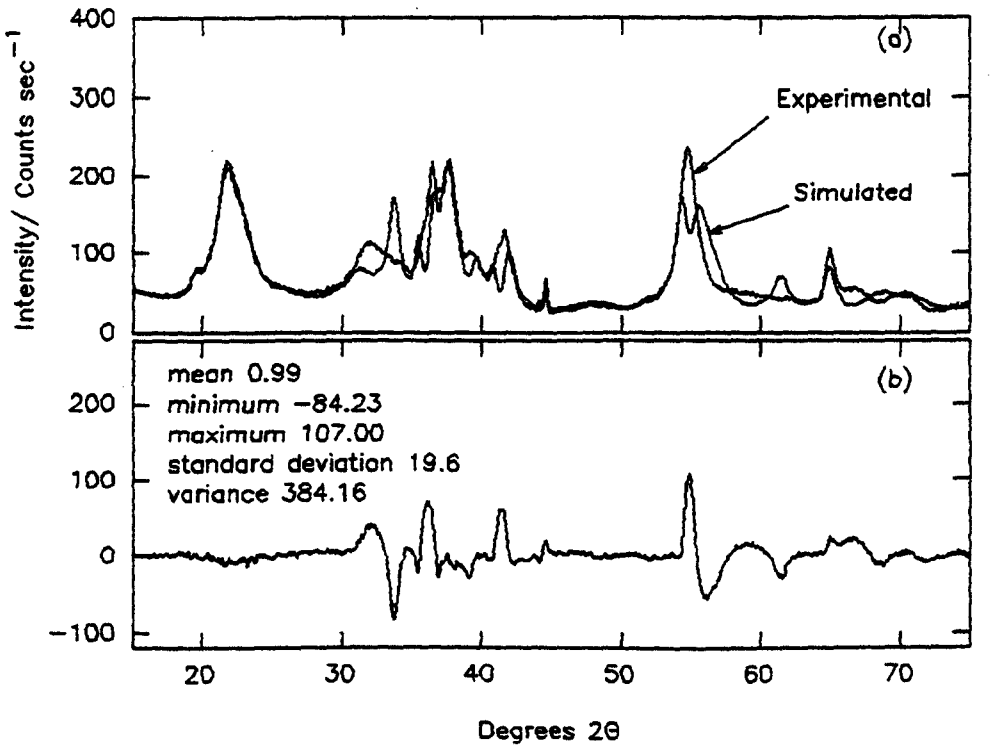


***Figure 5.9*** : Comparison of (a) experimental XRD pattern of $MnOOH_{0.560}$ with a mixture of 50% $MnOOH_{0.116}$ and 50% $MnOOH_{1.01}$ and (b) experimental−simulated difference spectrum; Non heat-treated CMD ( the statistical analysis is given for (b)).

*5.2.2 CMD heat-treated at 200°C.*

X-ray diffraction pattern changes during the reduction of this material are shown in figure 5.10 and selected regions of the XRD patterns are shown in 3D in figures 5.11 – 5.14. It can be seen from these patterns that a heterogeneous reaction occurred at a lower degree of H insertion than for the non heat-treated material (section 5.2.1). In figure 5.15 materials of a similar H insertion level are compared. The non and heat-treated (200°C) patterns look very similar although comparison of figure 5.16 with 5.7 would reveal differences. The importance of plotting the peak positions with respect to H insertion level was mentioned in section 4.2.1(ii). The reason for the differing behaviour between the non and heat-treated CMD could be either a structural one or a surface area effect. In figure 3.29 the XRD patterns during heat-treatment from 25 – 450°C were plotted and the patterns at 25 and 200°C were similar and chemical analysis (figure 3.8) showed that the stoichiometry had increased from 1.941 to 1.972 which indicated the oxidation of $Mn^{3+}$ to $Mn^{4+}$. Ruetschi (1984) and Shimzu *et al.* (1985) found that the electrochemical reactivity of undischarged $MnO_2$ increased with increasing structural water. Data on the change in the surface area (SA) of $MnO_2$ on heat-treatment were found in the papers given by Ikeda *et al.* (1980) and Swinkels *et al.* (1984). The former author gave an average decrease of the SA of 40% upon heat-treatment to 400°C (table 3) and the latter 35% (although only a 13% reduction at 200°C). If there was a large decrease in the SA then the concentration of inserted H would have been much higher in the heat-treated material and hence this is more likely to lead to a heterogeneous process. It is worth noting that data on the SA is to be regarded with caution because as Tye (1980) points out the BET equation is no longer valid for materials heated above 80°C. To summarize therefore the difference in the behaviour between the materials is more likely to be due to a structural change than a surface one. The proton diffusion could be facilitated in the non heat-treated material via the OH groups in a way that is similar to the Grotthus mechanism which is used to explain the electrolysis of water (see Hague 1971). Finally figure 5.18 demonstrates that heterogeneity begins at around $MnOOH_{0.637}$.

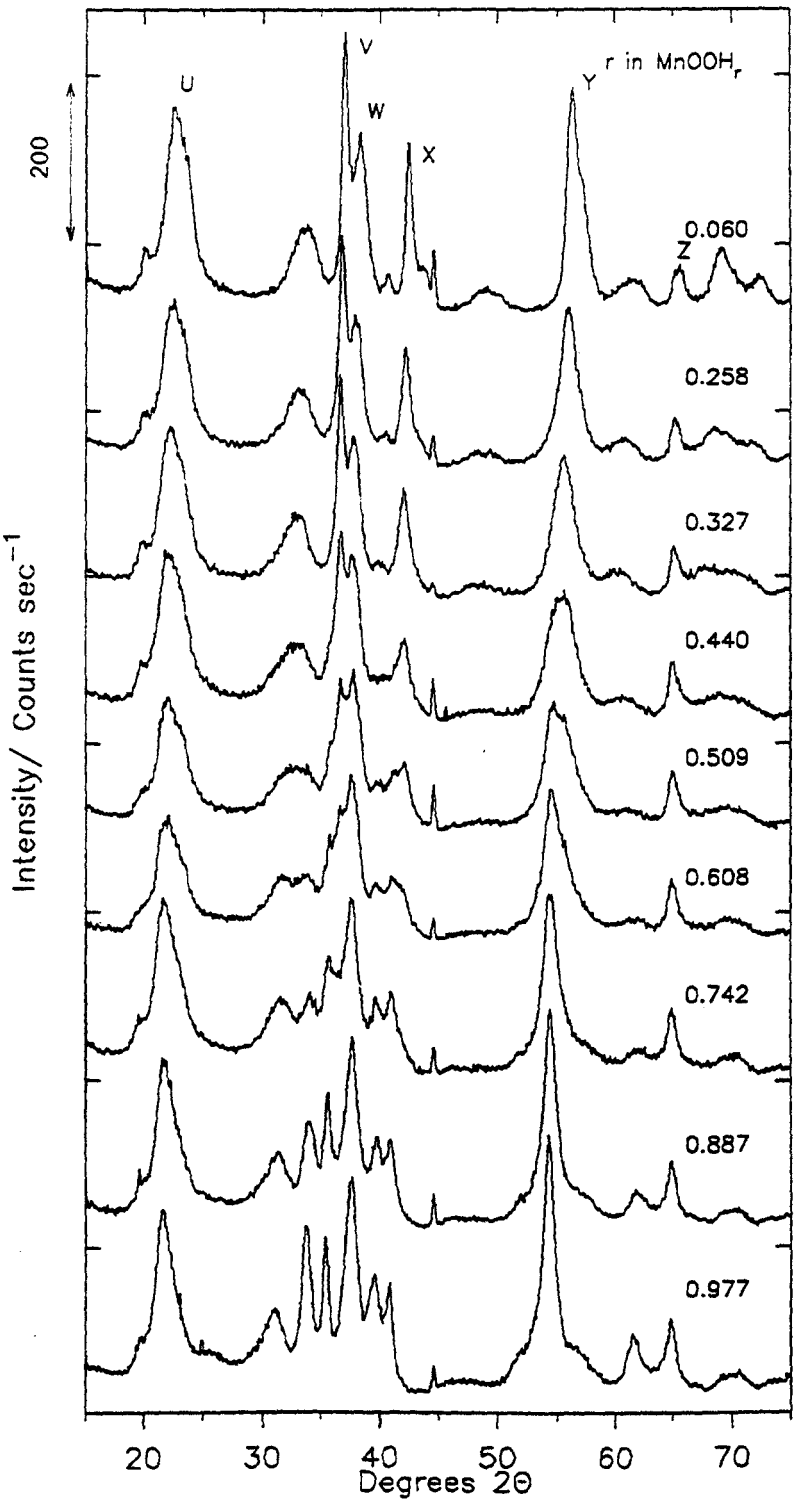


***Figure 5.10*** : X-ray diffraction spectra during the reduction of CMD (Faradiser WSLi); Heat-treated at 200°C; hydrazine hydrate reduction method (the level of H insertion is given above the XRD pattern).

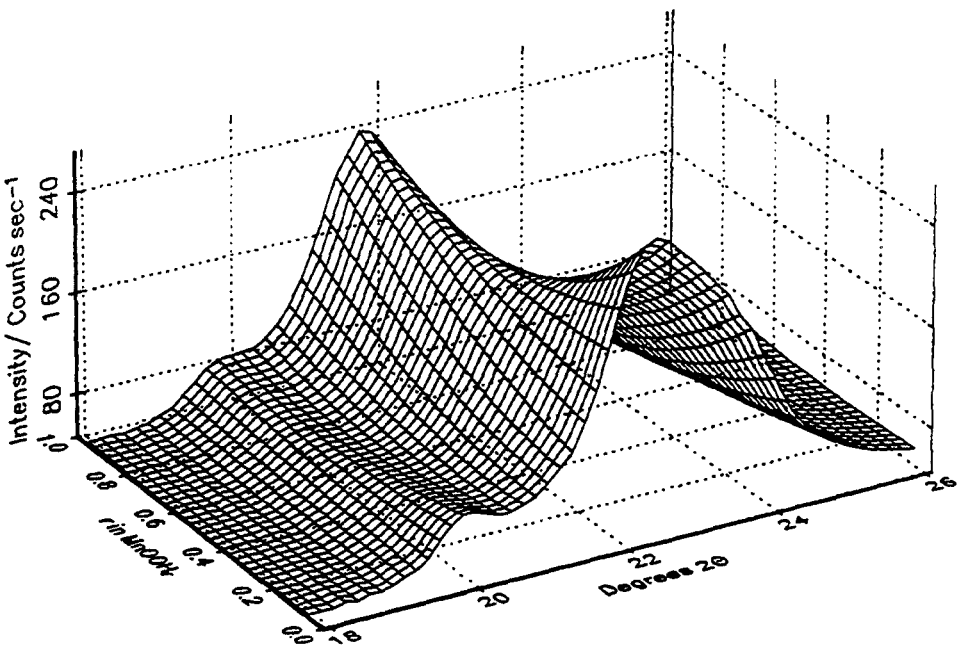


*Figure 5.11* : X-ray diffraction spectra in the region 18-26° 2Θ; CMD heat-treated at 200°C; hydrazine hydrate reduction method (data grid from 0.06–0.96 in 0.036 increments in r in $MnOOH_r$).

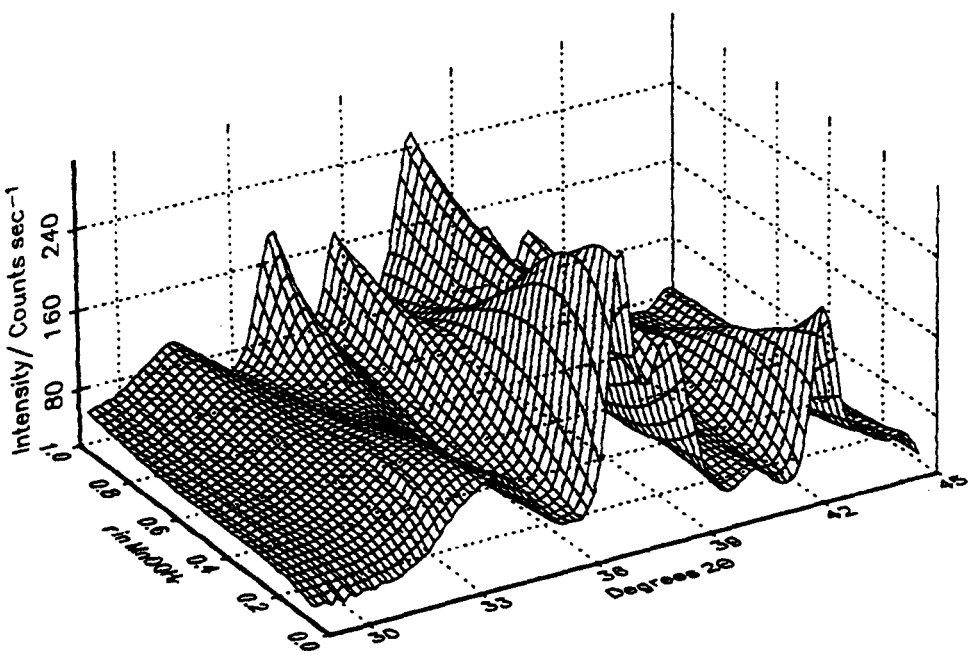


*Figure 5.12* :X-ray diffraction spectra in the region 29-45° 2Θ; CMD heat-treated at 200°C; hydrazine hydrate reduction method.

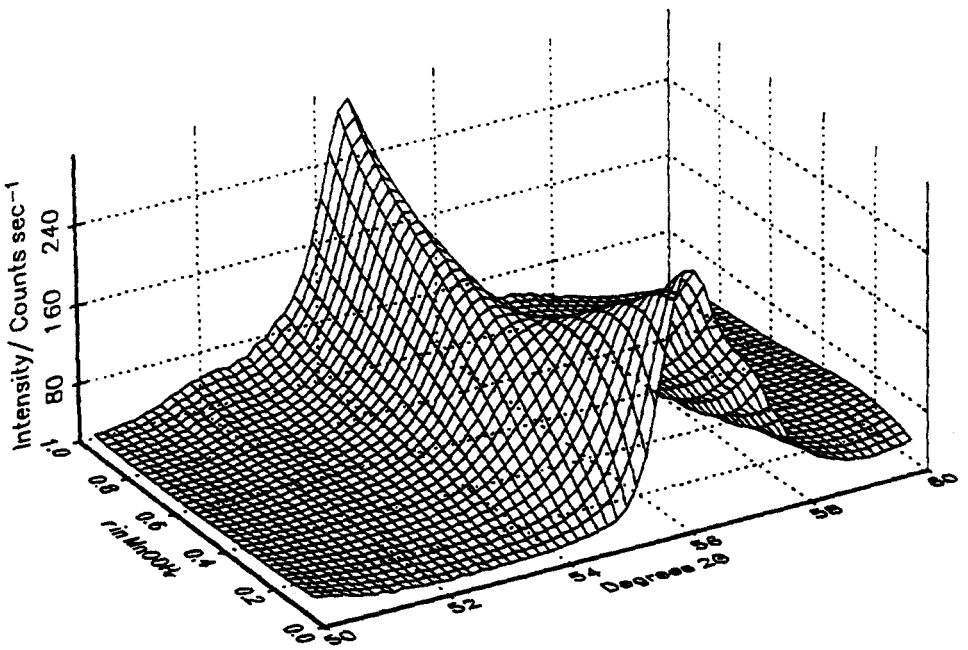


*Figure 5.13* : X-ray diffraction spectra in the region 50-60° 2Θ; CMD heat-treated at 200°C; hydrazine hydrate reduction method.

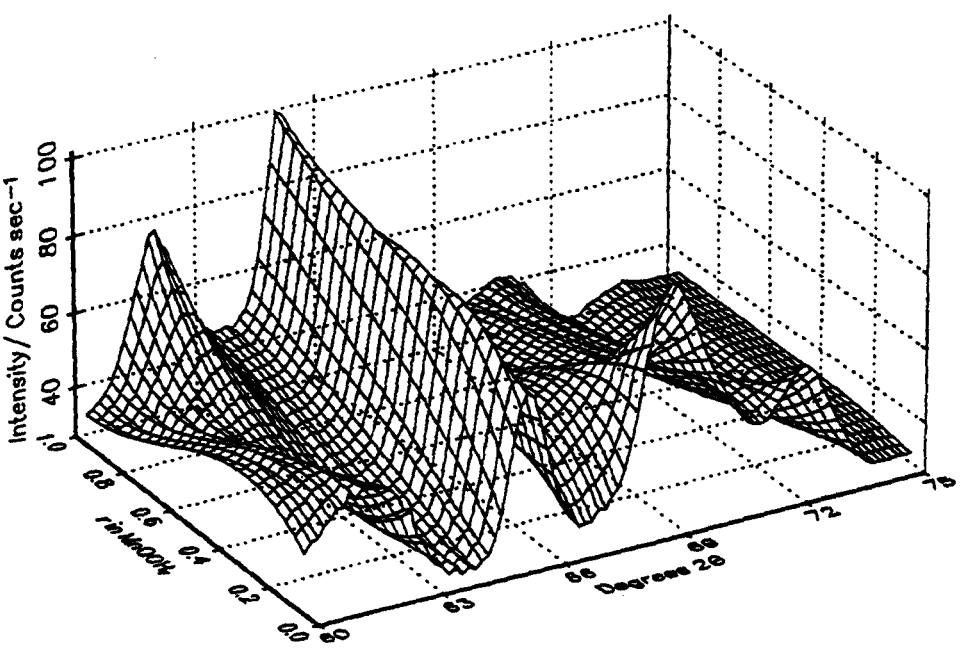


*Figure 5.14* :X-ray diffraction spectra in the region 60-75° 2Θ; CMD heat-treated at 200°C; hydrazine hydrate reduction method.

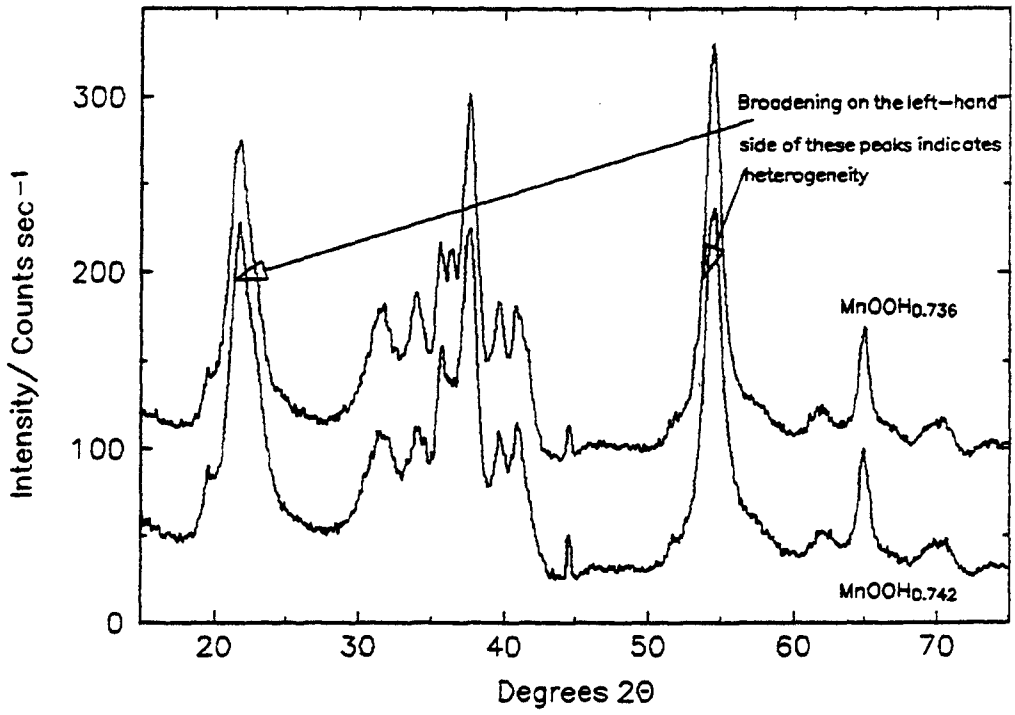


***Figure 5.15*** : Comparison of the X-ray diffraction patterns of $MnOOH_{0.736}$ and $MnOOH_{0.742}$ for non and heat-treated CMD at 200°C (the non heat-treated sample is displaced upwards by 60c $s^{-1}$).

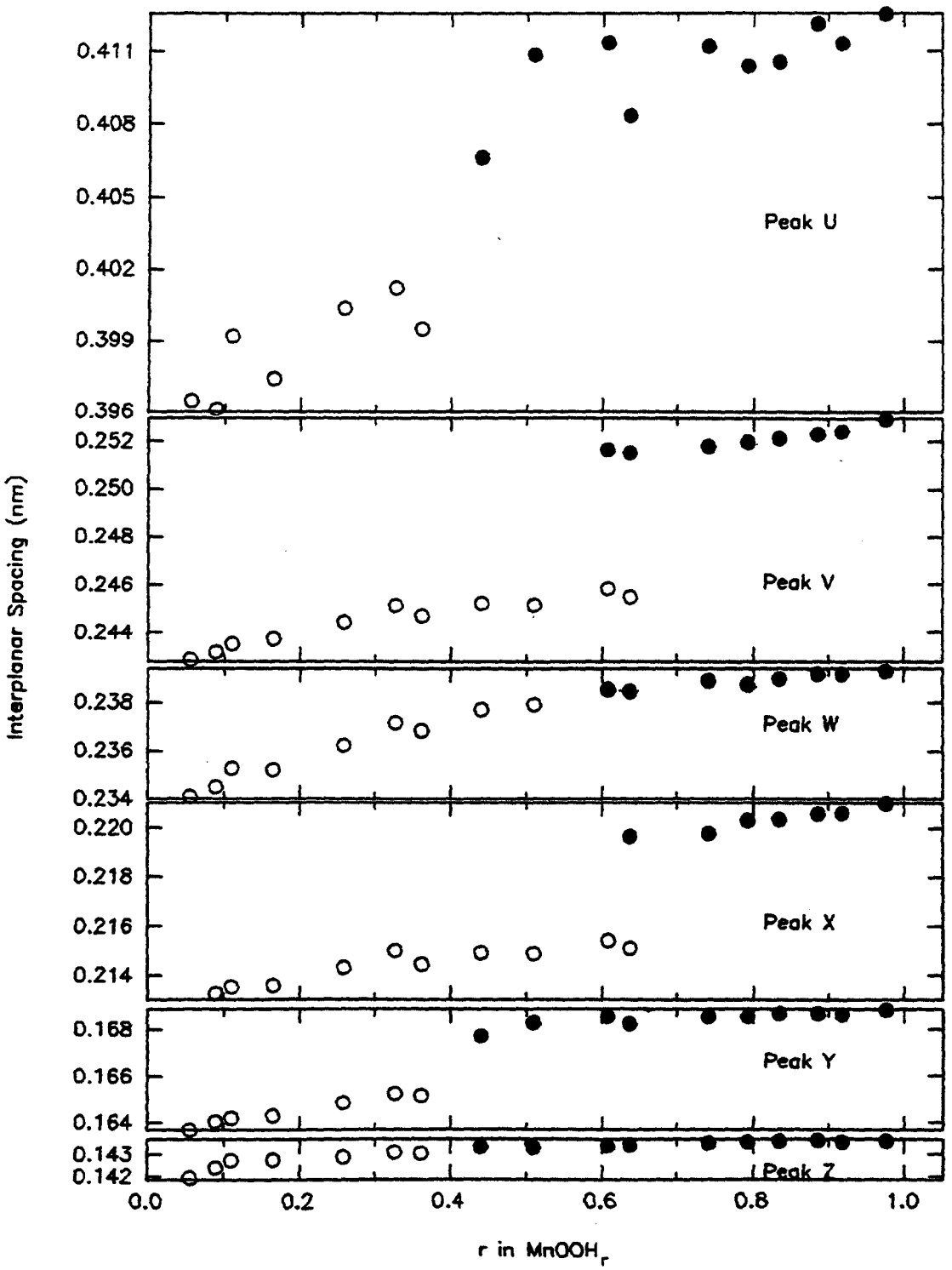


*Figure 5.16* : Interplanar spacing against H insertion level: CMD heat-treated at 200°C; hydrazine hydrate reduction method.

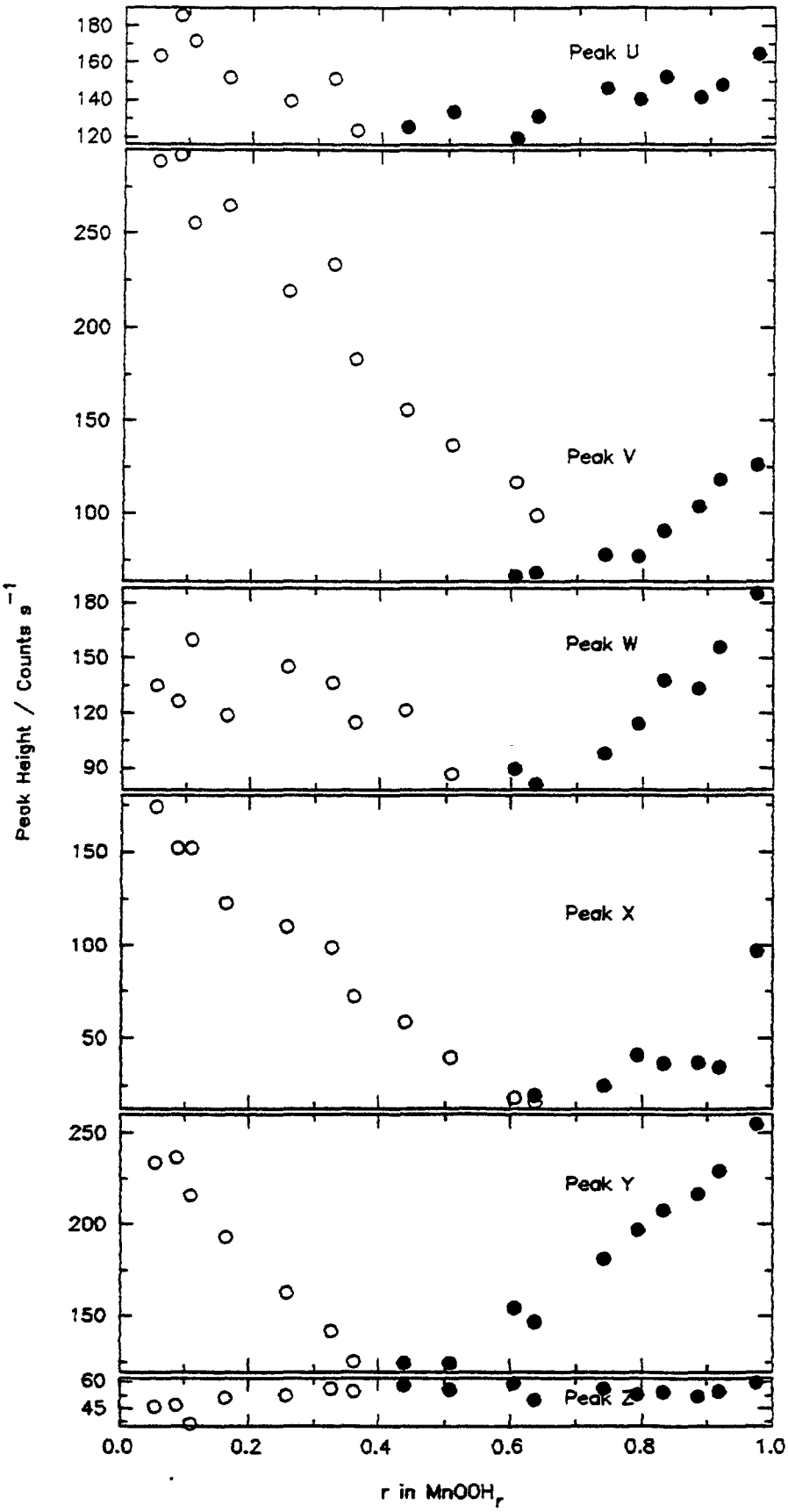


*Figure 5.17*: Peak height against H insertion level CMD heat-treated at 200°C (see figure 5.10 for peak labelling).

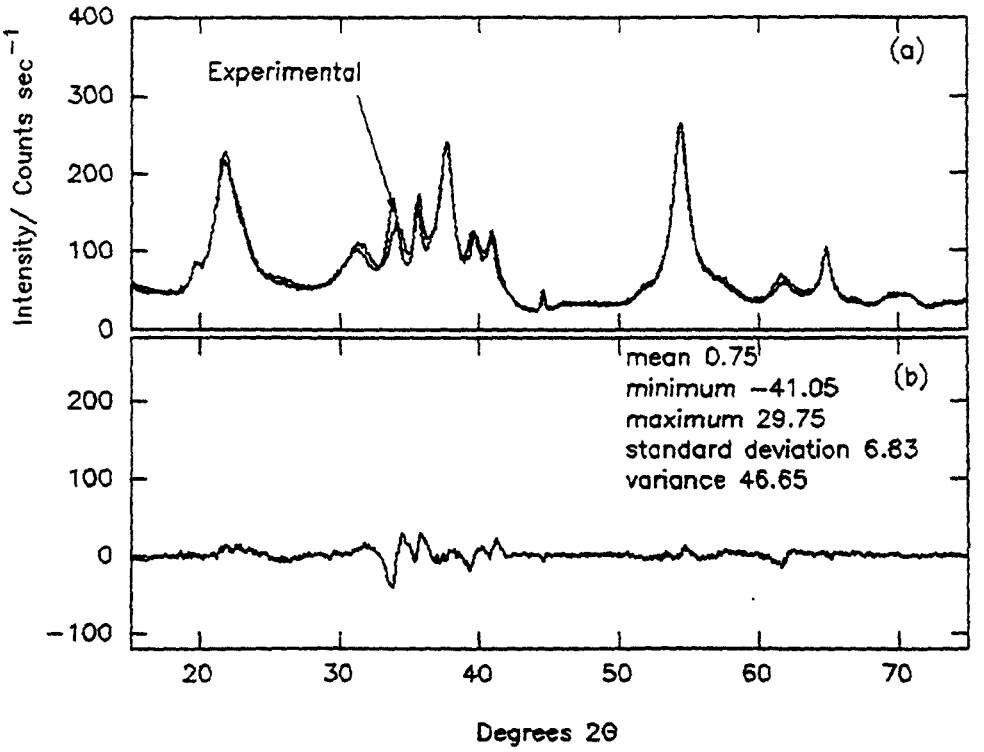


*Figure 5.18* : Comparison of (a) experimental XRD pattern of $MnOOH_{0.834}$ with a mixture of 41% $MnOOH_{0.637}$ and 59% $MnOOH_{0.977}$ and (b) experimental – simulated difference spectrum; CMD Heat-treated At 200°C ( the statistical analysis is given for (b)).

## *5.2.3 CMD heat-treated at 300°C.*

X-ray diffraction pattern changes during the reduction of the material that had been heat-treated at 300°C and reduced by hydrazine hydrate are shown in figure 5.19 and figures 5.20-5.23 show selected regions of the X-ray spectra in more detail in 3D. In figure 5.24 the variation of the interplanar spacings with H insertion are plotted and in figure 5.25 the peak heights are plotted. If these are compared with the analogous figures for the materials presented in the previous sections (figures 5.5, 5.6, 5.16 and 5.17) it can be seen that there is less peak movement for this set of samples and heterogeneity occurs at a lower level of H insertion. Examination of figure 5.26 would suggest that H insertion is heterogeneous after $MnOOH_{0.506}$.

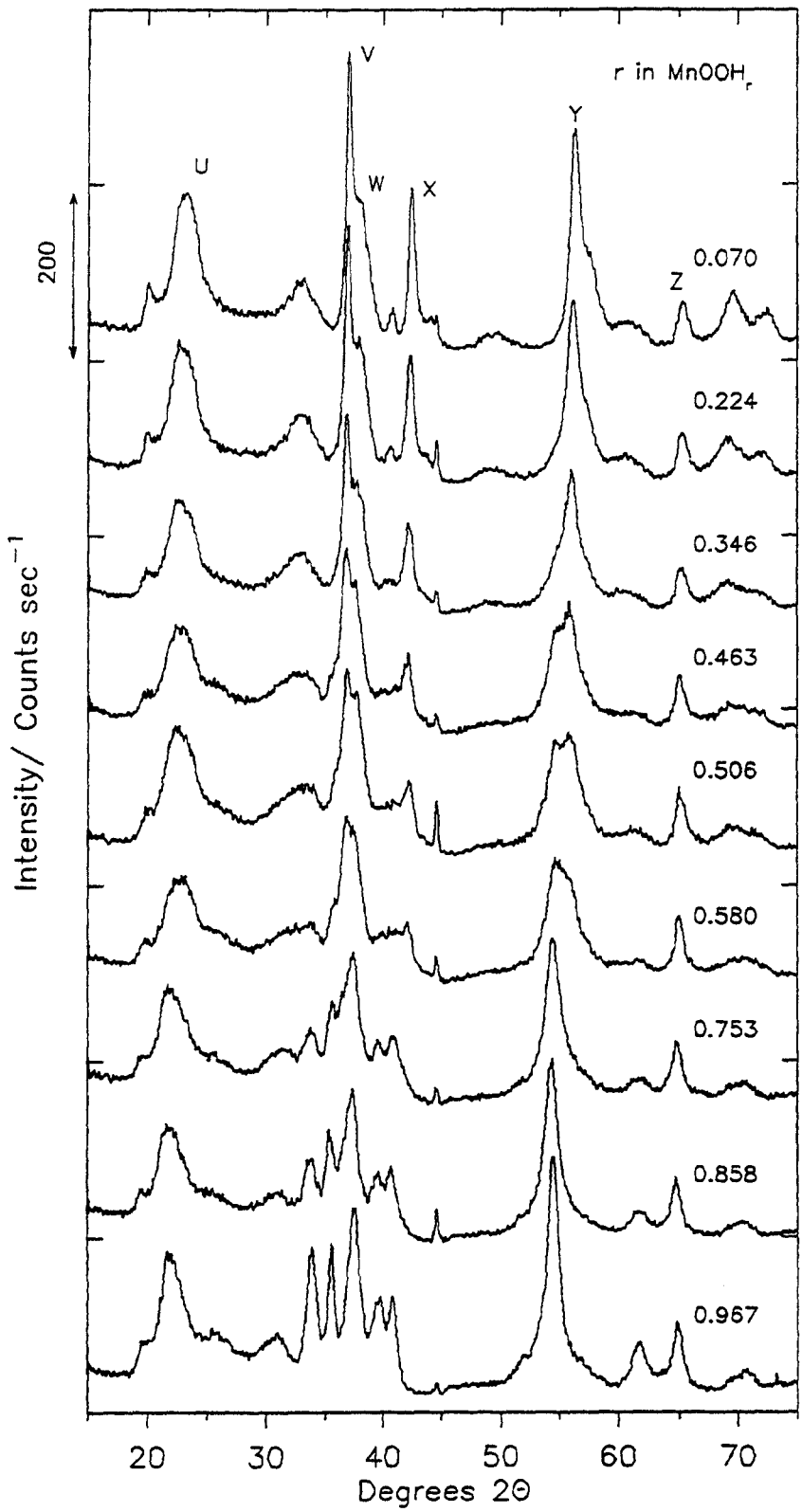


***Figure 5.19*** : X-ray diffraction spectra during the reduction of CMD (Faradiser WSLi); heat-treated at 300°C; hydrazine hydrate reduction method (the level of H insertion is given above the XRD pattern).

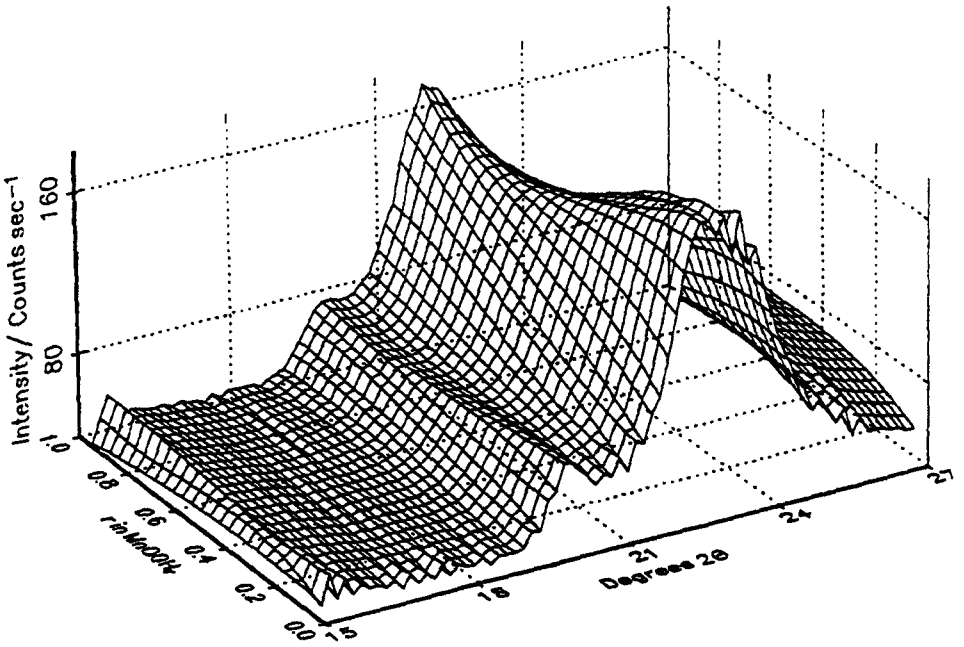


*Figure 5.20* : X-Ray Diffraction Spectra In The Region 15-27° 2Θ; CMD heat-treated at 300°C; hydrazine hydrate reduction method (data grid from 0.06 – 0.96 in 0.036 increments of r in $MnOOH_r$).

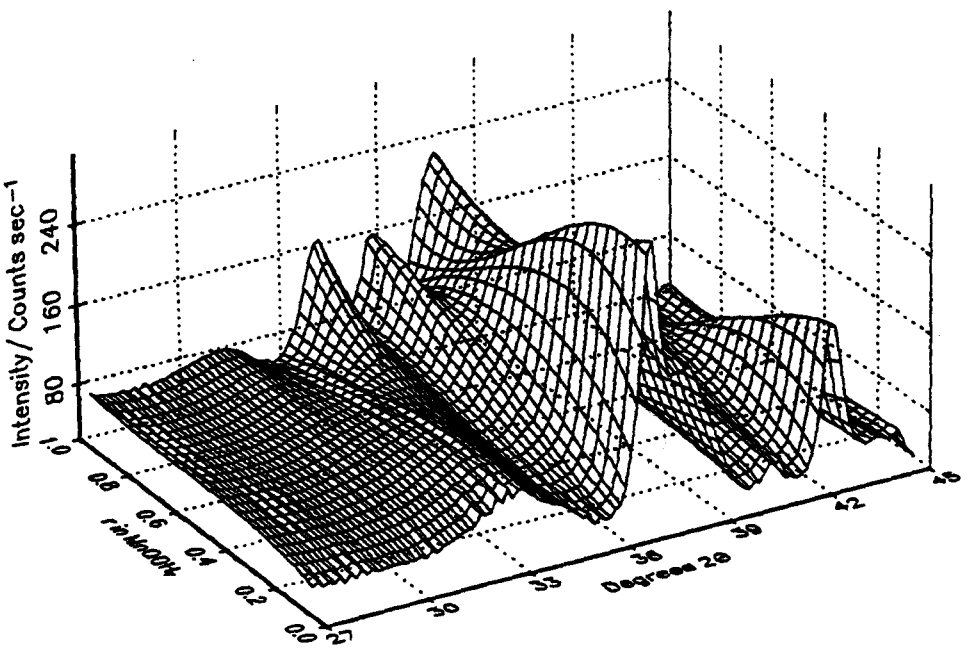


*Figure 5.21* :X-ray diffraction spectra in the region 27-45° 2Θ; CMD heat-treated at 300°C; hydrazine hydrate reduction method.

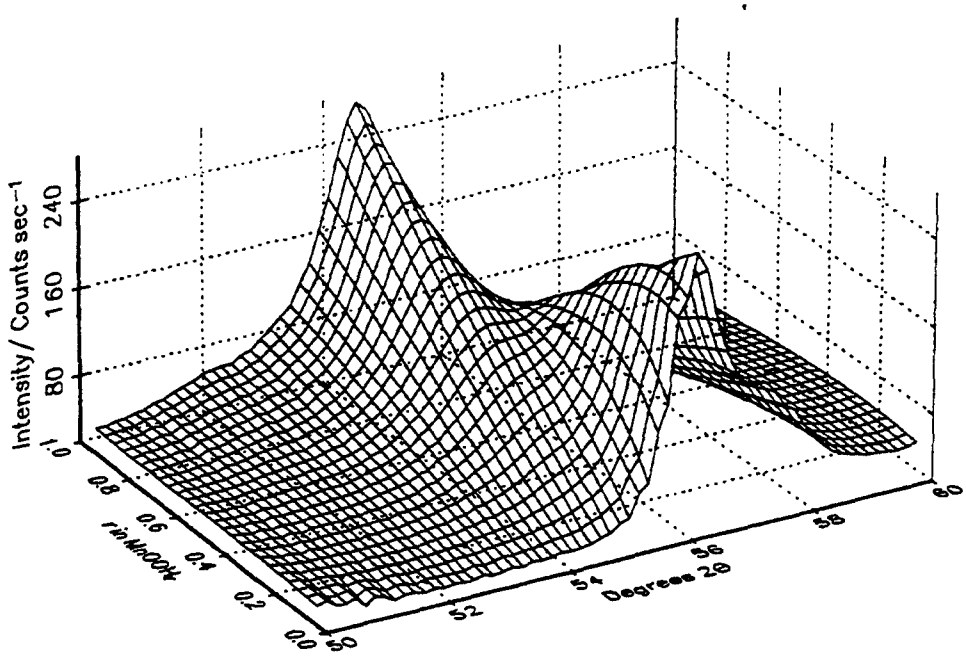


*Figure 5.22* : X-ray diffraction spectra in the region 50-60° 2Θ; CMD heat-treated at 300°C; hydrazine hydrate reduction method.

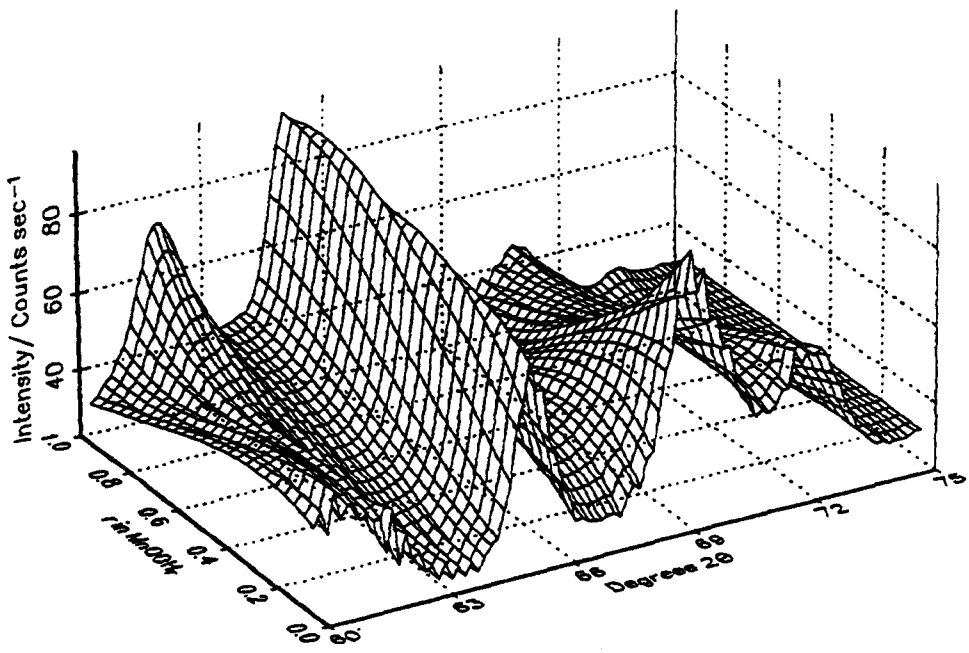


*Figure 5.23* :X-ray diffraction spectra in the region 60-75° 2Θ; CMD heat-treated at 300°C; hydrazine hydrate reduction method.

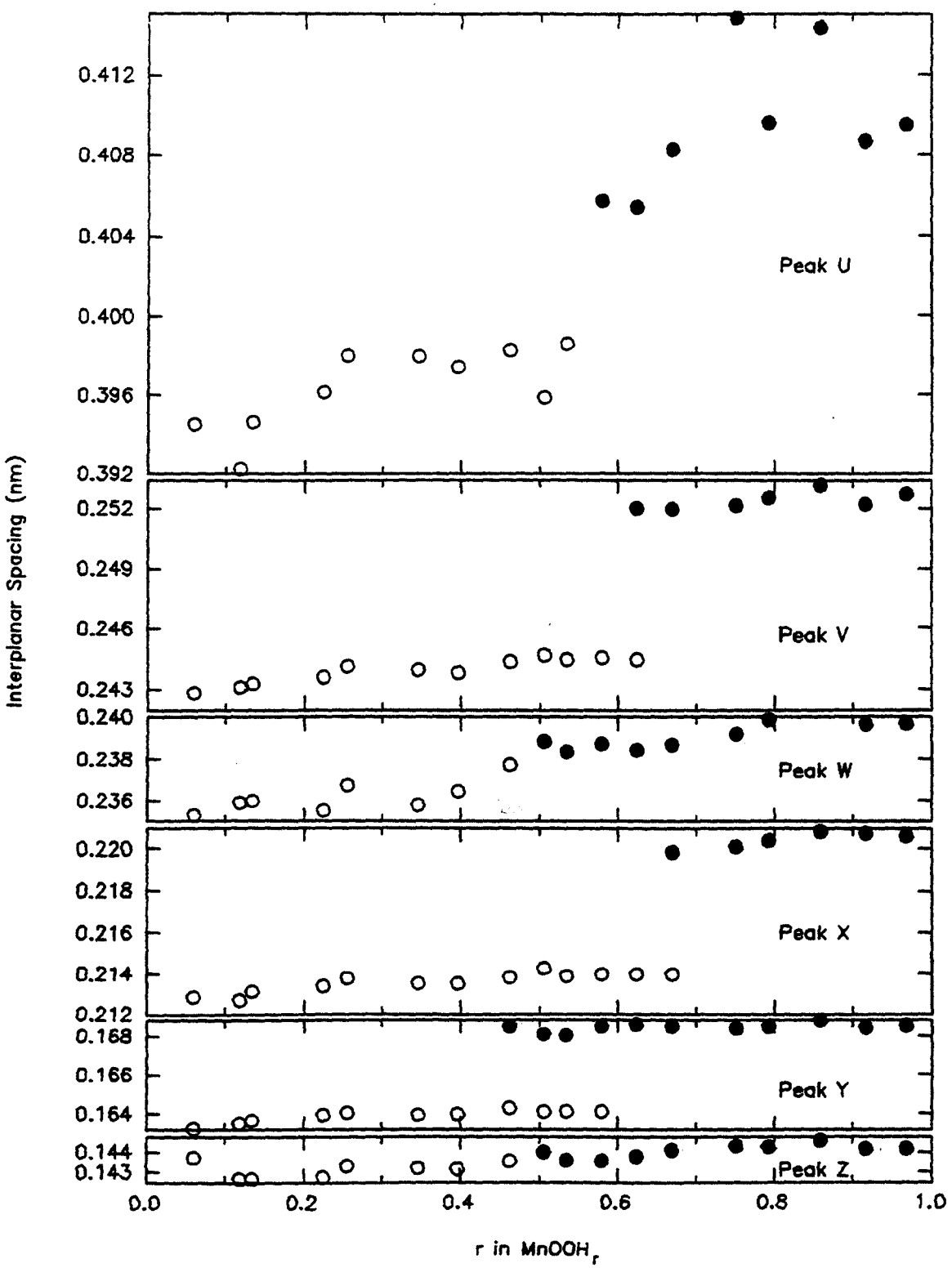


***Figure 5.24*** : Interplanar spacing against H insertion level: CMD heat-treated at 300°C; hydrazine hydrate reduction method.

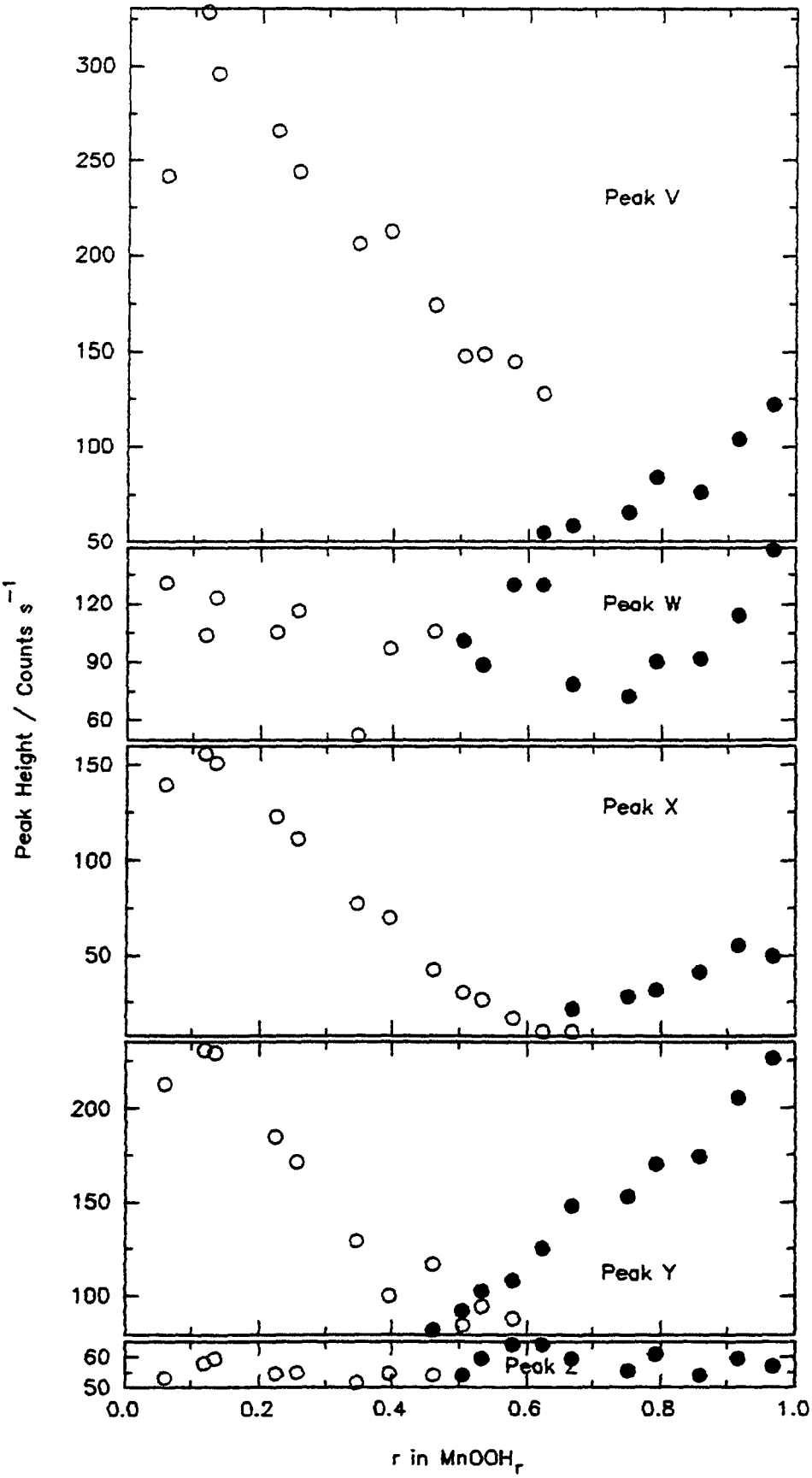


***Figure 5.25***: Peak height against H insertion level: CMD heat-treated at 300°C (see figure 5.19 for peak labelling).

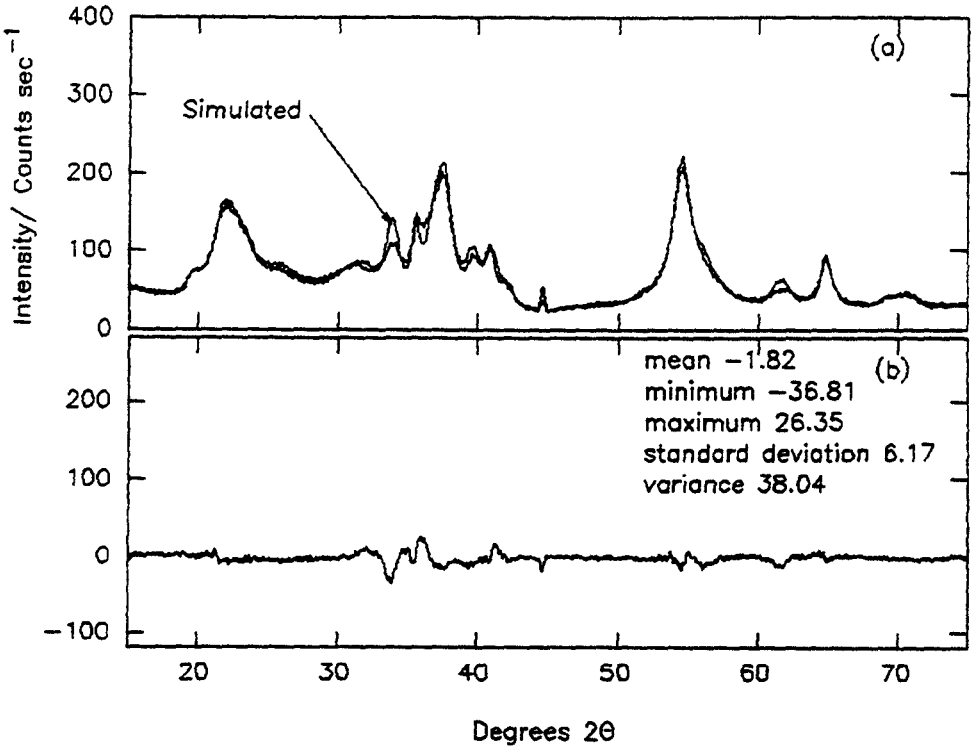


*Figure 5.26* : Comparison of (a) experimental $MnOOH_{0.753}$ with a mixture of 47% $MnOOH_{0.506}$ and 53% $MnOOH_{0.967}$ with (b) experimental-simulated difference spectrum; CMD heat-treated at 300°C; hydrazine hydrate reduction method (the statistical analysis is given for (b)).

## 5.2.4 CMD heat-treated at 400°C.

A selection of X-ray diffraction patterns during the reduction of this set of samples are shown in figure 5.27 and in 3D in figures 5.28-5.31. The interplanar spacings are plotted in figure 5.32. The XRD pattern of the starting material is referred to as "$\beta$-like" $MnO_2$ (Kozawa 1989 and Ohzuku 1988). This is in preference to simply $\beta$-$MnO_2$ (as exemplified by I.C. No 6) because "$\beta$-like $MnO_2$" performs well in lithium cells and a dramatic change in electrochemical properties, which is normally due to a phase transition, (see for example anatase to rutile Ohzuku *et al.* 1985) is not observed. The H insertion mechanism into the corresponding EMD material (section 4.2.3(i)) was found to be heterogeneous from $MnOOH_{0.110}$ and figure 5.33 compares two patterns of similar stoichiometries. Figure 5.34 also suggests that the reduction is heterogeneous from $MnOOH_{0.080}$. Figure 5.35 compares the peak movement of peak Y for the materials investigated in this chapter and figure 5.36 the peak height. Table 5.1 summarises the XRD data collected in this chapter.

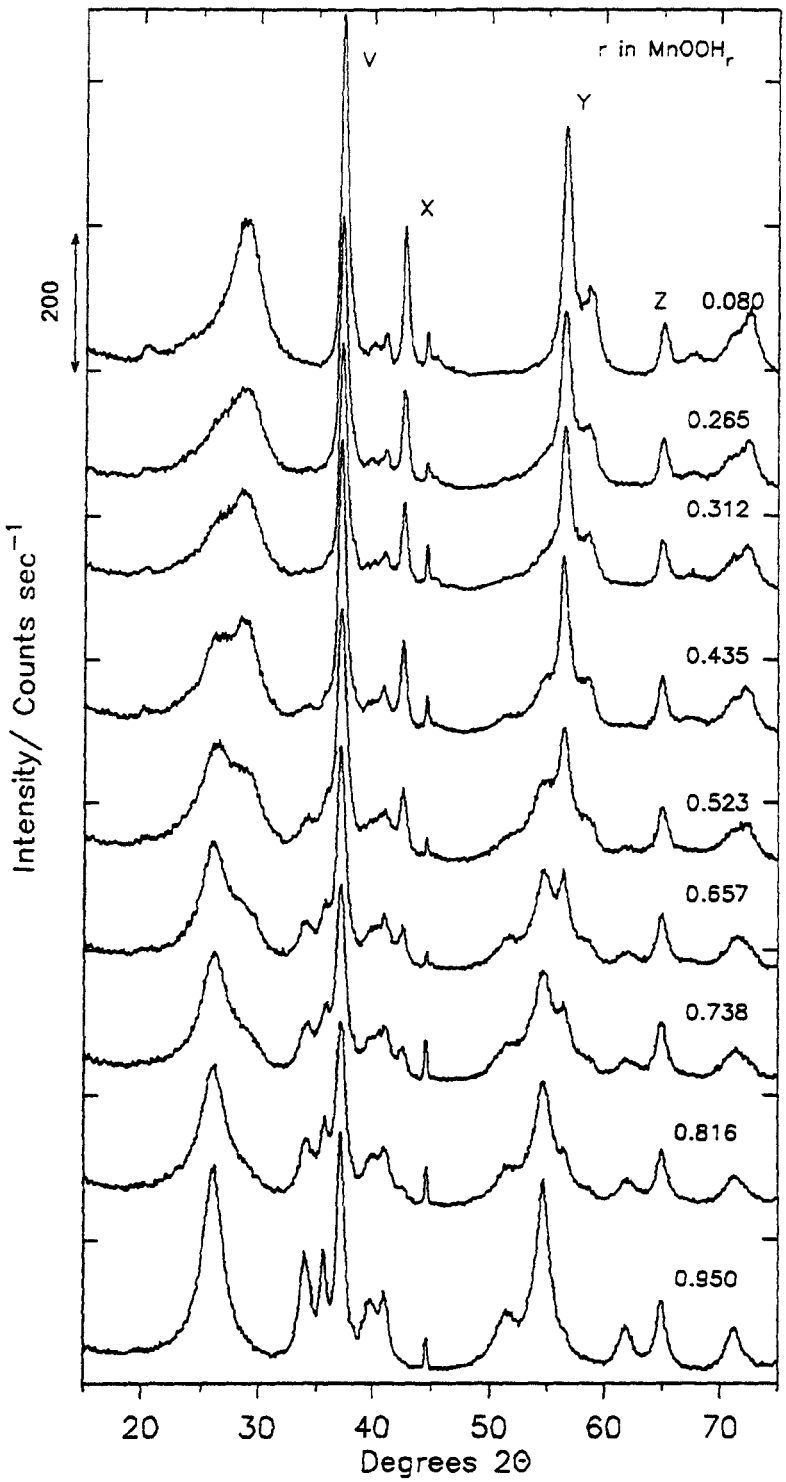


***Figure 5.27*** : X-ray diffraction spectra during the reduction of CMD (Faradiser WSLi); heat-treated at 400°C; hydrazine hydrate reduction method (the level of H insertion is given above the XRD pattern).

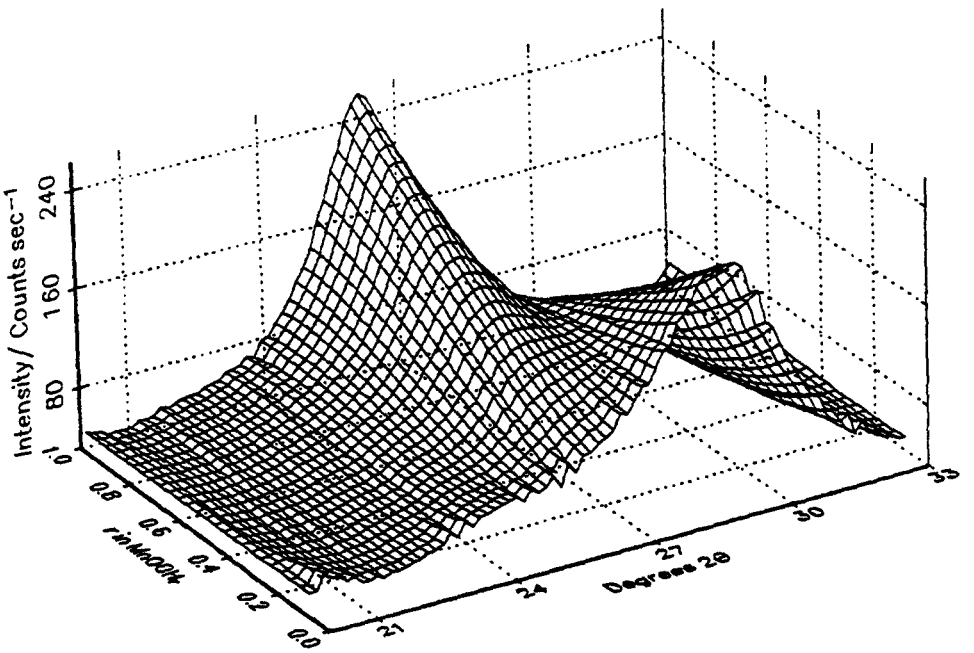


*Figure 5.28* : X-Ray Diffraction Spectra In The Region 20-33° 2Θ; CMD heat-treated at 400°C; hydrazine hydrate reduction method (data grid from 0.08 – 0.98 in 0.036 increments of r in $MnOOH_r$).

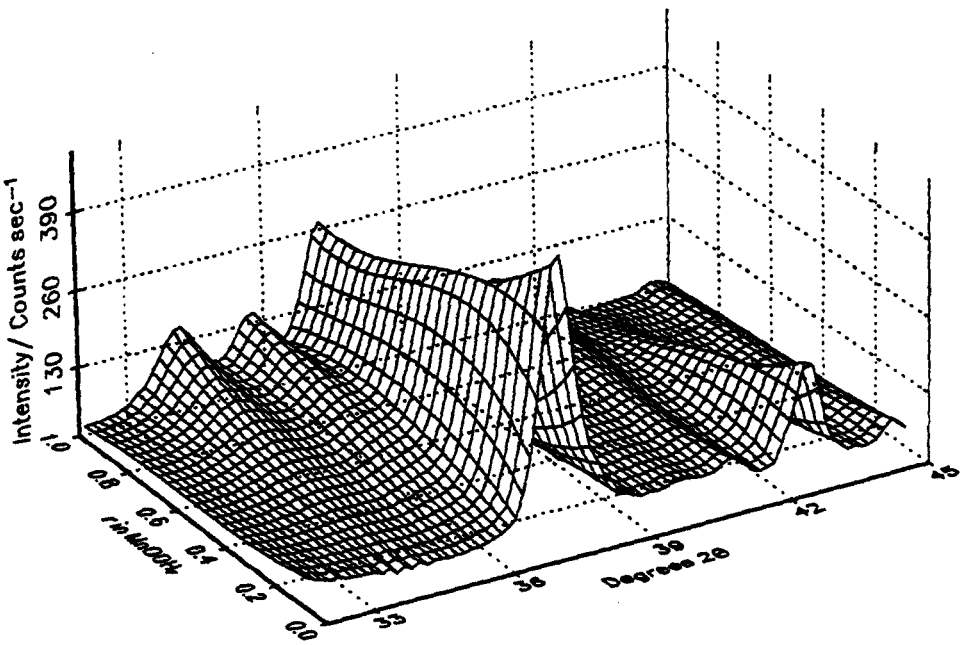


*Figure 5.29* :X-ray diffraction spectra in the region 32-45° 2Θ; CMD heat-treated at 400°C; hydrazine hydrate reduction method.

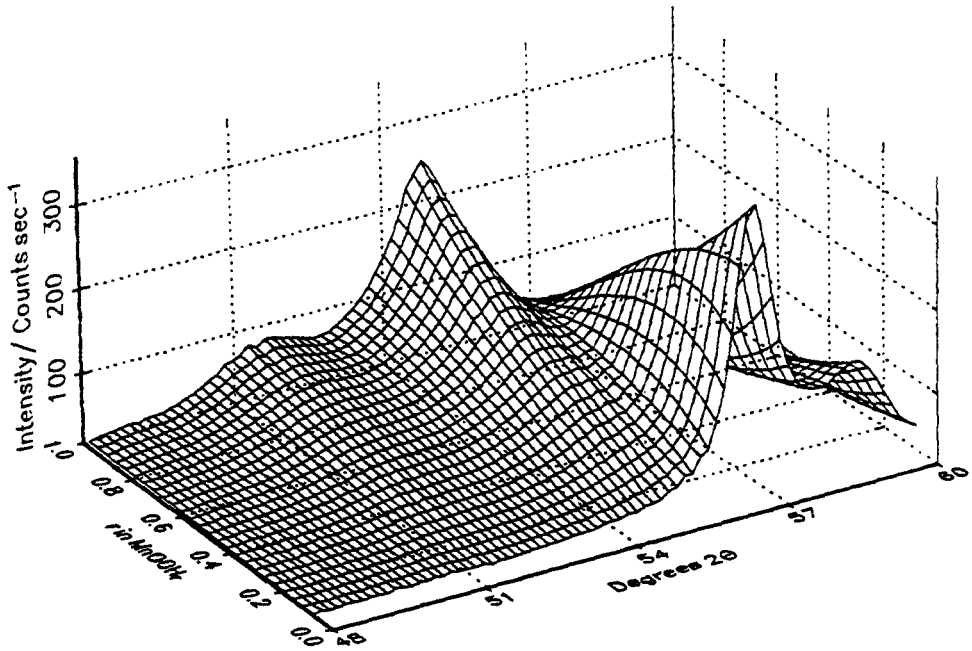


*Figure 5.30* : X-ray diffraction spectra in the region 48-60° 2Θ; CMD heat-treated at 400°C; hydrazine hydrate reduction method.

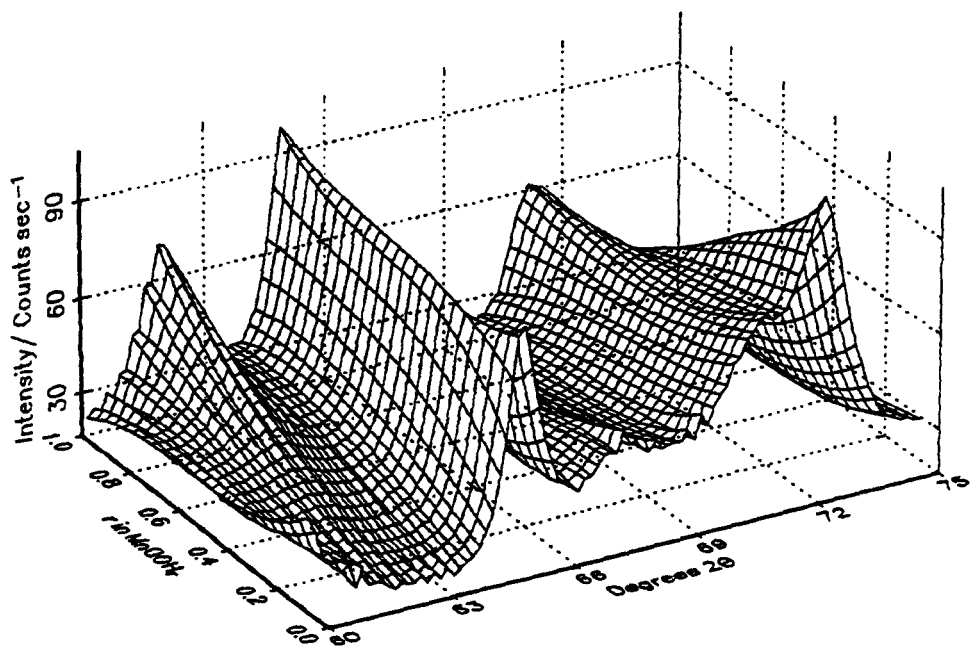


*Figure 5.31* :X-ray diffraction spectra in the region 60-75° 2Θ; CMD heat-treated at 400°C; hydrazine hydrate reduction method.

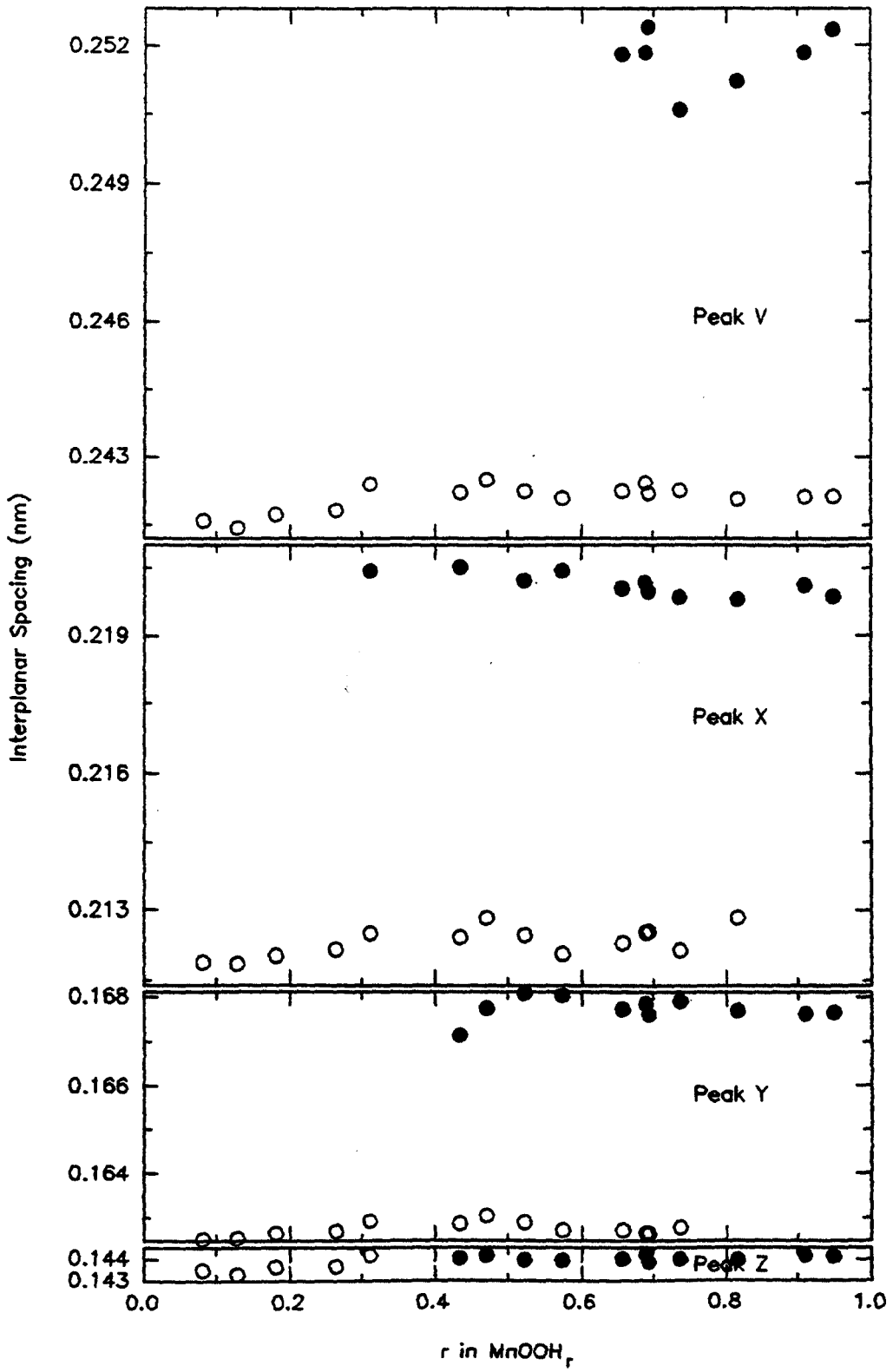


***Figure 5.32*** : Interplanar spacing against H insertion level: CMD heat-treated at 400°C; hydrazine hydrate reduction method.

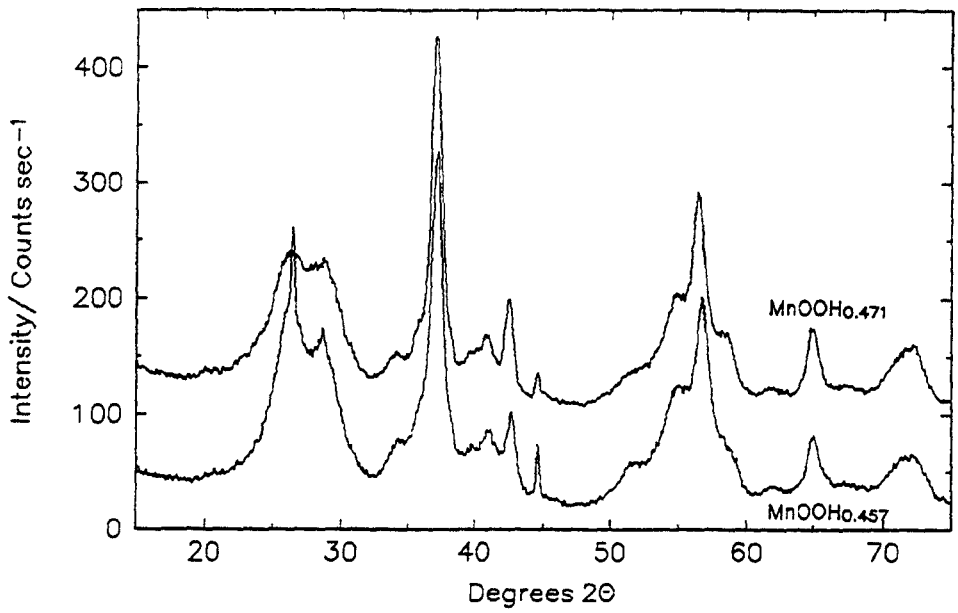


*Figure 5.33* : Comparison of the X-ray diffraction patterns of $MnOOH_{0.471}$ and $MnOOH_{0.457}$ for CMD and EMD heat-treated at 400°C and reduced by hydrazine hydrate (the CMD pattern is displaced upwards by 60 $cs^{-1}$).

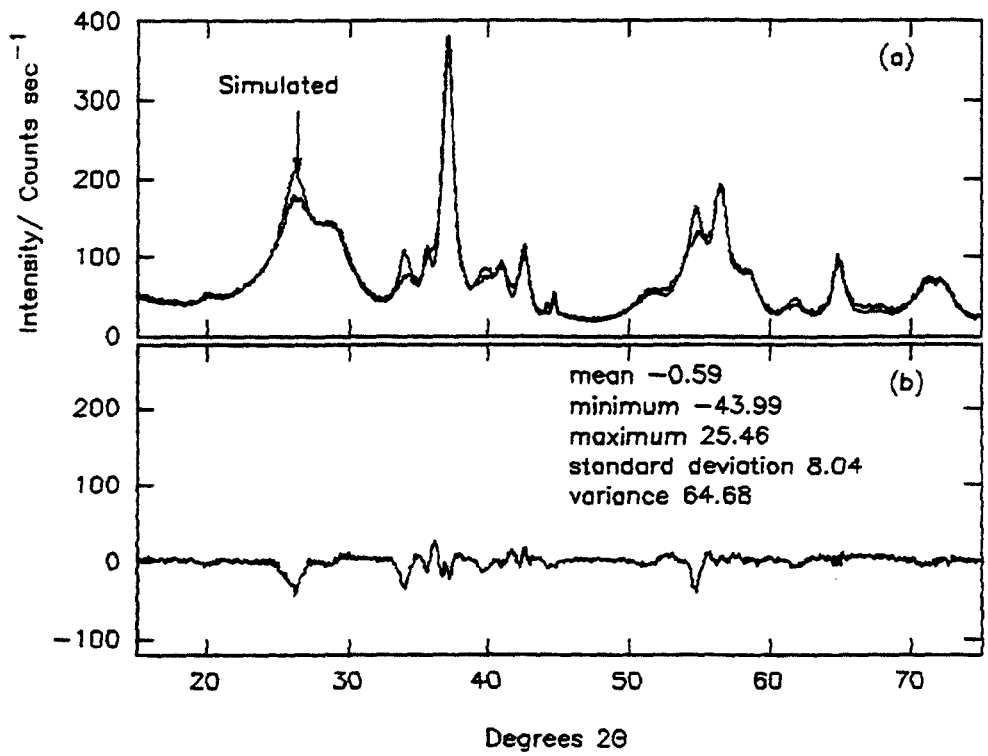


*Figure 5.34* : Comparison of (a) experimental XRD pattern of $MnOOH_{0.523}$ with a mixture of 49% $MnOOH_{0.080}$ and 51% $MnOOH_{0.950}$ and (b) experimental − simulated difference spectrum; CMD heat-treated at 400°C (the statistical analysis is given for (b)).

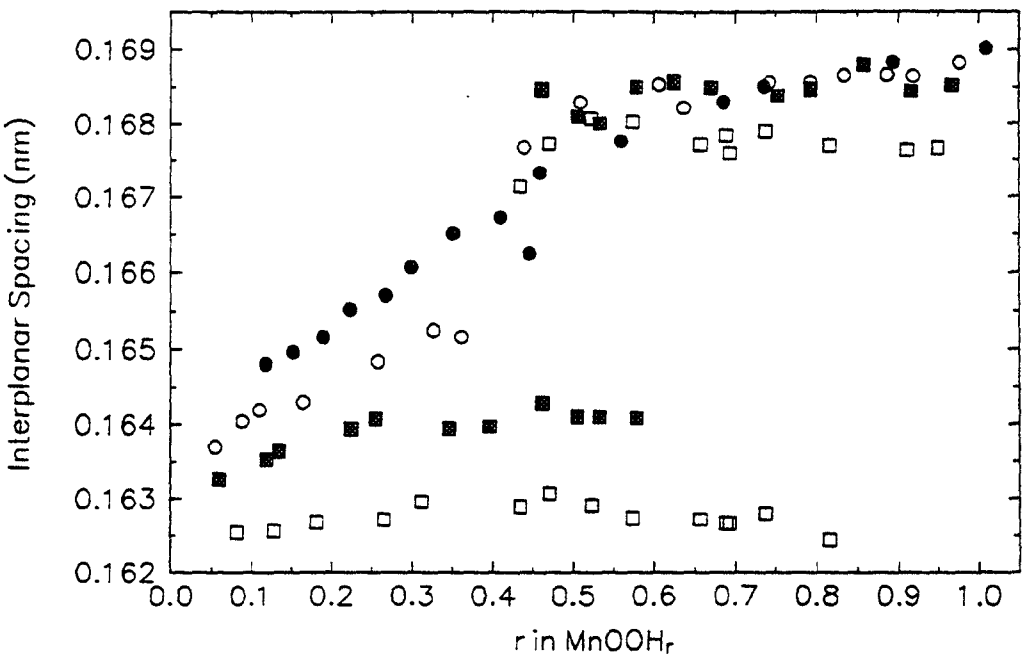


***Figure 5.35*** : **Comparison of the variation of the interplanar spacing of peak Y with H insertion level (●) non heat-treated, (○) 200, (■) 300 and (□) 400°C; CMD reduced by hydrazine hydrate.**

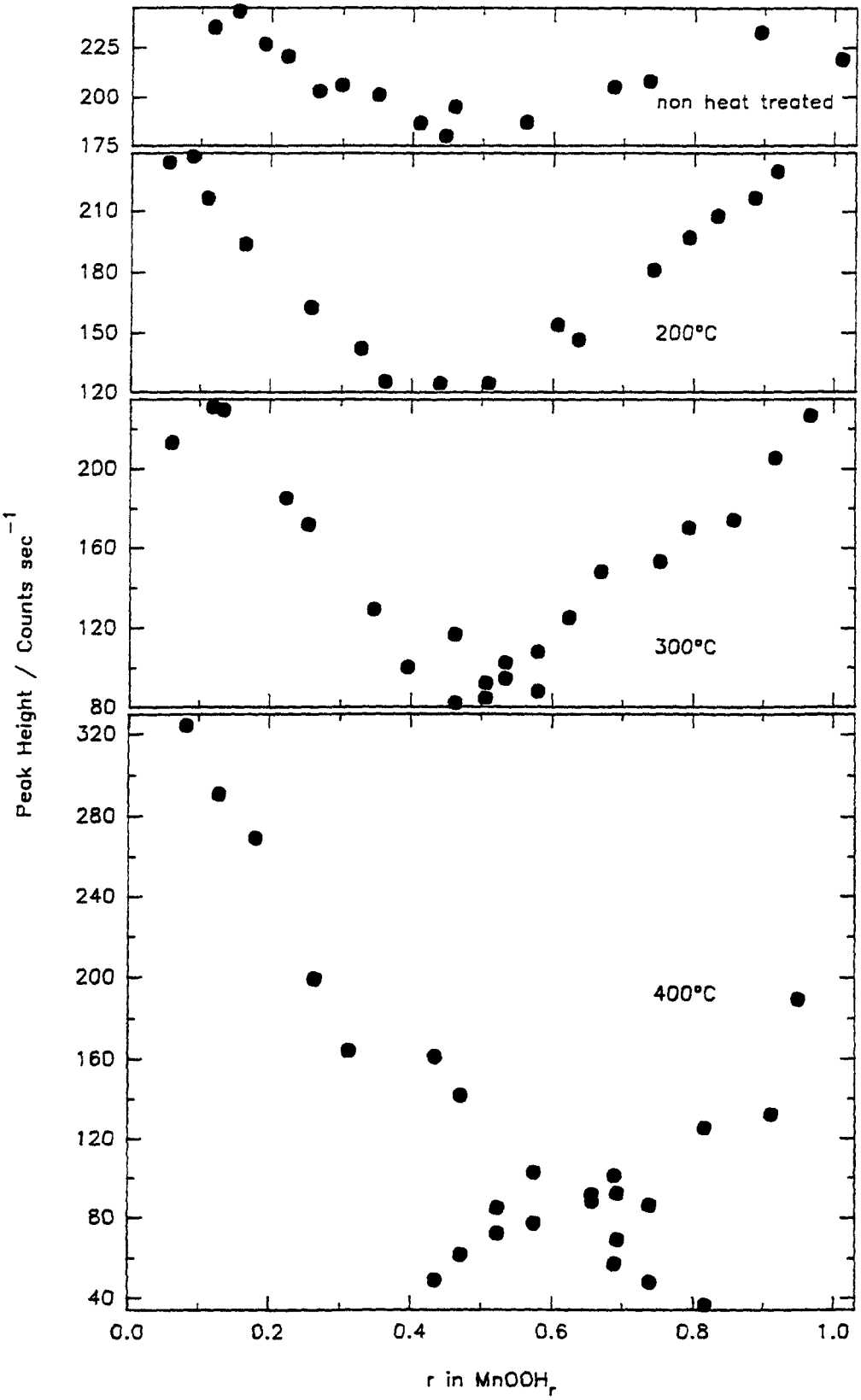


***Figure 5.36*** : Comparison of the peak height of peak Y with H insertion level for the CMD materials investigated in this chapter.

*Table 5.1*: Regions Where Heterogeneity Begin For The CMD Materials.

| Material | Region Where Heterogeneity Begins/ r in $MnOOH_r$ |
|---|---|
| non heat-treated | $0.736 \leq r \leq 0.894$ |
| 200°C | 0.637 |
| 300°C | 0.506 |
| 400°C | 0.110 0.08 |

*Table 5.2*: Comparison of the regions of heterogeneity of EMD (Chapter 4) and CMD (this Chapter).

| Heat-treatment temperature/°C | Reduction method | Material | Region where heterogeneity begins/ r in $MnOOH_r$ |
|---|---|---|---|
| 200 | hydrazine hydrate | CMD | 0.637 |
| 300 | hydrazine hydrate | CMD | 0.506 |
| 400 | hydrazine hydrate | CMD | 0.080 |
| 200 | hydrazine hydrate | EMD | 0.480 |
| 300 | hydrazine hydrate | EMD | 0.330 |
| 400 | hydrazine hydrate | EMD | 0.110 |

## 5.3 Comparison of the XRD reduction product spectra with published spectra of manganite and groutite.

Figure 5.37 compares the reduction product spectra obtained in this chapter with the JCPDS patterns of groutite and manganite. Recent evidence on the origin of the appearance of the new lines (labelled G,H,I and J in figure 5.38) that appear in the X-ray diffraction pattern have been given by Fitzpatrick and Tye (1991) and Tye (1992). In the former they found that there was some migration of inserted H between a mixture of the starting and reduction product materials and concluded that the new peaks were properly part of the solid solution system. In the linear cluster model developed by Tye (1992) protons and electrons were added independently to 200 paired sites and he found that large clusters of the inserted proton and electron occurred after $MnOOH_{0.80}$. This coincided with the appearance of the new lines and they were attributed to microcrystalline domains of the end-product. It would seem erroneous that the new lines are that of a new phase because the solid solution peaks continue to

shift after $MnOOH_{0.80}$ and this would be incompatible with a heterogeneous reduction. Figure 5.39 compares the peak positions of the new lines.

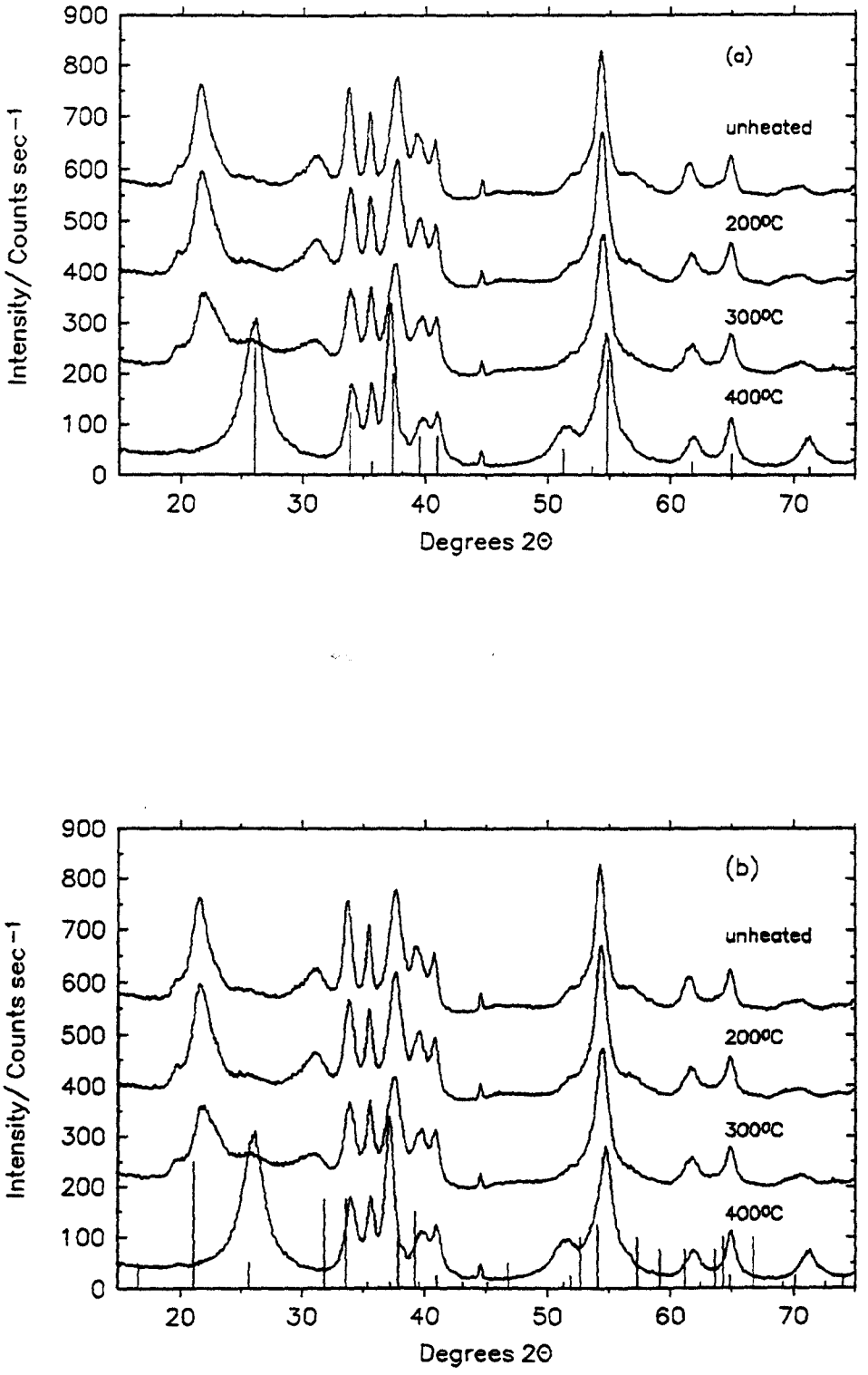


***Figure 5.37*** : Comparison of the X-ray diffraction reduction products with (a) manganite and (b) groutite. The stoichiometries of the compounds from top to bottom are $MnOOH_{1.010}$, $MnOOH_{0.977}$, $MnOOH_{0.967}$ and $MnOOH_{0.950}$.

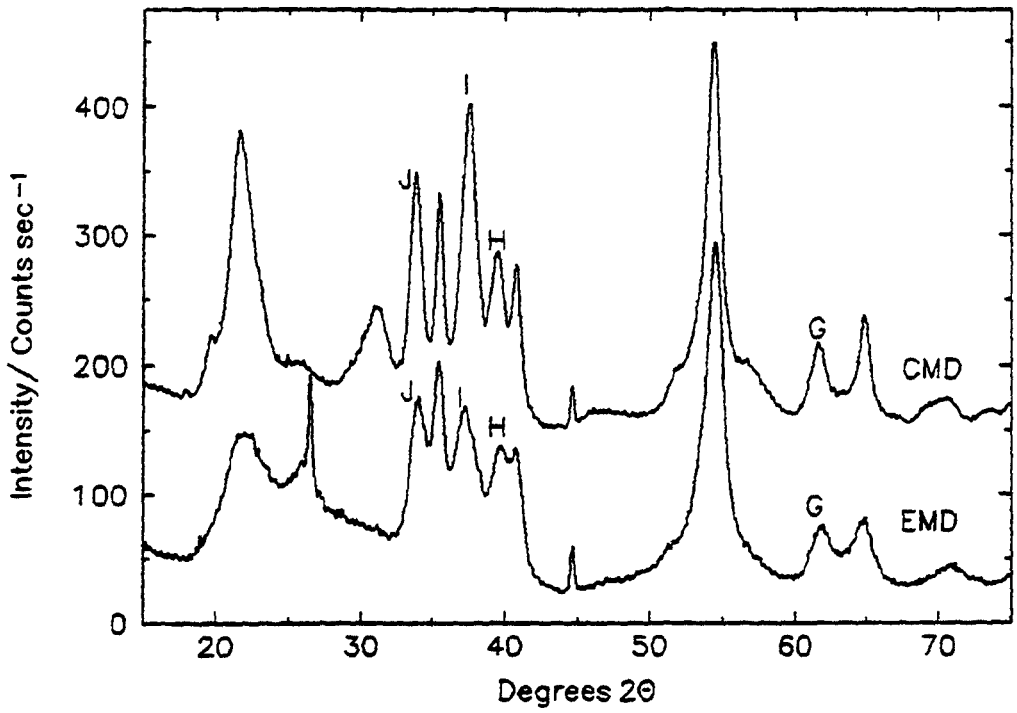


***Figure 5.38*** : Position of the "New Lines" (G,H,I and J) that appear in the latter part of the reduction of CMD and EMD.

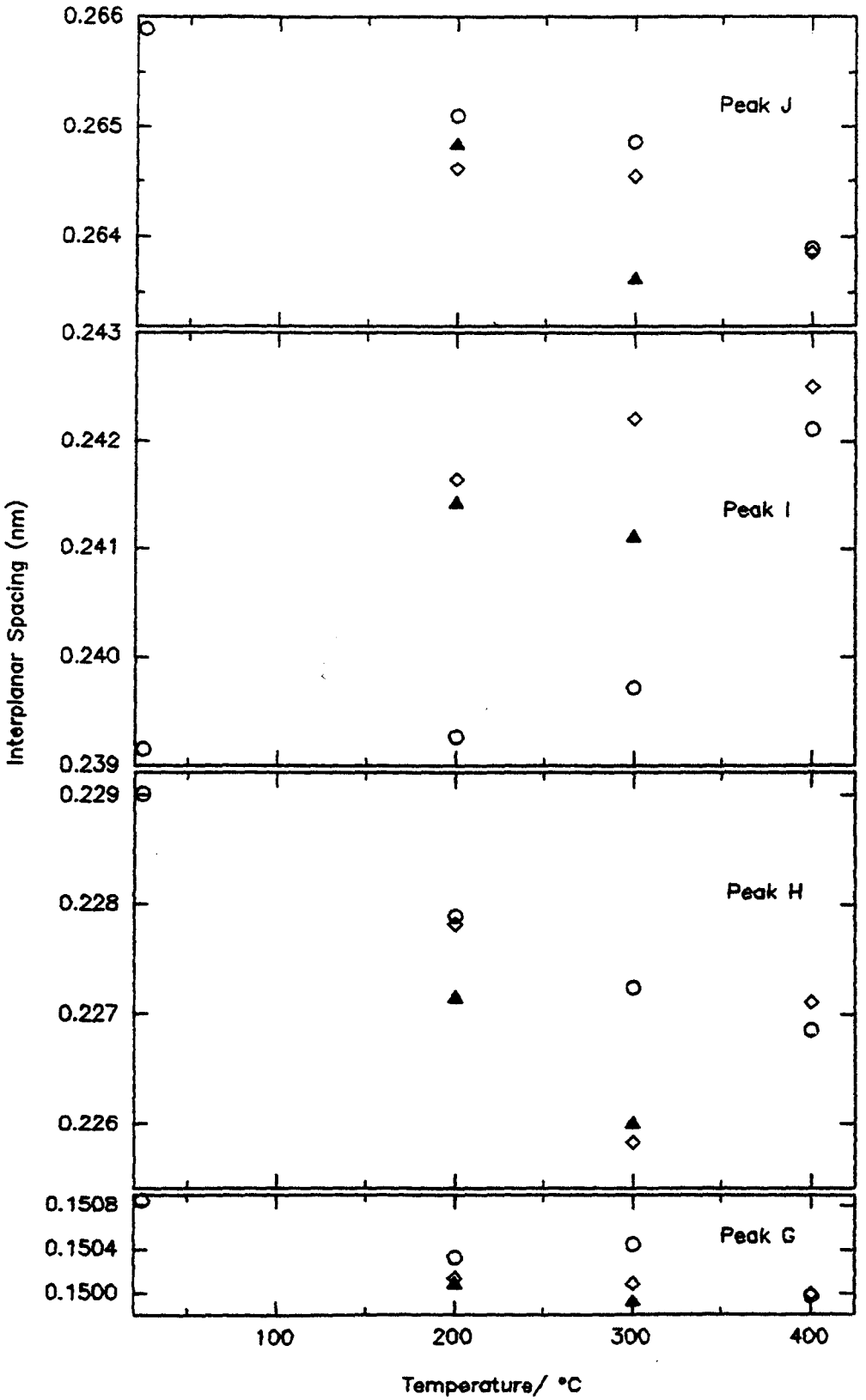


*Figure 5.39* : Comparison of the peak positions of the "New Lines" (G,H,I And J): (○) CMD; (▲) EMD reduced by propan-2-ol and (◇) EMD hydrazine hydrate.

## 5.4 Conclusion.

H has been chemically inserted into a range of heat-treated CMD materials and the resulting manganese oxyhydroxides studied by powder X-ray diffraction. As was observed in Chapter 4 differing regions of homogeneity/heterogeneity were found in the $\gamma$-$MnO_2$ – $\delta$MnOOH solid solution system. The non heat-treated CMD material exhibited the largest region of homogeneity and at 400°C the reduction was entirely heterogeneous. Between these extremes of behaviour intermediate levels of homogeneity/heterogeneity were observed (see Table 5.1). The crystal structure of the most reduced materials formed a similar range of intergrowth structures as was found for the EMD materials in Chapter 4. This was namely a $\delta$-MnOOH type structure at 200°C and a manganite structure at 400°C. The boundaries of the homogeneous/heterogeneous behaviour of EMD and CMD were compared in Table 5.2 and it was found that heterogeneity occurred at a higher level of H insertion for the CMD materials.

# Chapter 6 Lithium Insertion Into Heat-treated Electrodeposited and Chemical Manganese Dioxide

## 6.1 Introduction.

The capability of the lithium manganese dioxide cell was first shown by Ikeda in 1975. Since that time there has been world-wide interest in the development of suitable intercalation materials as well as the properties of the lithium electrode for use in a secondary lithium cell. The literature pertaining to Li insertion into $MnO_2$ was reviewed in section 1.7.1 and other insertion materials in section 1.8. In this chapter a range of Li inserted $MnO_2$ compounds analogous to the H inserted compounds that have been prepared in chapter 4 and 5 are investigated by XRD. Apart from the work of Ohzuku *et al.* (1989, 1990) which was concerned with electrochemical insertion of Li into $MnO_2$, most investigations have not focused on the effect of the initial heat-treatment temperature of $MnO_2$ with regard to the Li insertion process (this is of major importance in this investigation).

The use of n-butyllithium to chemically mimic an electrochemical reaction was first mentioned by Armand (1973) in connection with work on chromium oxide/graphite compositions. Since that time n-butyllithium has been used extensively to investigate Li insertion into various manganese oxides (see for example David *et al.* 1984, Mosbah *et al.* 1984, Murphy *et al.* 1978 and 1980 and Whittingham 1977). Organolithium synthetic methiods are discuused by Wakefield (1988). As was mentioned in section 4.1 with H insertion into $MnO_2$ the chemical insertion of Li with n-butyllithium is free from other phases that would be present in the electrochemical reduction. In particular P.T.F.E. which is used as a binding agent in Li/$MnO_2$ cells would have peaks that may interfere with those of the $Li_xMnO_2$ phase. In this chapter the effect of the heat-treatment process is investigated with regard to Li insertion into heat-treated EMD and CMD and direct comparisons can be made with the corresponding H inserted compounds in chapters 4 and 5.

## 6.2 Powder x-ray diffraction spectra of Li-inserted EMD compounds.

### *6.2.1 EMD heat-treated at 200°C.*

The experimental details for this section of work were given in section 2.5. It is worth repeating that all operations were carried out in argon filled glove box. In sections 6.2 and 6.3 the results are presented for the Li inserted EMD and CMD materials respectively. In section 6.4 the boundaries of homogeneity/heterogeneity are examined and in section 6.5 the results are interpreted in context to the literature on this subject. The X-ray diffraction patterns resulting from Li insertion into EMD heat-treated at 200°C are given in Figure 6.1 and greater detail is given in the 3-D plots in Figures 6.2 – 6.5. The interplanar spacings associated with the peaks labelled in Figure 6.1 are given in Figures 6.6 and 6.7.

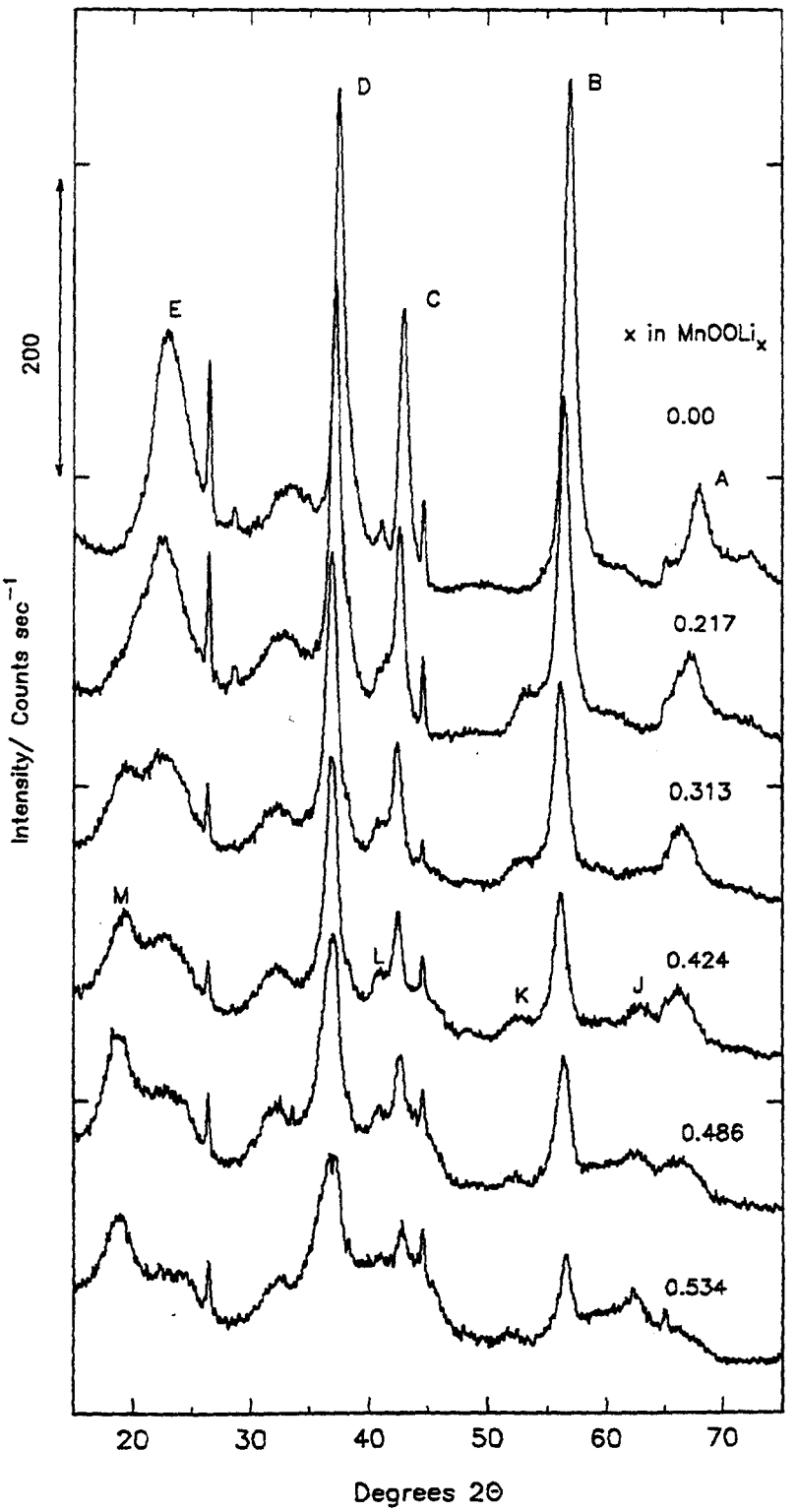


***Figure 6.1*** : X-Ray diffraction spectra resulting from Li insertion into EMD heat-treated at 200°C ( the level of Li insertion is given above the XRD pattern).

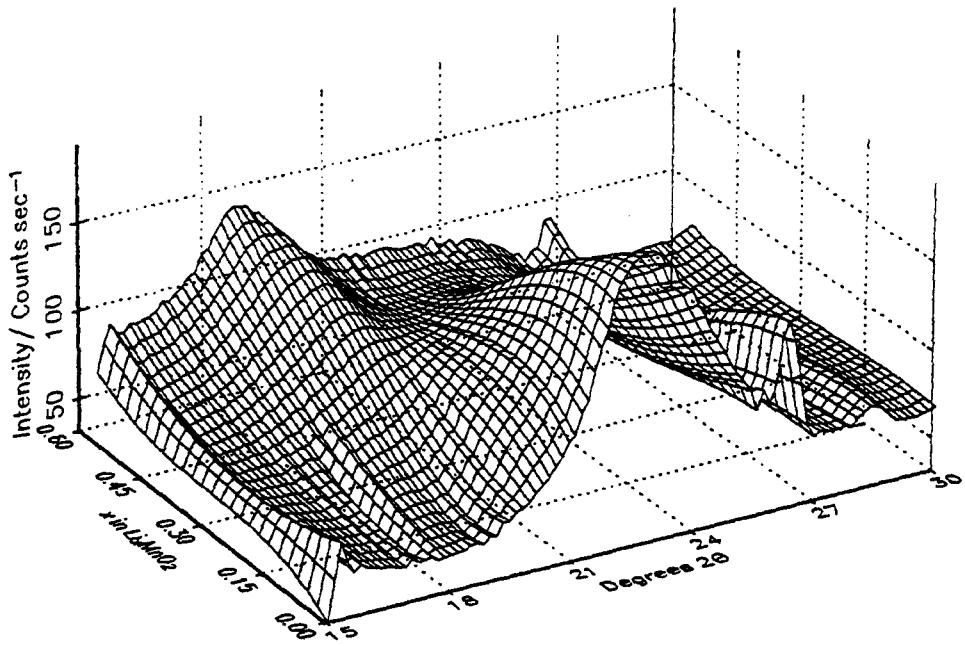


*Figure 6.2* : X-Ray diffraction spectra in the region 15 – 30°2Θ; EMD heat-treated at 200°C (data grid from 0.00-0.56 in 0.0224 increments of x in $Li_xMnO_2$).

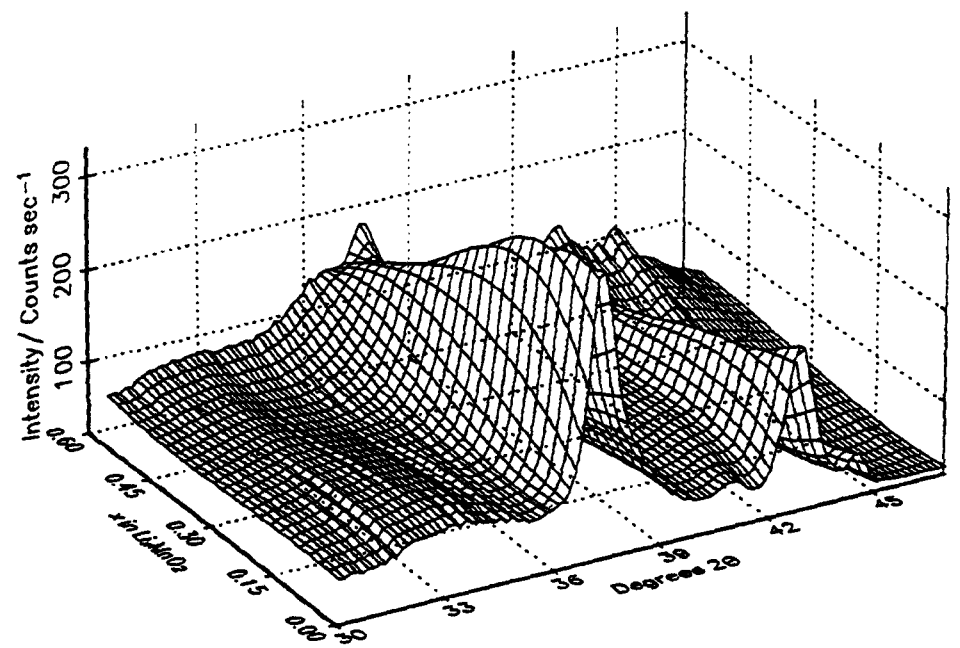


*Figure 6.3* : X-Ray Diffraction Spectra In The Region 30 – 47°2Θ; EMD Heat-treated At 200°C.

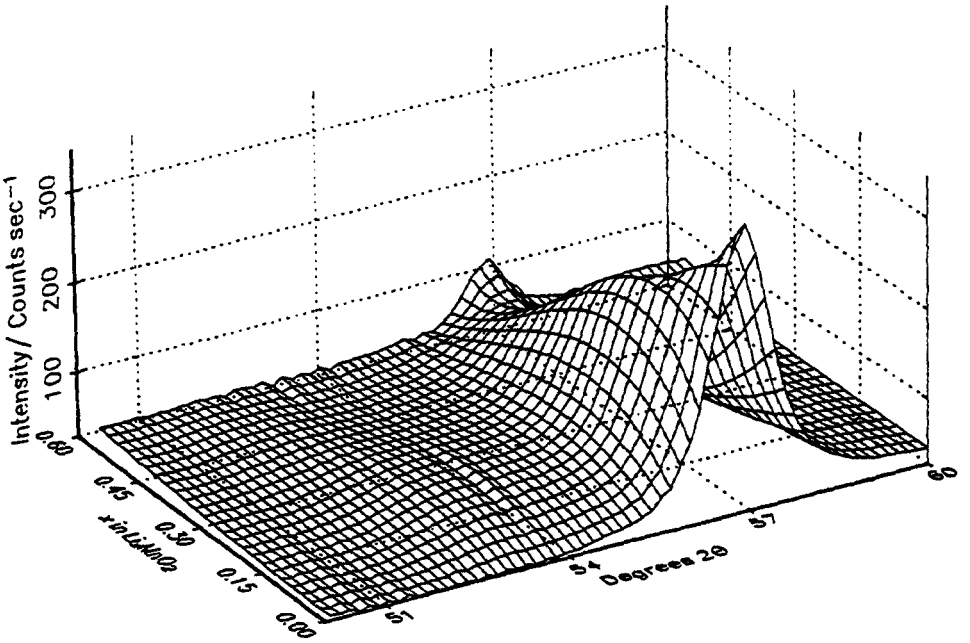


*Figure 6.4* : X-ray diffraction spectra in the region 50 – 60°2Θ; EMD heat-treated at 200°C.

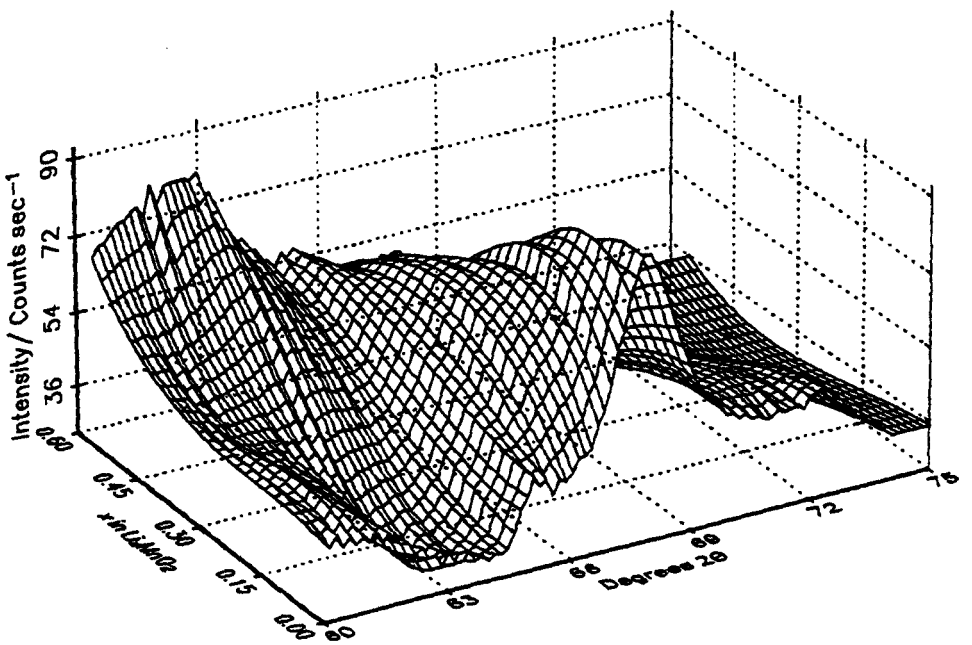


*Figure 6.5* : X-ray diffraction spectra in the region 60 – 75°2Θ; EMD heat-treated at 200°C.

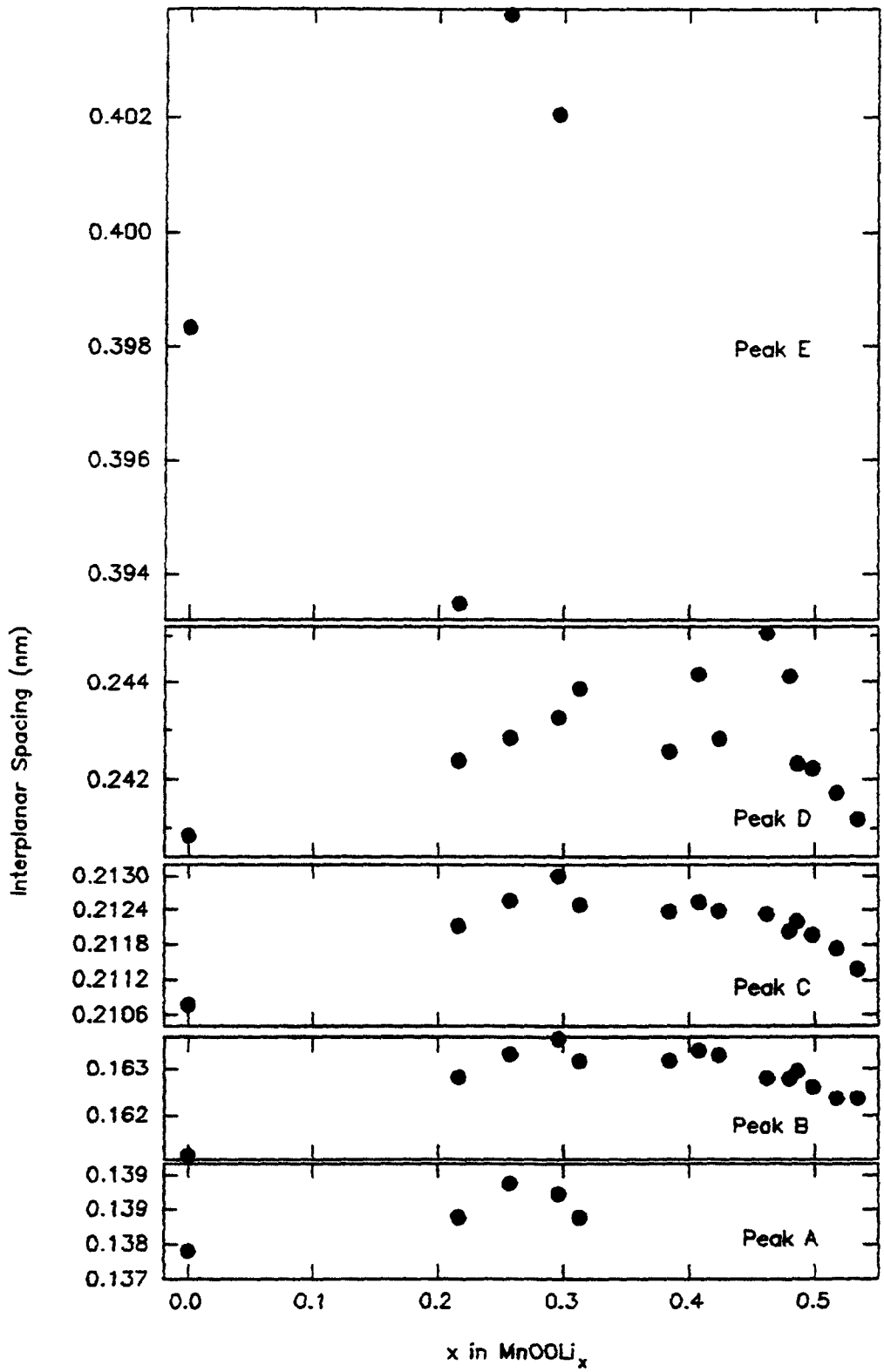


*Figure 6.6* : Interplanar spacing against Li insertion level for peaks A,B,C,D and E: EMD heat-treated at 200°C.

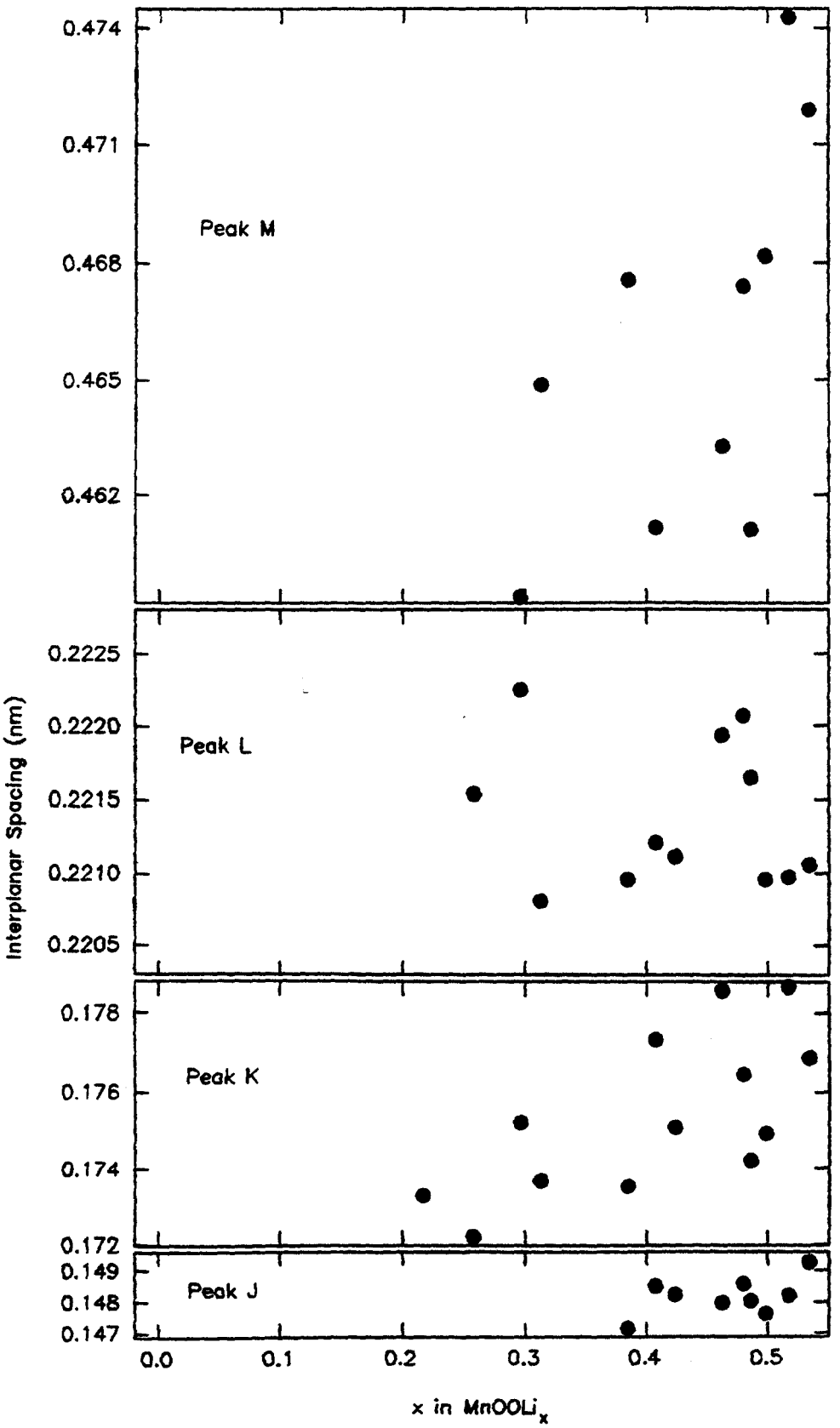


*Figure 6.7* : Interplanar spacing against Li insertion level for peaks J,K,L and M: EMD heat-treated at 200°C.

*6.2.2 EMD heat-treated at 300°C.*

The x-ray patterns resulting from Li insertion into EMD heat-treated at 300°C are given in figure 6.8 and the 3-D plots in figures 6.9 – 6.12. The interplanar spacings associated with the peaks labelled in figure 6.8 are given in figures 6.13 and 6.14.

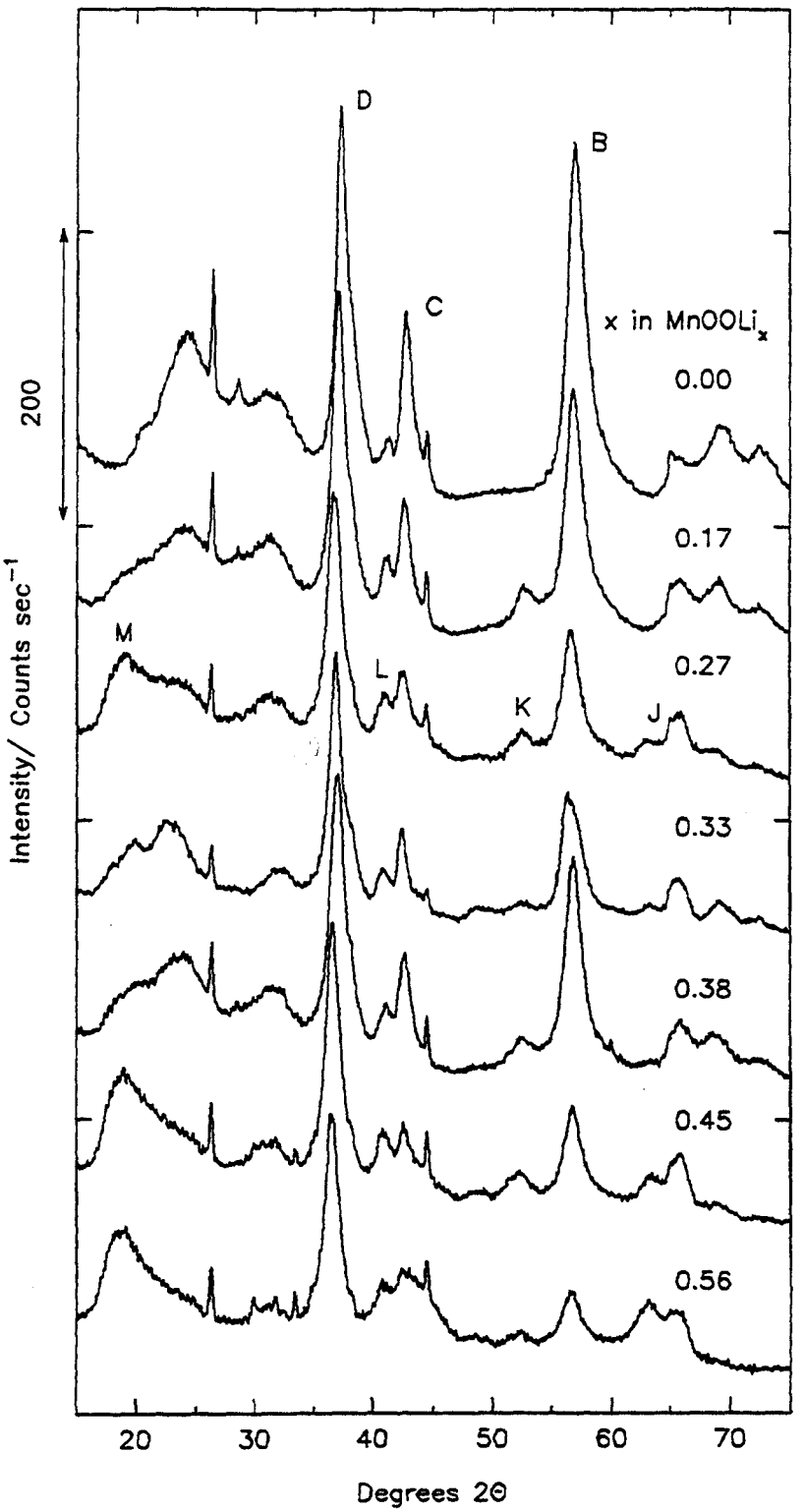


***Figure 6.8*** : X-ray diffraction spectra resulting from Li insertion into EMD heat-treated at 300°C (the level of Li insertion is given above the pattern).

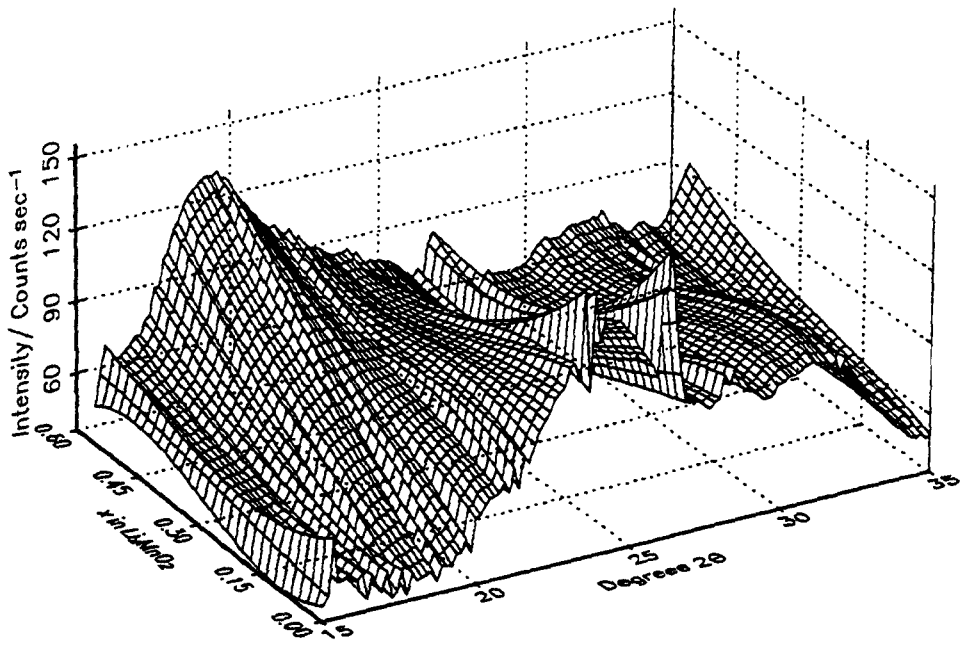


*Figure 6.9* : X-Ray diffraction spectra in the region 15 – 35°2Θ; EMD heat-treated at 300°C (data grid from 0.00-0.56 in 0.019 increments of x in $Li_xMnO_2$).

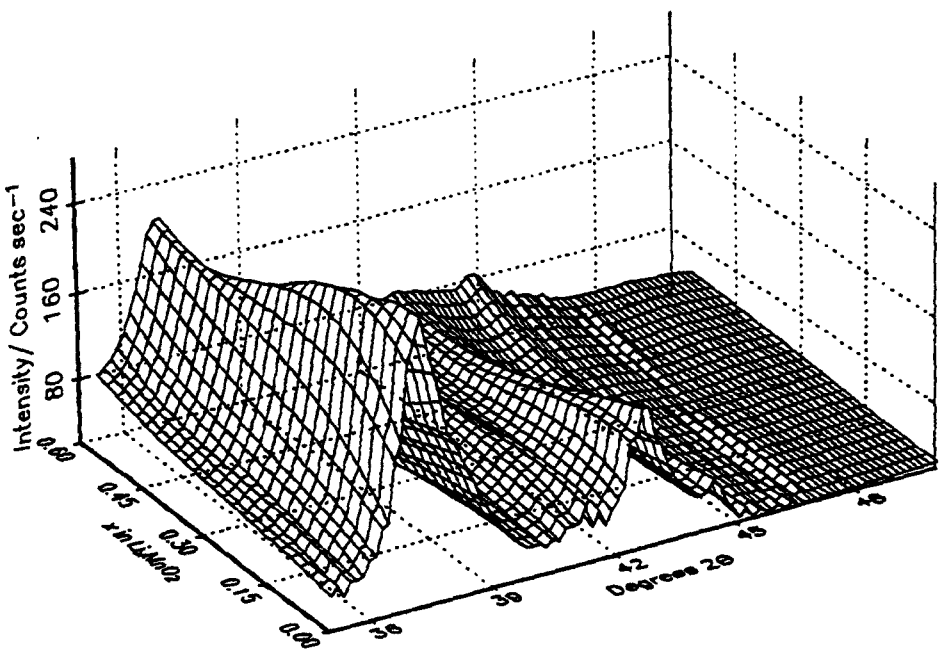


*Figure 6.10* : X-ray diffraction spectra in the region 35 – 50°2Θ; EMD heat-treated at 300°C.

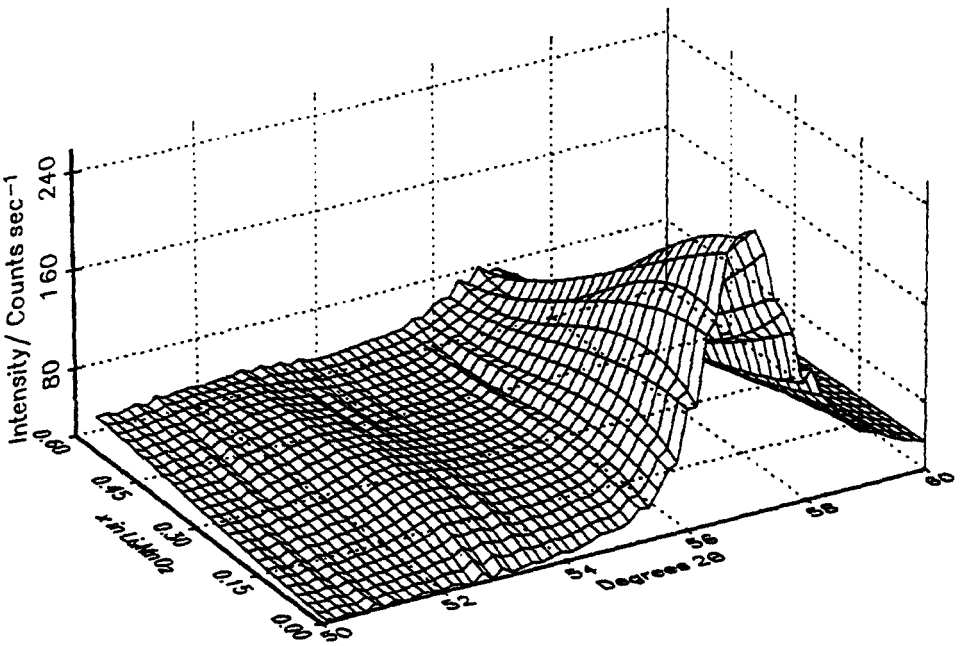


*Figure 6.11* : X-ray diffraction spectra in the region 50 – 60°2Θ; EMD heat-treated at 300°C.

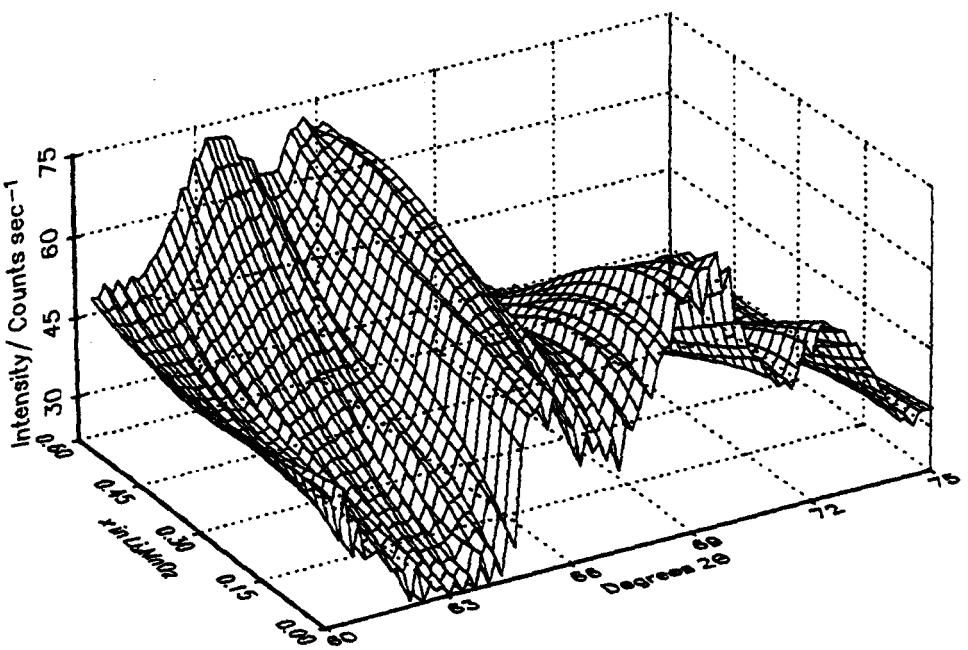


Figure 6.12 : X-ray diffraction spectra in the region 60 – 75°2Θ; EMD heat-treated at 300°C.

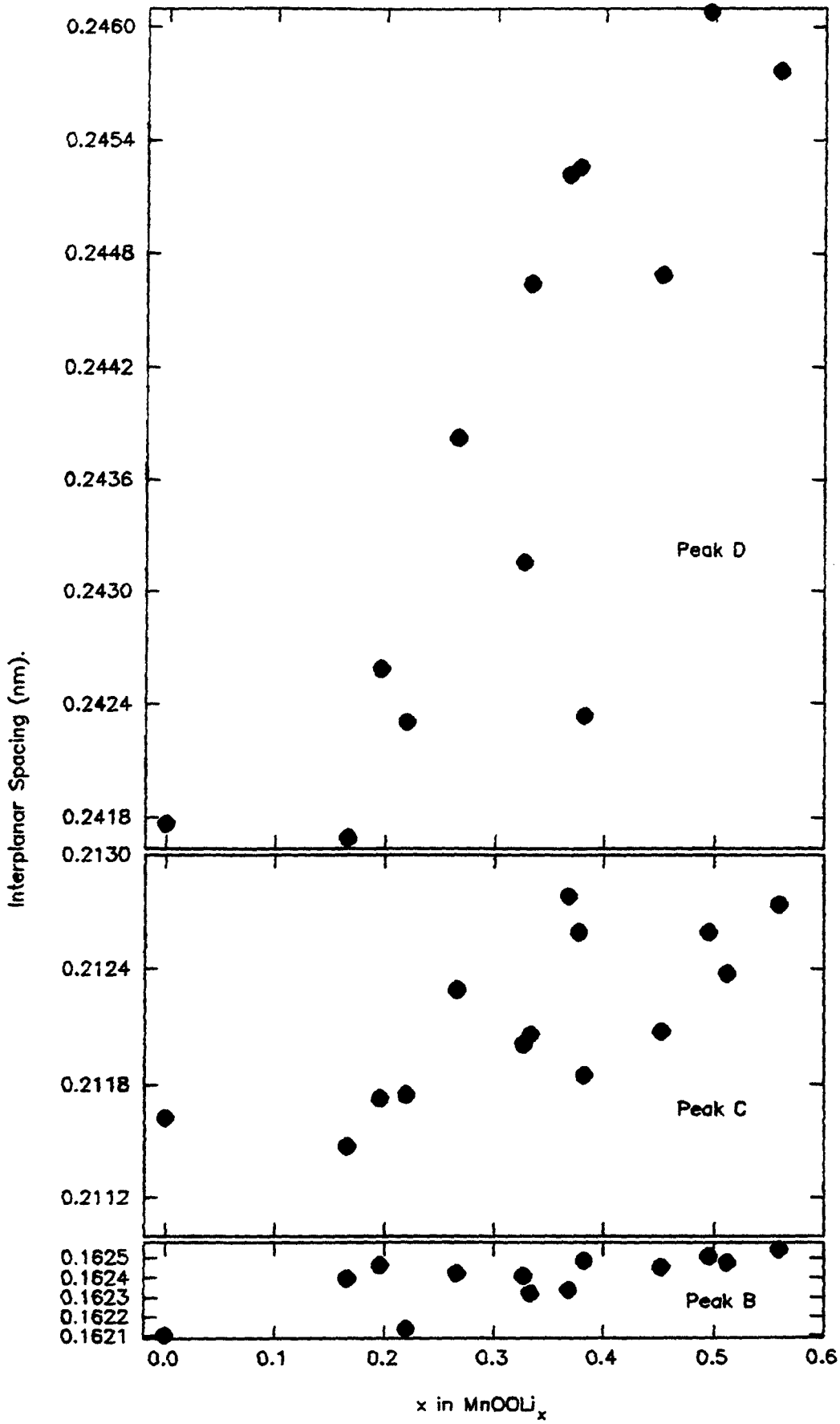


***Figure 6.13*** : Interplanar spacing against Li insertion level for peaks B,C and D: EMD heat-treated at 300°C.

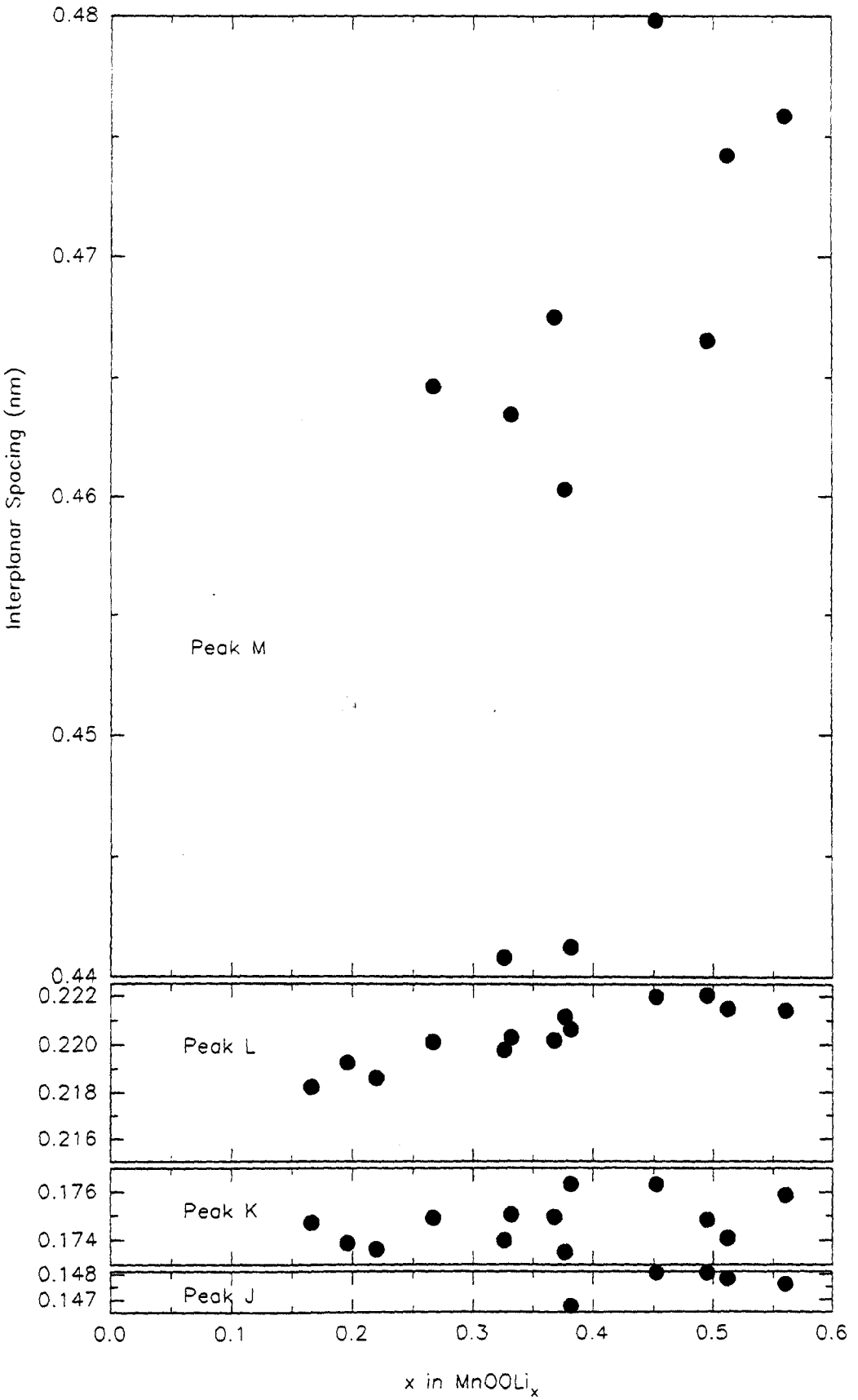


***Figure 6.14*** : **Interplanar spacing against Li insertion level for peaks J,K,L and M: EMD heat-treated at 300°C.**

*6.2.3 EMD heat-treated at 400°C.*

The x-ray patterns resulting from Li insertion into EMD heat-treated at 400°C are given in figure 6.15 and the 3-D plots in figures 6.16 – 6.19. The interplanar spacings associated with the peaks labelled in figure 6.15 are given in figures 6.20 – 6.22.

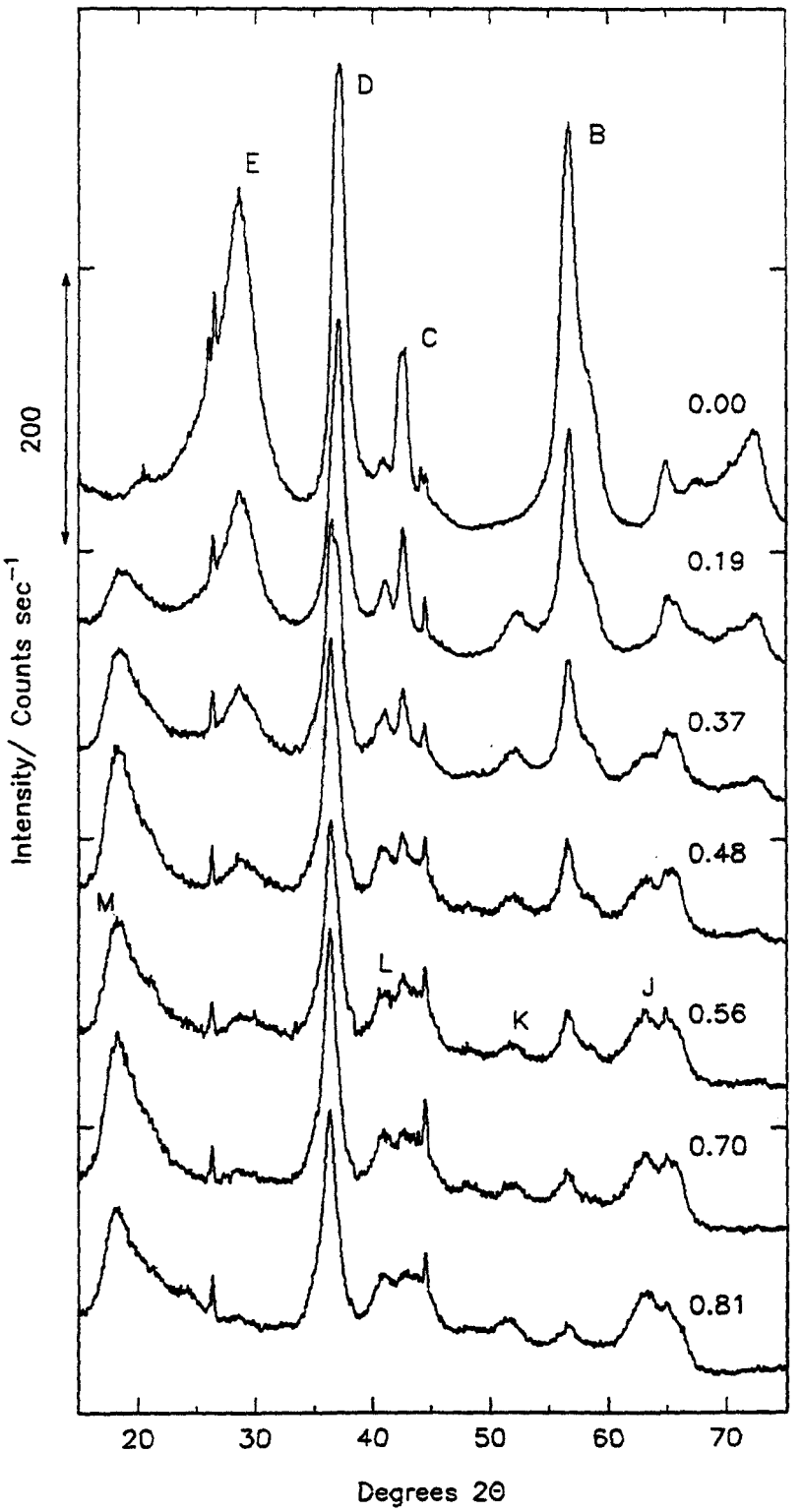


*Figure 6.15* : X-ray diffraction spectra resulting from Li insertion into EMD heat-treated at 400°C (the level of Li insertion is given above the XRD pattern).

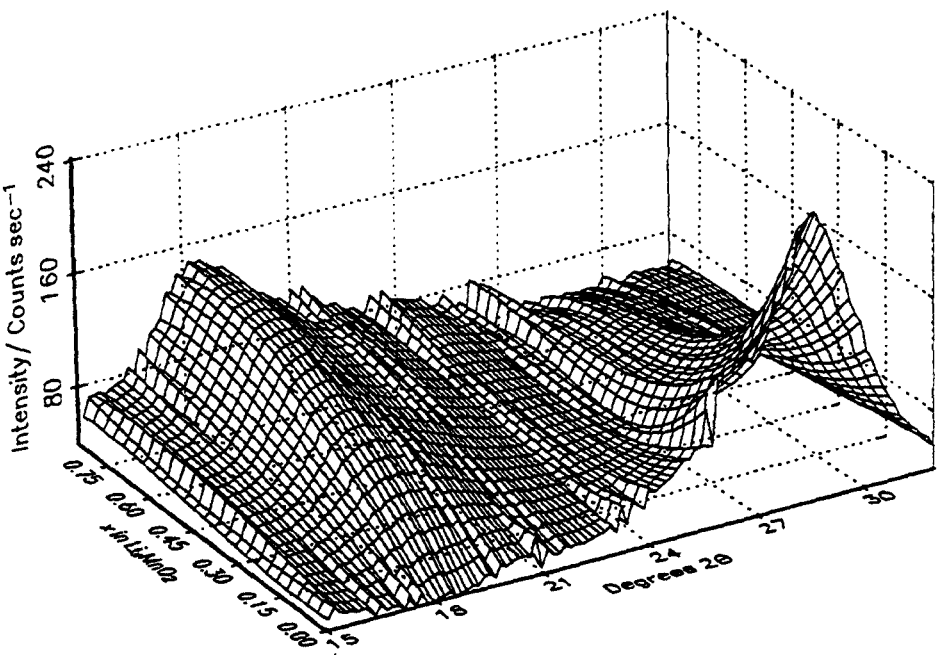


*Figure 6.16* : X-Ray diffraction spectra in the region 15 – 32°2Θ; EMD heat-treated at 400°C (data grid from 0.00-0.84 in 0.0336 increments of x in $Li_xMnO_2$).

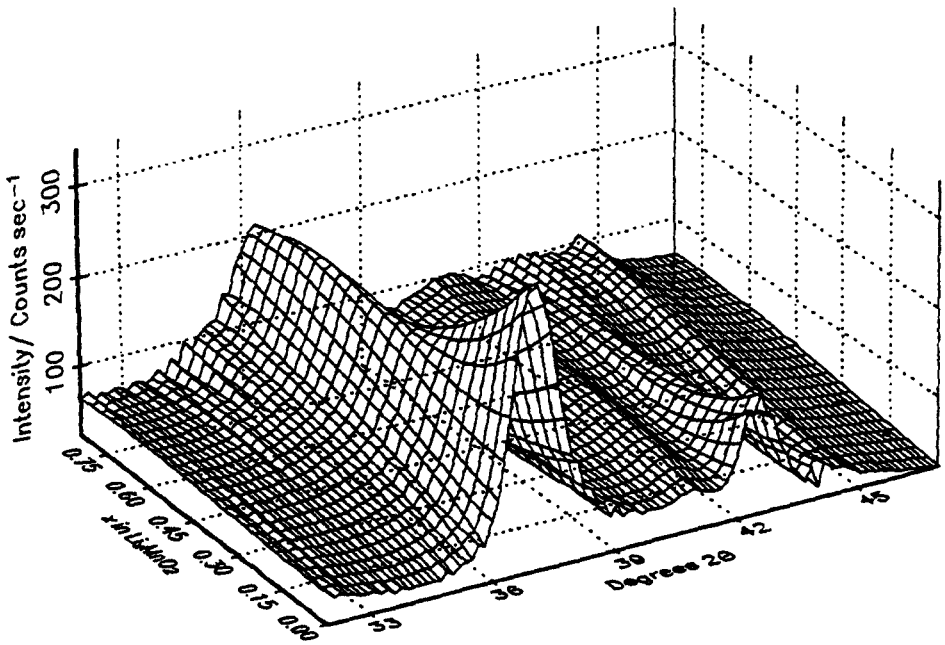


*Figure 6.17* : X-ray diffraction spectra in the region 32 – 48°2Θ; EMD heat-treated at 400°C.

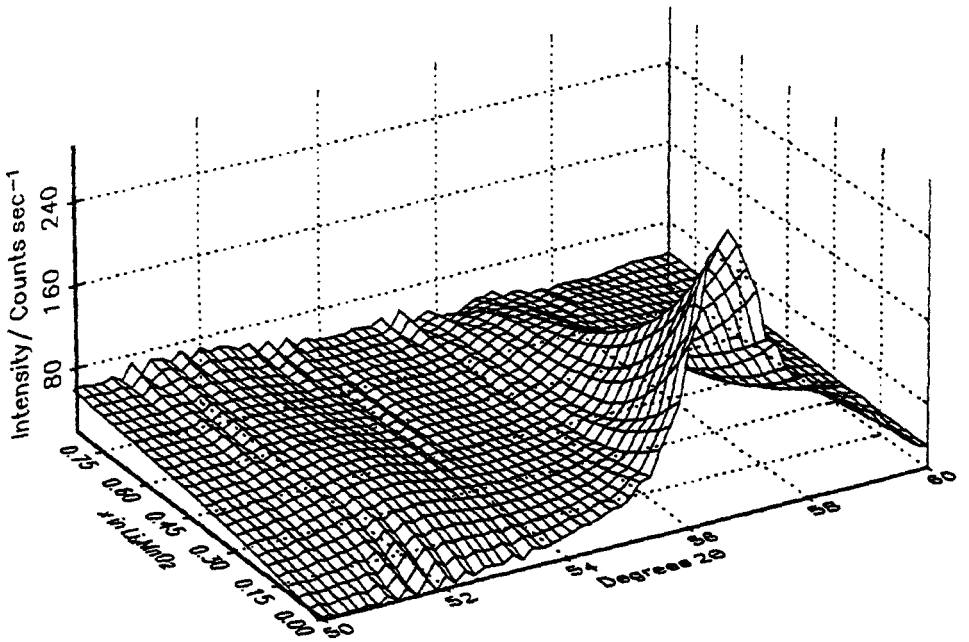


*Figure 6.18* : X-ray diffraction spectra in the region 50 – 60°2Θ; EMD heat-treated at 400°C.

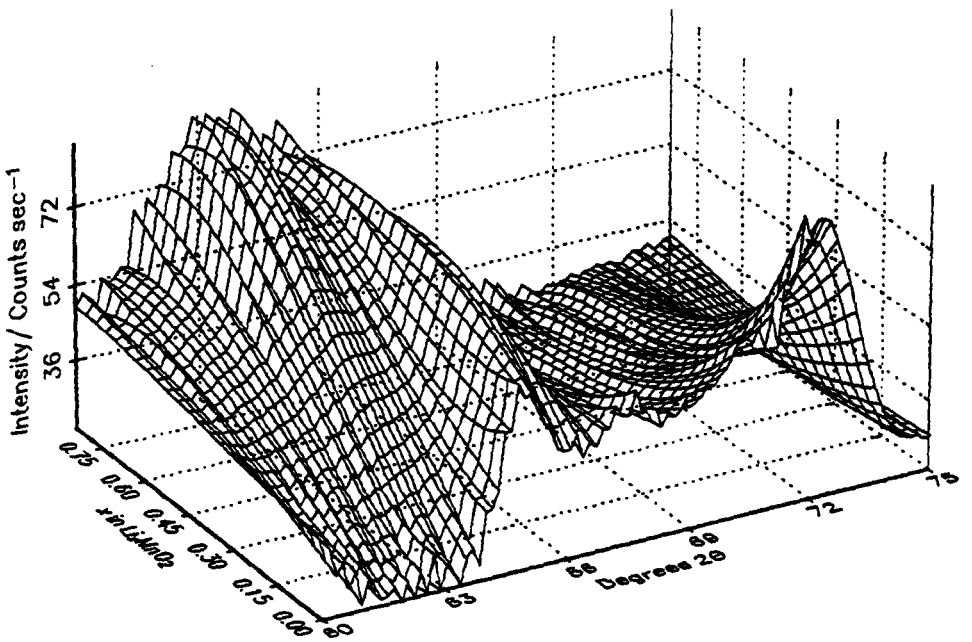


*Figure 6.19* : X-ray diffraction spectra in the region 60 – 75°2Θ; EMD heat-treated at 400°C.

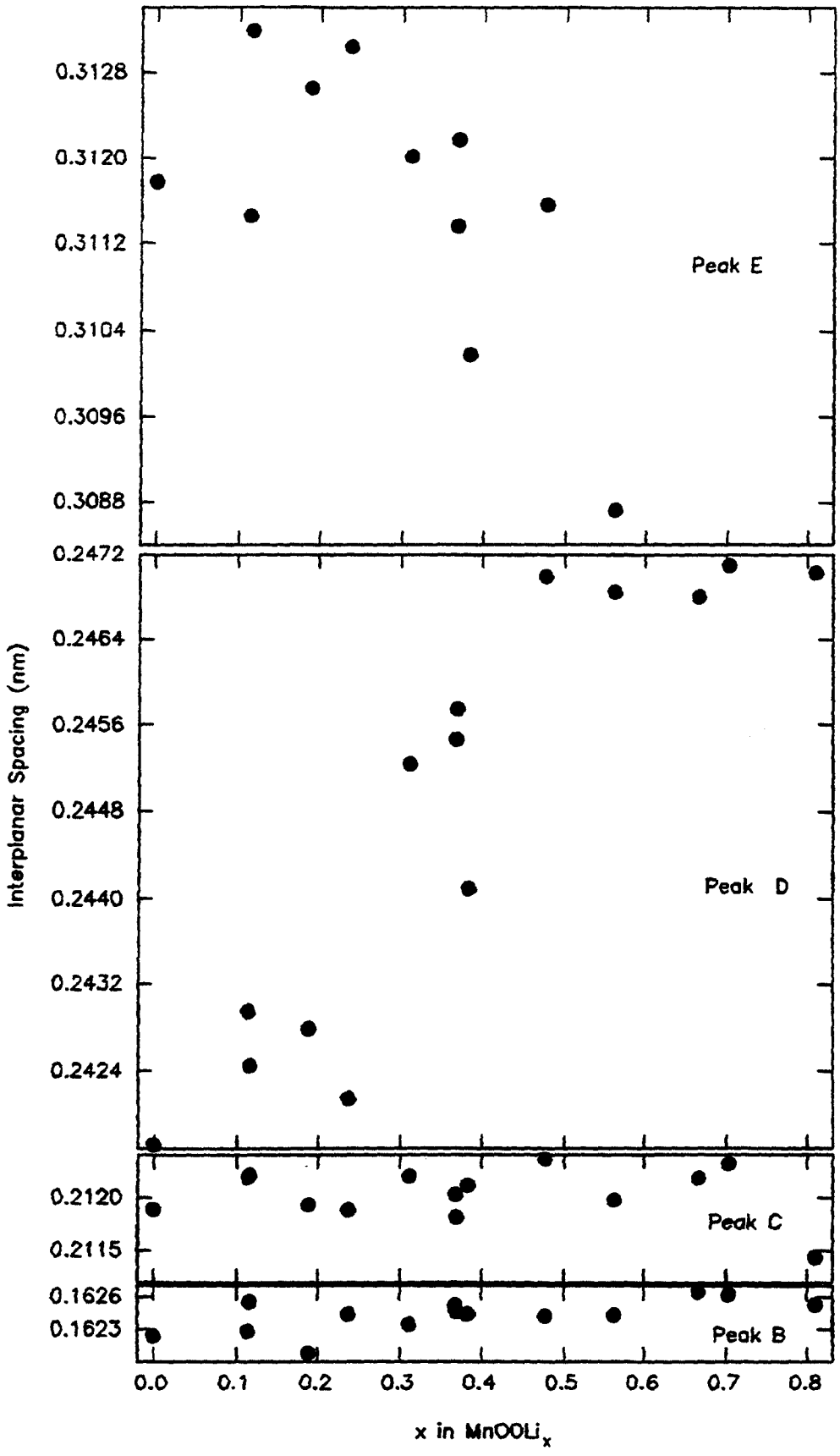


*Figure 6.20* : Interplanar spacing against Li insertion level for peaks B,C,D and E: EMD heat-treated at 400°C.

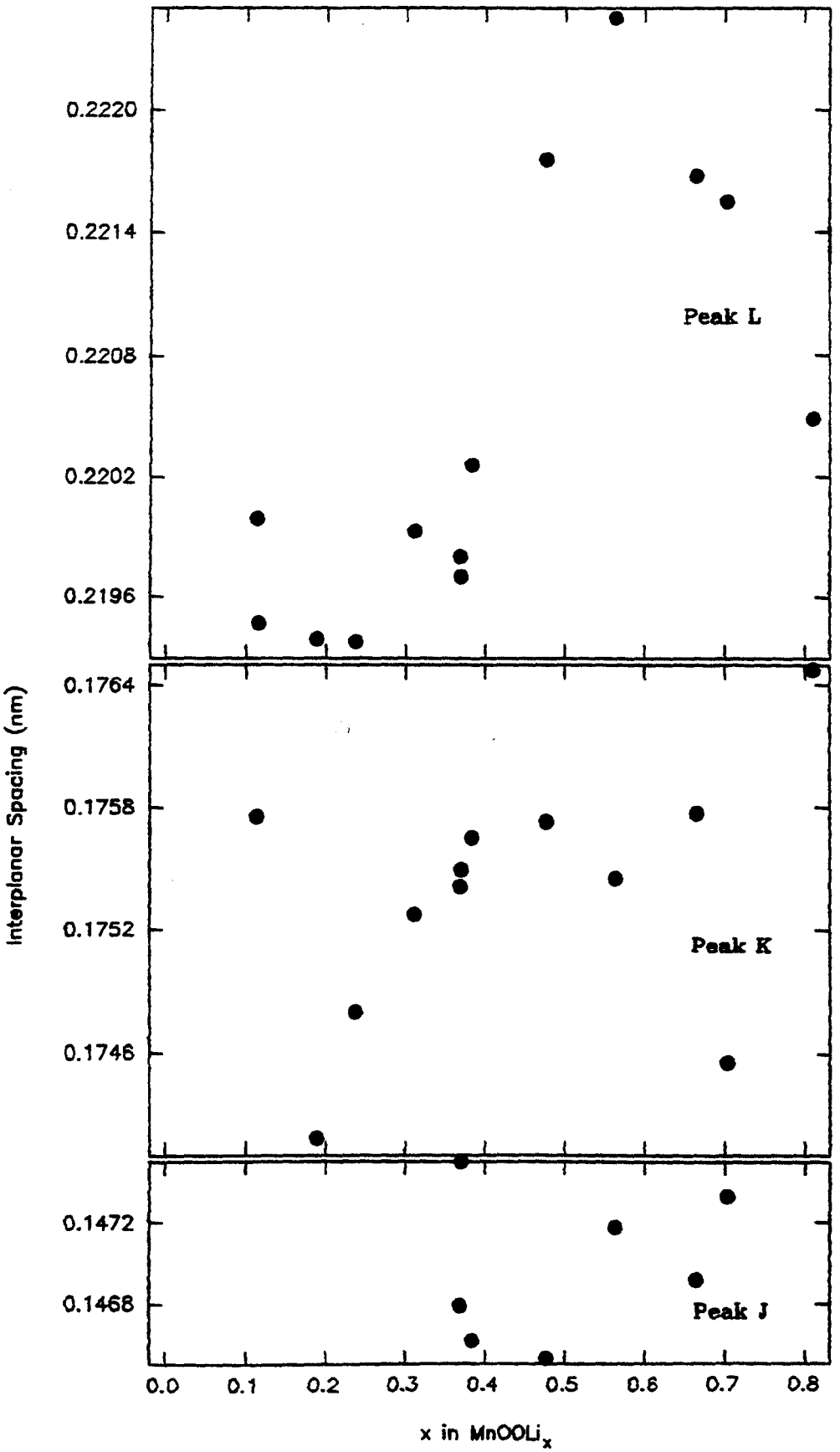


*Figure 6.21* : Interplanar spacing against Li insertion level for peaks J,K and L: EMD heat-treated at 400°C.

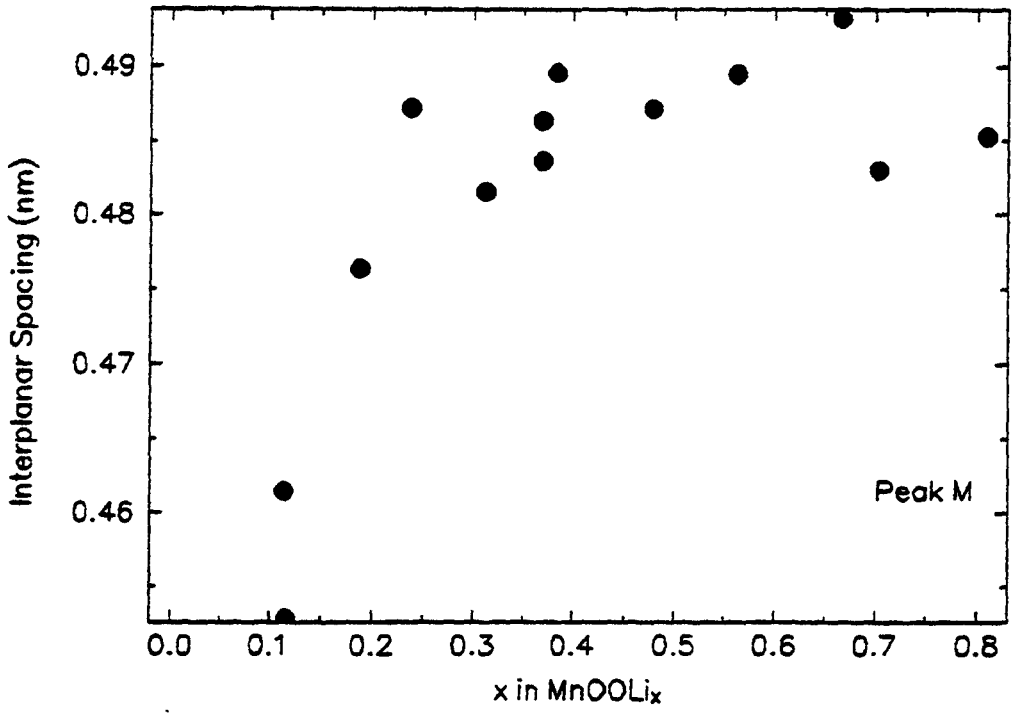


*Figure 6.22* : Interplanar spacing against Li insertion level for peak M: EMD heat-treated at 400°C.

## 6.3 Powder x-ray diffraction spectra of Li-inserted CMD compounds.

### *6.3.1 CMD heat-treated at 200°C.*

The x-ray patterns resulting from Li insertion into CMD heat-treated at 200°C are given in figure 6.23 and the 3-D plots in figures 6.24 – 6.27. The interplanar spacings associated with the peaks labelled in figure 6.23 are given in figures 6.28 – 6.29.

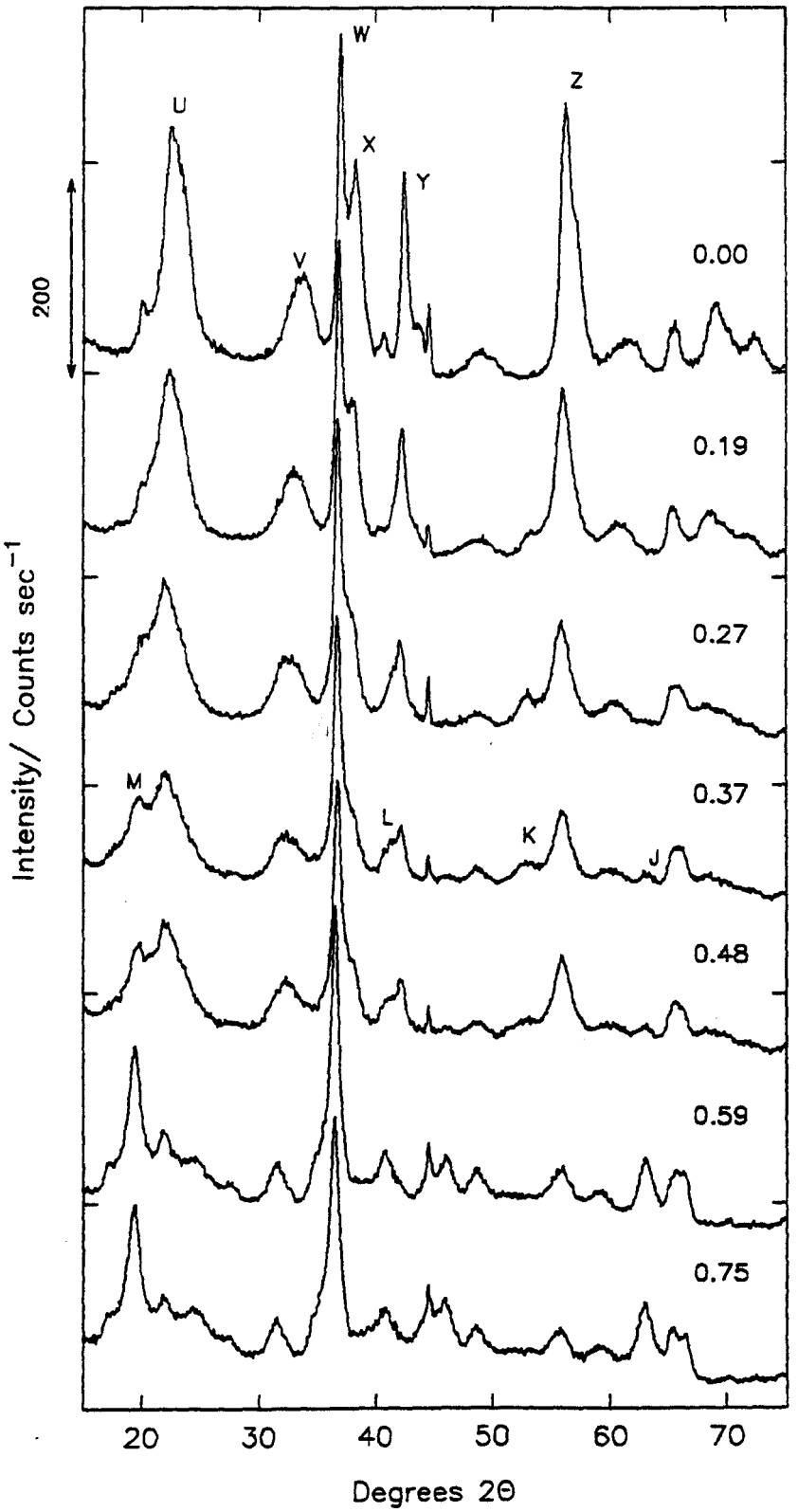


***Figure 6.23*** : X-ray diffraction spectra resulting from Li insertion into CMD heat-treated at 200°C (the degree of Li insertion is given above the XRD pattern).

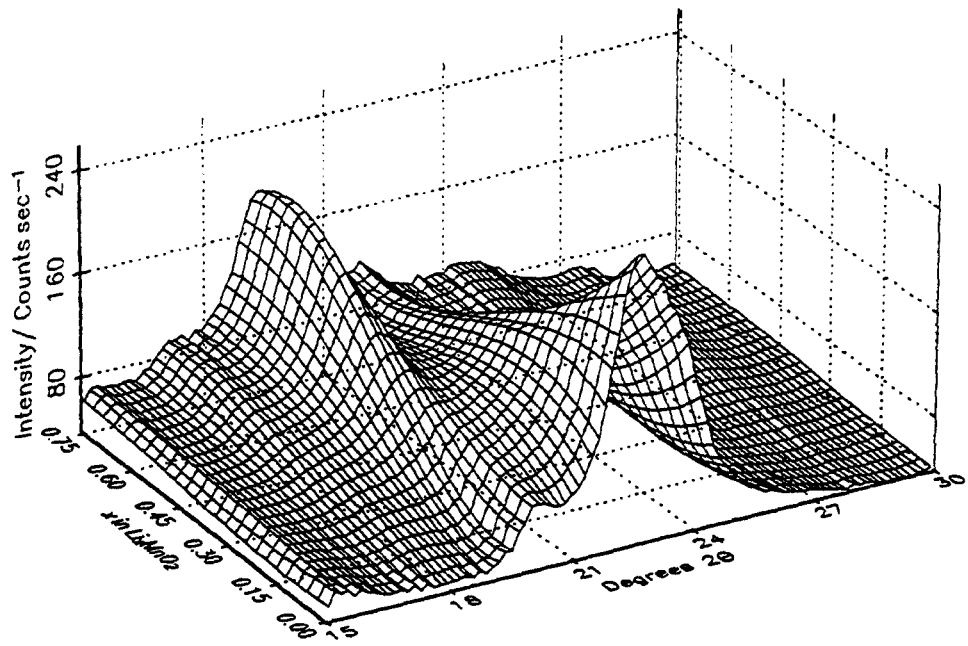


*Figure 6.24* : X-Ray diffraction spectra in the region 15 – 30°2Θ; CMD heat-treated at 200°C (data grid from 0.00-0.76 in 0.0304 increments of x in $Li_xMnO_2$).

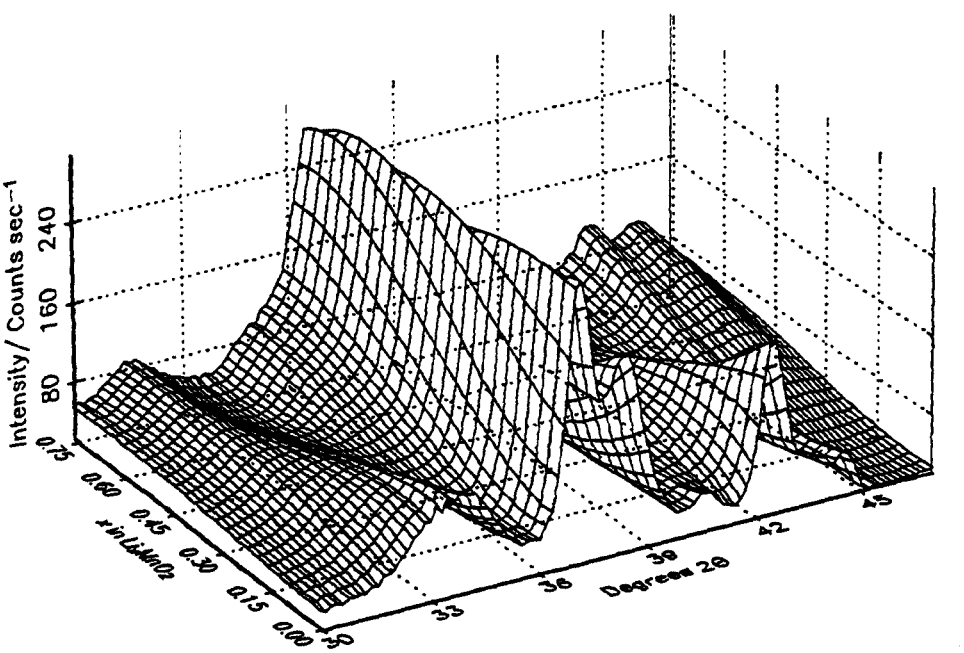


*Figure 6.25* : X-Ray diffraction spectra in the region 30 – 47°2Θ; CMD heat-treated at 200°C.

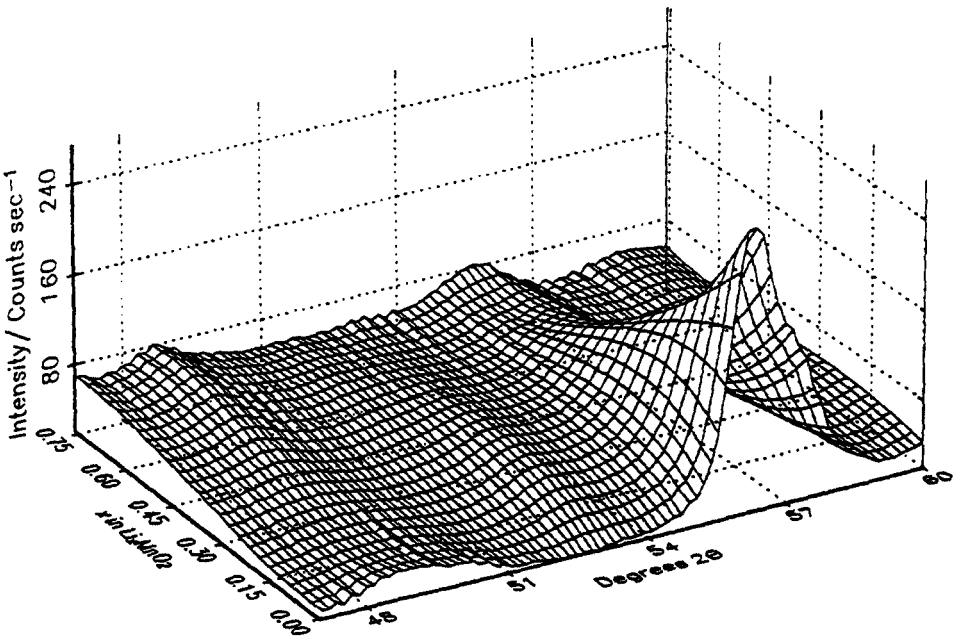


***Figure 6.26*** : X-ray diffraction spectra in the region 47 – 60°2Θ; CMD heat-treated at 200°C.

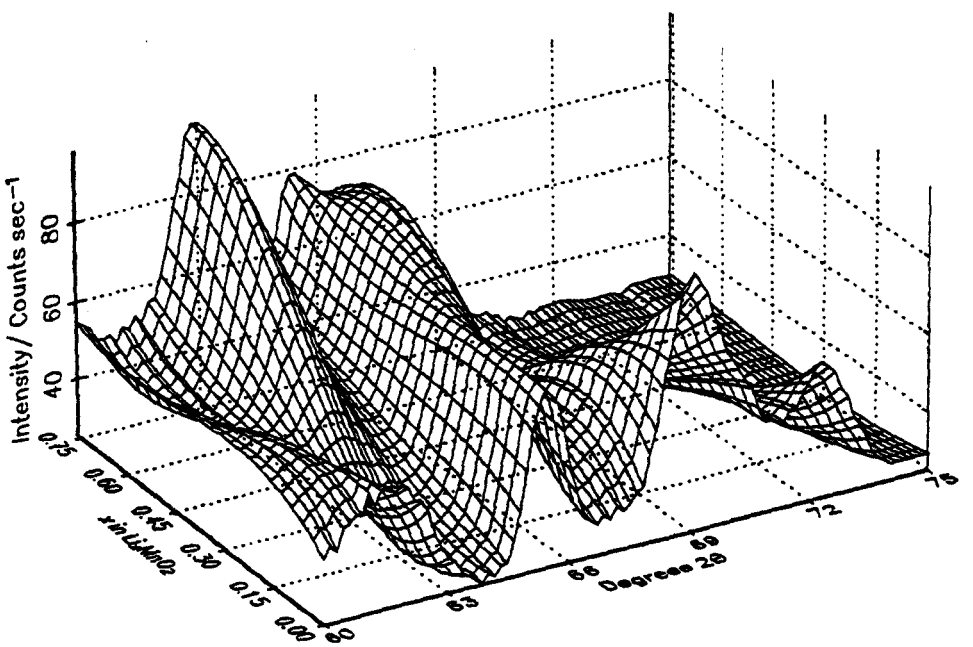


***Figure 6.27*** : X-ray diffraction spectra in the region 60 – 75°2Θ; CMD heat-treated at 200°C.

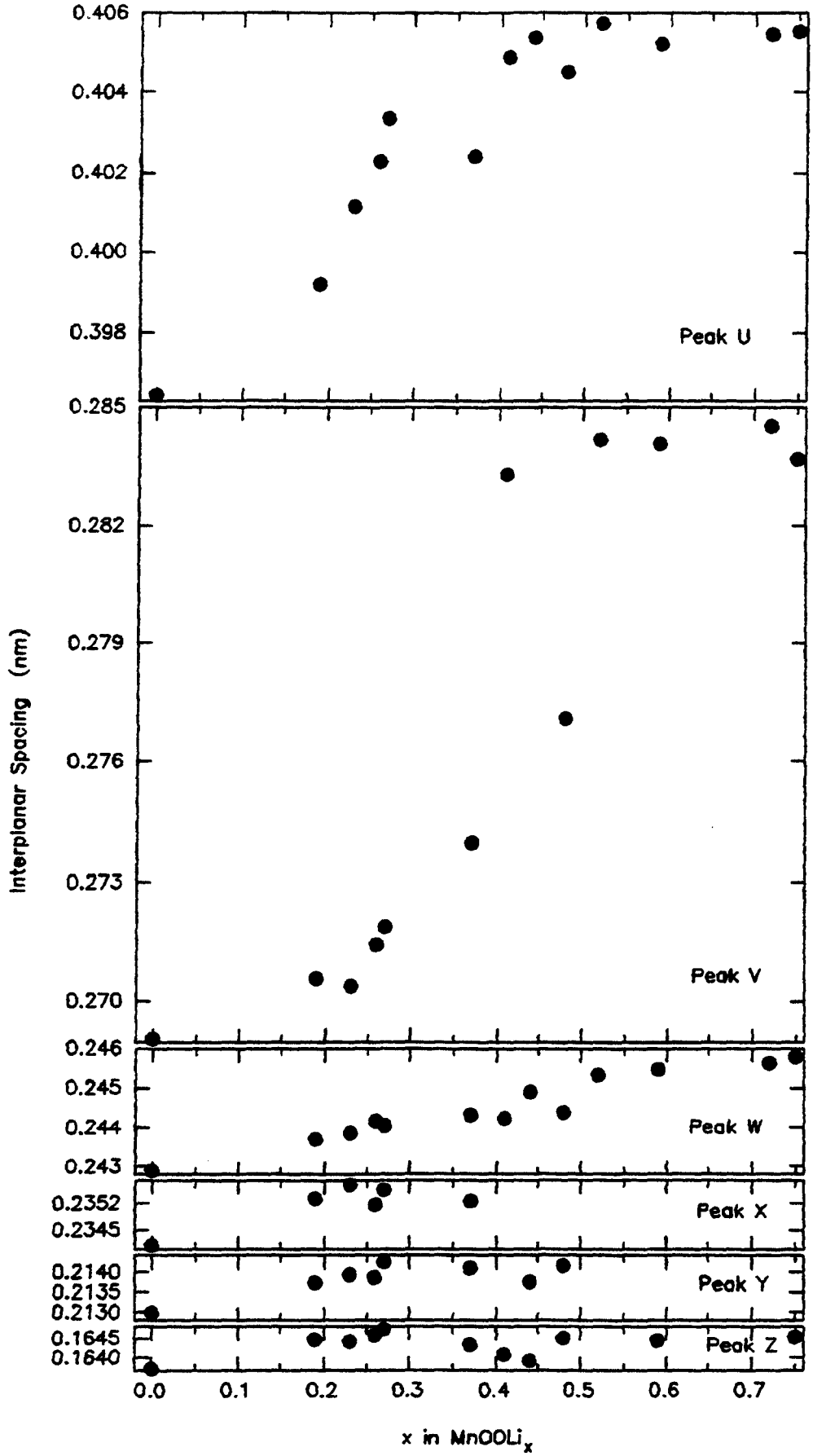


***Figure 6.28*** : Interplanar spacing against Li insertion level for peaks U,V,W,X,Y and Z: CMD heat-treated at 200°C.

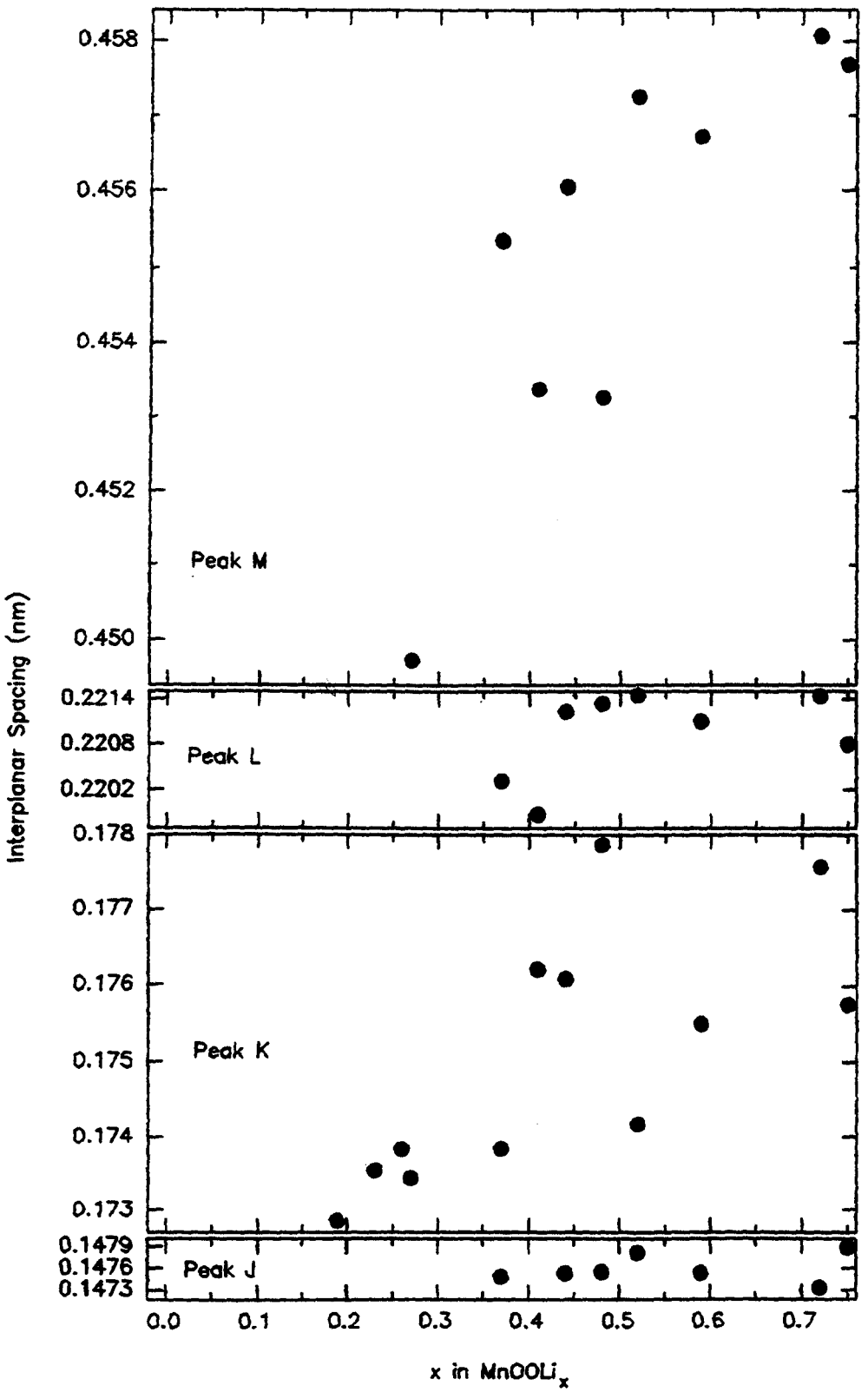


*Figure 6.29* : Interplanar spacing against Li insertion level for peaks J,K,L and M: CMD heat-treated at 200°C.

### *6.3.2 CMD heat-treated at 300 °C.*

The x-ray patterns resulting from Li insertion into CMD heat-treated at 300°C are given in figure 6.30 and the 3-D plots in figures 6.31 – 6.34. The interplanar spacings associated with the peaks labelled in figure 6.30 are given in figures 6.35 – 6.36.

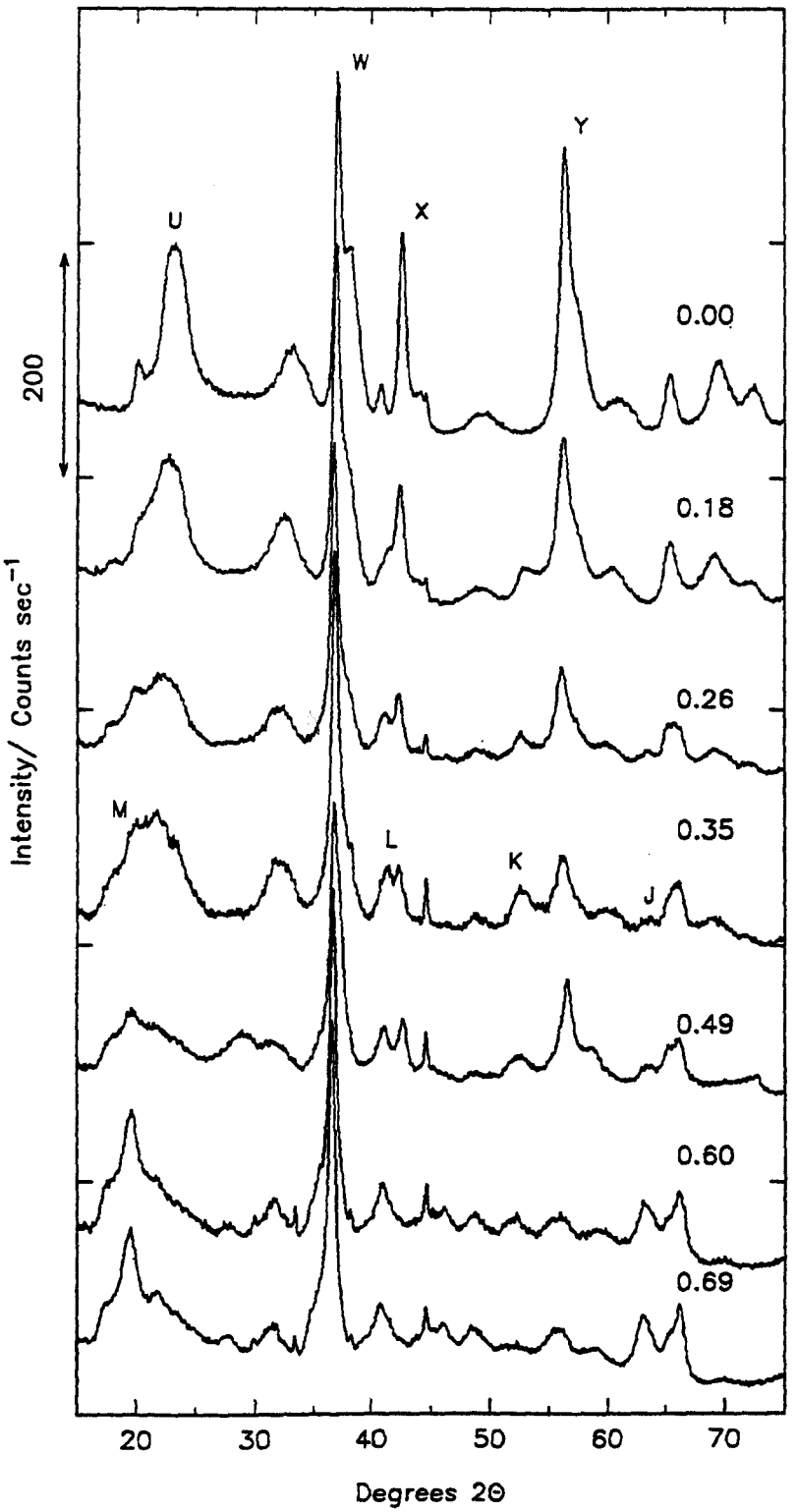


***Figure 6.30*** : X-ray diffraction spectra resulting from Li insertion into CMD heat-treated at 300°C (the degree of Li insertion is given above the XRD pattern).

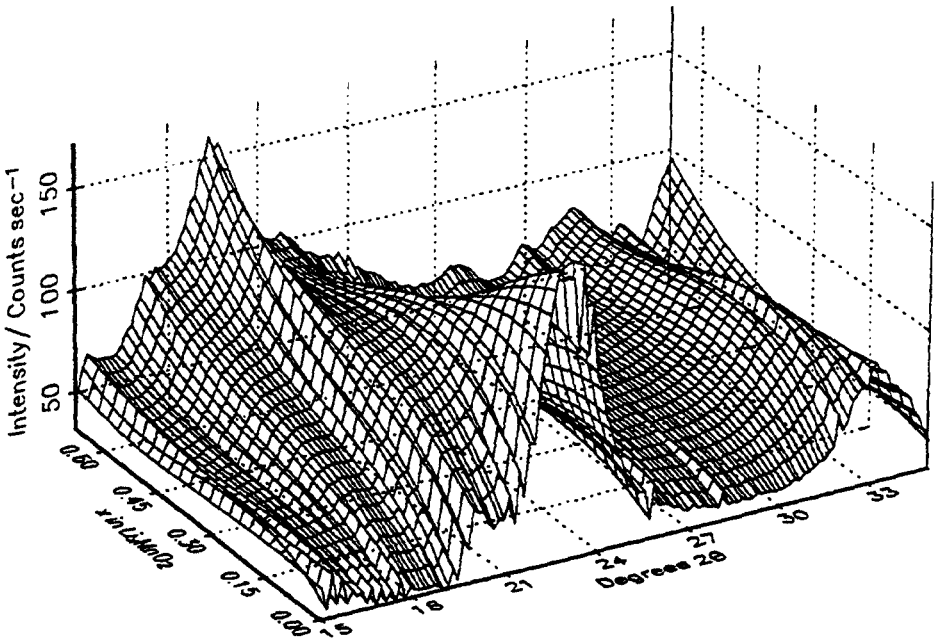


*Figure 6.31* : X-Ray diffraction spectra in the region 15 – 35°2Θ; CMD heat-treated at 300°C (data grid from 0.00-0.68 in 0.0272 increments of x in $Li_xMnO_2$).

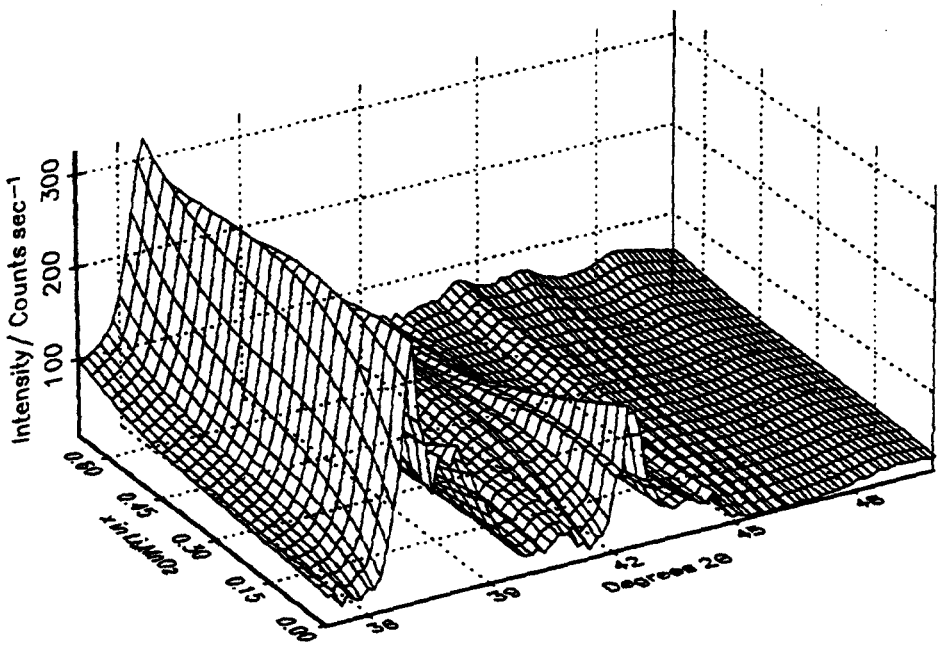


*Figure 6.32* : X-ray diffraction spectra in the region 35 – 50°2Θ; CMD heat-treated at 300°C.

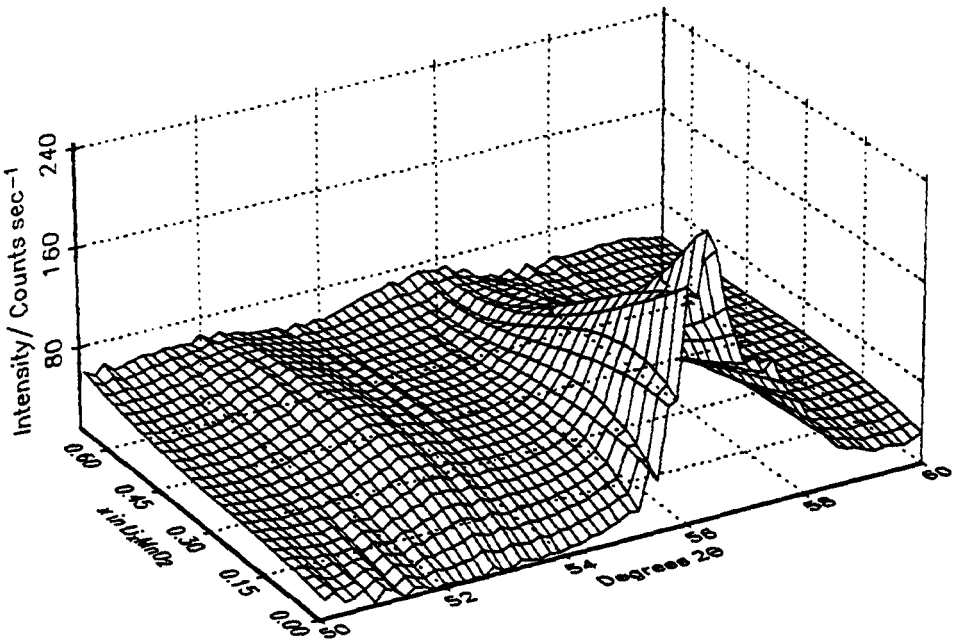


*Figure 6.33* : X-ray diffraction spectra in the region 50 – 60°2Θ; CMD heat-treated at 300°C.

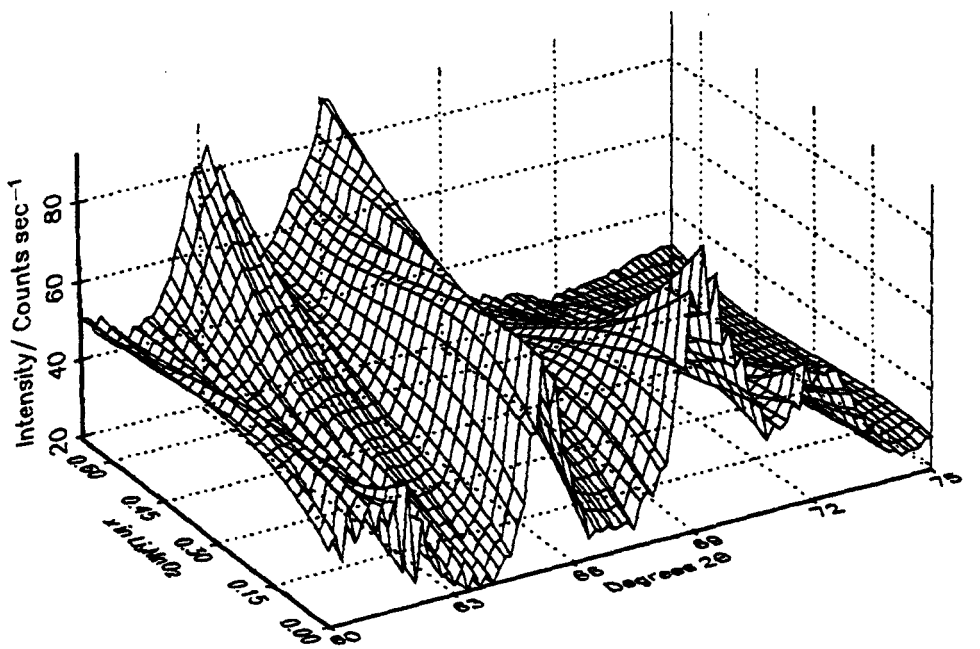


*Figure 6.34* : X-ray diffraction spectra in the region 60 – 75°2Θ; CMD heat-treated at 300°C.

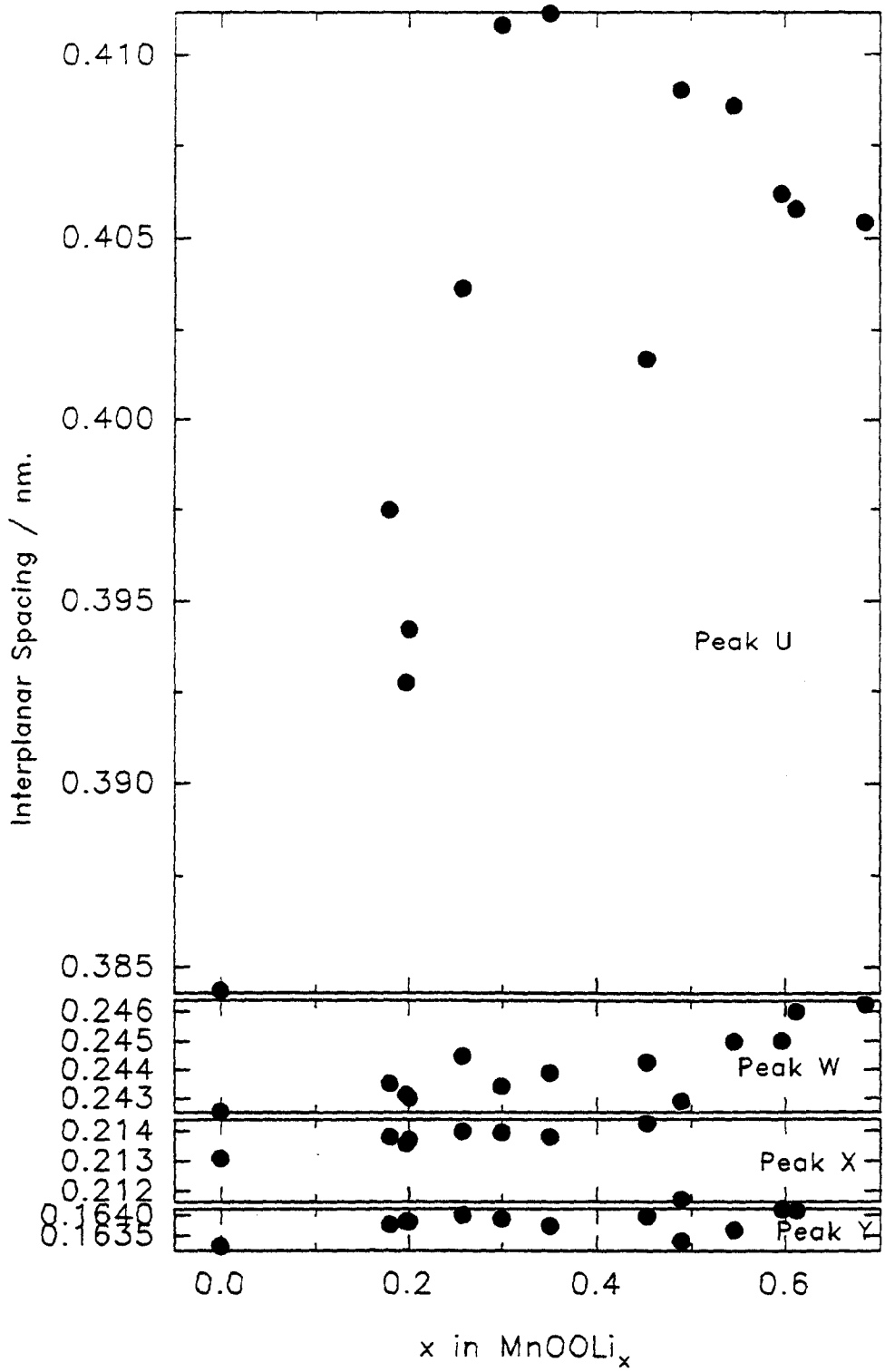


***Figure 6.35*** : Interplanar spacing against Li insertion level for peaks U,W,X,and Y: CMD heat-treated at 300°C.

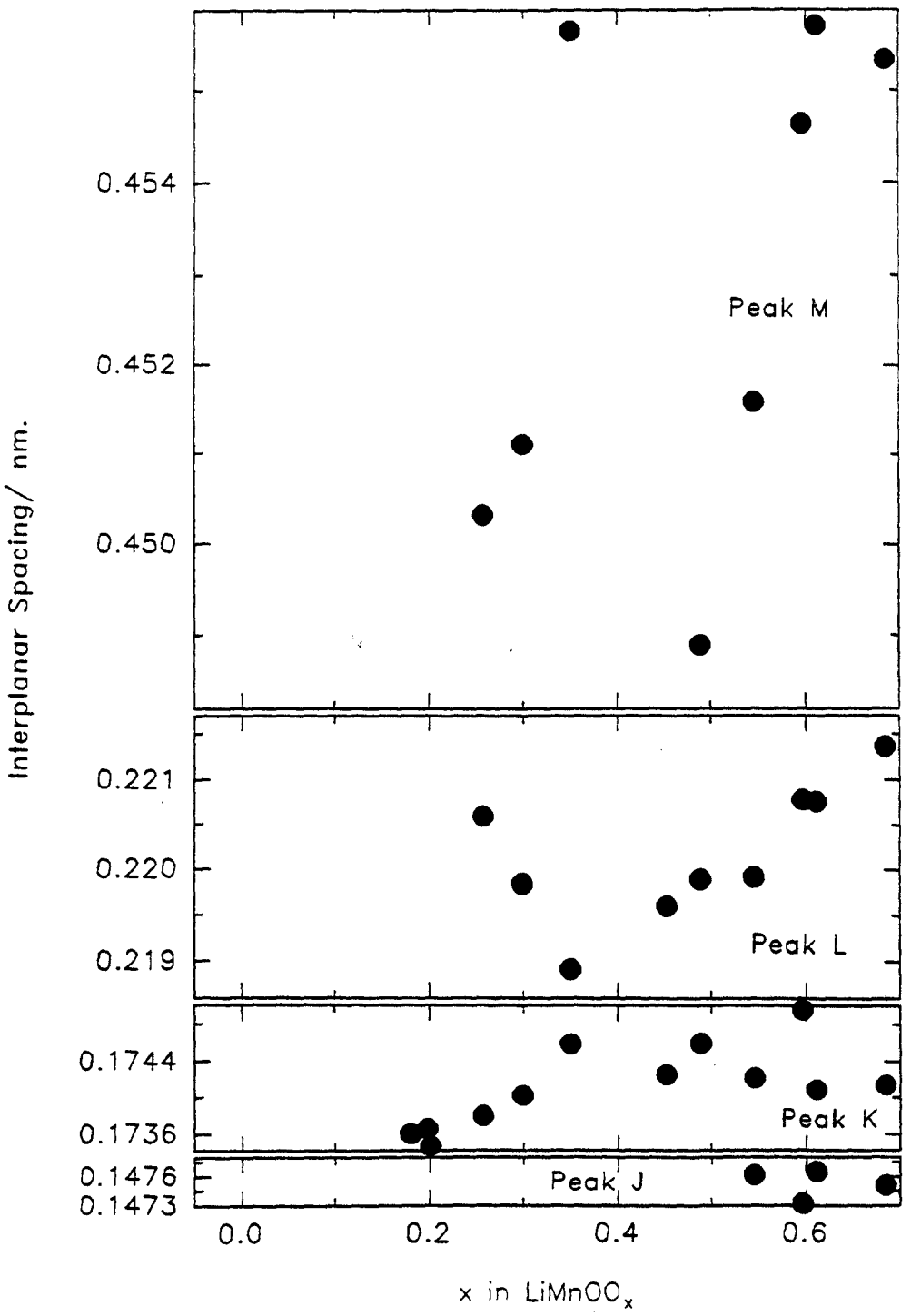


***Figure 6.36*** : Interplanar spacing against Li insertion level for peaks J,K,L and M: CMD heat-treated at 300°C.

*6.3.3 CMD heat-treated at 400°C.*

The x-ray patterns resulting from Li insertion into CMD heat-treated at 400°C are given in figure 6.37 and the 3-D plots in figures 6.38 – 6.41. The interplanar spacings associated with the peaks labelled in figure 6.37 are given in figures 6.42 – 6.43.

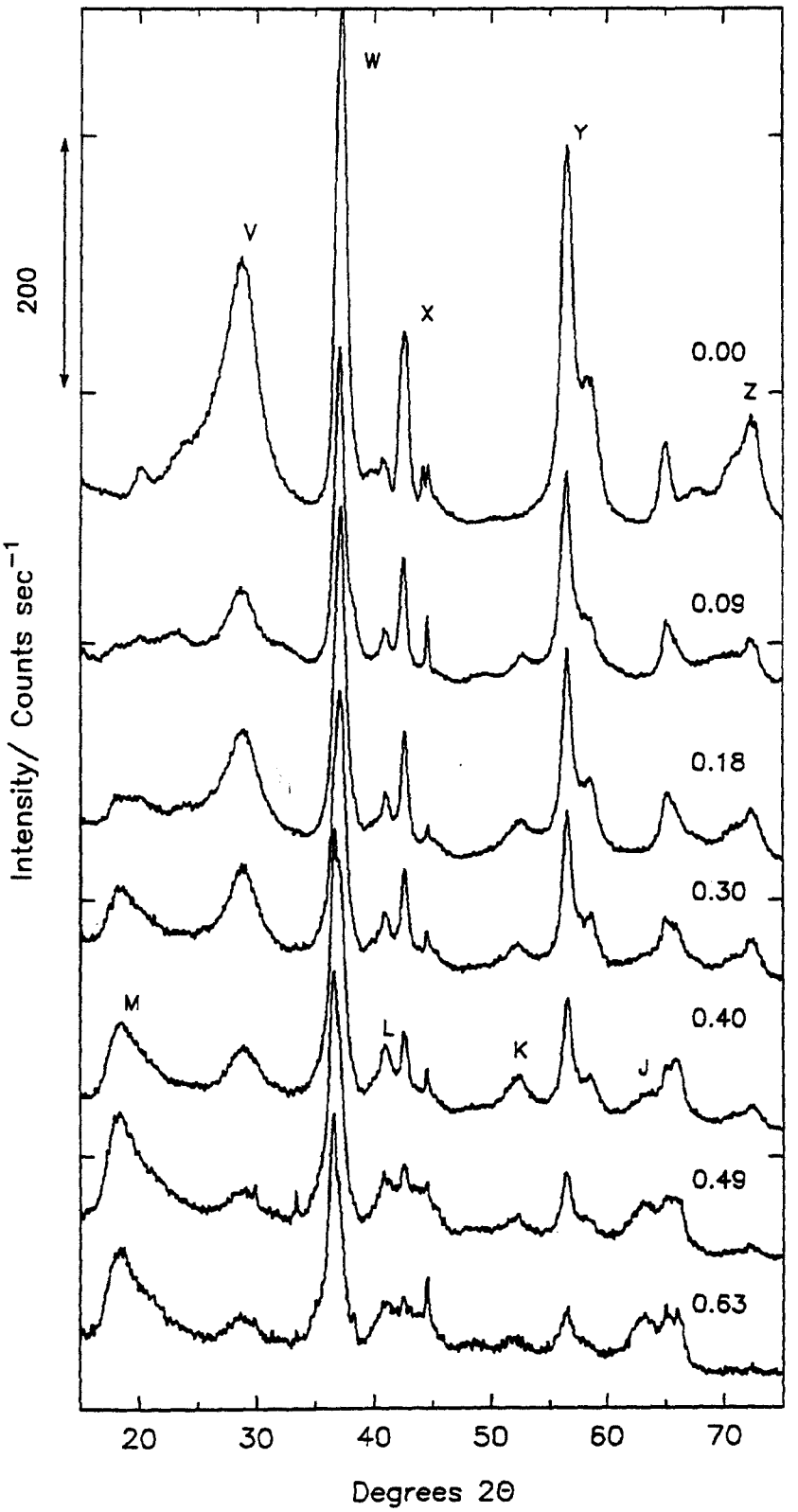


*Figure 6.37* : X-ray diffraction spectra resulting from Li insertion into CMD heat-treated at 400°C (the degree of Li insertion is given above the XRD pattern).

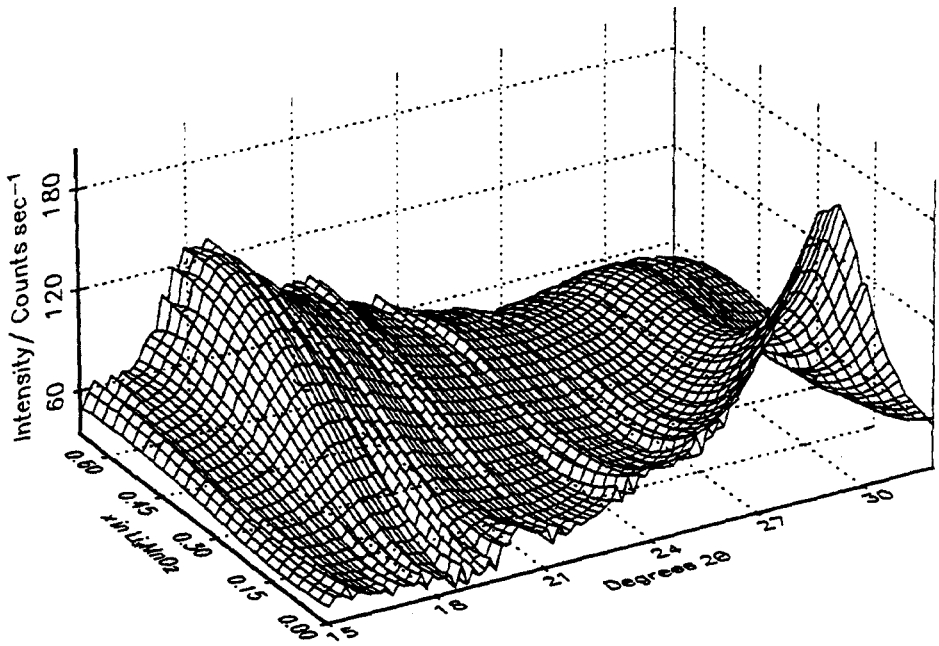


*Figure 6.38* : X-Ray diffraction spectra in the region 15 – 32°2Θ; CMD heat-treated at 400°C (data grid from 0.00-0.68 in 0.0272 increments of x in $Li_xMnO_2$).

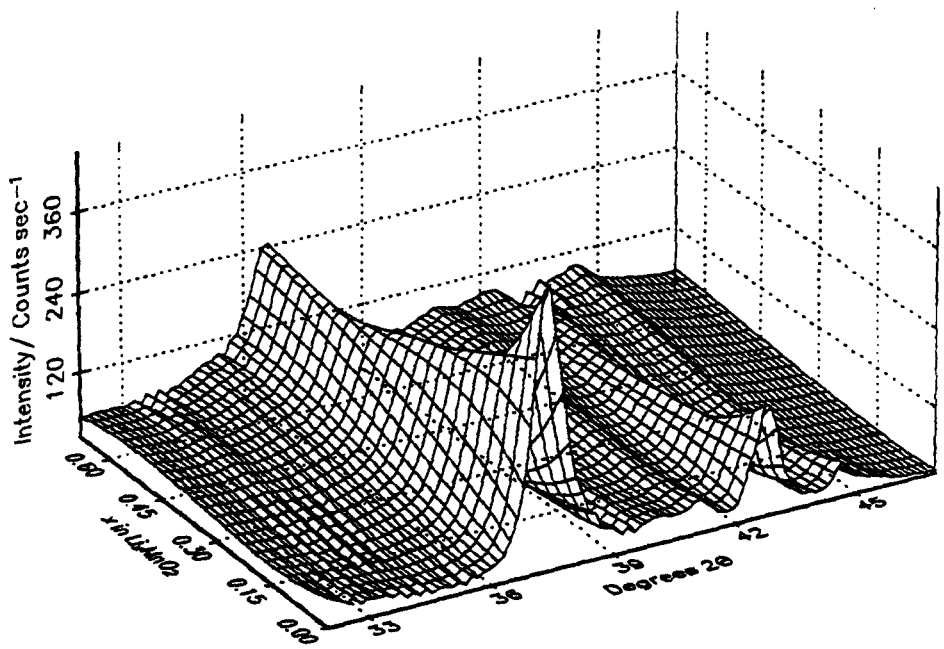


*Figure 6.39* : X-ray diffraction spectra in the region 32 – 47°2Θ; CMD heat-treated at 400°C.

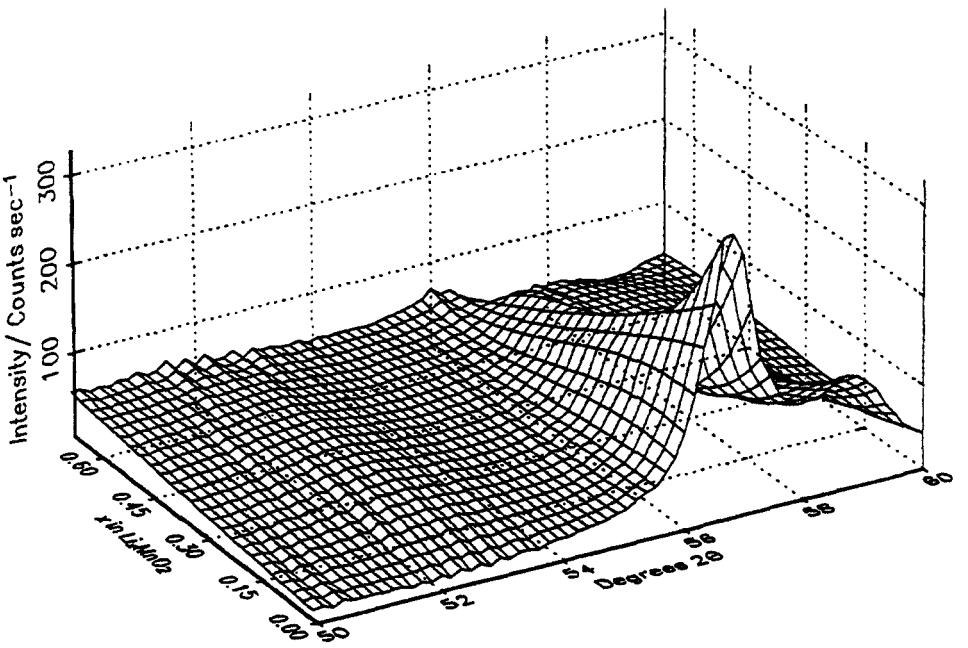


*Figure 6.40* : X-ray diffraction spectra in the region 50 – 60°2Θ; CMD heat-treated at 400°C.

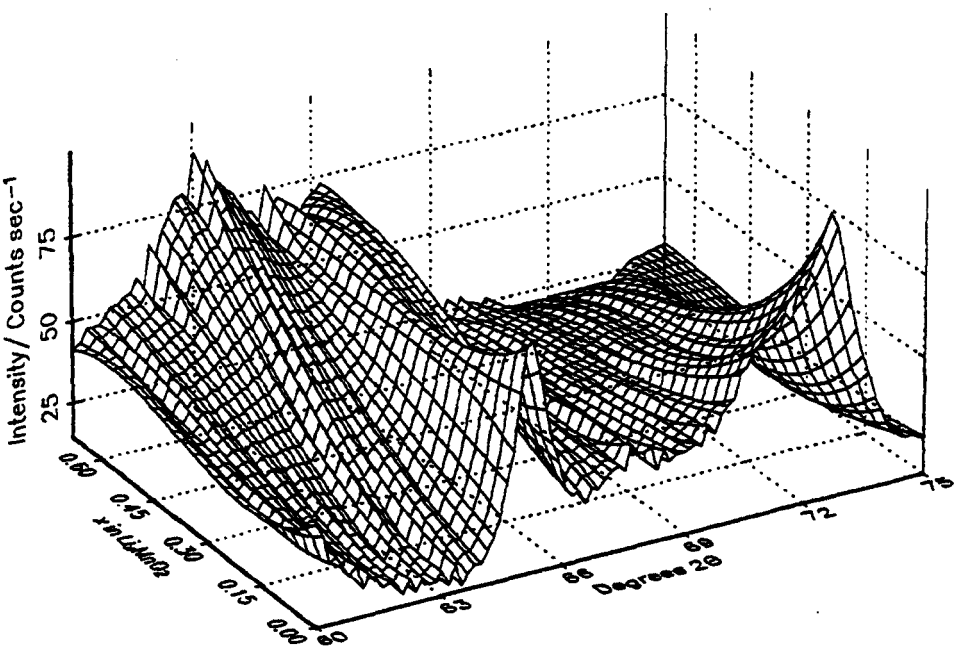


*Figure 6.41* : X-ray diffraction spectra in the region 60 – 75°2Θ; CMD heat-treated at 400°C.

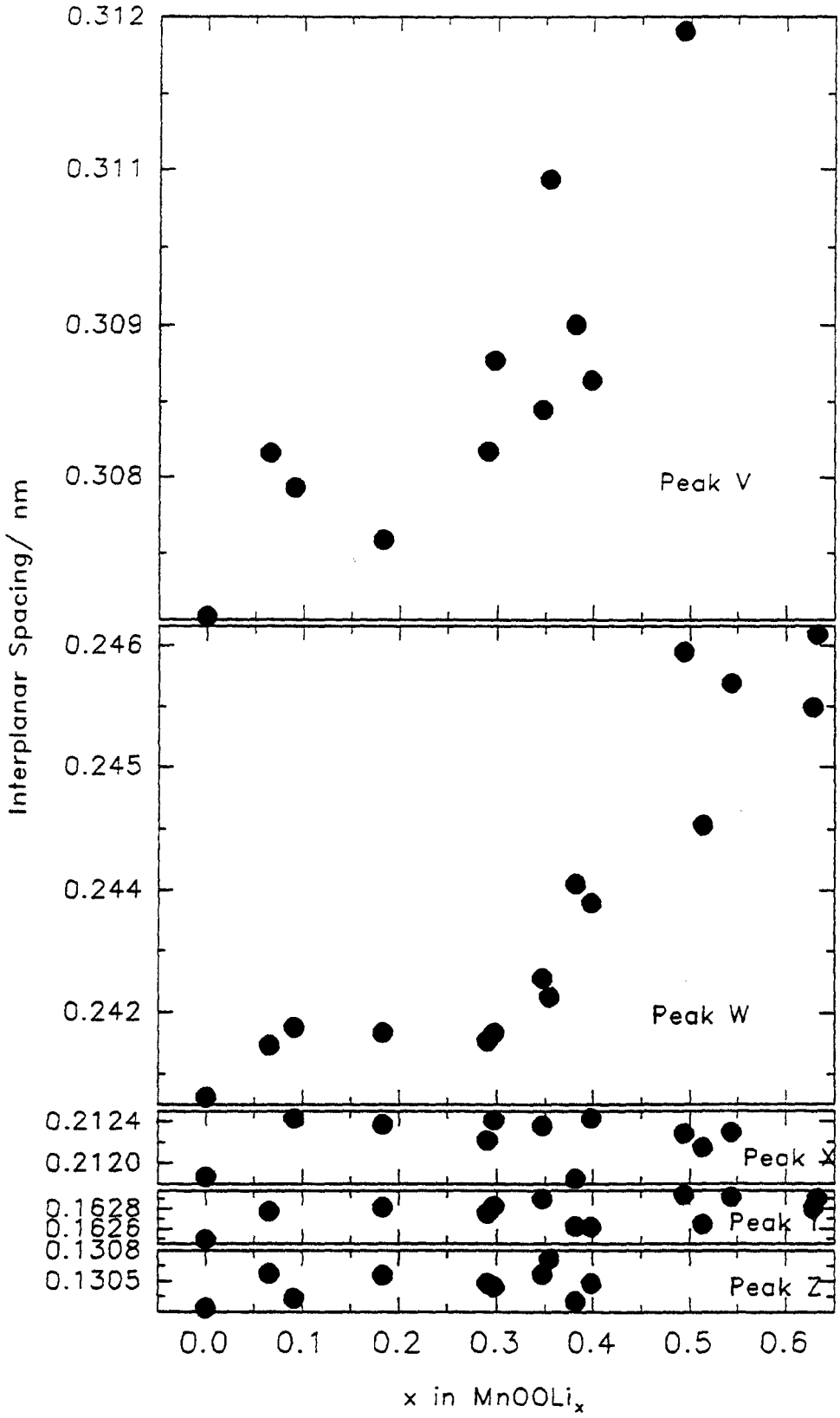


***Figure 6.42*** : Interplanar spacing against Li insertion level for peaks V,W,X,Y and Z: CMD heat-treated at 400°C.

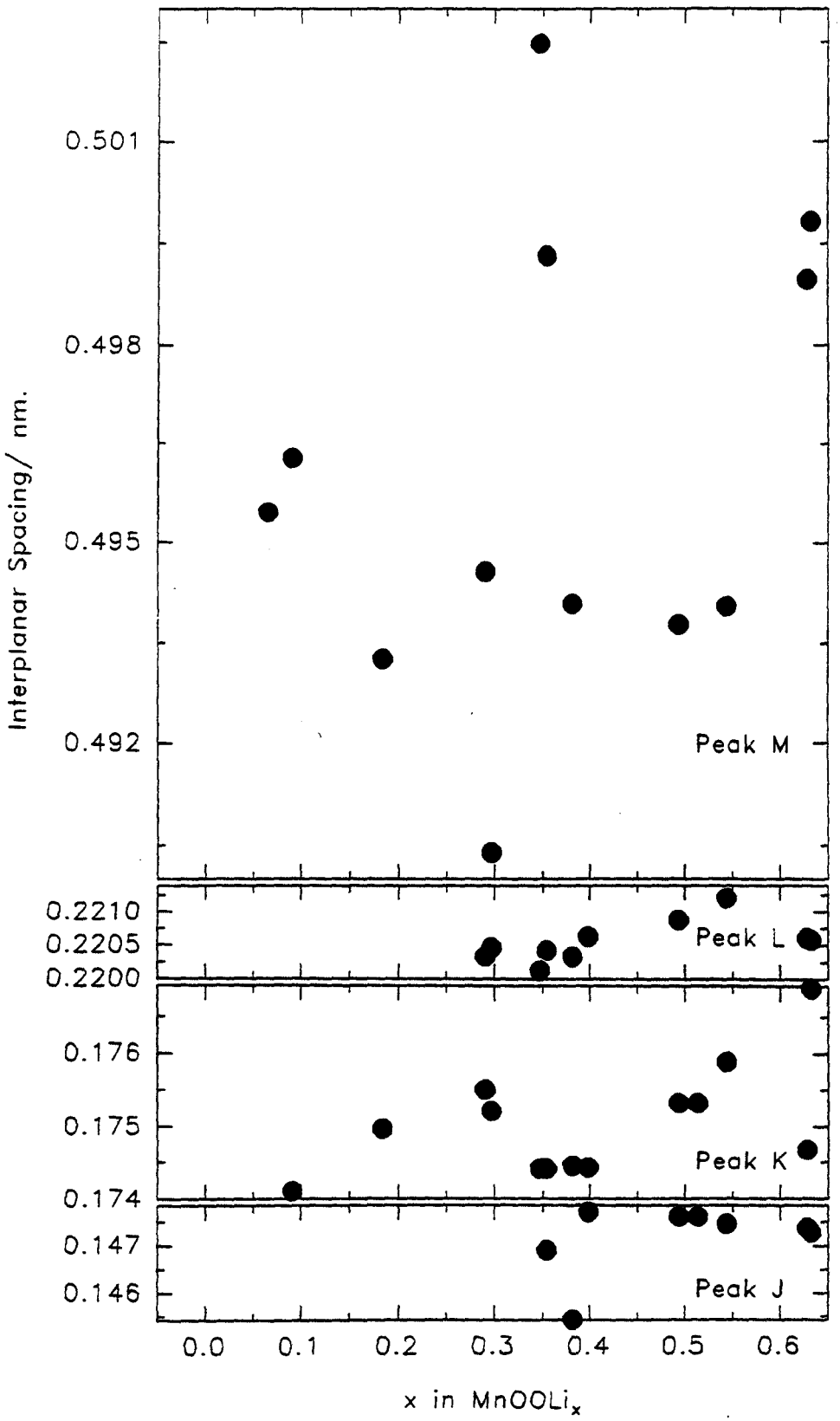


***Figure 6.43*** : Interplanar spacing against Li insertion level for peaks J,K,L and M: CMD heat-treated at 400°C.

## 6.4 Determination of homogeneity/heterogeneity in Li-inserted compounds

### *6.4.1 EMD heat-treated at 200, 300 and 400°C*

The purpose of this section is to determine whether the insertion of Li into $MnO_2$ occurs in a homogeneous or heterogeneous fashion using the powder XRD data. The method developed in section 4.5 for H insertion into EMD is used here. In the literature there has been disagreement over this question. Nardi (1985) found that there were three different stages in the insertion of Li into $MnO_2$. The first 10% of the discharge was a homogeneous reaction. The next step was a heterogeneous or two-phase reaction and this occurred in the region $Li_xMnO_2$ ($0.1 \leq x \leq 0.4$). The final stage of the reaction was a homogeneous one with $x > 0.4$ in $Li_xMnO_2$. The results of Nardi were based on the open-circuit voltage recovery curves of $Li/MnO_2$ cells at various depths of discharge. The open-circuit voltage profile of a $Li/MnO_2$ cell showed three distinct stages to a composition $LiMnO_2$ with interruptions in the profile at $x \approx 0.3$ and $x \approx 0.9$ as shown by Thackeray *et al.* (1993) and Zachau-Christiansen *et al.* (1994). The work of Ohzuku *et al.* (1989&1990a) was concerned with the electrochemical discharge of an EMD heat-treated at temperatures between 250-450°C. They found that the first part of the reaction was heterogeneous and in the range $Li_xMnO_2$ ($0.3 \leq x \leq 0.9$) the reaction proceeded in a homogeneous phase.

Returning to the question posed in the above paragraph it can be seen from figure 6.44 that the chemical insertion of Li into $MnO_2$ is not a heterogeneous reaction in the range $Li_xMnO_2$ ($0.0 \leq x \leq 0.81$) for an EMD heat-treated at 400°C. The agreement between the simulated and experimental $MnOOLi_{0.384}$ is not as good as in the equivalent H insertion process given in figure 4.51 (this reduction was considered to be heterogeneous from $MnOOH_{0.11}$-$MnOOH_{0.932}$). Examination of figure 6.45, however, shows that the reaction is heterogeneous in the range $Li_xMnO_2$ ($0.312 \leq x \leq 0.81$), the agreement between the experimental and simulated $MnOOLi_{0.563}$ spectra are similar to that given in figure 4.51 for the heterogeneous reduction of $\beta$-$MnO_2$ – $\gamma$-MnOOH. Figure 6.46 shows the case for EMD heat-treated at 300°C and it can be seen that the reaction is not heterogeneous in the range $Li_xMnO_2$ ($0.00 \leq x \leq 0.56$). Figure 6.47 shows that it is heterogeneous after $Li_{0.326}MnO_2$, this is similar to the result of

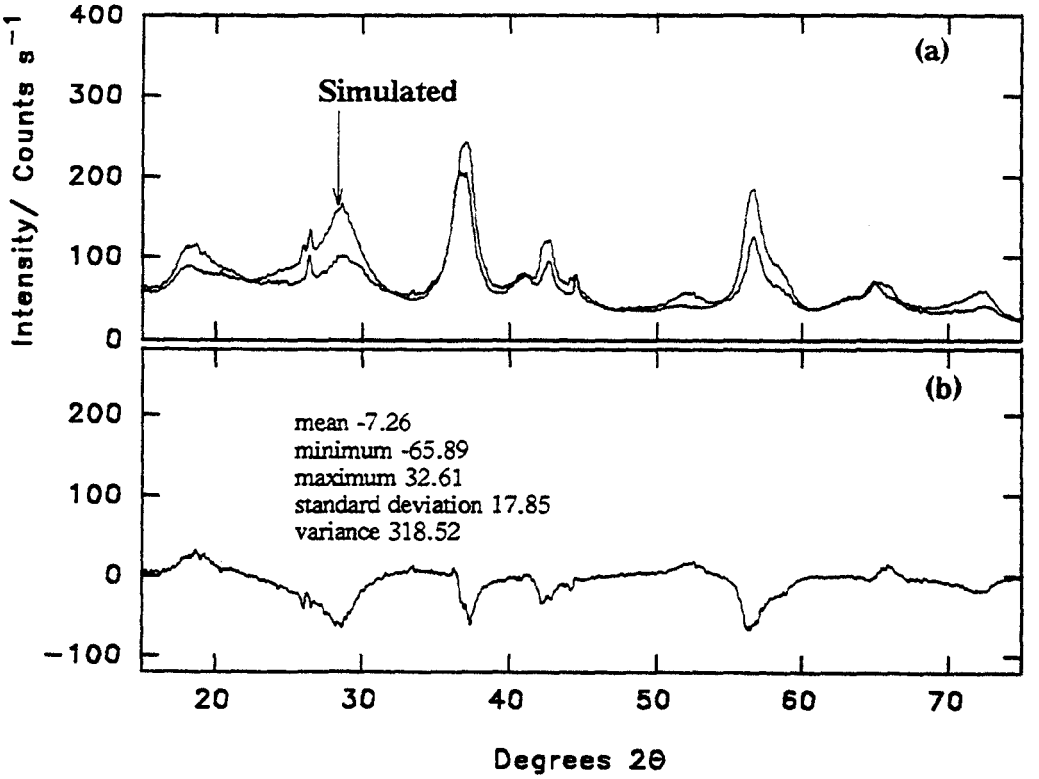


*Figure 6.44* : Comparison of (a) experimental XRD pattern of $MnOOLi_{0.384}$ with a mixture of 52% $MnOOLi_{0.00}$ and 48% $MnOOLi_{0.81}$ and (b) experimental-simulated difference spectrum; EMD heat-treated at 400°C; reduced with butyl-lithium.

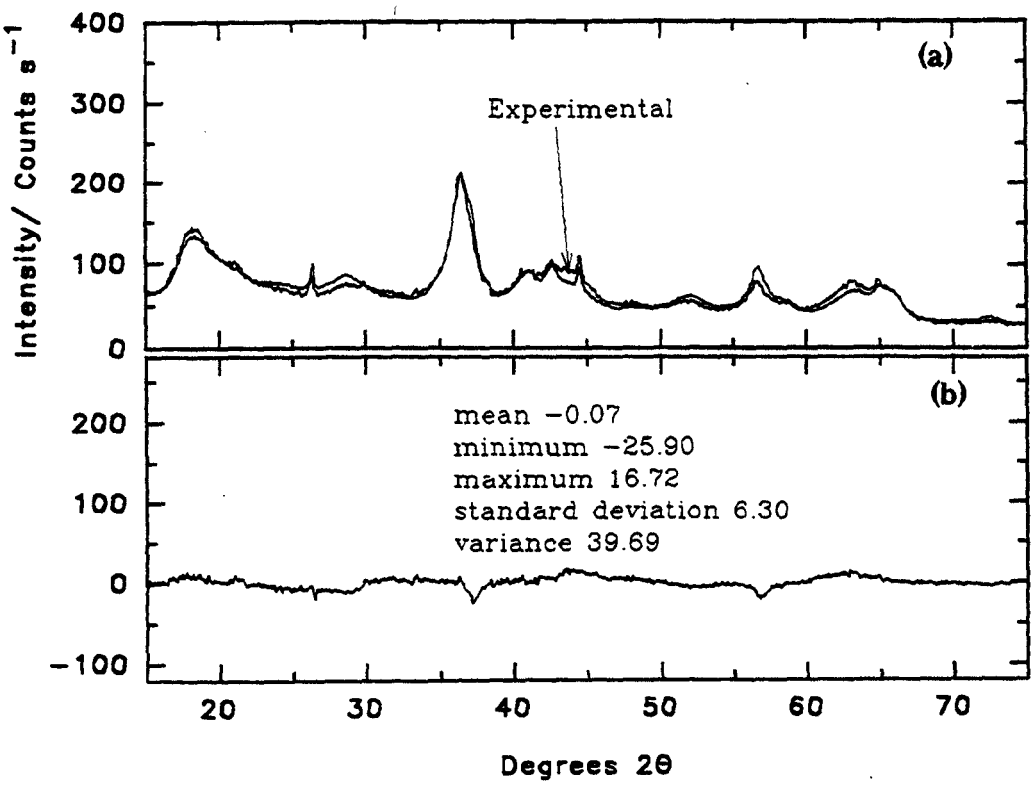


*Figure 6.45*: Comparison of (a) experimental $MnOOLi_{0.563}$ with a mixture of 49.5% $MnOOLi_{0.312}$ and 50.5% $MnOOLi_{0.81}$ (b) experimental-simulated difference spectrum; EMD heat-treated at 400°C; reduced with butyl-lithium.

the EMD material heat-treated at 400°C. Finally if the same analysis is applied to an EMD heat-treated at 200°C then figure 6.49 demonstrates that heterogeneity occurs after $Li_{0.313}MnO_2$. From the results presented so far an important difference has already been established in the H and Li insertion process. In chapter 4 it was shown that at 200°C H insertion (with propan-2-ol) occurred homogeneously with the end product being $\delta$-MnOOH and at 400°C a heterogeneous reaction took place leading to $\gamma$-MnOOH. In contrast, with Li insertion, the reaction is heterogeneous after about $MnOOLi_{0.3}$ regardless of the initial heat-treatment temperature. This also coincides with the appearance of the new peaks labelled J, K, L and M as shown in figures 6.7, 6.14 and 6.21. The data presented here support the work of Zachau-Christiansen *et al.* (1994) whereby in the electrochemical insertion of Li into ramsdellite and pyrolusite in the region $x > 0.35$ in $MnOOLi_x$ the potentials were similar although the discharge of ramsdellite proceeded at a higher potential until $MnOOLi_{0.3}$. It had already been established that the higher the heat treatment temperature of $MnO_2$ the lower the initial potential of the cell see, for example, figure 2 in the work of Ikeda *et al.* (1975) and Ohzuku *et al.* (1990a).

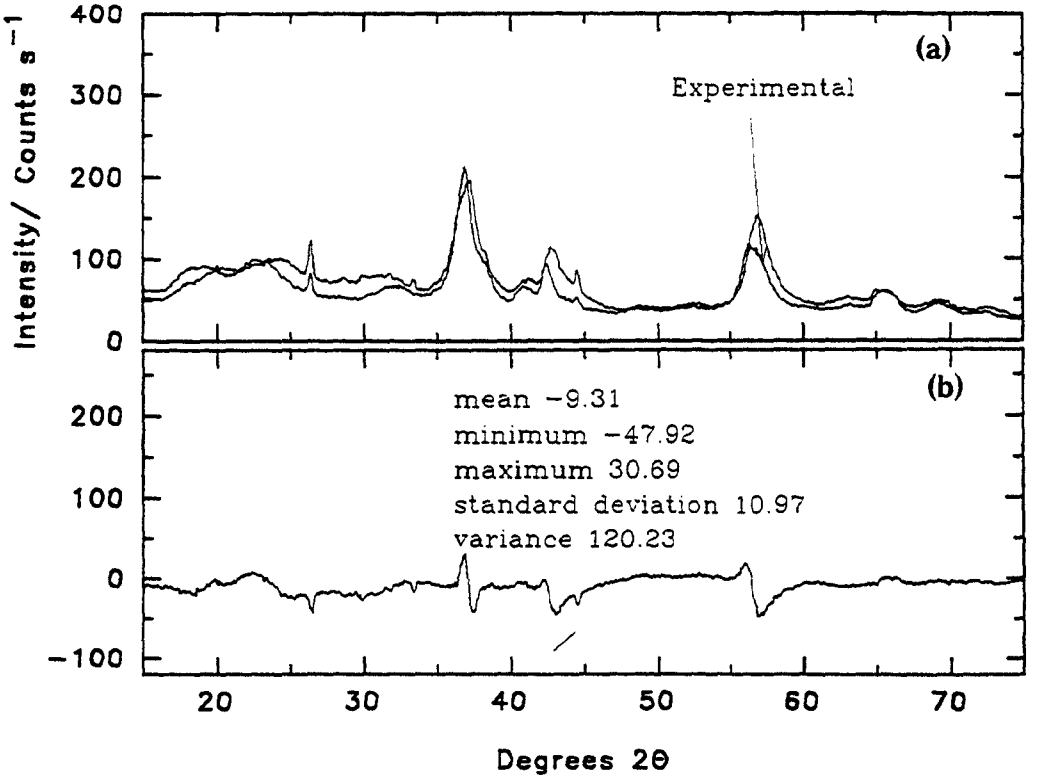


*Figure 6.46* : Comparison of (a) experimental XRD pattern of $MnOOLi_{0.332}$ with a mixture of 41% $MnOOLi_{0.00}$ and 59% $MnOOLi_{0.56}$ and (b) experimental-simulated difference spectrum; EMD heat-treated at 300°C; reduced with butyl-lithium.

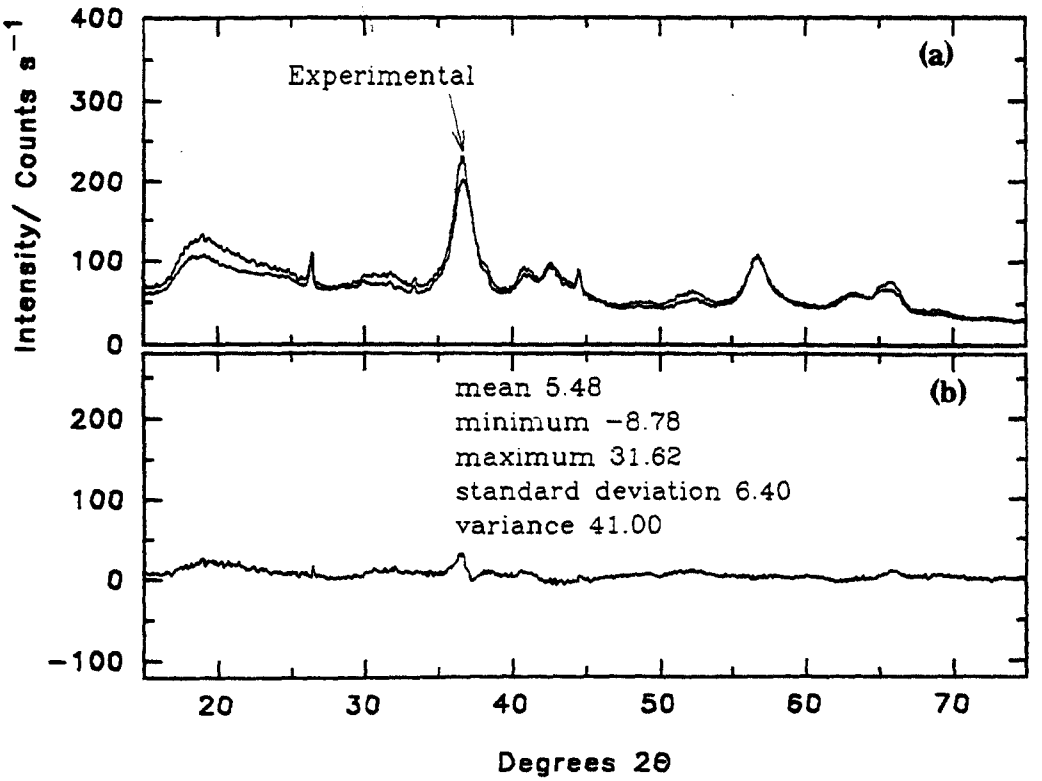


*Figure 6.47* : Comparison of (a) experimental XRD pattern of $MnOOLi_{0.452}$ with a mixture of 46% $MnOOLi_{0.326}$ and 54% $MnOOLi_{0.560}$ and (b) experimental-simulated difference spectrum; EMD heat-treated at 300°C; reduced with butyl-lithium.

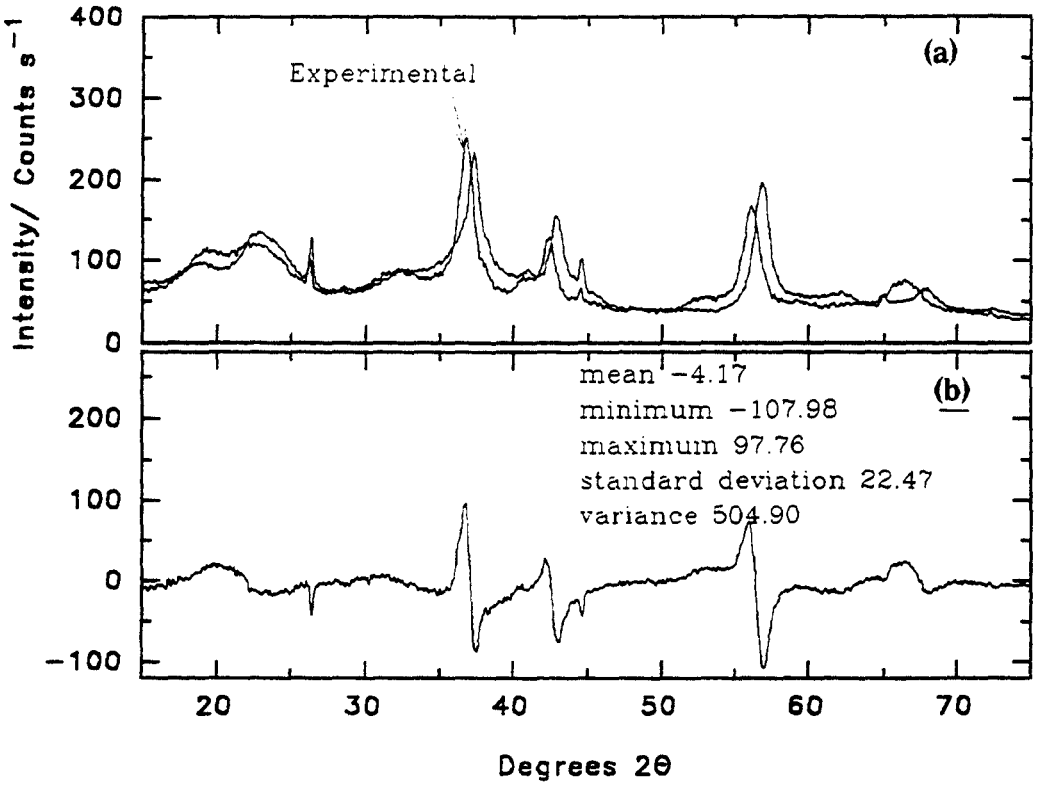


*Figure 6.48*: Comparison of (a) experimental XRD pattern of $MnOOLi_{0.313}$ with a mixture of 41% $MnOOLi_{0.00}$ and 59% $MnOOLi_{0.534}$ and (b) experimental-simulated difference spectrum; EMD heat-treated at 200°C; reduced with butyl-lithium.

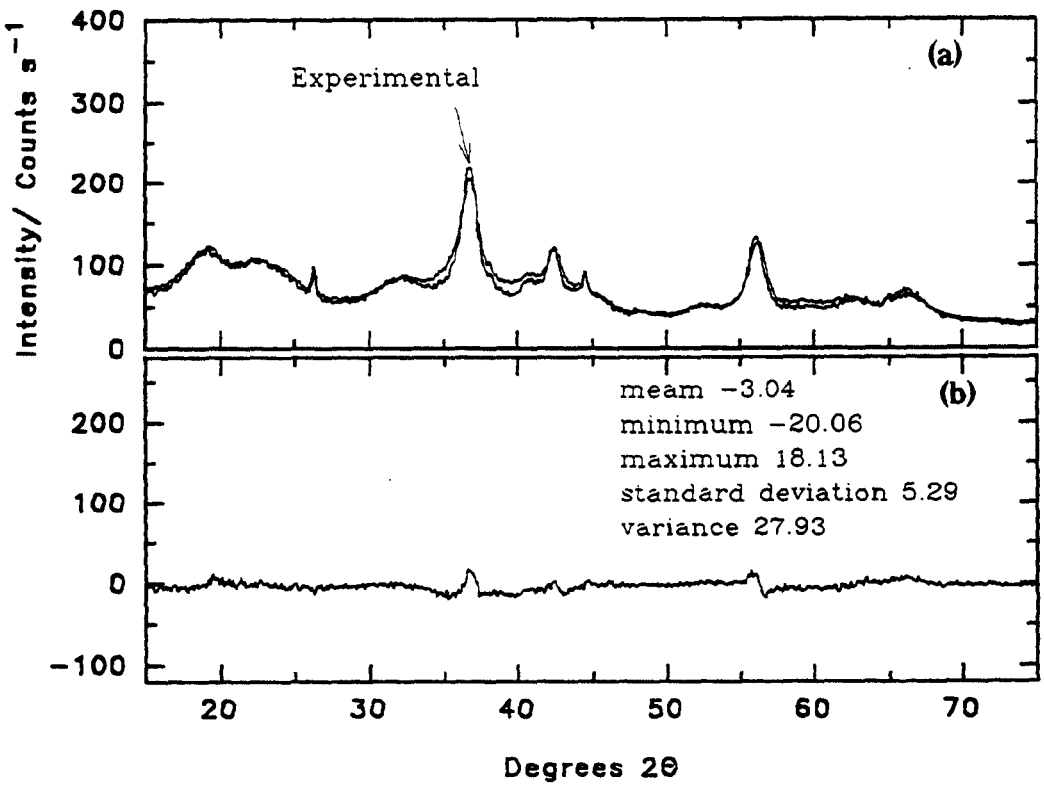


*Figure 6.49*: Comparison of (a) experimental XRD pattern of $MnOOLi_{0.424}$ with a mixture of 50% $MnOOLi_{0.313}$ and 50% $MnOOLi_{0.534}$ and (b) experimental-simulated difference spectrum; EMD heat-treated at 200°C; reduced with butyl-lithium.

*6.4.2 CMD heat-treated at 200, 300 and 400°C*

Examination of homogeneity/heterogeneity in the CMD Li inserted materials reveals that the results are sinilar to EMD. This is shown in figures 6.50-6.52. A heterogeneous reaction was observed after $MnOOLi_{0.35}$ for CMD heat-treated at 300 and 400°C and at $MnOOLi_{0.41}$ for heat-treatment at 200°C. The appearance of new peaks J, K, L and M as shown in figures 6.29, 6.36 and 6.43 occur at about $MnOOLi_{0.3}$. The mechanism of Li insertion is discussed in more detail in the next section.

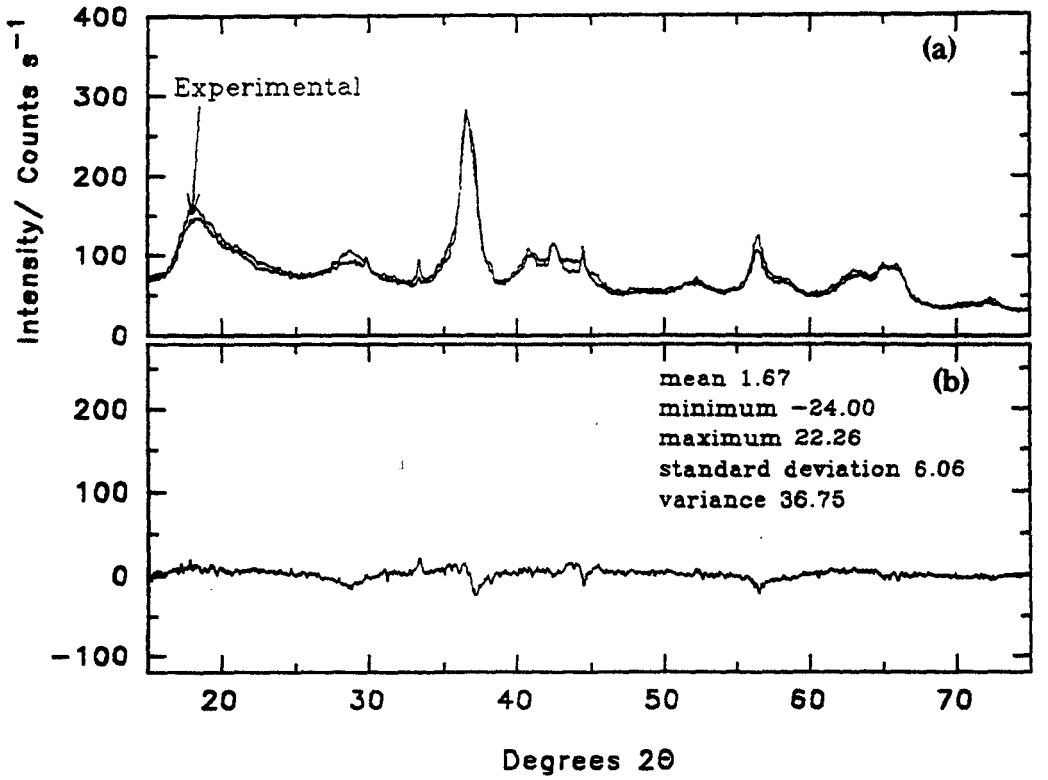


***Figure 6.50*** : Comparison of (a) experimental XRD pattern of $MnOOLi_{0.494}$ with a mixture of 50% $MnOOLi_{0.355}$ and 50% $MnOOLi_{0.633}$ and (b) experimental-simulated difference spectrum; CMD heat-treated at 400°C; reduced with butyl-lithium.

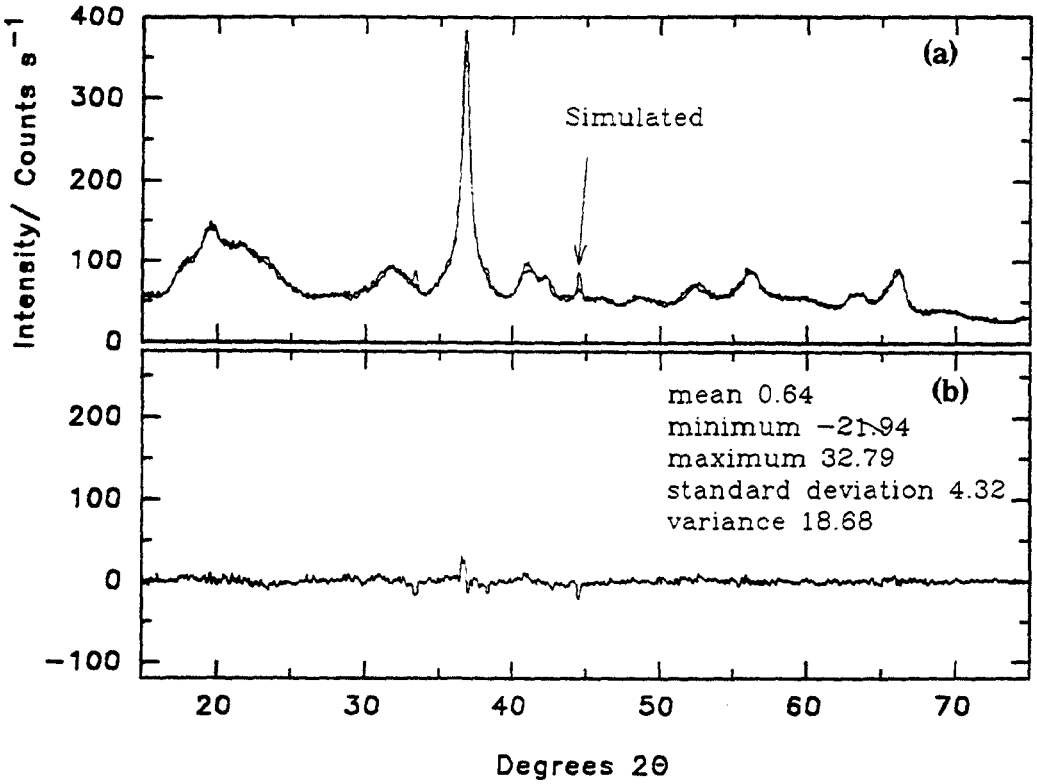


*Figure 6.51*: Comparison of (a) experimental XRD pattern of $MnOOLi_{0.490}$ with a mixture of 58% $MnOOLi_{0.350}$ and 42% $MnOOLi_{0.685}$ and (b) experimental-simulated difference spectrum; CMD heat-treated at 300°C; reduced with butyl-lithium.

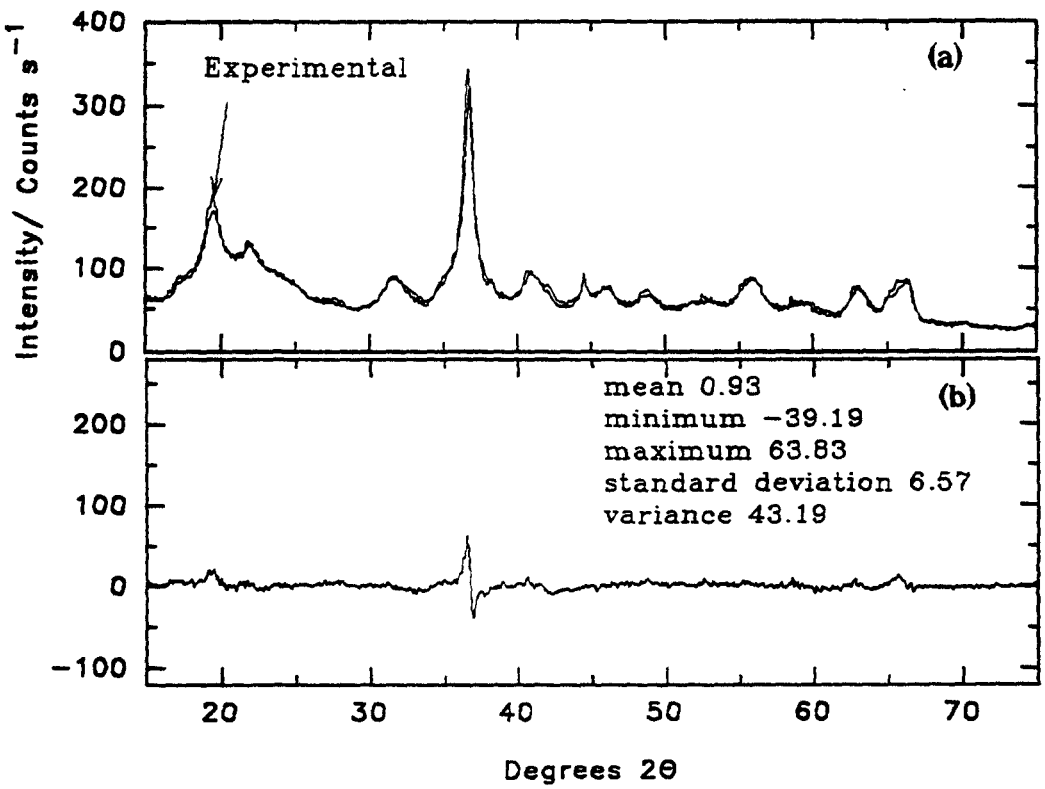


*Figure 6.52*: Comparison of (a) experimental XRD pattern of $MnOOLi_{0.520}$ with a mixture of 67% $MnOOLi_{0.410}$ and 33% $MnOOLi_{0.750}$ and (b) experimental-simulated difference spectrum; CMD heat-treated at 200°C; reduced with butyl-lithium.

## 6.5 Interpretation of the Li inserted x-ray diffraction patterns and comparison with H inserted compounds.

At this stage it is worthwhile reviewing the current literature regarding Li insertion into $MnO_2$ (this has previously been discussed in section 1.71). As far as structural data is concerned the most worthwhile studies have been carried out by Ohzuku *et al.* (1989, 1990a and 1991) and Thackeray *et al.* (1993). Although a number of other publications have dealt with discharge characteristics of Li/$MnO_2$ cells (see for example Ilchev 1989a, Voinov 1981 and Sleigh *et al.* 1990 and 1991). In this work concern is with structural information hence interest is focused on the work of Ohzuku *et al.* and Thackeray *et al.*. Table 6.1 compares the x-ray data, found in the literature, on the most reduced Li inserted materials with those of the ramsdellite-groutite crystal structures. The Li inserted materials in table 6.1 were obtained by different methods. Ohzuku electrochemically discharged an EMD that had been heat-treated at 400°C whereas Thackeray used a chemical method with LiI in acetonitrile from a ramsdellite-$MnO_2$ that had been prepared from acid treatment of the spinels $LiMn_2O_4$ and $LiMn_2O_9$. The synthetic ramsdellite had $P_r$ 0.27 and Tw 25% according to Chabre and Pannetier (1995). Natural ramsdellite used by Bystrom (1949) had $P_r$ and Tw 0%. MacLean *et al.* (1995) also prepared a synthetic ramsdellite (using a method based on Thackeray) with $P_r$ 0.20 and Tw 20%.

*Table 6.1*: Comparison of the lattice parameters of $Li_{0.9}MnO_2$ with ramsdellite and groutite.

| | Ohzuku *et al.* (1989) | Thackeray *et al.* (1993) | Ramsdellite[§] | Groutite[¶] |
|---|---|---|---|---|
| a (Å) | 10.27 | 9.910 | 9.27 | 10.699 |
| b (Å) | 4.93 | 5.208 | 4.533 | 4.565 |
| c (Å) | 2.85 | 2.812 | 2.86 | 2.852 |
| Unit cell volume (Å$^3$) | 144.3 | 145.1 | 120.4 | 139.24 |

[§] Bystrom (1949)
[¶] Dent Glasser *et al.* (1968).

The lattice parameters of the phase formed after $MnOOLi_{0.3}$ have been calculated using the method given in section 3.8. The Miller indices used for the calculation are shown in figures 6.53 and 6.54. The values of the lattice parameters are given in table 6.2 together with the standard error.

*Table 6.2*: Lattice parameters of the heterogeneous phase formed after $MnOOLi_{0.3}$.

| Material | Heat treatment temperature/°C | a(Å) | b(Å) | c(Å) | Unit cell volume (Å$^3$) |
|---|---|---|---|---|---|
| EMD | 400 | 10.387±0.017 | 5.109±0.022 | 2.764±0.005 | 146.69±0.53 |
| EMD | 300 | 10.437±0.017 | 4.998±0.039 | 2.766±0.003 | 144.28±1.14 |
| EMD | 200 | 10.528±0.024 | 5.067±0.057 | 2.746±0.008 | 146.47±1.60 |
| CMD | 400 | 10.421±0.016 | 5.160±0.022 | 2.739±0.005 | 147.28±0.69 |
| CMD | 300 | 10.406±0.008 | 4.828±0.018 | 2.773±0.003 | 139.33±0.48 |
| CMD | 200 | 10.425±0.008 | 4.951±0.035 | 2.779±0.002 | 143.46±1.05 |

The crystal structure of the electrochemically inserted MnOOLi reduction products have been discussed Ohzuku *et al.* (1990a). He stated that "the deep discharge products have almost the same crystal structure regardless of the EMD used". It was further discussed that the materials had the same diffraction lines in the region 30-75°2$\theta$ but were different between 15-30°2$\theta$. This is also observed in this work for the peak at 20°$\theta$ (figures 6.53 and 6.54). Possible structures of the unit cell were discussed based upon models of the ramsdellite-type structure having a [1x2]-tunnel structure and an intergrowth of [1x1]- and [1x3]-domains. This led to the conclusions that "visual inspection of the line shapes suggest that a [1x2]-structure predominates in the $Li_xMnO_2$ matrix" (EMD heat-treated at 250°) and of EMD heat-treated at 400°C "visual inspection of line shapes suggests a [1x3]- structure predominates in the $LiMnO_2$ matrix". In other words the crystal structure of the fully Li-inserted materials differ only in the arrangement of the $MnO_6$ octahedra. It is worth noting that in the work of MacLean (1993) the existence of triple chains of $MnO_6$ octahedra could not account for the features of the XRD patterns of $\gamma$-$MnO_2$'s. Therefore some doubt must be cast over the assertion that triple chains of $MnO_6$ octahedra predominate in the fully Li-inserted EMD material heat-treated at 400°C. Of course, the work of Ohzuku was done prior to the development of the comprehensive model developed by Chabre and Pannetier (1995).

Comparison of the lattice parameters for Li-inserted EMD (this work) in table 6.2 with the data in table 6.1 suggests reasonable agreement in the three sets of work. Exact agreement is highly improbable due to the crystal structure of $MnO_2$ and the fact that different $MnO_2$'s were used. The main difference is the assertion by Ohzuku of a homogeneous reaction in the range $MnOOLi_x(0.3 \leq x \leq 0.9)$ whereas in this work a heterogeneous reaction is

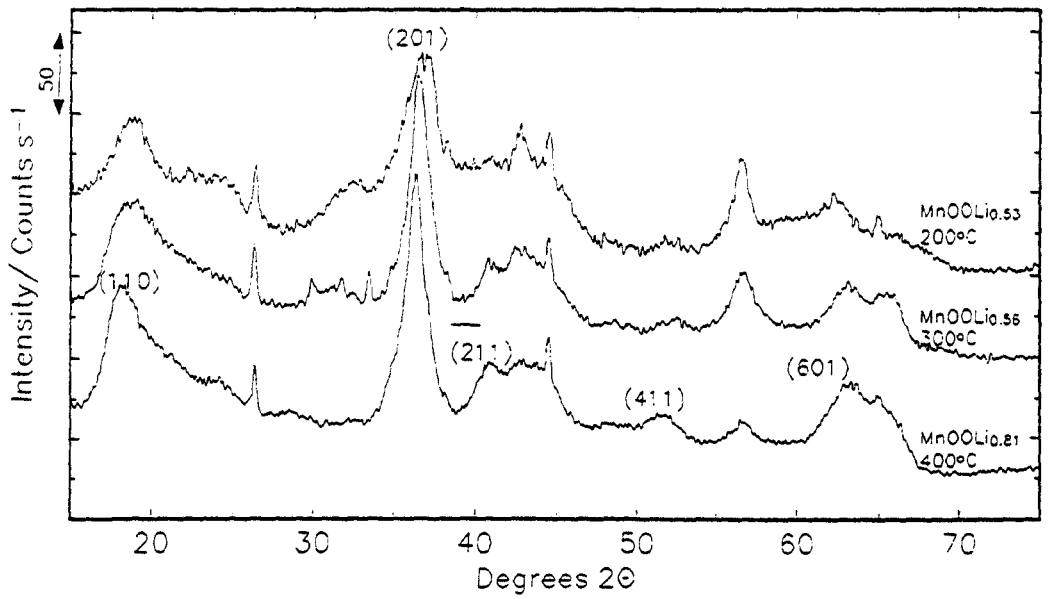


***Figure 6.53***: X-ray diffraction patterns of the most reduced Li inserted EMD materials with the Miller indices used to calculate the orthorhombic unit cell parameters (200 and 300°C patterns are displaced for clarity).

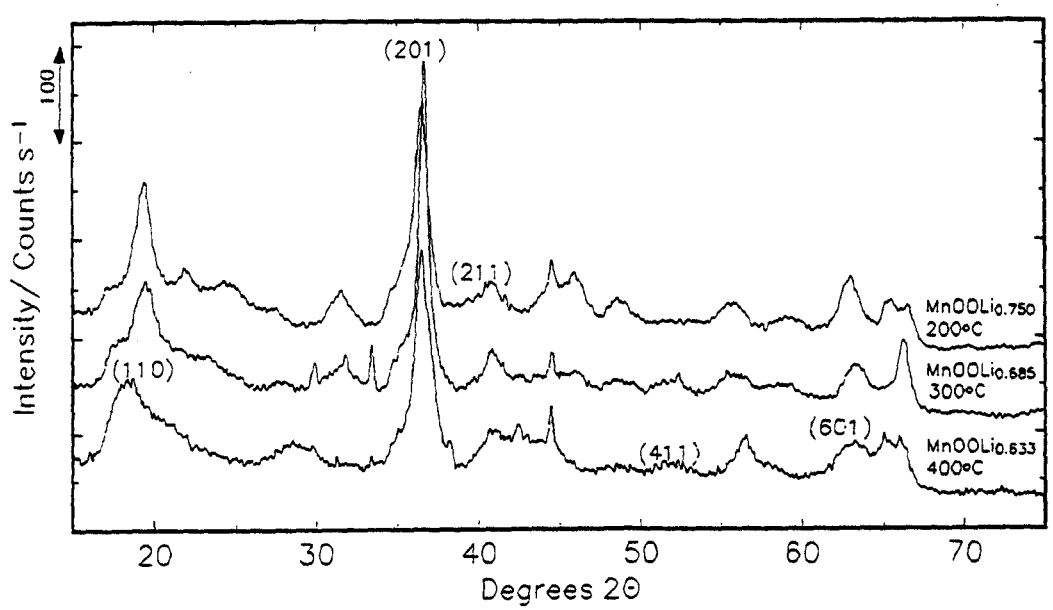


***Figure 6.54***: X-ray diffraction patterns of the most reduced Li inserted CMD materials with the Miller indices used to calculate the orthorhombic unit cell parameters (200 and 300°C patterns are displaced for clarity).

observed in the range $MnOOLi_x(0.3 \leq x \leq 0.8)$. Even though the results were obtained by different means, one electrochemical and the other chemical it has been shown that the crystal structure of the reduction products are similar. A plausible explanation could be that the chemical reduction was carried out at too fast a rate, in a manner similar to that observed with hydrazine hydrate in chapter 4. Although the data has not been shown here, a number of Li-inserted samples were prepared at a slower rate over an eight week period and there were no discernible differences in their XRD patterns.

The mechanism proposed by Thackeray *et al.* (1993) for Li insertion into synthetic ramsdellite is the one favoured here. It essentially consists of two stages: in the first one ($MnOOLi_x$ $0 \leq x \leq 0.3$), lithium is inserted into the hexagonally-close-packed $MnO_2$ structure and in the second stage $0.3 \leq x \leq 0.9$, Li insertion causes a shear of the [1x2] ramsdellite blocks and a buckling of the structure in response to an increase in electrostatic interactions between lithium and manganese ions in face-shared octahedra. The shear transforms the structure such that the layering of the oxygens is a combination of hexagonal-close-packing and cubic-close-packing.

Comparison of the most reduced Li-inserted compounds with their H-inserted counterparts are shown in figures 6.55 and 6.56 for EMD and CMD respectively. Obviously some differences would be expected with H and Li insertion. Steric considerations suggest that the $MnO_2$ lattice does not need to expand to accomodate H whereas it must expand for Li insertion. The octahedral and tetrahedral holes in $MnO_2$ can accomodate ions of 0.58 and 0.32Å (Jaffe 1988), whereas the ionic radius of $Li^+$ is 0.6Å. The fundamental difference found in this work has been the differing regions of homogeneity/heterogeneity with H insertion into heat-treated $MnO_2$'s whereas with Li insertion there is a critical value ($MnOOLi_{0.3}$ for EMD and $MnOOLi_{0.35}$ for CMD) where a new phase is formed. The question as to whether the Li-inserted materials form a series of intergrowth structures (going from 200-400°C) as has been found with H-insertion has not been resolved. Although this has been mentioned by Ohzuku *et al.* (1990a) in his interpretation of the fully Li-inserted materials. The best way to solve this question would be to prepare Li-inserted ramsdellite and pyrolusite materials and compare those XRD patterns with the fully Li-inserted heat treated

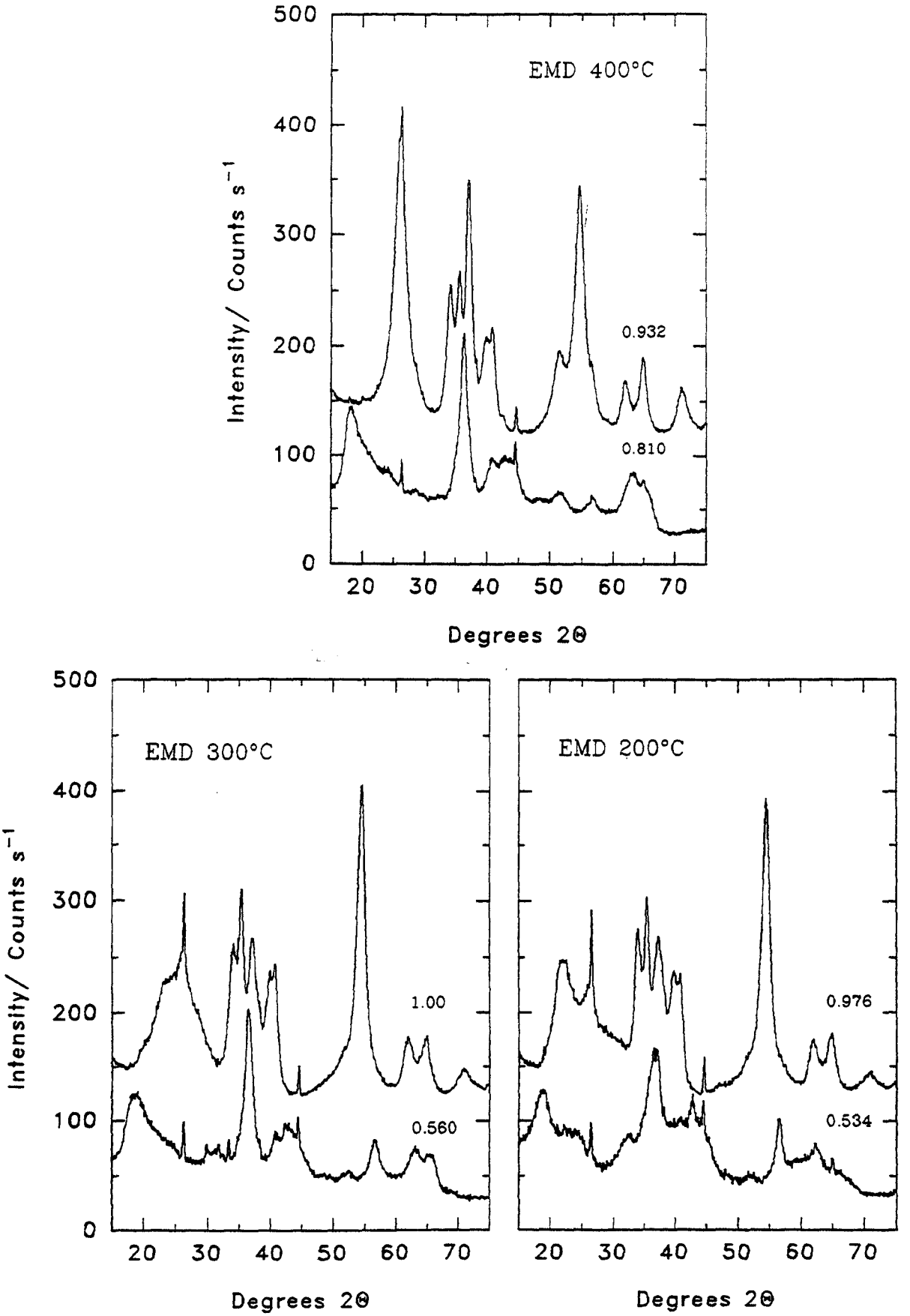


***Figure 6.55*** : Comparison of the EMD XRD patterns for the most reduced Li and H inserted samples (the H inserted patterns are displaced by 100 $Cs^{-1}$ for clarity and the level of H or Li insertion is given above the XRD pattern).

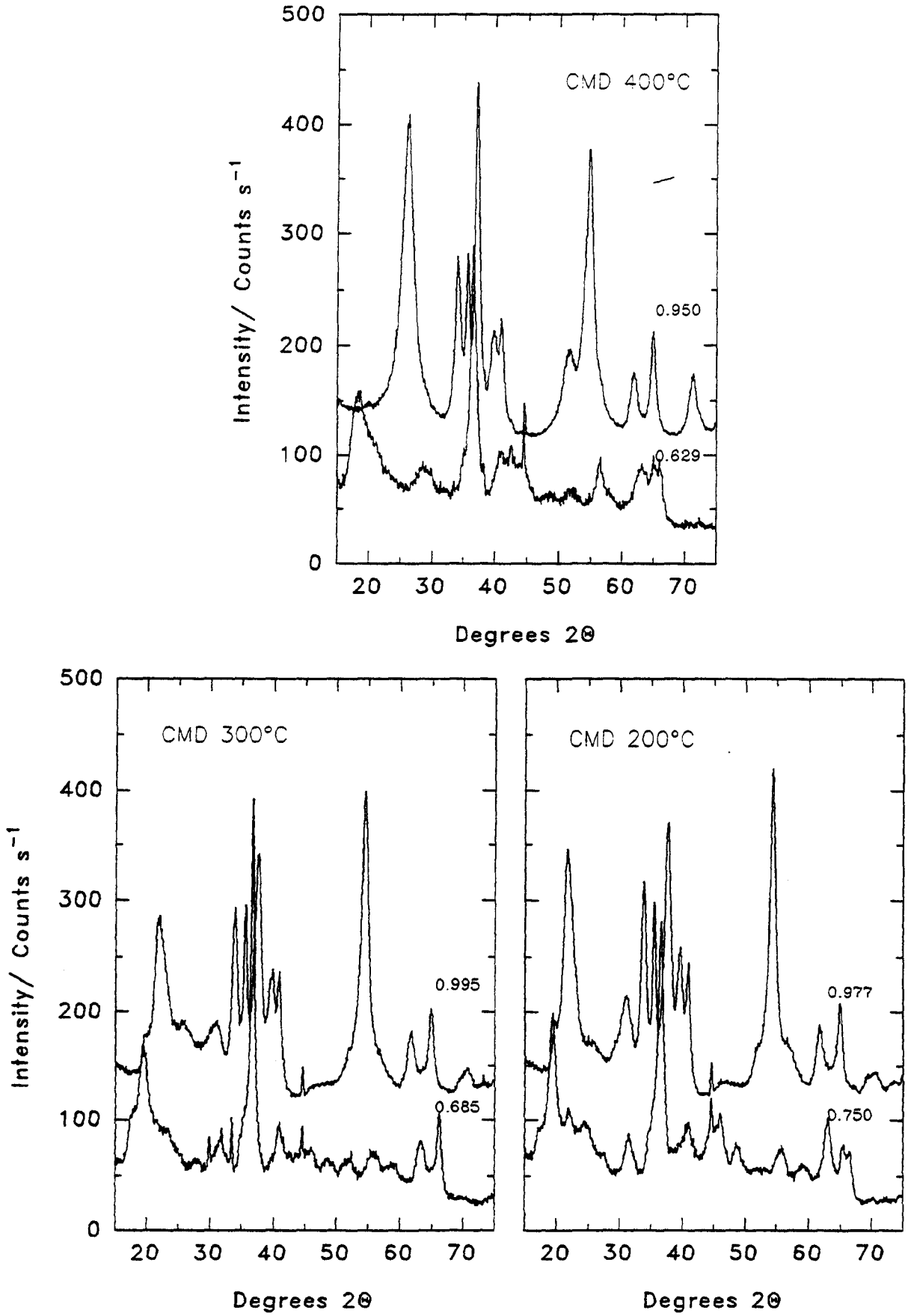


***Figure 6.56*** : Comparison of the CMD XRD patterns for the most reduced Li and H inserted samples (the H inserted patterns are displaced by 100 $Cs^{-1}$ for clarity and the level of H or Li insertion is given above the XRD pattern).

compounds.

## 6.6 Conclusions.

An electrodeposited (R2) and chemical (Faradiser WSLi) $MnO_2$ were heat-treated at 200, 300 and 400°C for 24 hours in air and then a range of Li-inserted compounds were prepared in an argon filled glove-box using n-butyllithium. The resulting compounds were studied by XRD. New peaks appeared in the XRD patterns at low levels of Li insertion. From the results shown in chapters 4 and 5 this seemed indicative of a heterogeneous process. This was confirmed by mixing of the XRD spectra in section 6.4 and it was shown that the reaction was heterogeneous after $MnOOLi_{0.3}$ for EMD and $MnOOLi_{0.35\text{-}0.40}$ for CMD. In contrast to H insertion the onset of heterogeneity was independent of the heat treatment temperature. The X-ray diffraction patterns of the new phase could be indexed to an orthorhombic unit cell. The lattice parameters were calculated and were in reasonable agreement with those found in the literature. Again, in contrast to H insertion, the crystal structure of the most reduced Li-inserted materials seemed to be the same regardless of the initial heat treatment temperature.

# Chapter 7 Statistical Analysis of Powder X-Ray Diffraction and FTIR Spectra.

## 7.1 Statistical analysis of powder X-ray diffraction spectra.

In this chapter some of the X-ray powder diffraction spectra and FTIR spectra that were presented in chapters 4 and 5 are analysed using linear regression. The method can be used to pinpoint possible peak movement in a spectral dataset using the coefficient of determination ($R^2$) as the parameter. It is particularly noteworthy that the method to be presented can be used in other spectroscopic applications. In order to demonstrate the validity of the method the two extremes of behaviour that were observed in sections 4.2.1(i) and 4.2.4 (i) are analysed this is namely the single phase reduction of $\gamma$-$MnO_2$ – $\delta$-MnOOH and the heterogeneous reduction of $\beta$-$MnO_2$ – $\gamma$MnOOH respectively

### *7.1.1 EMD heat-treated at 200°C; propan-2-ol reduction method.*

The data set that was used for the linear regression analysis is shown in Figure 7.1. There were 29 samples from $MnOOH_{0.07}$ – $MnOOH_{0.976}$ and, so that the x (r in $MnOOH_r$) and y (Intensity/ Counts $s^{-1}$) axes had comparable scales, the maximum intensity in the data set was given the value of 1. This was done because in the raw data the intensity would vary from approximately 25 – 425 Counts $s^{-1}$ and r in $MnOOH_r$ varied from 0.07 – 0.976. As mentioned in section 2.7 the samples were scanned from 15 – 75°2Θ at a speed of 0.01°2Θ $s^{-1}$ therefore each pattern consisted of 6000 points. In order to keep the data set to a manageable size the linear regression was performed on the smoothed data files where each pattern consisted of 376 points i.e. every 0.16°2Θ. The regression analyses can be performed easily in a spreadsheet package running on a personal computer. Figure 7.2 shows how the intensity varied with r in $MnOOH_r$ for a range of degree 2Θ values; the magnitude of $R^2$ and the slope of the regression line are also given in the Figure. $R^2$ is called the coefficient of determination and varies from 0 to 1. This is distinct from the normally quoted correlation coefficient r which varies from – 1 to 1. A value of – 1 is given for a perfect negative correlation and, conversely 1 for a perfect positive correlation. The results of the linear regression analyses, from 15-75°2Θ, are shown in

Figure 7.3. The slope of the regression line changes sign (from positive to negative) at 36.56, 41.84, 55.44 and 65.84°2Θ and this corresponds to the mid-point of the reduction range as can be seen from Figure 7.4. Another feature of the analysis is that whenever the slope of the regression line is zero $R^2$ is also zero. This is shown in Figure 7.2 at the values of 28.48 and 45.44°2Θ. This is an unsatisfactory arrangement and means that little useful information can be assimilated from Figure 7.3. To examine why this is the case it is necessary to look closely at how $R^2$ is calculated. Figure 7.5 shows two examples of how $R^2$ is calculated, one where $R^2$ is zero (28.48°2Θ) and the other where $R^2$ is close to one (54.72°2Θ). The top two Figures show how the intensity varies with H insertion and the bottom two Figures how $R^2$ is computed. The two important quantities in calculating $R^2$ are the residual sum of squares (designated RSS) and the total sum of squares (designated SYY). These are defined in equations 7.1 and 7.2, $R^2$ is given in 7.3.

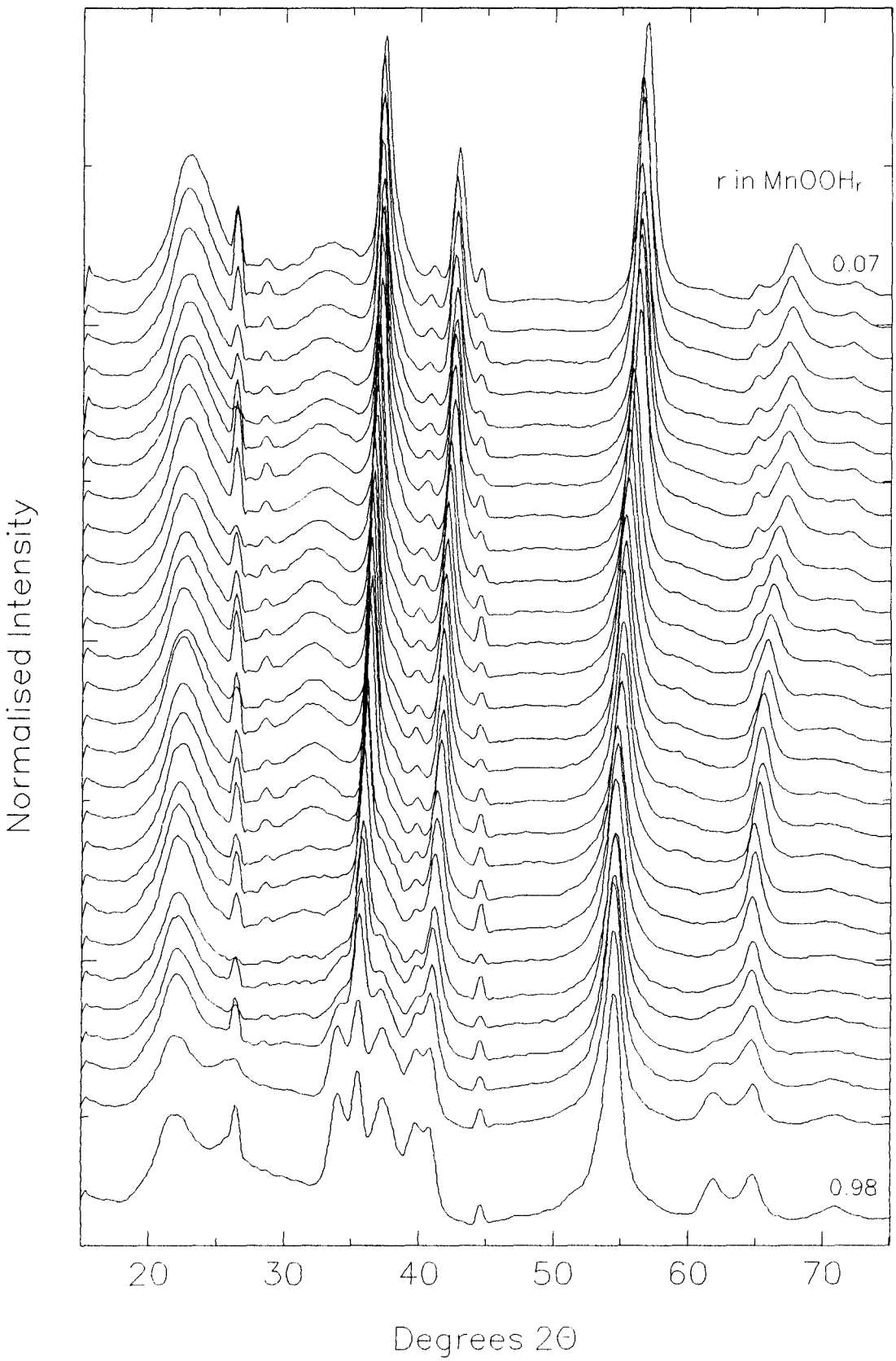


***Figure 7.1***: Dataset that was used for the linear regression analysis: EMD heat-treated at 200°C; propan-2-ol reduction method.

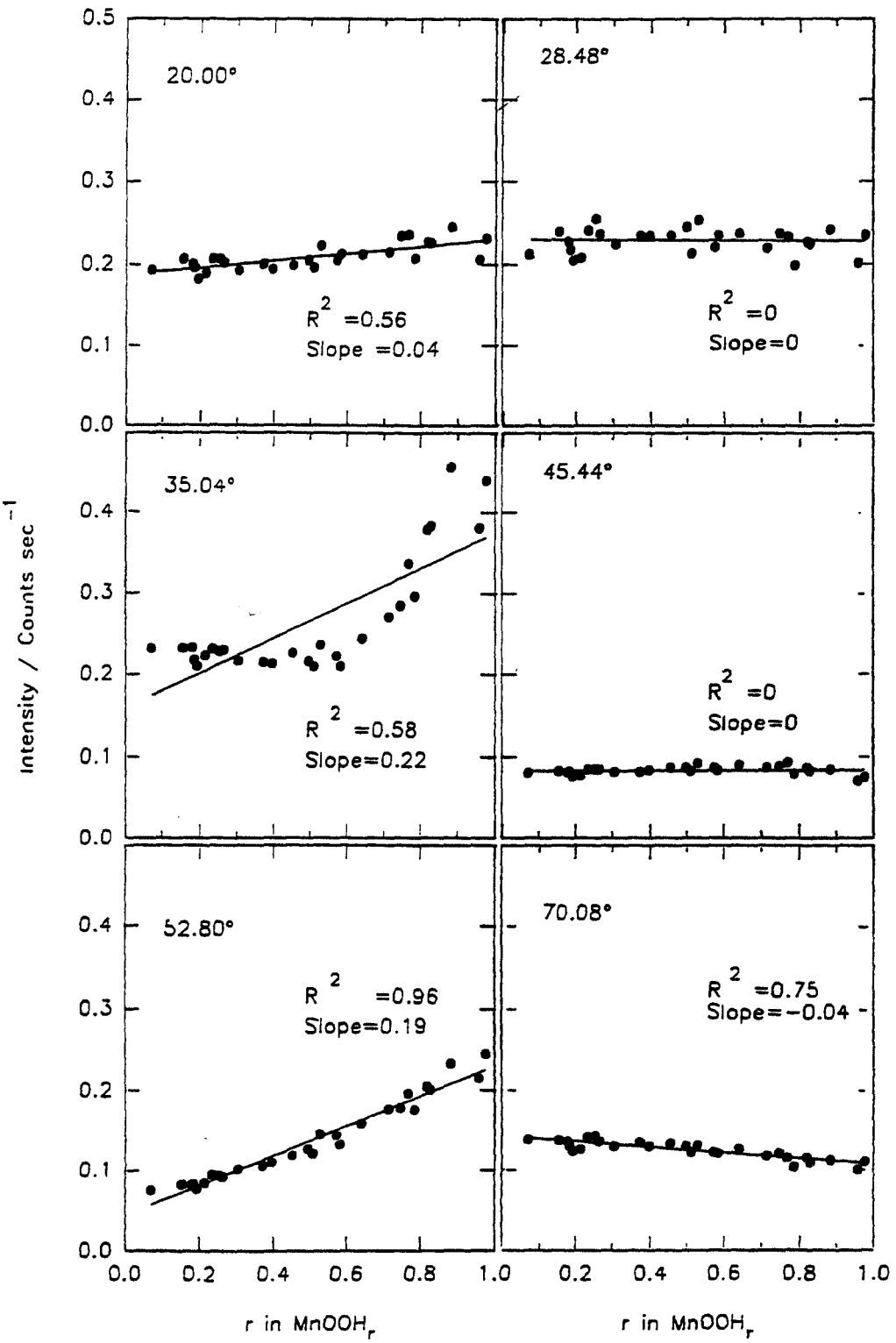


***Figure 7.2*** : Plots of intensity against r in $MnOOH_r$ for a range of Degree 2Θ values (this is given in the top left of each figure): EMD heat-treated at 200°C; propan-2-ol reduction method.

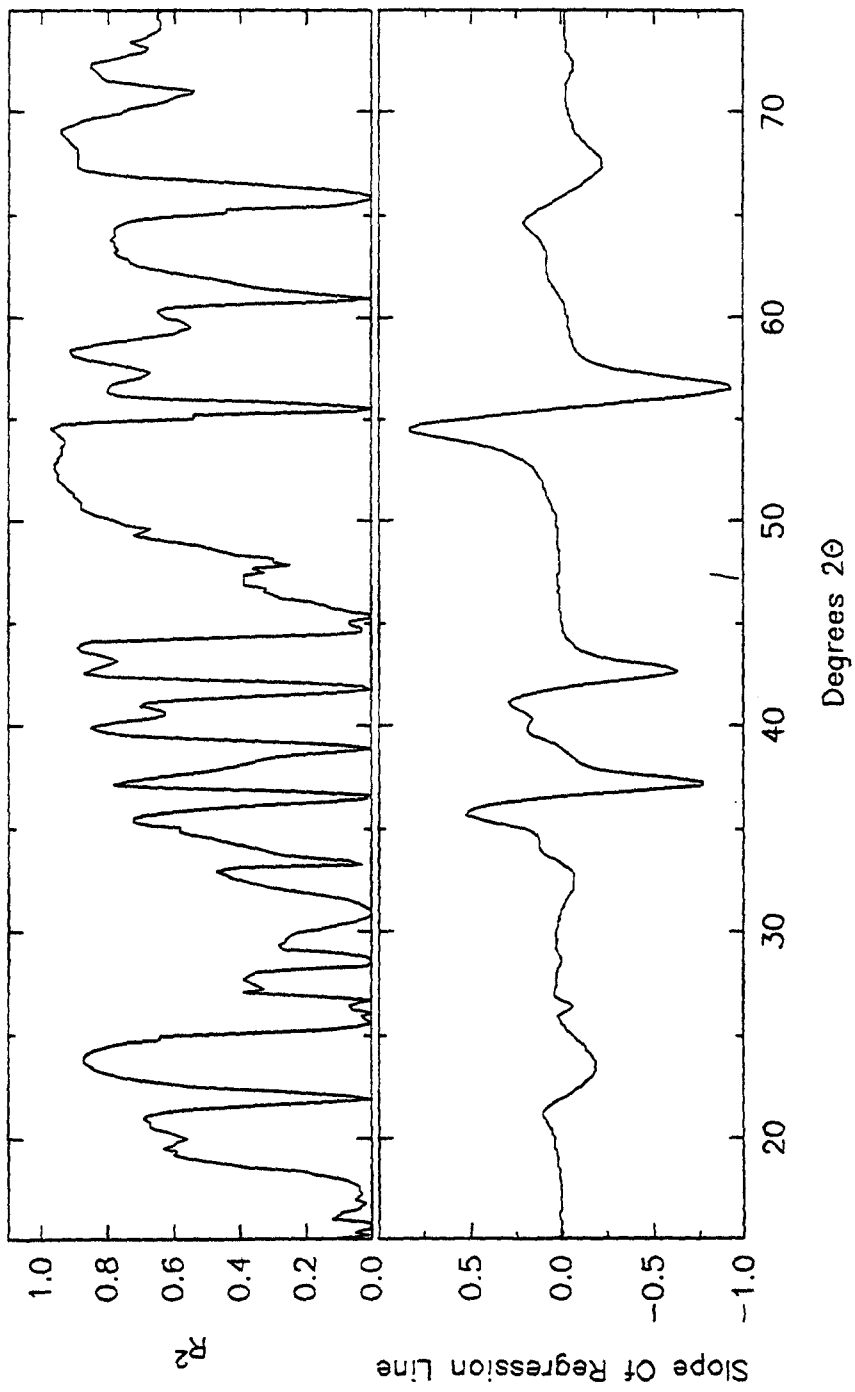


***Figure 7.3*** : Slope of regression line and $R^2$ against Degrees 2Θ; EMD heat-treated At 200°C: propan-2-ol reduction method.

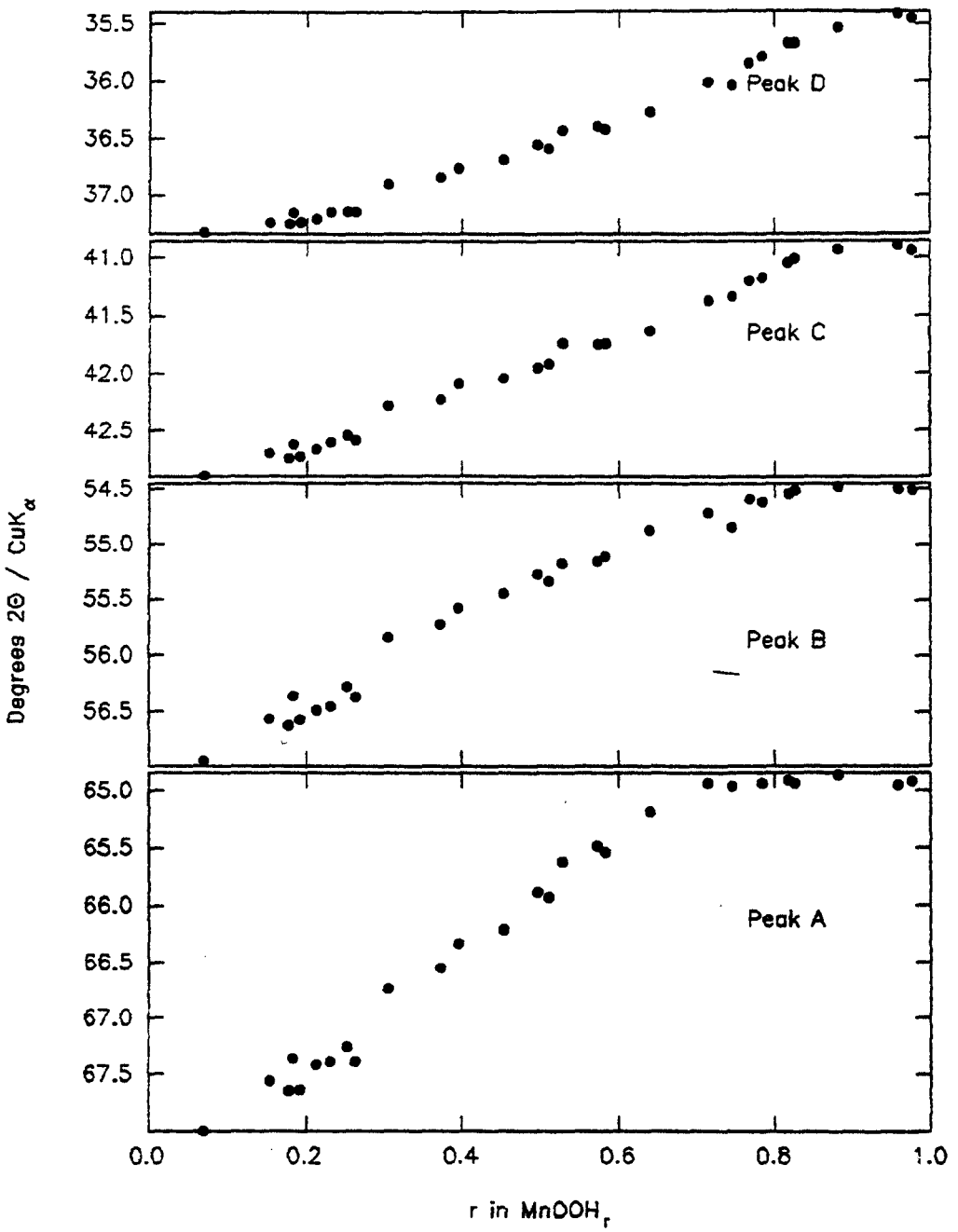


***Figure 7.4*** : Movement of peaks A,B,C and D during the reduction of EMD heat-treated At 200°C; propan-2-ol reduction method.

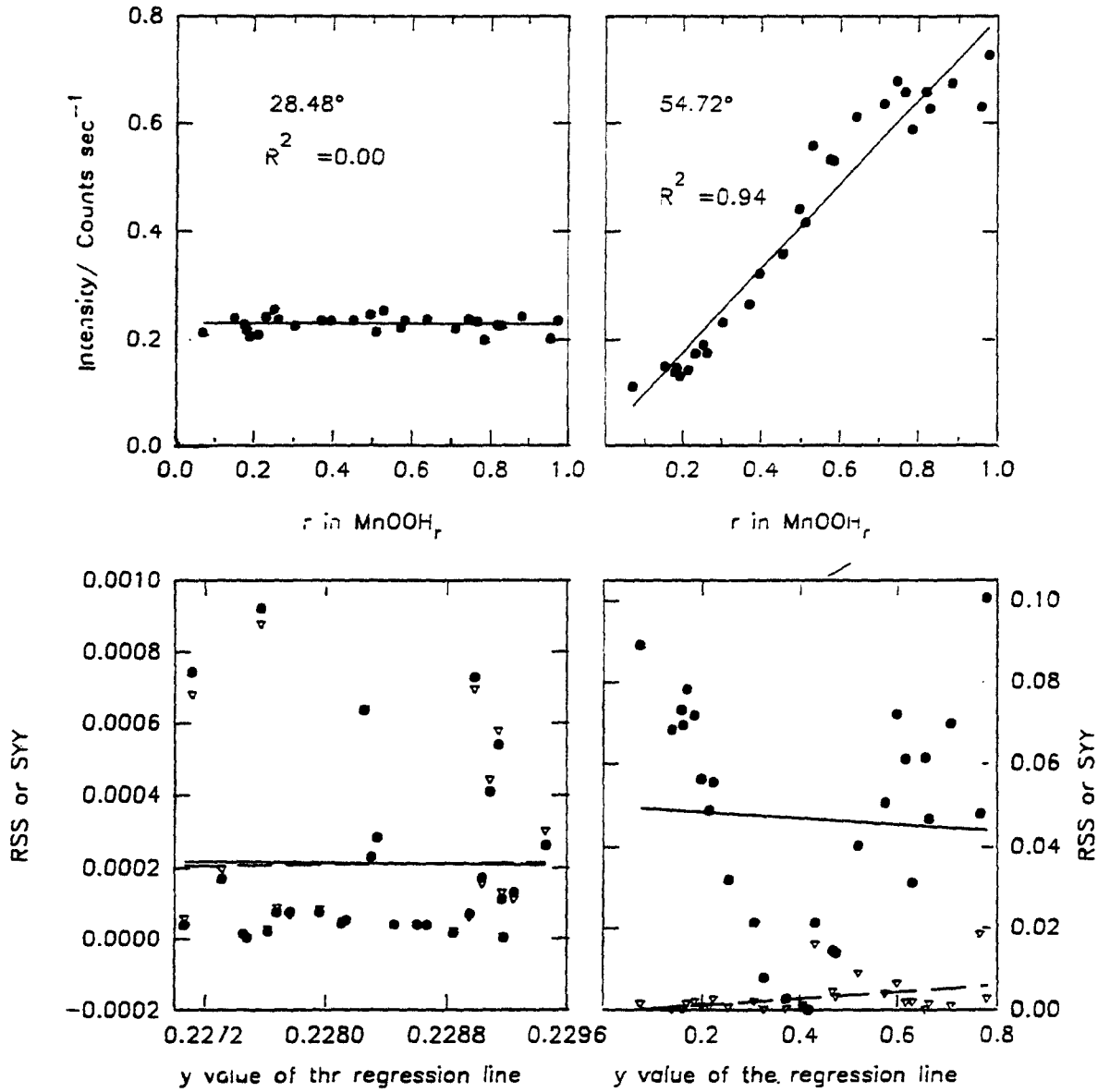


***Figure 7.5*** : An example of how $R^2$ was calculated: EMD heat-treated at 200°C; propan-2-ol reduction method. In the bottom two figures (●)SYY and (▽) RSS.

$$RSS = \sum (y_i - \hat{y})^2 \qquad (7.1)$$

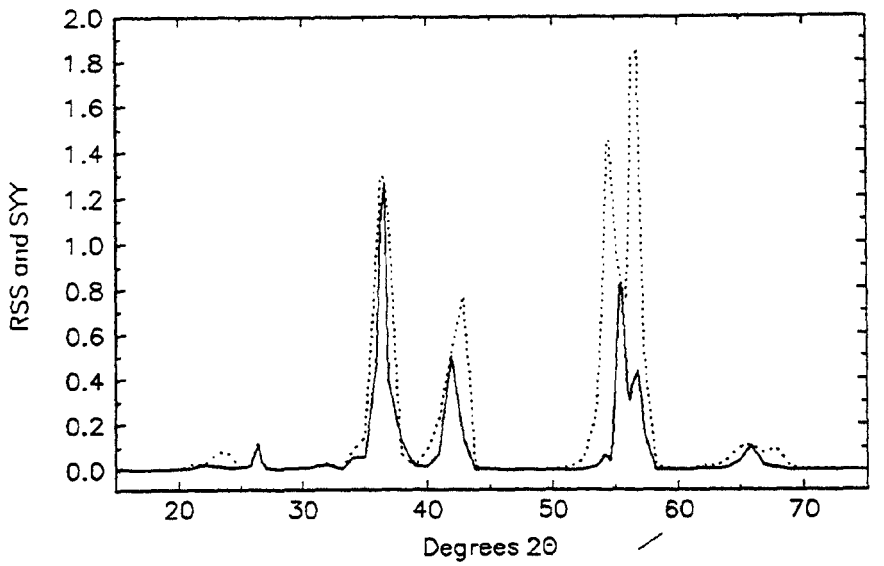


*Figure 7.6* : The summation of the RSS ( – ) or SYY (···) against Degrees 2Θ: EMD heat-treated at 200°C; propan-2-ol reduction method.

$$SYY = \sum (y_i - \bar{y})^2 \qquad (7.2)$$

$$R^2 = 1 - \frac{RSS}{SYY} \qquad (7.3)$$

$y_i$ is the individual value of the intensity, $\bar{y}$ is the average value of the intensity and $\hat{y}$ is y value that is computed in the regression line (a full description of $R^2$ is given by Chatfield 1970 and Weisberg 1980). The RSS is the difference between the experimental y values and those computed in the regression line and SYY is the difference between the experimental y values and the average y experimental value. From equation 7.3 it can be seen that when RSS and SYY have the same value the ratio will be close to one and consequently $R^2$ is then close to zero. This is demonstrated for the calculation of $R^2$ at 28.48°2Θ in figure 7.5 where SYY and RSS have similar values. Examination of RSS and SYY at 54.72°2Θ in figure 7.5 reveals that SYY is much larger than RSS and so $R^2$ has a higher value. Figure 7.6 shows the summation of RSS and SYY against Degrees 2Θ. In the literature there are numerous papers that are concerned with

the best straight line through a set of points when both variables have uncertainties (see for example Pearson 1901, York 1966, Lybanon 1984 and Reed 1989). This has received attention because in a linear regression analysis the independent variable is assumed to be free of errors and often in an analysis this is not the case. No papers, however, were found which dealt with the dependence of $R^2$ on the slope of the regression line and in the following section a method is presented whereby the data is transformed so that the slope of the regression line is the same throughout the data set.

**Transformation of the data to achieve a slope of unity.**

In the previous paragraph it was found that when the slope of the regression line was zero $R^2$ was also zero. In this section the data is transformed so that the slope of the regression line is the same throughout the data set; figure 7.7 shows how this can be done. The method uses Pythagoras' theorem and trigonometry. Each transformation consisted of the following steps:

$$\alpha = \tan^{-1}m \tag{7.4}$$

$$\theta = 45 - \alpha \tag{7.5}$$

$$\phi = \gamma - \theta \tag{7.6}$$

$$\gamma = \tan^{-1}\left[\frac{x_i}{y_i}\right] \tag{7.7}$$

$$x_i^2 + y_i^2 = X_i^2 + Y_i^2 \tag{7.8}$$

$$Y_i = \sqrt{(x_i^2 + y_i^2)}\ \cos\phi \tag{7.9}$$

$$X_i = \pm\sqrt{(x_i^2 + y_i^2) - Y_i^2} \tag{7.10}$$

Figure 7.8 shows some examples of the rotation of the data and Table 7.1 gives the values of $R^2$ in the original data (figure 7.3) and $R^2$ in the rotated data (figure 7.8). Figure 7.9 shows $R^2$ against Degrees $2\Theta$ when all the data has the same slope it can be seen that there are four regions in the data set where $R^2$ is varying and these correspond to the movement of peaks A,B,C and D (figure

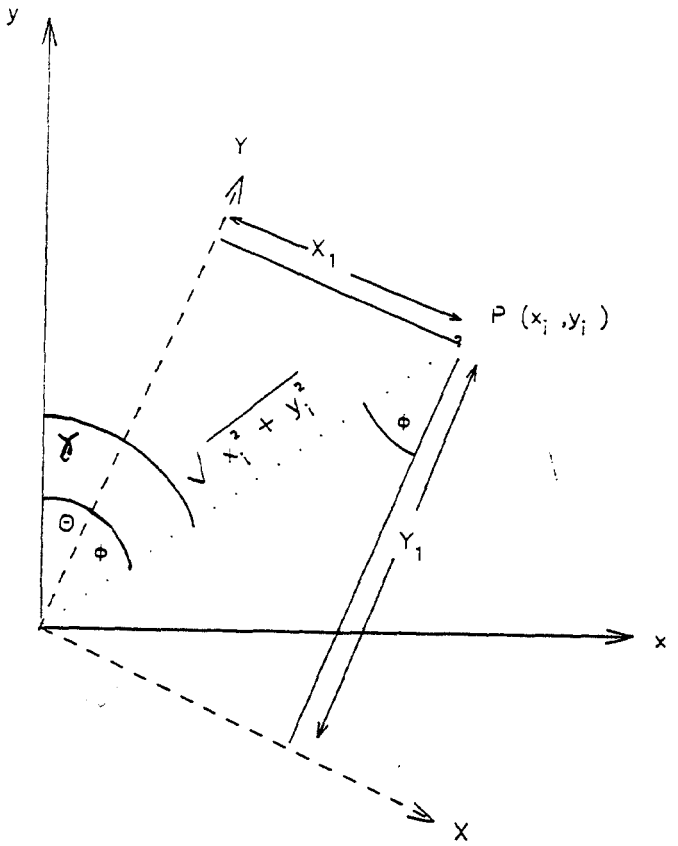


*Figure 7.7* : Transformation of the intensity ($y_i$) against degrees 2Θ ($x_i$) data to obtain a Slope of unity

7.4). In other words when a peak moves in a spectrum this is seen in a decrease of $R^2$, figure 7.10 shows that this is indeed the case and this can be compared with figure 7.8.

*Table 7.1* : Comparison Of $R^2$ In The Original And Rotated Data.

| Degrees 2Θ/ $CuK_\alpha$ | $R^2$ (original data) | $R^2$ (rotated data) |
|---|---|---|
| 21.92 | 0.000 | 0.958 |
| 31.04 | 0.000 | 0.968 |
| 40.00 | 0.834 | 0.976 |
| 47.36 | 0.396 | 0.975 |
| 54.56 | 0.972 | 0.972 |
| 69.12 | 0.944 | 0.999 |

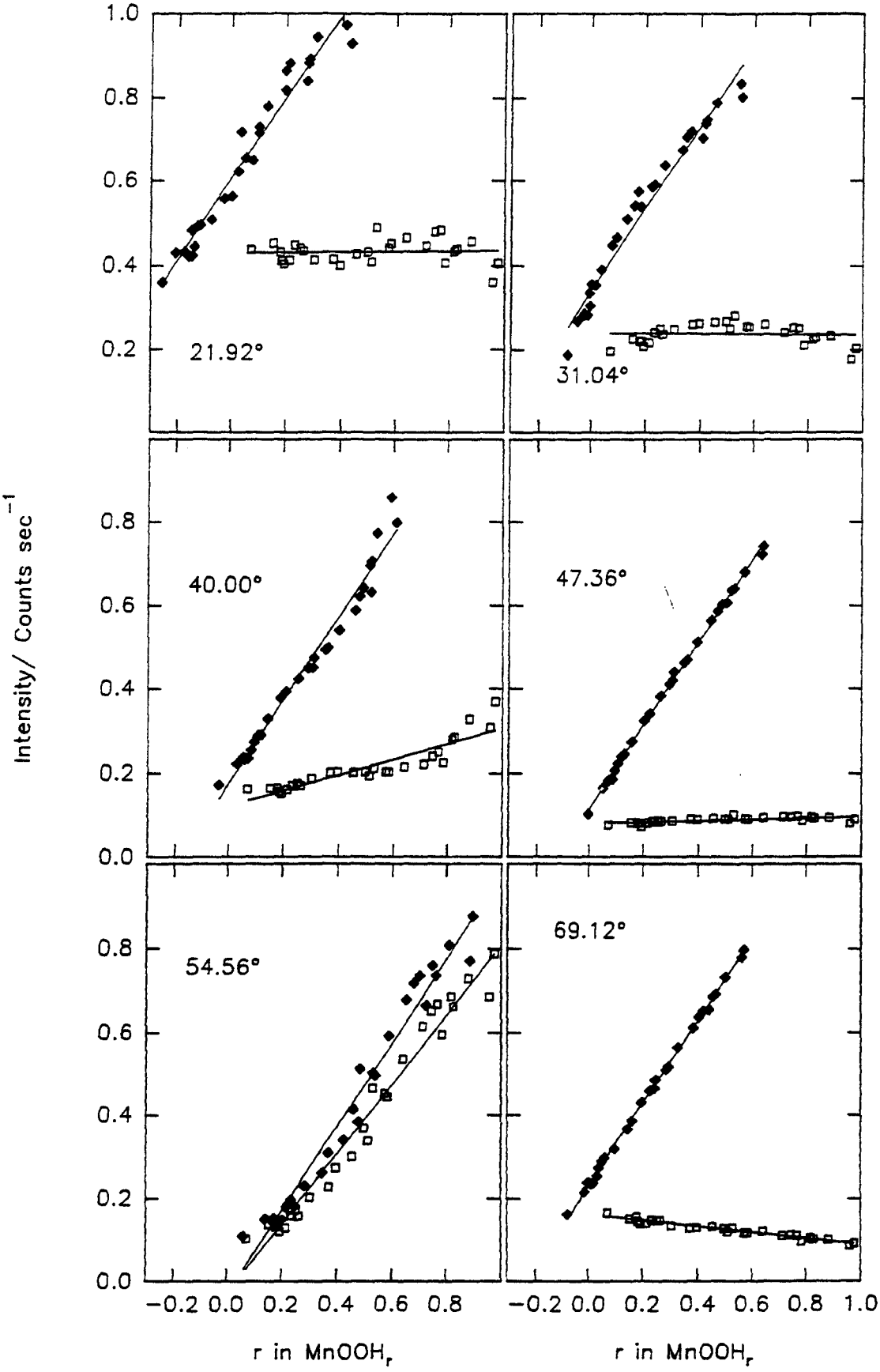


*Figure 7.8* : Plots of intensity against r in $MnOOH_r$ for a range of degree 2Θ values; (□) original data (◆) rotated data: EMD heat-treated at 200°C; propan-2-ol reduction method (see Table 7.1 for the computed $R^2$ values).

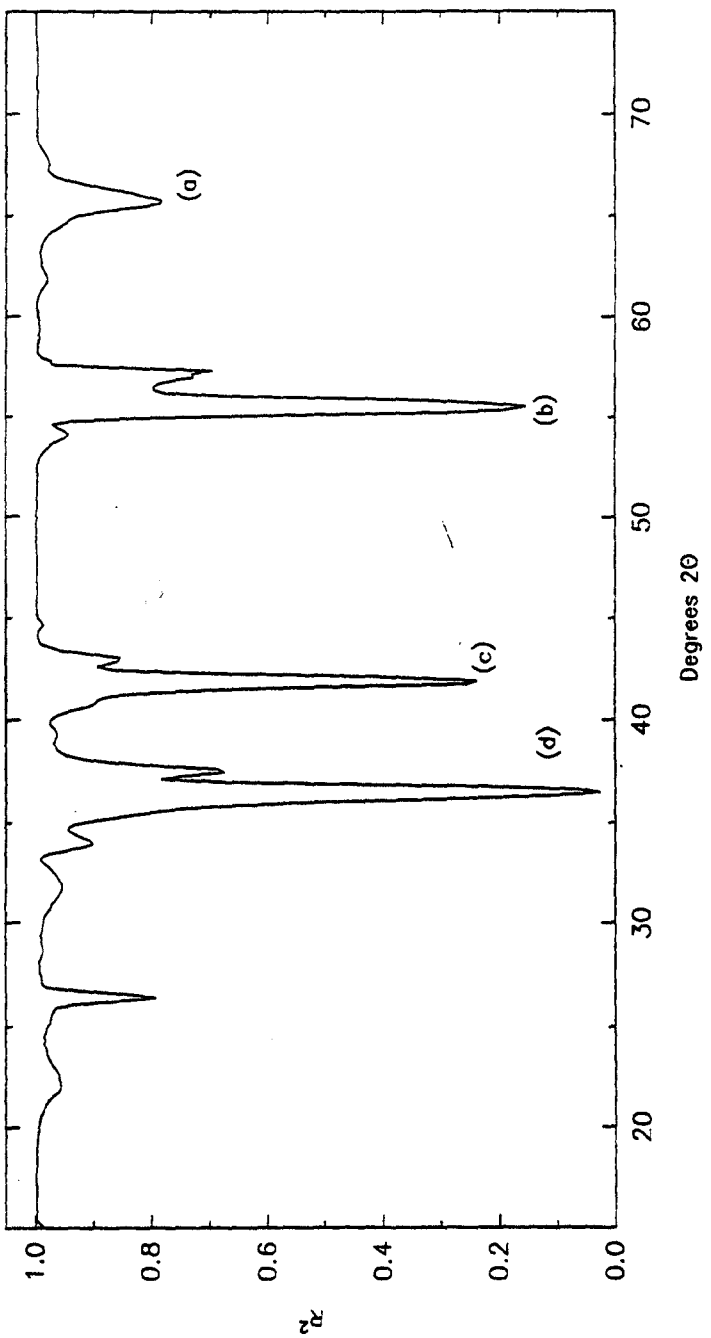


***Figure 7.9*** : $R^2$ against degrees 2Θ when the data has been transformed to a slope of unity; EMD heat-treated at 200°C; propan-2-ol reduction method.

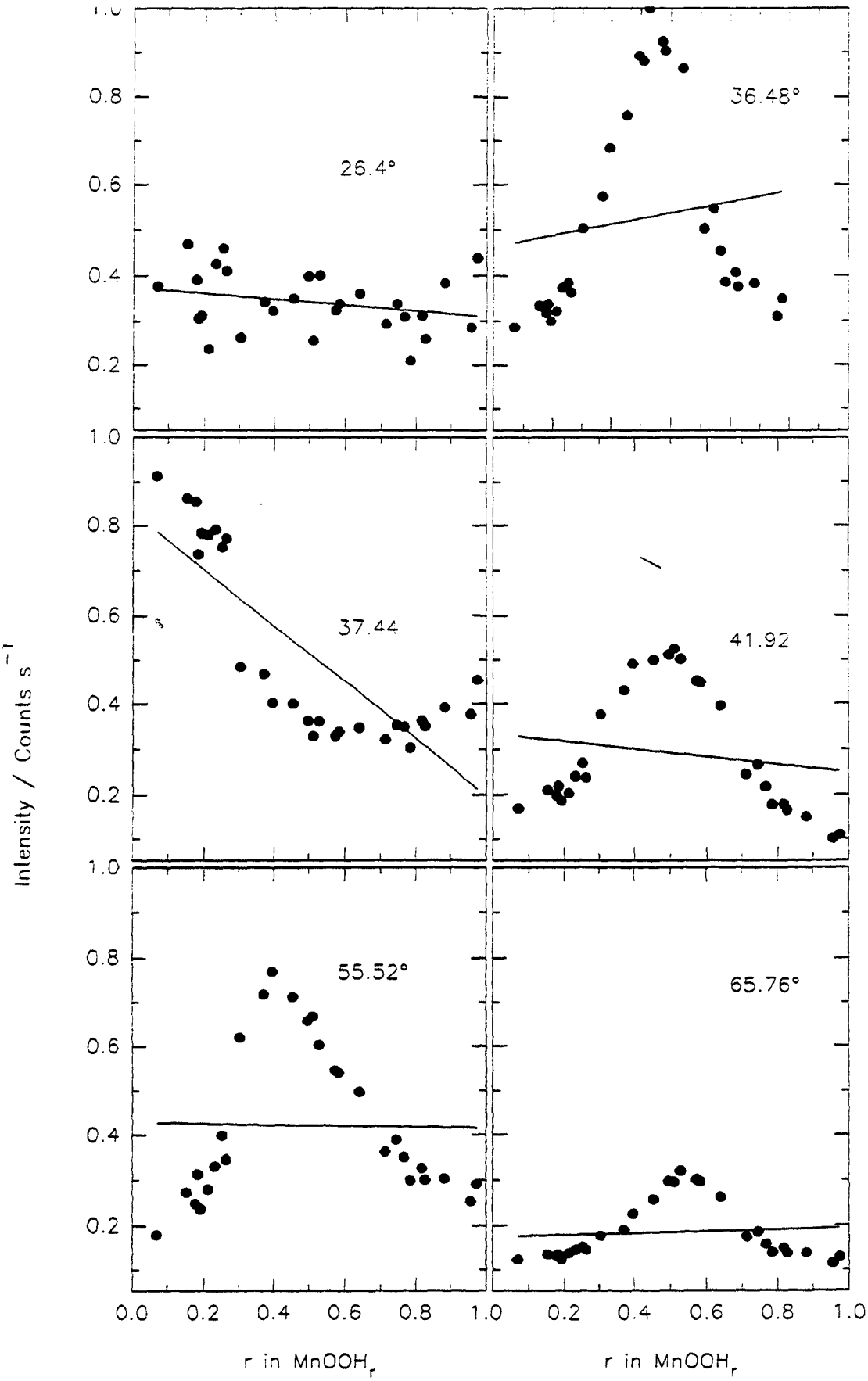


***Figure 7.10***: Plots of intensity against r in MnOOH, corresponding to low values of $R^2$ in figure 7.9 (the value of °2Θ is given in each of the plots).

**The dependence of $R^2$ on the angle of rotation.**

In the previous section the original data was rotated so that the slope of the regression line was the same throughout the dataset and it was found that when a peak moved this was seen as a decrease in $R^2$. In this section emphasis is placed on the effect of the angle of rotation on $R^2$ and the slope of the regression line. Figure 7.11 shows rotation of the data at various angles (45, 90, 135 and 180°) for a range of Degree 2Θ values and Table 7.2 lists the $R^2$ and slope of regression line data from figure 7.11.

*Table 7.2* : Slope Of Regression Line And $R^2$ For The Data Depicted In Figure 7.11

| Degrees/ | Angle Of Rotation/ Degrees | | | | | | | | | |
|---|---|---|---|---|---|---|---|---|---|---|
| 2Θ | 0 | | 45 | | 90 | | 135 | | 180 | |
| | Slope | R2 | Slope | R2 | Slope | R2 | Slope | R2 | Slope | R2 |
| 21.92 | 0.01 | 0.00 | 0.97 | 0.95 | 0.42 | -0.00 | -0.98 | 0.95 | -0.004 | 0.00 |
| 36.8 | -0.35 | 0.23 | 0.48 | 0.30 | 0.34 | -0.64 | -0.65 | 0.309 | -0.13 | 0.06 |
| 41.92 | -0.08 | 0.03 | 0.60 | 0.37 | 0.10 | 0.00 | -0.63 | 0.37 | -0.02 | 0.00 |
| 50.08 | 0.08 | 0.03 | 0.90 | 1.00 | 17.99 | 0.09 | -1.11 | 1.00 | -0.05 | 0.93 |
| 55.52 | -0.01 | 0.00 | 0.42 | 0.18 | 0.02 | 0.00 | -0.43 | 0.18 | -0.01 | 0.00 |
| 65.72 | 0.02 | 0.01 | 0.88 | 0.79 | -0.01 | 0.00 | -0.88 | 0.79 | -0.13 | 0.06 |

Figure 7.12 shows how $R^2$ and the slope of the regression line vary with the degree of rotation. An important factor that was not mentioned in the previous section was that at 36.8, 41.92 and 55.52°2Θ it was not possible to have a slope of one through the data, for example the maximum slope obtained at 55.52°2Θ is 0.42 and $R^2$ is 0.181 but this is still an improvement on the original data where $R^2$ is 0.

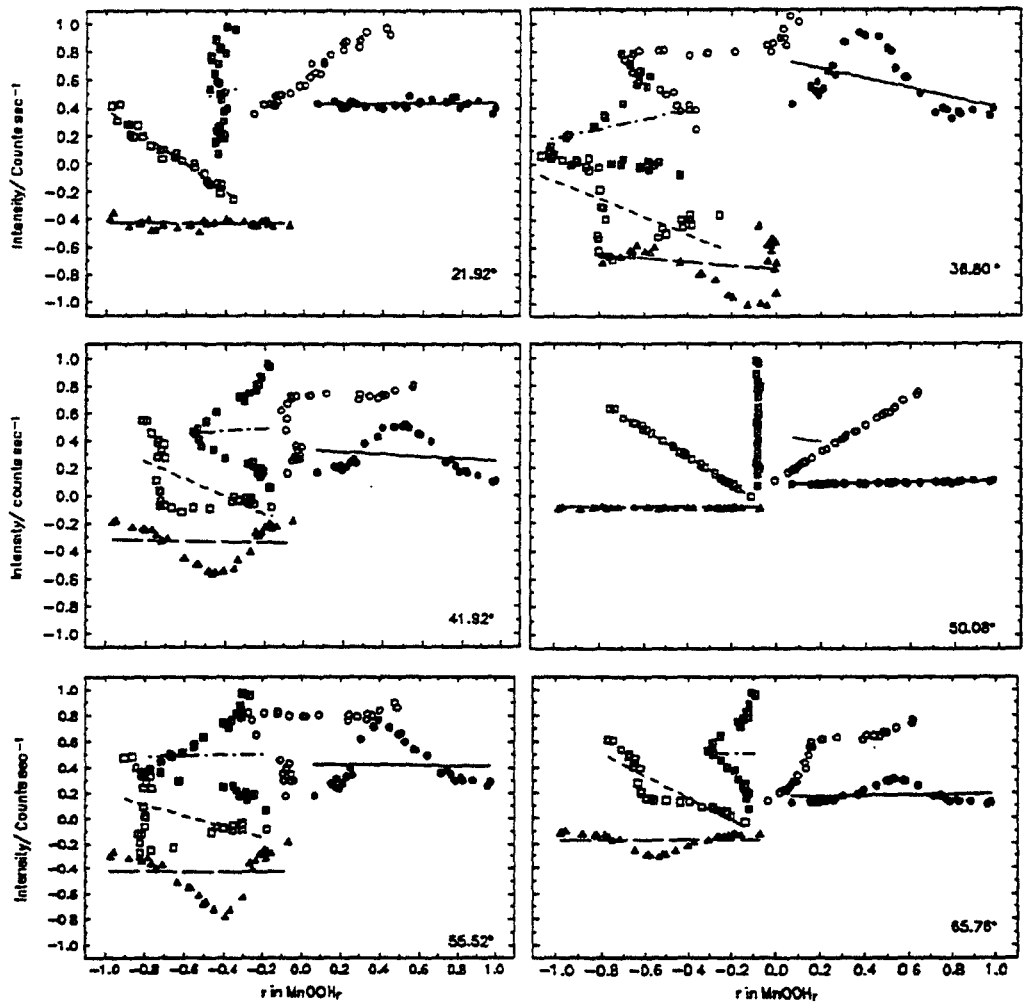


*Figure 7.11* : Rotation of the data at (●) 0°; (○) 45°; (■) 90°; (□) 135° and (▲) 180° : EMD heat-treated at 200°C; propan-2-ol reduction method (see Table 7.2 for the $R^2$ values).

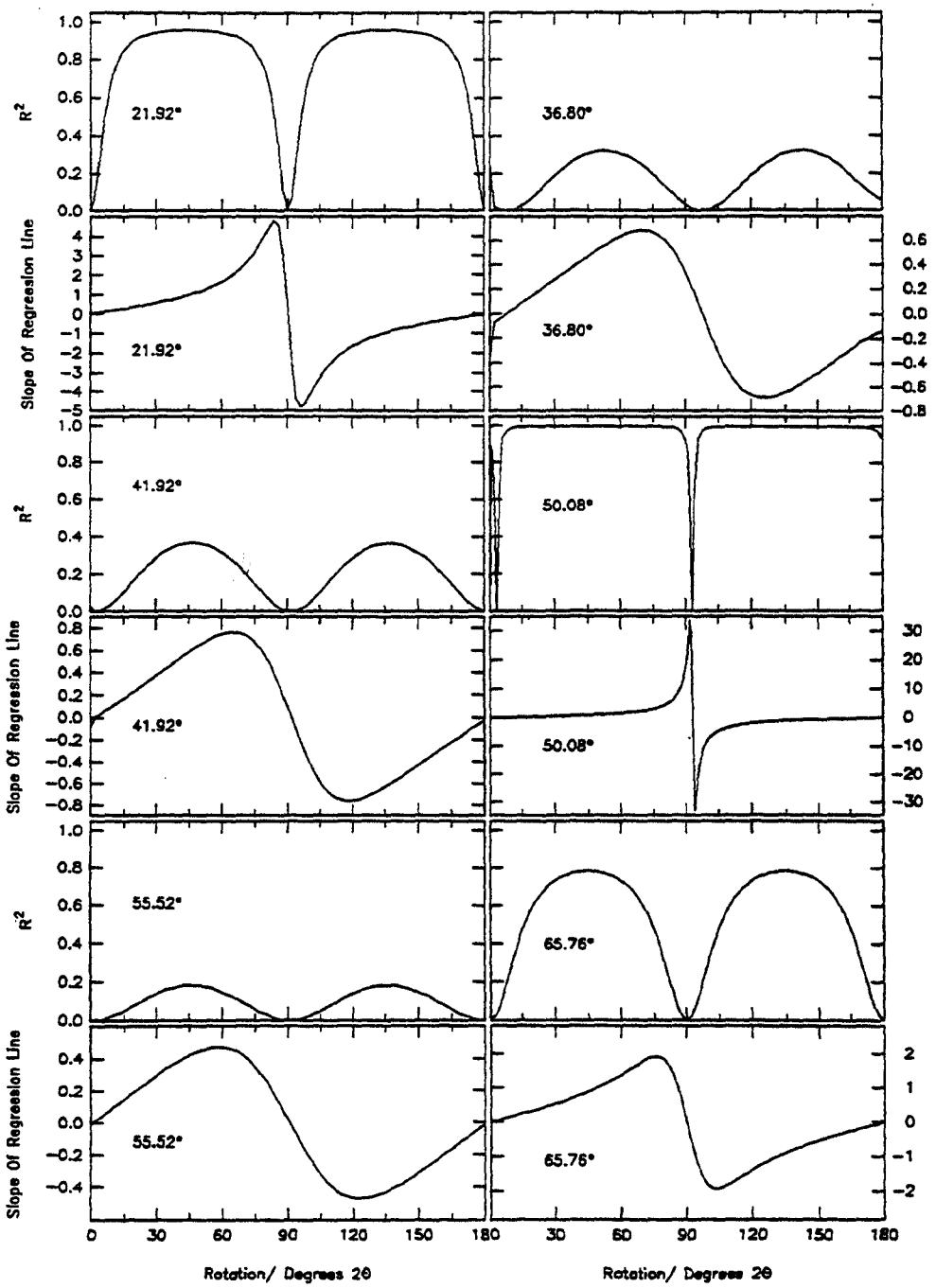


Figure 7.12 : The dependence of $R^2$ on the angle of rotation for a range of degrees 2Θ: EMD heat-treated at 200°C; propan-2-ol reduction method.

## *7.1.2 EMD heat-treated at 400°C: hydrazine hydrate reduction method.*

The analysis that was performed in section 7.1.1 is now applied to the X-ray diffraction dataset that was presented in section 4.2.4.1 and the patterns are shown in figure 7.13 (there are 13 patterns in this dataset compared to 28 in section 7.1.1). As the theory of the rotation method has already been presented in section 7.1.1 only the salient features of the analysis are shown. The results of the linear regression analysis are shown in figure 7.14 and the rotated data in figure 7.15. Comparison of figure 7.16 with 7.4 reveals that there is little or no movement of peaks B, C and D in figure 7.14 with their counterparts in figure 7.4. This is substantiated by the fact that the minimum value of $R^2$ in figure 7.15 is 0.79. The theory presented in section 7.1.1 has now been successfully applied to two sets of data: one where peaks move throughout the dataset and another where the original peaks diminish at the expense of new peaks (this section). It has been found that, in the former, low values of $R^2$ are found and in the latter high values of $R^2$.

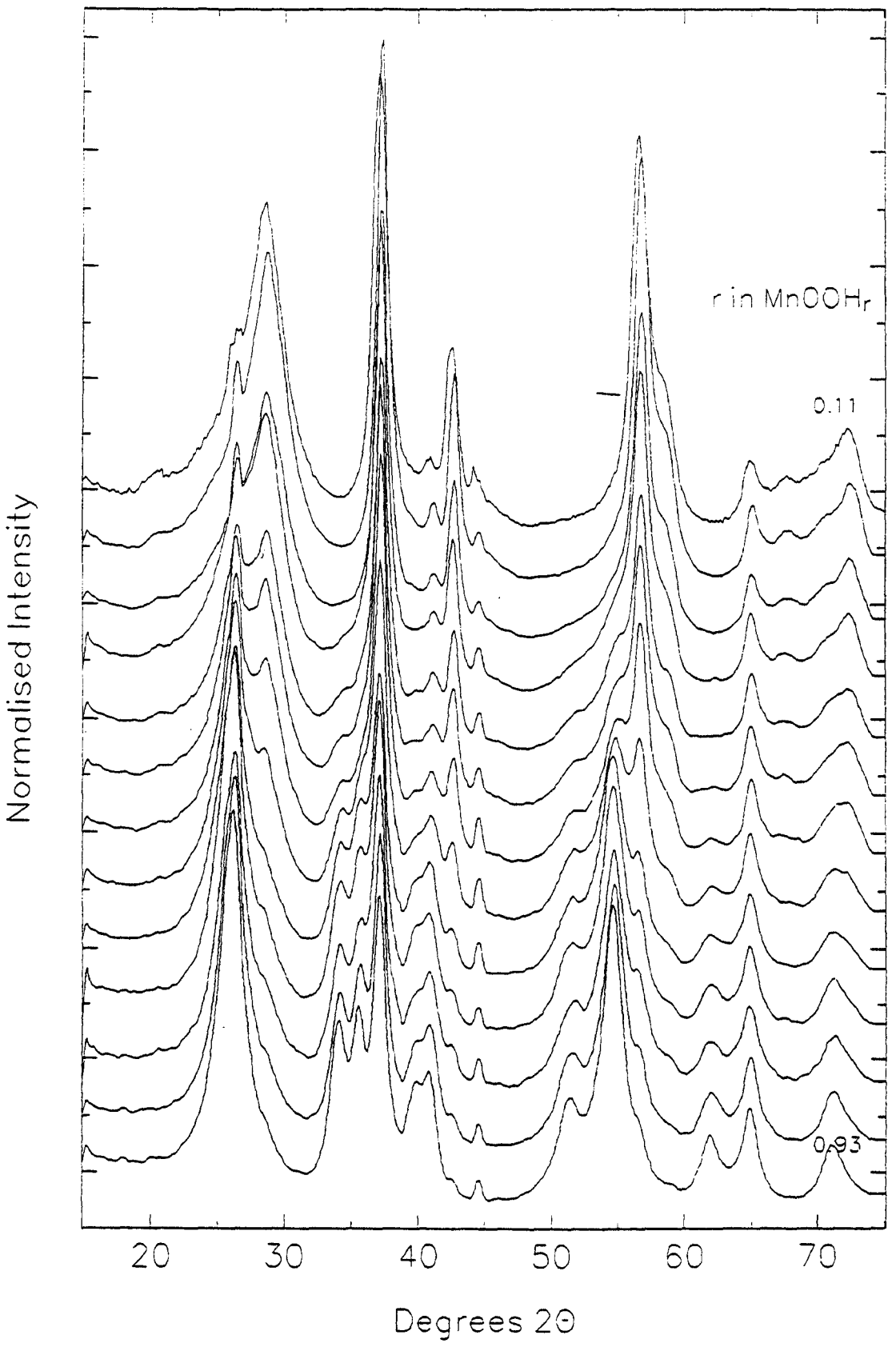


***Figure 7.13***: **Dataset that was used for the linear regression analysis EMD heat-treated at 400°C; hydrazine hydrate reduction method.**

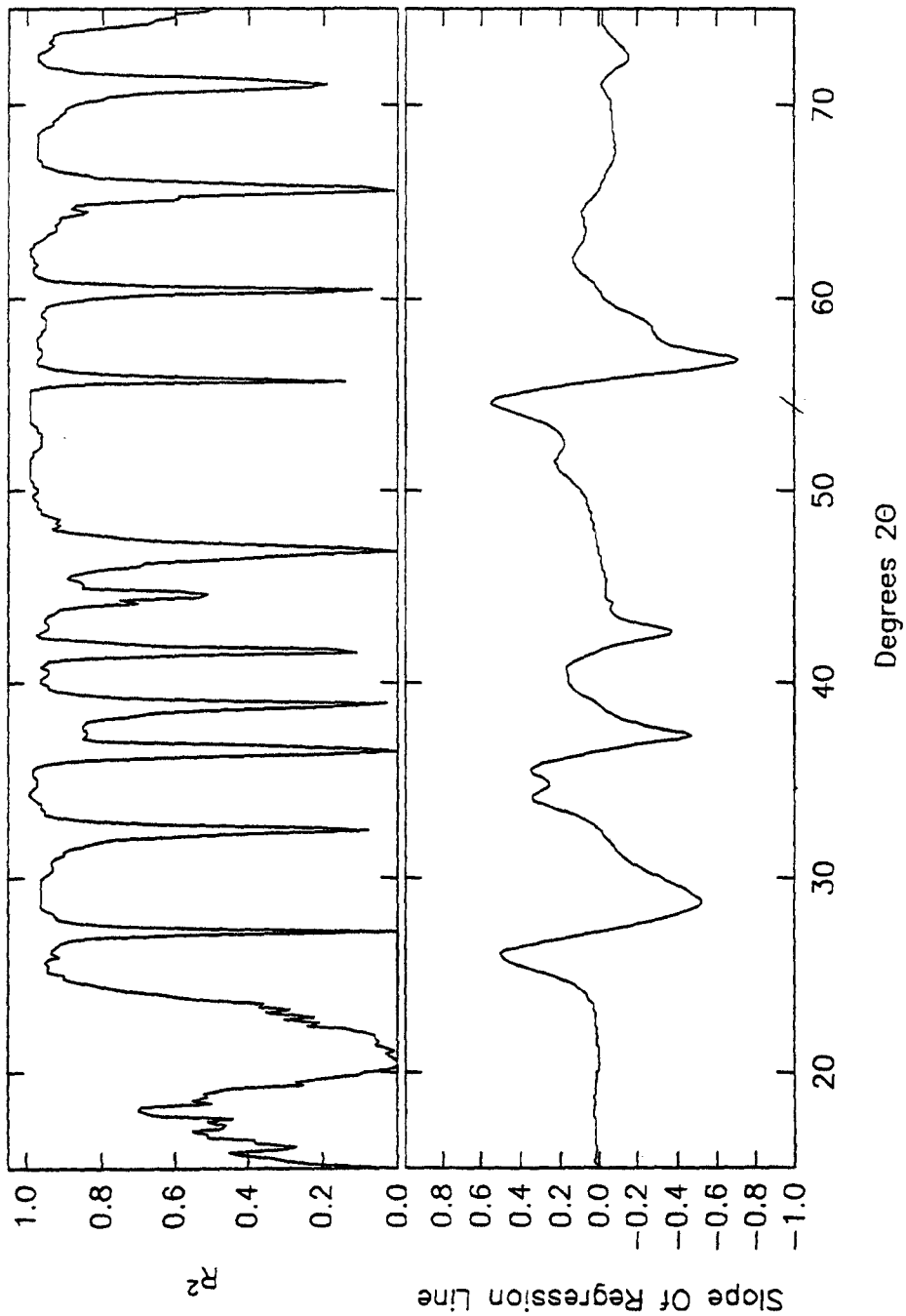


***Figure 7.14*** : Slope of the regression line and $R^2$ against degrees 2Θ: EMD heat-treated at 400°C; hydrazine hydrate reduction method.

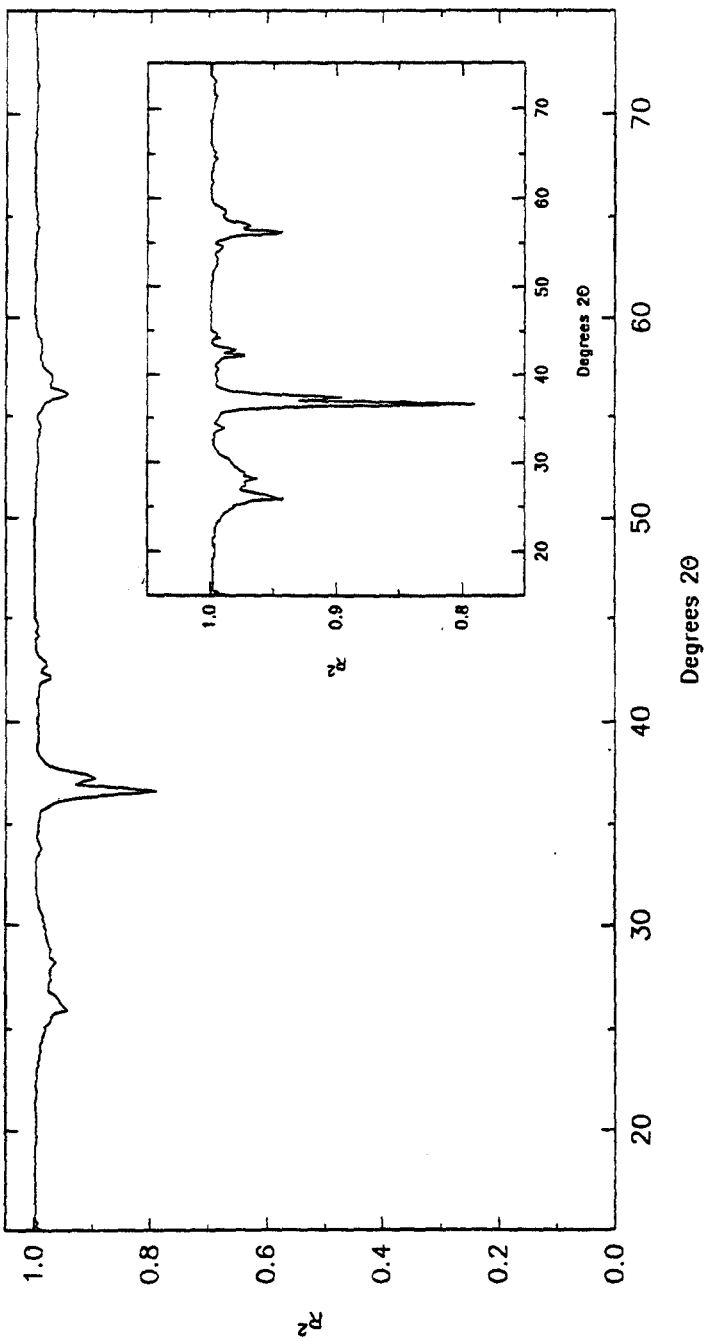


*Figure 7.15* : $R^2$ against degrees 2Θ when all the data has a slope of unity: EMD Heat-treated at 400°C; hydrazine hydrate reduction method.

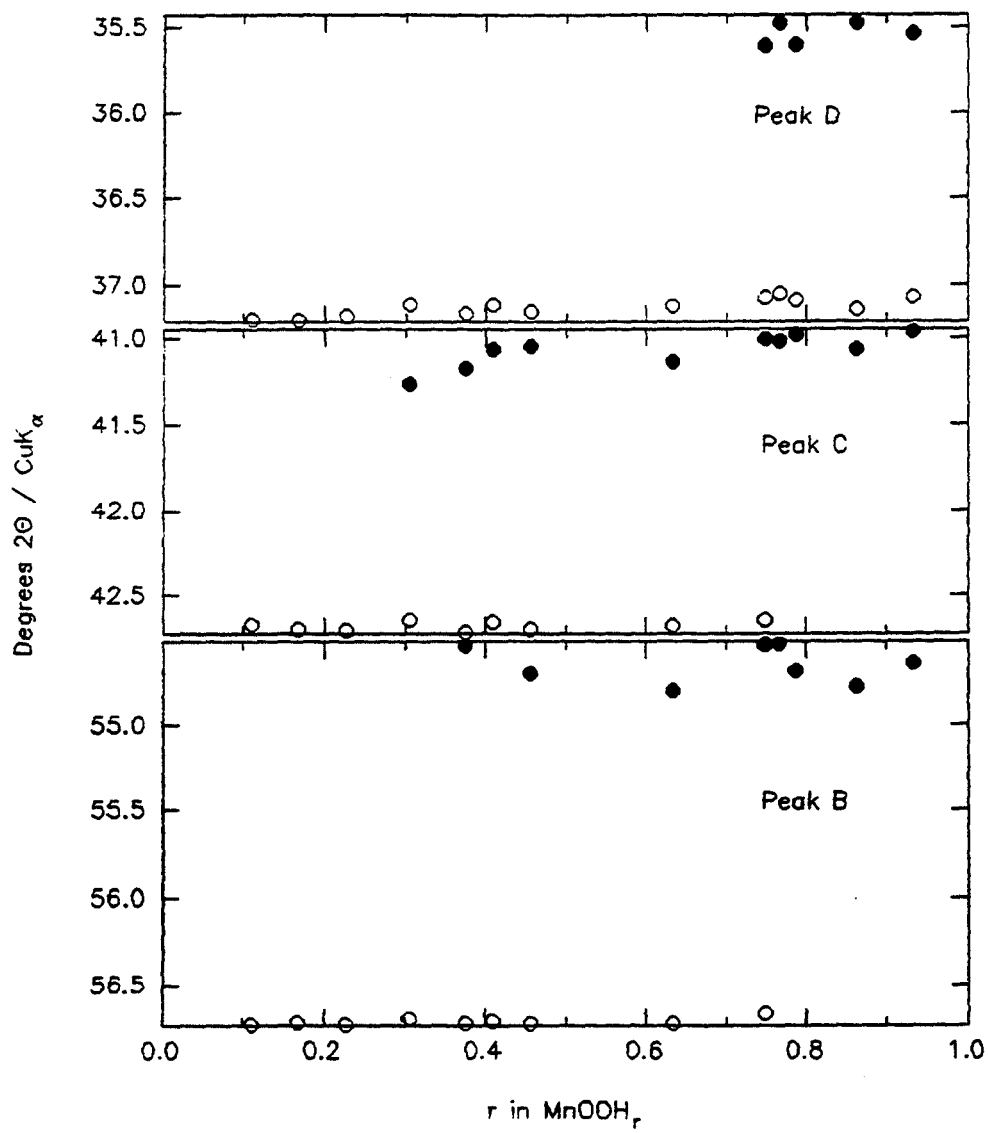


***Figure 7.16*** : Movement of peaks B,C and D against H Insertion Level: EMD heat-treated at 400°C; hydrazine hydrate reduction method.

## *7.1.3 Further statistical analysis of data to substantiate the regions of homogeneity/ heterogeneity.*

Examination of the intensity against r in MnOOHr at 55.52°2Θ (figure 7.10) shows that the data is peak shaped and if the equivalent data were shown for EMD heat-treated at 400°C then the data would be linear. Figure 7.17 shows

a schematic representation of the trends in intensity against H insertion level for a range of °2Θ values on either side of the top of a peak. In the homogeneous case because a peak is moving throughout the range of reduction the intensity values will be either rising or falling with respect to r in $MnOOH_r$. In the heterogeneous case the plots will be either linearly rising or falling with H insertion level as shown in case (b). It is proposed that this method can be used to determine the regions of homogeneity/heterogeneity that were observed in chapters 4 & 5.

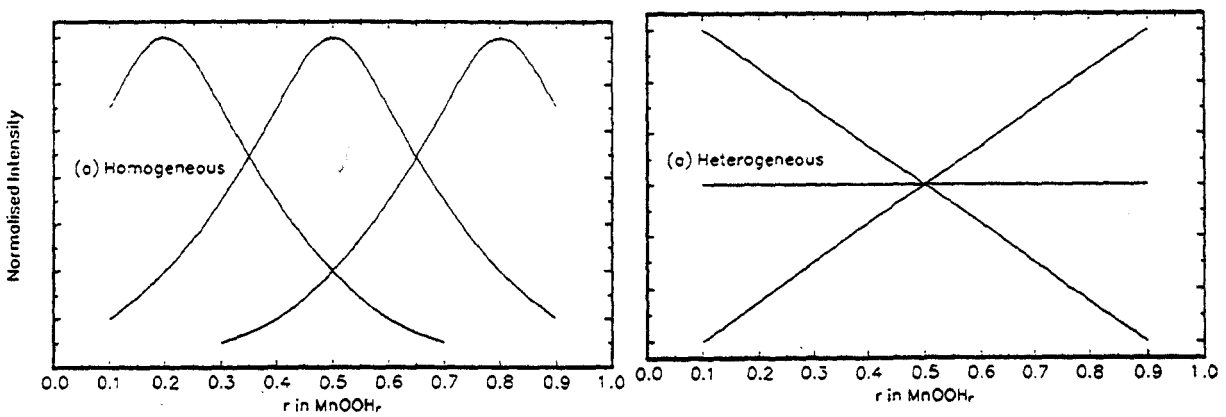


*Figure 7.17*: Schematic representation of the trends of intensity against H insertion level on either side of the top of a peak for a homogeneous and heterogeneous case.

Only one peak is suitable for this type of exercise and that is the one at 55.5°2Θ. This is because in the other regions of the data where there is peak movement "new" lines appear in the dataset and so would interfere in the intensity values (this is shown in figure 7.10 for the plot at 37.44°2Θ). For the purpose of this exercise the minimum value of $R^2$ in the rotated data in the region of 55.5°2Θ was taken and six points on either side of that position were plotted to investigate the trends in intensity with H insertion level. The results of these plots for the EMD materials investigated in chapter 4 are shown in figures 7.18-7.22. The regions of heterogeneity that were found in chapter 4 are marked with a dashed line and it can be seen that after this level of H insertion the intensity is rising, falling or horizontal with respect

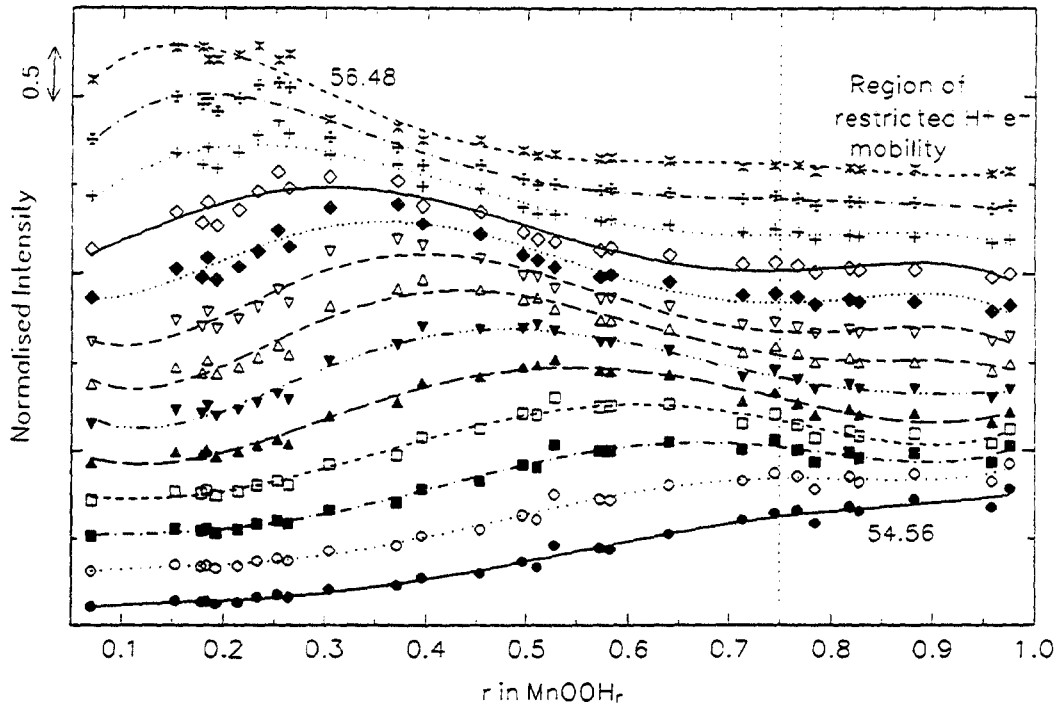


***Figure 7.18***: Trends in intensity against H insertion level to determine the regions of homogeneous behaviour (the maximum and minimum values of °2Θ are given in the figure): EMD heat-treated at 200°C; propan-2-ol reduction.

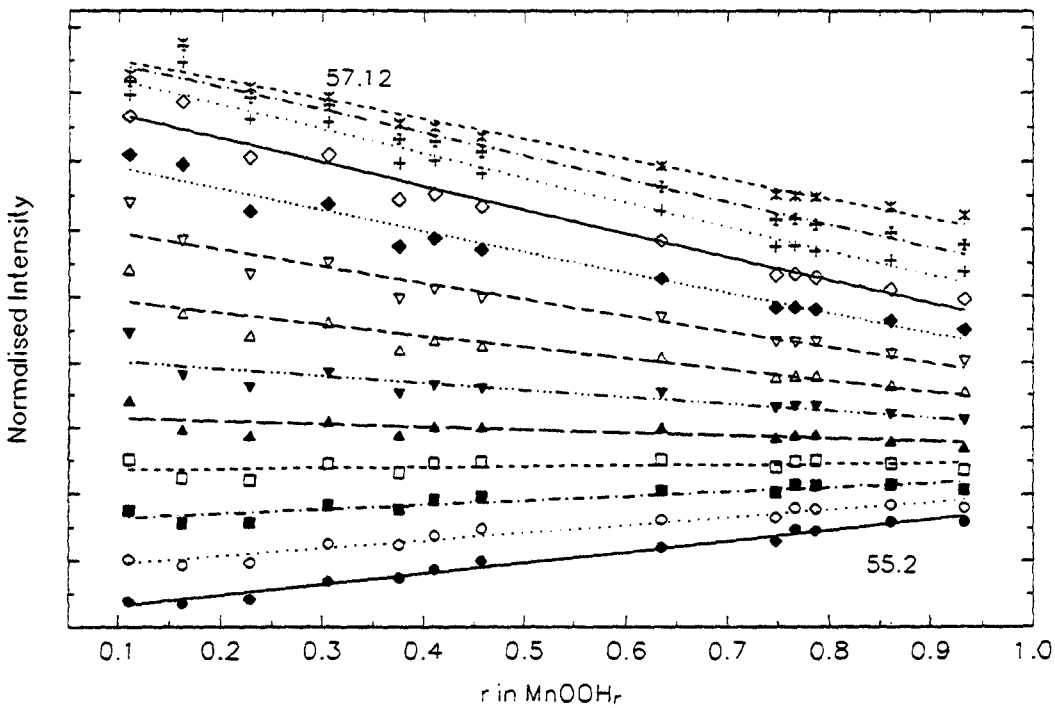


***Figure 7.19***: Trends in intensity against H insertion level to determine the regions of homogeneous/heterogeneous behaviour (the maximum and minimum values of °2Θ are given in the figure): EMD heat-treated at 400°C; hydrazine hydrate reduction.

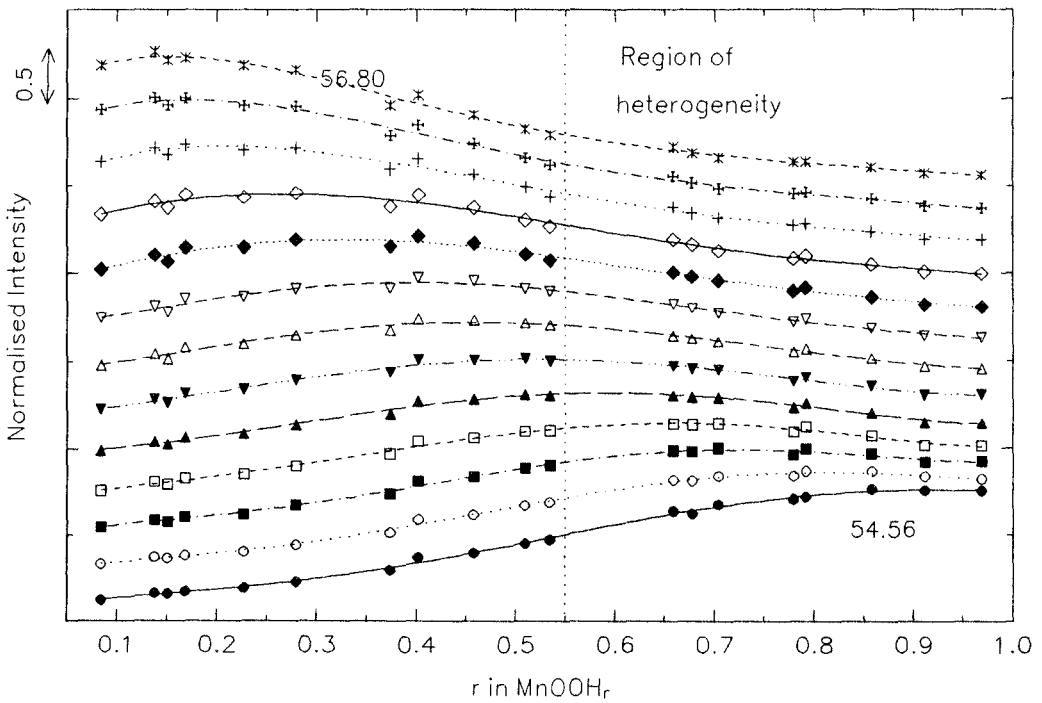


***Figure 7.20***: Trends in intensity against H insertion level to determine the regions of homogeneous/heterogeneous behaviour (the maximum and minimum values of °2Θ are given in the Figure): EMD heat-treated at 300°C; propan-2-ol reduction.

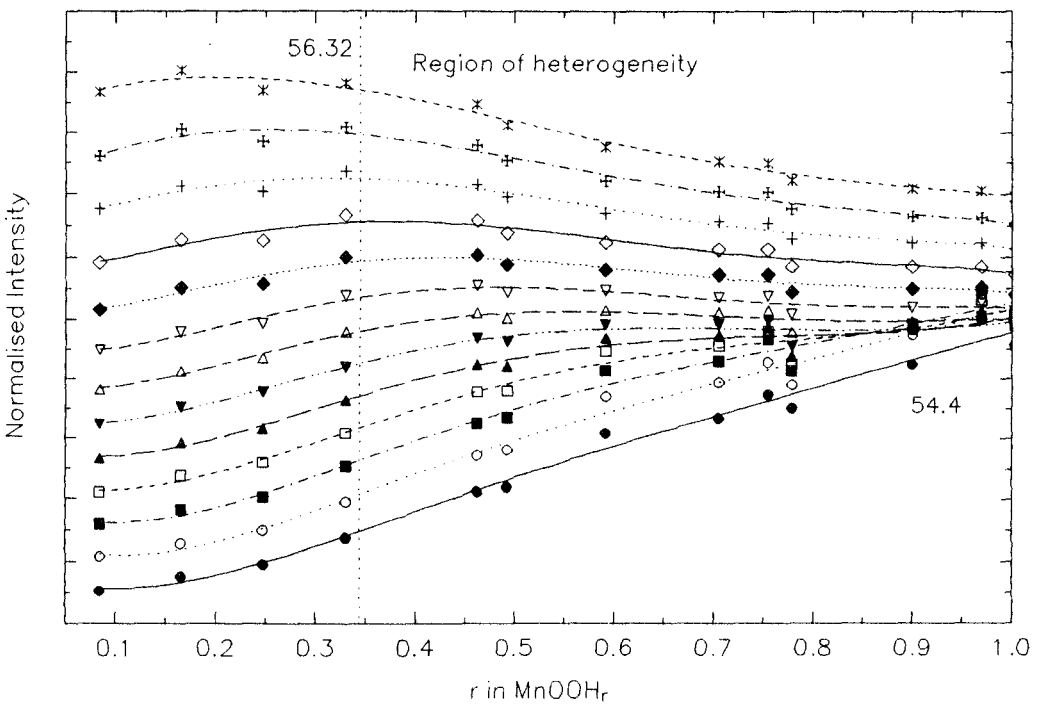


***Figure 7.21***: Trends in intensity against H insertion level to determine the regions of homogeneous/heterogeneous behaviour (the maximum and minimum values of °2Θ are given in the Figure): EMD heat-treated at 300°C; hydrazine hydrate reduction.

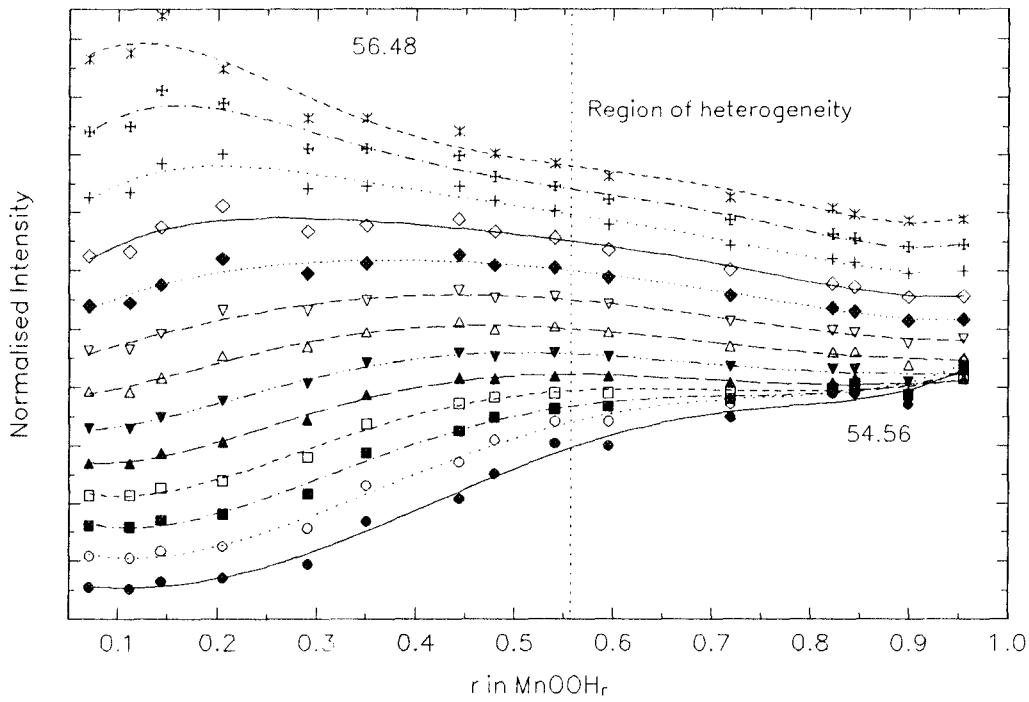


***Figure 7.22***: Trends in intensity against H insertion level to determine the regions of homogeneous/heterogeneous behaviour (the maximum and minimum values of °2Θ are given in the Figure): EMD heat-treated at 200°C; hydrazine hydrate reduction.

to the H insertion level. The data represented in this section represents another method of determining the regions of homogeneity/heterogeneity that had previously been observed.

## 7.2 Statistical analysis of FTIR spectra.

### *7.2.1 EMD heat-treated At 200°C; hydrazine hydrate reduction method.*

The final dataset to be shown is that of the FTIR spectra that were presented in section 4.3.1.2. The spectra are plotted in Figure 7.23 and trends in absorbance at a particular wavenumber (the actual value is given in the plot) against r in $MnOOH_r$ are plotted in Figure 7.24. The absorbance decreases in an approximately linear fashion at 3600, 2648, 1200 and 752 $cm^{-1}$ but is independent of r in $MnOOH_r$ at 500$cm^{-1}$. This is manifested in the low $R^2$ (0.005). As the range in the absorbance values (0.15 – 1.3) is comparable to r in $MnOOH_r$ (0.07 – 0.955) it was not necessary to set the highest point in the

dataset to one which was carried out with the XRD data in sections 7.1.1 and 7.1.2. The RSS and SYY for the wavenumbers shown in figure 7.24 are plotted in figure 7.25 and the summation of RSS and SYY against wavenumber are shown in figure 7.26. At 500cm$^{-1}$ it can be seen that RSS and SYY have the same value and therefore $R^2$ is close to zero. Figure 7.27 shows the results of the initial regression analysis and figure 7.28 the rotated data. Figure 7.28 shows that $R^2$ is less than 0.7 from approximately 575-620 cm$^{-1}$ and this corresponds with the position of the absorbance due to the $MnO_6$ octahedral framework. The peak position of this absorbance against r in $MnOOH_r$ is plotted in figure 7.29 where the movement of this peak is confirmed.

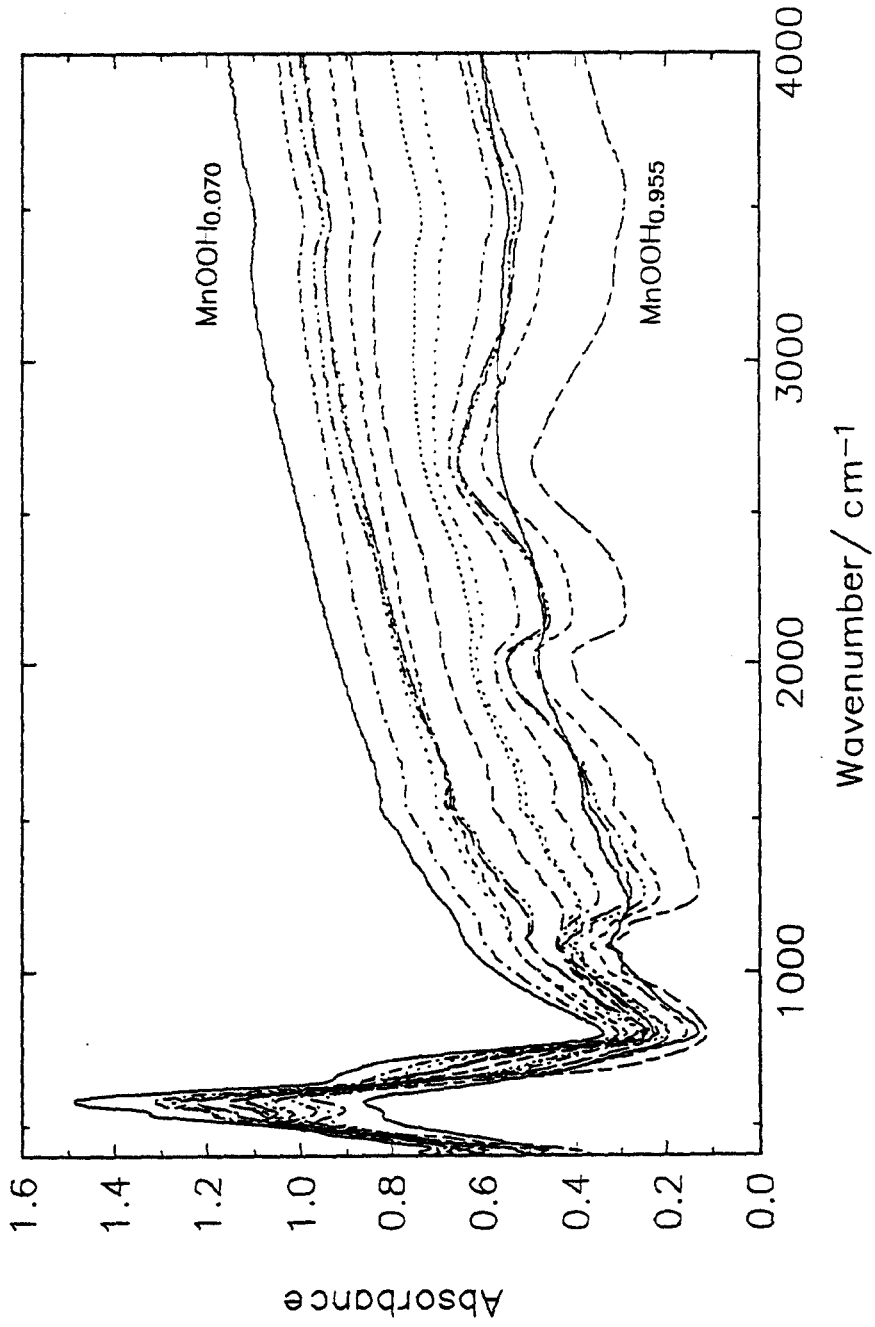


***Figure 7.23*** : Data set that was used for the linear regression analysis for the FTIR spectra of EMD heat-treated at 200°C; hydrazine hydrate reduction method.

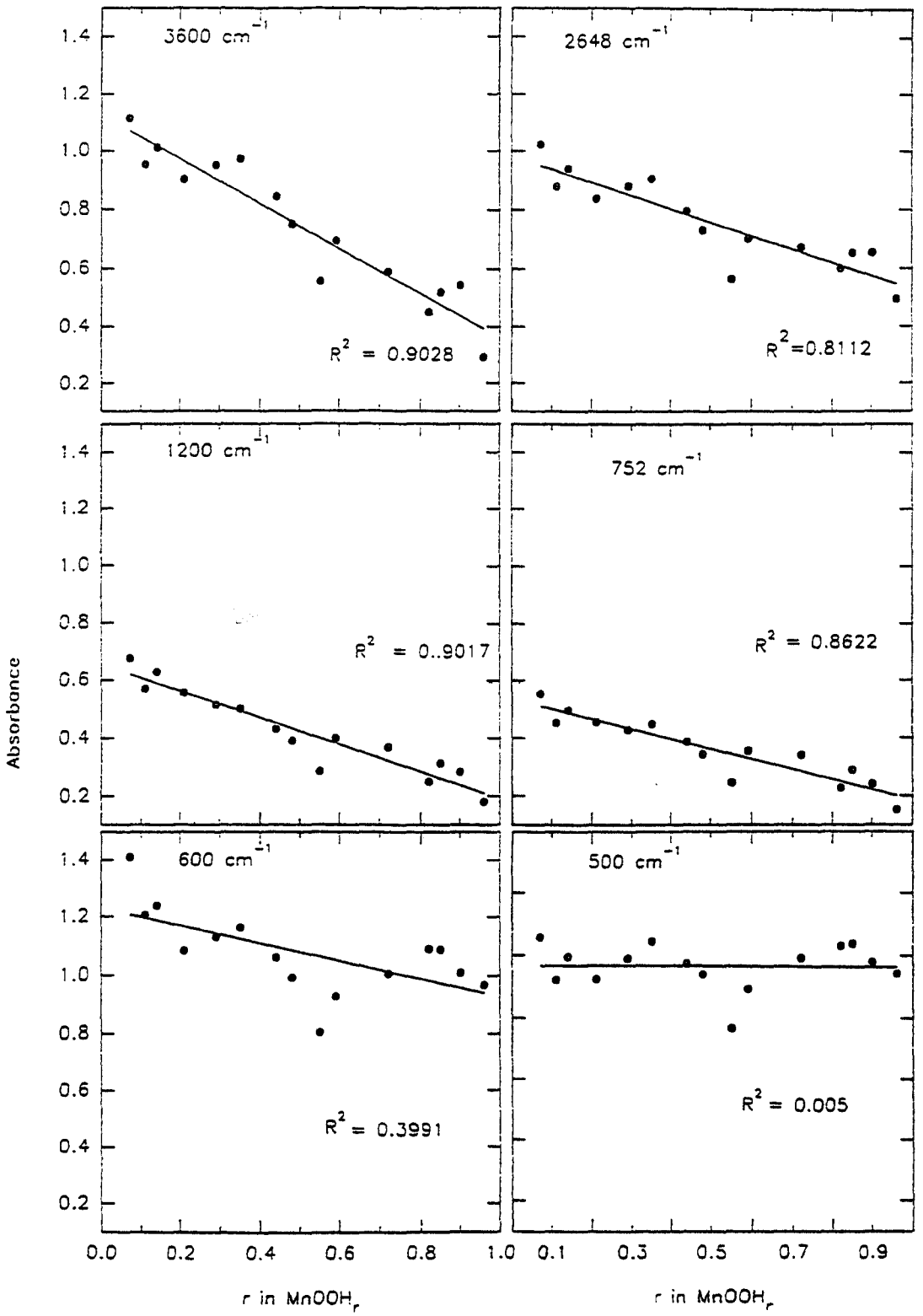


*Figure 7.24* : Plots of absorbance against H insertion level for a range of wavenumbers: EMD heat-treated at 200°C; hydrazine hydrate reduction method.

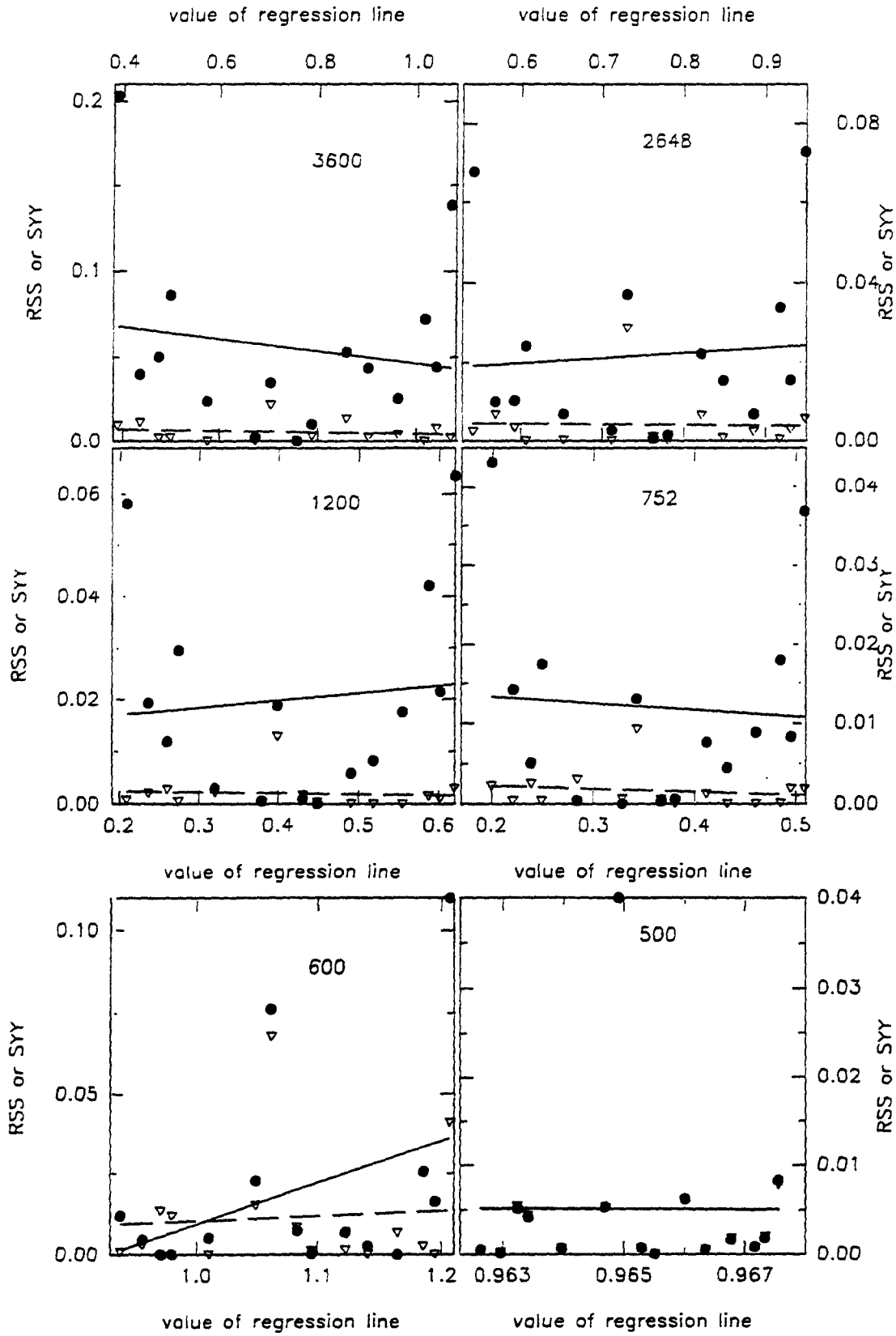


***Figure 7.25*** : Plots of SYY (●) and RSS (▽) against the y value of the regression line for the wavenumbers shown in Figure 7.24.

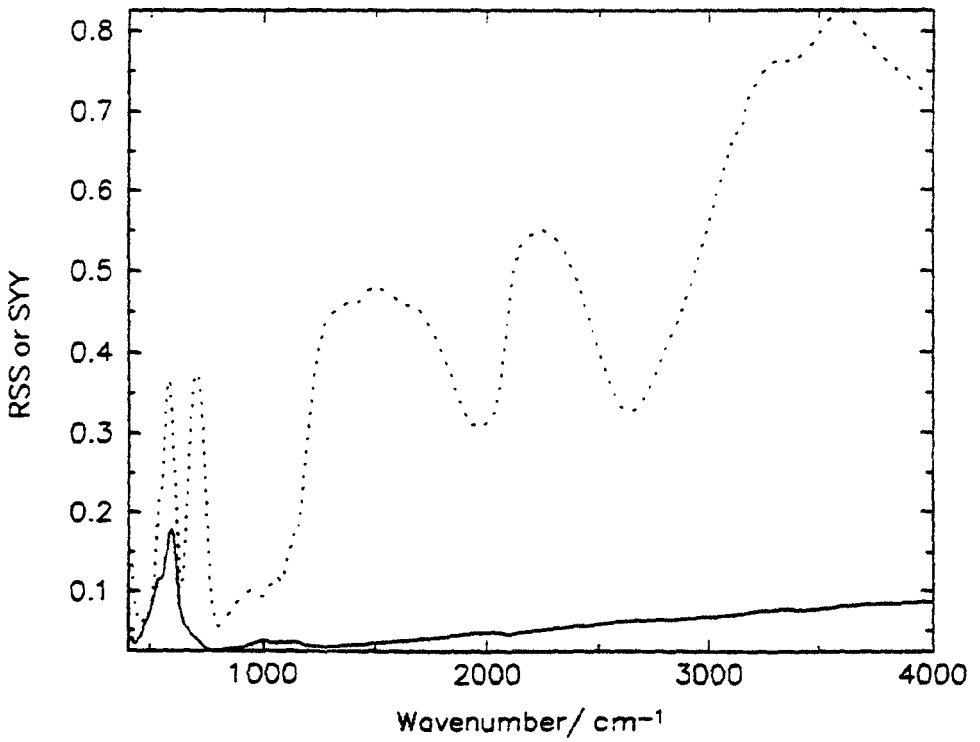


*Figure 7.26* : The summation of RSS (—) or SYY (···) against wavenumber: FTIR spectra; EMD heat-treated at 200°C; hydrazine hydrate reduction method.

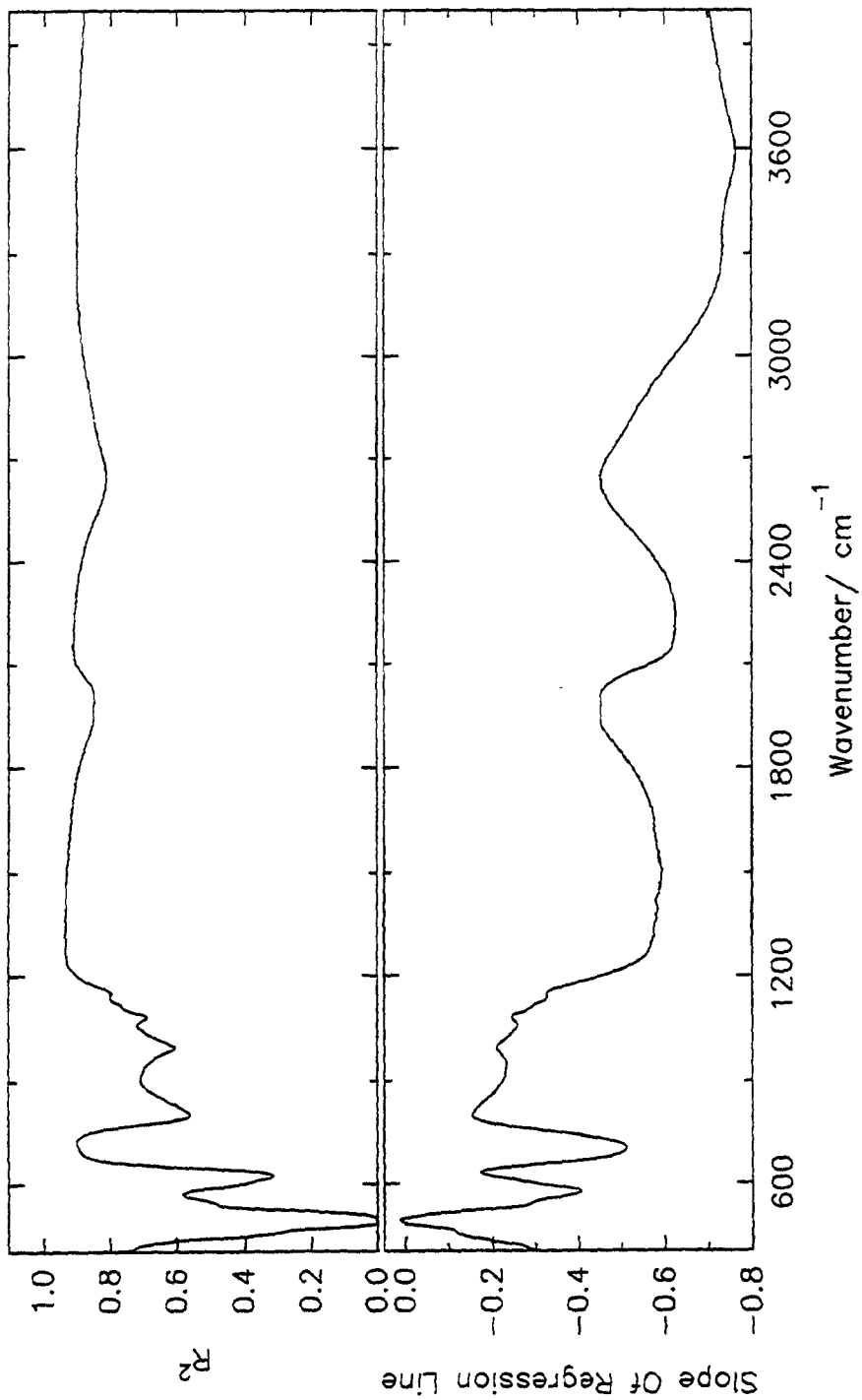


***Figure 7.27*** : Slope of the regression line and $R^2$ against wavenumber: EMD heat-treated at 200°C; hydrazine hydrate reduction method.

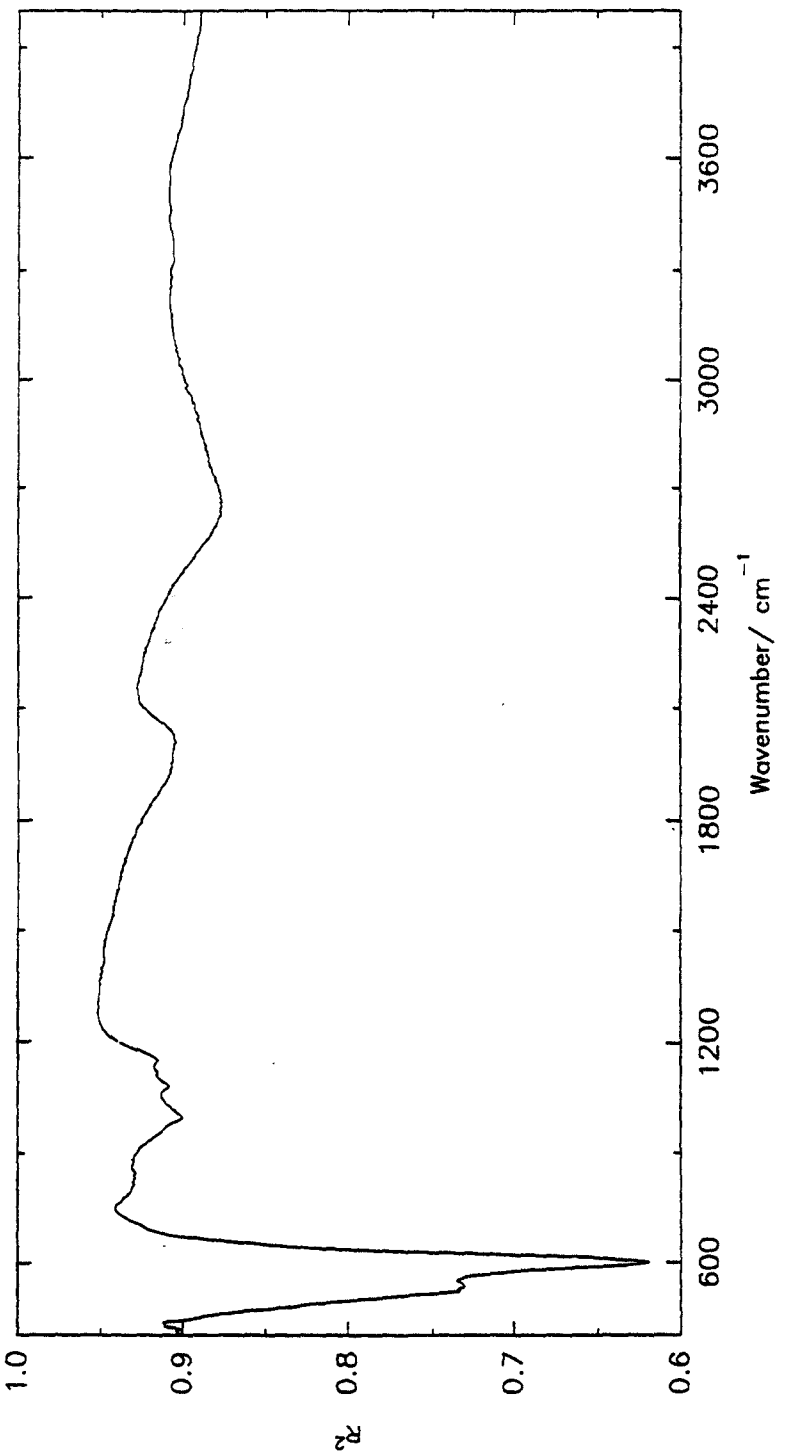


***Figure 7.28*** : $R^2$ against wavenumber when all the data has a slope of one: EMD heat-treated at 200°C; hydrazine hydrate reduction method.

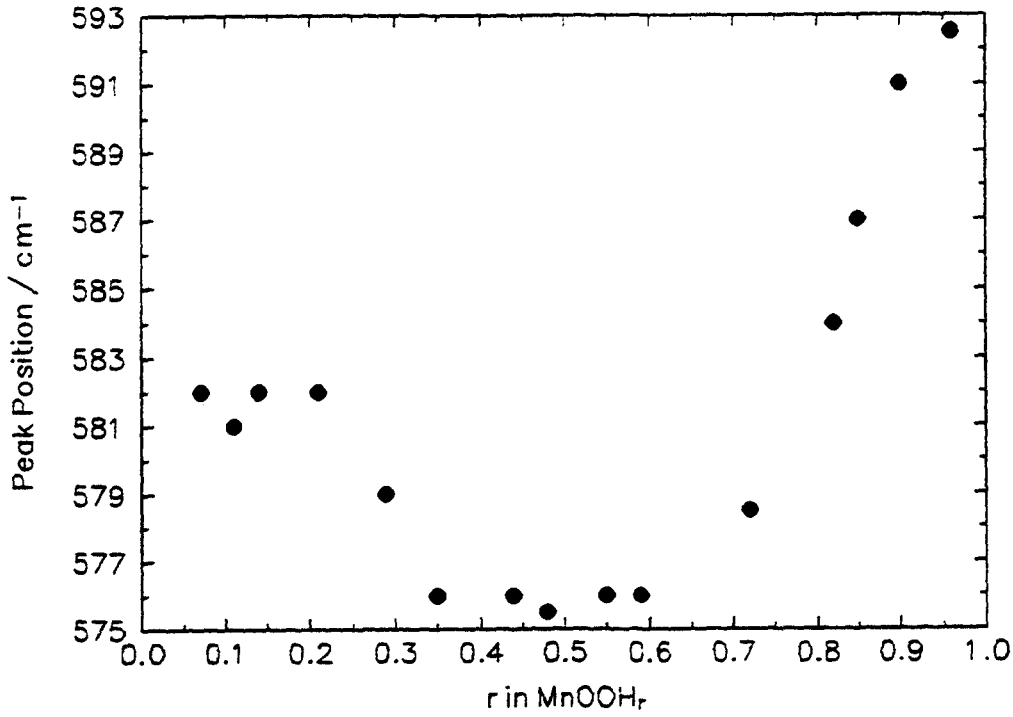


*Figure 7.29* : Peak position due to the absorbance of the $MnO_6$ octahedral framework: EMD heat-treated at 200°C; hydrazine hydrate reduction method.

## 7.3 Conclusion.

A novel applied linear regression analysis was developed that can be used to determine particular trends in a spectral dataset. The analysis consisted of two parts: first of all a linear regression analysis was performed at a fixed value of either Degrees 2Θ (XRD) or wavenumber (FTIR) with the intensity or absorbance as the dependent variable against r in $MnOOH_r$ as the independent variable. It was found (in the first part of the analysis) that when a peak moved in a set of data a low value of $R^2$ was obtained although the analysis was complicated by the fact that $R^2$ was zero whenever the slope of the regression line was zero (see figure 7.3). To overcome this the original data was transformed so that the slope of the regression line was the same throughout the dataset and in the subsequent plot of $R^2$ against °2Θ the observation of peak movement was confirmed (see figure 7.9). In addition to this three important pieces of information could be obtained from the data when the slope of the regression line was unity. They were as follows (see figure 7.10):

(i) The variability in the peak height of the graphite peak at 26.48°2Θ.

(ii) The appearance of new lines in the XRD pattern at 37.44°2Θ.

(iii) Peak movement at 36.48, 41.92, 55.52 and 65.76°2Θ.

In section 7.1.3 a new method was presented to determine the regions of homogeneity/heterogeneity that had been observed in chapter 4. This involved plotting the intensity against H insertion level for a range of °2Θ values on either side of the minimum value of $R^2$ in the rotated data. Only the peak at 55°2Θ was suitable and it was found that in the heterogeneous region (see Figures 7.18-7.22) the intensity was rising, falling or horizontal with respect to H insertion level.

# Chapter 8 Conclusions and Further Work.

## 8.1 Conclusions.

This investigation was primarily concerned with the water content of $MnO_2$ and the effect of that with regard to proton and lithium insertion in the temperature range 25-400°C. Until this investigation most of the work found in the literature had been focussed on H insertion into non heat-treated $\gamma$-$MnO_2$ and electrochemical insertion of Li into heat-treated EMD. In this work a series of H and Li inserted compounds were prepared which enabled direct comparison of their behaviour to be made.

The water content of manganese dioxide had been the subject of numerous investigations (section 1.2) and this work was an extension of that but with emphasis on temperatures from 120-450°C with regard to the use of $\gamma$-$MnO_2$ in lithium cells. In section 3.4 four different types of $\gamma$-$MnO_2$ (two EMD's and two CMD's) were heat-treated in an air or argon environment. The rate of water evolution was measured by collecting the evolved water in tubes containing magnesium perchlorate and the uptake/loss of oxygen by chemical analysis of the heat-treated material. The EMD materials behaved in a similar fashion in terms of the rate and amount of water evolution in air and argon. The stoichiometry reached a maximum at 250°C in air whereas in argon the stoichiometry remained unchanged from 25-250°C. Oxygen loss was observed in an argon environment from 300°C whereas in air loss was seen after 350°C. The CMD materials behaved differently, the stoichiometry of Faradiser WSLi increased markedly in air whereas no increase was found for Faradiser M. Oxygen loss (in argon) was observed after 250°C for Faradiser M in contrast to 300°C for the other materials. Pyknometric density measurements of $MnO_2$ were performed to determine the type of water being removed at a particular temperature. It was found that water removed up to 120°C had the same density as that of normal water (0.997 g $cm^{-3}$). Between 120-160°C water of a higher density was removed and the removal of hydroxyl groups between 200-250°C generated microporosity in $MnO_2$ and a surface which reacted with water. Powder X-ray diffraction spectra of the heat-treated materials (section 3.7) showed that there was little change in structure from 25-300°C and between 300-400°C the structure from a $\gamma$-phase to a $\beta$-like phase. It was found

that a $\gamma$-$MnO_2$ heat-treated from 300-400°C should not be referred to as $\beta$-$MnO_2$ or $\gamma/\beta$-$MnO_2$ (as is often quoted in the literature) but instead as "$\beta$-like" or "pyrolusites containing random ramsdellite defects". Application of the latest structural model of $\gamma$-$MnO_2$ (section 3.8) in terms of de Wolff disorder and microtwinning was applied to the XRD patterns of Faradiser WSLi. It was found that there was decrease in microtwinning from 25-300°C but the amount of de Wolff disorder was essentially unchanged. Simulation of XRD patterns by taking appropriate amounts of two materials and comparing them with one obtained experimentally showed a heterogeneous transformation from $\gamma$ to $\beta$-$MnO_2$ in the temperature range 300-400°C. FTIR spectra of the heat-treated materials showed a progressive shift of the peaks associated with the $MnO_6$ octahedra. Comparison of the peak positions with the published data of ramsdellite and pyrolusite suggested a ramsdellite phase in the unheated material and a pyrolusite phase at 400°C. This was in agreement with the XRD data. The potential of $MnO_2$ became more negative by approximately 200mV during heat-treatment from 25-450°C. The potential decreased at a greater rate after 200°C and this was attributed to structural changes that had been observed with XRD and FTIR spectra.

In chapter 4 H insertion was investigated in an electrodeposited $MnO_2$ (R2) that had been heat-treated at 200, 300 and 400°C in air for 24 hours and then reduced to $MnOOH_{1.0}$ by either hydrazine hydrate or propan-2-ol. Different behaviour was observed and this depended on the heat-treatment temperature and the reduction method. When EMD was heat-treated at 200°C and reduced by propan-2-ol a homogeneous phase from $MnOOH_{0.07}$-$MnOOH_{0.976}$ was observed in the X-ray diffraction spectra (section 4.2.1(i)). At 400°C the reduction was heterogeneous from $MnOOH_{0.11}$-$MnOOH_{0.932}$ and within these extremes of behaviour different regions of homogeneity/heterogeneity were found. A new finding was that hydrazine hydrate caused the heterogeneous reduction of EMD heat-treated at 200°C (section 4.2.1 (ii)) even though a homogeneous phase was found for the same material reduced with propan-2-ol (section 4.2.1 (i)). At 300°C the reduction of $MnO_2$ was found to be heterogeneous whatever the mode of reduction although heterogeneous reduction was observed at lower levels of H insertion with hydrazine hydrate. FTIR spectroscopy was used as a

complementary technique to X-ray diffraction (section 4.3) and it was found that the spectra could be divided into two regions. Vibrations in the region 400-1400cm$^{-1}$ were due to the $MnO_6$ octahedral framework and from 1400-4000 cm$^{-1}$ they were due to OH bending and stretching vibrational modes. The changes in the $MnO_6$ octahedral framework were related to the Jahn-Teller deformation associated with the $Mn^{3+}$ ion (section 4.3.1 (i)). Peaks relating to OH bond formation centred at 2050 and 2650cm$^{-1}$ dominated the spectra at $MnOOH_{1.0}$. It was found that for a homogeneous reduction (section 4.3.1 (i)) peaks relating to OH bond formation only appeared after $MnOOH_{0.70}$ and this demonstrated delocalisation of the inserted proton and electron without significant OH bond formation which was a new finding (Figure 4.36). When the reduction of $MnO_2$ was heterogeneous peaks relating to OH bond formation appeared much earlier in the reduction process. The crystal structure of the sample heat-treated at 200°C was similar to $\delta$-MnOOH which was the name given to the chemical reduction product of non heat-treated EMD by Maskell *et al.* (1981) and Fitzpatrick and Tye (1991). At 400°C the crystal structure was the same as manganite. Mixing of the X-ray diffraction spectra was used to establish the onset of the heterogeneous behaviour and the following levels of H insertion were found at which heterogeneity set in: 200°C hydrazine $MnOOH_{0.48}$, 300°C hydrazine $MnOOH_{0.33}$ and 300°C propan-2-ol $MnOOH_{0.534}$.

In chapter 5 a range of chemically inserted CMD non heat-treated and heat-treated H insertion materials analogous to those prepared in chapter 4 were made. The resulting powder XRD patterns revealed differing regions of homogeneity/heterogeneity in the reduction process. The non heat-treated material exhibited the largest region of homogeneity and at 400°C the reduction was entirely heterogeneous. Between these extremes of behaviour intermediate levels of homogeneity/heterogeneity were observed (see Table 5.1). The crystal structure of the most reduced materials formed a similar range of intergrowth structures as was found for the EMD materials in Chapter 4. The boundaries of the homogeneous/heterogeneous behaviour of EMD and CMD were compared in Table 5.2 and it was found that heterogeneity occurred at a higher level of H insertion for the CMD materials.

Lithium insertion into an electrodeposited (R2) and chemical (Faradiser

WSLi) $MnO_2$ heat-treated at 200, 300 and 400°C for 24 hours in air and reduced using n-butyllithium in an argon filled glove-box was investigated in chapter 6. The resulting compounds were studied by XRD. New peaks appeared in the XRD patterns at low levels of Li insertion. From the results shown in chapters 4 and 5 this seemed indicative of a heterogeneous process. This was confirmed by mixing of the XRD spectra in section 6.4 and it was shown that the reaction was heterogeneous after $MnOOLi_{0.3}$ for EMD and $MnOOLi_{0.35\text{-}0.40}$ for CMD. In contrast to H insertion the onset of heterogeneity was independent of the heat treatment temperature. The X-ray diffraction patterns of the new phase could be indexed to an orthorhombic unit cell. The lattice parameters were calculated and were in reasonable agreement with those found in the literature. Again, in contrast to H insertion, the crystal structure of the most reduced Li-inserted materials seemed to be the same regardless of the initial heat treatment temperature.

A novel applied linear regression analysis was developed to be used to pinpoint possible peak movement in a spectral dataset using the coefficient of determination ($R^2$) as the parameter. The analysis consisted of two parts: first of all a linear regression analysis was performed at a fixed value of either Degrees 2Θ (XRD) or wavenumber (FTIR) with the intensity or absorbance as the dependent variable against r in $MnOOH_r$ as the independent variable. In the second part of the analysis the original data was transformed so that the slope of the regression line was the same throughout the dataset and it was found that when a peak moved in set of data this showed up as a decrease in $R^2$. Three important pieces of information could be obtained from the data when the slope of the regression line was unity. They were as follows (see Figure 7.10):

(i) The variability in the peak height of the graphite peak at 26.48°2Θ.

(ii) The appearance of new lines in the XRD pattern at 37.44°2Θ.

(iii) Peak movement at 36.48, 41.92, 55.52 and 65.76°2Θ.

In the heterogeneous reduction of $\beta$-$MnO_2$-$\gamma$-MnOOH (section 7.1.2) little or no peak movement was observed and consequently the values of $R^2$ were close to one when all the data had the same slope. In section 7.1.3 a new method was presented to determine the regions of homogeneity/heterogeneity that had been observed in chapter 4. This involved plotting the intensity against H insertion

level for a range of °2Θ values on either side of the minimum value of $R^2$ in the rotated data. Only the peak at 55°2Θ was suitable and it was found that in the heterogeneous region the intensity was rising, falling or horizontal with respect to H insertion level.

## 8.2 Further Work.

In the following paragraphs a number of suggestions are made for further study which should complement this investigation.

The pyknometric density measurements performed in section 3.5 gave valuable information on the type of water that was being removed at each particular temperature and it would be interesting to expand the range of heat treatment temperatures and times of $MnO_2$ that were used. This may help determine the type of water being removed and therefore complement the XRD data as to the optimum heat treatment temperature for $MnO_2$ in lithium cells.

The FTIR study of the H inserted EMD compounds in chapter 4 gave valuable data about the $MnO_6$ octahedral framework and it would be worthwhile assigning vibrational modes to the peaks in that region. Also additional FTIR investigations in the region below $400cm^{-1}$ where other peaks occur may lead to a greater understanding of the H insertion process. A study of the potential against degree of reduction (r in $MnOOH_r$) for the manganese oxyhydroxides prepared in chapter 4 and 5 would be worthwhile and breaks in the curves should correlate with those obtained in the XRD patterns. In chapter 5 the series of CMD H inserted compounds were reduced by hydrazine hydrate and a series of samples reduced with propan-2-ol would enable a direct comparison to be made with the EMD materials prepared in chapter 4.

In chapter 6 samples of composition $MnOOLi_x$ ($0 \leq x \leq 1$) covering the full range of Li-insertion were not prepared and it would be important to prepare samples with $x > 0.7$ $MnOOLi_x$ for a complete elucidation of the Li-insertion process. For a complete investigation it would be also be necessary to have electrochemical discharge data of Li-insertion to complement the chemically prepared samples.

# Appendixes

## Appendix A

Statistical Analysis Graphs

The data that was discussed in Chapter 7 is presented here. First of all the XRD patterns are shown. Then results of the initial linear regression analysis with $R^2$ and the slope of the regression line are displayed. Results are then shown when all the data has a slope of unity (this was outlined in section 7.11). Finally plots of intensity against H insertion level which correspond to the minimum values of $R^2$ in the rotated data are presented.

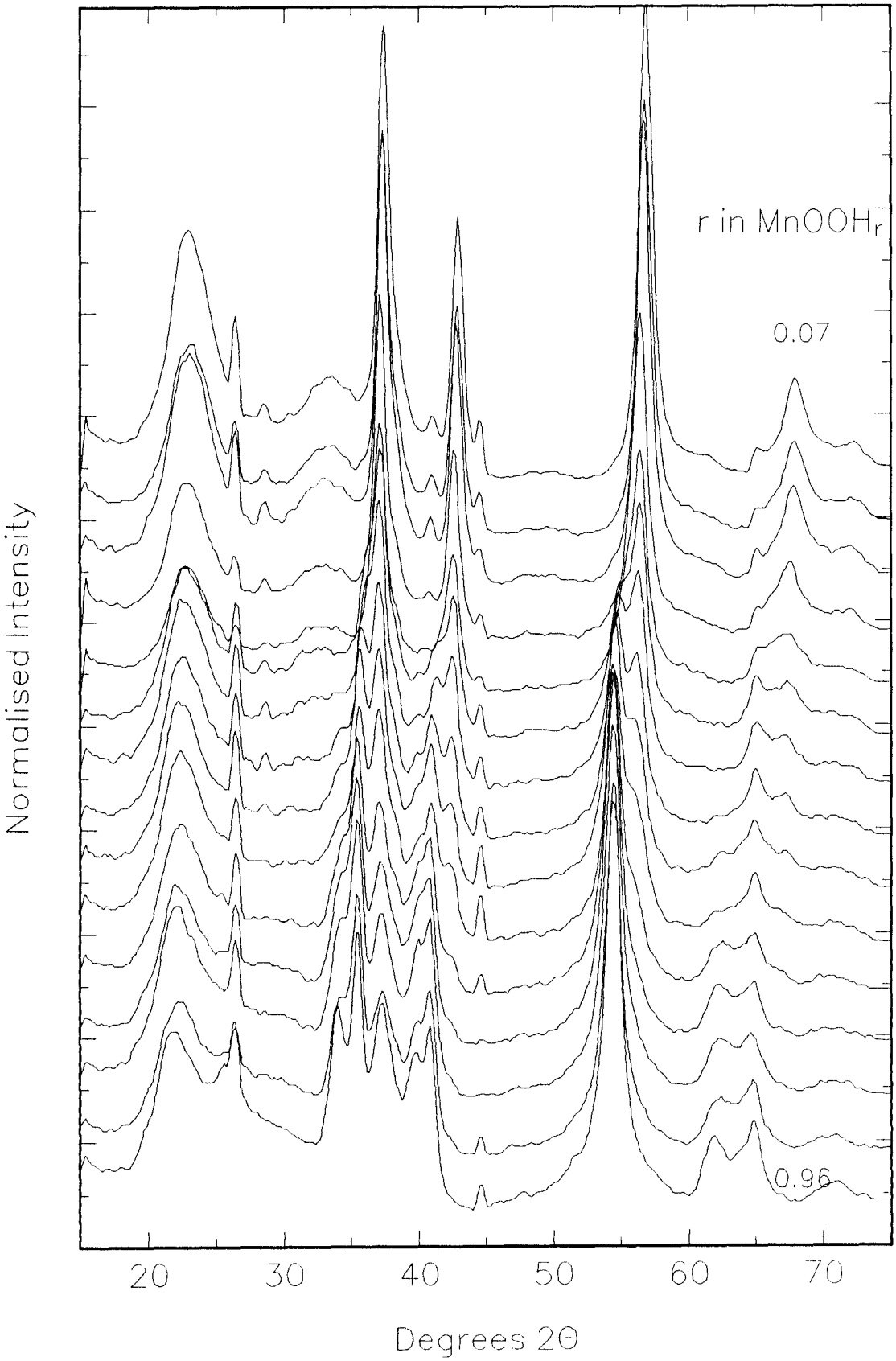


***Figure A1***: Dataset that was used for the linear regression analysis: EMD heat-treated at 200°C; hydrazine hydrate reduction method.

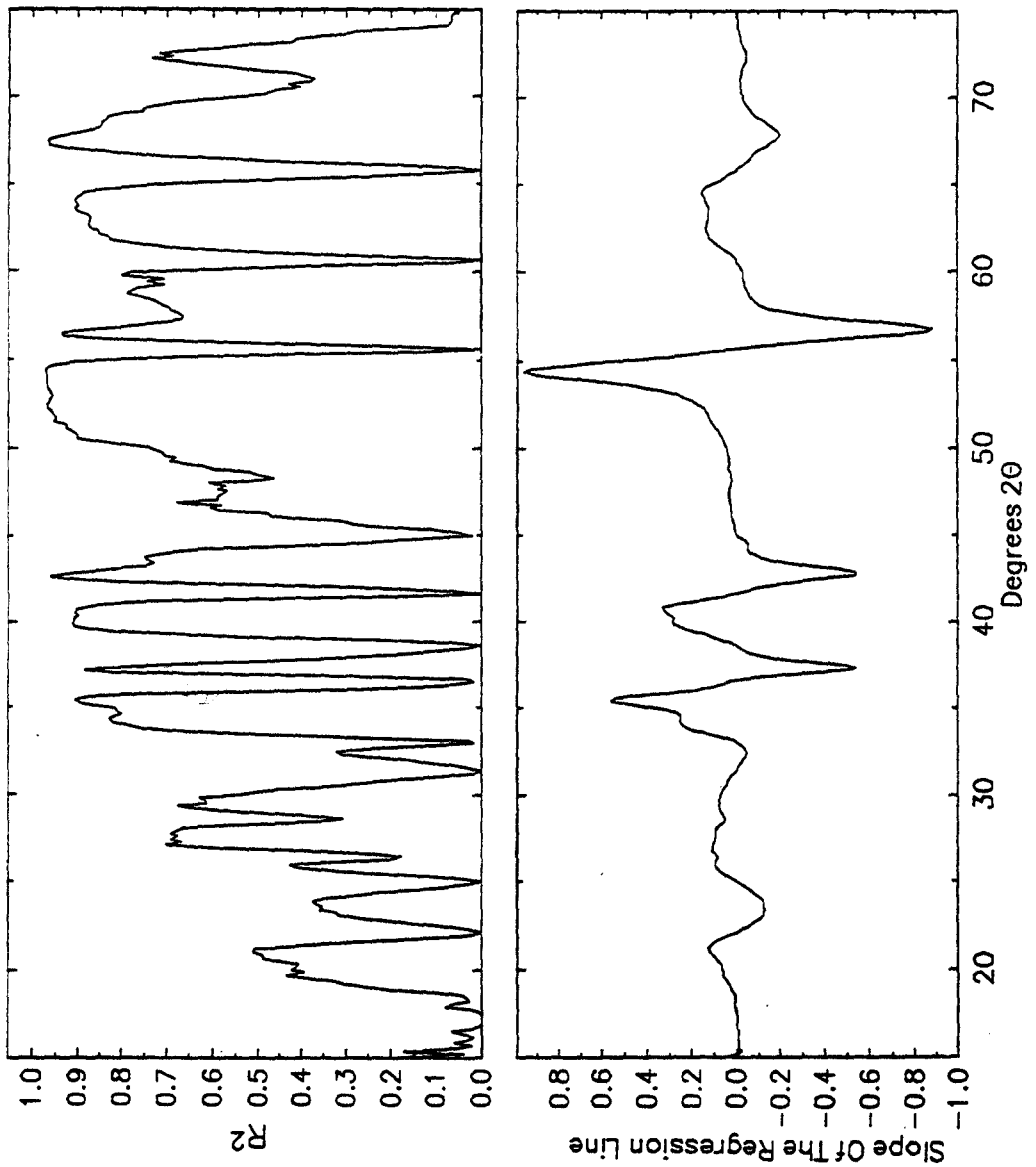


*Figure A2*: Slope of the regression line and $R^2$ against degrees 2Θ; EMD heat-treated at 200°C; hydrazine hydrate reduction method.

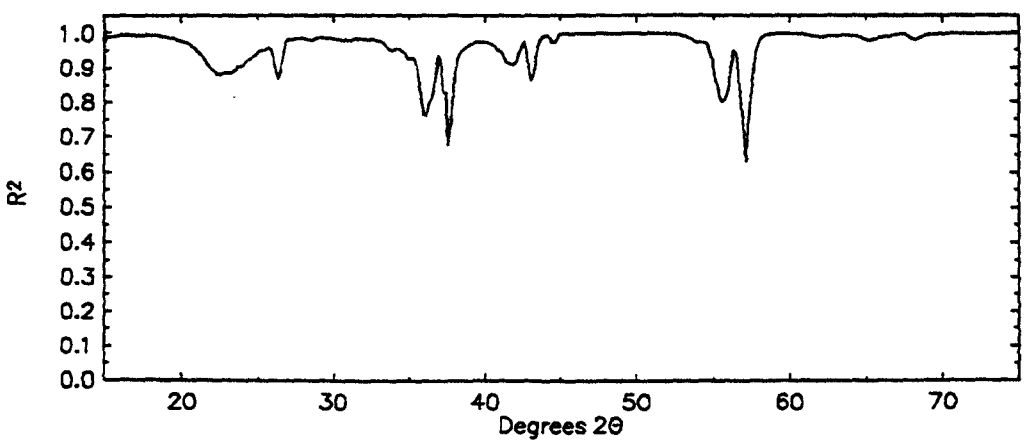


*Figure A3*: $R^2$ against Degrees 2Θ when the data has the same slope; EMD heat-treated at 200°C; hydrazine hydrate reduction method.

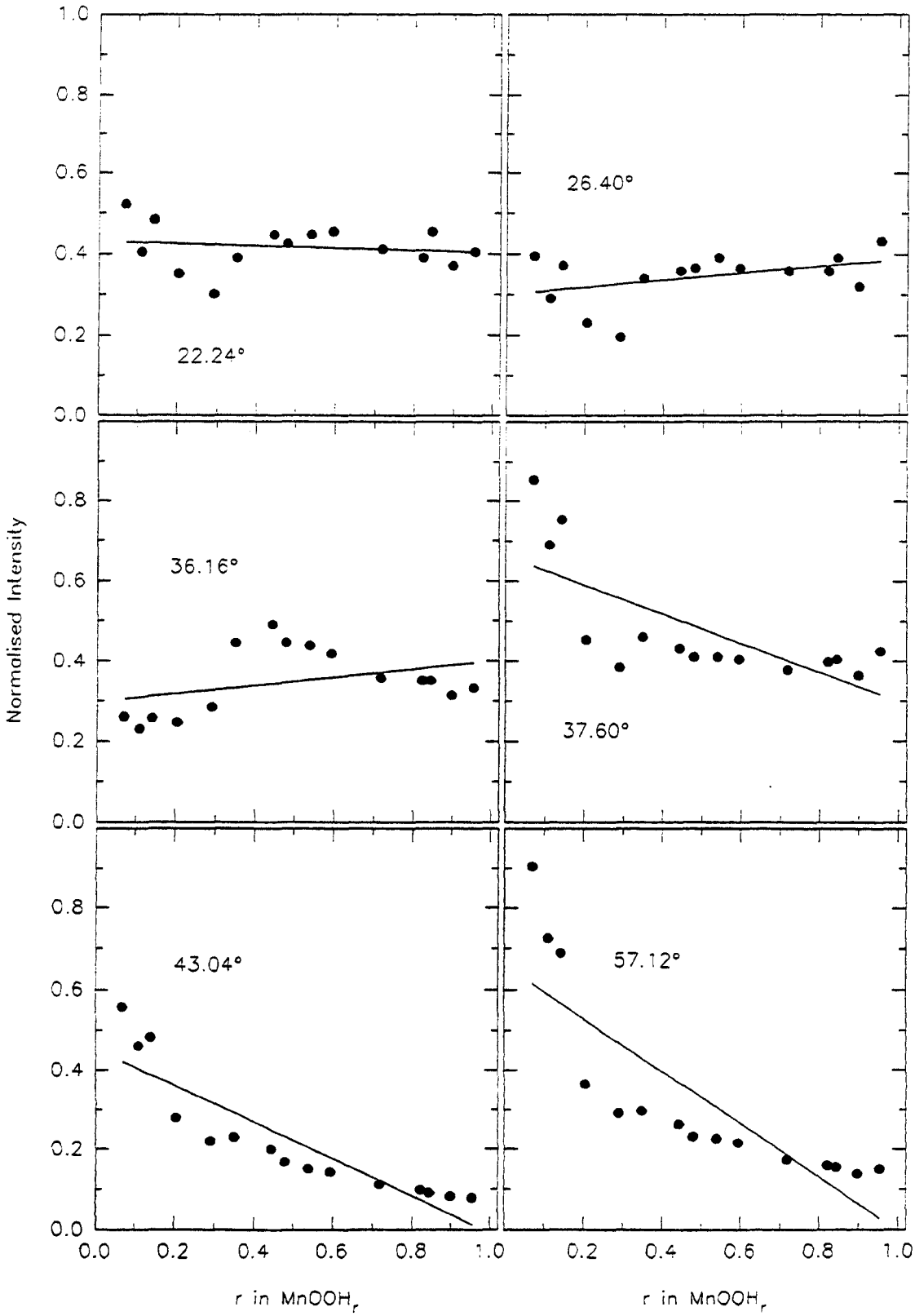


***Figure A4***: Plots of intensity against H insertion level corresponding to the minimum values of $R^2$ given in figure A3 (the value of °2Θ is given in the plot): EMD heat-treated at 200°C; hydrazine hydrate reduction.

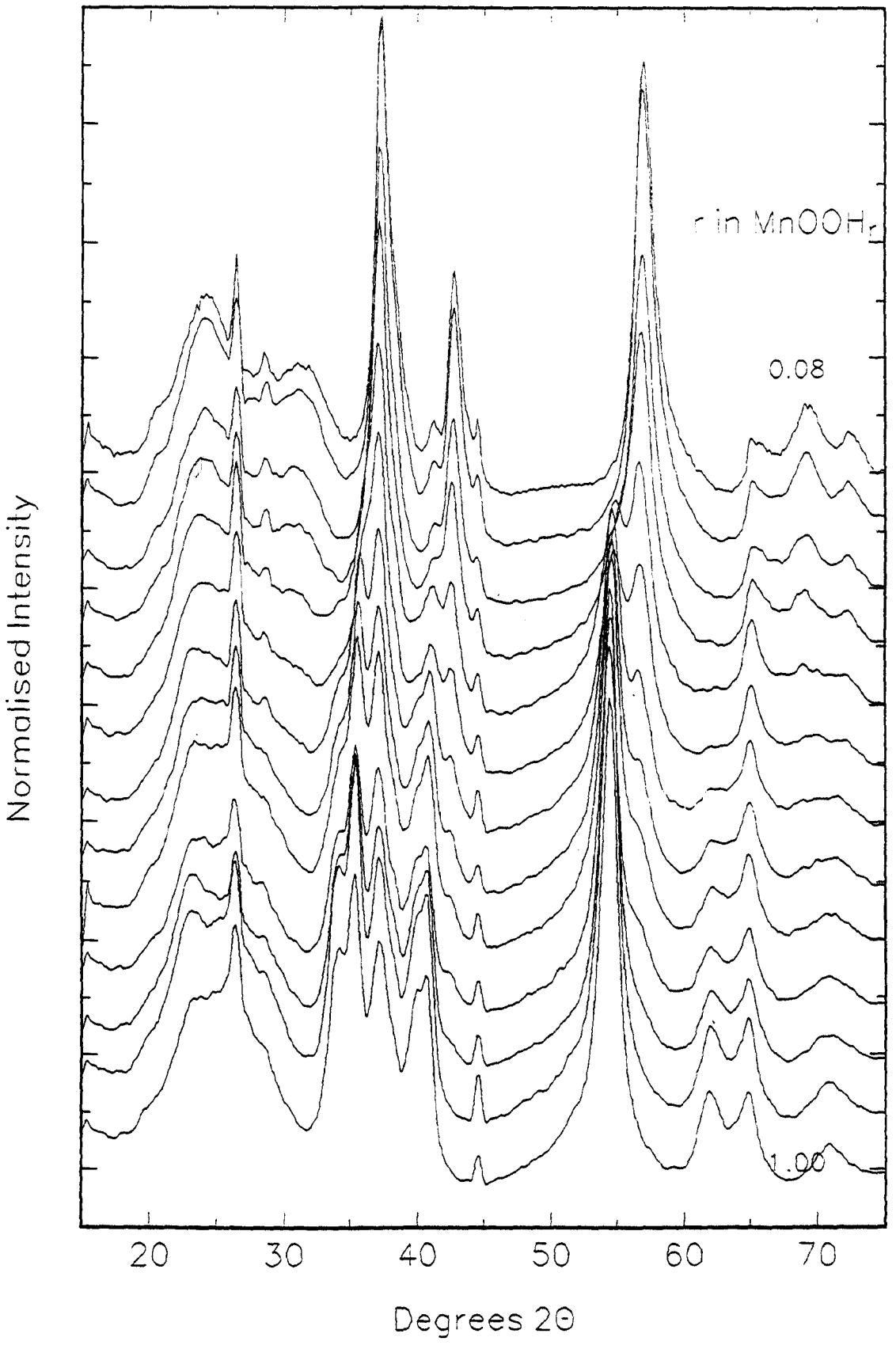


***Figure A5***: Dataset that was used for the linear regression analysis: EMD heat-treated at 300°C; hydrazine hydrate reduction.

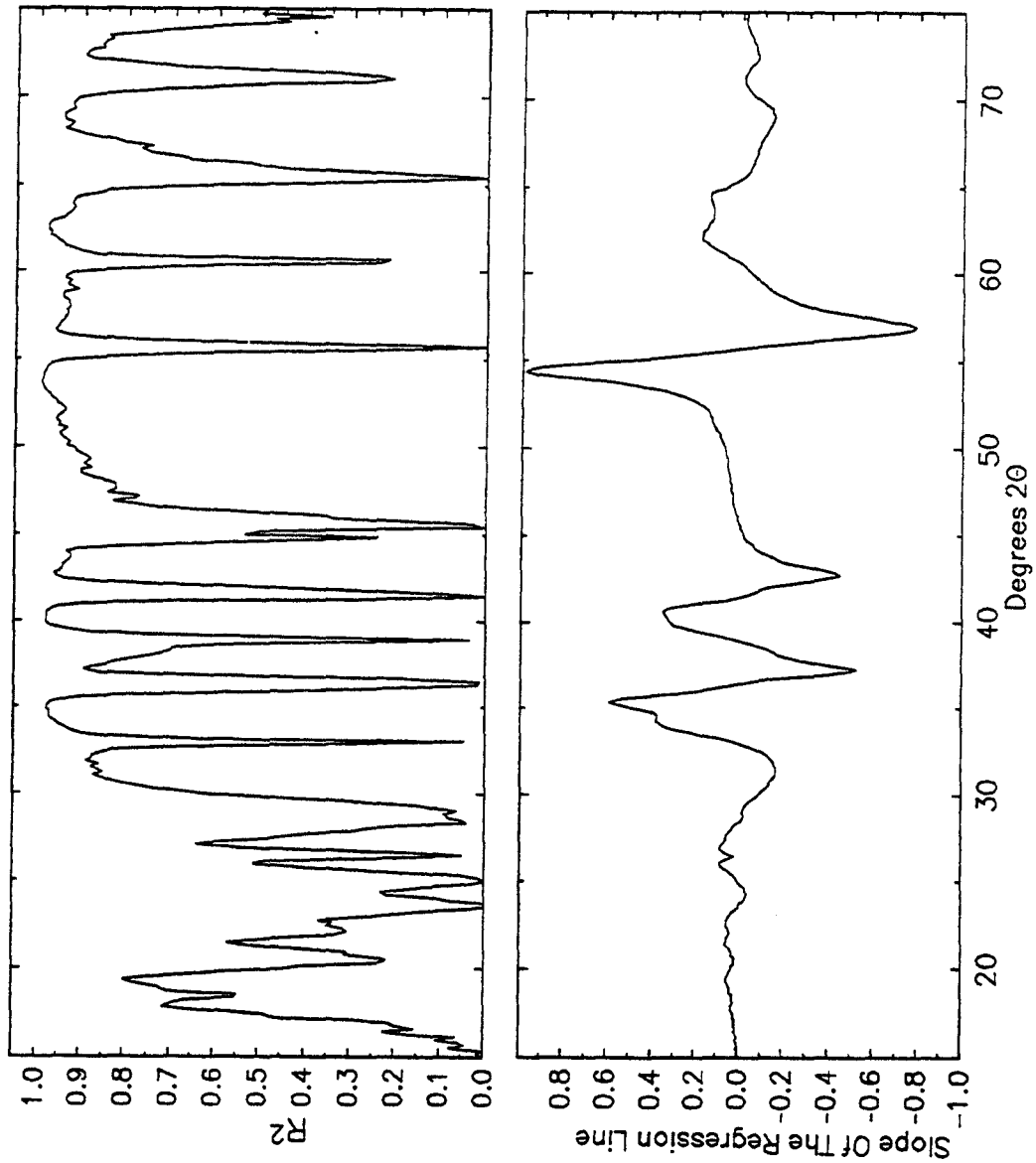


***Figure A6***: Slope of the regression line and $R^2$ against Degrees 2Θ; EMD heat-treated at 300°C; hydrazine hydrate reduction method.

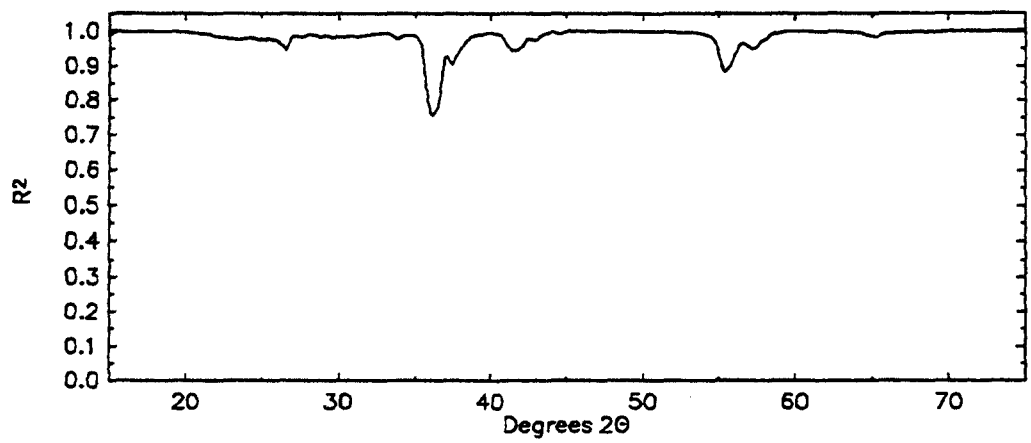


***Figure A7***: $R^2$ against Degrees 2Θ when the data has the same slope; EMD heat-treated at 300°C; hydrazine hydrate reduction method.

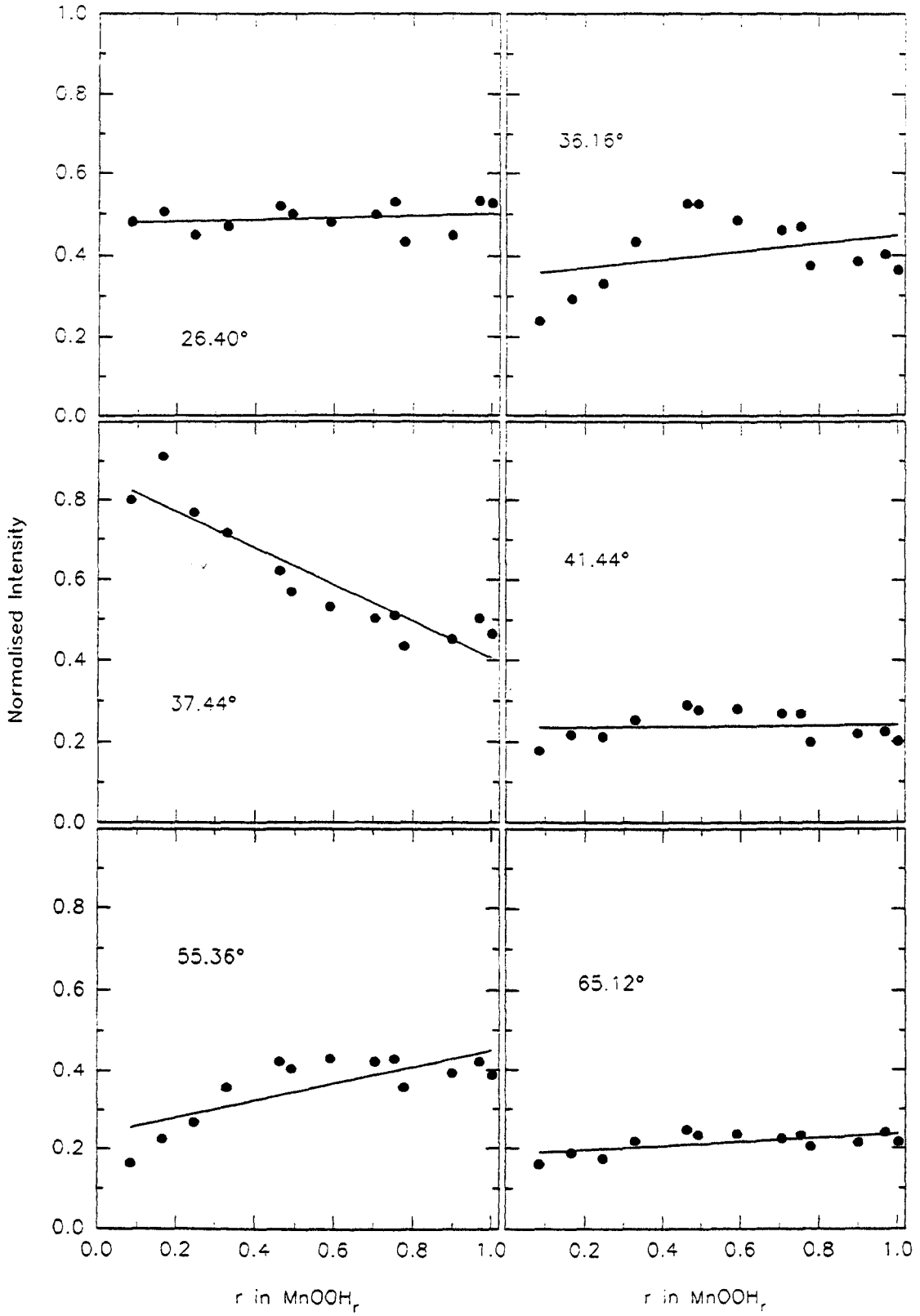


***Figure A8***: Plots of intensity against H insertion level corresponding to the minimum values of $R^2$ given in figure A7 (the value of °2Θ is given in the plot): EMD heat-treated at 300°C; hydrazine hydrate reduction.

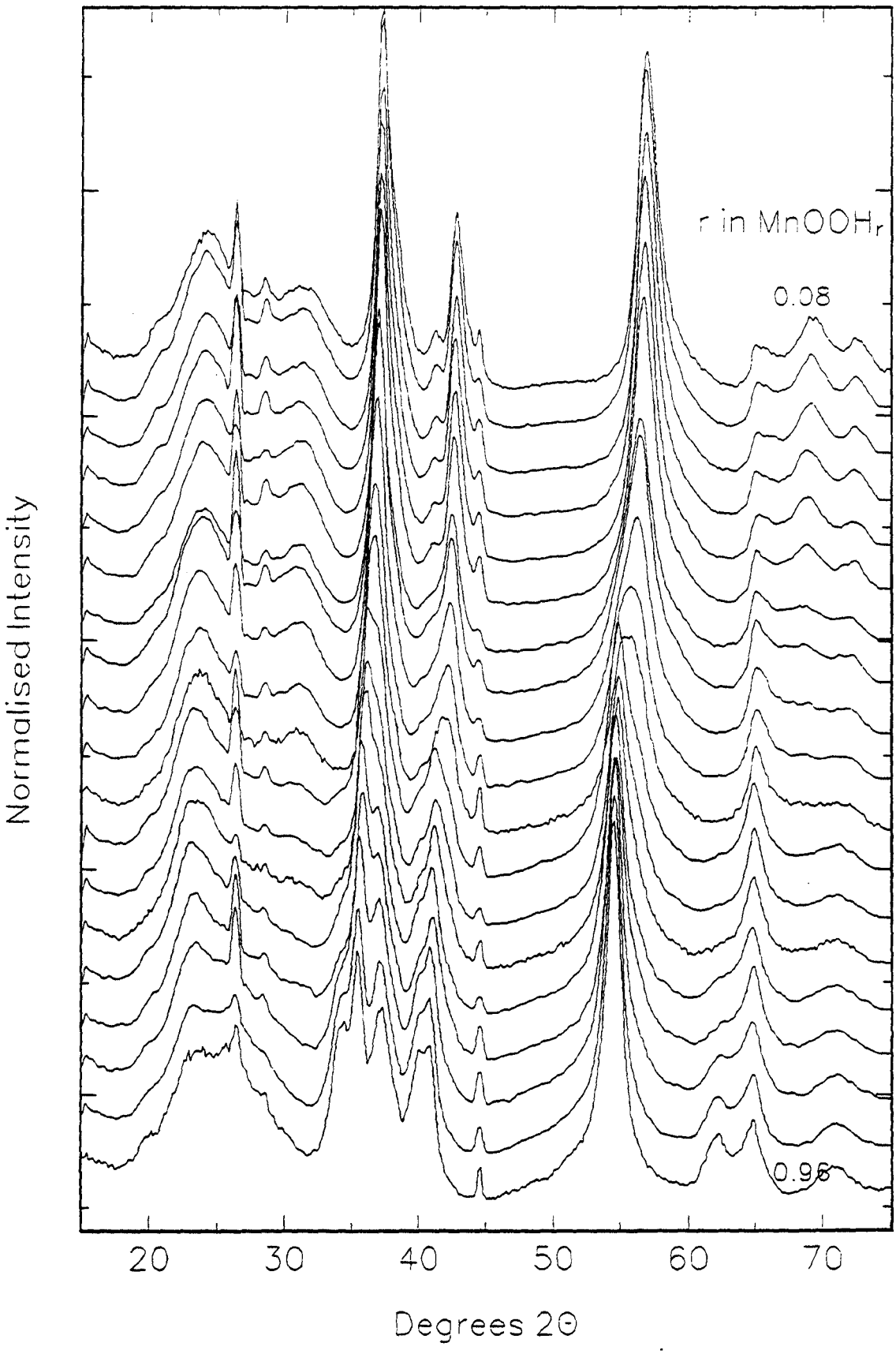


***Figure A9***: **Dataset that was used for the linear regression analysis: EMD heat-treated at 300°C; propan-2-ol reduction method.**

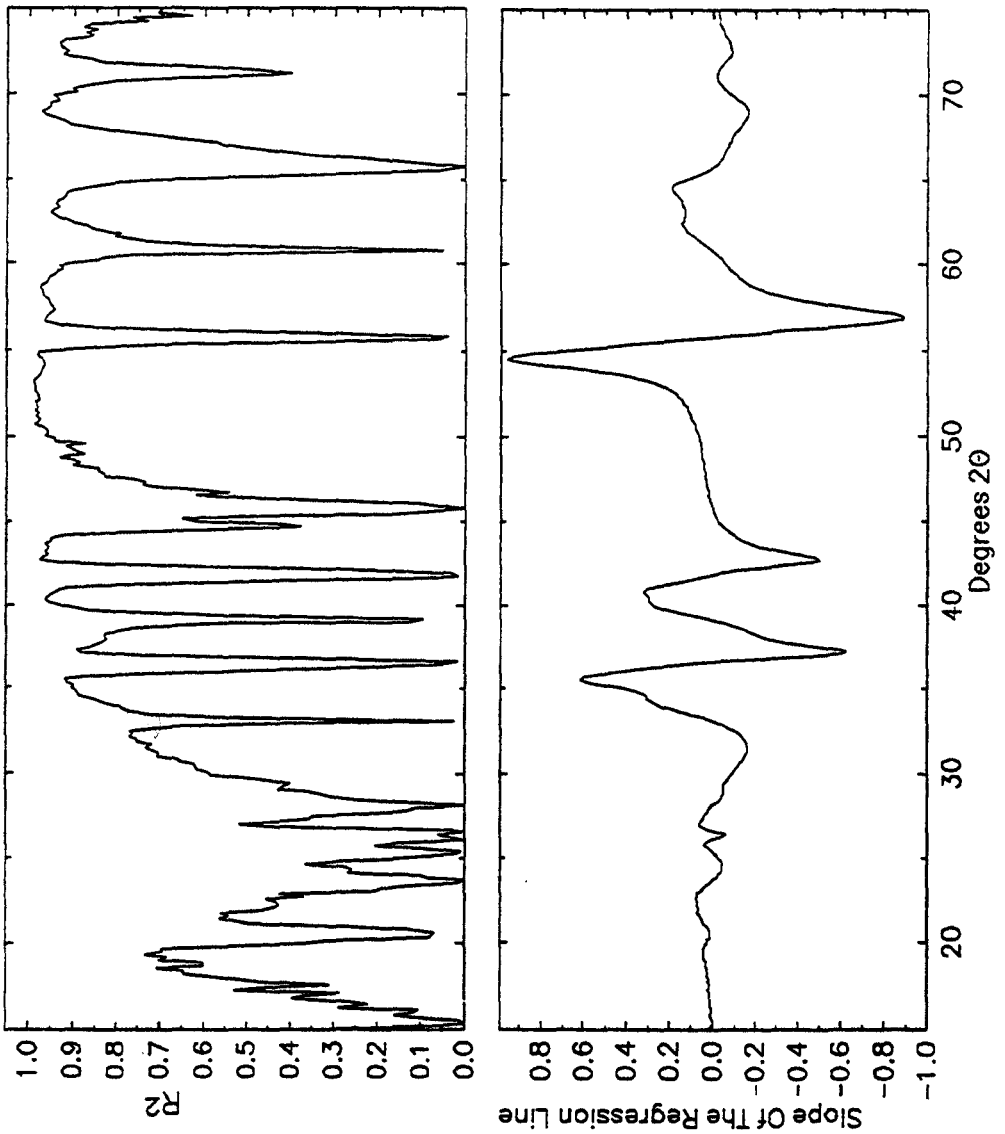


*Figure A10*: Slope of the regression line and $R^2$ against Degrees 2Θ; EMD heat-treated at 300°C; propan-2-ol reduction method.

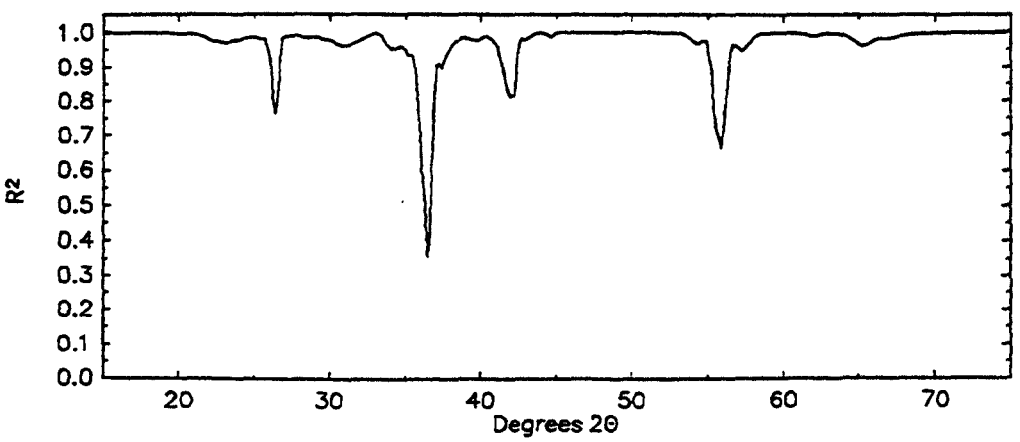


*Figure A11*: $R^2$ against Degrees 2Θ when the data has the same slope; EMD heat-treated at 300°C; propan-2-ol reduction method.

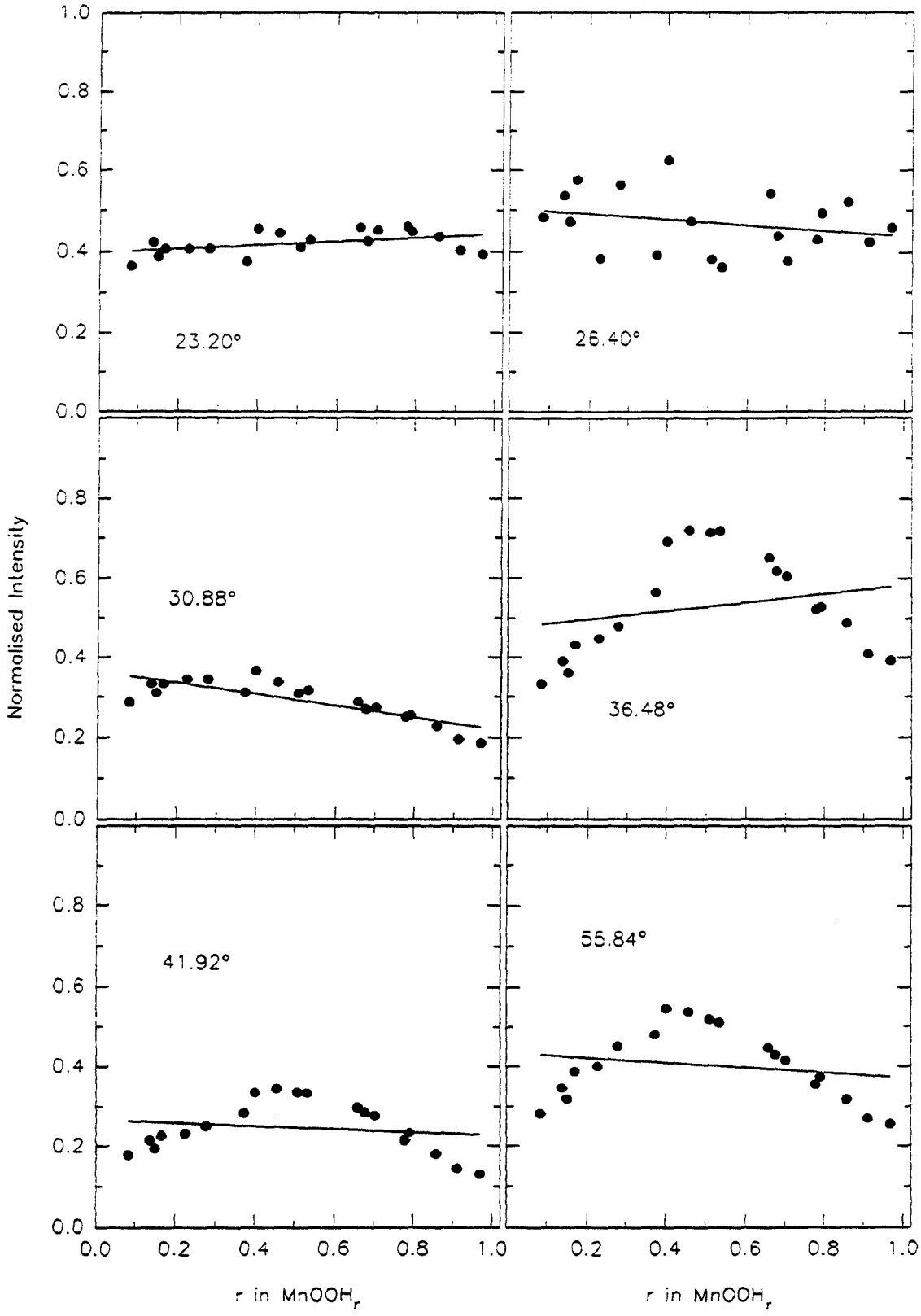


***Figure A12***: Plots of intensity against H insertion level corresponding to the minimum values of $R^2$ given in figure A11 (the value of °2Θ is given in the plot): EMD heat-treated at 300°C; propan-2-ol reduction.

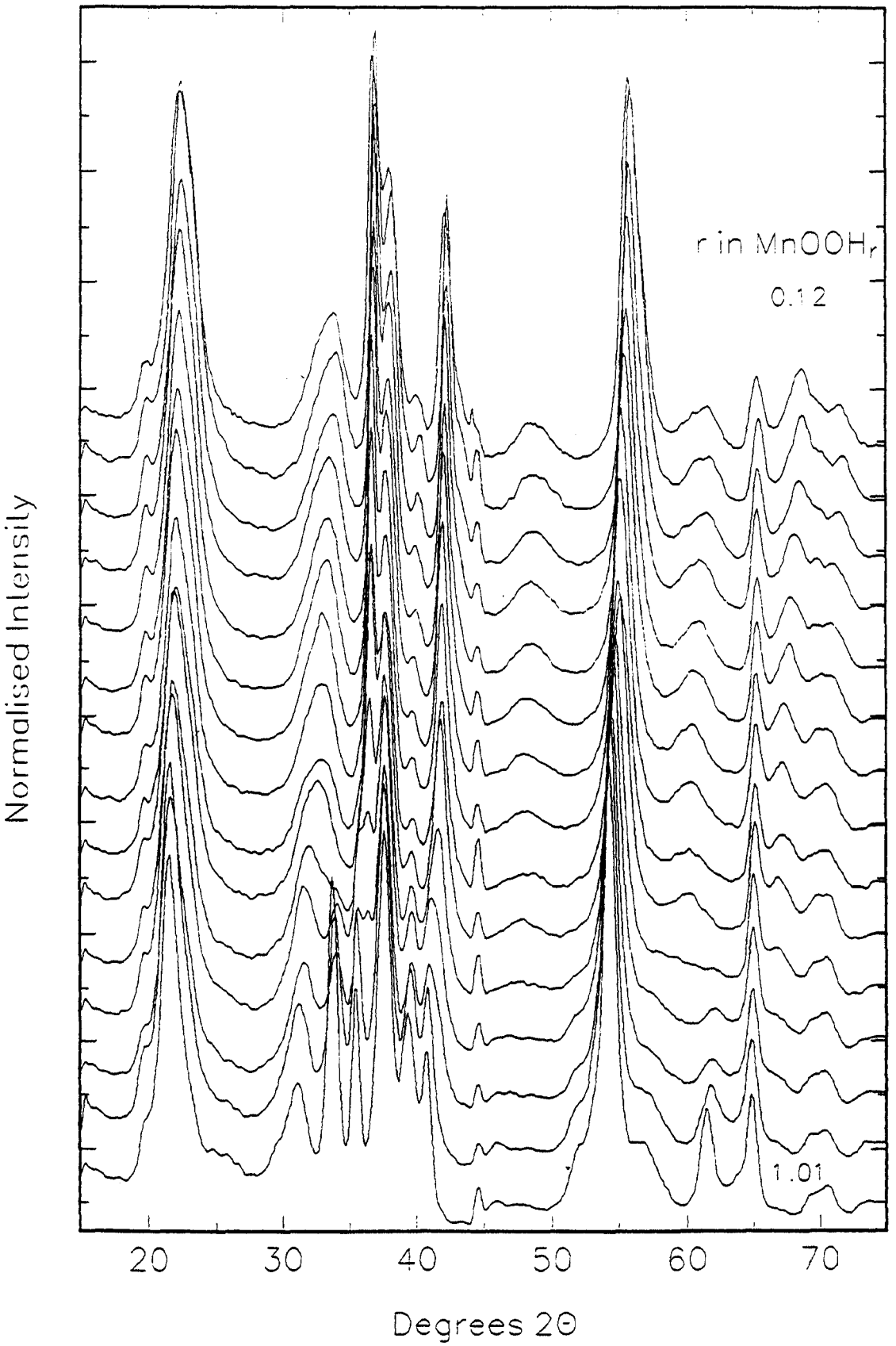


***Figure A13***: **Data set that was used for the linear regression analysis: non heat-treated CMD; hydrazine hydrate reduction method.**

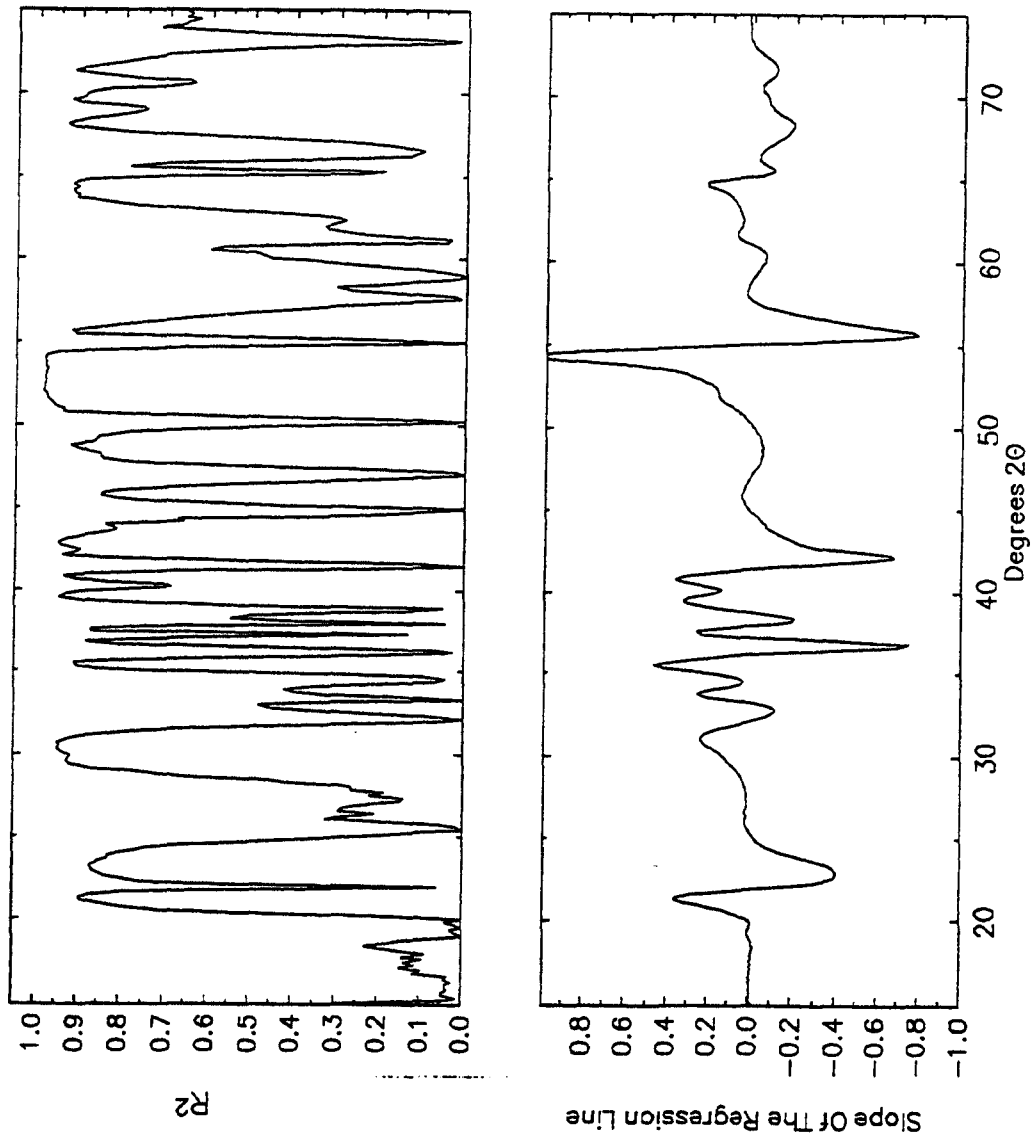


***Figure A14***: Slope of the regression line and $R^2$ against Degrees 2Θ; non heat-treated CMD; hydrazine hydrate reduction method.

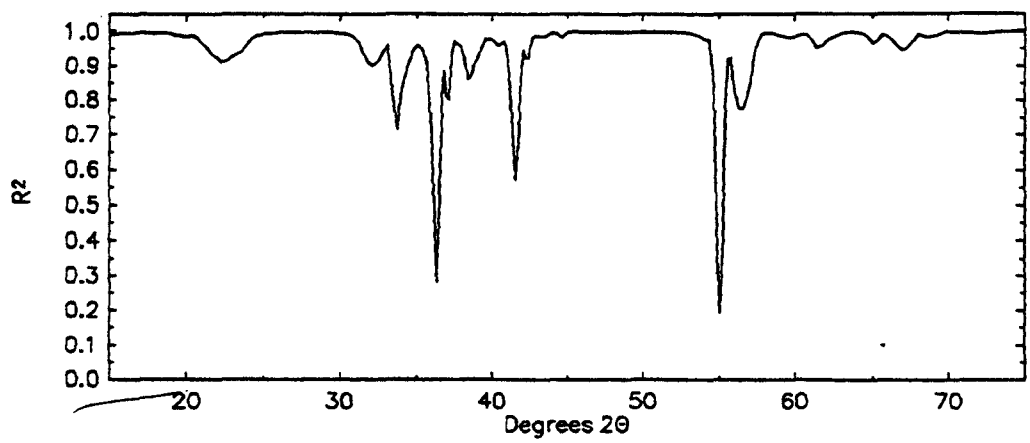


***Figure A15***: $R^2$ against Degrees 2Θ when the data has the same slope; non heat-treated CMD; hydrazine hydrate reduction method.

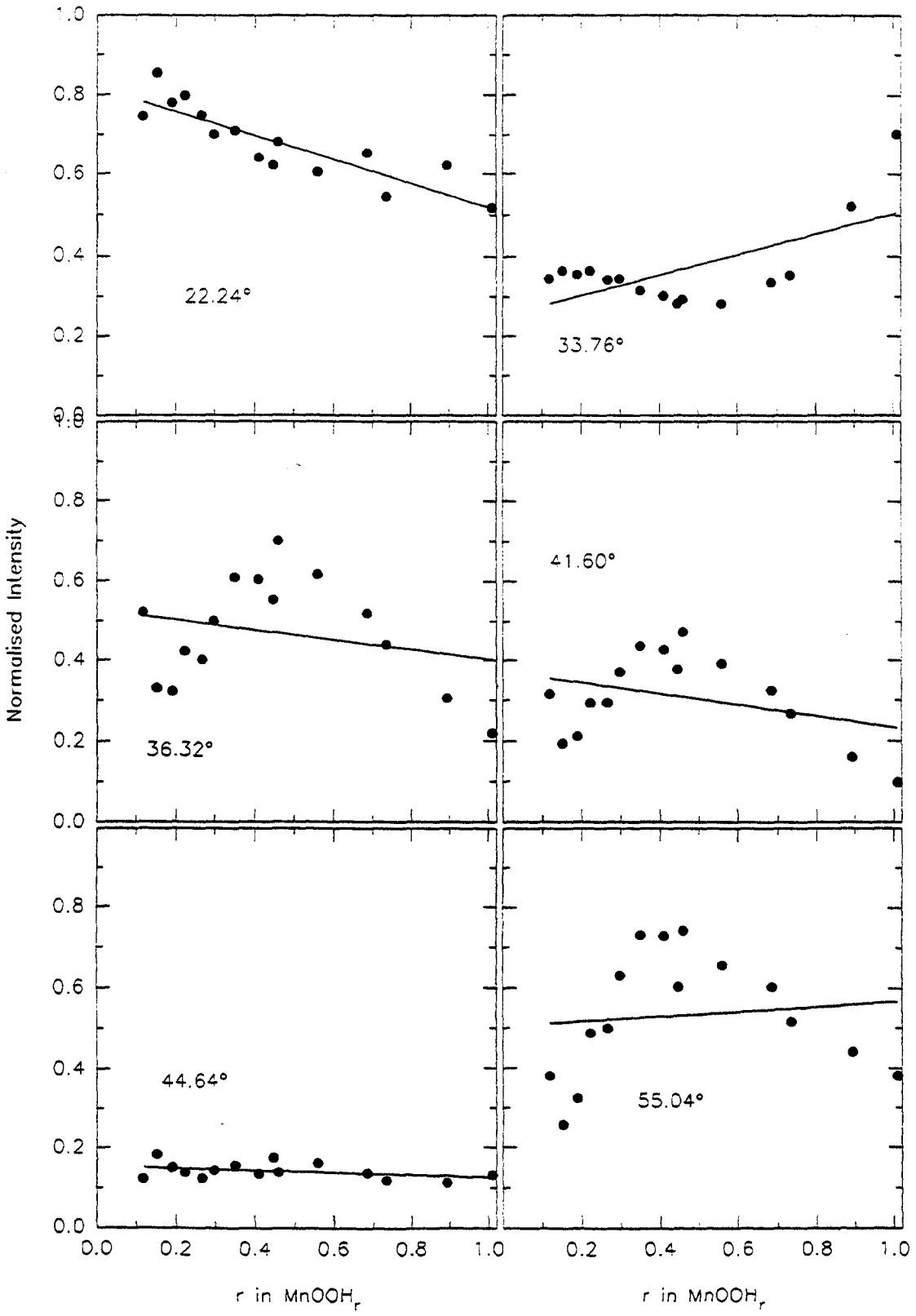


***Figure A16***: Plots of intensity against H insertion level corresponding to the minimum values of $R^2$ given in figure A15 (the value of °2Θ is given in the plot): non heat-treated CMD; hydrazine hydrate reduction.

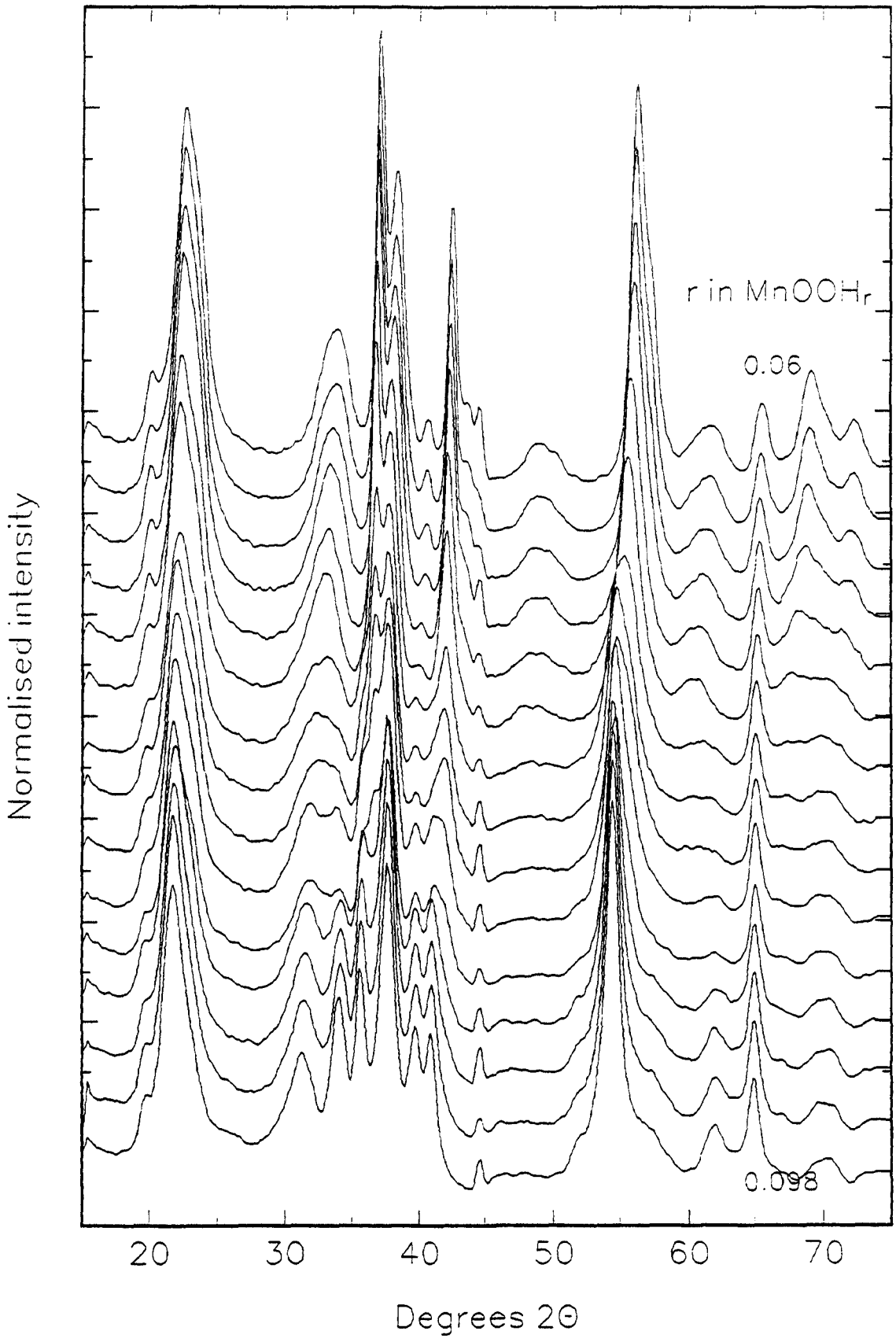


***Figure A17*: Dataset that was used for the linear regression analysis: CMD heat-treated at 200°C; hydrazine hydrate reduction method.**

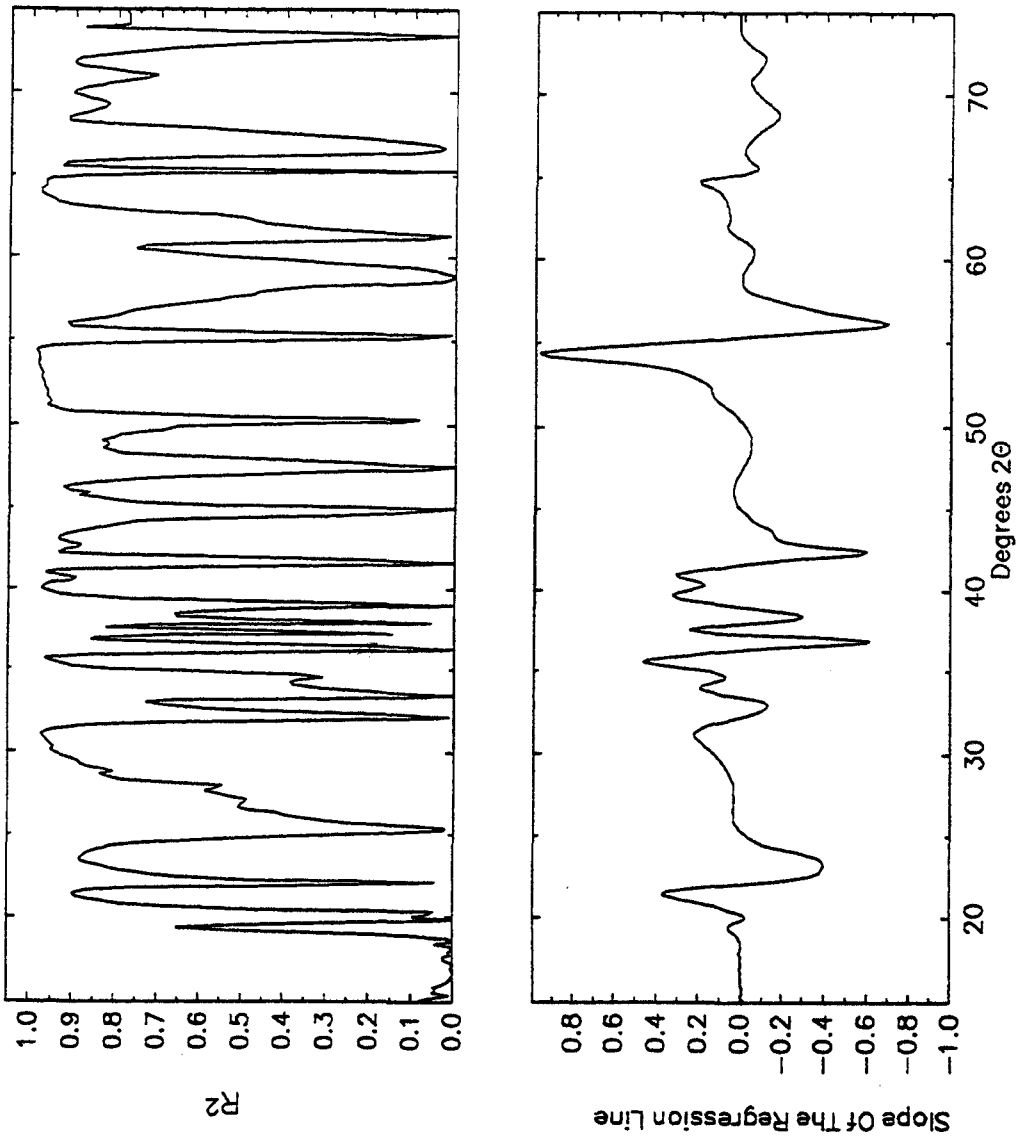


***Figure A18***: Slope of the regression line and $R^2$ against Degrees 2Θ; CMD heat-treated at 200°C; hydrazine hydrate reduction method.

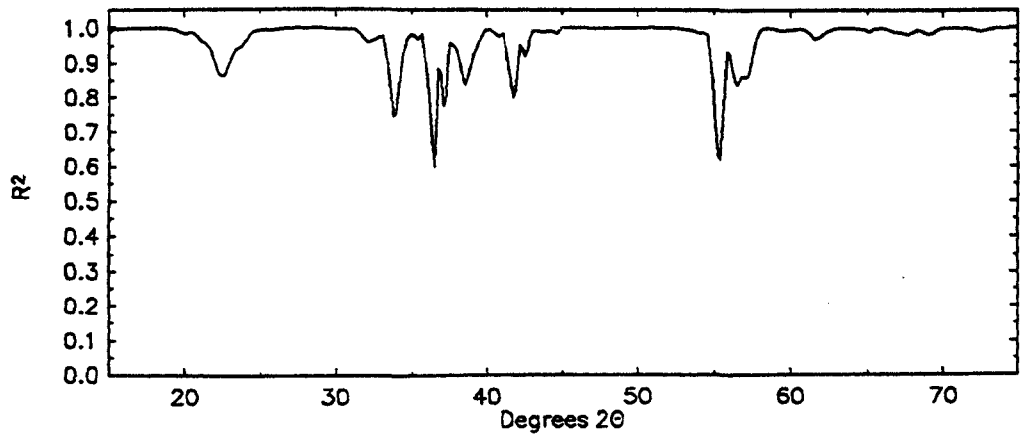


***Figure A19***: $R^2$ against Degrees 2Θ when the data has the same slope; CMD heat-treated at 200°C; hydrazine hydrate reduction method.

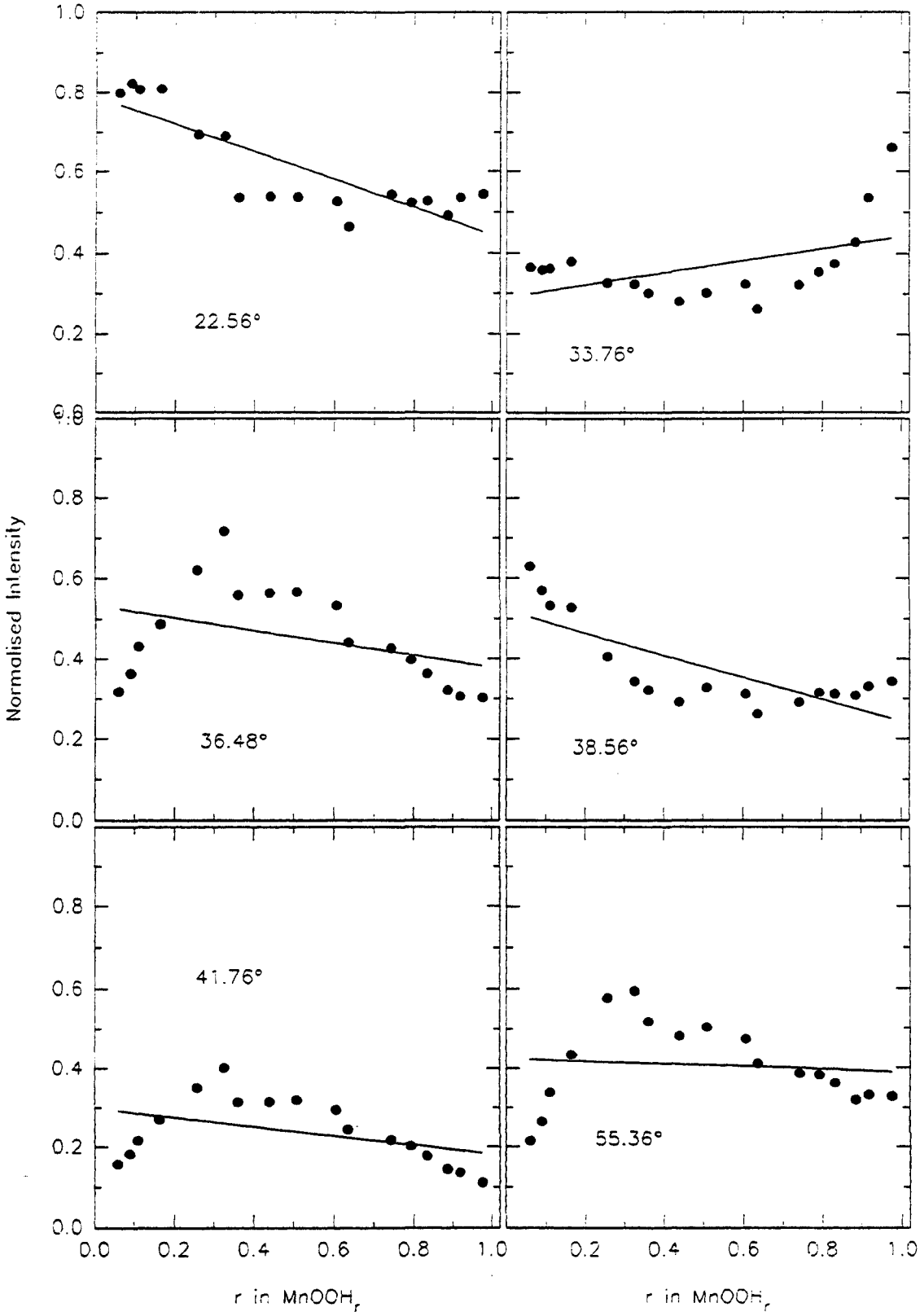


***Figure A20***: Plots of intensity against H insertion level corresponding to the minimum values of $R^2$ given in figure A19 (the value of °2Θ is given in the plot): CMD heat-treated at 200°C; hydrazine hydrate reduction.

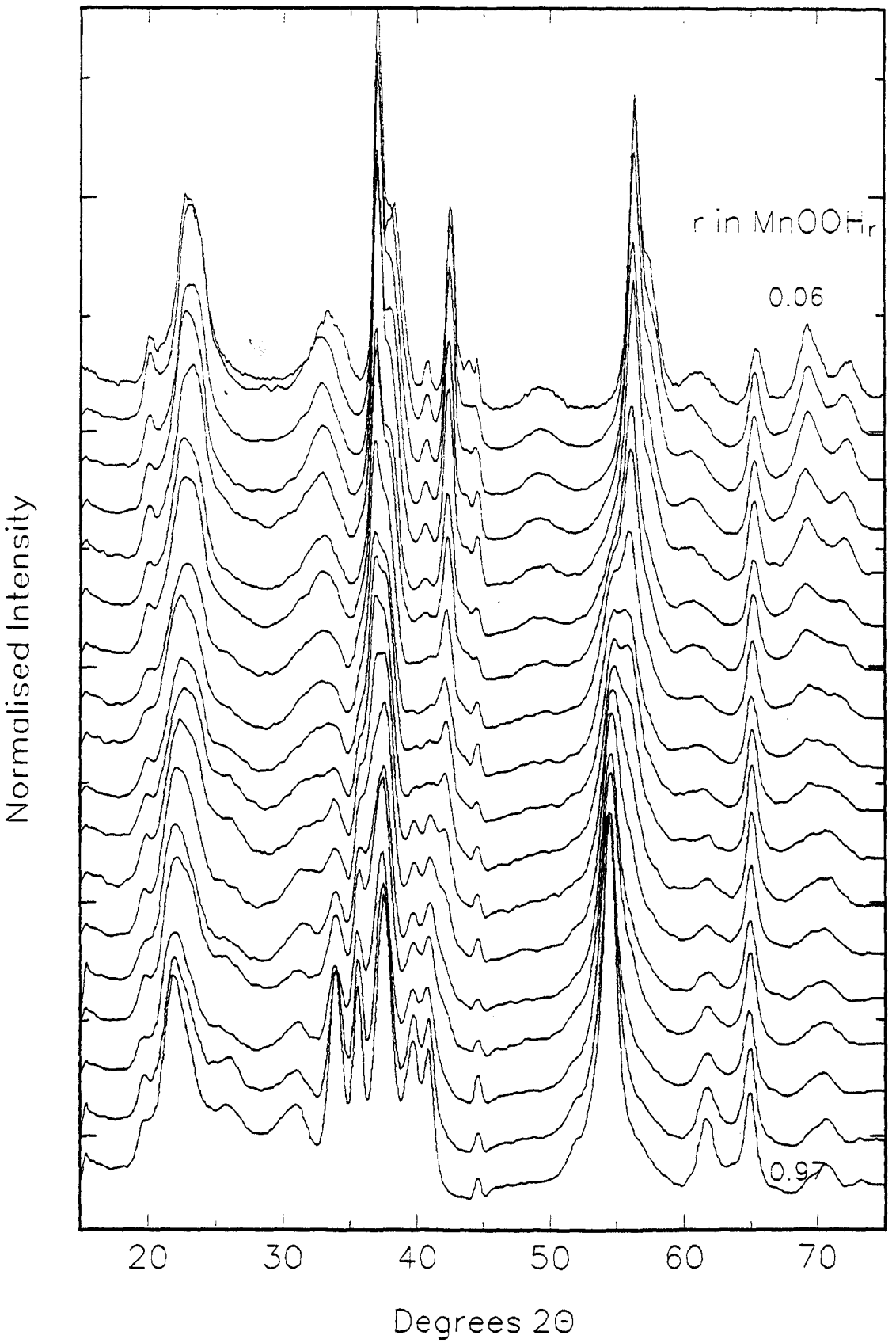


***Figure A21***: Dataset that was used for the linear regression analysis: CMD heat-treated at 300°C; hydrazine hydrate reduction.

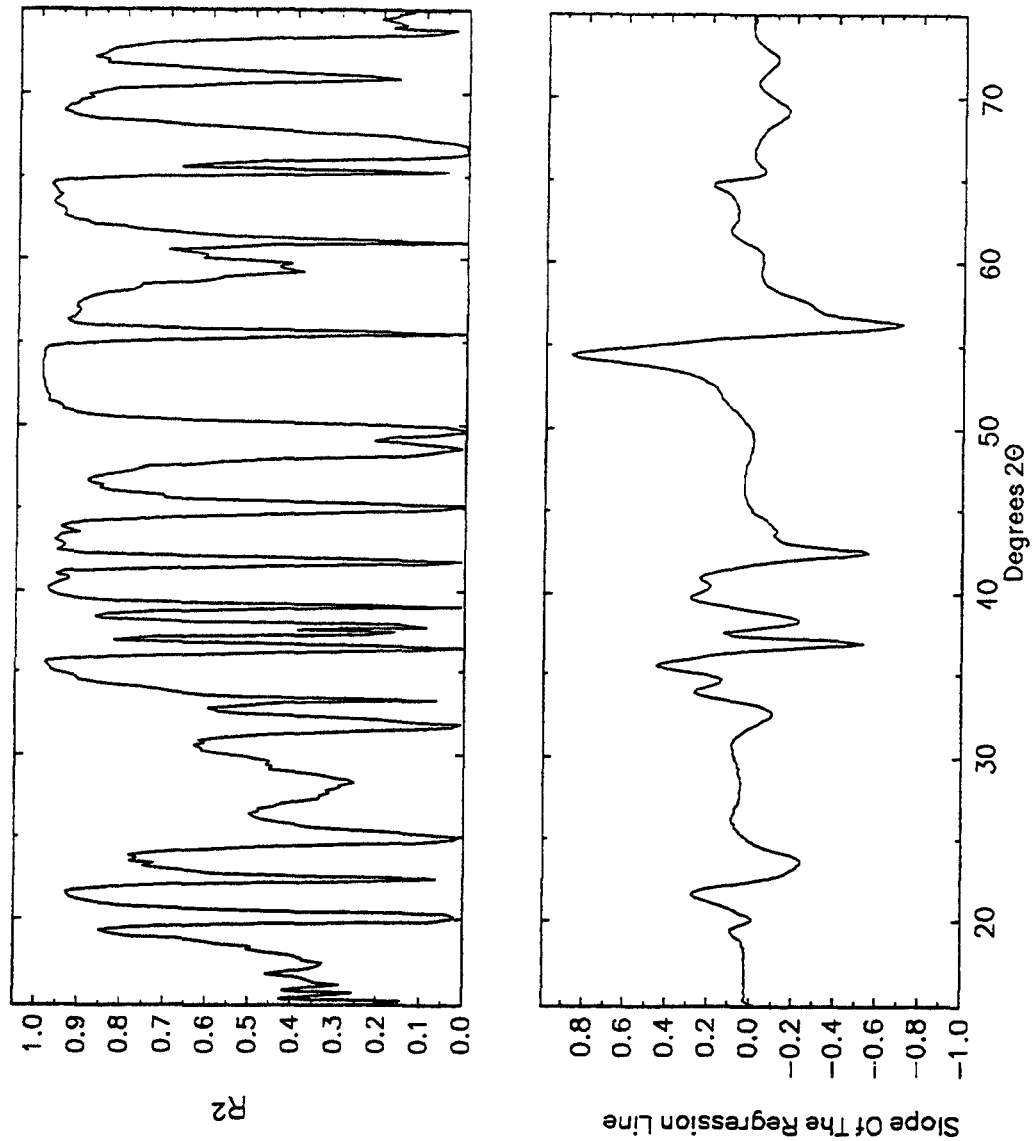


*Figure A22*: Slope of the regression line and $R^2$ against Degrees 2Θ; CMD heat-treated at 300°C; hydrazine hydrate reduction method.

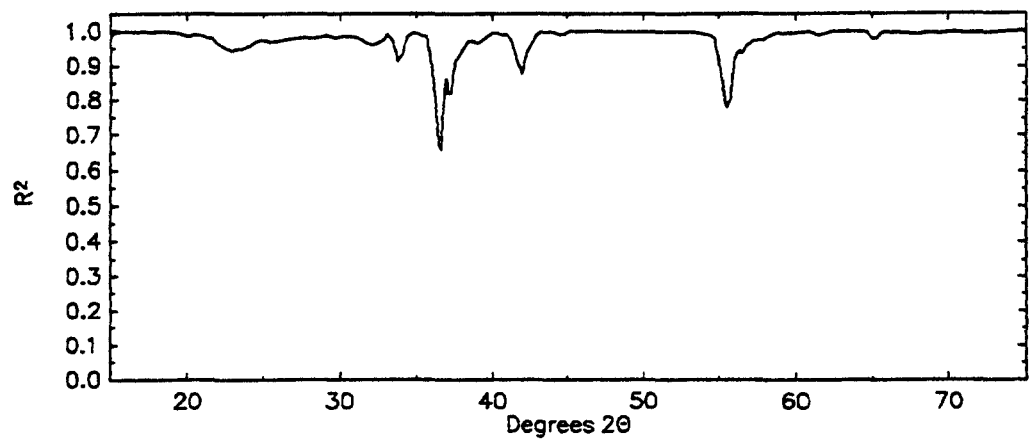


*Figure A23*: $R^2$ against Degrees 2Θ when the data has the same slope; CMD heat-treated at 300°C; hydrazine hydrate reduction method.

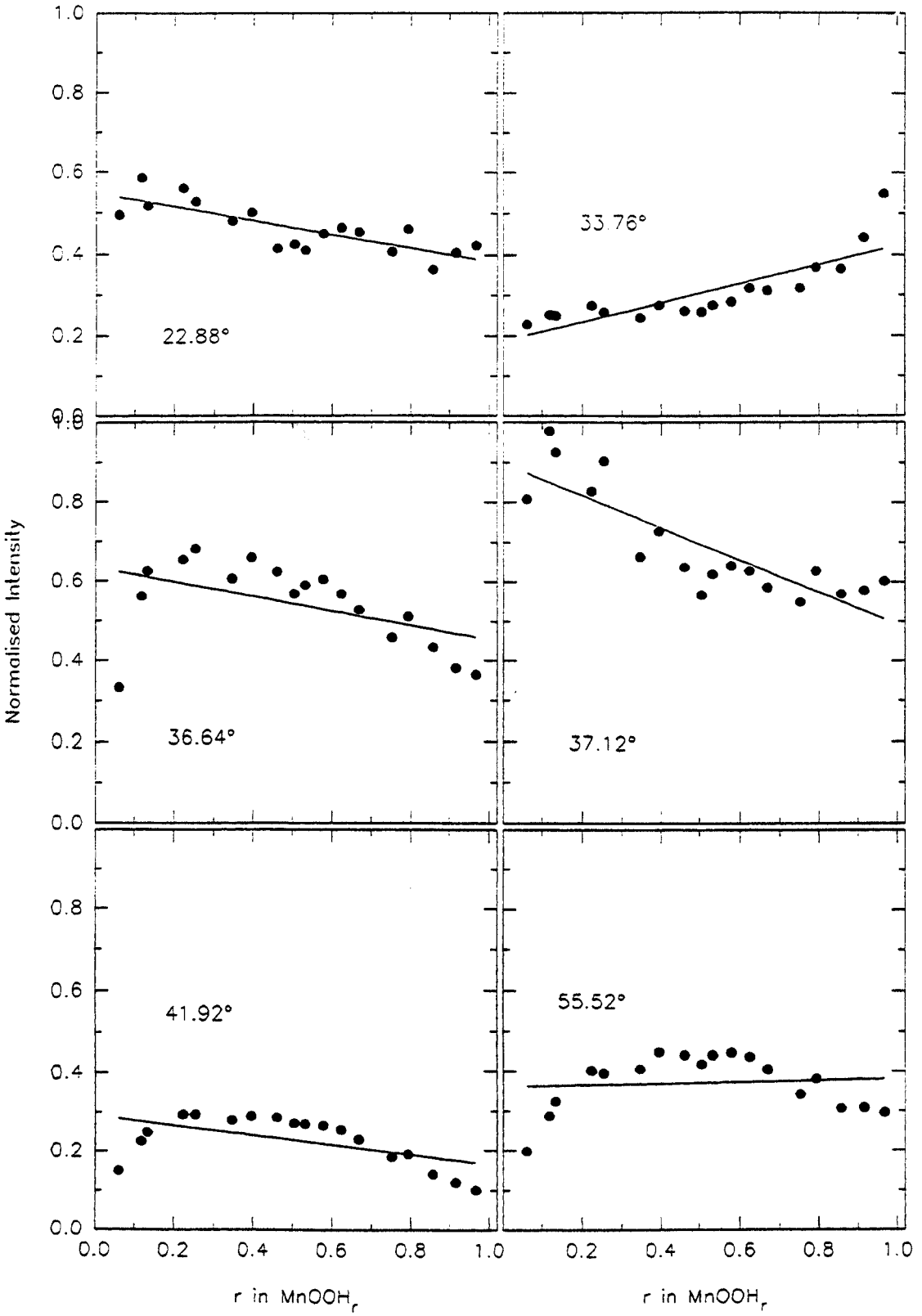


*Figure A24*: Plots of intensity against H insertion level corresponding to the minimum values of $R^2$ given in figure A23 (the value of °2Θ is given in the plot): CMD heat-treated at 300°C; hydrazine hydrate reduction.

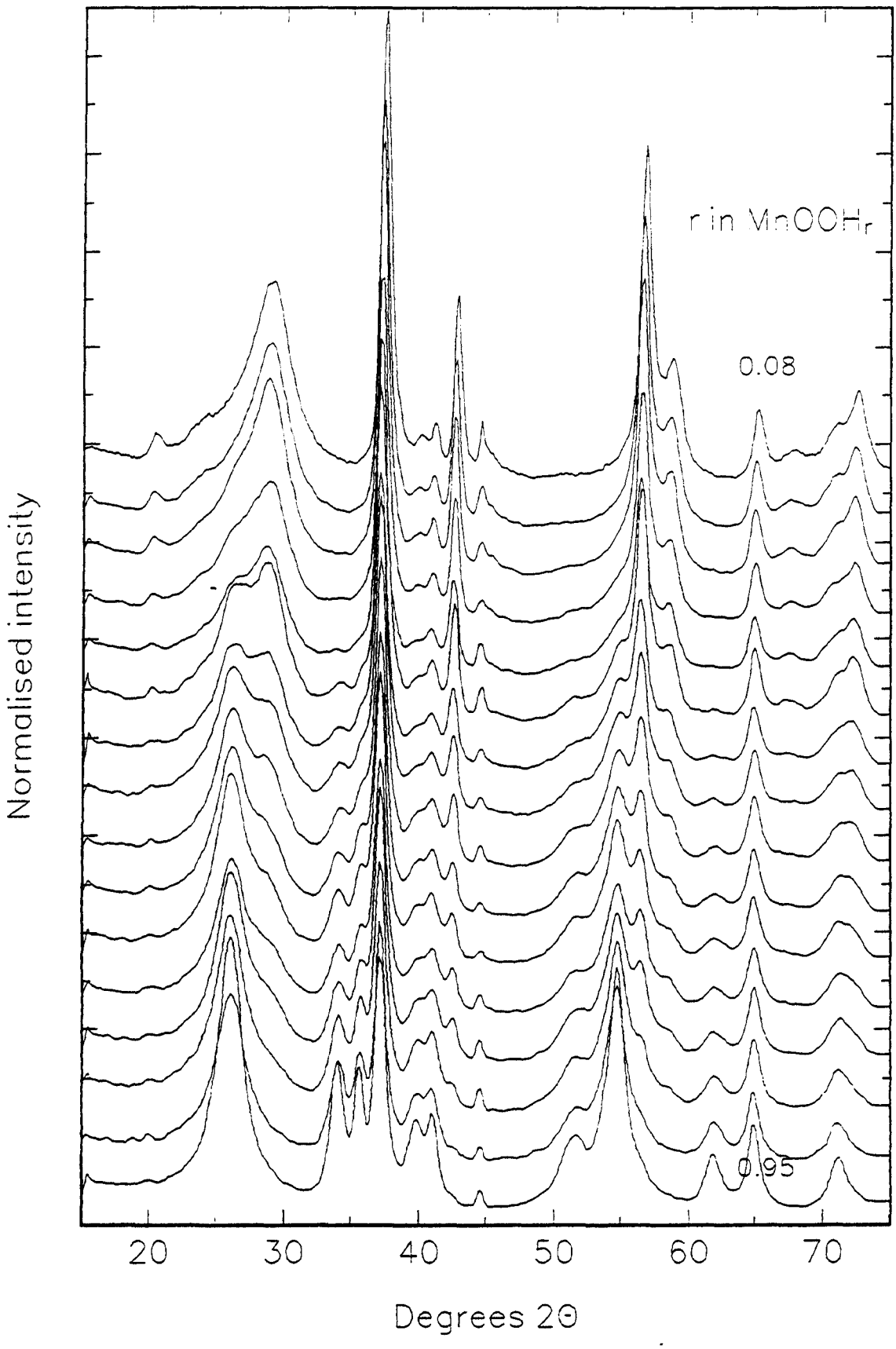


***Figure A25***: Dataset that was used for the linear regression analysis: CMD heat-treated at 400°C; hydrazine hydrate reduction.

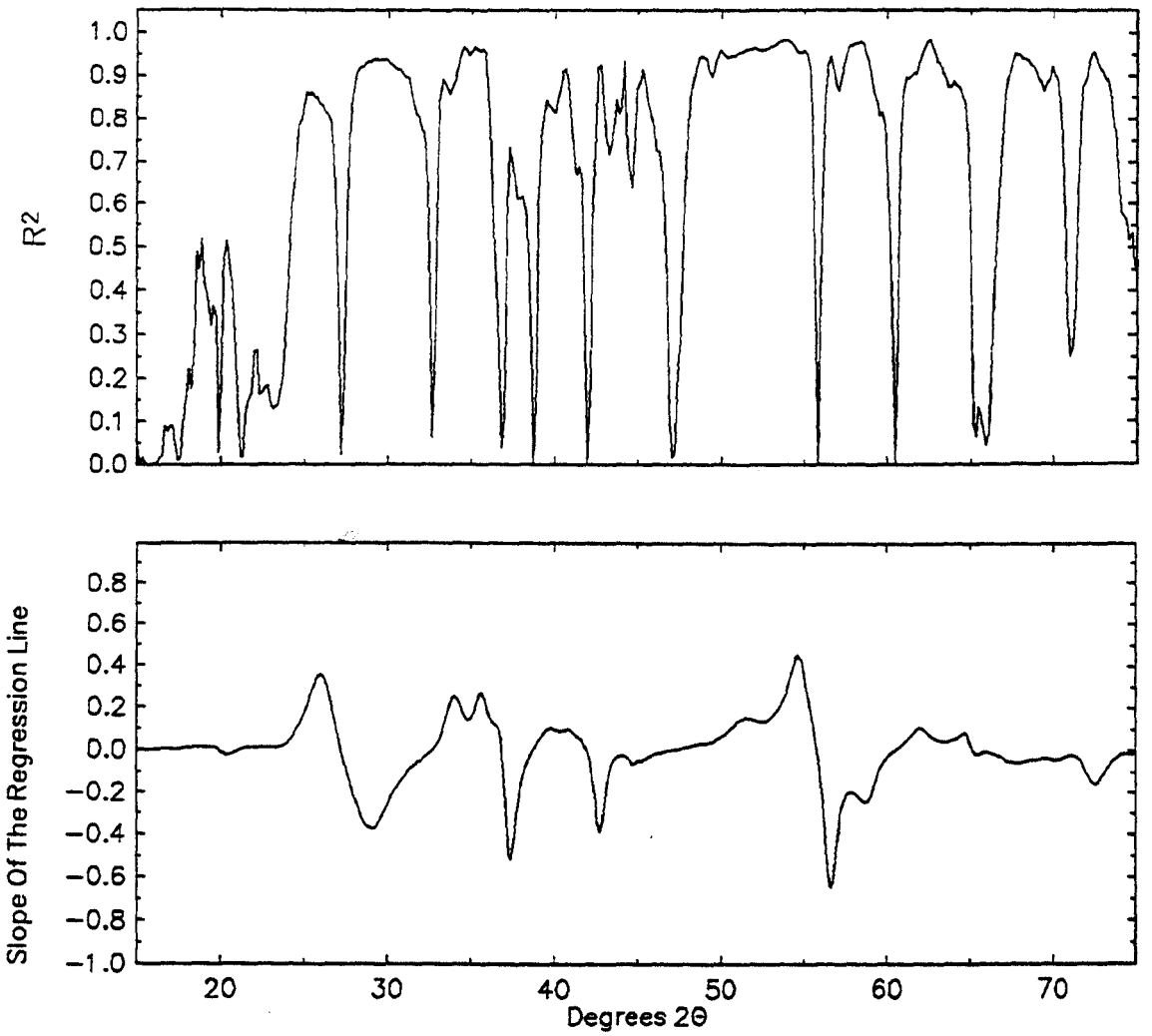


***Figure A26***: Slope of the regression line and $R^2$ against Degrees 2Θ; CMD heat-treated at 400°C; hydrazine hydrate reduction method.

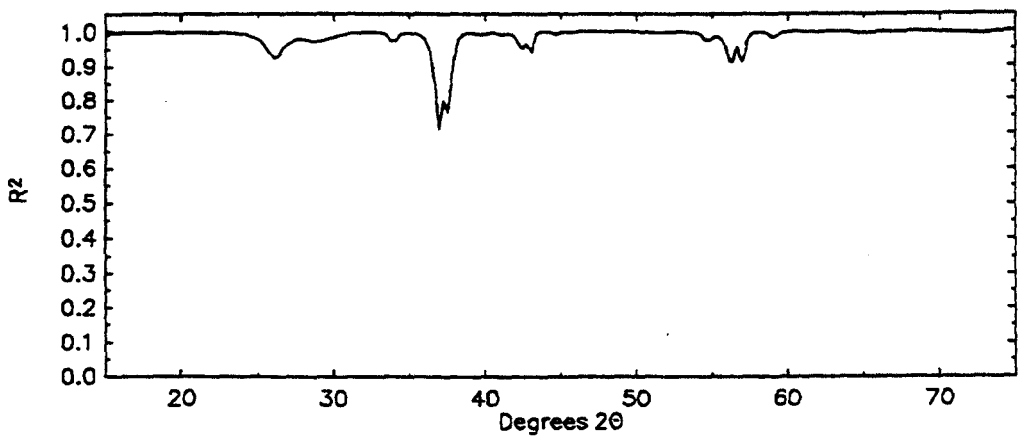


***Figure A27***: $R^2$ against Degrees 2Θ when the data has the same slope; CMD heat-treated at 400°C; hydrazine hydrate reduction method.

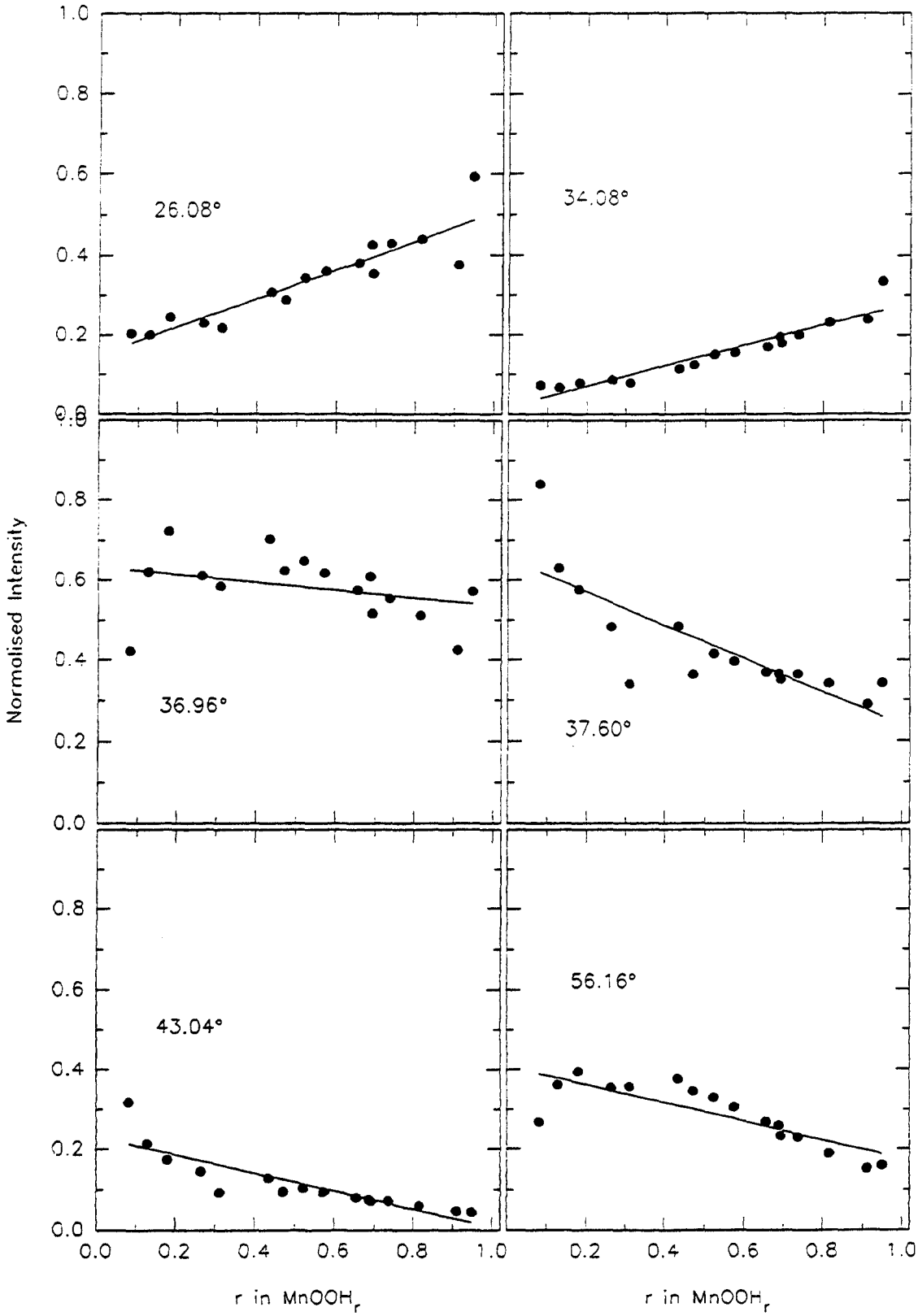


***Figure A28***: Plots of intensity against H insertion level corresponding to the minimum values of $R^2$ given in figure A27 (the value of °2Θ is given in the plot): CMD heat-treated at 400°C; hydrazine hydrate reduction.

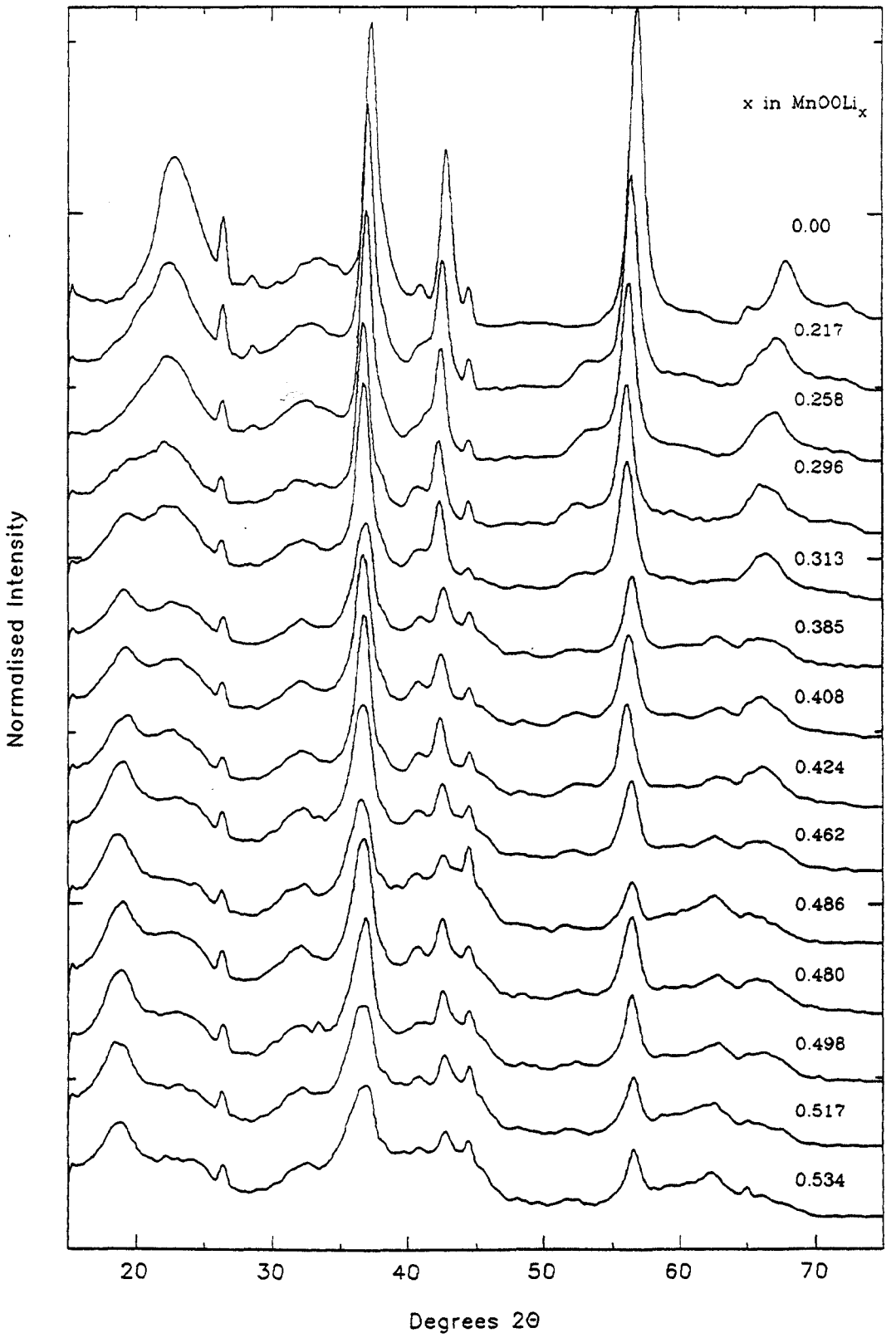


***Figure A29***: Dataset that was used for the linear regression analysis: EMD heat-treated at 200°C; n-butyllithium reduction.

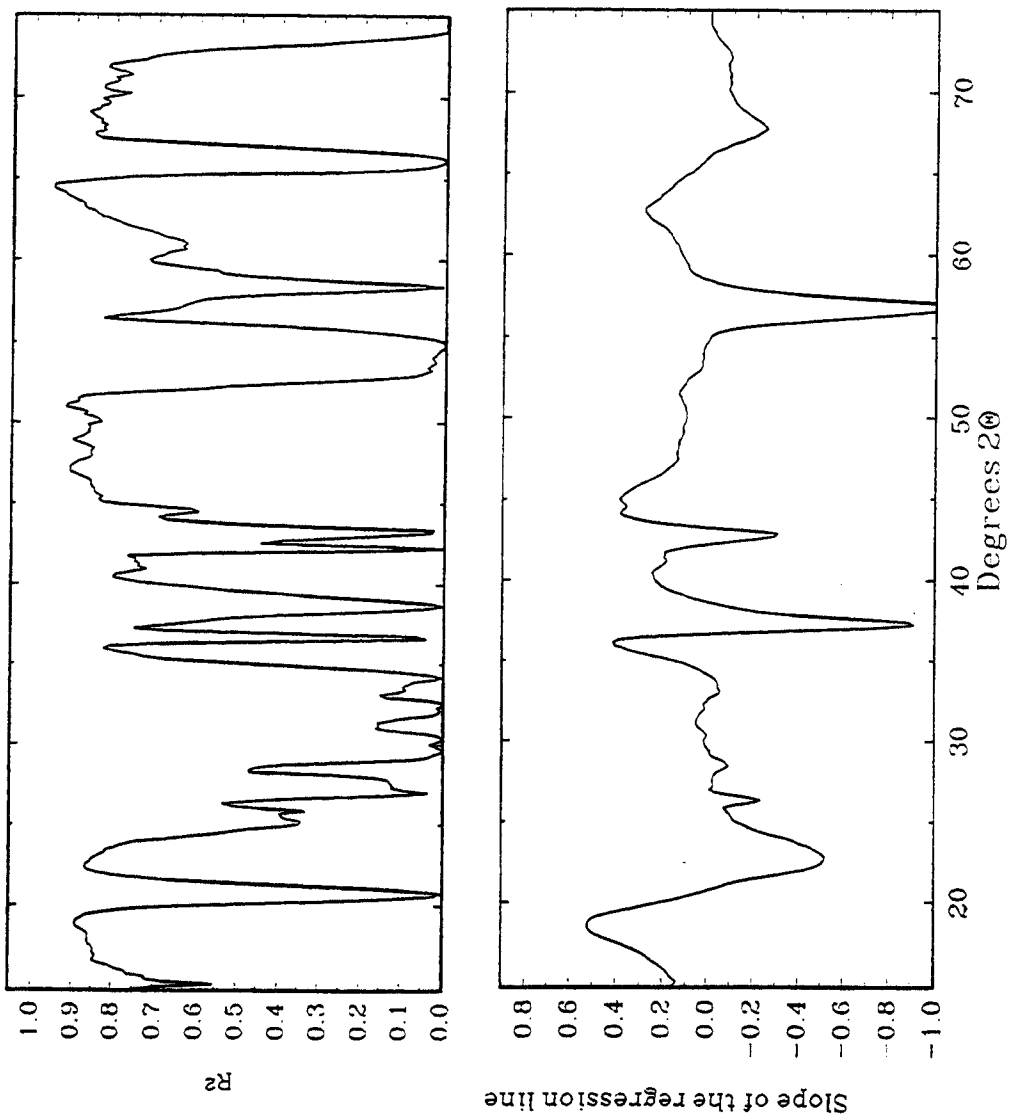


***Figure A30***: Slope of the regression line and $R^2$ against Degrees 2Θ; EMD heat-treated at 200°C; n-butyllithium reduction method.

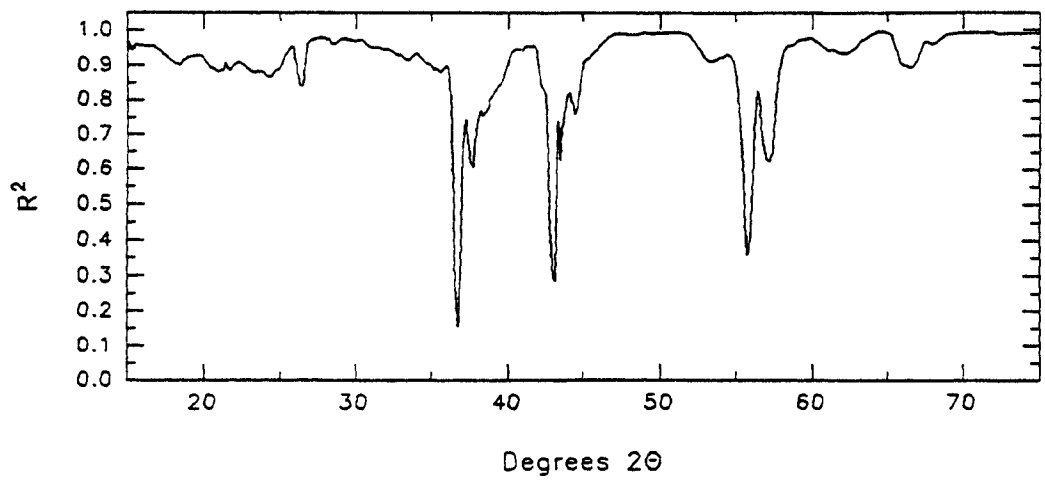


***Figure A31***: $R^2$ against Degrees 2Θ when the data has the same slope; EMD heat-treated at 200°C; n-butyllithium reduction method.

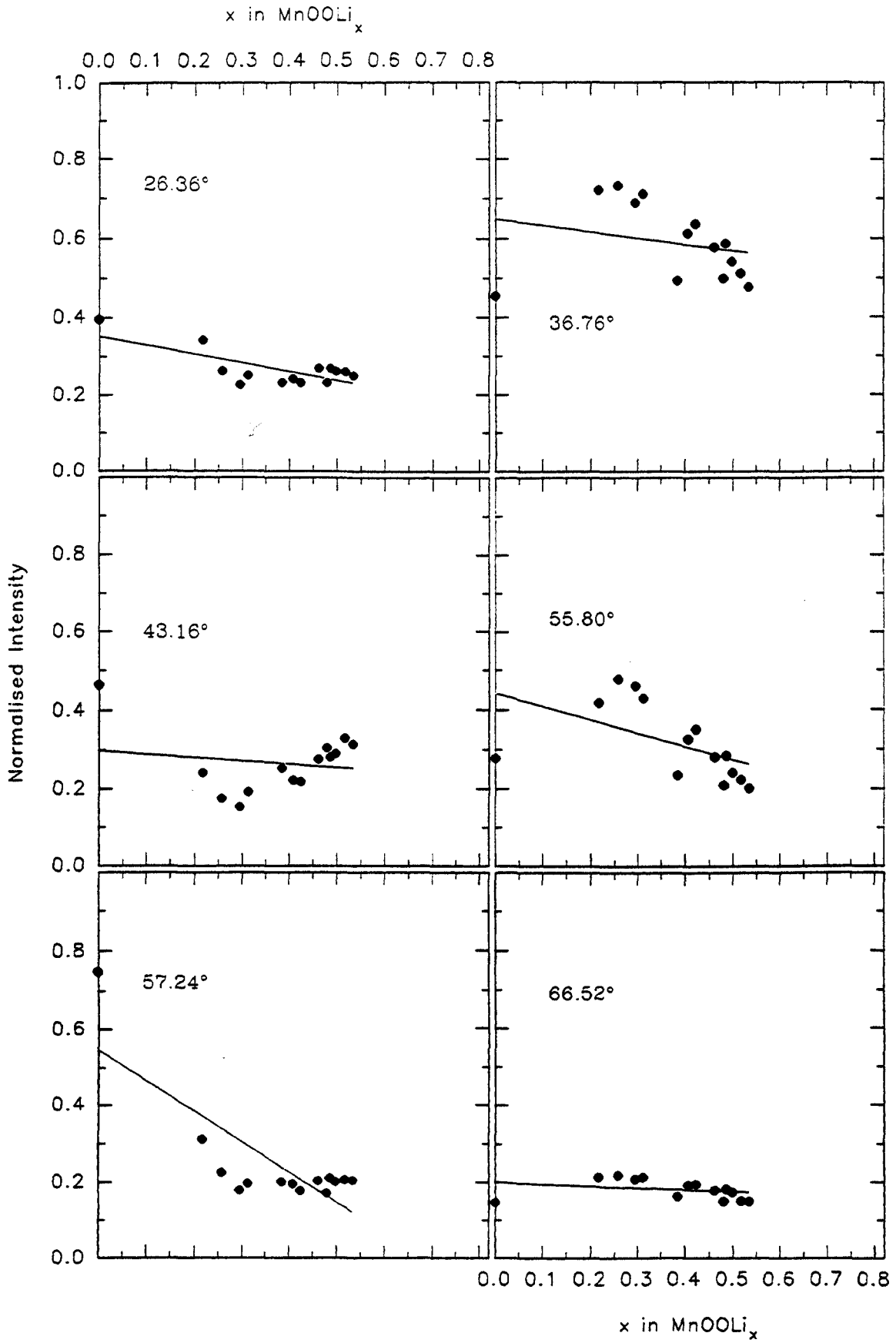


***Figure A32***: Plots of intensity against Li insertion level corresponding to the minimum values of $R^2$ given in figure A31 (the value of °2Θ is given in the plot): EMD heat-treated at 200°C; n-butyllithium reduction.

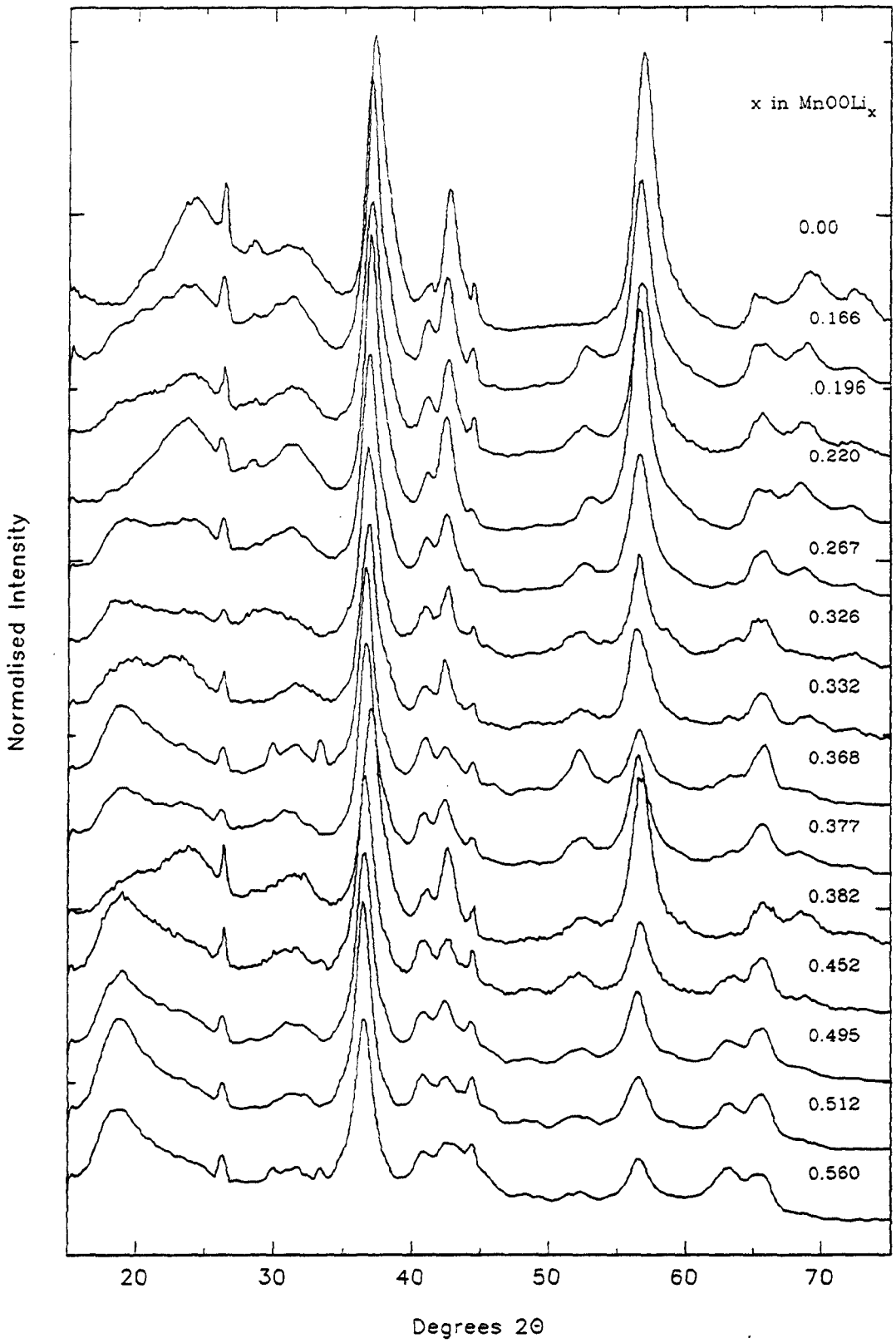


***Figure A33***: Dataset that was used for the linear regression analysis: EMD heat-treated at 300°C; n-butyllithium reduction.

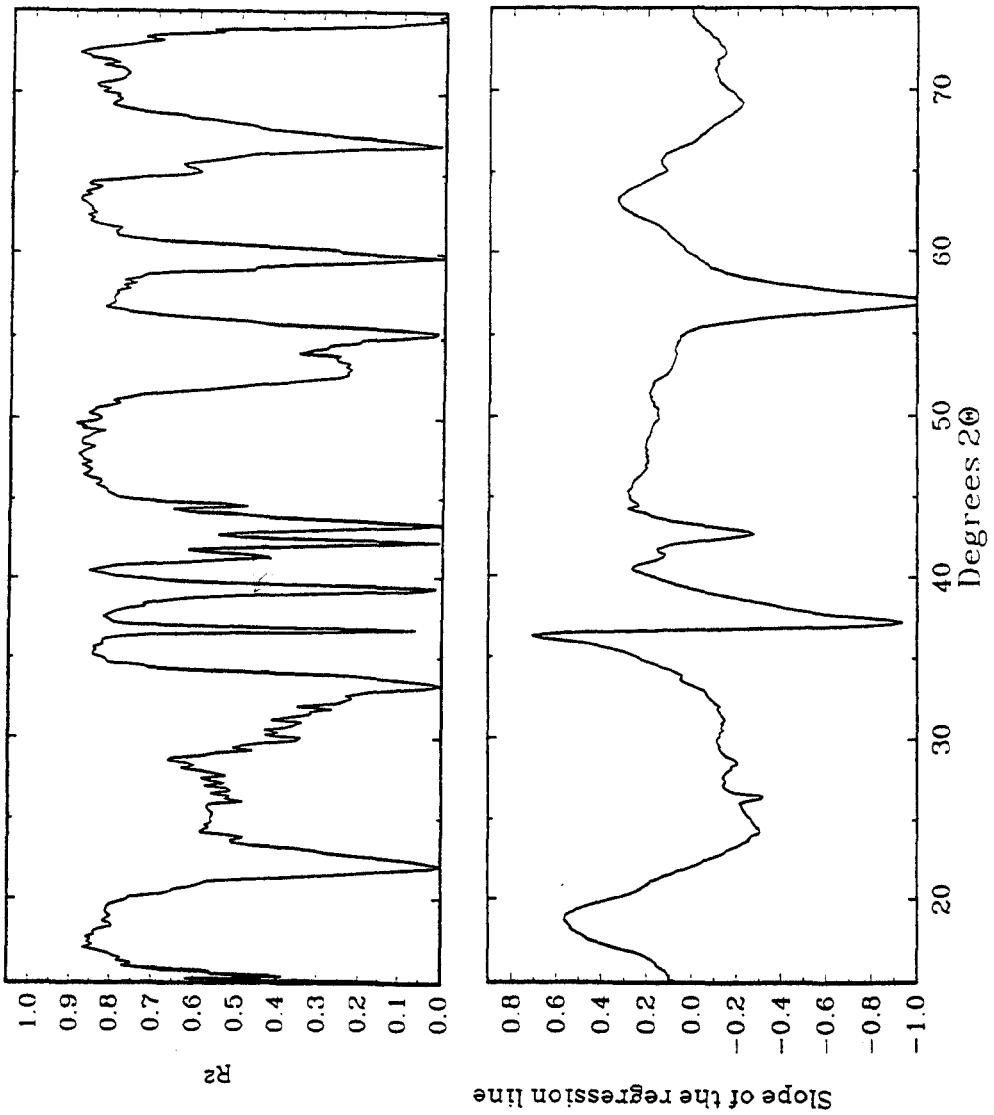


***Figure A34***: Slope of the regression line and $R^2$ against Degrees 2Θ; EMD heat-treated at 300°C; n-butyllithium reduction method.

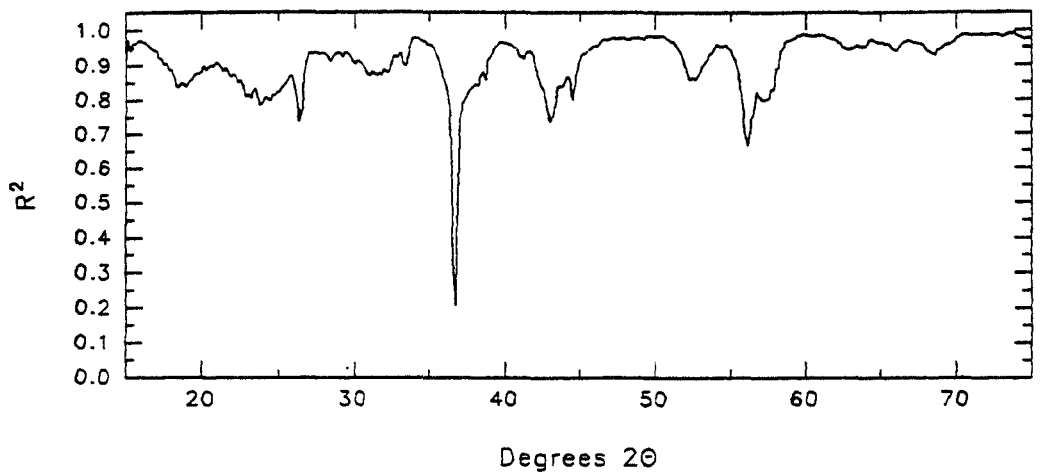


***Figure A35***: $R^2$ against Degrees 2Θ when the data has the same slope; EMD heat-treated at 300°C; n-butyllithium reduction method.

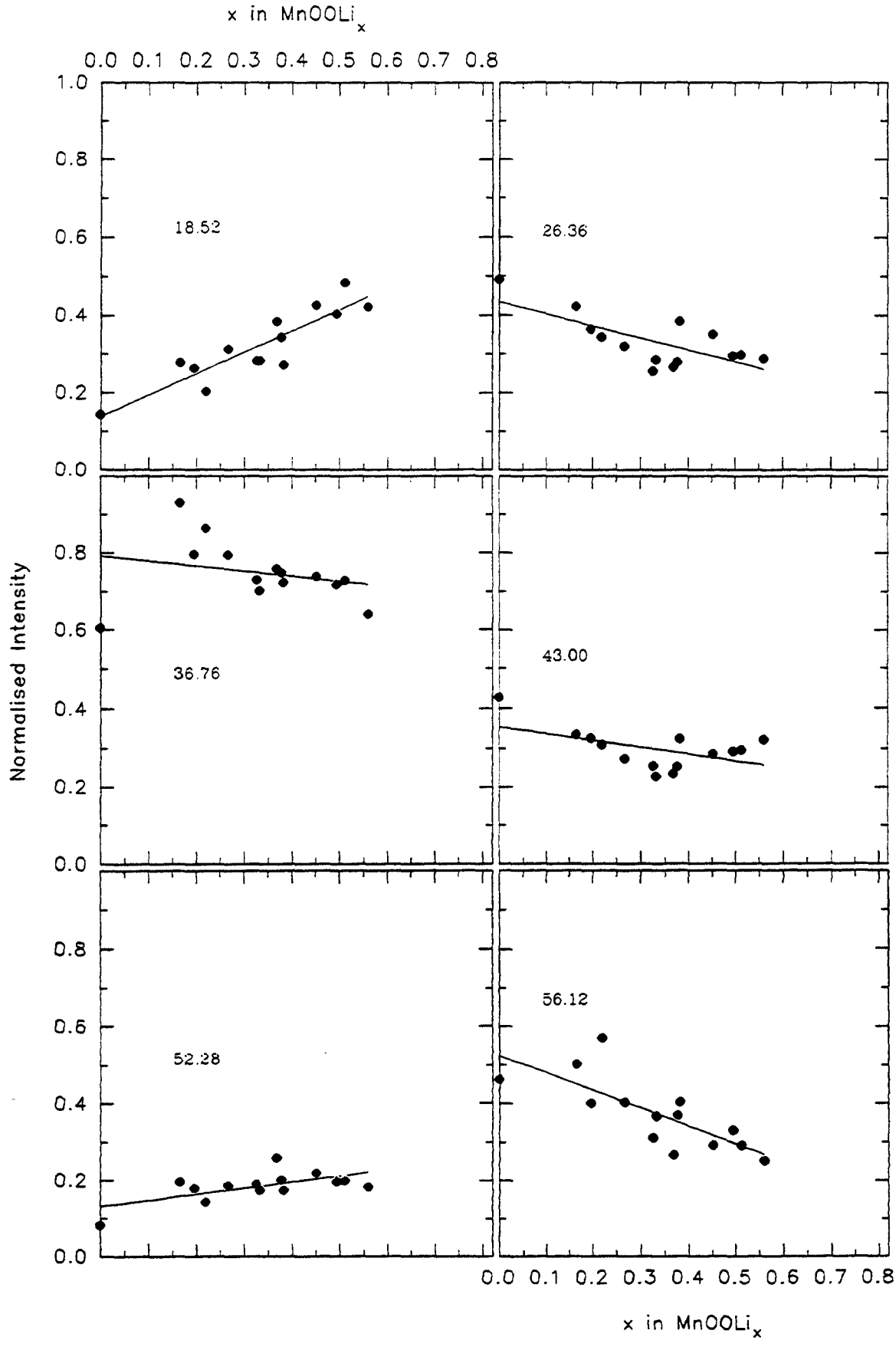


***Figure A36***: Plots of intensity against Li insertion level corresponding to the minimum values of $R^2$ given in figure A35 (the value of °2Θ is given in the plot): EMD heat-treated at 300°C; n-butyllithium reduction.

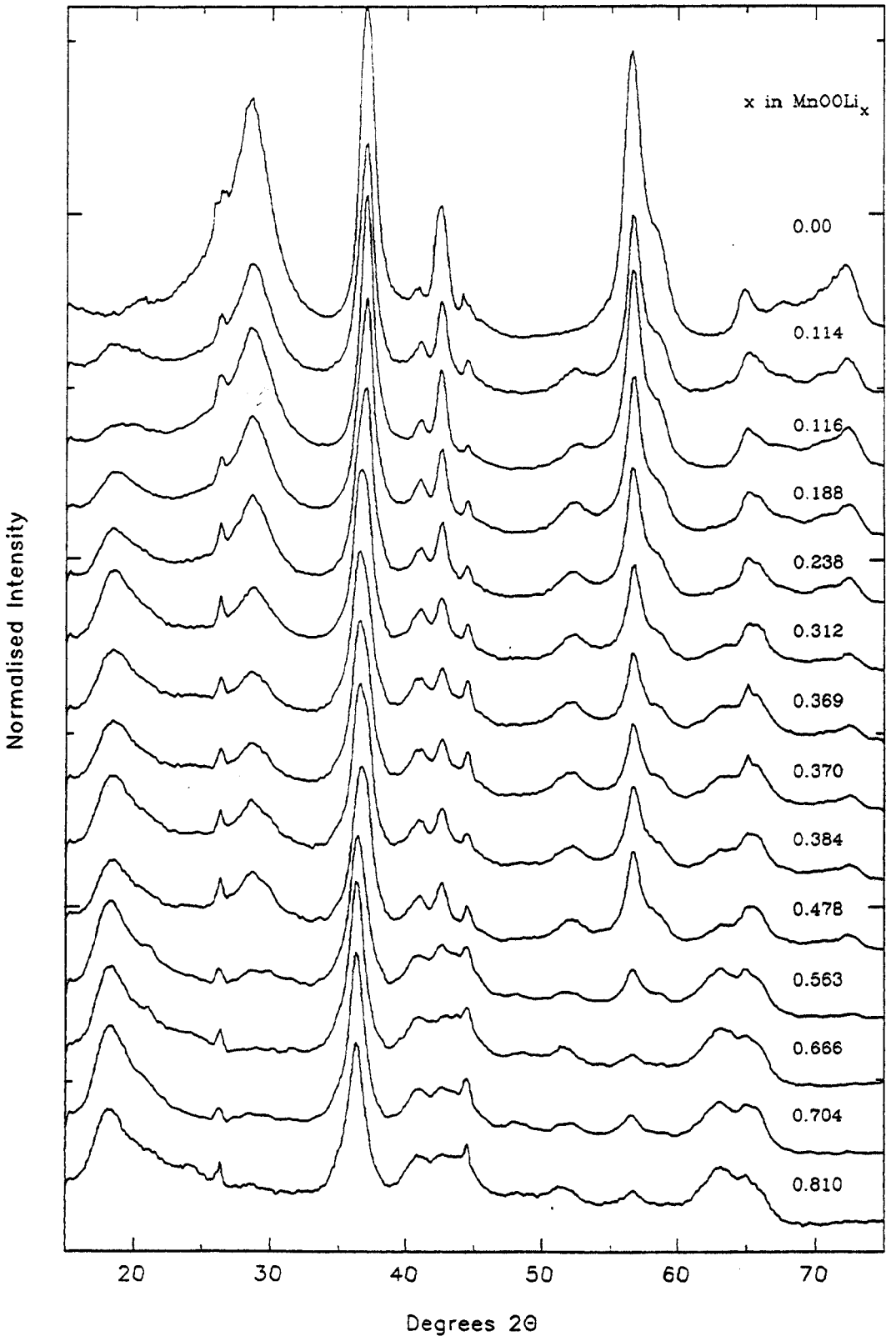


***Figure A37***: Dataset that was used for the linear regression analysis: EMD heat-treated at 400°C; n-butyllithium reduction.

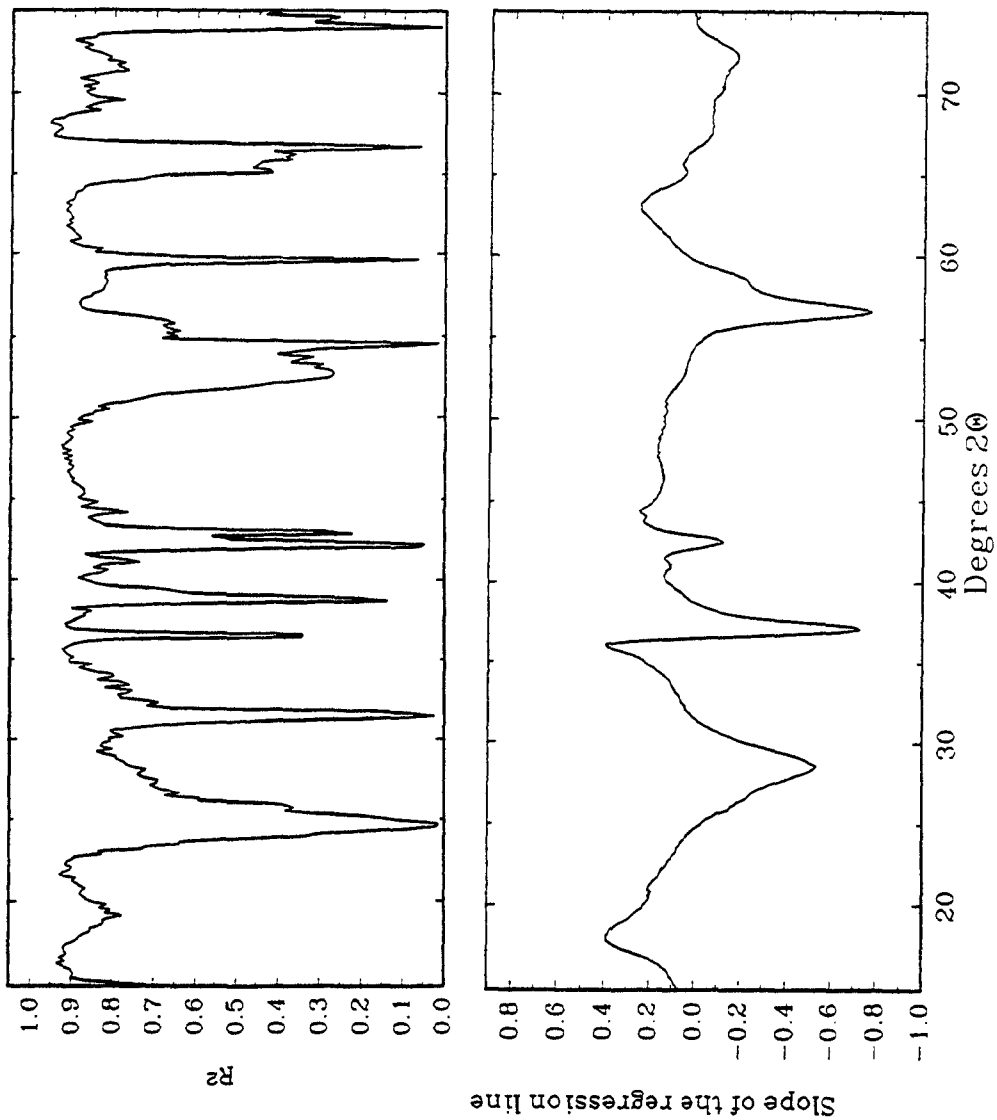


***Figure A38***: Slope of the regression line and $R^2$ against Degrees 2Θ; EMD heat-treated at 400°C; n-butyllithium reduction method.

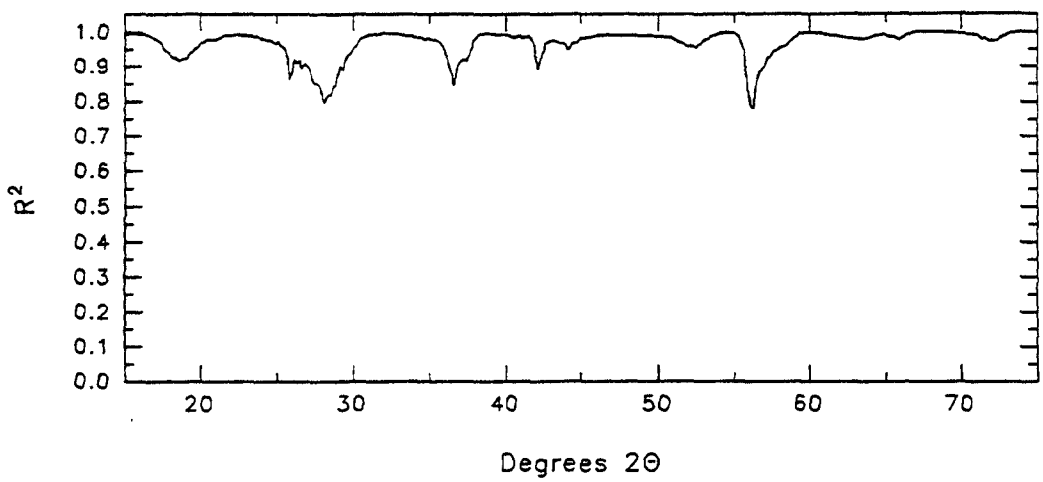


***Figure A39***: $R^2$ against Degrees 2Θ when the data has the same slope; EMD heat-treated at 400°C; n-butyllithium reduction method.

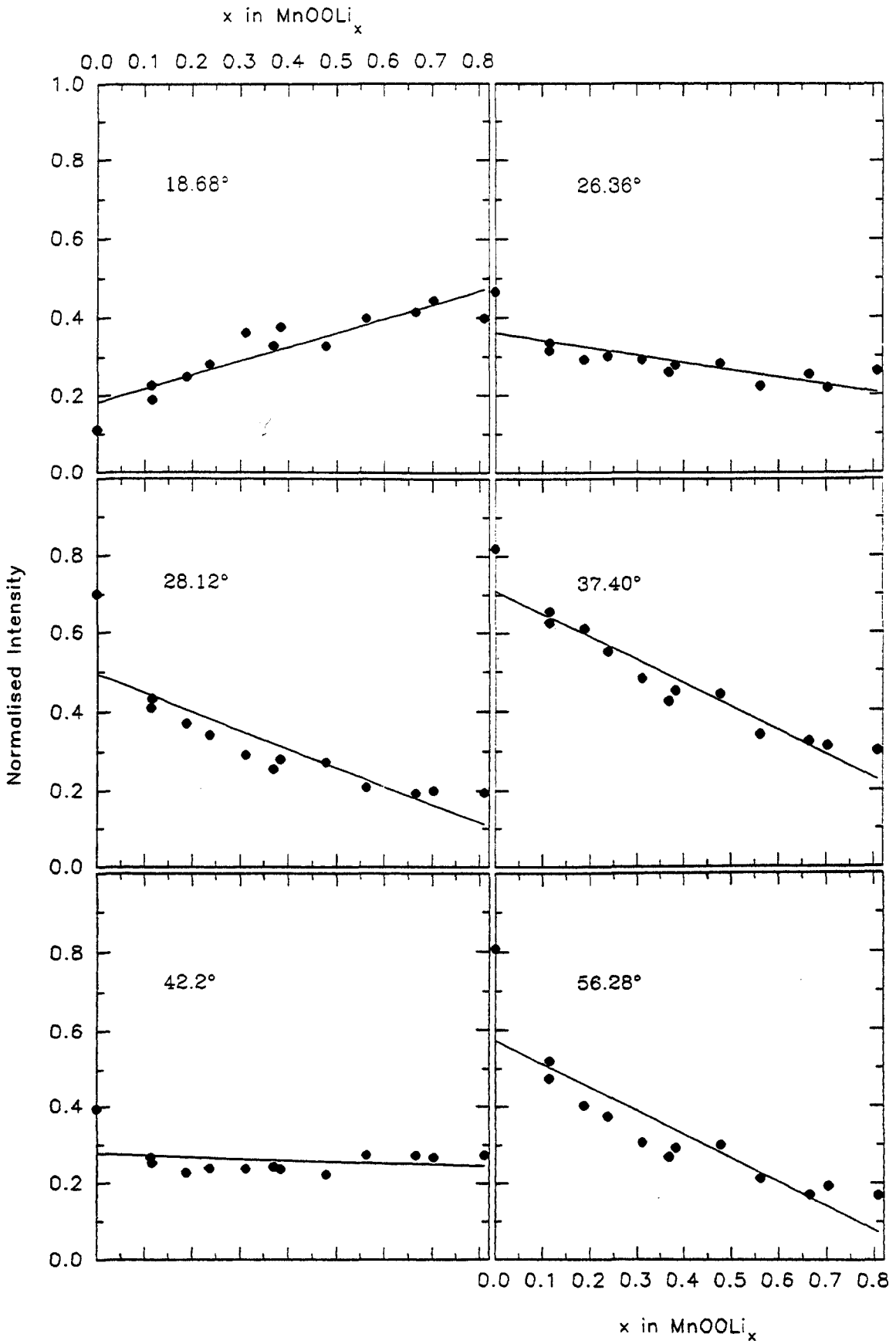


***Figure A40***: Plots of intensity against Li insertion level corresponding to the minimum values of $R^2$ given in figure A39 (the value of °2Θ is given in the plot): EMD heat-treated at 400°C; n-butyllithium reduction.

# Appendix B

Calculation of Tw and $P_r$.

The following table shows the lines that were used for the calculation of Tw and $P_r$ for a non heat-treated sample of Faradiser WSLi.

| °2θ | h | k | l | d/Å |
|---|---|---|---|---|
| 36.8992 | 0 | 2 | 1 | 2.436 |
| 40.2575 | 2 | 0 | 0 | 2.240 |
| 42.2413 | 1 | 2 | 1 | 2.139 |
| 55.7775 | 2 | 2 | 1 | 1.648 |
| 65.3708 | 0 | 0 | 2 | 1.428 |
| 68.6475 | 0 | 6 | 1 | 1.367 |

Using the analysis given in section 3.8 this yields the apparent orthorhombic unit cell parameters a=4.478, b=9.344 and c=2.855Å and b/2c 1.636.

Calculation of the amount of Tw.

From the b/2c ratio and equation 3.9 Tw = 16.36%

From the splitting of 002/061 ($\Delta°2\theta$=3.277) and equation 3.10 Tw = 17.43. This is corrected to 21.79% because the splitting of lines 002/061 is overestimated due to the presence of other lines in the vicinity (see Table 3.2).

Calculation of the amount of de Wolff disorder.

The position of line 110 is 22.264°2θ

The correction of line 110 is calculated from equation 3.11:

$$\delta(Tw) = -0.0054\ Tw - 8.9\ 10^{-5}\ Tw^2 = -0.16°$$

this gives a shift of line 110 due to de Wolff defects:

$$\delta(DW) = 22.3237 + 0.16 - 21.808 = 0.6160°$$

substituting these values into equation 3.12 gives $P_r$ = 0.30. Neglect of microtwinning yields 0.28.

# References

Alday, J. (1993) MPhil Thesis, Middlesex University, London, (unpublished).

Amlie, R.F. and Tvarusko, A. (1964) *J. Electrochem. Soc.* 111 pp496-501.

Armand, M.B. (1973) *Fast Ion Transport in Solids.* (edited by W. Van Gool) North-Holland.

Atlung, S. and West, K. (1989) *J. Power Sources* 26 pp139-159.

Baur, W. H. (1976) *Acta Cryst.* 32 pp2200-2206.

Bode, H., Scheimer, A. and Berndt, D. (1962) *Z. Electrochem.* 66 pp586-593.

Brown, A.J., St Claire Smith, C.R., Tye, F.L. and Whiteman, J.L. (1975) *J. Colloid and Interfac. Sci.* 45 pp516-522.

Brown, A.J., Tye, F.L. and Wood, L.L. (1981) *J. Electroanal. Chem* 122 pp337-346

Buerger, M.J. (1936) *Zeit. Cryst.* 95 pp163-174.

Burns, R.G. and Burns, V.M. (1975) *Manganese Dioxide Symposium Vol. 1.* Cleveland, (edited by A. Kozawa and R.J. Brodd) I.C. Sample Office pp306-327.

Burns, R.G. and Burns, V.M. (1985) *Manganese Dioxide Electrode Theory and Practice for Electrochemical Applications* (edited by B. Schumm, R.L. Middaugh, M.P. Grotheer and J.C. Hunter) The Electrochem. Soc., Pennington, New Jersey pp97-111.

Buseck, P.R., Miner, B. and Turner, S. (1985) *Manganese Dioxide Electrode Theory And Practice for Electrochemical Applications* (edited by B. Schumm, R.L. Middaugh, M.P. Grotheer and J.C. Hunter) The Electrochem. Soc., Pennington, New Jersey pp48-76.

Bystrom, A.M. (1949) *Acta. Chem. Scand.* 3 pp163-173.

Cartier, C., Tranchant, A., Verdaguer, M., Messina, R. and Dexpert, H. (1990) *Electrochim Acta* 35 pp889-898.

Chabre, Y.P. (1991) *J. Electrochem. Soc.* 138 pp329-330.

Chabre, Y. and Pannetier, J. (1995) *Prog. Solid St. Chem.* 23 pp1-130.

Charenton, J.C. and Strobel, P. (1988) *J. Solid State Chem.* 77 pp33-39.

Chatfield, C. (1976) *Statistics For Technology* Chapman and Hall.

Chen, C.J. and Greenblatt, M. (1985) *Mat. Res. Bull.* 20 pp1347-1352.

Cisak, A., Werblan, L. (1993) *High Energy Non-Aqueous Batteries*, Ellis

Horwood pp197-253.

Cox, D.E., Cava, R.J., McWhan, D.B. and Murphy, D.W. (1982) *J. Phys. Chem. Solids.* 43 pp657-666.

Crespi, A.M., Merritt, D.R. and Skarstad, P.M. (1990) *Extended Abstracts of the 175th Meeting of the Electrochemical Society,* Abstract No. 49.

Dahn, J.R., Py, M.A. and Haering, R.R. (1982) *Can. J. Phys* 60 pp307-313.

David, W.I.F., Thackeray, M.M., Bruce, P.G. and Goodenough, J.B. (1984) *Mat. Res. Bull.* 19 pp99-106.

Davidson, I.J. and Greedan, J.E. (1984) *J. Solid State Chem.* 51 pp104-117.

Dent Glasser, L.S. and Ingram, L. (1968) *Acta Cryst.B.* 24 pp1233-1236.

Desai, B., Dhume, R.A.S. and Kamat Dalal, V.N. (1988) *J. Appl. Electrochem* 18 pp62-74.

Desilvestro, J. and Hass, O. (1990) *J. Electrochem. Soc.* 137 pp5C-22C.

de Wolff, P.M. (1959) *Acta. Cryst.* 12 pp341-345.

de Wolff, P.M., Visser, J.W., Giovanoli, R. and Brutsch, R. (1978) *Chimia* 32 pp257-259.

Dickens, P.G., French, S.J., Hight, A.T. and Pye, M.S. (1979) *Mat. Res. Bull.* 14 pp1295-1301.

Dickens, P.G. and Reynolds, G.J. (1981) *Solid State Ionics* 5 pp331-334

Fernandes, J.B., Desai, B. and Kamat Dalal, V.N. (1983) *Electrochim Acta*, 28 pp309-315.

Fillaux, F., Ouboumour, H., Tomkinson, J. and Yu, L.T. (1991) *Chemical Physics* 149 pp459-469.

Fillaux, F., Ouboumour, H., Cachet, C., Tomkinson, J., Kearley, G.J. and Yu, L.T. (1992a) *Chemical Physics* 164 pp311-319.

Fillaux, F., Ouboumour, H., Cachet, C., Tomkinson, J and Yu, L.T. (1992b) *Physica B* 180 & 181 pp680-682.

Fillaux, F., Cachet, C.H., Ouboumour, H., Tomkinson, J., Levy-Clement, C. and Yu, L.T. (1993a) *J. Electochem. Soc.* 140 pp585-591.

Fillaux, F., Ouboumour, H., Cachet, C.H., Tomkinson, J., Levy-Clement, C. and Yu, L.T. (1993b) *J. Electochem. Soc.* 140 pp592-598.

Fitzpatrick, J. and Tye, F.L. (1991) *J. Appl. Electrochem.* 21 pp130-135.

Freeman, D.S., Pelter, P.F., Tye, F.L. and Wood, L.L. (1971) *J. Appl. Electrochem* 1 pp127-136.

Freund, F., Konen, E. and Preisler, E. (1975) *Manganese Dioxide Symposium Vol. 1.* Cleveland, (edited by A. Kozawa and R.J. Brodd) I.C. Sample Office pp328-348.

Gabano, J.P., Morignat, B., Fidales, E., Emery, B. and Laurent, J.F. (1965) *Z. Phys. Chem* 46 pp359-372.

Gabano, J.P., Seguret, J. and Laurent, J.F. (1970) *J. Electochem. Soc.* 117 pp147-151.

Giovanoli, R. and Leuenberger, U. (1969) *Helv. Chim. Acta*. 52 pp2333-2347.

Giovanoli, R. (1980) *Manganese Dioxide Symposium Vol. 2.* Tokyo, (edited by B. Schumm, J.M. Joseph and A. Kozawa) I.C. Sample Office pp113-133.

Goodenough, J.B., Thackeray, M.M., David, W.I.F. and Bruce, P.G. (1984) *Rev. Chim. Min.* 21 pp435-455.

Goodenough, J.B. (1985) *Manganese Dioxide Electrode Theory and Practice for Electrochemical Applications* (edited by B. Schumm, R.L. Middaugh, M.P. Grotheer and J.C. Hunter) The Electrochem. Soc., Pennington, New Jersey pp77-96.

Gruner, J.W. (1947) *American Mineralologist.* 32 pp654-659.

Hague, D.N. (1971) *Fast Reactions* Wiley Interscience.

Holton, D.M., Tye, F.L. (1980) *Manganese Dioxide Symposium Vol. 2.* Tokyo, (edited by B. Schumm, J.M. Joseph and A. Kozawa) I.C. Sample Office pp244-250.

Hughes, M., Hampson, N.A. and Karunathilaka, S.A.G.R. (1984) *J.Power Sources* 12 pp83-144.

Hunter, J.C. (1981) *J. Solid State Chem*. 39 pp142-147.

Hunter, J.C. and Tudron, F.B. (1985) *Manganese Dioxide Electrode Theory and Practice for Electrochemical Applications* (edited by B. Schumm, R.L. Middaugh, M.P. Grotheer and J.C. Hunter) The Electrochem. Soc., Pennington, New Jersey pp444-451.

Ikeda, H., Saito, T. and Tamura, H. (1975) *Manganese Dioxide Symposium Vol. 1.* Cleveland, (edited by A. Kozawa and R.J. Brodd) I.C. Sample Office pp384-401.

Ikeda, H., Narukawa, S. and Suenaga, S. (1980) *Manganese Dioxide Symposium Vol. 2.* Tokyo, (edited by B. Schumm, J.M. Joseph and A. Kozawa) I.C. Sample Office pp414-430.

Ilchev, N., Manev, V. and Hampartzumian, K. (1989a) *J.Power Sources* 25 pp177-185.

Ilchev, N. (1989b) *J. Power Sources* 27 pp261-269.

Jacobsen, A.J. (1981) *Solid State Ionics* 5 pp65-70.

Jaffe, H. W. (1988) *Introduction to Crystal Chemistry*, Cambridge University Press p51.

Klingsberg, C. and Roy, R. (1959) *Am. Mineralologist.* 44 pp819-838.

Klug, H.P. and Alexander, L.E. (1974) *X-Ray Diffraction Procedures For Polycrystalline And Amorphous Materials.* John Wiley & Sons.

Kozawa, A. and Sasaki, K. (1954) *J. Electrochem. Soc. Japan* 25 E57-62.

Kozawa, A. and Vosburgh, W.C. (1958) *J. Electochem. Soc.* 105 pp59-63.

Kozawa, A. and Powers, R.A. (1967) *Electrochem Tech.* 5 pp535-542.

Kozawa, A. (1985) *Manganese Dioxide Electrode Theory and Practice for Electrochemical Applications* (edited by B. Schumm, R.L. Middaugh, M.P. Grotheer and J.C. Hunter) The Electrochem. Soc., Pennington, New Jersey pp384-390.

Kozawa, A. (1989) *Progress In Batteries And Solar Cells* 8 pp25-27.

Laig-Horstebrock, H. (1990) *Electrochim. Acta* 35 pp1889-1895.

Larcin, J. (1991) PhD Thesis, Middlesex University, London.

Laudy, J.H.A. and de Wolff, P.M. (1963) *Appl. Sci. Res. Sect. B.* 10 pp157-168.

Lee, J.A., Newnham, C.E. and Tye, F.L. (1973a) *J. Colloid Interface Sci.* 42 pp372-380.

Lee, J.A., Newnham, C.E., Stone, F.S. and Tye, F.L. (1973b) *J. Colloid Interface* Sci. 45 pp289-294.

Lee, J.A., Newnham, C.E., Stone, F.S. and Tye, F.L. (1978) *J. Chem. Soc. Faraday Trans. I* 74 pp237-248.

Levy-Clement, C., Godart, C., Mondoloni, C. and Cortes, R. (1992) *Solid State Ionics* (edited by M. Balkanski T. Takahashi and H.L. Tuller), Elsevier Science Publishers pp153-158.

Li, J-B., Koumoto, K. and Yanagida, H. (1988) *J. Mater. Sci.* 23 pp2595-2600.

Lingane, J.J. and Karplus, R. (1946) *Ind. Eng. Chem. Anal. Ed.* 18 pp191-194.

Lybanon, M. (1984) *Am. J. Phys.* 52 pp22-26.

MacLean, L.A.H. (1993) PhD Thesis, Middlesex University, London.

MacLean, L.A.H., Poinsignon, C., Amarilla, J.M., Le Cras, F. and Strobel, P. (1995a) *J. Mater. Chem.* 5 pp1183-1189.

MacLean, L.A.H. and Tye, F. L. (1995b) submitted to *J. Solid State Chem.*

Malpas, D.G. and Tye, F.L. (1989) *Handbook Of Manganese Dioxides Battery Grade*, (edited by D. Glover B.Schumm and A. Kozawa), International Battery Material Association, Brunswick, Ohio, USA pp177-209.

Manev, V., Ilchev, N. and Nassalevska, A. (1989) *J. Power Sources* 25 pp167-175.

Maskell, W.C. (1976) PhD Thesis, University College London.

Maskell, W.C., Shaw, J.E.A. and Tye, F.L. (1981) *Electrochim. Acta*. 26 pp1403-1410.

Maskell, W.C., Shaw, J.E.A. and Tye, F.L. (1982) *J. Appl. Electochem*. 12 pp101-108.

Maskell, W.C., Shaw, J.E.A. and Tye, F.L. (1982a) *J. Appl. Electochem*. 12 pp101-108.

Maskell, W.C., Shaw, J.E.A. and Tye, F.L. (1982b) *J. Power Sources* 8 pp113-120.

Maskell, W.C., Shaw, J.E.A. and Tye, F.L. (1982c) *Electrochim. Acta* 27 pp425-428.

Maskell, W.C., Shaw, J.E.A. and Tye, F.L. (1983a) *Electrochim. Acta* 28 pp225-230.

Maskell, W.C., Shaw, J.E.A. and Tye, F.L. (1983b) *Electrochim. Acta* 28 pp231-235.

Miyazaki, K. (1975) *Manganese Dioxide Symposium Vol. 1.* Cleveland, (edited by A. Kozawa and R.J. Brodd) I.C. Sample Office pp111-131.

Mosbah, A., Verbaere, A. and Tournoux, M. (1983) *Mat. Res. Bull* 18 pp1375-1381.

Murphy, D.W., DiSalvo, F.J., Carides, J.N. and Waszczak, J.V. (1978) *Mat. Res. Bull.* 13 pp1395-1402.

Murphy, D.W. (1980) *Lithium Nonaqueous Battery Electrochemistry* (edited by E.B. Yeager, B. Schumm, G.E. Blomgren, V.Z. Leger, D.R. Blankenship and J. Akridge), The Electrochem. Soc. pp197-205.

Murphy, D.W., Cava, R.J., Zahurak, S.M. and Santoro, A. (1983) *Solid State*

*Ionics* 9-10 pp413-418.

Murphy, D.W. (1986) *Solid State Ionics* 18-19 pp847-851.

Murray, J.J., Sleigh, A.K. and McKinnon, W.R. (1991) *Electrochim. Acta* 36 pp489-498.

Naraukawa, S. and Furukawa, N. (1991) *Modern Battery Technology* (edited by Clive D.S. Tuck), Ellis Horwood pp348-365.

Nardi, J.C. (1985a) *J. Electrochem. Soc.* 132 pp1787-1791.

Nardi, J.C. (1985b) *Manganese Dioxide Electrode Theory And Practice For Electrochemical Applications* (edited by B. Schumm, R.L. Middaugh, M.P. Grotheer and J.C. Hunter), The Electrochem. Soc., Pennington, New Jersey pp419-443.

Nohma, T., Yoshimura, S., Nishio, K. and Saito, T. (1994) *Lithium Batteries, New Materials, developments and perspectives* (edited by G. Pistoia), Elsevier pp417-456.

Ohzuku, T., Kodama, T. and Hirai, T. (1985a) *J. Power Sources* 14 pp153-165.

Ohzuku, T. and Hirai, T. (1985b) *Manganese Dioxide Electrode Theory And Practice for Electrochemical Applications* (edited by B Schumm, R.L.Middaugh, M.P. Grotheer and J.C. Hunter), The Electrochem. Soc.,Pennington, New Jersey pp141-157.

Ohzuku, T. and Hirai, T. (1988) *Progress In Batteries And Solar Cells* 7 pp31-36.

Ohzuku, T., Kitagawa, M. and Hirai, T. (1989) *J. Electrochem. Soc.* 136 pp3169-3174.

Ohzuku, T., Kitagawa, M. and Hirai, T. (1990a) *J. Electrochem. Soc.* 138 pp40-46.

Ohzuku, T., Kitagawa, M. and Hirai, T. (1990b) *J. Electrochem. Soc.* 138 pp769-775.

Ohzuku, T., Kato, J., Sawai, K. and Hirai, T. (1991) *J. Electrochem. Soc.* 138 pp2556-2560.

Pannetier, J., Chabre, Y. and Poinsignon, C. (1990) *ISSI Lett.* 1 pp5-7.

Pannetier, J. (1992) *Progress In Batteries And Battery Materials* 11 pp51-55.

Parida, K.M. and Kanungo, S.B. (1983) *Themochim. Acta* 66 pp275-287.

Pearson, K (1901) *Phil. Mag* 2 pp559-572.

Pistoia, G. (1982) *J. Electrochem. Soc.* 120 pp1861-1865.

Pistoia, G. (1983) *J. Power Sources* 9 pp307-320.

Preisler, E. (1976) *J. Appl. Electrochem.* 6 pp311-320.

Preisler, E. (1980) *Manganese Dioxide Symposium Vol. 2.* Tokyo, (edited by B. Schumm, J.M.Joseph and A. Kozawa) I.C. Sample Office pp184-206.

Preisler, E. (1989a) *J. Appl. Electrochem.* 19 pp540-546.

Preisler, E. (1989b) *J. Appl. Electrochem.* 19 pp559-565.

Potter, R.M. and Rossman, G.R. (1979) *Amer. Mineral.* 64 pp1199-1218.

Ravdel, B.A., Pozin, M.Y., Tikhonov, K.I. and Rotinyan, A.L. (1988) *Soviet Electrochemistry* 23 pp1369-1374.

Reed, C. B. (1989) *Am. J. Phys.* 57 pp642-646.

Ripert, M., Pannetier, J., Chabre, Y. and Poinsignon, C. (1991) *Mat.Res.Soc.Symp.Proc.* 210 pp359-365.

Rossouw, M.H., de Kock, A., de Picciotto, L.A. and Thackeray, M.M. (1990) *Mat.Res.Bull.* 25 pp173-182.

Rossouw, M.H. and Thackeray, M.M. (1991) *Mat. Res Bull.* 26 pp463-473.

Ruetschi, P. (1984) *J. Electrochem. Soc.* 131 pp2737-2744.

Ruetschi, P. (1988a) *J. Electrochem. Soc.* 135 pp2657-2663.

Ruetschi, P. and Giovanoli, R. (1988b) *J. Electrochem. Soc.* 135 pp2663-2669.

Shimzu, K. and Koshiba, J. (1985) *Manganese Dioxide Electrode Theory and Practice for Electrochemical Applications*, (edited by B.schumm, R.L. Middaugh, M.P. Grotheer and J.C. Hunter), The Electrochem. Soc., Pennington, New Jersey pp391-402.

Sleigh, A.K. and McKinnon, W.R. (1990) *Electrochim. Acta* 35 pp1849-1854.

Sleigh, A.K., Murray, J.J. and McKinnon, W.R. (1991) *Electrochim. Acta* 36 pp1469-1474.

Swinkels, D.A.J., Anthony, K.E., Fredericks, P.M. and Osborn, P.R. (1984) *J. Electroanal. Chem.* 168 pp430-450.

Swinkels, D.A.J. (1989) *Handbook Of Manganese Dioxides Battery Grade*, (edited by D. Glover B.Schumm and A. Kozawa), International Battery Material Association, Brunswick, Ohio, USA pp249-258.

Tarascon, J.M., Wang, E., Shokoohi, F.K., McKinnon, W.R. and Colson, S. (1991) *J. Electrochem. Soc.* 138 pp2859-2864.

Tarascon, J.M. and Guyomard, D. (1993a) *Electrochim. Acta.* 38 pp1221-

1231.

Tarascon, J.M. and Guyomard, D. and Baker, G. L. (1993b) *J. Power Sources* 43-44 pp689-690.

Tarascon, J.M., Coowar, F., Amatuci, G., Shookoohi, F.K. and Guyomard, D.G. (1995) *J. Power Sources* 54 pp103-108.

Tarte, P., Liegeois-Duyckaerts, M., Cahay, R. and Winand, J.M. (1990) *Solid State Ionics* 42 pp177-196.

Tedjar,F. and Guitton, J. (1991) *Thermochim. Acta*. pp13-22.

Thackeray, M.M., David, W.I.F., Bruce, P.G. and Goodenough, J.B. (1983) *Mat. Res. Bull.* 18 pp461-472.

Thackeray, M.M., Johnson, P.J., de Picciotto, L.A., Bruce, P.G. and Goodenough, J.B. (1984) *Mat. Res. Bull* 19 pp179-187.

Thackeray, M.M., de Picciotto, L.A., de Kock, A., Johnson, P.J., Nicholas, V.A. and Adenorff, K.T. (1987) *J. Power Sources*.21 pp1-8.

Thackeray, M.M., de Kock, A., Rossouw, M.H., Liles, D., Bittihn, R. and Hoge, D. (1992a) *J. Electrochem. Soc*. 139 pp363-366.

Thackeray, M.M. (1992b) *Progress In Batteries And Battery Materials* 11 pp150-157.

Thackeray, M.M., Rossouw, M.H., Gummow, R.J., Liles, D.C., Pearce, K., De Kock, A., David, W.I.F. and Hull, S. (1993a) *Electrochim. Acta.* 38 pp1259-1267.

Thackeray, M.M., Rossouw, M.H., de Kock, A., de la Harpe, A.P., Gummow, R.J., Pearce, K. and Liles, D.C. (1993b) *J. Power Sources*.43-44 pp289-300.

Tinsley, D.M. and Sharp, J.H. (1971) *J. Therm. Anal.* 3 pp43-48.

Treacy, M.M.J., Newsam, J.M. and Deam, M.W. (1991) *Proc. Royal Soc. London*, A433 pp499-507.

Tvarusko, A. (1964) *J. Electrochem. Soc.* 111 pp125-131.

Tye, F.L. (1980) *Electrochemical Power Sources,* (edited by M. Barak), Peter Peregrinus Ltd pp50-150.

Tye, F.L. (1985a) *Manganese Dioxide Electrode Theory and Practice for Electrochemical Applications*, (edited by B.schumm, R.L. Middaugh, M.P. Grotheer and J.C. Hunter), The Electrochem. Soc., Pennington, New Jersey pp301-341.

Tye, F.L. (1985b) *Electrochim. Acta.* 30 pp17-23.

Tye, F.L. (1991) Private Communication.

Tye, F.L. (1992) *Progress In Batteries And Battery Materials* 11 pp1-15.

Vetter, K.J. (1963) *J. Electrochem. Soc.* 110 pp597-605.

Vetter, K.J. and Jaeger, N. (1966) *Electrochim. Acta.* 11 pp401-419.

Voinov, M. (1981) *Electrochim. Acta.* 26 pp1373-1376.

Vondrak, J., Jakubec, I. and Bludska (1985) *J. Power Sources* 14 pp141-147.

Wakefield, B.J. (1988) *Organolithium Methods* Academic Press Ltd.

Weisberg, S. (1980) *Applied Linear Regression* John Wiley and Sons

West, K., Zachau-Christiansen, B. and Jacobsen, T. (1983) *Electrochim. Acta.* 12 pp1829-1833.

West, K., Zachau-Christiansen, B. and Jacobsen, T. (1985) *J. Power Sources* 14 pp235-245.

White, W.B. and Roy, R. (1964) *Amer. Mineral.* 49 pp1670-1687.

Whittingham, M.S. and Dines, M.B. (1977) *J. Electrochem. Soc.* 124 pp1387-1388.

Whittingham, M.S. *Prog. Solid State Chem* (1978) 12 pp41-99

Xia, Xi., Hong, Li. and Chen, Z-H. (1989) *J. Electrochem. Soc* 136 pp266-271.

Yoffe, A.D. (1983) *Solid State Ionics* 9-10 pp59-70.

York, D. (1966) *Can J. Phys.* 44 pp1079-1086.

Yoshimori, T., Kato, M., Nippashi, K. and Murayama, J. (1980) *Manganese Dioxide Symposium Vol. 2.* Tokyo, (edited by B. Schumm, J.M. Joseph and A. Kozawa) I.C. Sample Office pp369-383.

Zachau-Christiansen, B., West, K.,Jacobsen, T. and Atlung, S. (1988) *Solid State Ionics* 28-30 pp1176-1182.

Zachau-Christiansen, B., West, K.,Jacobsen, T. and Skaarup, S. (1994) *Solid State Ionics* 70-71 pp401-406.2